The development of quantitative live cell imaging techniques and their applications in the study of inter-cellular communication and sarcoma cell motility

James Edward Monypenny

University College London

And

Cancer Research UK

Principal supervisor: Dr Daniel Zicha

Second supervisor: Dr Anne Ridley

A thesis submitted in partial fulfilment of the requirements of the degree of Doctor of Philosophy, University of London.

June 2003

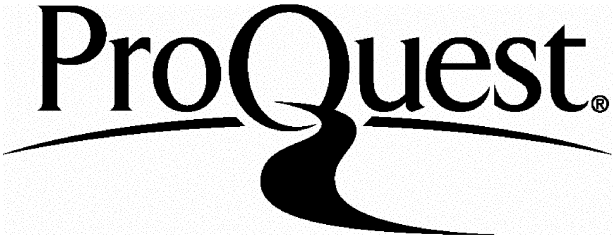

ABSTRACT

The aim of the project was to develop and apply quantitative light microscopy and image analysis techniques to the study of two essential aspects of cell behaviour: *gap junction-mediated intercellular communication* and *cell motility and chemotaxis*.

Gap junction-mediated intercellular communication is essential for the regulated diffusion of small molecules and ions between adjacent cells. Mutations in connexin proteins, the main components of gap junctions, result in a variety of diseases that include skin disorders, neuropathy, and deafness. In this study a combination of microinjection, multi-channel time-lapse microscopy, and image processing was used to investigate *in vitro* the effects of different disease associated connexin 31 mutations on intercellular communication and cell survival. This study revealed that a deafness/peripheral neuropathy mutation and a mutation previously reported as a polymorphic variant of connexin 31 were associated with impaired intercellular communication, while mutations linked to skin disorders were associated with cell death.

Cell motility and chemotaxis are believed to play an important role in the metastatic spread of cancer. In order to investigate the role of cytoskeletal signalling molecules in the motility and chemotaxis of metastatic sarcoma cells, the Dunn chemotaxis chamber was applied in combination with microinjection and time-lapse microscopy. The study focused on the Rho GTPases Cdc42, and Tc10 and their effectors PAK1 and N-WASP, proteins previously identified as regulators of polarity in other cell systems. This study revealed that PAK1 was required for efficient chemotaxis and motility of the sarcoma cells. While Cdc42, Tc10 and

N-WASP were all necessary for efficient motility they were not found to be important for chemotaxis. Comparative studies in fibroblasts confirmed the importance of Cdc42 in motility but not directionality. In additional studies the novel fluorescence localisation after photobleaching technique revealed increased actin dynamics in metastatic sarcoma cells compared to non-metastatic cells. Finally, the subcellular interaction of Cdc42 with PAK1 and N-WASP was explored using fluorescence lifetime imaging microscopy in order to reveal the dynamics of Cdc42/effector interactions in single cells. Cdc42 and N-WASP associated constitutively in the majority of cells studied, and this interaction was largely confined to a perinuclear region. In contrast, Cdc42 and PAK1 association was inducible, requiring growth factor stimulation.

AKNOWLEDGEMENTS

Foremost I would like to thank Daniel Zicha for giving me the opportunity to work within his laboratory and for his constant guidance, supervision and support. I am also indebted to all the members of the Department of Light Microscopy for their support, and above all tolerance over the past four years: special thanks go to Colin Gray, Ian Dobbie, Debbie Aubyn, Peter Jordan, Alastair Nicol, Yan Gu, and Tamara Cavanna. I would especially like to thank Tony Ng for his interest in my work and for many useful discussions. Above all I would like to thank those people who, either through financial donation or investment of time, have provided the excellent facilities at Cancer Research UK, within which I have had the great privilege to work.

TABLE OF CONTENTS

3 THE CHEMOTAXIS AND MOTILITY OF SARCOMA CELLS AND FIBROBLASTS 84

LIST OF FIGURES

LIST OF TABLES

1 PREFACE

In order to maintain a logical structure this thesis is presented in two parts: the first is a study of connexin mutation and gap junction-mediated intercellular communication, while the second is a study of sarcoma cell chemotaxis and motility. While both parts essentially represents independent bodies of work, the similarities in the experimental approach adopted in each provide a common theme. A key feature of this work has been the development and application of novel microscopy and image analysis techniques to the study of specific biological problems. The use of fluorescence imaging has been essential for the study of cell behaviour in both parts. The development of techniques that combine multi-channel time-lapse microscopy with post-acquisition image processing and analysis has enabled observations of cell behaviour to be interpreted objectively, in a quantifiable and statistically testable manner.

2 GAP JUNCTION-MEDIATED INTERCELLULAR COMMUNICATION

2.1 INTRODUCTION

The regulated exchange of ions and small metabolites between adjacent cells is essential for the maintenance of tissue homeostasis and the control of synchronised cellular responses (De Maio et al., 2002). This process is mediated by gap junctions, intercellular channels that directly couple the cytoplasm of neighbouring cells (Evans and Martin, 2002). Gap junctions couple cells in most, if not all, metazoan organisms (Simon and Goodenough, 1998). In mammals gap junctions are found within a variety of tissues where they adopt diverse functional roles including the coordination of biomechanical processes, the synchronisation of neuronal activity and cellular metabolism, the control of differentiation, and tumour suppression. Abnormalities in gap junction communication have been found to underlie a wide range of human disorders.

2.1.1 The structure of gap junctions

Gap junction channels are multimeric structures comprised of protein subunits known as connexins. Each connexin is an integral membrane protein consisting of four transmembrane domains, two extracellular loops, a cytoplasmic loop, and cytoplasmic amino and carboxyl termini (Oviedo-Orta and Evans, 2002). During transit to the plasma membrane individual connexins associate to form hexameric hemichannels known as connexons. The six subunits of each connexon are arranged in a radial manner such that they form an aqueous pore at the centre of the hemichannel. Intercellular channels are formed via the docking of connexons

that reside within the plasma membrane of apposing cells. Clusters of tens to thousands of intercellular channels, often arranged in tight, regular arrays, form the gap junctions, ultrastructures that directly link the cytoplasm of adjacent cells (Figure 1, page 13).

Connexins are encoded by a large gene family comprising at least twenty family members (De Maio et al., 2002). Individual connexin proteins are classified according to their molecular weight (e.g. the nomenclature for the 31 kDa connexin is Cx31) and groups of connexins assigned to subfamilies according to their homology (α, β, γ, and unclassified). Hemichannels can be composed of connexins of either the same or different types enabling the formation of either homomeric or heteromeric connexons respectively. Furthermore, selective interactions between homomeric and heteromeric connexons on the surface of apposing cells enable the creation of both homotypic and heterotypic intercellular channels. The extracellular loops of the connexin subunits govern the interactions of apposing connexon hemichannels while their intracellular loops and carboxyl termini, which represents the regions of greatest sequence divergence between connexin family members, provide sites for channel regulation which include phosphorylation, and pH and voltage sensing. The molecular permeabilities, conductance properties, and modes or regulation of individual gap junction channels can vary and are determined by the properties of the individual connexins from which they are derived (Beyer et al., 2001). Given the capacity for different connexin types to associate with one another and given that many of these proteins are co-expressed in a wide range of tissues, the potential exists for the generation of tremendous channel diversity.

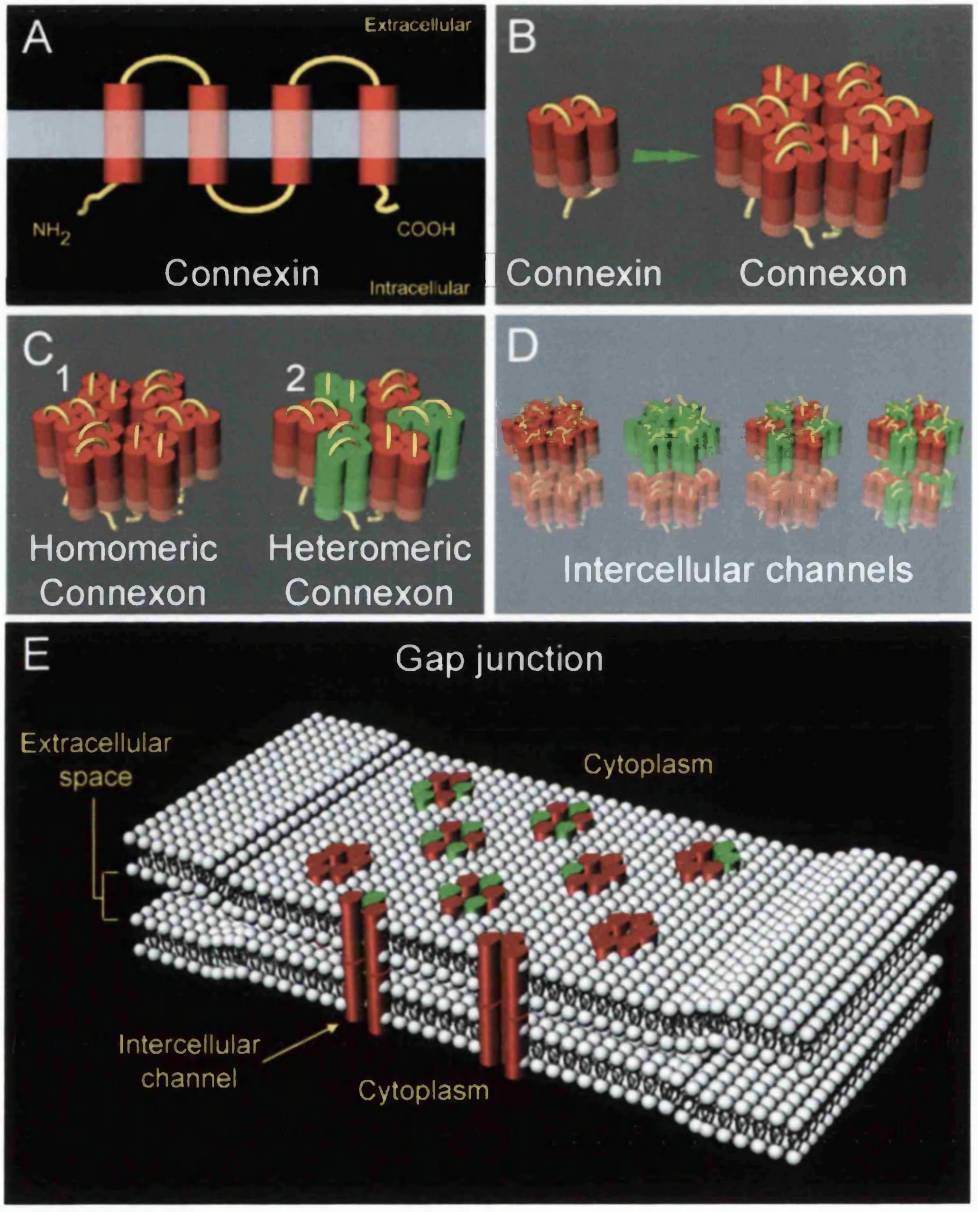

Figure 1. The structure of gap junctions

Each connexin is a four trans-membrane spanning protein with intracellular N- and C-termini (A). Six connexins combine within the endoplasmic reticulum to form a hexameric connexon hemi-channel (B). Connexins of the same type interact to form homomeric connexons (C1) while the interaction of different family members produce heteromeric connexons (C2). Connexons from neighbouring cells couple to produce intercellular membrane channels directly linking the cytoplasm of adjacent cells (D). The interaction of homomeric and heteromeric connexons enables the formation of both homotypic and heterotypic channels (D). Selective interactions between different connexons allow the formation of a large variety of channels with varying conductance properties. Large clusters of channels form gap-junctions plaques (E).

The exchange of ions and small molecules between adjacent cells through gap junction channels occurs due to passive diffusion. Owing to the relatively small pore size of these channels passage is restricted to molecules of less than approximately 1.0 - 1.2 kDa in size. Consequently gap junctions are primarily involved in the transfer of inorganic ions and low molecular weight metabolites such as calcium ions, potassium ions, glucose, and cyclic nucleotides (De Maio et al., 2002). However, pore size is not the sole determinant of channel permeability. Indeed many gap junction channels display highly selective conductances, permitting the passage of only those ions or molecules of a particular charge. For instance Cx32 is selectively permeable to anionic molecules while Cx26 permits the passage of molecules independent of their charge (Elfgang et al., 1995). Furthermore the specific conductance properties conferred by a single connexin type can be modified when incorporated into channels with other connexin species. Therefore, a heterotypic channel can acquire electrophysiological properties that are markedly different from those of homotypic channels formed from single connexin types. Indeed, some connexins (e.g. Cx29) are unable to form functional homotypic channels and appear to have evolved specifically to modify the electrophysiological properties of other connexin types through heterotypic associations (Altevogt et al., 2002). The ensemble of different connexins expressed within a particular organ or tissue is therefore likely to reflect the specific function bestowed upon the gap junctions within that physiological system.

2.1.2 Connexins in physiology and pathology

Connexin proteins are associated with many hereditary and acquired human disorders that range from mild hearing loss and cataractogenesis (Donaldson et al., 2001; Kelsell et al., 2001) to cardiovascular disease and cancer (Carystinos et al., 2001; Severs et al., 2001). Furthermore, different germline mutations in the same connexin gene can result in profoundly different clinical phenotypes (Kelsell et al., 2001). Table 1, page 16 provides a summary, but by no means an exhaustive list, of many of the connexins identified to date, their respective tissue distributions, ascribed functions, and known disorders associated with their dysfunction. Some of these examples are also discussed further below. It is interesting to note that while some connexins are expressed extensively in many tissues others are more restricted in their distribution; for instance Cx43 is the most abundantly expressed connexin and is found in most tissues including the heart, smooth muscle, brain, bone, and kidney, while Cx50 appears to be expressed exclusively within the lens of the eye.

Gap junctions are crucial for the coordination of many biomechanical processes. Within the walls of the cardiac chambers gap junctions permit the interconnection of vast networks of myocytes, enabling the synchronised transmission of calcium waves required for coordinated heart contraction (Severs et al., 2001). They are also found in abundance in smooth muscle tissue where they have been implicated in the control and maintenance of vascular tone (Hill et al., 2001) and the peristaltic movements of the gastrointestinal tract (Suzuki, 2000). Also, an increase in the formation of gap junctions between cells of the myometrium is observed during mid- to late-term pregnancy and is believed to occur in preparation for the synchronisation of uterine contractions required during labour (Carbillon et al., 2001). Cx43

The connexins

Connexin	Gene	Subfamily	Tissue distribution	Proposed functions	Disease association
Cx43	GJA1	α	A widely expressed connexin found in most gap junction containing tissues including heart [1], smooth muscle [1], CNS* [2], bone [3], ovary [4], adrenal gland [5], term pregnant myometrium [6].	Control of heart contraction [1], vascular tone [1], myometrial activation [6].	Cardiovascular disease [1]: Ventricle arhythmia, coronary arteriosclerosis, possibly hypertension.
Cx46	GJA3	α	lens of eye [7].	Regulation of lens microcirculation [7].	Cataractogenesis [8].
Cx37	GJA4	α	CNS [2], vascular endothelium [9], ovary [10].	Control of vascular tone [1], development of ovarian follicles [10].	Arteriosclerosis [9], possibly female infertility [10].
Cx40	GJA5	α	CNS [2], heart [1], vascular endothelium [1], vascular smooth muscle [1], kidney [5].	Control of heart contraction [1] and vascular tone [1].	Cardiovascular disease [1]: atrial fibrillation, possibly hypertension.
Cx45	GJA7	α	CNS [2], heart [1], restricted expresion in vascular smooth muscle [1].	Control of heart contraction [1].	Of unknown significance.
Cx50	GJA8	α	lens of eye [7].	Regulation of lens microcirculation [7].	Cataractogenesis [11].
Cx32	GJB1	β	CNS [2], PNS** [12], Liver [13].	Control of liver metabolism [13], peripheral nerve function [12].	X-linked Charcot-Marie-Tooth disease [12].
Cx26	GJB2	β	CNS [2], Epidermis [14], Inner ear [12].	Epidrmal growth and differentiation [14], auditory transduction [12].	Nonsyndromic and syndromic hearing loss [12], Vohwinkel syndrome [14].
Cx31	GJB3	β	PNS[15], Epidermis [14], Inner ear [12].	Epidrmal growth and differentiation [14], auditory and peripheral nerve transduction [12, 15].	Erythrokeratoderma variablis [14], Nonsyndromic and syndromic hearing loss [12], peripheral neuropathy [15].
Cx30.3	GJB4	β	Epidermis [14].	Epidrmal growth and differentiation [14].	Erythrokeratoderma variablis [14].
Cx30	GJB6	β	Epidermis [16], Inner ear [12].	Epidrmal growth and differentiation [14], auditory transduction [12].	Hydrotic Ectodermal Dysplasia [16], Nonsyndromic and syndromic hearing loss [12].
Cx36	CX36	U/C***	CNS [2], retunal tissue: rod photoreceptors, cone pipolar cells, All amicrine cells [17, 18].	Vision [19], Neuronal development [17].	Retinitis pigmentosa (proposed indirect pathological effect) [19].

*CNS, Central nervous system
**PNS, Peripheral nervous system
***U/C, Unclassified

[1](Severs et al., 2001),[2](Rouach et al., 2002),[3](Rodriguez., E),[4](Simon et al., 1998),[5](Serre-Beinier et al., 2002), [6](Carbillon et al., 2001),[7](Donaldson et al., 2001),[8](Pal et al., 2000),[9](Boerma et al., 1999),[10](Simon et al., 1997),[11](Pal et al., 1999),[12](Rabionet et al., 2002),[13](Nelles et al., 1996),[14](Kelsell et al., 2001),[15](Lopez-Bigas et al., 2001),[16](Common et al., 2002),[17](Sohl et al., 1998),[18](Deans et al., 2002),[19](Ripps., 2002)

Table 1. The physiology and pathology of connexins

Table summarising the tissue distributions, ascribed functions, and known disorders associated with various connexin family members.

is expressed extensively in cardiac and smooth muscle and is a major component of gap junctions in these tissues. It is also becoming increasingly evident that Cx43 is of significant importance in the progressive development of cardiovascular disease: abnormalities in Cx43 expression and inappropriate patterns in Cx43-dependent gap junctional coupling in myocardial tissue have been associated with lethal ventricular arrhythmias, while conversely the early stages of coronary arteriosclerosis have been linked with an increase in Cx43 expression within the smooth muscle of vascular tissue (Severs et al., 2001).

Gap junction communication has also been implicated in neuronal signalling and dysfunction (Rouach et al., 2002). Within the central nervous system gap junctions provide an alternative to chemical synaptic transmission, enabling the direct electronic coupling of adjacent neurones. These electrical synapses are thought to synchronise neuronal activity. Neurological disorders such as epileptic seizure, which are characterised by excessive and highly synchronised neuronal firing, are in part believed to be the consequence of abnormalities in gap junction signalling (Perez Velazquez and Carlen, 2000). Gap junctions also appear to be of importance in the peripheral nervous system where they interconnect the many layers of the myelinating Schwann cells (Baker, 2002) and mutations in connexins expressed in these tissues have been associated with peripheral nerve dysfunction and neuropathy (Rabionet et al., 2002). Within the mammalian eye the propagation of rod signals across the retina requires the coupling of adjacent cells via gap junction channels (Deans et al., 2002). In the congenital disorder retinitis pigmentosa, a disease characterised by severe visual impairment due to mutations in the rhodopsin gene, the transfer of apoptotic signal from dying rod cells to adjacent healthy cone cells is thought to be mediated by gap junctions

(Ripps, 2002). Although not functionally impaired themselves, the gap junctions contribute to the pathogenesis of this disease by permitting the spread of cytotoxic signals from one cell type to another. Within the inner ear gap junction channels enable the recycling of potassium ions within the cochlea, a requirement for the normal function of the mammalian hearing system. Cx26 is expressed in all inner ear cells presenting gap junctions, and as much as 30 - 50 % of all hereditary hearing loss is a result of congenital mutations in this protein (Avraham, 2001).

Gap junctions are also necessary for coordinating the metabolic activities of a number of organ tissues. For instance glucose metabolism within the liver is synchronised via the extensive coupling of hepatocytes via gap junction channels (Nelles et al., 1996). Similarly, the coordinated production and release of secretary factors from endocrine and exocrine glands such as the pituitary, adrenal gland, and pancreas is believed to be mediated by gap junction communication (Serre-Beinier et al., 2002). The specialised anatomical design of the mammalian lens relies heavily on the properties of gap junctions; intercellular channels permit the formation of a highly specialised internal microcirculation between the fibre cells of the lens, enabling tissue transparency by removing the need for a true vasculature (Donaldson et al., 2001). Disruption of this microcirculation results in tissue necrosis and the development of cataracts (Pal et al., 1999; Pal et al., 2000). Intercellular communication mediated by gap junctions is also critical for the normal development and differentiation of the epidermis, and mutations in at least four different connexins expressed in epidermal related tissues have been associated with a range of hyperproliferative skin disorders (Kelsell et al., 2001)(see section 2.1.3 below).

The importance of gap junctions in cancer biology has been known for many years. A loss of gap junctionial communication is invariably associated with carcinogenisis and strongly correlates with the metastatic potential of a number of different cell lines (Carystinos et al., 2001; Nicolson et al., 1988; Saunders et al., 2001). Furthermore, re-induction of gap junctionial communication has been shown to inhibit the growth of transformed cells (Goldberg et al., 2000). A variety of known chemical tumour promoters (e.g. phorbol esters) have been shown to disrupt gap junction signalling while, conversely, various anticancer agents (e.g. retinoids) seem to promote gap junction-mediated cell communication (Trosko and Chang, 2001).

2.1.3 Cx31 mutation and disease

The majority of hereditary disorders linked to connexin abnormalities have been associated with mutations in β-connexin genes (GJB). The β-connexins, which include Cx32, Cx26, Cx31, Cx30.3, and Cx30, are highly expressed in tissue of ectodermal origin including the epidermis, neuronal tissue, and the epithelium of the inner ear. Germline mutations in β-connexins underlie a range of clinically diverse human disorders including deafness, skin disease, and peripheral neuropathy (Kelsell et al., 2001; Rabionet et al., 2002). These disorders can occur either in isolation or in combination with one another and present with varying degrees of severity depending upon the specific connexin and mutation in question. Mutations in Cx26 and Cx30, which are co-expressed in various tissues of the inner ear and the epidermis are associated with both dominant and recessive hearing loss and a range of hyperproliferative skin disorders including the aggressive and mutilating Vohwinkel

syndrome (Cx26, MIM 124500) and Hidrotic Ectodermal Dysplasia (Cx30, MIM 129500). Mutations in the epidermally expressed Cx30.3 result in the skin disease erythrokeratoderma variables (EKV) (MIM 133200), while mutations in Cx32 which is expressed to a high degree in peripheral nervous tissue result in the X-linked form of the neurodegenerative disorder Charcot-Marie-Tooth disease (CMTX)(MIM 302800) (reviewed, Kelsell et al., 2001).

An interesting phenomenon associated with many β-connexin-associated disorders is the widely differing clinical phenotypes that can arise from various mutations within the same connexin protein. On of the most striking example of this is provided by Cx31. Cx31 is expressed in the epidermis (Di et al., 2001), the myelinating cells of peripheral nerves, and the spiral ligament and limbus of the inner ear (Lopez-Bigas et al., 2001a), and mutation in this protein can result in disorders associated with all these tissues. As with many β-connexins Cx31 has been implicated in the normal growth and development of the epidermis (Di et al., 2001; Kelsell et al., 2001). Various dominant germline mutations in this protein have been associated with EKV, a skin disorder characterised by localised hyperkeratrosis and generalised erythema (Rook et al., 1998). The disease typically presents as a diffuse thickening of the palmoplantar epidermis due to the growth of hyperkeratotic plaques, but patients can also suffer from independent and transient erythematous patches that affect the whole body and which only persist for short periods. Both hyperkeratotic plaques and erythematous patches can be triggered by a number of environmental factors ranging from trauma to the skin, and exposure to ultraviolet irradiation to emotional stress. To date six independent dominant mutations in Cx31 have been identified that are linked to EKV

(Gottfried et al., 2002; Kelsell et al., 2001). Interestingly, these mutations do not seem to be confined to specific functional domains but instead are distributed throughout the molecule. For instance single amino acid changes in the amino terminus (G12D/R), the first extracellular loop (R42P), or the second transmembrane domain (C86S) of Cx31 have all been associated with EKV.

That mutations located in many of the different functional domains of Cx31 cause EKV would suggest that any impairment of protein function *per se* should result in this skin disorder. However, two dominant mutations identified in the second extracellular loop of Cx31 (R180X and E183K) have both been associated with non-syndromic (i.e. of single clinical phenotype) hearing loss with no additional abnormalities associated with the epidermis (Xia et al., 1998). Cx31 is expressed both within the inner ear and the auditory nerve and therefore it is not surprising that disruptions in Cx31-related gap junction signalling can result in hearing dysfunction. However, what is surprising is that different mutations within the same molecule can result in independent and unrelated clinical phenotypes. A further complication to the pathology of Cx31 has been provided by the recent identification of an additional and rare dominant mutation within the first extracellular loop of Cx31 (66DelD), which has been associated with syndromic hearing loss (i.e. of multiple clinical phenotype) (Lopez-Bigas et al., 2001a). This mutation is also associated with reduced conduction velocities in motor and sensory nerves, resulting in diminished muscle reflexes and severe peripheral neuropathy. Cx31 is co-expressed with Cx32 in the myelinating Schwann cells of peripheral nerves. Mutations in Cx32 result in the neurodegenerative disorder CMTX as mentioned, and therefore the recent

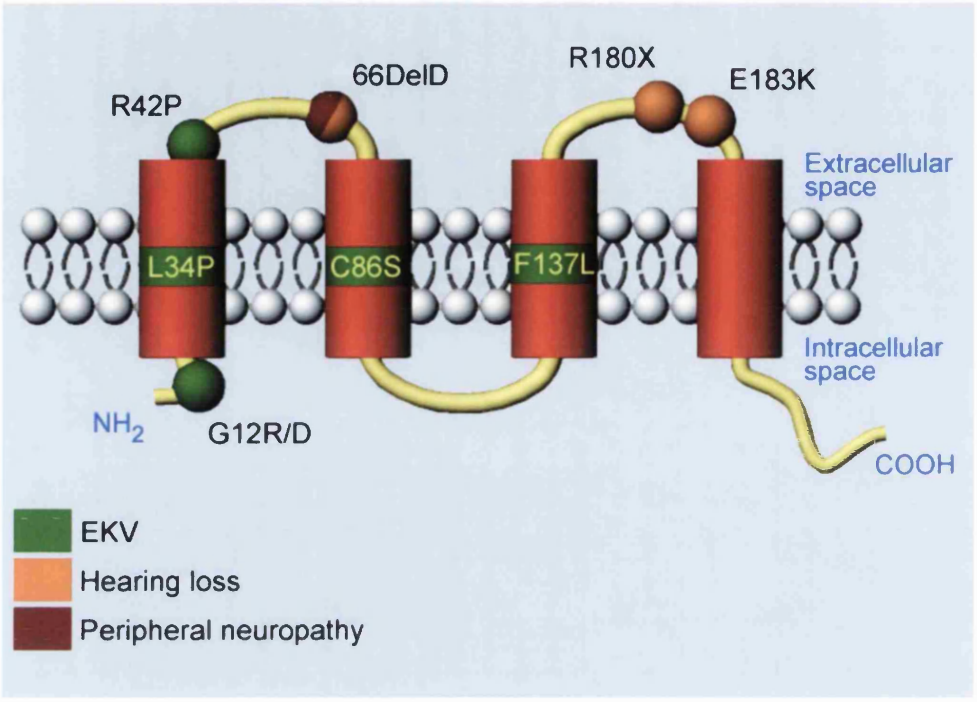

Figure 2. The germline mutations of Cx31 and their associated disorders

A schematic depicting the functional domains of Cx31 and the localisation of disease-associated mutations. Diseases are defined by the accompanying colour key. Deafness mutations are confined to the extracellular loops of the protein, while EKV mutations are more varied in their distribution, but tend to lie adjacent to or within transmembrane domains. X = stop codon. Cx31 is unique among the connexins in that three separate clinical disorders have been associated with mutations in this protein; the skin disorder erythrokeratoderma variables (EKV), non-syndromic hearing loss, and a syndromic hearing disorder associated with peripheral neuropathy.

identification of the 66DelD mutation in Cx31 confirms the importance of both these connexins in peripheral nerve function.

Cx31 mutation can therefore result in multiple and varying clinical phenotypes. The factors that determine the differential effects that particular mutations confer on various tissues are likely to be complex and many possible explanations exist. For instance the co-expression of different connexin types within a particular tissue may allow for a degree of redundancy, enabling one connexin type to adopt the role of another. In tissues where redundancy is not permitted due to the relatively restricted expression of other connexin types, the severity of a particular mutation may be greater. However, it has been reported that at least ten connexin types are expressed in the human epidermis (Di et al., 2001), while only four have been detected in the inner ear (Rabionet et al., 2002), and yet certain Cx31 mutations can have deleterious effects on the former tissue and not the latter. Redundancy alone is therefore unlikely to provide a sufficient explanation for the variation in clinical phenotypes observed. The severity of a particular mutation may also be governed by the capacity for Cx31 to form heterotypic associations with other connexins within a particularly tissue. For instance a specific Cx31 mutation may confer a more detrimental effect on homotypic channel function than on heterotypic channel function as the presence of other connexin types within the same channel may in part compensate for the deleterious effects of the mutation. Therefore in tissues where the protein is largely incorporated into heterotypic channels the effects of the mutation may be more subdued than in those tissues where homotypic channels are the predominant type. It is interesting to note that no apparent correlation exists between the position of a particular mutation within the Cx31 molecule and the resulting clinical disorder;

specific skin disease and deafness mutations are spread across the length of the molecule and appear within various functional domains (Figure 2, page 19). It is therefore of particular interest to determine whether Cx31 mutations associated with specific disorders elicit differing effects at the cellular level.

2.1.4 Study aims

Although much is known about the genotype-phenotype differences between distinct Cx31 mutations at the clinical level, little is known about these differences at the cellular level. This study represents an attempt to bridge this gap. A number of functional assays combining microinjection, wide-field multi-channel digital time-lapse microscopy, and image processing were used to investigate *in vitro* the effects of specific disease associated Cx31 mutations on both intercellular channel function and cell morphology in cultured keratinocyte and fibroblast cell lines. The EKV-associated mutations, R42P & C86S, the deafness and peripheral neuropathy mutation 66DelD, and a Cx31 polymorphic variant, R32W, of unknown disease significance provided the main focus of this study. Here new insights are provided into how distinct Cx31 mutations elicit different effects on epidermal growth, auditory transudation and peripheral neuronal function.

2.2 METHODS

2.2.1 Cell Culture

NIH 3T3 mouse fibroblasts were grown in Dulbecco's Modified Essential Medium (DMEM) supplemented with 10 % foetal calf serum (FCS) (Sigma), 1.6 % L-glutamine, 5 mM glucose, and 100 U/μg/ml penicillin-streptomycin, and phenol red indicator. Adherent cell cultures were passaged every 2 to 3 days to maintain continuous cell growth. Cells were maintained in culture up until their 10^{th} passage and individual cultures never permitted to grow to confluency. Cultures were kept in a humidified incubator (Heraeus Instruments) set to 37°C with 10 % ambient CO_2. The periodic passaging of cells involved a brief wash with phosphate-buffered saline (PBS) followed by treatment with a 0.02 % porcine trypsin (Beckton Dickinson)/5 mM EDTA solution to induce cell detachment. Culture medium was subsequently added to the cell suspension to inhibit further trypsin/EDTA activity and the cells then used to re-seed new cell cultures of varying densities. Sterile tissue culture plastics were used throughout (Falcon).

NEB-1 cells, originally derived from HPV16 immortalized human keratinocytes (Morley et al., 1995), were kindly grown and maintained by Wei-Li Di, Centre for Cutaneous Research, Queen Mary Hospital, London. Cells were cultured in 3:1 DMEM/F12 medium supplemented with 10 % FCS, 0.4 μg/ml hydrocortisone, 5 μg/ml insulin, 10 ng/ml epidermal growth factor (EGF), 10×10^{-10} M choleratoxin, 5 μg/ml transferrin, 2×10^{-11} M lyothyronine, and 100 U/μg/ml penicillin-streptomycin.

2.2.2 Microinjection

Nuclear microinjection provided the main tool for introducing expression constructs into cells while cytoplasmic microinjection was used to introduce fluorescent dye into the cells during dye transfer experiments. Microinjection needles were generated from glass capillaries (GC120TF-10, Fisher Scientific) using an electronic microfilament puller (P-97, Sutter Instrument Co.). Solutions prepared for microinjection containing either cDNA constructs, fluorescent antibodies, or fluorescent dyes were spun at 14000 rpm for 20 min in a desktop microcentrifuge (Eppendorf) pre-cooled to 4 °C in order to sediment particles that could otherwise have blocked the microinjection needle. Samples were kept on ice throughout the microinjection process and microinjection needles were loaded with solution taken from only the very top of the spun sample.

Nuclear Microinjection: All nuclear microinjection was carried out using a transjector and micromanipulator (Eppendorf) mounted on a Zeiss Axiovert 135 TV inverted microscope (Carl Zeiss) equipped with a tungsten lamp for bright field illumination, a long-working distance condenser, and long-working distance objectives. The microscope body rested on an optical table isolator (Melles Griot) to prevent ambient vibrations from disturbing the microinjection needle. A heated stage enabled cell cultures to be maintained at 37 °C during the microinjection process. A conventional CCD camera (Sony) was fitted to the front camera port of the microscope to enable microinjection to be visualized on an analogue monitor. All microinjection was carried out using a ×20, NA 0.3, long-working distance, phase contrast objective.

Cytoplasmic microinjection: During dye transfer experiments cytoplasmic microinjection was used to introduce Alexa 568 dye into cells expressing enhanced green fluorescent protein (EGFP) fusions of different Cx31 variants. A modified microscope configuration was therefore required that permitted fluorescence imaging. The microscope system used for cytoplasmic microinjection was the same as that used for time-lapse microscopy.

2.2.3 Time-lapse microscopy

Digital time-lapse microscopy was used to record cell behaviour during dye transfer and cell death experiments. All time-lapse experiments were conducted on the same Zeiss Axiovert TV 135 (Carl Zeiss) inverted microscope. The microscope was optimised for multi-channel digital time-lapse microscopy and to accommodate the long-term imaging of mammalian cells in culture. The addition of a transjector and micromanipulator unit (Eppendorf) also enabled cells to be microinjected and subsequently filmed on the same system. This was particularly crucial for dye transfer experiments where the time between microinjection and imaging had to be kept to a minimum.

The microscope was fitted with tungsten and mercury lamps to enable both bright field and fluorescence imaging, and was equipped with separate bright field and fluorescence shutters (Uniblitz), a shutter controller (Sutter Instruments), and a highly sensitive CCD camera (Orca ER, Hamamatsu). All peripheral devices were under the control of image acquisition software (Acquisition Manager, Kinetic Imaging). The CCD camera was mounted directly under the sample on the lower camera port of the microscope in order to minimise the number of optical elements in the path from the objective to the camera, therefore

maximising the fluorescence signal. Blocks containing excitation and emission filters and compatible dichromatic mirrors enabled a range of fluorophore species to be imaged. In addition, motorised excitation and emission filter wheels containing a selection of different fluorescence filters enabled the rapid sequential imaging of multiple fluorophores during a single time-lapse experiment when used in conjunction with appropriate multiple dichromatic mirrors. Filters and dichromatic mirrors were purchased from Omega Optical, Inc. and permitted the imaging of EGFP (FX100-2 Alpha Vivid: Ex 475 AF40, DRLP 505, Em 535 AF45), Alexa 568/Cy3/Cy3.5 (FX108-2 Alpha Vivid: Ex 525 AF45, DRLP 560, Em 695 AF55), and Cy5 (FX110-2 Alpha Vivid: Ex 630 AF50, DRLP 650, Em 535 AF45) fluorescence.

The microscope was housed in a purpose built Perspex environment chamber accurately maintained at 37 °C using an in-house built controlled heater. The main body of the microscope rested on an optical table isolator (Melles Griot) in order to minimize the effects of ambient vibrations on both microinjection and image acquisition. A choice of short-working and long-working distance condensers enabled experiments to be conducted either with or without the additional use of microinjection. Cytoplasmic microinjection was conducted using a ×20, NA 0.5, short working distance, phase contrast objective. A conventional CCD camera (Sony) was mounted on the front camera port of the microscope and connected to an analogue monitor for use during microinjection.

The time-lapse interval, total duration of the recording, and the specific filter configurations depended upon the experimental assay in question and are therefore described in their relevant sections.

2.2.4 EGFP fusion constructs

Expression constructs encoding EGFP fusions of wild type Cx31 and the mutant variants R42P, C86S, R32W, and 66DelD were constructed and kindly provided by Wei-Li Di. All Cx31 variants were encoded in the pEGFP-N1 expression vector (ClonTech) in-frame and upstream of EGFP. The native Cx31 stop codon was altered (TGA to GGA) to enable read-through and consequently transcription of the downstream fluorophore. Cx31 variants were therefore expressed as N-terminal fusions to the EGFP. The wild-type and R42P mutant form of Cx31 were originally generated via PCR from human genomic DNA, while the R32W, C86S, and 66DelD mutations were generated independently via site directed mutagenesis using the wild-type Cx31-EGFP template (Di et al., 2002).

2.2.5 The conjugation of fluorescent dyes to antibodies

Fluorescent dyes were conjugated to antibodies for use as microinjection markers during various experiments. Conjugation reactions were performed as follows: lyophilised, reagent-grade sheep IgG (Sigma) was reconstituted to a concentration of 2 mg/ml in 100 mM Na_2CO_3, pH 9.3. 1 ml of IgG solution was then applied to a single pre-packed vial of either Cy3.5 or Cy5 fluorescent dye (Amersham Biosciences, cat: PA23500 & PA25000). The suspension was gently agitated with a pipette to ensure thorough mixing of the dye. The

reaction was then incubated at room temperature for 30 min with one brief additional mixing step half way through. Conjugation reactions were always protected from light. Dye-conjugated antibodies were then separated from free dye using the QuickSep dialysis system (Tripple Red). Briefly, the 1 ml reaction volume was placed into a dialysis cassette containing a 16,000 MW cut-off membrane and subsequently immersed in 400 ml of phosphate buffered saline, pH 7.5 (PBS). Dialysis was preformed over 48 hours at 4 °C with periodic buffer changes. A magnetic stirrer ensured thorough mixing throughout. Dialysed Cy3.5-IgG and Cy5-IgG stocks were stored at -20 °C until required.

2.2.6 In vitro dye transfer assay for the study of intercellular communication

Preparation of experimental cultures: Freshly trypsinised NEB1 keratinocytes and NIH 3T3 fibroblasts were seeded in 35 mm diameter glass-bottomed microwell dishes (MatTek) containing 3 ml of the appropriate tissue culture medium for the cell type in question. Cells were allowed three days to grow to confluency before experimentation.

For all microinjection and imaging cells were transferred to fresh phenol red-free tissue culture medium supplemented with 20 mM HEPES, pH 7.5 (experimental culture medium). The presence of phenol red in culture medium was not desirable during fluorescence imaging due to the autofluorescent properties of this compound. HEPES was added to culture medium to compensate for the low ambient levels of CO_2 during both microinjection and imaging, therefore removing the need for more complicated CO_2 delivery systems.

Nuclear microinjection: A confluent region of cells within the central microwell of the culture dish was selected and groups of adjacent cells microinjected in the nucleus with

plasmid DNA encoding one of the EGFP-Cx31 variants. Expression constructs were all microinjected at a concentration of 0.05 μg/μl. Following microinjection cells were transferred to fresh tissue culture medium and returned to the incubator. Cells were allowed 4-5 hours to express the microinjected constructs.

Cytoplasmic microinjection and time-lapse microscopy: The cytoplasmic microinjection of fluorescent dye into cells was conducted on the same Zeiss Axiovert 135 TV inverted microscope (Carl Zeiss) that was subsequently used for the imaging of dye-transfer through cells. For a detailed description of the microscope specifications see section 2.2.3, page 19. The culture dish was positioned on the stage of the microscope in a glass-topped, steel humidity chamber (constructed in-house) that was designed to prevent evaporation during the course of time-lapse experiments. The lid of the chamber was removed during microinjection. For all dye transfer experiments patches of fluorescent cells were identified under the microscope and single cells close to the patch perimeter were microinjected in the cytoplasm with 2 mM Alexa 568 dye (Molecular Probes). Upon the successful cytoplasmic microinjection of a single fluorescent cell the microinjection needle was quickly removed from the microscope and the lid of the steel humidity chamber replaced, completely enclosing the culture dish. The occurrence of dye transfer between adjacent cells was then determined using multi-channel digital time-lapse microscopy. The acquisition software was used to acquire images every 20 seconds in three separate channels (phase contrast, EGFP fluorescence, and Alexa 568 fluorescence) using the 20 × NA 0.5 objective, the CCD camera and the multiple dichromatic mirror in conjunction with motorised excitation and emission filter wheels. Cell cultures were monitored for a total duration of 33 min (100 acquisition

rounds). Although the exposure times used for imaging EGFP fluorescence tended to vary between dye transfer experiments, the exposure time used for imaging Alexa 568 fluorescence was kept constant as fluorescence intensity of the dye did not vary considerably. The time elapsed from the injection of dye to commencement of image acquisition was approximately a minute. The procedure for studying intercellular dye transfer is summarised in Figure 3, page 19.

2.2.7 Measurement of dye transfer rate

The time-lapse acquisition of Alexa 568 fluorescence images over the course of dye transfer experiments provided accurate information concerning the temporal dynamics of dye spread through cell populations expressing different Cx31 variants. Image processing software was specially developed in order to numerically quantify this process, enabling the statistical comparison of the effects of different Cx31 mutations on the rate of dye transfer. By comparing the various rates at which dye transferred through cell populations expressing the wild type Cx31 protein with those found for cell populations expressing particular Cx31 variants, significances could be derived that reflected the relative degree to which different Cx31 mutations impeded or enhanced intercellular communication.

Preparation of film sequences for image analysis: Prior to image analysis film sequences were cropped (IMD analysis, Kinetic Imaging) to incorporate a region that contained the EGFP expressing cells and dispersing dye. Interactive tracking (Motion Analysis, Kinetic Imaging) was then used to mark, using the mouse pointer, the position of the cell originally microinjected with Alexa 568 dye. Cell position was represented by a single *xy* co-ordinate

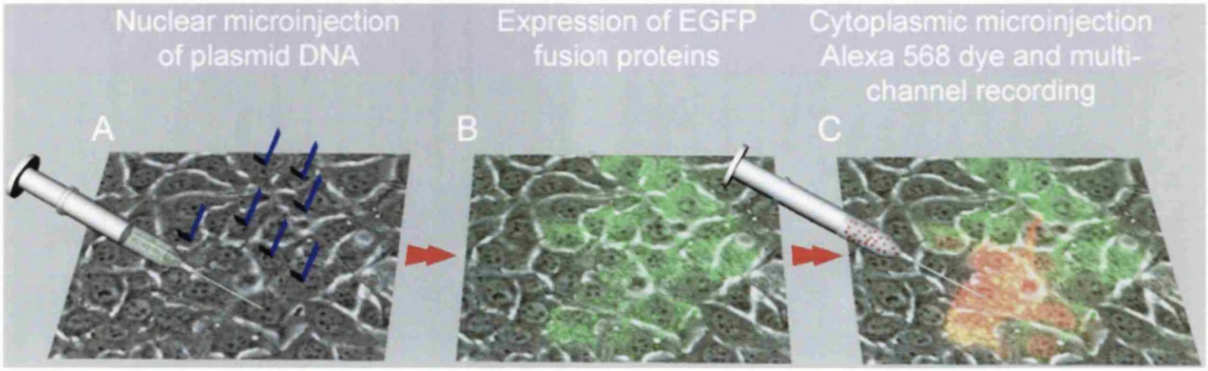

Figure 3. Summary of the in vitro dye transfer assay for the assessment connexin function

(A) Groups of adjacent cells within a monolayer culture were microinjected in the nucleus with 0.05 μg/μl plasmid DNA encoding one of the Cx31-EGFP fusion constructs under investigation. (B) Cultures were left for 4 – 5 hours to allow the expression of microinjected constructs. This resulted in the formation of tight patches of fluorescent cells. (C) A single expressing cell close to the patch perimeter was then selected and microinjected in the cytoplasm with 2 mM Alexa 568 dye. Multi-channel time-lapse microscopy was then used to monitor the spread of Alexa dye through the surrounding cell population: Images were acquired at 20 s time intervals in three separate channels (phase contrast, EGFP, and Cy3.5 fluorescence). Each film sequences consisted of 100 acquisition rounds (33 min duration).

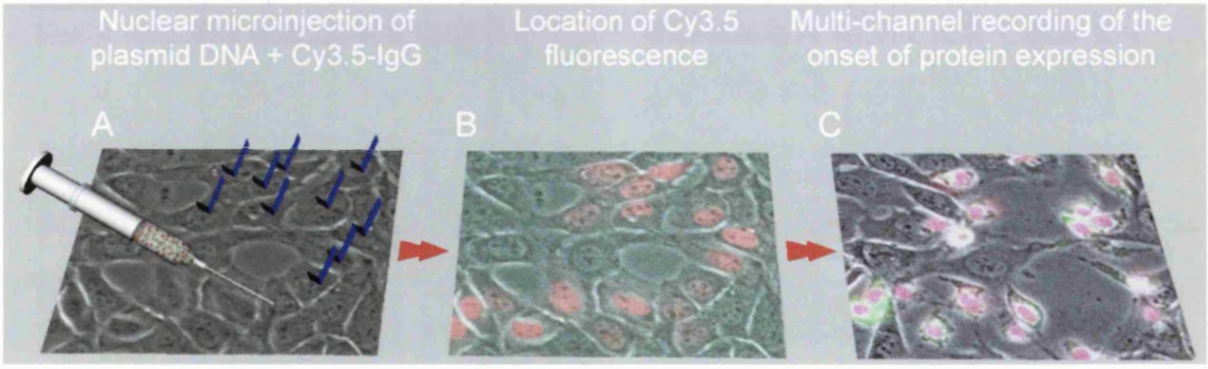

Figure 4. Summary of the in vitro assay for the assessment of NIH 3T3 cell death

(A) Groups of adjacent cells within a monolayer culture were microinjected in the nucleus with a mixture of 1 μg/μl Cy3.5-IgG and 0.05 μg/μl plasmid DNA encoding one of the EGFP Cx31 fusion constructs under investigation. Cultures were allowed 20 min to recover from microinjection. (B) Propidium iodide was added to the culture medium to a final concentration of 0.5 μg/ml and the microinjected cells then relocated under the microscope via detection of their Cy3.5-IgG labelled nuclei. (C) Multi-channel time-lapse recording was then used to monitor the onset of protein expression and any subsequent change in cell behaviour: Sequential phase contrast, EGFP, Cy3.5, and propidium iodide fluorescence images were acquired every 60 s in order to monitor the effects of protein expression on cell viability. The concentration of propidium iodide within the medium was sufficiently low that it could only be detected upon accumulation within the nuclei of dead cells. Cells were imaged for a 100 min duration.

and was defined as the centroid of the microinjected cell within the first frame of the film sequence. Cell movement within the monolayer was minimal over the course of time-lapse experiments and so it was considered unnecessary to score the cell position for each frame within the film sequence.

Image analysis: A single numerical value representing the normalised mean distance of dye transfer (*NMD*) was generated for each Alexa 568 fluorescence image within a film sequence and collectively these values then used to calculate the mean rate of dye transfer for a particular experiment. Alexa 568 fluorescence images were extracted from film sequences, binned to a pixel size of 2.6 × 2.6 μm (4 × 4 pixel binning) in order to remove high frequency noise, and thresholded in order to remove background. Single *NMD* values were then calculated for each image as:

$$NMD(t) = \frac{\sum (I_{xyt} \times d_{xyt})}{\sum I_{xyt}}$$

where I is the intensity at pixel (x, y) at time t and d is the distance of that pixel from the site of dye microinjection (defined by the pixel co-ordinate of the centroid of the cell initially microinjected with Alexa 568 dye). In multiplying pixel intensity by distance ($I_{xyt} \times d_{xyt}$), increasing bias was given to those intensity values that lay furthest from the site of initial dye microinjection. By increasing the significance of distant pixel values, greater discrimination could be made between those treatments that enhanced the rate of dye transfer and those that impeded this process. All pixel intensity-distance values were summed, $\Sigma(I_{xyt} \times d_{xyt})$, to produce a single value that represents the degree of dye displacement for that image time point. This value was then divided by the total image intensity in order to mean and normalise the data, thus deriving the *NMD* value for the image. *NMD* values calculated for

all Alexa 568 images within the first 10 min of a film sequence were then used to derive a single value that represented the mean rate of dye transfer for that particular experiment. Linear regression analysis (least squares fit) was applied to the *NMD* data and the slope of the resulting regression function taken to represent the mean rate of dye transfer. Significances in the differences in the mean rate of dye transfer between groups of sequences were evaluated by the two-sided t-test. All image-analysis software was written in the Mathematica programming language (Wolfram Research). The software code for the derivation of *NMD* values can be found in Appendices 5.1, page 19.

2.2.8 Evaluation of cell death in NEB1 keratinocytes

Nuclear microinjection: Confluent cell cultures of NEB-1 keratinocytes were prepared as described in section 2.2.6, page 19. Cells were transferred to experimental culture medium and confluent patches of cells within the central microwell of each dishes then selected for microinjection. Cells were microinjected in the nucleus with 0.05 μg/ml of plasmid DNA encoding either (wt)Cx31-EGFP, (R42P)Cx31-EGFP, or (C86S)Cx31-EGFP. Following microinjection cultures were transferred to fresh tissue culture medium and returned to the incubator where they were allowed 5 hours to express the microinjected constructs.

Assessment of cell death: Cells were treated with 0.5 μg/ml of the membrane-impermeable fluorescent dye propidium iodide (Sigma). After a 10 min incubation at 37 °C, expressing cells were located under the microscope and imaged in three separate channels (phase contrast, EGFP fluorescence, and propidium iodide fluorescence). Propidium iodide fluorescence was imaged using the Cy3/TRITC filter configuration. Cells were imaged on

the same Zeiss Axiovert 135 TV inverted microscope described in section 2.2.3, page 19 using the 20 × objective, NA 0.5, the CCD camera and the multiple dichromatic mirror in conjunction with motorised excitation and emission filter wheels. Once acquired propidium iodide and EGFP fluorescence images were overlaid and interactive tracking subsequently used to label cells as either dead or viable. Expressing cells were assigned to one of three possible categories: either (1) dead cells which exhibited bright propidium iodide nuclear staining and nuclear shrinkage, (2) cells in the process of dying which exhibited nuclear shrinkage but which were not yet positive for propidium iodide staining, and (3) viable cells that displayed a normal morphology and which were also negative for propidium iodide staining. Only cells that clearly exhibited nuclear staining with propidium iodide were scored as dead while only cells that exhibited an unaltered morphology as well as propidium iodide-negative staining were scored as viable. Therefore, cells that fell into the second category were regarded as indeterminate and ignored. Data were presented as percentages of the total number of cells scored for each treatment group, and tested for significant differences by analysis of variance (ANOVA).

2.2.9 Dynamic assessment of cell death in NIH 3T3 fibroblasts

Nuclear microinjection: Confluent cultures of NIH 3T3 fibroblast were prepared as described in section 2.2.6, page 19. Cells were transferred to experimental culture medium and confluent patches of cells within the central microwell of each dish selected for microinjection. Patches of adjacent cells were microinjected in the nucleus with a mixture of 1 μg/μl Cy3.5-conjugated sheep IgG (Cy3.5-IgG) and 0.05 μg/μl of plasmid DNA encoding either (wt)Cx31-EGFP, (R42P)Cx31-EGFP, or (C86S)Cx31-EGFP. Cells were transferred to

fresh tissue culture medium and returned to the incubator where they were allowed 20 min to recover from the process of microinjection.

Time-lapse microscopy: The occurrence of cell death following the expression of microinjected constructs was determined using multi-channel digital time-lapse microscopy. All experiments were conducted using the same Zeiss Axiovert 135 TV inverted microscope used for dye transfer experiments (see section 2.2.3, page 19). Prior to time-lapse recording cells were transferred to fresh experimental medium supplemented with 0.5 μg/ml propidium iodide. The culture dish was placed on the stage of the microscope in a steel humidity chamber to protect the sample from evaporation during the course of the experiment. The co-microinjection of Cy3.5-IgG provided a fluorescent nuclear marker that enabled microinjected cells to be re-located under the microscope prior to the expression of EGFP fusion constructs. A single patch of microinjected cells was selected for observation using time-lapse recording. Images were acquired every 60 seconds in four separate channels (phase contrast, EGFP fluorescence, Cy3.5 fluorescence, and propidium iodide fluorescence) using the 20 × objective NA 0.5, the CCD camera and the multiple dichromatic mirror in conjunction with motorised excitation and emission filter wheels. Cell behaviour was recorded for 100 min (100 acquisition rounds).

Three-channel fluorescence imaging: A specially developed technique enabled the sequential imaging of EGFP, Cy3.5, and propidium iodide fluorescence despite the partial overlap that existed between their excitation and emission spectra. The technique exploited the versatility

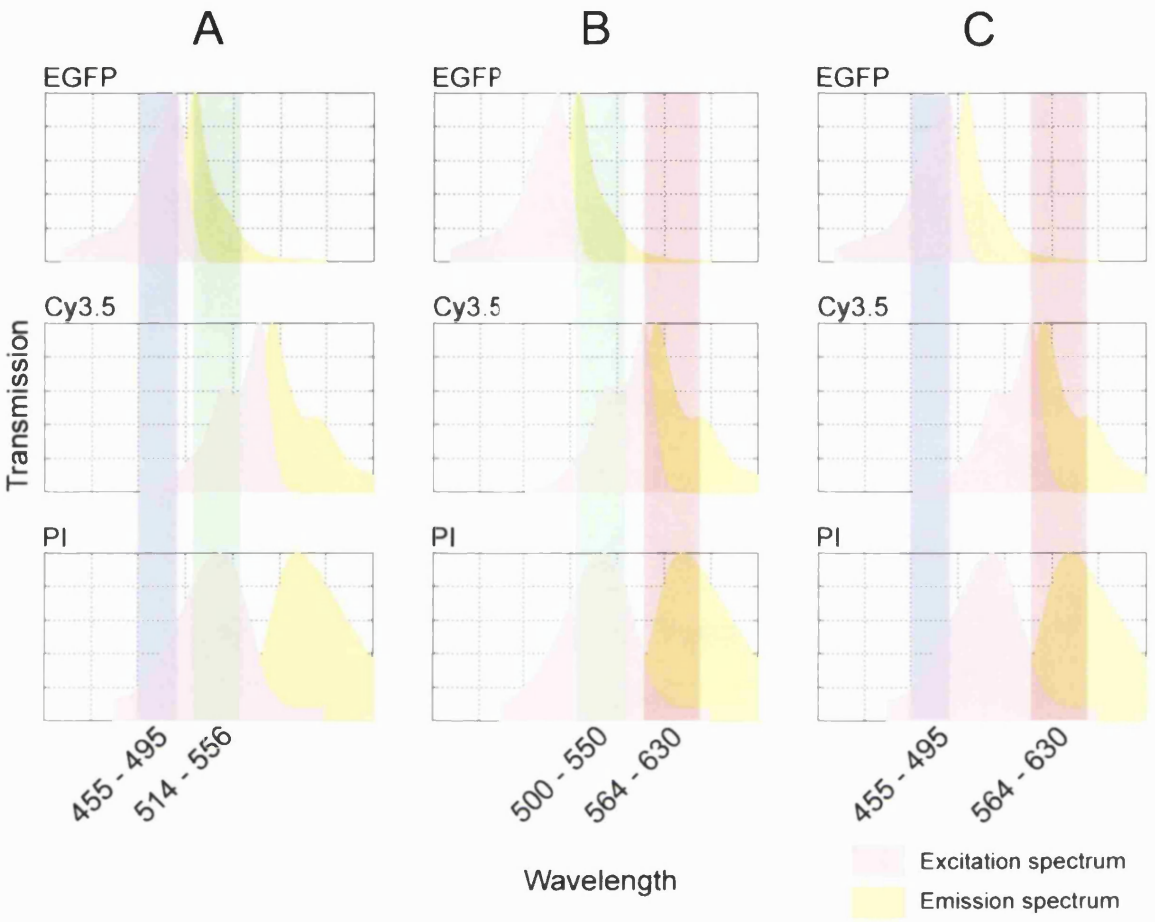

Figure 5. Three-channel fluorescence imaging

The sequential acquisition of EGFP, Cy3.5, and propidium iodide fluorescence was achieved by combining different excitation and emission filter combinations. The use of motorised excitation and emission filter wheels and a multiple dichromatic mirror enabled the different filter configurations to be selected automatically during the filming process. (A) EGFP fluorescence was imaged using a conventional configuration enabling fluorophore excitation between 455 – 495 nm and detection of fluorescence emission between 514 – 556 nm. This configuration did not allow significant excitation of Cy3.5 but did enable a degree of propidium iodide excitation. However, the emission filter only permitted the collection of EGFP fluorescence emission. (B) A conventional TRITC filter configuration was used to image Cy3.5 fluorescence providing excitation between 500 – 550 nm and detection of fluorescence emission between 564 – 630 nm. This enabled the effective excitation and fluorescence detection of Cy3.5 and propidium iodide but not EGFP. (C) The selective imaging of propidium iodide fluorescence was enabled by using the EGFP excitation filter (455 – 495 nm) in combination with the TRITC emission filter (564 – 630 nm). This enabled excitation of both EGFP and propidium iodide but not Cy3.5, while enabling the detection of propidium iodide and Cy3.5 fluorescence emission but not EGFP. Therefore, this filter combination only permitted the simultaneous excitation and detection of propidium iodide. PI = propidium iodide.

afforded by the use of motorised excitation and emission filter wheels and is described in detail in Figure 5, page 19. Briefly, while EGFP fluorescence and Cy3.5 fluorescence could be monitored independently using separated EGFP and TRITC filter configurations, propidium iodide fluorescence was detected using a miss-matched filter combination that is similar in principle to that used in sensitised emission FRET studies. By exploiting the relatively broad excitation spectrum of propidium iodide EGFP excitation light could be used to excite the fluorophore while its fluorescence emission could be detected using the TRITC/Cy3.5 emission filter specification. This allowed effective discrimination between all three fluorophores, while using filter sets essentially designed to discriminate between only two. The acquisition of EGFP fluorescence enabled the onset of protein expression to be monitored while the occurrence of cell death was determined by the subsequent uptake and accumulation of propidium within cell nuclei. Fluorescence images were pseudocoloured so that EGFP fluorescence appeared green, Cy3.5 fluorescence appeared red, and propidium iodide fluorescence appeared blue. Dead cells were therefore detected by a gradual change in the colour of nuclei from red (Cy3.5) to purple (Cy3.5 + propidium iodide). If expressed proteins did not result in death then cell nuclei would remain red throughout the entire recording period. The ambient concentration of propidium iodide within the surrounding culture medium was sufficiently low that it was undetectable. The assay developed for the study of NIH cell death is summarised in Figure 4, page 19.

Assessment of cell death: Acquisition Manager software was used to overlay the three separate fluorescence channels of film sequences applying the pseudocolour combinations described above. The final frame of the resulting merged film sequences was then extracted and used for scoring cell death. Motion Analysis software was used to interactively label

cells expressing the microinjected constructs. Cells expressing EGFP constructs were scored as dead if they exhibited purple nuclei and viable if their nuclei remained red. Data were expressed as percentages of total cells scored. The ANOVA comparison of the (R42P)Cx31-EGFP and (C86S)Cx31-EGFP treatment groups with the (wt)Cx31-EGFP treatment group by was used to derive significances that reflected the degree of cytotoxicity conferred by the different mutations.

2.2.10 Assay for assessing the intercellular transmission of a cell death signal

Nuclear microinjection: Confluent cultures of NEB-1 keratinocytes were prepared as described in section 2.2.6, page 19. Cells were transferred to experimental culture medium prior to nuclear microinjection, which was performed on the same microinjection system previously used for cytoplasmic microinjection (see section 2.2.3, page 19) due to the additional requirement for fluorescence detection. A confluent region within the central microwell of the dish was selected and adjoining cells then microinjected in the nucleus with a mixture of 1 μg/μl Cy3.5-IgG and 0.05 μg/μl of (wt)Cx31-EGFP plasmid DNA. This resulted in a tight patch of microinjected cells with Cy3.5-IgG labelled nuclei. A fresh microinjection needle was then used to microinject a mixture of 1 μg/μl Cy5-IgG and 0.05 μg/μl (C86S)Cx31-EGFP plasmid DNA into the nuclei of cells directly adjacent to the first patch, using the fluorescent lamp of the microscope to detect the position of previously microinjected cells. This resulted in the formation of two directly neighbouring patches of cells, which could be distinguished from one another on account of their different fluorescent nuclear markers. Following microinjection cells were transferred to fresh tissue culture

medium and returned to the incubator where they were allowed 1 hour to express the microinjected constructs.

Multi-channel imaging: 1 hour after microinjection cells were transferred to experimental culture medium and imaged on a Zeiss Axiovert 135 TV inverted microscope (see 2.2.3, page 19). Patches of expressing cells were identified and single phase contrast, EGFP, Cy3.5, and Cy5 fluorescence images then acquired using the relevant filter blocks in order to record the positions of the two cell patches. Cells were imaged using the 20 × NA 0.5 objective lens. Cells were then returned to the incubated and allowed to express constructs for a further 4 hours before re-imaging as described.

2.3 RESULTS

In this study a combination of microinjection, wide-field multi-channel digital time-lapse microscopy, and image processing was used to investigate *in vitro* the effects of different disease associated Cx31 mutations on intercellular communication and cell viability. Nuclear microinjection was used to introduce expression constructs encoding EGFP fusions of wild type and mutant forms of Cx31 into cells. The study focused on the skin disease-associated mutations, R42P and C86S, a deafness and peripheral neuropathy-associated mutation 66DelD and a Cx31 polymorphic variant, R32W, of unknown disease significance. The effects that different Cx31 mutations conferred on intercellular communication were assessed using dye transfer assays conducted on monolayer cell cultures. The use of EGFP fusion and the application of dye transfer assays to monitor gap junction mediated intercellular communication have previously been used successfully (Martin et al., 2001; Falk 2002). A novel technique combining multi-channel time-lapse microscopy and image analysis was developed that permitted the rate of dye transfer between adjacent cells to be numerically quantified, enabling any variations in the efficiency of intercellular dye transfer to be assessed in a statistically testable manner. Multi-channel time-lapse microscopy was also applied to the analysis of cell death and a novel assay was developed that exploited three-channel fluorescence imaging in order to monitor and confirm the onset of cell death following the ectopic expression of cytotoxic proteins.

2.3.1 Expression of (wt)Cx31-EGFP results in the formation of functional intercellular channels

Dye transfer rates between cells ectopically expressing (wt)Cx31-EGFP were used as a baseline comparison for the effects of Cx31 mutation on intercellular communication. It was

therefore important to assess the functionality of the wild-type protein in the cell lines studied. Adjacent cells in confluent monolayers were microinjected in the nucleus with an expression construct encoding (wt)Cx31-EGFP in order to generate tight patches of fluorescent cells. A single expressing cells on the perimeter of each patch was then selected for cytoplasmic microinjection with Alexa 568 dye and the process of intercellular dye transfer subsequently monitored by multi-channel time-lapse microscopy.

NEB1 cells expressing (wt)Cx31-EGFP exhibited an enhanced rate of dye transfer when compared to non-expressing cells (Figure 6, page 19, compare A & C with E & G). Alexa 568 dye transferred most rapidly through adjoining (wt)Cx31-EGFP expressing cells when compared to their non-expressing neighbours, indicating that the expressed protein could form functional intercellular channels (E & G). Interestingly, the extent to which dye transferred between NEB1 cells varied considerably between experiments, possibly reflecting a variation in the expression levels of the endogenous protein or channel activity states between cells in the local population. While some (wt)Cx31-EGFP expressing cells exhibiting a significant ability to transfer dye others showed relatively poor transfer rates in comparison. A similar variation in dye transfer efficiency could also be seen in the uninjected cell population. However, in all cases dye transferred preferentially through the (wt)Cx31-EGFP expressing cell population. (wt)Cx31-EGFP exhibited both a punctate cytoplasmic and plasma membrane localisation. The aggregation of protein at the plasma membrane was most common at sites of cell-cell contact, suggesting the formation of gap-junction plaques (E & F, arrows).

The functionality of (wt)Cx31-EGFP was also assessed in NIH 3T3 fibroblasts (Figure 7, page 19). Although NIH 3T3s express endogenous Cx31 (Di et al., 2002) the basal level of dye transfer in the non-expressing cell population was poor. Indeed, dye rarely propagated further than those cells directly bordering the microinjected cell over the entire duration observed (A & C). In dramatic contrast however Alexa 568 dye rapidly propagated through the (wt)Cx31-EGFP expressing cell population (E & G). Indeed, in the short time interval that elapsed between the cytoplasmic microinjection of a single fluorescent cell with dye and the commencement of filming, the dye had often already spread significantly through the adjoining (wt)Cx31-EGFP expressing cells. The steady rate at which dye transferred through NIH 3T3s expressing (wt)Cx31-EGFP suggested that channels exhibited uniform activity in these cells and that levels of endogenous protein were sufficiently low not to influence the effects of the exogenous protein. The subcellular localisation of the expressed protein was similar to that seen in NEB1 cells with (wt)Cx31-EGFP displaying a predominantly punctate cytoplasmic and plasma membrane localisation.

Collectively these experiments demonstrated that (wt)Cx31-EGFP could form functional intercellular channels in both NEB1 keratinocytes and NIH 3T3 fibroblasts. These cell lines therefore provided useful models for the study of Cx31 mutation. Furthermore these studies validate the use of Alexa 568 dye as a suitable fluorescent tracer for the assessment of intercellular channel function, indicating that this 0.731 kDa fluorophore of net negative charge could efficiently pass through functional, homotypic Cx31 channels.

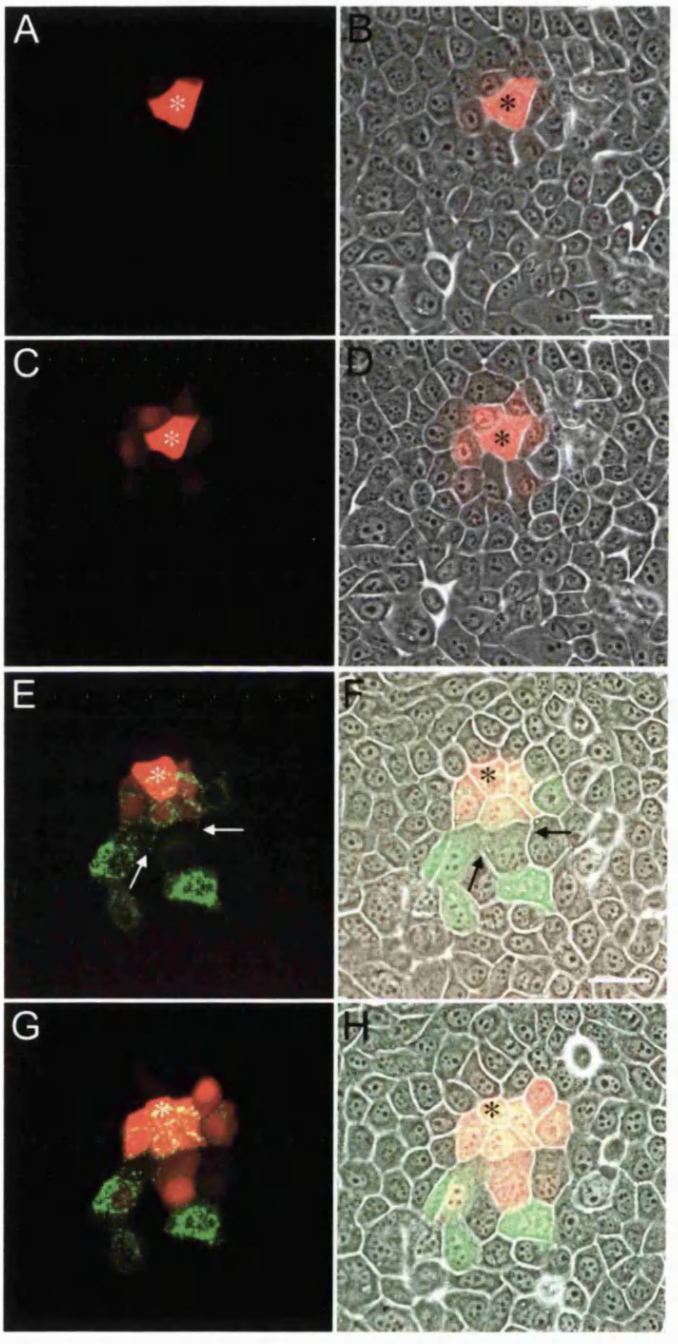

Figure 6. Expression of (wt)Cx31-EGFP enhances dye transfer in NEB1 keratinocytes

Preferential spread of Alexa 568 dye through (wt)Cx31-EGFP expressing cells. Images (A – D) demonstrate the basal level of dye transfer in NEB1 cells. Images (A & C) show Alexa 568 fluorescence and (B & D) Alexa 568 fluorescence with additional phase contrast overlaid. Images (A & B) represent the first time point of the time-lapse sequence and (C & D) the last, and were acquired 33 min later. An asterix indicates the cell initially microinjected with dye. Over the whole period observed basal levels of dye transfer were poor, with dye spreading only as far as the immediately adjoining cells. Images (E – H) demonstrate the enhanced rate of dye transfer observed in cell expressing (wt)Cx31-EGFP. Images show EGFP fluorescence (green) and Alexa 568 fluorescence (red) either without (E & G) or with (F & H) phase contrast overlaid to indicate the surrounding non-expressing cells. Image time points as described for (A – D). The expressed protein displayed a predominantly punctate cytoplasmic localisation but protein aggregation at sites of cell-cell contact was also evident (arrows), suggesting the formation of intercellular channels. Asterix indicate the cell initially microinjected with dye. Alexa 568 dye transferred rapidly and preferentially through the expressing cell population indicating that the expressed protein could form functional gap junctions. Scale bars = 50 μm.

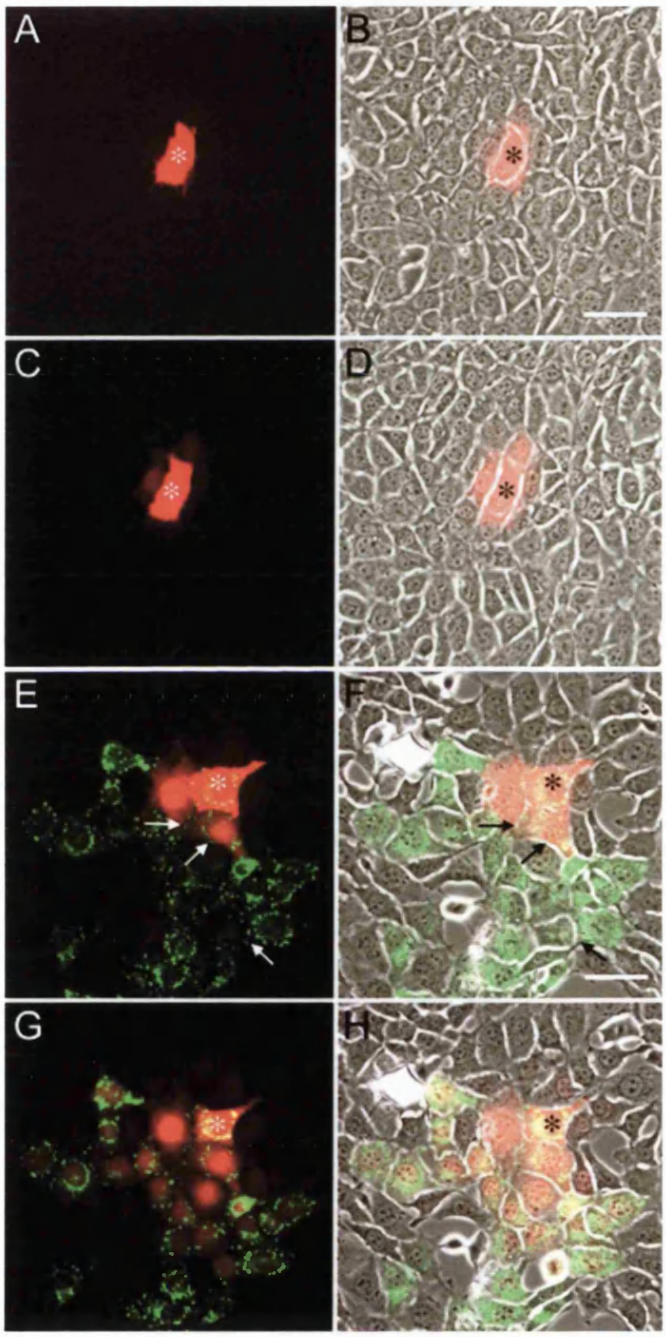

Figure 7. Expression of (wt)Cx31-EGFP enhances dye transfer in NIH 3T3 fibroblasts

Preferential spread of Alexa 568 dye through (wt)Cx31-EGFP expressing cells. Images (A – D) demonstrate the basal level of dye transfer in NIH 3T3 cells, while images (E – H) demonstrate the enhanced rate of dye transfer through (wt)Cx31-EGFP expressing cells. All image compositions and time points are as described for Figure 6. In each case an asterix indicates the cell initially microinjected with dye. The basal level of dye transfer in the non-expressing cell population was consistently poor (A & C). In dramatic contrast dye spread rapidly through (wt)Cx31-EGFP expressing cells (E & G). Phase contrast overlays reveal the surrounding non-expressing cells and clearly demonstrate the preferential transfer of dye through expressing cells. As with NEB1 cells the expressed protein displayed a predominantly punctate cytoplasmic localisation but protein aggregation at sites of cell-cell contact was also evident (arrows), again suggesting the formation of intercellular channels.
Scale bars = 50 μm.

2.3.2 The R32W and 66DelD Cx31 mutations inhibit channel function

Dye transfer studies were performed in order to assess the effects of the polymorphic variant R32W and the deafness and peripheral neuropathy mutation 66DelD on Cx31 mediated intercellular communication. Adjacent cells in confluent monolayers of either NEB1 keratinocytes or NIH 3T3 fibroblasts were microinjected in the nucleus with expression constructs and dye transfer assays subsequently performed on the resulting patches of fluorescent cells.

In contrast to observations made with the wild type protein the ectopic expression of (R32W)Cx31-EGFP in NEB1 cells did not seem to elevate the rate of dye transfer above that of basal levels, indicating that this polymorphic variant could not form functional intercellular channels (Figure 8 E & G). Alexa 568 dye was largely confined to the microinjected cell and rarely spread beyond the immediately adjoining cells over the entire duration observed. The effects that the R32W polymorphism conferred on intercellular channel formation were most apparent from additional studies performed in NIH 3T3s. In striking contrast to observations made with the wild type protein, little to no dye transfer was observed following the microinjection of dye into (R32W)Cx31-EGFP expressing cells. This is clear from the film sequence in (Figure 9 E & G), where, even after a period of 30 min dye is barely detectable in the cells surrounding the microinjected cell.

In both NEB1 and NIH 3T3 cells (R32W)Cx31-EGFP exhibited a punctate cytoplasmic localisation similar to that observed with the wild type protein but with less pronounced

protein aggregation at the plasma membrane. It is interesting to note that, although previously reported to be a Cx31 polymorphism with no associated disease phenotype (Kelsell et al., 2000; Lopez-Bigas et al., 2000), the R32W variant evidently constitutes a dysfunctional connexin protein. It is therefore possible that this variant may be of some significance in disease.

(66DelD)Cx31-EGFP also did not form functional intercellular channels, as expression of the protein did not enhance the rate of dye transfer above that of basal levels in either NEB1 or NIH 3T3 cells (Figure 8 I & K, Figure 9 I & K). Again the effects of this mutation were most apparent from studies performed in NIH 3T3s where the basal level of dye transfer was almost undetectable. In both cell types the protein exhibited a largely diffuse cytoplasmic localisation, although some punctate localisation within the cytoplasm was observed at higher levels of expression. Therefore the subcellular localisation of this mutant was distinct from both that of the wild type protein and the R32W polymorphic variant. The detection of (66DelD)Cx31-EGFP at the plasma membrane was rare, suggested that a trafficking defect may underlie the inability of this protein to form functional intercellular channels.

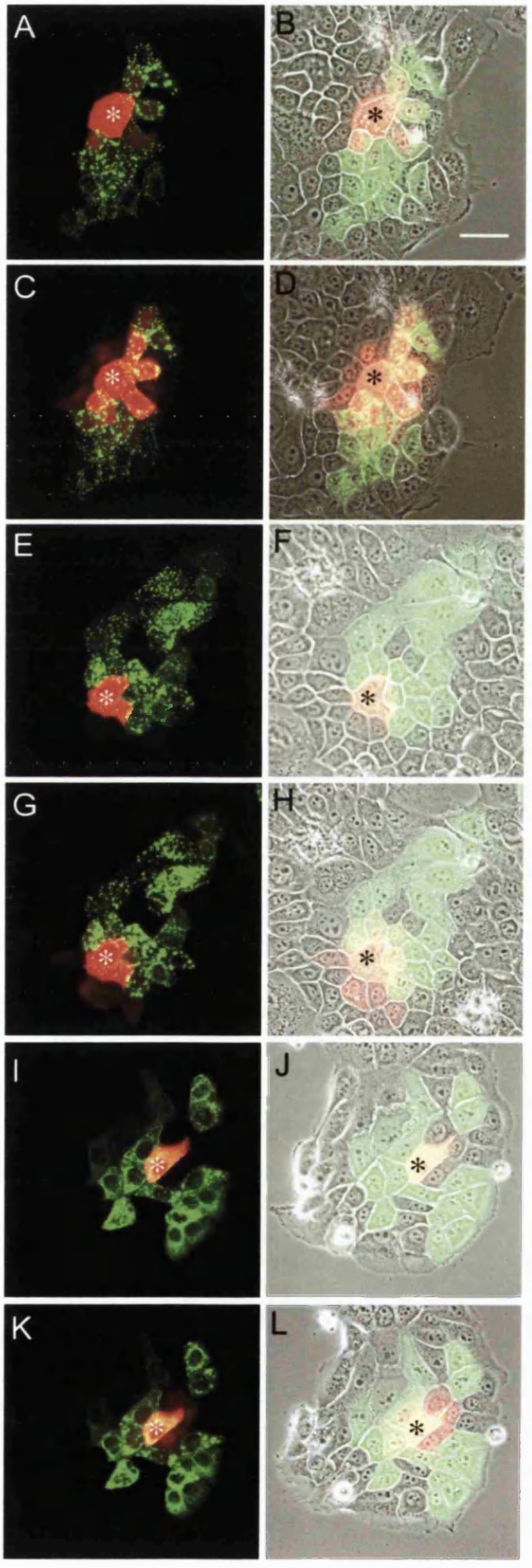

Figure 8. Intercellular dye transfer in NEB1 keratinocytes

Effects of Cx31 mutations on Alexa 568 dye transfer in NEB1 keratinocytes. Images show EGFP fluorescence and Alexa 568 fluorescence overlays either with or without phase contrast to reveal surrounding non-expressing cells (right and left columns respectively). Images are taken from representative NEB1 dye transfer film sequences and show cells expressing either (wt)Cx31-EGFP (A - D), (R32W)Cx31-EGFP (E - H), or (66DelD)Cx31-EGFP (I & L). Images A & B, E & F, I & J represent the first time point of the time lapse sequence while images C & D, G & H, K & L represent the last time point of the time lapse sequence and were acquired 33 min later. For each dye transfer experiment a group of fluorescent cells were located and a single cell close to the patch perimeter then selected for cytoplasmic microinjection with Alexa 568 dye. Filming commenced immediately after dye injection. For each image an asterix identifies the cell originally microinjected with Alexa dye. Note the relatively efficient dye transfer between cells expressing the wild type protein compared to cells expressing either the (R32W)Cx31-EGFP, or the (66DelD)-Cx31-EGFP variants. Scale bar = 50 μm.

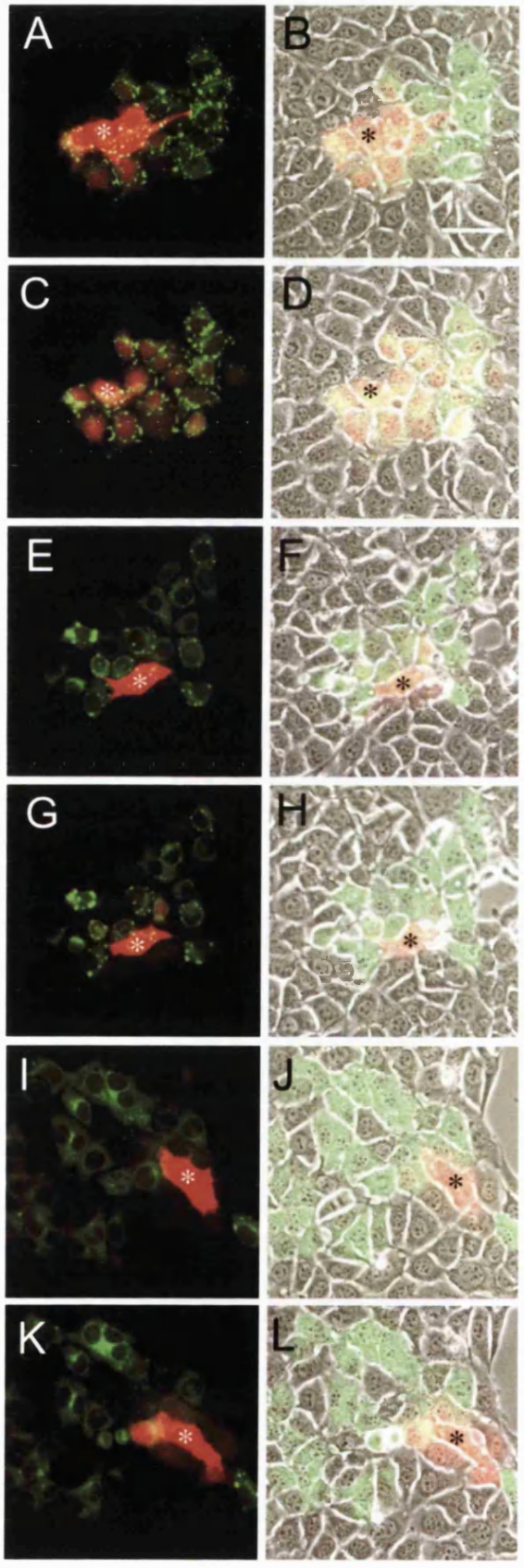

Figure 9. Intercellular dye transfer in NIH 3T3 fibroblasts

Effects of Cx31 mutations on Alexa 568 dye transfer in NIH 3T3 fibroblasts. Images show EGFP fluorescence and Alexa 568 fluorescence overlays either with or without phase contrast to reveal surrounding non-expressing cells (right and left columns respectively). Images are taken from representative NIH 3T3 dye transfer film sequences and show cells expressing either (wt)Cx31-EGFP (A - D), (R32W)Cx31-EGFP (E - H), or (66DelD)Cx31-EGFP (I - L). Image time points are the same as those described for NEB1 experiments (see Figure 8) and represent the first and last images of film sequences. For each image an asterix identifies the cell originally microinjected with Alexa dye. As with NEB1 experiments, dye transfer between NIH 3T3 fibroblasts expressing the wild type protein was far more efficient that between cells expressing either the (R32W)Cx31-EGFP, or the (66DelD)-Cx31-EGFP variants. Note that dye transfer into the non-expressing cell population was almost undetectable (C & D).
Scale bar = 50 μm.

2.3.3 Quantitative analysis of the effects of Cx31 mutation on the rate of dye transfer

The unequivocal confirmation that dye transfer rates differed significantly between cell populations expressing different Cx31 variants required the statistical comparison of experimental data. This was especially important with respect to observations made in NEB1 cells where the basal level of dye transfer was often highly variable and the functionality of the wild type protein less uniform. In order to assess experimental observations objectively image processing and analysis techniques were specially developed that numerically quantified the rate at which dye spread through cell populations. For a full description of the image processing and analysis techniques developed see methods section 2.2.7, page 19. Briefly, individual Alexa 568 fluorescence images extracted from the first ten minutes of time-lapse sequences were normalised and converted to single values that represented the normalised mean distance of dye transfer (*NMD*) at each given image time point. Linear regression analysis was then applied to the *NMD* data calculated for a particular film sequence and the slope of the regression function taken to represent the mean rate of dye transfer for that experiment. Therefore each experiment yielded a single value that represented the mean rate of dye transfer. Significances of the differences of the dye transfer rates between groups of sequences could then be evaluated using the two-sided *t*-test.

Figure 10, Figure 11, and Figure 12 (pages 19 - 19) demonstrate the processing involved in the derivation of *NMD* values and dye transfer rates and represent images and data from the same (wt)Cx31-EGFP, (R32W)Cx31-EGFP, (66DelD)Cx31-EGFP NIH film sequences shown in Figure 9, page 19. These examples clearly show that *NMD* values provided an effective means of representing the extent of dye transfer within individual Alexa 568

images. The *NMD* plots generated for the first 10 min of each film sequence also demonstrate that a linear function could effectively approximate the change in dye dispersal over this period and therefore linear regression analysis provided an appropriate means of representing the mean rate of dye transfer for individual experiments. However, it should be noted that the application of a more complex function would have been required if longer time points were assessed due to the non-linear properties of diffusion. Comparison of the linear regression functions derived for each film sequences clearly reveals the differing rates at which dye transferred between cells expressing (wt)Cx31-EGFP and cells expressing either (R32W)Cx31-EGFP or (66DelD)Cx31-EGFP. Mean rates of dye transfer were calculated as shown for all (wt)Cx31-EGFP, (R32W)Cx31-EGFP, and (66DelD)Cx31-EGFP dye transfer experiments conducted in both the NEB1 and NIH 3T3 cell lines. The data are summarised in Figure 13, page 19. The statistical analysis of group data revealed significant differences between the mean dye transfer rates calculated for (wt)Cx31-EGFP expressing cells and those calculated for cells expressing either (R32W)Cx31-EGFP or (66DelD)Cx31-EGFP, therefore confirming that these mutations prevented the formation of functional intercellular channels (Table 2, page 19).

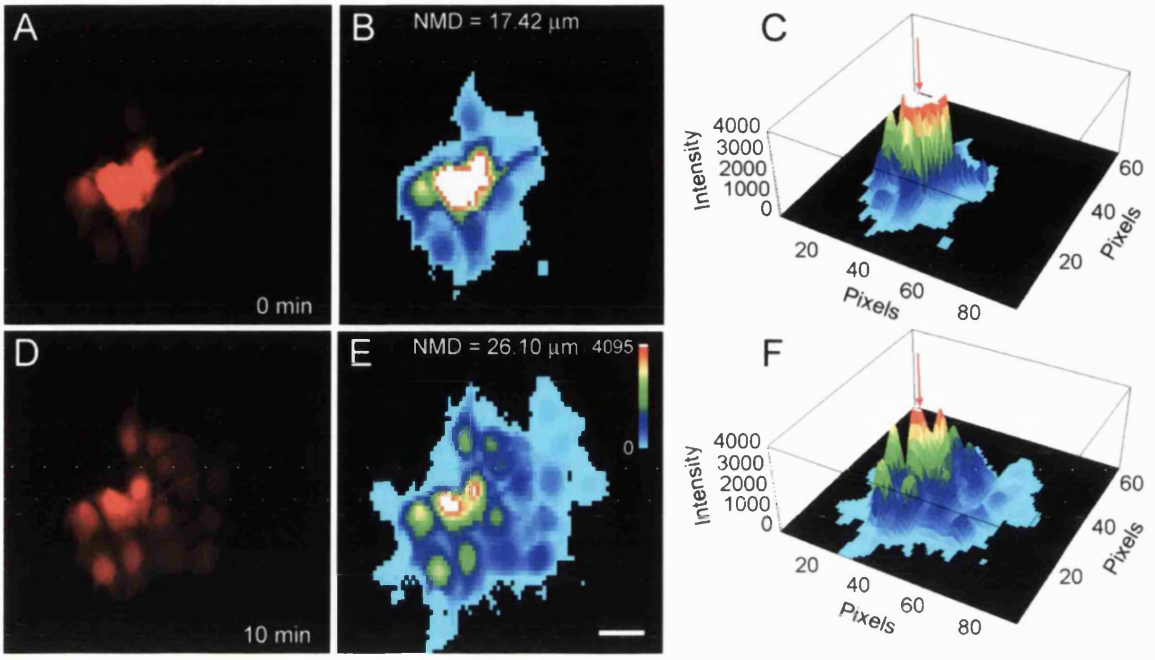

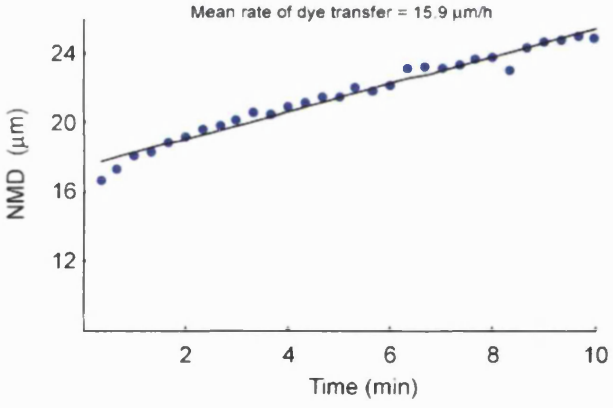

Figure 10. Derivation of the dye transfer rate for a (wt)Cx31-EGFP film sequence

Processing of Alexa 568 fluorescence images from a single (wt)Cx31-EGFP experiment for the calculation of the rate of dye transfer. (A & D) represent fluorescence images of Alexa 568 dye taken from the same NIH 3T3 (wt)Cx31-EGFP dye transfer experiment shown in Figure 9 (A - D). Images represent 0 & 10 min time points respectively. (B & E) represent post-processed pseudocoloured images of (A & D): images were cropped, binned to a pixel size of 2.6 × 2.6 µm and automatically thresholded before the calculation of the normalised mean distance of dye transfer (NMD). (C & F) are three-dimensional representations of (B & E), and are also displayed in pseudocolour. 3D plots demonstrate effectively the degree to which dye spread between adjoining cells over the first 10 min of the film sequence (red arrow indicates the position of the cell originally microinjected with dye). A single NMD value was calculated for each processed image and was taken to represent the mean distance of dye transfer for that image time point. NMD values derived from a sequence of images were used for the calculation of the mean rate of dye transfer: Plot (C) shows the NMD values calculated for Alexa 568 fluorescence images from the first 10 min of the film sequence (20 s time points). The slope of the regression function (line of least squares fit) of the NMD data was taken to represent the mean rate of dye transfer over the period analysed (calculated in µm/h). A single film sequence therefore yielded a single value that represented the mean rate of dye transfer. Pseudocoloured images are defined by the accompanying scale. Scale bar = 30 µm.

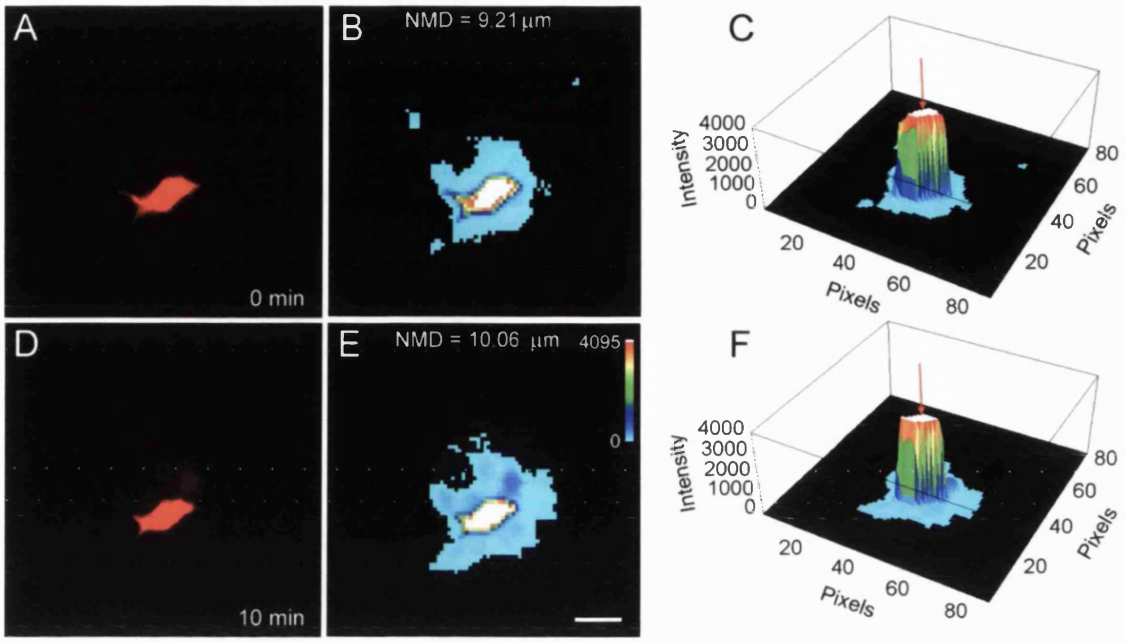

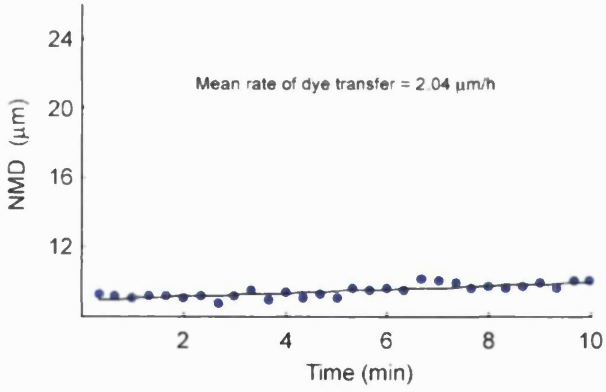

Figure 11. Derivation of the dye transfer rate for a (R32W)Cx31-EGFP film sequence

(A and D) represent fluorescence images of Alexa 568 dye taken from the same NIH 3T3 (R32W)Cx31-EGFP dye transfer experiment shown in Figure 9 (E – H). Images represent 0 & 10 min time points respectively. (B & E) represent post-processed pseudocoloured images of (A & D). Images were processed as described in Figure 10. (C & F) are three-dimensional representations of (B & E), and are also displayed in pseudocolour (red arrow indicates the position of the cell originally microinjected with dye). (C) A plot of NMD values calculated for Alexa 568 fluorescence images from the first 10 min of the film sequence. The slope of the least squares fit of the NMD data was taken to represent the mean rate of dye transfer over the period analysed (calculated in µm/h). Pseudocoloured images are defined by the accompanying scale. Scale bar = 30 µm.

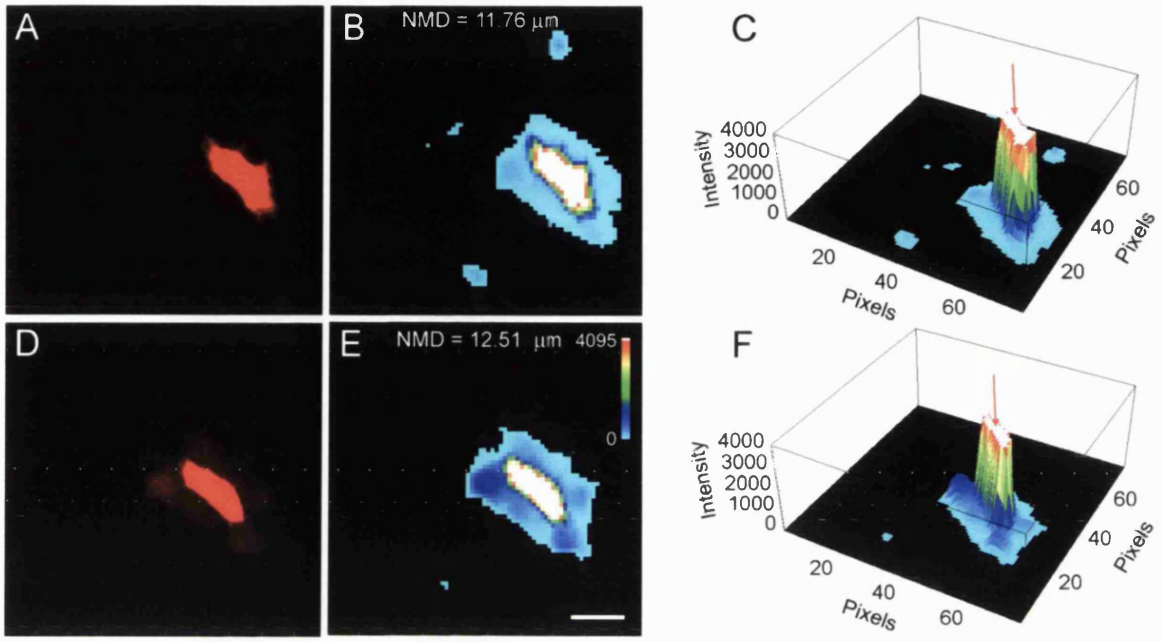

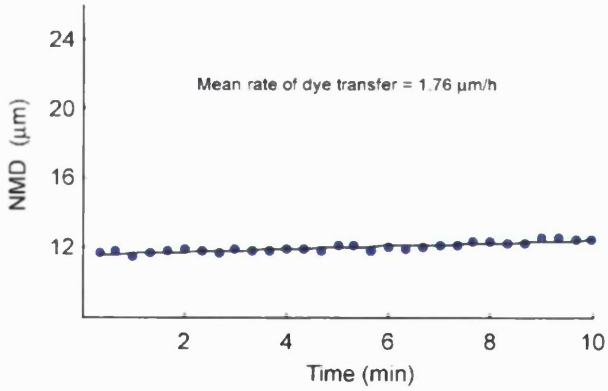

Figure 12. Derivation of the dye transfer rate for a (66DelD)Cx31-EGFP film sequence

(A and D) represent fluorescence images of Alexa 568 dye taken from the same NIH 3T3 (66DelD)Cx31-EGFP dye transfer experiment shown in Figure 9 (I - L). Images represent 0 & 10 min time points respectively. (B & E) represent post-processed pseudocoloured images of (A & D). Images were processed as described in Figure 10. (C & F) are three-dimensional representations of (B & E), and are also displayed in pseudocolour (red arrow indicates the position of the cell originally microinjected with dye). (C) A plot showing the NMD values calculated for Alexa 568 fluorescence images from the first 10 min of the film sequence. The slope of the least squares fit of the NMD data was taken to represent the mean rate of dye transfer over the period analysed (calculated in µm/h). Pseudocoloured images are defined by the accompanying scale. Scale bar = 30 µm.

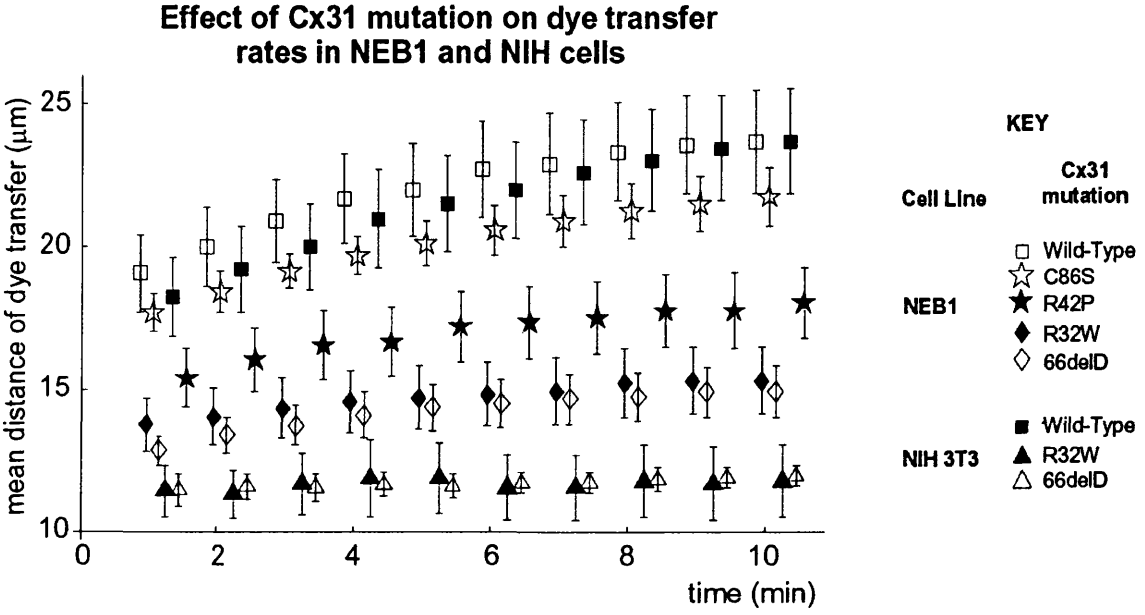

Figure 13. Effects of Cx31 mutation on dye transfer rates in NEB1 and NIH 3T3 cells

Plot summarising time courses of normalised mean distances of dye transfer (NMD) for different experimental groups of NEB1 and NIH 3T3 cells expressing various EGFP-Cx31 mutations. Normalised mean distances, partitioned into 60 s time bins, are represented by mean values (points) and standard errors of sample mean (bars). NMD values were calculated for Alexa 568 fluorescence images taken from the first 10 min of film sequences and each plot represents data pooled from multiple experiments within the same treatment group. For both cell lines plots clearly show that dye transfer rates were significantly reduced in cells expressing either the R32W or the 66DelD mutants when compared to cells expressing the wild type protein. In NEB1 cells the C86S mutation did not significantly impair dye transfer. The R42P mutation did however appear to reduce the rate of dye transfer, although to less of a degree than the R32W and 66DelD mutations.

	Dye Transfer Analysis				
Cell Line	**Cx31 mutation**	**Number of films**	**Mean rate of dye transfer (μm/h)**	**Standard error**	**Two sided t-test sig.**
NEB1	Wild-Type	10	10.06	1.92	-
	C86S	4	8.80	1.02	n.s.
	R42P	5	5.38	0.79	*
	R32W	8	3.47	0.65	**
	66delD	5	4.39	1.03	*
NIH 3T3	Wild-Type	11	11.98	1.50	-
	C86S	N/A	N/A	N/A	N/A
	R42P	N/A	N/A	N/A	N/A
	R32W	7	0.62	1.46	***
	66delD	5	1.02	0.97	***

Table 2. The statistical evaluation of dye transfer data

The above table summarises data from all dye transfer experiments, and indicates the significance of the effects of different Cx31 mutations on the rate of dye transfer in NEB1 and NIH 3T3 cells. For individual experiments the rate of dye transfer was defined as the slope of the regression function calculated for NMD values derived for the first ten minutes of the film sequence. For a particular cell line data calculated for each treatment group were compared to those calculated for the wild type control group using a two-sided t-test in order to derive significances that represented the degree to which various Cx31 mutations effected dye transfer. The mean rate of dye transfer is calculated as the mean slope of the linear regression functions representing a particular treatment group and is expressed in μm/h. Note that dye transfer experiments could not be conducted in NIH 3T3 fibroblasts expressing either the R42P or the C86S Cx31 mutants due to the extremely high instance of death that these proteins caused in this cell line.

2.3.4 *The R42P and C86S Cx31 mutations induce death in NEB1 keratinocytes but only C86S permits channel function*

EGFP-Cx31(R42P): It was apparent from microinjection studies that the EKV-associated Cx31 mutations R42P and C86S conferred a detrimental effect on NEB1 keratinocytes, resulting in an increased instance of cell death. This phenomenon was not observed following expression of any of the other Cx31 variants studied. Multi-channel time-lapse microscopy was used to further characterise the effects of the R42P and C86S mutations on cell morphology. Where possible, dye transfer studies were also performed in order to establish whether expressed proteins could form functional intercellular channels.

Expression of (R42P)Cx31-EGFP resulted in two distinct cellular phenotypes. The first was characterised by a dramatic change in cell morphology including extensive cell blebbing and nuclear shrinkage, two phenotypes often associated with cell death (Figure 14, page 19). These cells adhered poorly to the substrate and were difficult to microinject during dye transfer experiments. In cases where microinjection was successful dye did not transfer to neighbouring cells but merely leaked out from the cell into the surrounding medium (B – D). The mutant protein was often found to express poorly and localised to a predominantly perinuclear region. Additional studies revealed that cells displaying this phenotype often exhibited positive nuclear staining for the DNA inter-collating fluorescent marker propidium iodide, indicating that plasma membrane integrity had been lost (Figure 15 A & B, page 19). This was a clear indication that protein expression had resulted in cell death.

The second phenotype associated with the expression of (R42P)Cx31-EGFP was similar to that of the surrounding non-expressing cells. In these cells the expressed protein was, to some

extent, observed at the plasma membrane (Figure 16, page 19 A & B arrows). However, dye transfer experiments revealed that channel function was significantly impaired (Figure 16 A - D, Figure 13, page 19, Table 2, page 19), although, not as severely as seen for the R32W and 66DelD mutations. Cells that exhibited this second phenotype did not stain positive for propidium iodide indicating that (R42P)Cx31-EGFP expression was not always lethal. Indeed, the frequency of death was low following (R42P)Cx31-EGFP expression, occurring in approximately 10 % of cells (Figure 18A, page 19, & Table 3, page 19). Interestingly, there did not seem to be a clear correlation between the onset of cell death and the intensity of protein expression suggesting that corresponding levels of endogenous protein expression may in part have determined cell survival. This, however, was not explored further.

EGFP-Cx31(C86S): As with (R42P)Cx31-EGFP, NEB1 cells expressing (C86S)Cx31-EGFP exhibited two major phenotypes; those that showed profound blebbing and nuclear shrinkage, and those that were similar to the surrounding non-expressing cell population. Again cell blebbing and nuclear shrinkage corresponded with positive nuclear labelling with propidium iodide, indicating that protein expression resulted in cell death (Figure 15 C & D, page 19). In the normal phenotype where membrane integrity remained intact, the protein displayed a largely punctate cytoplasmic localisation. However, to some extent, aggregation of protein at the plasma membrane was also observed, although this was not as striking as that seen with the wild-type protein. The cytotoxicity of the C86S mutation was far greater than that observed for the R42P mutation, resulting in the death of over 50 % of expressing cells (Figure 18A, page 19 & Table 3, page 19). Interestingly, however, although often lethal the C86S mutation did not inhibit the formation of functional intercellular channels and dye

transfer rates in (C86S)Cx31-EGFP expressing cells were comparable to those observed in cells expressing the wild type protein (Figure 16 E - H, page 19, Figure 13, page 19, Table 2, page 19).

Figure 17 (page 19) represents images taken from a (C86S)Cx31-EGFP time-lapse sequence where the onset of cell death coincided with the recording of a dye transfer experiment. Initially the (C86S)Cx31-EGFP expressing cells exhibited a normal healthy phenotype and the microinjected dye was observed to spread preferentially through the fluorescent cell population, indicating the formation of functional intercellular channels (Figure 17B). However, as time progressed the cells began to die. Note the progressive nuclear shrinkage commonly associate with the cytotoxic effects of this protein (Figure 17 B – D, white arrow). As plasma membrane integrity was finally lost, the Alexa 568 dye leaked out into the surrounding medium and was no longer detectable. The onset of cell death was unlikely to be the cause of cytoplasmic microinjection as four other independent dye transfer experiments were conducted in (C86S)Cx31-EGFP expressing cells where cell death was not observed. Furthermore, cells that had not yet received the Alexa 568 dye were also observed to die.

Interestingly, the C86S and R42P mutants differed significantly with respect to both cytotoxicity and their capacity to form functional intercellular channels when expressed in NEB1 cells. The toxicity of the C86S mutation was five-fold that of the R42P mutation while, in contrast the C86S mutant was far more effective at forming functional intercellular channels than the R42P mutant. Cell death was, however, a common feature of EKV-associated Cx31 mutation.

A common phenomenon associated with both R42P and C86S related cell death was that the onset of cell death appeared to be synchronised. Cells were always microinjected with expression constructs in tight patches and following protein expression either all the cells within a single patch would die or all would survive. Indeed, separate patches of dead or viable cells would often be observed within a single tissue culture dish. Since both dead and viable cells were never found to occur within the same patch it was hypothesised that synchronised cell death was triggered by the generation of an intercellular diffusible second-messenger signal. This would have also accounted for the greater cytotoxic effects associated with (C86S)Cx31-EGFP expression as the C86S mutation did not significantly impair the formation of functional intercellular channels. In an attempt to test this hypothesis patches of (wt)Cx31-EGFP and (C86S)Cx31-EGFP expressing cells were created that directly bordered one another. In principle, assuming that Cx31-mediated heterologous coupling was possible between the two cell populations, any diffusible signal generated in the (C86S)Cx31-EGFP expressing population would be free to pass through to the (wt)Cx31-EGFP expressing population and therefore ultimately result in the death of both cell populations. Co-microinjection of fluorescent-IgG markers with expression constructs enabled the effective discrimination of (C86S)Cx31-EGFP and (wt)Cx31-EGFP expressing cells (Figure 19, page 19). Eight independent experiments revealed that, in all cases, the onset of cell death in the (C86S)Cx31-EGFP expressing cell population had no effect on the adjoining (wt)Cx31-EGFP expressing cell population. This suggests that cell death was not the consequence of a Cx31-mediated diffusible second-messenger signal.

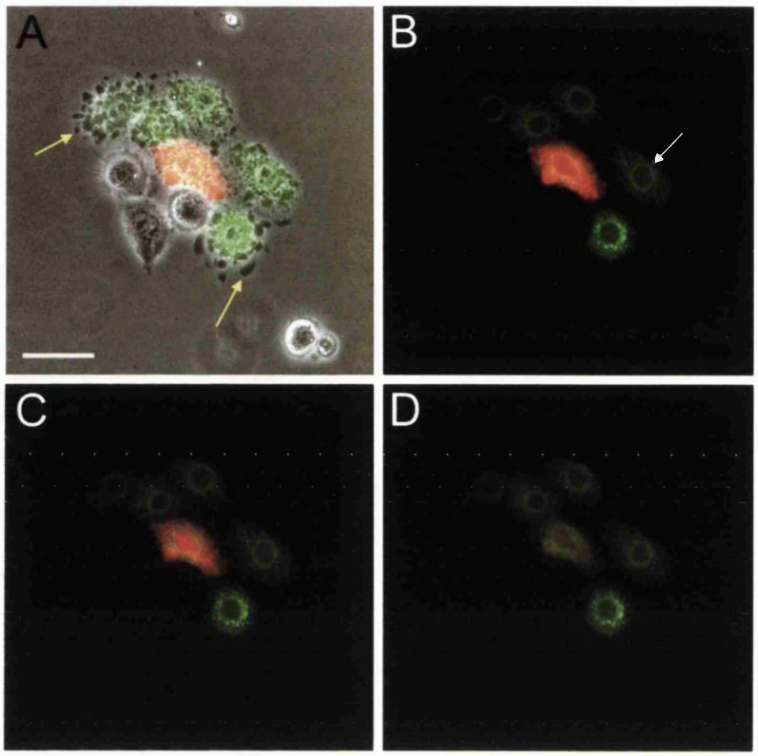

Figure 14. (R42P)Cx31-EGFP expression induces death in NEB1 cells

Expression of (R42P)Cx31-EGFP induced death in NEB1 keratinocytes. Images are derived from an (R42P)Cx31-EGFP time-lapse experiment and show EGFP and Alexa 568 fluorescence overlays either with (A) or without phase contrast (B, C & D). Images represent 0 min, (A & B), 15 min (C), and 30 min (D) time points. The mutant protein displayed a largely perinuclear localisation and induced membrane blebbing, nuclear shrinkage and cell detachment from the underlying substrate. Following microinjection Alexa 568 dye rapidly leaked out from the cell indicating a loss of plasma membrane integrity, a clear indication that the cell had died. White and yellow arrows highlight example of membrane blebbing and nuclear shrinkage respectively. Scale bar = 50 μm.

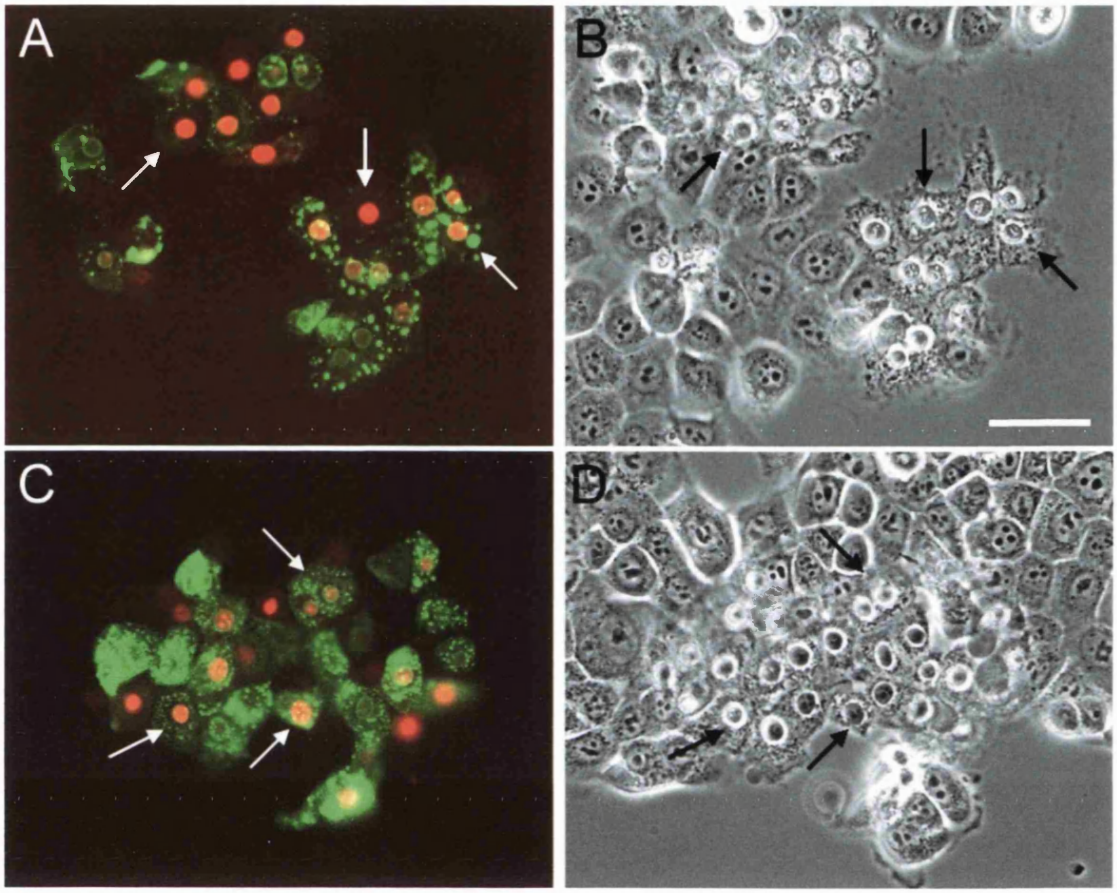

Figure 15. Confirmation of cell death in NEB1 cells

The nuclear uptake of propidium iodide confirmed the onset of cell death following expression of either (R42P)Cx31-EGFP or (C86S)Cx31-EGFP in NEB1 keratinocytes. (A & C) represent EGFP and propidium iodide fluorescence overlays for (R42P)Cx31-EGFP and (C86S)Cx31-EGFP expressing cells respectively. (B & D) represent phase contrast images of the same observation fields shown in (A & C). Cell death was specific for the expressing cell population: propidium iodide staining of nuclei indicated a loss of membrane integrity following the expression of the R42P and C86S Cx31 mutants, a clear sign that cells had died. White arrows indicate examples of positive nuclear staining and corresponding black arrows in phase contrast images highlight the associated cellular phenotype. Scale bar = 50 μm.

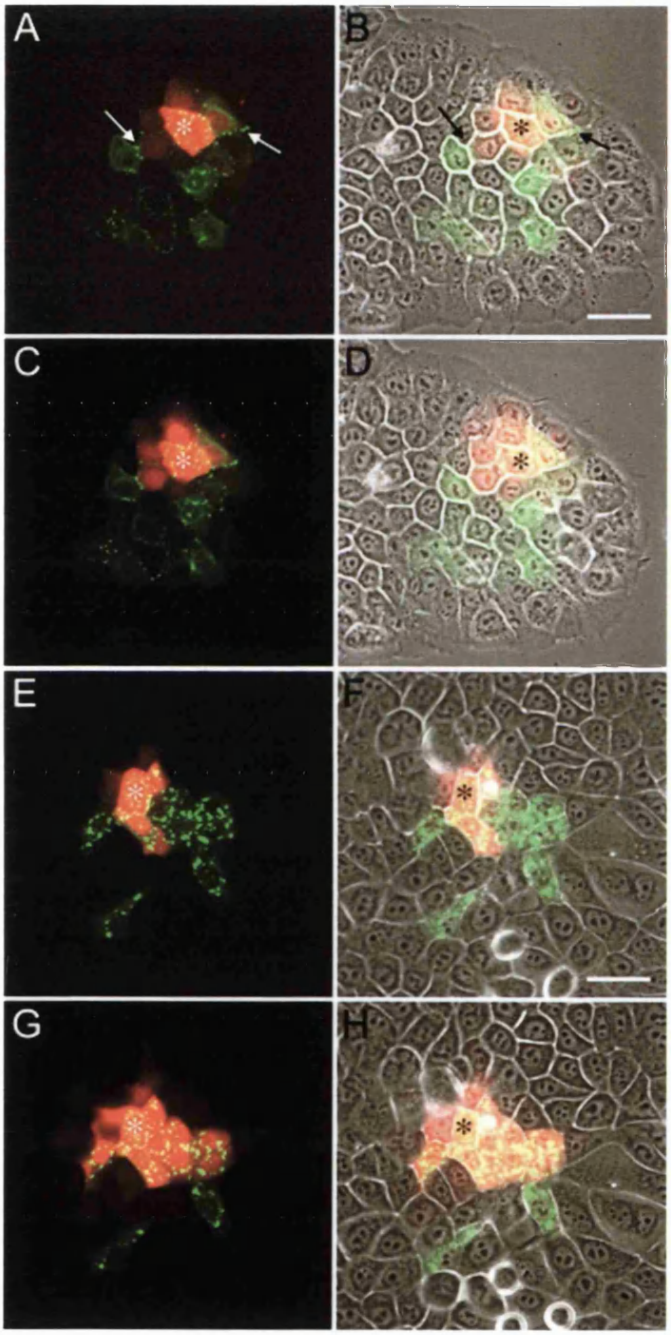

Figure 16. Effects of EKV-associated mutation on channel function

The skin disease associated Cx31 mutations R42P and C86S had differential effects on the formation of functional intercellular channels. Images are taken from representative NEB1 dye transfer experiments conducted in viable NEB1 cells expressing either the R42P (A – D) or C86S (E – H) Cx31 mutants. Images show EGFP fluorescence (green) and Alexa 568 fluorescence (red) overlays either with or without phase contrast (right and left columns respectively). Images (A & B), and (E & F) represent the first time point of the time-lapse sequence while images (C & D), and (G & H) represent the final time point and were acquired 33 min later. In each image an asterix identifies the cell originally microinjected with dye. Although some protein was observed at the plasma membrane in cells expressing the R42P mutant (A & B, arrows) dye transfer rates were poor indicating impaired intercellular channel function. However, in contrast, dye rapidly spread through cells expressing the C86S Cx31 mutant, indicating that functional channels could form despite the presence of this mutation. Scale bars = 50 μm.

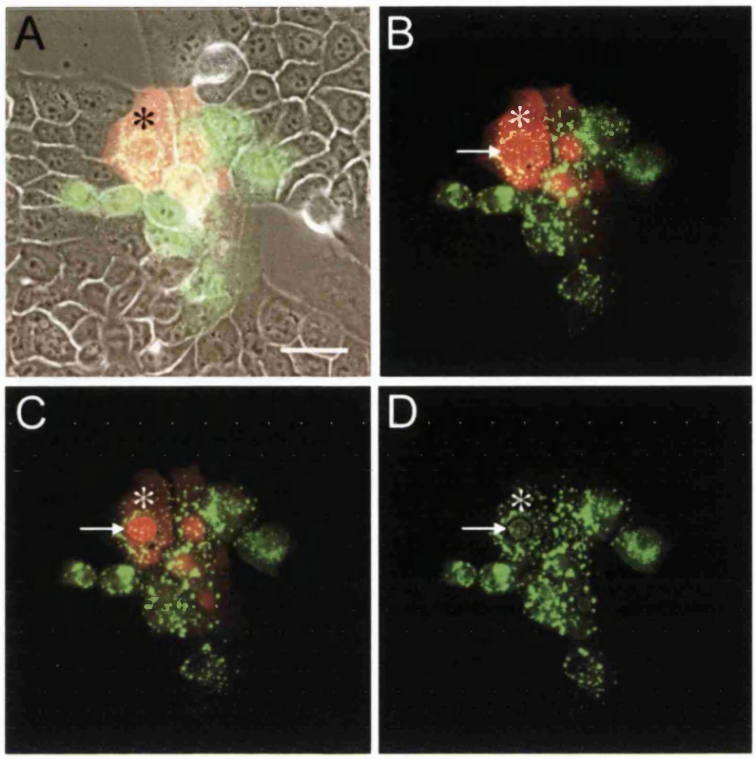

Figure 17. Dye transfer and death in (C86S)Cx31-EGFP expressing NEB1 cells

Expression of (C86S)Cx31-EGFP resulted in the formation of functional intercellular channels prior to death in NEB1 keratinocytes. Images are derived from a (C86S)Cx31-EGFP dye transfer experiment where the onset of cell death coincided with filming. Images represent 0 min, (A & B), 15 min (C), and 30 min (D) time points. Image (A) represents overlaid EGFP, Alexa 568, and phase contrast channels. (B,C & D) as for (A) except without phase contrast. Initially Alexa 568 dye transferred through adjacent fluorescent cells indicating that the mutant protein could form functional intercellular channels. However, as the expressing cells began to die the fluorescent dye was lost into the surrounding medium (indicated by a rapid fall in Alexa 568 fluorescence intensity). Cell death was accompanied by nuclear shrinkage (arrow) and blebbing, two phenotypes also associated with (R42P)Cx31-EGFP expression. An asterix indicates the position of the cell originally microinjected with dye. Scale bar = 50 μm.

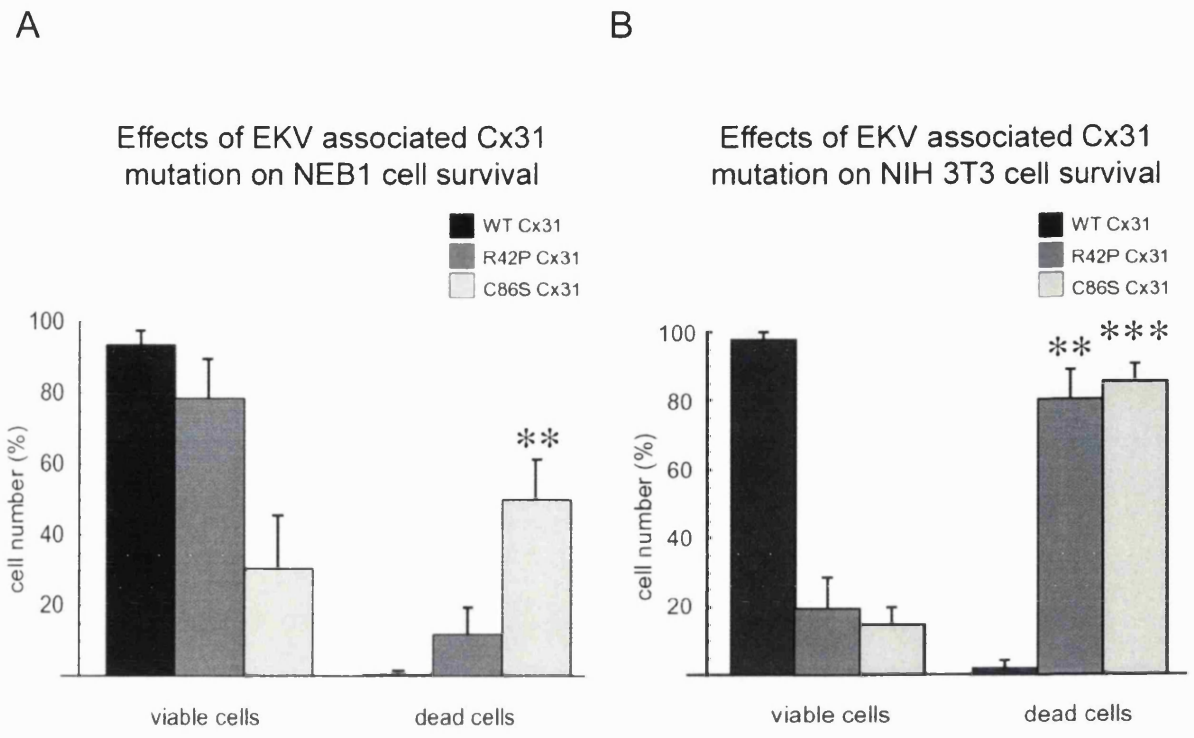

Figure 18. Summary of the effects of EKV associated Cx31 mutations on cell survival

Bar charts representing the means and standard errors of the relative incidence of cell death and survival following expression of the EKV associated Cx31 mutations R42P and C86S for NEB1 keratinocytes (A) and NIH 3T3 fibroblasts (B). 0.5 μg/ml propidium iodide was applied to cell cultures 10 min before scoring cell death. Cells were scored as dead only when positive for nuclear labelling with propidium iodide. Cells that did not display an altered phenotype and which did not show positive propidium iodide staining were scored as viable. Cells that displayed an altered phenotype indicative of the onset of cell death but that were not yet positive for propidium iodide staining were discounted. The cytotoxic effects of the EKV associated Cx31 mutations were far more evident in the NIH 3T3 cell line resulting in death in over 80 % of cells observed. Significances are derived from the ANOVA comparison of the wild type treatment group with the R42P and C86S treatment groups (two stars, $p < 0.01$; three stars, $p < 0.001$).

		Cell Death Analysis		
Cell Line	**Cx31 mutation**	**Number of cells scored**	**Cell Death (%)**	**ANOVA sig.**
NEB1	Wild-Type	212	<1	-
	C86S	207	50	**
	R42P	334	12	n.s.
	R32W 66delD	No apparent cell death		
NIH 3T3	Wild-Type	50	2	-
	C86S	82	80	***
	R42P	66	85	**
	R32W 66delD	No apparent cell death		

Table 3. The statistical evaluation of cell death data

The above table provides a numerical summary of all data from NEB1 and NIH 3T3 cell death experiments. The statistical significances of the effects of EKV associated Cx31 mutations on NEB1 and NIH 3T3 cell survival are also presented. Significances were derived from the ANOVA comparison of the wild type treatment group with the R42P and C86S treatment groups (two stars, $p < 0.01$; three starts, $p < 0.001$). Note that the relatively low instance of cell death caused by the R42P mutant in NEB1 cells did not achieve significance. Cell death was not evaluated for the R32W and 66DelD mutations as it was clear from the numerous experiments performed that they had no deleterious effect on cell survival.

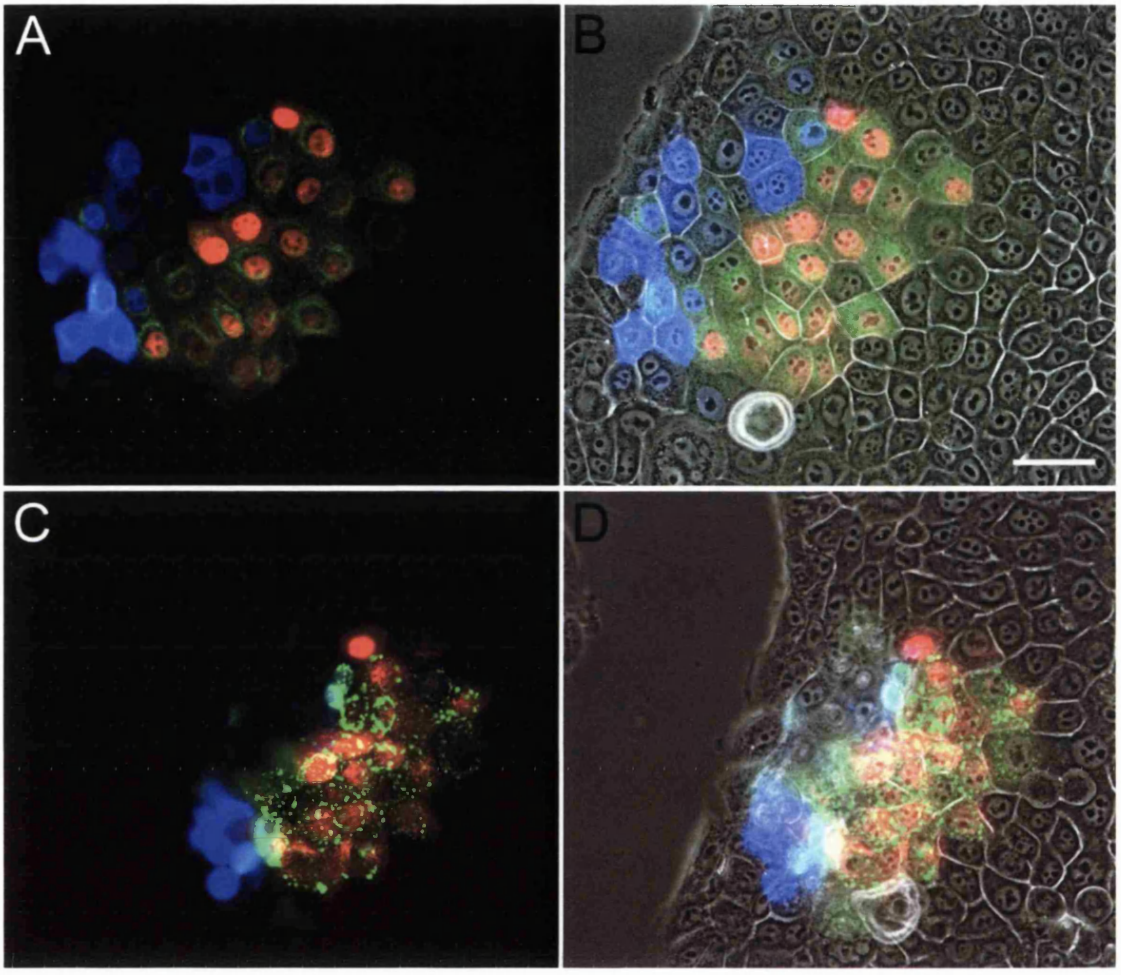

Figure 19. Cell death is confined to the (C86S)Cx31-EGFP expressing population

Adjacent patches of cells were microinjected with either (wt)Cx31-EGFP + Cy3.5-IgG marker or (C86S)Cx31-EGFP + Cy5-IgG marker in order to determine whether cell death associated with expression of the C86S mutation would be conferred to the wild type expressing population. Images represent EGFP (green), Cy3.5 (red), and Cy5 (blue) fluorescence overlays either with (B & D) or without (A & C) phase contrast. Images (A & B) and (C & D) represent 1 hour and 5 hour time points respectively. Although cell death was apparent in the (C86S)Cx31-EGFP expressing population (C & D, blue cells) directly adjacent (wt)Cx31-EGFP expressing cells remained viable (C & D, red cells). Scale bar = 50 μm.

2.3.5 Skin disease-associated Cx31 mutations are lethal in NIH 3T3 fibroblasts

Dye transfer experiments were typically conducted 4 – 5 h following the microinjection of expression constructs. NIH 3T3 fibroblasts microinjected with either the (R42P)Cx31-EGFP or (C86S)Cx31-EGFP expression constructs were never detectable following this length of incubation. However, the frequent observation of fluorescent debris within experimental cultures suggested that protein expression had resulted in the death of all microinjected cells, an indication that EKV-associated Cx31 mutations were highly toxic in these cells. In order to further explore this possibility, a multi-channel time-lapse microscopy assay was developed that enabled cell death to be directly monitored during the onset of exogenous protein expression. Confluent patches of NIH 3T3 fibroblasts were co-microinjected in the nucleus with a Cy3.5-IgG fluorescent marker and expression constructs encoding either (R42P)Cx31-EGFP, (C86S)Cx31-EGFP, or (wt)Cx31 EGFP. The fluorescent marker permitted the identification of cells prior to the expression of microinjected constructs, enabling cells to be filmed during the onset of protein expression. Propidium iodide was included in the culture medium during time-lapse experiments enabling cell death to be assessed directly. Three channel florescence imaging and the employment of specialised filter configurations were required in order to effectively discriminate between EGFP, Cy3.5 and propidium iodide fluorescence (see methods 2.2.9, page 19 for a detailed description).

Multi-channel time-lapse experiments revealed that expression of either (R42P)Cx31-EGFP or (C86S)Cx31-EGFP rapidly induced cell death in NIH 3T3 fibroblasts (Figure 20, page 19 & Figure 21, page 19). Indeed, the R42P and C86S mutations were highly toxic, inducing death at extremely low levels of expression. The effects of protein expression on cell

morphology were profound, resulting in cell contraction, loss of adhesion, and nuclear shrinkage. In contrast, expression of (wt)Cx31-EGFP had no discernible effect on cell survival or morphology Figure 22, page 19. The differing degrees of toxicity that the R42P and C86S mutations exhibited in the different cell lines studied were striking. The R42P mutation caused death in only 10 % of NEB1 cells, but induced death in over 80 % of NIH 3T3s within two hours of microinjection (Figure 18B, page 19). The C86S mutation was also far more potent when expressed in NIH 3T3s inducing levels of cell death comparable to that of the R42P mutation. Table 3, page 19 summarises the data from NEB1 and NIH 3T3 experiments, and shows the statistical significances of the effects of different Cx31 mutations on cell death.

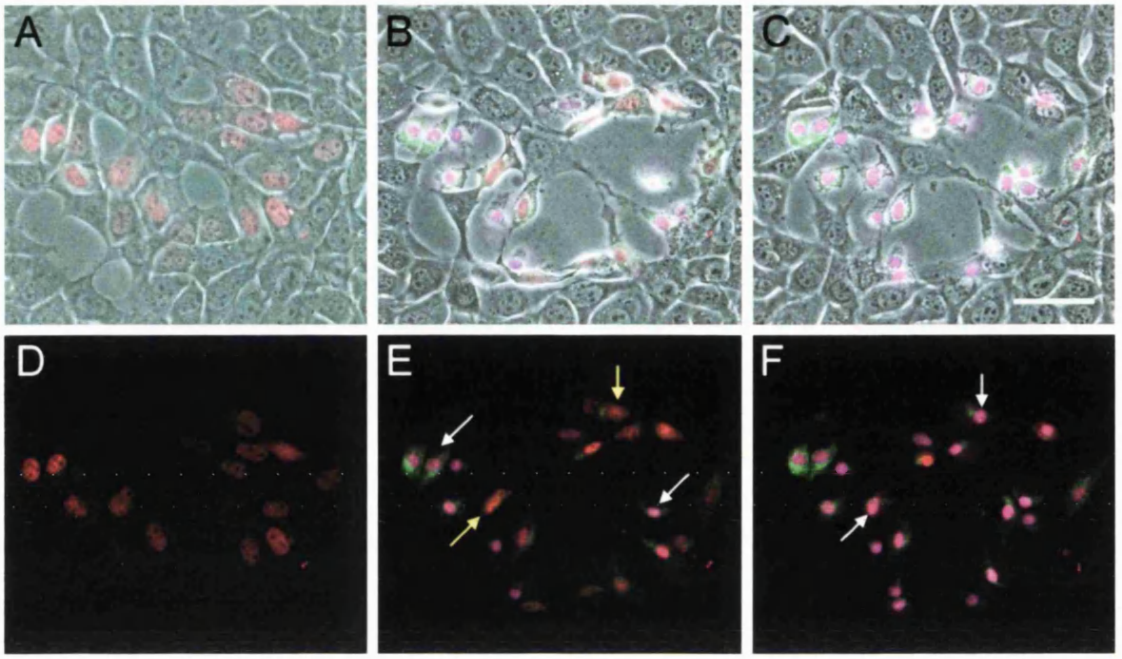

Figure 20. (R42P)Cx31-EGFP expression rapidly induces death in NIH 3T3 cells

Imaging the onset of (R42P)Cx31-EGFP expression in NIH 3T3 cells in the presence of 0.5 μg/ml propidium iodide. Images represent EGFP(green), Cy3-IgG (red), and propidium iodide (blue) fluorescence overlays either with (A – C) or without (D - F) phase contrast to reveal the surrounding non-expressing cells. Time points are as follows; (A & D) 0 min, (B & E) 50 min, and (C & F) 100 min. Cy3.5-IgG was co-microinjected with plasmid DNA to enable the location of microinjected cells prior to the onset of protein expression. Cells were relocated 20 min after microinjection and filmed using multi-channel time-lapse microscopy for 100 min (1 min time-lapse intervals) in order to record the onset of cell death. 0.5 μg/ml propidium iodide was added to cell cultures prior to the filming process. Expression of the (R42P)Cx31-EGFP mutant rapidly lead to cell death revealed by the accumulation of propidium iodide within cell nuclei. The nuclei of dead cells appeared purple due to the overlay of red Cy3.5-IgG and blue propidium iodide fluorescence channels. White arrows in image (E) highlight examples of dead cells that took up propidium iodide following the expression of the microinjected plasmid. Yellow arrows within the same image indicate cells with intact nuclei that had yet to die. In image (F) white arrows indicate cells previously marked by yellow arrows in (E). Note the change of cell nuclei from red to purple indicating that cell death had finally occurred. Note also the nuclear shrinkage that followed protein expression, an observation also made in NEB1 keratinocytes. Cell death occurred at very low levels of protein expression indicating that the R42P mutation was highly toxic. A specially developed technique allowed the imaging of all three fluorophores despite their overlapping spectra (see methods 2.2.9, page 36). Scale bar = 50 μm.

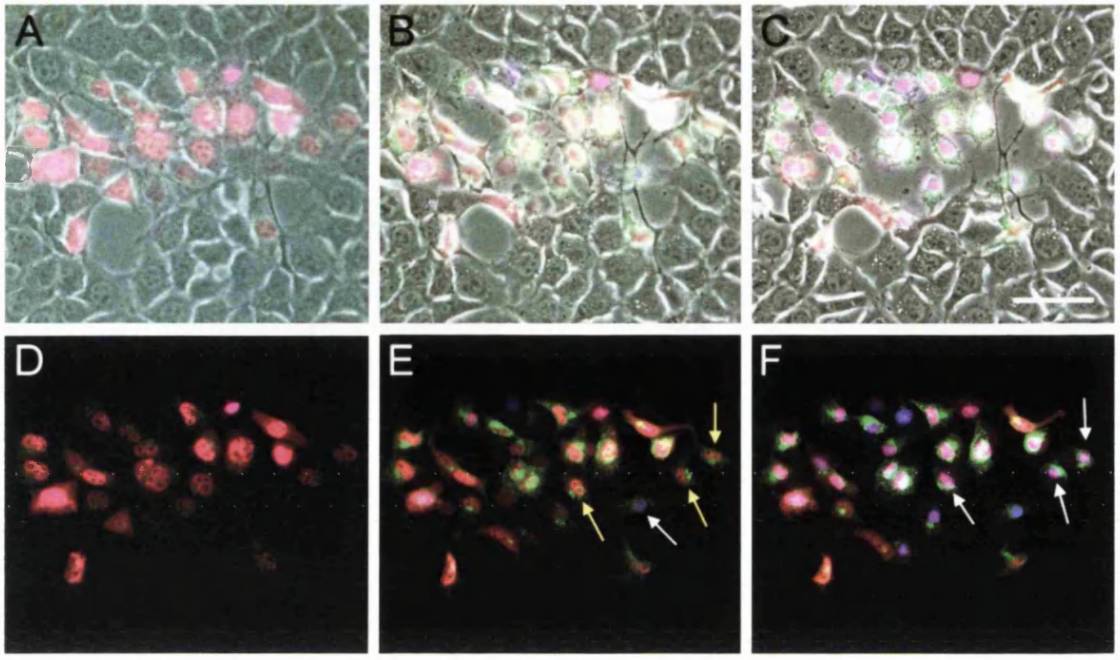

Figure 21. (C86S)Cx31-EGFP expression rapidly induces death in NIH 3T3 cells

Imaging the onset of (C86S)Cx31-EGFP expression in NIH 3T3 cells in the presence of 0.5 μg/ml propidium iodide. Image compositions and time courses are the same of for Figure 20 except that cells were microinjected with (C86S)Cx31-EGFP plasmid DNA. Again, Cy3.5-IgG was co-microinjected with plasmid DNA to enable the location of microinjected cells prior to the onset of protein expression. Film duration and time-lapse intervals were as described in Figure 20. Expression of the (C86S)Cx31-EGFP mutant rapidly lead to cell death as revealed by the accumulation of propidium iodide within cell nuclei. In image (E) white arrows highlight examples of dead cells that had taken up propidium iodide following the expression of the microinjected plasmid. Yellow arrows within the same image indicate cells with intact nuclei that had yet to die. In image (F) white arrows indicate cell previously marker by yellow arrows in (E). Note that cell nuclei changed from red to purple indicating that cell death had finally occurred. As with the R42P mutation, cell death occurred at very low levels of protein expression and was accompanied by nuclear shrinkage.
Scale bar = 50 μm.

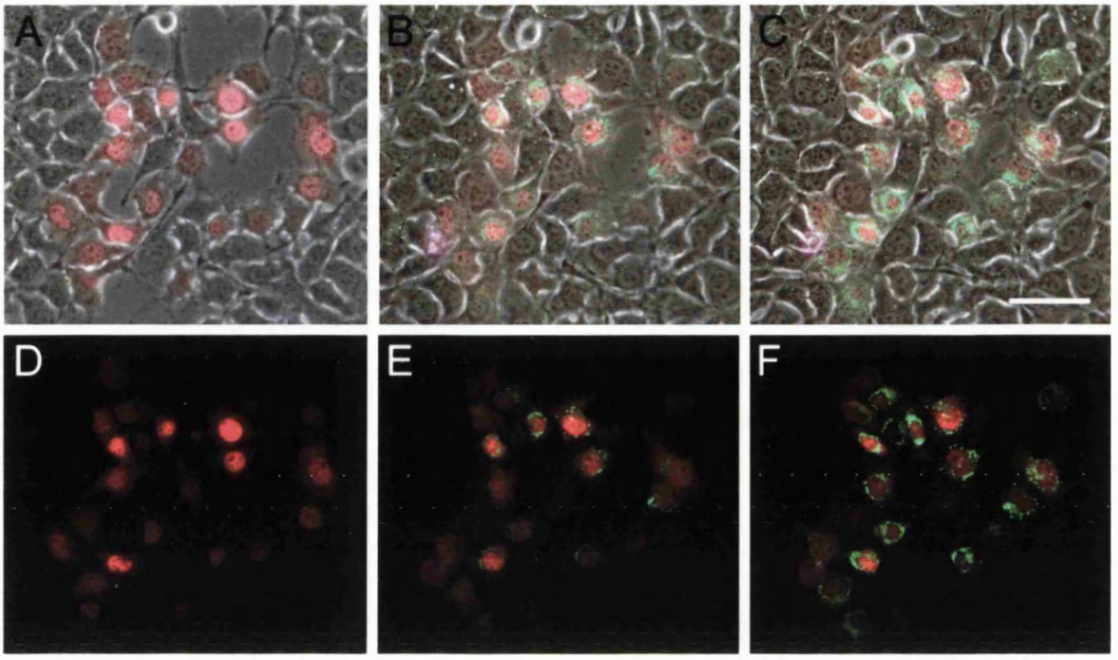

Figure 22. (wt)Cx31-EGFP expression has no effect on NIH 3T3 survival

Imaging the onset of (wt)Cx31-EGFP expression in NIH 3T3 cells in the presence of 0.5 μg/ml propidium iodide. Image compositions and time courses are the same as for Figure 20 except that cells were microinjected with (wt)Cx31-EGFP plasmid DNA. Propidium iodide was not taken up by cell nuclei over the course of the film sequence indicating that cell death did not occur. Cy3.5-IgG was co-microinjected with plasmid DNA to enable the location of microinjected cells prior to the onset of protein expression. Note that wild type Cx31 achieved far higher levels of expression that the Cx31 variants harbouring either the R42P or C86S mutations. Scale bar = 50 μm.

2.4 DISCUSSION

Germline mutations in the Cx31 gene *GJB3* lead to a number of disorders including skin disease, deafness and peripheral neuropathy (Kelsell et al., 2001; Rabionet et al., 2002). Although the clinical effects of these nutations are well established little is known about their effects at the cellular level. This study aimed to address these outstanding questions. Microscopy based assays were applied to the *in vitro* study of Cx31 function. Dye transfer assays were applied to the study of intercellular communication in order to determine the effects of Cx31 mutation on channel function. A novel analytical technique was developed that enabled dye transfer rates to be directly quantified allowing the statistical comparison of different treatment groups. The development of a technique that permitted the discrimination of multiple fluorophores with overlapping spectra also enabled the effects of protein expression on cell viability to be assessed directly during time-lapse experiments.

Studies revealed that impaired channel function was associated with two distinct Cx31 mutations; a deafness/peripheral neuropathy mutation (66DelD), and a mutation previously considered to be a rare Cx31 polymorphism with no known disease significance (R32W). These mutations had no effect on the viability of cells. In contrast two mutations associated with the skin disorder EKV (R42P and C36S) induced rapid death in certain cell populations. However these mutations had either no or only mild inhibitory effects on channel function. These studies have therefore identified some key cellular phenotypic differences with respect to disease-associated Cx31 mutations.

2.4.1 The R32W polymorphism and 66DelD deafness/peripheral neuropathy mutation disrupt Cx31-mediated intercellular communication

This study demonstrated that the R32W mutation inhibited the ability of Cx31 to form functional homotypic channels, as measured by the inability of cells to efficiently transfer fluorescent dye. The expressed protein was primarily confined to the cytoplasm and, unlike the wild type protein, rarely formed significant aggregates or 'plaques' at the plasma membrane. These findings strongly suggest that R32W is a non-functional variant of Cx31.

The R32W mutation has previously been reported as a polymorphic variant of Cx31 with no proven disease association (Kelsell et al., 2000; Lopez-Bigas et al., 2000). However, it has been postulated that this mutation may confer a modifying effect with respect to the severity of epidermal disease or hearing loss when associated with other connexin mutations (Lopez-Bigas et al., 2001b). The mutation exhibits an allelic frequency of 1.43 %, and demonstrates a degree of ethnic variability (3 % in Irish, 0.7 % of Afro-Caribbeans, and 2.5 % of Asians, n = 488) (John Common, personal communication). However, as yet no homozygotes have been detected for this allele. Given that the data from this study demonstrates that R32W confers an inhibitory effect on Cx31-dependent intercellular communication, it may be that homozygosity for this polymorphism results in an, as yet, unassociated recessive disease phenotype. The argenine to tryptophan substitution in this polymorphism represents a positive to neutral shift in residue charge within the first transmembrane domain of Cx31, a region that is highly conserved amongst connexins (Gottfried et al., 2002). This change may therefore result in structural abnormalities within a domain that appears to be of particular importance in connexin function. Indeed, the recently identified L34P mutation in Cx31,

which also resides within the first transmembrane domain of the protein, has been associated with a recessive form of EKV (Gottfried et al., 2002), while the change M34T in Cx26 results in a recessive form of hearing loss. Further genetic studies will need to be performed to assess the disease significance of the R32W Cx31 variant. However, given the findings from this study, it is not unreasonable to suggest that R32W may be of some importance in an, as yet, unassociated recessive disease.

The rare 66DelD mutation that resides within the first extracellular loop of Cx31 is associated with a dominant syndrome of hearing loss and peripheral nerve dysfunction and neuropathy (Lopez-Bigas et al., 2001a). Dye transfer experiments and observations of protein localisation performed within this study support the deleterious nature of this mutation with respect to Cx31 function. Dye transfer studies revealed that the 66DelD mutation significantly impaired the ability of Cx31 to form functional homotypic channels. Furthermore, unlike the wild-type protein, the 66DelD mutant did not reveal significant aggregation at the plasma membrane but instead exhibited a largely diffuse cytoplasmic localisation. These findings may therefore reflect a membrane trafficking or folding defect associated with this mutation. Interestingly, a mutation of the same residue in Cx26 also results in a similar cytoplasmic localisation suggesting that this region may be of importance in general for connexin function. Indeed the Cx26 mutation is also associated with a dominant syndrome of hearing loss although, in contrast to the 66DelD mutation in Cx31, this is additionally accompanied by skin disease (Kelsell et al., 2001).

Cx31 is expressed in the spiral limbus and ligament of the cochlea and also within the auditory nerve and therefore impaired channel function is likely to provide a direct mechanism for the hearing loss associated with the Del66D mutation. Detailed audiological examinations of patients who harbour this mutation have previously revealed that hearing impairment arises due to abnormalities in both the cochlea and the auditory nerve (Lopez-Bigas et al., 2001a) and thus hearing loss is the consequence of multiple dysfunctions within the auditory transduction pathway. A disruption of ionic homeostasis is likely to underlie the main cause of cochlear dysfunction associated with this disease: within the cochlea hair cells are bathed in endolymph fluid rich in potassium ions. Upon acoustic stimulation these ions rapidly flood into the hair cells and must subsequently be removed and recycled in order to main correct hearing function (Rabionet et al., 2002). Potassium recycling occurs via a syncytium of supporting cells and fibrocytes interconnected by gap junction channels. This cellular network draws potassium ions away from the hair cells and delivers them back to the endolymph via the spiral ligament. Given that Cx31 is expressed in the spiral ligament and given that the 66DelD mutation inhibits the formation of functional gap junction channels, an impairment of potassium recycling may provide the mechanism of cochlea dysfunction in this disease. Additional abnormalities in the function of the auditory nerve, which compound the severity of this hearing disorder, are likely to arise as a consequence of the independent function of Cx31 in the peripheral nervous system.

Cx31 is expressed in the myelinating Schwann cells of the peripheral nervous system (Lopez-Bigas et al., 2001a). Schwann calls are the satellite cells that surround nerve axons and motor nerve terminals. The plasma membrane of a single Schwann cell can wrap many

(often hundreds) of times around the underlying nerve axon, a process that is essential for efficient neuronal function (Baker, 2002). The connexins of Schwann cells are believed to form 'reflexive gap junctions' - intracellular gap junctions that directly couple the many layers of overlapping plasma membrane found in these cells. The spiralling cytoplasm of the Schwann cell provides a long convoluted pathway for the diffusion of metabolites and other factors important for cellular function. It has therefore been postulated that these reflexive gap junctions permit radial diffusion across the many membranous layers of the cell, allowing a relatively short pathway for the cytoplasmic distribution of metabolites and ions (Altevogt et al., 2002; Baker, 2002). Loss of this pathway may impair cellular function; ultimately resulting in the death of the Schwann cell and the underlying neurone. This study revealed that although the 66DelD mutation inhibited the formation of functional Cx31 channels it did not confer any direct cytotoxic effects on NEB1 and NIH 3T3 cells. The dysfunctional protein was therefore not toxic in itself. This suggests that the extensive demyleination and neuropathy seen in patients harbouring the 66DelD mutation may result as a long-term consequence of impaired cellular function as opposed to an acute cytotoxic effect resulting directly from the expression of the mutated protein. However firm conclusion concerning the effects of Cx31 mutation on peripheral nervous tissue cannot be drawn from studies performed in keratinocytes and fibroblasts and therefore additional studies performed in more appropriate cells will be required.

2.4.2 Cell death is a characteristic of skin disease-associated Cx31 mutations

The dominant Cx31 mutations R42P and C86S result in EKV, a hyperproliferative skin disorder that primarily affects the palmoplantar surfaces of the epidermis. Functional assays

conducted in this study demonstrated that these mutations conferred a cytotoxic effect on keratinocyte and fibroblast cells, an observation that was not made for the R32W and 66DelD mutations. In keratinocytes, death associated with both these mutations appeared sporadic, often only killing a subpopulation of cells expressing the protein within a single culture. Furthermore, the cytotoxicity associated with the expression of the (C86S)Cx31-EGFP mutant was five fold that observed for the (R42P)Cx31-EGFP mutant, reflecting a difference in potency between these proteins. (R42P)Cx31-EGFP was often expressed poorly in keratinocytes and in cell populations where death was apparent the protein exhibited a predominantly perinuclear localisation. This pattern of expression is consistent with that observed from the immunohistochemical analysis of Cx31 expression in a skin biopsy taken from the epidermis of a patient harbouring the R42P mutation (Di et al., 2002). In cell populations where death did not occur protein aggregation could be observed at the plasma membrane for both (R42P)Cx31-EGFP and (C86S)Cx31-EGFP, although this was less apparent than that observed for the wild type protein. However, dye transfer experiments revealed that the R42P mutation did confer an inhibitory effect on channel function although to a lesser degree than that observed for non-EKV mutations. The C86S mutation did not, however, have a significant deleterious effect on channel function, allowing dye to transfer between cells at a comparable rate to that observed for the wild type protein. Subtle functional differences therefore existed between these mutations. Interestingly, in dramatic contrast to observations made in keratinocytes, expression of either (R42P)Cx31-EGFP or (C86S)Cx31-EGFP resulted in the rapid death of all fibroblast cells.

To date five dominant mutations and one recessive mutation have been identified in Cx31 that result in EKV (Gottfried et al., 2002; Kelsell et al., 2001). None of these mutations are associated with additional clinical phenotypes. Therefore, in theory, the search for a common cellular mechanism shared by the EKV-associated Cx31 mutations should prove less of a complicated task than for many of the other skin disease-associated β-connexin mutations, which often exhibit a varying background of additional clinical phenotypes. This study provides the first indication that cell death is a common mechanism of EKV-associated Cx31 mutation. More recent studies lend further credence to this idea: Diester and co-workers have reported that the dominant EKV-associated Cx31 mutation G12R, which resides within the highly conserved amino terminus of the protein, is lethal in HeLa cells (Diestel et al., 2002). Furthermore, this mutation, and additionally the G12D and L34R mutations, have also been found to be lethal in NEB1 keratinocytes (Wei-Li Di, Colin Gray - personal communication). Therefore, although these mutations are disseminated amongst a number of functional domains within Cx31 they all promote the same cellular phenotype. Furthermore, this phenotype does not appear to be associated with non-EKV Cx31 mutations. Collectively data presented in this study and that more recently obtained by others indicate that cell death is a common mechanism of EKV-associated Cx31 mutation.

The importance of Cx31-dependent intercellular communication in EKV is unclear. This study has demonstrated that the formation of functional Cx31 homotypic channels is essentially unaffected by the C86S mutation while, in contrast, the R42P mutation does confer a mild but significant inhibitory effect. To further complicate the picture it has been reported that the G12R mutation actually functions to enhance intercellular communication

(Diestel et al., 2002), while it has been suggested that the recessive L34P mutation inhibits channel function (Gottfried et al., 2002). Interestingly, Diestel and co-workers postulate that channel function may be important for lethality. They argue that the G12R mutation may result in defective channel closure and therefore may promote cell death by preventing the control of cellular homeostasis. It is also conceivable that this may also enable uncoupled connexon hemichannels on the cell surface to permit the free exchange of ions and metabolites between the intracellular and extracellular space, a process that would rapidly result in cell death. Defective channel closure would certainly provide a fitting explanation for the relative differences in efficiency with which the R42P and C86S mutations were observed to induced cell death in NEB1 keratinocytes in this study: if this explanation held then the greater efficiency with which cells expressing (C86S)Cx31-EGFP were able to transfer dye compared to those expressing (R42P)Cx31-EGFP would explain why the former protein resulted in a far higher instance of cell death, as the loss of cellular homeostasis would be more rapid. Further studies will be required to determine the precise nature of the mechanism of cell death associated with mutations that cause EKV.

Findings from the *in vitro* study of EKV-associated Cx31 mutations have provided somewhat of a paradox: an increased instance of cell death appears to underlie a disorder that is ultimately characterised by hyperproliferation. This presents an intriguing dichotomy which will require additional study. For instance the role of Cx31 during the different stages of keratinocyte differentiation remains to be explored, and moreover the precise relationships that exist between Cx31 and the many other connexin types that are co-expressed in epidermal tissue has yet to be elucidated. Given that at least ten different connexin types are

expressed in epidermal tissue, this presents a formidable task (Di et al., 2001). The findings presented in this study provide new insights into the differing effects that distinct Cx31 mutations confer on channel function and cellular phenotype, and therefore constitute a step towards understanding the intriguing phenotype-genotype relationships produced due to β-connexin mutations.

25 CONCLUSION

This study has demonstrated that Cx31 harbouring either the rare 66DelD hearing loss/peripheral neuropathy mutation or the R32W polymorphism cannot to assemble into functional homotypic channels. Loss of channel function associated with the 66DelD mutation is likely to result in the impaired recycling of potassium ions within the cochlea of the inner ear, and the impaired radial diffusion of ions and metabolites in the Schwann cells of the peripheral nervous system. Together these abnormalities are likely to underpin the hearing loss and peripheral neuropathy found in individuals who harbour this mutation. The R32W polymorphism results in a dysfunctional protein and so may prove to be of importance in an as yet unassociated recessive disease. Finally, cell death appears to be a common characteristic of EKV-associated Cx31 mutation. Therefore distinct Cx31 mutations that influence either the epidermis or the auditory and peripheral nerve transduction process elicit different effects at the cellular level. In conclusion, this study has identified some key phenotypic differences with respect to disease-associated Cx31 mutations.

3 THE CHEMOTAXIS AND MOTILITY OF SARCOMA CELLS AND FIBROBLASTS

31 INTRODUCTION

31.1 Chemotaxis in physiology and pathology

The migration of cells towards and away from the source of diffusible chemical signals is known as chemotaxis (Bray, 2001). Chemotactic behaviour first evolved with the earliest life forms providing a mechanism of bacterial translocation towards nutrient sources and enabling cell aggregation during periods of environmental stress (Budrene and Berg, 1991). As organism complexity has increased so too has the range of biological processes in which chemotaxis can be found to play a role. In mammals chemotactic behaviour is essential for the efficient function of a broad range of homeostatic mechanisms: the recruitment of leukocytes to regions of infection and tissue trauma is a chemotactic driven process that is essential for effective immune system function (Wilkinson, 1987). During wound repair the chemotactic migration of keratinocytes and fibroblasts into the exposed region is believed to be important for wound closure (Gillitzer and Goebeler, 2001). Homeostatic mechanisms that regulate the constant turnover of bone are believed to include chemotaxis as calcium signals guide mineral-reabsorbing osteoblasts to sites of bone degradation (Yamaguchi et al., 1998). During embryogenesis selective neurotransmitters and growth factors regulate the chemotactic migration of neurons from zones of proliferation to their appropriate destinations within the developing brain (Nguyen et al., 2001). Furthermore, the tight regulation of chemotactic signals that attract and repel the highly motile axonal growthcone during neurite outgrowth is believed to enable the precise synaptic formations required during the

development of the central nervous system (Xiang et al., 2002). Many such homeostatic mechanisms require various cell types to exhibit only transient chemotactic responses and therefore it is essential that the multitude of signals that collectively promote and inhibit this behaviour are under strict control. Any breakdown in this control can result in inappropriate chemotactic responses that can have detrimental rather than beneficial effects on the organism.

Inappropriate chemotactic responses and loss of chemotactic function underlie a wide range of pathological states. Wiscott Aldrich Syndrome (WAS), a rare X-linked congenital immune-deficiency disorder characterised by heightened susceptibility to infection and autoimmune complications, is in part, believed to be the consequence of poor leukocyte chemotaxis (Badolato et al., 1998; Zicha et al., 1998). Inappropriate chemotactic responses also promote the development of a range of pathological conditions that are often associated with inappropriate inflammatory responses such as autoimmunity and type II hypersensitivity (allergy). The accumulation of large populations of neutrophils within the synovial joints of Rheumatoid Arthritis patients is a chemotactic driven process that results in the eventual destruction of the surrounding cartilage due to excessive elastase secretion by these cells (Podolin et al., 2002). The chemotaxis of microglia towards amyloid β-peptide is believed to be responsible for the accumulation of these cells in regions of peptide build-up and deposition in the Alzheimer's diseased brain (Smits et al., 2002). Microglial accumulation results in much of the secondary inflammatory damage associated with this disease; release of neurotoxins and other cytotoxic agents results in the dendritic pruning and localised synaptic loss that is believed to underlie the cognitive impairment associated with

Alzheimer's disease (Strohmeyer and Rogers, 2001). The abnormal recruitment of large numbers of eosinophils to the asthmatic lung underlies much of the pathology associated with this condition including endothelial cell destruction and bronchial constriction (Conroy and Williams, 2001). The chemotactic driven migration of blood monocytes into the early atheroma is a key step in the progressive development of arteriosclerosis, the most common underlying cause of coronary hear disease. Once resident within the atheroma monocytes mature into macrophages and ultimately foam cells that secrete proteases and coagulating factors that collectively promote plaque breakdown and thrombosis (Libby, 2002). However, one of the most striking examples of how chemotaxis can contribute to the development of a disease is provided by the metastatic spread of cancer.

3.1.2 Metastatic disease

Metastatic disease is the major cause of death in cancer (Ahmad and Hart, 1997). Yet the process by which subpopulations of cells within a primary tumour acquire the ability to establish sites of secondary growth in other areas of the body remains poorly understood. A primary neoplastic growth often consists of different zones of morphologically and biologically distinct cell populations which, through a gradual process of tumour progression, may have arisen from a single transformed cell (Fidler and Hart, 1982). Different cell populations can exhibit markedly different metastatic potentials and resistances to chemotherapeutic agents. It is this inherent biological heterogeneity that, through a process of cell selection, determines a cancer's ability to survive and spread in the face of host defence mechanisms and current therapeutic strategies.

The metastatic cascade defines a set of, as yet, poorly understood processes that enable cells from the primary tumour to seed new sites of secondary growth within other regions of the host. Escape from the primary tumour, entry into the blood stream and/or local lymphatics, arrest in the capillary bed of a target organ, subsequent infiltration of the surrounding tissue, and finally, initiation of secondary tumour growth are all requirements of a metastasising cell population (Ahmad and Hart, 1997; Fidler and Hart, 1982). Furthermore, metastasising cells must evade a constant barrage of host defence mechanisms in order to sustain the progressive spread of the disease. The main stages of the metastatic cascade are defined in Figure 23.

The metastatic cascade is a highly complex process usurping host mechanisms as well as the inherent properties of the cancer. The initial process of intravasation whereby metastasising cells escape from the primary tumour into the local lymphatics or blood stream is a multi-component process involving the exploitation of host angiogenic mechanisms, the dynamic regulation of cell attachment to extracellular substrates, the local degradation of these substrates, and the detection and response to local gradients of soluble or matrix-bound signalling factors. Metastasising cells may not need to fulfil all these requirements as other cell populations within the tumour or from the host may contribute in part to providing an environment that is conducive to tumour cell spread. However, the ability to chemotax is likely to be an important property common to all metastasising cells: chemotactic signals commonly associated with the vasculature and chemotactic peptides that are solubilised and liberated as a consequence of matrix degradation are believed to guide metastasising cells from the primary tumour towards the local bloodstream or lymphatics

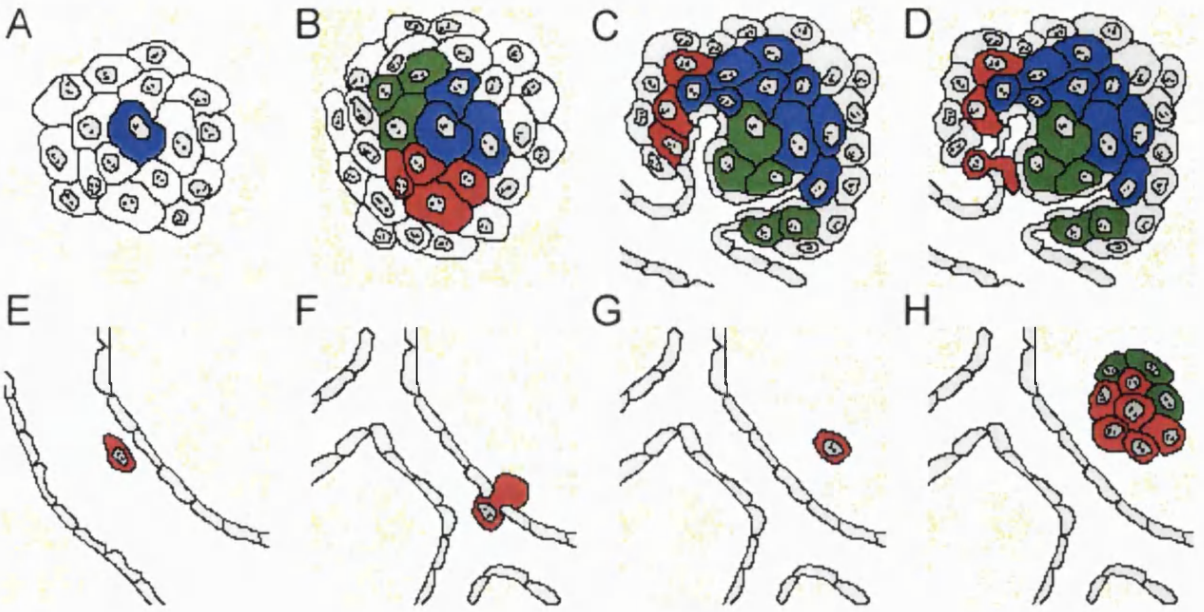

Figure 23. The metastatic cascade

(A) The initial process of cell transformation that results in uncontrolled cell growth. Most primary neoplasms are likely to be monoclonal in origin (Fidler and Hart, 1982). (B) Tumour growth and evolution resulting in the emergence of subpopulations of cells of varying biological phenotypes e.g. varying metastatic potentials and cytotoxic resistances. (C) New angiogenic growth required for any tumour mass exceeding approximately 2 mm in diameter (Fidler and Ellis, 1994). New vessel growth is often disorganised and highly permeable – this may aid the process of intravasation (Ahmad and Hart, 1997). (D) Subpopulations of cells acquire the ability to detach from the main tumour mass and infiltrate the local vasculature or lymphatics, a process requiring the dynamic regulation of cell-cell and cell-substrate attachments, local matrix degradation, chemotaxis, and resistance to high shear forces upon entering the blood stream. (E) Cell trafficking via the bloodstream. The tumour cell finally arrests in the capillary bed of a target organ. (F) During extravasation chemotactic signals can guide the tumour cell into the surrounding tissue, a process requiring further matrix degradation and dynamic regulation of cell attachments. (G) Now resident within the target organ the cell must survive and persist within a foreign tissue environment. The cell may possibly require additional genetic and/or regulatory changes before initiation of secondary tumour growth and may persist for years without division, a phenomenon known as minimum residual cancer (Klein et al., 2002). (H) Initiation of secondary tumour growth and establishment of full-blown metastases. The tumour cells successfully adapt and survive in the foreign tissue possibly due to autonomous regulation of cell growth resulting from acquired autocrine signalling mechanisms (Rusciano and Burger, 1992).

(Vyckoff et al., 2000a; Wyckoff et al., 2000b). Additionally, during the latter stages of the metastatic cascade chemotactic signals are likely to be important for promoting the extravasation of metastasising cells that have arrested in the capillary beds of target organs.

Evidence of a role for chemotaxis in intravasation: Recent studies confirm the ability of metastatic cells to chemotax away from primary tumours in response to growth factors commonly associated with the vasculature (Wyckoff et al., 2000b). In these studies the authors inserted microneedles loaded with matrigel and growth factors into rat tumours in order to assess the chemotactic ability of metastatic and non-metastatic tumour cells *in vivo*. It was found that while tumour cells readily infiltrated microneedles inserted into metastatic tumours only modest infiltration was found in the case of non-metastatic tumours. The subsequent genetic analysis of the two tumour populations used in these studies revealed that metastatic tumour cells expressed significantly higher levels of the EGF receptor when compared to non-metastatic tumour cells (Wang et al., 2002b). Therefore EGF, which is abundant in serum, platelets, and vascular smooth muscle cells, may provide an essential signal for the chemotactic driven intravasation of certain tumour cells.

Both the intravital imaging of living tumours and the analysis of histopathological sections of fixed tumours reveal that cells often polarize towards blood vessels in metastatic tumours but are essentially randomly polarised in non-metastatic tumours (Wyckoff et al., 2000a). Cells of metastatic tumours are therefore able to detect directional cues in the tumour microenvironment that actively guide them towards the local vasculature, while cells of non-metastatic tumours are either blind or unable to respond to these signals. Large numbers of immune cells can also be found to infiltrate metastatic tumours, something that is less

apparent in non-metastatic tumours. Growth factors and other cytokines released by immune cells as they enter the tumour may attract metastatic cells towards blood vessels and thus further enhance the process of intravasation.

Evidence of a role for chemotaxis in extravasation: A potential role for chemotaxis during the final stages of metastasis could also be inferred from the fact that many cancers exhibit organ-specific metastases (Fidler and Hart, 1982; Rusciano and Burger, 1992). Although many target organs of metastases are usually dense with microvasculature such as bone, lungs and liver, passive cell trapping alone is insufficient to explain the organ-specific aspect of this process. For instance, the spleen is a highly vascular organ and yet represents a rare site of metastasis (Pollock, 1999). Furthermore, although sites of secondary tumour growth often reside in organs that represent the first significant vascular network downstream of the site of primary tumour growth, this is certainly not the rule: lung carcinomas often shed metastasis to the adrenal gland which represents a surprisingly distant anatomical target for this cancer, while neuroblastomas target the liver and bone, but rarely the lung, which is otherwise a common site of metastasis for many other cancers (Pollock, 1999; Rusciano and Burger, 1992).

A large body of experimental data now exists that indicates that sites of metastases are not determined by the mere anatomical distribution of target organs. The intravenous injection of the M5076 murine sarcoma cell line into mice results in the rapid accumulation of tumour cells within the lung, the first dense vascular network that these cells encounter. However, over a period of 3-4 days the cells slowly filter through the pulmonary capillary network and

subsequently traffic to the liver where they finally establish metastases (Hart et al., 1981). More recent studies have also shown that mixed populations of cells from tumours that shed metastasis to differing locations show distinctive trafficking *in vivo*, revealing the preferential persistence of one population over the other in different body tissues (Koike et al., 1997). The phenomenon of organ-specific metastasis is likely to be a consequence of a multitude of factors that include the preferential adhesion of metastasising cells to organ-specific endothelial cell markers, the chemotactic response of these cells towards growth factors associated with the target organ, and the ability of these cells to persist and finally grow in a foreign organ environment. Adhesion interactions between circulating cancer cells and cells of the endothelium are likely to play a key role in the initial process of target organ selection. Indeed, *in vitro* studies reveal that metastatic cell lines preferentially adhere to endothelial sheets derived from those organs that represent the cancer cells' *in vivo* targets (Auerbach et al, 1987). However, once adhered to the endothelium the subsequent process of extravasation is likely to depend on the ability of the metastasising cells to detect and respond to chemotactic signals that direct cell migration into the organ itself (Hujanen and Terranova, 1985; Rusciano and Burger, 1992).

A wealth of evidence exists that strongly links the chemotactic behaviour of metastatic cells to extravasation. Chemokines, which bind to growth factor receptors specifically upregulated in breast cancer cells, exhibit peek levels of expression in those organs most commonly targeted by metastasis in this disease (Muller et al., 2001): the expression of the CXCR4 receptor promotes the metastatic spread of the 1231 breast carcinoma cell line to the regional lymph nodes and liver when injected into the tail vein of nude mice. Both these organs

represent abundant sources of SDF-1, the specific ligand for this receptor, and are both common targets of breast cancer metastasis. The pre-treatment of cells with a blocking antibody specific for the CXCR4 receptor prior to intravenous injection prevents the formation of metastases at these sites, implicating a role for chemotaxis in organ-specific targeting and extravasation. *In vitro* studies reveal the preferential chemotaxis of prostate cancer cells towards tissue extracts from bone marrow, a common target for prostate cancer metastasis, whilst extracts from other tissues have poor chemotactic effects (Jacob et al., 1999). Similar examples of the preferential chemotaxis of cancer cells towards tissue extracts derived from their *in vivo* target organs have been shown for melanoma, sarcoma, and breast carcinoma cell lines (Hujanen and Terranova, 1985). It has also been demonstrated that the injection of chemotactic factors into the peritoneal cavity of rats promotes the formation of multiple metastases in the surrounding mesenchymal tissue upon the intravenous injection of Walker carcinosarcoma cells (Lam et al., 1981). Taken together, these findings strongly implicate an important role for chemotaxis in both the initial intravasive and final extravasive stages of the metastatic cascade. A knowledge of the cellular mechanisms involved in the promotion and regulation of cancer cell chemotaxis could, therefore, provide additional targets for the development of new cancer therapies.

Additional requirements for metastasis: Chemotaxis is not the sole requirement for efficient metastasis as other mechanisms such as matrix degradation, regulated adhesion, and angiogensis are also required for efficient cancer spread. It is now believed that cells of non-tumour origin that are either recruited to, or resident within the local tumour vicinity may provide some of these additional requirements. For instance, fibroblasts isolated from basal

cell carcinomas show elevated levels of protease production, and so are likely to aid the metastatic process through the solubilisation of local matrix, a major barrier to cell motility (Pauli et al., 1983). The abnormal behaviour of host cells within the vicinity of the tumour is a consequence of both paracrine signalling and direct tumour cell-stromal cell interactions. Through these mechanisms tumour cells are able to modify the gene expression of local fibroblast populations, promoting their production and secretion of numerous proteolytic enzymes. *In vitro* studies reveal that co-cultures of human fibroblasts and MCF7 human breast carcinoma cells induce the production of collagen and lamanin proteases in the fibroblast population (Ito et al., 1995). Indeed, the importance of matrix degradation in cancer spread is paramount as the degree of protease activity within a tumour often directly correlates with progression to a malignant phenotype, characterised by increased local tissue invasion and metastasis (Murphy et al., 1989; Pauli et al., 1983).

Local inflammatory responses are also likely to aid tumour survival and spread. Mast cells, which accumulate in high numbers at regions of tumour invasion, degranulate and release potent proteases and chemical factors that promote neovascularisation. As vascular endothelial cells penetrate the tumour mass in response to these angiogenic signals they further promote matrix degradation through the release of additional proteolytic enzymes (Pauli et al., 1983). The exploitation of host angiogenic mechanisms is likely to be crucial for metastasis as dense vascular growth within the tumour provides a local route into the wider blood stream. This is aided further by the fact that much of this new vascular growth is thin-walled and consequently leaky (Ahmad and Hart, 1997). Furthermore, angiogenesis is essential for the progressive growth of both primary and metestatic tumours, as any tumour

mass that exceeds a radius of approximately 1- 2 mm must establish an independent blood supply (Fidler and Ellis, 1994).

31.3 Mechanisms of chemotaxis

Chemotaxis is a motile response that is well defined at the level of cell behaviour. The intracellular signalling cascades and molecular machinery that control the chemotactic response, however, are likely to be highly complex. The key to cell motility lies in the cytoskeleton, a dynamic network of filaments and associated proteins whose organisation dictates cell morphology (Machesky and Insall, 1999; Pollard and Borisy, 2003). An effective chemotactic response requires that a cell polarise in the direction of the chemotactic gradient (Bray, 2001). Such a process can only be achieved through a dramatic spatial and temporal reorganisation of the actin cytoskeleton. For a number of vertebrate cell types it has been suggested that the chemotactic response requires the initial protrusion of actin rich extensions or filopodia towards the stimulus (Ridley et al., 1995; Zicha et al., 1998). Once established these extensions can function as the primary scaffold that guides the forward propagation of an actin filament array that constitutes the underlying structural framework of the lamellipodium or cell leading edge whilst the constant pinocytosis of activated receptor at the leading edge may function to intensify the signalling gradient within the cell and further enhance polarity (Bailly et al., 2000). Once established this asymmetric shape, with appropriate adhesion to the substrate, enables the cell to migrate along the axis of polarisation using its acto-myosin machinery.

A directed motile response such as in chemotaxis requires the effective processing of spatial and temporal cues in the cell's microenvironment and the transmission of this information to the cytoskeleton to enable correct morphological responses. The plethora of actin binding proteins that directly modify filaments through capping, severing, bundling, cross-linking, nucleating and extracellular matrix anchoring lie at the heart of this process (Machesky and Insall, 1999). They translate cell surface signals into the mechanics of cell movement. Understanding chemotaxis therefore lies in understanding the mechanisms that control the spatial and temporal activity of these proteins. Many molecules have been identified as signalling intermediates between cell surface receptors and the actin cytoskeleton including protein kinases (Kiley et al., 1992; Kiosses et al., 1999), scaffold proteins (Takenawa and Miki, 2001), and the Rho family of GTPases (Aspenstrom, 1999; Bishop and Hall, 2000; Ridley, 1996) all of which are likely to operate through their effects on the actin binding proteins.

3.1.4 Regulators of cell polarity

A number of signalling molecules have previously been identified as important regulators of cell polarity in a variety of cell systems and thus provide logical candidates for study in the chemotaxis of cancer cells. Many of these molecules are found to exhibit a high degree of functional conservation, regulating polarity in unicellular and multicellular organisms and in cells of a broad range of tissue types. Those regulators of polarity that have been directly implicated in the chemotaxis of various mammalian cell types formed the primary focus of this study.

3.1.5 Cdc42

Cdc42, an extensively characterised member of the Rho family of GTPases, is likely to regulate polarity in most, if not all, eukaryotic cells (Etienne-Manneville and Hall, 2002; Johnson, 1999). It represents an important signalling intermediate in the transmission of receptor signals to the actin cytoskeleton, mediating its effects through interactions with various downstream target proteins that either directly or indirectly regulate actin assembly. Many of these targets have themselves been identified as important regulators of polarity suggesting the existence of a network of interconnected and highly conserved proteins involved in cell polarity control.

Cdc42 belongs to the Rho family of GTPases, small monomeric proteins 20 kDa – 30 kDa in size that catalyze GTP hydrolysis (Bishop and Hall, 2000; Hall, 1998; Ridley, 1996). Their activity is dictated by the nature of their bound nucleotide: in the GTP bound form the protein is active, can localize to membranes, and interact with effector molecules, thereby initiating downstream signalling events. In the GDP bound form the protein is inactive and largely sequestered in the cytoplasm by inhibitory proteins that prevent membrane localization and spontaneous nucleotide exchange. Activation of Cdc42, as with the other Rho family members, is largely governed by interactions with the guanine nucleotide exchange factors (GEFs), GTPase activating proteins (GAPs) and GDP-disassociation inhibitors (GDIs) that regulate both the nature of the bound nucleotide and the inherent GTPase activity of the protein. The GEFs associate with the inactive form of Rho-family proteins and catalyze the exchange of bound GDP for GTP that is required for activation. The Rho-family members exhibit intrinsic GTPase activity and the eventual hydrolysis of bound

GTP to GDP+P_i renders the protein inactive once more. However, their intrinsic GTPase activity is inefficient and the process of GTP hydrolysis inherently slow. The GAPs therefore act to greatly enhance this process and upon GTPase binding, promote the rapid conversion of bound GTP to GDP+P_i terminating further downstream signalling events. The post-translational modification of Cdc42 and various other Rho-family members result in the prenylation of the carboxy terminus of the protein providing the addition of a geranylgeranylation isopropene group, a prerequisite for membrane targeting and protein function. When inactive, inhibitory proteins (GDIs) mask this c-terminal lipid anchor sequestering and solubilising the protein within the cytoplasm. However, upon activation Cdc42 is delivered to the membrane where it is free to interact with potential signalling partners (Figure 24, page 19).

Interactions with effector proteins are likely to be mediated through the switch I and switch II domains of Cdc42, two surface loops which undergo conformational alterations that depend on the nature of the bound guanine nucleotide. Interactions between the active conformation of the switch I domain and a conserved GTPase consensus site, the CRIB (Cdc42/Rac interactive binding) domain, found within many Cdc42 target proteins provides the major mechanism of Cdc42/effector binding. CRIB domain binding induces subsequent conformational changes in the target protein, often through the disruption of intermolecular auto-inhibitory interactions, resulting in protein activation and further downstream signalling (Bishop and Hall, 2000).

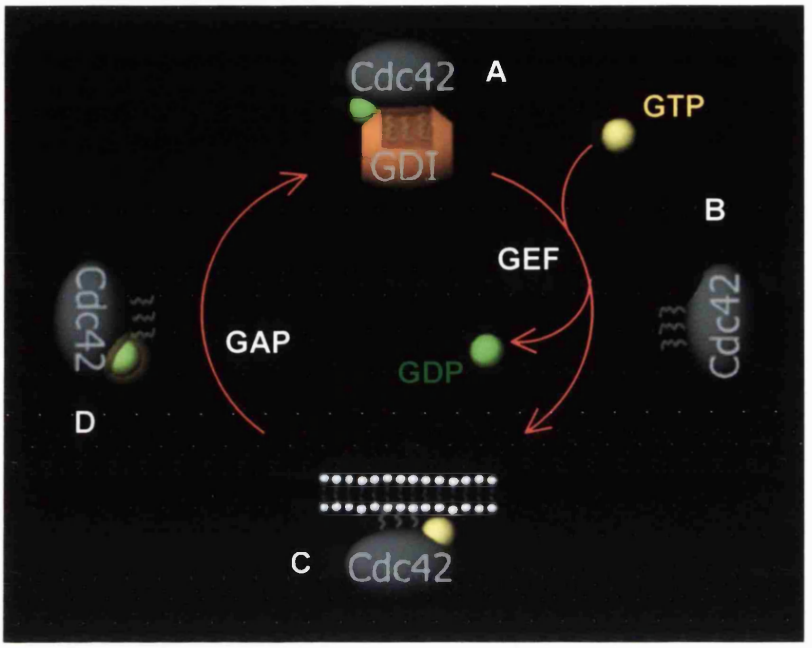

Figure 24. The Rho GTPases

The Rho GTPases function as molecular switches, cycling between active GTP-bound and inactive GDP-bound states. They are regulated by their associated guanine nucleotide exchange factors (GEFs), GTPase activating proteins (GAPs) and GDP-disassociation inhibitors (GDIs). (A) GDIs function as inhibitors of Rho proteins, sequestering the inactive/GDP-bound form of the protein within the cytoplasm. (B & C) GEFs activate Rho proteins by catalysing the exchange of the bound GDP for GTP, allowing membrane localisation and interaction with downstream effector molecules. The intrinsic GTPase activity of Rho family proteins results in the eventual hydrolysis of bound GTP and a return to the inactive state, thus terminating signalling. (D) GAPs, however, greatly enhance this process and rapidly down-regulate signalling upon association with the Rho protein.

Cdc42 and polarity: The importance of Cdc42 in cell polarity was first established as a consequence of studies performed in *Saccharomyces Cerevisiae.* In these studies cells that carried temperature sensitive mutants of Cdc42 were found to have markedly disorganised actin structures and exhibited both a loss of polarised cell growth and an inability to form buds during mitosis (Adams et al., 1990). Additional localisation studies revealed that wild-type Cdc42 was highly concentrated at sites of bud emergence and within pheromone-induced mating projections, further indicating the importance of Cdc42 in yeast polarity (Ziman et al., 1993). Since these initial studies Cdc42 has been implicated in the control of cell polarity in almost all eukaryotic organisms in which this protein has been studied. Polarised outgrowth of the fungus *Penicillium marneffei* is dependent upon Cdc42 activity, inhibition of which results in aberrant haephae outgrowth and disorganised septum formation (Boyce et al., 2001). Recent studies demonstrate the importance Cdc42 function in establishing the polarity of the single-cell embryo of the worm *Caenorhabditis elegans* (Gotta et al., 2001), while Cdc42 dependent actin rearrangements control neurite outgrowth in the *drosophila* fly (Johnson, 1999).

Cdc42 has also been shown to govern a range of polarity events in mammalian cell systems: The selective diffusion of lipids and membrane proteins across tight junctions, and the regulation of vesicular trafficking to basolateral and apical membranes are essential for the maintenance of epithelial sheet polarity, and are two cellular processes in which Cdc42 function is known to play a role (Rojas et al., 2001). The correct alignment of the Golgi apparatus towards antigen presenting cells and the accompanying increase in actin polymerisation at areas of cell-cell contact are disrupted in helper T-lymphocytes following

Cdc42 inhibition (Stowers et al., 1995), while in rat embryonic fibroblasts inhibition of Cdc42 disrupts the orientation of the Golgi apparatus along the axis of cell migration (Nobes and Hall, 1999). A more recent and striking discovery is the dependence of the chemotaxis of certain cells of the mammalian immune system on Cdc42 function: the chemotaxis of either T-lymphocytes to gradients of SDF-1 (Haddad et al., 2001) or Bac1 macrophages to gradients of CSF-1 (Allen et al., 1998) is abolished following Cdc42 inhibition.

Given the importance of Cdc42 function in the chemotaxis of cells of the mammalian immune system, as well as the central role for this protein in the regulation of cellular polarity *per se*, Cdc42 provides an obvious candidate for study in the chemotaxis of cancer cells. Indeed, with respect to cancer biology, one key question that arises is whether metestatic cancer cells acquire the ability to exploit the same signalling mechanisms that cells of the immune system use to regulate their motile and chemotactic machinery.

3.1.6 Tc10

The recent characterisation of the Rho GTPase Tc10 has revealed that this protein shares many common downstream targets with Cdc42, including proteins involved in the regulation of actin assembly (Neudauer et al., 1998). Tc10 and Cdc42 exhibit a high degree of sequence homology (> 65 %) (Murphy et al., 1999). The switch I domains of these proteins are highly homologous (> 70 %), permitting their association with a similar range of CRIB domain containing effector proteins including N-WASP, and PAK1, key regulators of actin dynamics. The ectopic expression of constitutively active variants of Tc10 in fibroblasts and neurones induces the formation of filopodia, actin-rich structures commonly associated with

Cdc42 activation (Neudauer et al., 1998). Taken together these finding make Tc10 an obvious candidate for the additional regulation of polarity events in mammalian cells.

Tc10 and polarity: Despite their similarities, recent studies have established a role for Tc10 in the regulation of mammalian cell polarity that appears to be distinct to that of Cdc42. For instance, Tc10 has been shown to induce new neurite outgrowth in the N1E-115 mouse neuroblastoma cell line (Abe et al., 2003), while Cdc42 has no effect. Organ culture studies reveal that Tc10 mRNA expression is dramatically upregulated in dorsal root ganglia neurones following axotomy, promoting the regeneration and polarised outgrowth of new neurite extensions (Tanabe et al., 2000). The expression levels of other GTPases are, however, unaffected. The importance of Tc10 in polarity has largely come from studies performed in tissue-cultured neurones and, to a lesser extent, fibroblasts cell lines. The role of Tc10 in the regulation of polarity in other cell types remains to be established. However, recent findings make it is easy to speculate that this protein may provide an additional mechanism of GTPase-dependent polarity regulation in a number of other cell systems and that Tc10 signalling may both complement and also function independently from Cdc42 associated signalling processes.

3.1.7 The WASP-family proteins

Actin filament assembly is essential for cell protrusion and therefore polarity and motility. Consequently, Cdc42 and Tc10 must mediate much of their control on cell polarity through the remodelling of the actin cytoskeleton. However, as GTPases do not interact directly with

actin monomers or filaments their effects must be mediated through downstream effector molecules that target the actin cytoskeleton either directly or indirectly.

Nucleation is the limiting factor in filamentous actin assembly. Consequently signalling events that induce actin assembly must utilize mechanisms that promote actin nucleation either through the uncapping or severing of pre-existing filaments to provide exposed sites for further filament elongation, or through the activation of specific actin nucleating proteins that promote *de novo* filament production. The Wiskott-Aldrich syndrome protein (WASP) family members represent key regulators of actin assembly, providing a common mechanism for the *de novo* polymerization of actin filaments (Takenawa and Miki, 2001). The WASP family members include WASP, expression of which is restricted to cells of haematopoietic origin, neuronal WASP (N-WASP), which is ubiquitously expressed, and the SCAR/WAVE proteins. WASP family members collectively integrate signals from a number of upstream pathways and translate them into filamentous actin assembly through a common effector; the Arp2/3 actin-nucleating complex (Machesky and Gould, 1999). Their ability to converge signalling in this way is reflected in the nature of their structure: the amino terminus that dictates the binding of upstream regulators varies widely in sequence homology between WASP-family members, while the carboxyl terminus that recruits actin and the Arp2/3 complex remains highly conserved. The VCA domain (for verproline homology, cofilin homology, acidic region) that lies within the carboxyl termini of all WASP-family members is responsible for actin and Arp2/3 binding, and upon recruitment of these molecules an actin assembly complex is formed that catalyses the rapid nucleation of actin and thereby the polymerization of new filaments.

N-WASP is likely to mediate Cdc42/Tc10 dependent actin assembly in a variety of mammalian cell types. The carboxyl-terminus of N-WASP contains the VCA region common to all WASP family members while the amino-terminus contains a unique GTPase binding domain (GBD) specific for Cdc42/Tc10 binding and which is crucial for the regulation of N-WASP function (Kim et al., 2000). The GBD region consists of a core 16 residue CRIB motif and flanking sequences that stabilize GTPase binding. Upon Cdc42/Tc10 binding N-WASP undergoes a dramatic conformational change that provides a scaffold for the assembly of a multimeric actin nucleating and polymerising complex.

The mechanism of activation of Rho-family effectors commonly involves the disruption of an autoinhibitory state that reveals catalytic or adaptor domains within the target molecule, which once exposed, can initiate further downstream signalling events. N-WASP adheres to this theme and in the inactive state adopts a folded, autoinhibitory conformation that results from intramolecular associations between the GBD and VCA domains (Kim et al., 2000). This association occludes VCA-Arp2/3 binding and thus inhibits actin assembly. However, active Cdc42/Tc10 competes with the VCA domain for GBD binding, thereby disrupting the autoinhibitory association. Once exposed the VCA region is available to recruit the Arp2/3 complex and initiate actin assembly. Acidic phospholipids such as phosphoinositide-(2,4)-bisphosphate ($PI(4,5)P_2$) are believed to further modify and/or enhance the effects of N-WASP activation, possibly by stabilising active GTPase/N-WASP complexes at the membrane (Prehoda et al., 2000). Once localised at the membrane the N-WASP/actin assembly complex can stimulate actin filament production and the subsequent cell protrusion

required for cell motility. The mode of N-WASP activation is summarized in Figure 25, page 19.

N-WASP and polarity: WASP-family proteins are likely to mediate much of the actin reorganisation that underlies Cdc42/Tc10 dependent changes in cell morphology and polarity. Mutations in haematopoetic WASP lead to the congenital disorder Whiskott-Aldrich Syndrome, the condition from which the protein acquires its name, and in which macrophage and monocyte chemotaxis is found to be greatly impaired (Badolato et al., 1998; Zicha et al., 1998). Given the importance of Cdc42 signalling in the chemotaxis of Bac1 macrophages it is likely that a Cdc42/WASP pathway regulates chemotaxis in these cells. Furthermore, activation and direct interaction of Cdc42 with WASP has been reported as essential for the chemotaxis of T-lymphocytes toward SDF-1 (Haddad et al., 2001), suggesting that this pathway plays a common role in the regulation of chemotaxis in cells of haematopoietic origin.

N-WASP has been associated with polarity events in cells of non-haematopoetic origin, regulating axonal outgrowth in hippocampal neurons (Banzai et al., 2000), and invasion and tubulogenesis in epithelial cells (Yamaguchi et al., 2002). Although the importance of WASP in the chemotaxis of cells of haematopoitic origin is now well established, a possible role for N-WASP in the chemotaxis of cells of non-haematopoetric origin has only recently begun to be explored. The similarities between these proteins both in sequence homology (> 50 %), their effects on cytoskeletal remodelling, and their shared upstream regulators make N-WASP an obvious candidate for study in the chemotaxis of cancer cells.

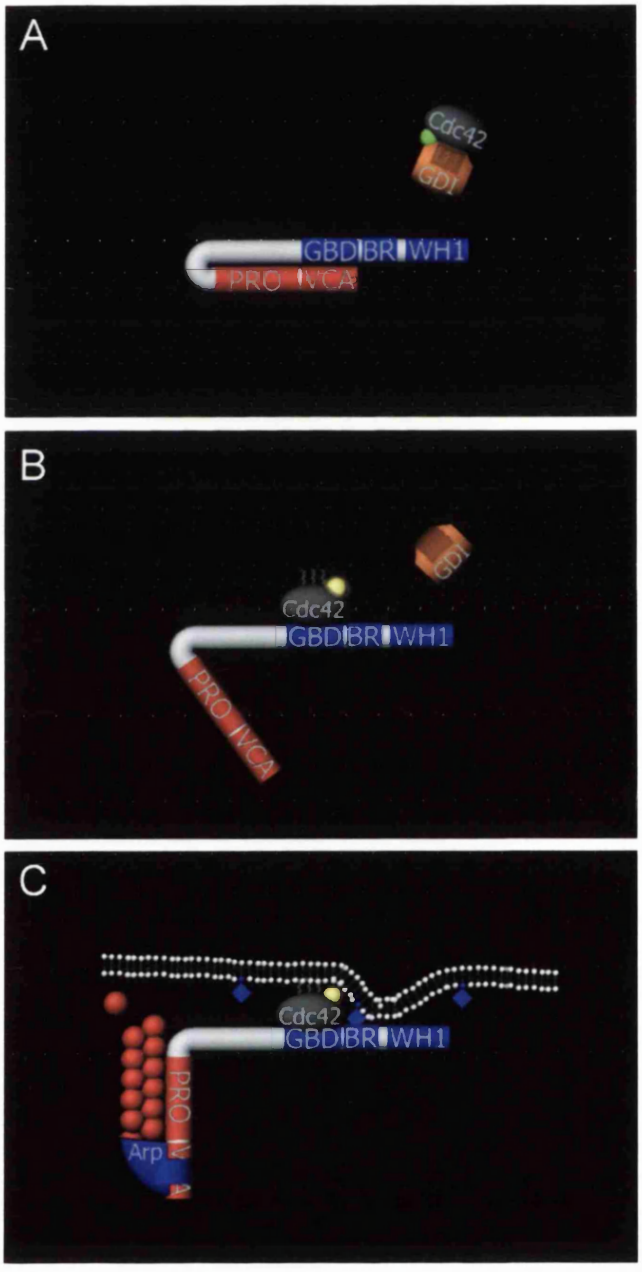

Figure 25. Activation of N-WASP

(A) When inactive N-WASP adopts a folded, autoinhibited conformation due to intramolecular associations between the VCA domain and the GTPase binding domain (GBD). (B) Upon activation and liberation from sequestering Rho-GDI Cdc42 can bind the GBD domain of N-WASP, disrupting these intramolecular associations and exposing the VCA region. (C) Cdc42 and PIP_2 synergistically function to stabilize active N-WASP at the membrane. Recruitment of Arp2/3 to the exposed VCA domain initiates de novo actin polymerisation, initiating cytoskeletal changes.
GBD: GTPase binding domain.
BR: Basic region.
PR: Proline rich domain.
WH1: WASP homology 1.
VCA: verproline homology, cofilin homology, acidic region.

31.8 PAK serine/threonine kinases

The p21-activated kinases (PAKs) represent a family of highly conserved serine/threonine knases that regulate cell morphology and motility through their effects on the actin cytoskeleton and cell adhesion (Edwards et al., 1999; Kiosses et al., 1999; Sells et al., 1999; Sells et al., 1997). Four mammalian PAK isoforms have been identified to date, all of which represent downstream targets for regulation by Rho family GTPase. With the potential to both regulate and be regulated by a wide range of proteins PAK signalling is, to say the least, complex. Furthermore although the kinase activity of PAK is essential for certain signalling processes it seems to be largely irrelevant for others, and although originally characterised by their ability to both bind and become activated by GTPases, it is now clear that PAKs can also function in a GTPase independent manner.

PAK1 is the most highly characterized of all the mammalian PAK isoforms. In keeping with the characteristics of other GTPase effectors, PAK1 activation is believed to initially involve the disruption of autoinhibitory interactions (Lei et al., 2000). Indeed the functional organization of PAK1 is remarkably similar to that of N-WASP, although they are essentially unrelated proteins. PAK1 is divided into two basic functional regions; a kinase domain within the carboxyl-terminus and a regulatory domain within the amino-terminus. In the inactive, autoinhibited state PAK1 exists as a soluble dimer, the kinase domain of one molecule bound tightly to an autoregulatory domain within the amino-terminus of the other (Figure 26A). The autoregulatory domain consists of a p21 binding domain (PBD) (70 – 113) that binds to the active form of Rho GTPases, and an overlapping, upstream inhibitory sequence (83 – 149) that binds and masks the catalytic site of the kinase domain when the

protein is in the autoinhibitory conformation. The PBD domain of PAK1 contains a CRIB motif and is analogous in function to the GBD domain of N-WASP. Upon binding to the PBD domain active GTPases disrupt protein dimerisation and therefore the intermolecular autoinhibitory conformation, resulting in the liberation of active PAK1 monomer (Figure 2.6B). Autophosphorylation events that follow the liberation of the kinase domain further stabilize the activity of molecule. Interestingly, it has been reported that, for at least PAK3, the phosphorylated protein exhibits a reduced affinity for GTPases *in vitro*, possibly reflecting an intrinsic feedback mechanism for the down regulation of PAK activity (Hashimoto et al., 2001). The autoregulatory sequence of PAK1 is very similar in structure to that of N-WASP and this has lead to speculation that these proteins may potentially form heterodimeric complexes *in vivo* (Lei et al., 2000).

Other sites for protein targeting are provided by proline-rich sequences that flank the autoregulatory domain of PAK1. Proline rich sequences upstream of the autoregulatory region provide competitive targets for both paxillin and Nck providing independent links to both focal adhesion-associated signalling and growth factor receptor-associated signalling pathways respectively: Paxillin is an adaptor protein that acts as a scaffold in the formation of integrin assembly complexes and has been reported to localise both kinase-active and kinase-inactive forms of PAK1 to focal adhesion complexes (Hashimoto et al., 2001). Nck, on the other hand, is an adaptor protein that is recruited to receptor tyrosine kinases upon growth-factor stimulation (Lu et al., 1997; Lu and Mayer, 1999). Therefore Nck provides a mechanism for PAK1 membrane localization that may further help to stabilise GTPase/PAK1 complexes and to specifically localize PAK1 to sites of receptor activation

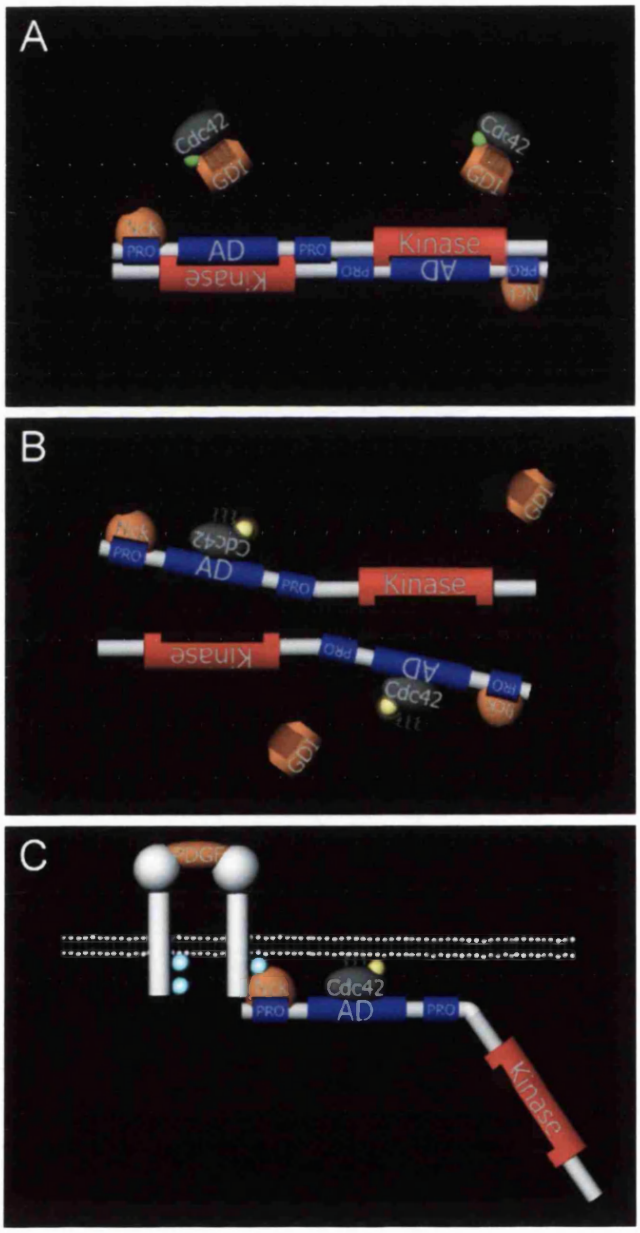

Figure 26. Activation of PAK1

(A) Inactive PAK1 exists as a soluble dimmer in the cytoplasm, the kinase domain of each respective monomer blocked by the autoregulatory domain of the other. (B) Upon activation and liberation from sequestering Rho-GDI Cdc42 can bind the autoregulatory domain of PAK1, disrupting the dimer and exposing the catalytic domain. (C) Cdc42 can then stabilise active PAK1 monomer at the membrane. Localization of active Cdc42/PAK1 complexes to sites of receptor activation could be mediated by the adaptor protein Nck, which is constitutively bound to the amino terminus of PAK1.
AD: Autoregulatory domain.
PRO: Proline rich domain.
Kinase: Catalytic domain.

(figure 26C). The degree to which PAK1 preferentially associates with either paxillin or Nck is unknown although it has been suggested that the latter constitutively associate with PAK1 in unstimulated cells (Lu et al., 1997). Additional proline rich sequences downstream of the autoregulatory domain of PAK1 provide targets for the guanine nucleotide exchange factor PIX (PAK-interacting exchange factor) (Lei et al., 2000). The recruitment and subsequent phosphorylation and activation of PIX by PAK1 may provide a feedback loop for PAK1 activation: PIX is a GEF and once active may therefore promote further GTPase activity and further drive and amplify PAK1 activation pathways.

Upon activation PAK1 has been reported to orchestrate cytoskeletal rearrangements through the phosphorylation of a number of target substrates including LIM kinase (Edwards et al., 1999), filamin (Vadlamudi et al., 2002), and both Myosin Light Chain (MLC)(Sells et al., 1999) and Myosin Light chain Kinase (MLCK) (Sanders et al., 1999). The phosphorylation and subsequent activation of LIM kinase is likely to influence cytoskeleton turnover through the subsequent downstream phosphorylation and inhibition of cofilin, an actin filament severing protein. Activation of the actin binding protein filamin provides a mechanism for the orthogonal cross-linking of actin filaments, a process believed to be required for the formation of actin ultra-structures such as membrane ruffles. An increase in myosin light-chain phosphorylation following PAK1 activation could directly effect morphology and motility by regulating Myosin-based cell contractility. However, the identification of MLCK as a potential substrate for PAK1 suggests that in certain circumstances PAK1 can also inhibit Myosin function. Therefore, although it is clear that PAK1 is important for the

regulation of Myosin function, the extent to which PAK1 up regulates or down regulates the activity of this protein remains to be established.

PAKs also have the capacity to regulate cytoskeletal changes through kinase independent mechanisms, indicating that these proteins exhibit more than one mode of action. For instance it has been shown that upon recruitment to the plasma membrane PAK1 can induce changes in the actin cytoskeleton that are independent of either kinase activity (Frost et al., 1998; Sells et al., 1999), or GTPase binding (Bokoch et al., 1998; Vadlamudi et al., 2002). PAK signalling is therefore likely to be complex, offering multiple methods of activation and of relaying downstream signals. The degree to which PAK1 exhibits either GTPase dependent/independent and/or kinase dependent/indenpendent signalling *in vivo* to orchestrate cytoskeletal rearrangements remains unclear. It is possible that PAK1 may be employed in polarity mechanisms that are both related and independent of GTPase signalling. However, it is clear that PAK1 is a key regulator actin dynamics and a crucial regulator of polarity in many biological systems.

PAK1 and polarity: The role of the PAK-family proteins in cell polarity is wide ranging. The PAK homologue STE20 regulates actin assembly and morphogenesis in Saccharomyces cerevisiae (Eby et al., 1998) and overexpression of this protein can compensate for much of the morphological defects associated with loss of Cdc42 function, highlighting the importance of PAK in Cdc42 dependent signalling to the cytoskeleton. In protozoa PAK-related proteins have been implicated in the chemotaxis of Dictyostilum discoideum (Chung and Firtel, 1999) and in the efficient polarization and motility of the pathogenic parasite

Entamoeba histolytica the underlying cause of the human disease amoebiasis (Labruyere et al., 2003). In Drosophila PAK proteins are believed to regulate actin assembly in the motile growth cone during axonal guidance and neuron migration (Hing et al., 1999).

In mammalian cells PAK family members have been identified as key regulators of polarity and motility, regulating protrusion, ruffling, and contractility: in NIH 3T3 fibroblasts PAK1 has been reported to function as a potent stimulator of cell motility, irrespective of its kinase activity (Sells et al., 1999). However, both the persistence of cell movement and the co-ordination of lamellipodial protrusion in these cells are highly dependent upon the kinase function of this protein. Indeed, the over-expression of a constitutively active kinase variant of PAK1 greatly enhances the haptotactic response of NIH 3T3 fibroblasts to immobilised collagen gradients. In other studies the Cdc42-dependent activation of PAK1 kinase activity has been reported to be required for the CXCL1 driven chemotaxis of human embryonic kidney cells, directly implicating a role for PAK1 in the chemotaxis of mammalian cells (Wang et al., 2002a). Therefore, it is possible that WASP-family and PAK-family proteins provide divergent pathways downstream of Cdc42 in the regulation of mammalian cell chemotaxis.

3.1.9 Sarcoma cell lines derived from inbred rats as a model for metastasis

In this study the RPSL4T15 rat sarcoma cell line (T15) was used to examine *in vitro* the signalling molecules involved in the chemotaxis of metastatic sarcoma cells. Sarcomas are malignant neoplastic growths of mesenchymal origin that exhibit incredibly high instances of metastasis. They are commonly anaplastic (undifferentiated) growths that shed metastasis

primarily to the lungs and liver preferentially through venous networks. Cancers of the epithelium (carcinomas) are generally less aggressive in comparison and typically favour the lymphatics as a route for metastatic spread. Although cancers of the mesenchyme are uncommon, accounting for less than 1 % of annually diagnosed adult malignancies, they are associated with an exceptionally high instance of mortality (close to 50 %) (Pollock, 1999).

The T15 rat sarcoma cell line provides a useful tool for understanding both the *in vivo* and *in vitro* behaviour of metastatic sarcoma cell populations. Derived *in vitro* from spontaneously transformed rat embryonic fibroblast, the T15 cell line has been established through the progressive selection *in vivo* in of cell populations of increasing malignant phenotype (Vesely et al., 1987). The cell line, although largely maintained in culture, is subjected to periodic cycles *in vivo* in singeneic, inbred rats to confirm and maintain its metastatic potential. The T15 cell line differs considerably with respect to morphology, motile behaviour, and metastatic potential when compared to the less aggressive LW13K2 cell line (K2) from which it was originally derived. A striking difference lies in the chemotactic potential of each cell line: T15 sarcoma cells exhibit strong chemotaxis in gradients of PDGF-BB and IGF-1, two growth factors commonly associated with the vasculature, while non-metastatic K2 cells show little or no directional response (Zicha and Dunn, 1995). Therefore, the T15 cell line provides a valuable model for the study of the subcellular signalling mechanisms involved in the chemotaxis of metastatic sarcoma cells. That the potential to chemotax is a characteristic of T15 cell line and not the related non-metastatic K2 cell line is analogous to findings made by others: Wycoff *et al* have shown that the MTLn3 metastatic cell line can exhibit EGF dependent chemotaxis *in vivo* while the non-

metastatic but related MTC cell line cannot (Wyckoff et al., 2000b). The PDGF-BB/IGF-1 dependent chemotaxis of T15 sarcoma cells is therefore likely to be an important feature of their metastatic phenotype, as these chemotactic factors are likely to guide cells towards local venous networks within the tumour microenvironment *in vivo*. The chemotaxis of T15 sarcoma cells was used here as a model for the study of chemotactic behaviour associated with the initial stages of sarcoma cell intravasation. Using this model a range of signalling molecules previously associated with the control of chemotaxis and/or polarity in other mammalian systems were assessed to determine their role, if any, in the regulation of sarcoma cell chemotaxis.

3.1.10 Methods of analysing chemotactic behaviour

The in vitro study of chemotaxis: A variety of assays have been developed for the analysis of chemotaxis *in vitro,* all of which have their merits and shortcomings. The most common *in vitro* assay for the study chemotaxis is provided by the Boyden chamber, a trans-well assay in which a chemotactic response in inferred by the ability of cells to migrate across a polycarbonate membrane filter separating two compartments, one of which contains the chemoattractant (Boyden, 1962). The Boyden chamber has been heavily employed in the study of leukocyte chemotaxis, and has provided a sensitive technique for the large scale screening of various putative chemokines. The technique allows large cell numbers to be assayed quickly providing important quantitative information concerning the chemotactic potential of a specific cell line or type. However, observations are prone to misinterpretation if insufficient measures are taken to enable the experimenter to effectively discriminate between the chemokinetic and chemotactic effects of particular treatments: the ability of cells

to migrate across a membrane in the presence of a putative chemoattractant does not, in itself, provide unequivocal confirmation of chemotaxis, as the experimenter cannot preclude the possible chimokinetic effects of the treatment providing the same outcome. However, if a system of Zigmond-Hirsch checkerboard analysis is adopted in Boyden chamber chemotaxis assays then any chemokinetic effects associated with a particular treatment can be controlled for (Zigmond and Hirsch, 1973). When checkerboard analysis is applied, the Boyden chamber can provide a very powerful and sensitive method for assessing chemotactic behaviour. Indeed, the Boyden chamber has contributed significantly to our understanding of the chemotaxis of mammalian cells. That this technique represents the first reliable assay for the reproducible study of chemotaxis and that it remains, to this day, the most common method for studying chemotaxis is a testament to its simple but highly effective design.

The major limitation of the trans-well assay is that it does not permit the direct observation of cell behaviour, and consequently chemotaxis can only be inferred from the final distribution of the cell population. The effects that a particular treatment may confer on the speed, persistence, and morphology of cells during the course of a chemotaxis experiment cannot therefore be assessed. If this information is desirable then specialised chemotaxis assays designed specifically for use in conjunction with light microscopy techniques are required. A broad range of such techniques have been developed and applied with varying degrees of success. Early efforts to combine the study of chemotaxis with microscopy involved relatively crude techniques such as the use of sephadex beads containing soluble chemotactic factors as point sources of radially diffusing chemoattractants (Allan and Wilkinson, 1978). This is similar in principle to more recent techniques involving the use of microinjection

needles containing soluble chemotactic factors as a means of establishing short-term chemotactic gradients (Bailly et al., 2000). Chemotactic gradients have also been established effectively using agarose based techniques such as the under agarose assay (Nelson et al., 1975) and collagen gel assays, which also enable the simultaneous observation of the effects of mechanical stress on cell migration (Shreiber et al., 2001).

The two most significant advances in the microscopy-based study of chemotaxis have come from the development of the Zigmond (Zigmond, 1988) and Dunn (Zicha et al., 1991) direct viewing chemotaxis chambers. Both chambers permit linear steady-state gradients to establish and therefore allow chemotaxis to be assessed under reproducible and definable conditions. While the Zigmond chamber is effective for the short term study of highly motile cells such as neutrophils, it is less practicle for the study of slow moving cells such as fibroblasts, as it is prone to gradient instability due to mechanical stress and thermal effects (Zicha et al., 1997). The Dunn chamber offers improved gradient stability by adopting a concentric layout for the inner and outer wells (Figure 27, page 19). The primary advantage of the concentric design is to isolate the inner well from the influence of mechanical and thermal effects that can otherwise effect a well sealed with wax, which is susceptible to volume change. Any mechanical or thermal effects that act upon the outer well of the Dunn chamber (which is sealed with wax) have no effect on gradient stability due to the incompressibility of the medium within the 'blind' central well. The Dunn chemotaxis chamber is therefore well suited for the long-term study of fibroblast-like cells.

In this study the Dunn chemotaxis chamber was combined with multi-channel time-lapse microscopy in order to examine in detail the chemotactic behaviour of T15 sarcoma cells in PDGF-BB/IGF-1 gradients. The major advantage of this technique was that it enabled changes in many aspects of cell motility, including chemotaxis, persistence, and speed, to be assessed in response to different treatments. Furthermore, by applying a range of analytical techniques to acquired film data, cell behaviour could be quantified enabling the effects of different treatments to be assessed statistically. However, the major disadvantage of this technique was that it required multiple experiments to be performed for a single treatment in order to accumulate sufficient data sets for statistically meaningful results. The chemotactic behaviour of thousands of cells can be assessed in a single Boyden chamber experiment whereas approximately 30 – 40 fibroblast-like cells can be assessed in a single, low magnification observation field in the Dunn chamber. This number is reduced further when the behaviour of only a subpopulation of cells within the observation field in under investigation (e.g. microinjected or transfected cells expressing various proteins of interest). For the foreseeable future the microscopy-based analysis of cell behaviour will, therefore, remain a relatively low throughput exercise.

The in vivo study of chemotaxis: Although a variety of novel assays have been developed for the analysis of chemotaxis *in vivo* they have tended to be highly specialised, developed with a specific cell type or physiological mechanism in mind. Examples of techniques used include the insertion of hypodermic needles loaded with matrigel and soluble chemoattractants into subcutaneous tumours induced in rats in order to collect motile populations of cells (Wyckoff et al., 2000b); the injection of metastatic cells into the tail vein

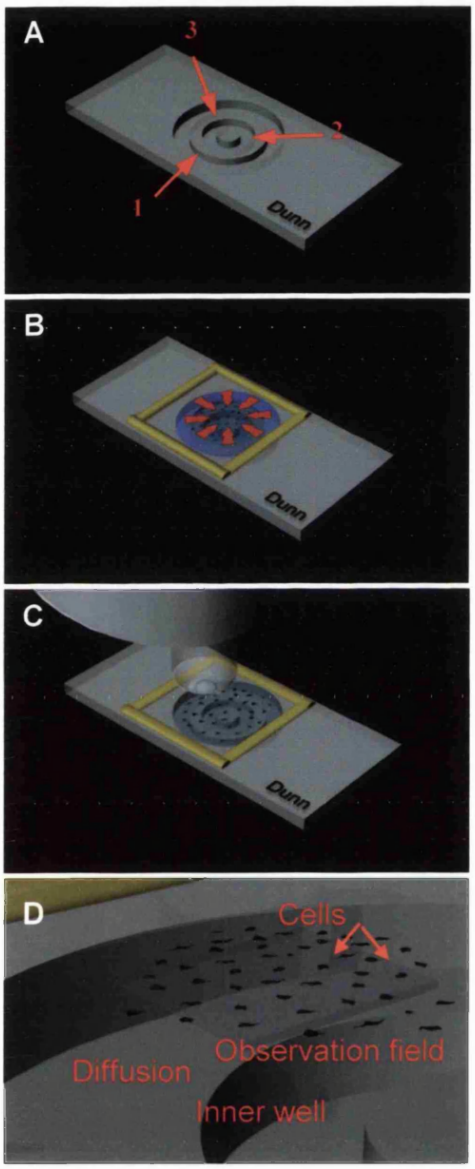

Figure 2'. The Dunn chemotaxis Chamber

The Dunn chemotaxis chamber enables the long-term observation of adherent cells exposed to gradients of diffusible chemotactic signals. Manufacured from glass, the chamber is suited for use in conjunction with light microscopy techniques. The chanber is engineered such that the concentric layout of the wells and the height of the intervening diffusion gap collectively enable the formation of highly sable diffusion gradients that can be maintained for long periods, and consequently represent a significant improvement on the Zigmond chamber design.

The chanber (A) consists of an outer (1) and inner annular (2) well separated by an annular platform (3) engineered 20 μm below the main chamber surface. A glass coverslip with adherent cells is inverted and positioned over the central region of the chanber such that a small annular gap separating the inner and outer wells is formed between the surface of the platform and the underside of the coverslip. When a chemoattractant is applied to the outer well a stable diffusion gradient establishes across this gap as the chemoattractant diffused between the outer and inner wells (B). The time for the gradient to stabilize and the duration that it persists depends on the molecular weight of the chemoattractant used. A field of cells directly within the diffusion gap is selected for observation via microscopy (C & D – close up). Cells will translocate towards the outer well if chemotactic to the signalling factor used. When assembled the chamber provides a hermetically sealed environment designed for use with CO_2 independent medium. Consequently, complications that often arise in live cell imaging experiments due to gradual medium loss through evaporation are avoided.

of mice either in the presence or absence of chemokine receptor-blocking antibodies in order to assess their effects on metastasis (Muller et al., 2001); and finally, the injection of putative chemotactic agents into the peritoneal cavity of mice and/or rats in order to assessthe chemotactic ability of cells of the host immune system or of cell lines administered intravenously (Lam et al., 1981). Although such techniques can be highly informative, they cannot be applied generally in the study of chemotaxis. *In vitro* assays therefore provide the most reliable methods of assessing the chemotaxis of cultured cells.

3.1.11 Imaging protein dynamics in living cells

Understanding actin dynamics in cultured cells is the key to understanding cell motility and polarity. In turn, understanding the spatiotemporal relationships of the various proteins involved in remodelling the actin cytoskeleton is the key to understanding how actin dynamics is regulated within the cell. In this study attempts to discern the role of various polarity proteins in the chemotaxis and motility of sarcoma cells were complemented by additional studies that permitted both actin dynamics and the mechanisms that regulate actin dynamics to be monitored in intact living cells. The recently developed FLAP (fluorescence localisation after photobleaching) technique was applied to the study of actin dynamics. Additionally, FLIM (fluorescence lifetime imaging microscopy) was used to monitor FRET (fluorescence resonance energy transfer) between various signalling molecules implicated in the control of actin dynamics in order to determine where and when these molecules interact within cells.

3.1.12 Fluorescence localisation after photobleaching (FLAP)

FLAP represents a novel and relatively simple method for the localised photolabelling and subsequent tracking of specific molecules within living cells and can be achieved using a conventional laser scanning confocal microscope (Dunn et al., 2002). In this method two subpopulations of the same species of molecule are labelled with differing and spectrally separable fluorophores that are amenable to photobleaching. When present at similar levels within the cell the separate fluorophores demonstrate perfect co-localisation because the proteins to which they are attached are the same. The selective and localised photobleaching of only one fluorophore within the cell is then used as a means of photolabelling. If the fluorescent signals of the two fluorophores are carefully matched prior to photobleaching then simple image differencing can be used to subsequently monitor the distribution of the bleached molecules within the cell. Alternatively, by calculating the ratio of bleached-to-unbleached molecules within each image pixel the relative concentration of photolabelled molecules can be mapped across the cell (Zicha et al., 2003). FLAP therefore provides a powerful method of directly monitoring protein dynamics *in situ*.

For FLAP to work effectively the specific protein under investigation should ideally be expressed directly by the cell as a fusion to a biofluorescent molecule such as ECFP (enhanced cyan fluorescent protein) or EYFP (enhanced yellow fluorescent protein) in order to ensure a constant protein-to-fluorophore ratio of 1:1. Furthermore ECFP and EYFP are particularly amenable to photobleaching, an essential prerequisite for the FLAP technique. However, in principle the technique should also work using proteins biochemically conjugated to separate fluorescent dyes, although efforts must be made to ensure that a

constant protein-to-fluorophore ratio is naintained. Localised photobleaching and subsequent monitoring of protein localisation is most effectively achieved using a laser scanning confocal microscope that allows bleacl regions to be defined within the scanning area and which enables the alternating line-by-line scanning of the sample for each fluorescent channel in order to minimise the delaybetween separate acquisition events. The Zeiss LSM 510 laser scanning confocal microscopeis ideally suited for this purpose.

FLAP is essentially an extension of :he related methods of fluorescence recovery after photobleaching (FRAP) and fluorescence loss in photobleaching (FLIP) (Cole et al., 1996; Lippincott-Schwartz et al., 2001). Hbwever, unlike these methods FLAP permits the distribution of the photobleached molecules themselves to be tracked due to the use of a reference fluorophore, and therefore the FLAP technique is in effect a specialised form of photoactivation. Conventional methods of photoactivation have typically involved the use of a caged fluorescent probe biochemically conjugated to a protein of interest which is then introduced into cells via microinjection (Politz, 1999). Photoactivation is then achieved using an intense flash of excitation light which results in the de-caging of the fluorescent probe, rendering it amenable to subsequent excitation and fluorescent emission. Like FLAP, localised photoactivation enables a subpopulation of labelled molecules to be traced through the cell. However, the major disadvantage of many caged fluorophores is that their photoactivation commonly requires intense, short-wavelength excitation light. For instanced the commonly used caged resorufin iodoacetamide has a photo-activation wavelength of 390 nm. Such harmful UV irradiation can have deleterious effects on the cell and therefore alternatives to these methods are desirable. An advantage of FLAP over the use of many

caged fluorescence probes is that it enables the photolabelling and tracing of biofluorescent proteins directly expressed by cells. However, the chief advantage of FLAP is that the use of a reference fluorophore permits ratiometric imaging, enabling the relative concentration of photolabelled molecules to be determined at different regions within the cells. Given the distinct lack in the availability of suitable photoactivatable biofluorescent proteins, FLAP represents a valuable addition to the repertoire of imaging techniques currently available for monitoring protein dynamics within living cells.

3.1.13 Fluorescence resonance energy transfer (FRET)

FRET is a quantum event that involves the non-radiative transfer of energy from an electronically excited donor fluorophore to an unexcited acceptor fluorophore (Lakowicz, 1999). During the process of energy transfer the donor fluorophore returns to the ground state without photon emission while the sensitised acceptor disperses the energy in a radiative manner (i.e. through photon emission). FRET is subject to highly limiting spectral and spatial constraints. For efficient energy transfer to occur a significant degree of overlap must exist between the emission and excitation spectra of the respective donor and acceptor fluorophores. Moreover, energy transfer is highly dependent on the proximity and orientation of the interacting fluorophores: the mechanism of energy transfer is non-radiative and therefore is not merely the consequence of photon emission and re-absorption between the respective donor and acceptor fluorophores. In fact, FRET occurs due to intermolecular dipole coupling events that require the two fluorophores to be in extreme close proximity. As the distance between putative donor and acceptor fluorophores increases the probability of FRET falls dramatically. Indeed, the probability of FRET occurring between donor and

acceptor fluorophores is inversely proportional to the sixth power of the distance that separates them.

FRET has been exploited as a tool for the non-invasive study of biochemical interactions in single cells (Wouters et al., 2001). The continuous discovery and development of biofluorescent proteins and fluorescent dyes suitable for protein conjugation is providing an ever-growing pool of fluorescent tools that are at the disposal of the cell biologist. By coupling appropriate donor and acceptor fluorophores to two separate species of protein whose potential interaction is the subject of investigation, FRET can be used to monitor the dynamics of their association *in situ* (Figure 28, page 19). The strict spatial constraints that apply to FRET mean that efficient energy transfer will occur only when donor and acceptor fluorophores are separated by distances of less than approximately 7 nm (Bastiaens and Squire, 1999). Consequently any occurrence of FRET can be taken to reflect direct interactions between the proteins to which the donor and acceptor fluorophores are coupled.

Modern molecular biology procedures and simple biochemistry provide effective methods of coupling fluorophores to proteins for use in FRET studies. When coupling fluorophores directly to proteins either molecular cloning can be used to generate cDNA constructs that encode a fusion between the protein of interest and a biofluorescent protein such as GFP, or the protein can be directly conjugated biochemically to a fluorescent dye such as Cy3. Alternatively, indirect probes can be generated that consist of fluorescent dyes conjugated to antibodies that are specific for the protein of interest. Many of these techniques have been

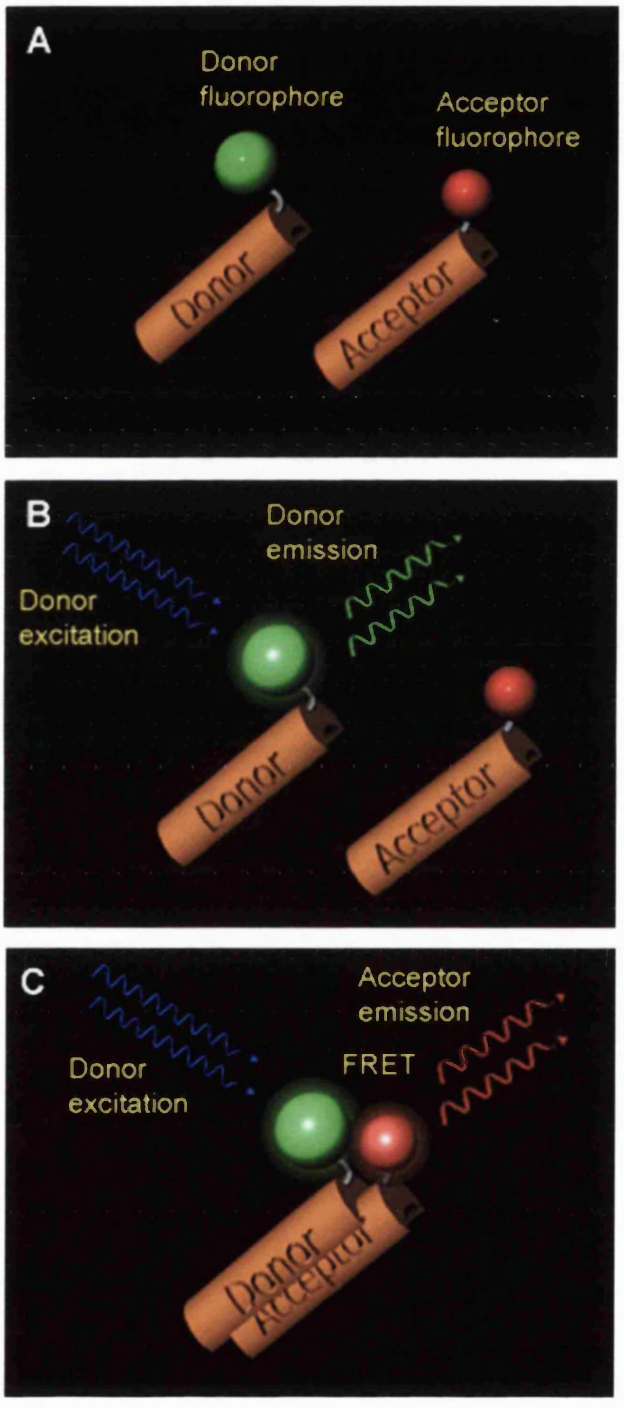

Figure 28. Fluorescence resonance energy transfer (FRET)

(A) Donor and acceptor fluorophores are coupled to two different species of protein in order to monitor their interactions in situ. (B) In the absence of protein binding selective donor excitation results in donor emission. (C) However, when proteins interact donor and acceptor fluorophores are brought into close proximity and FRET can occur. The excited donor fluorophore can transfer energy to the proximal acceptor fluorophore resulting in acceptor excitation and emission. Energy transfer returns the donor fluorophore to the ground state without photon emission.

used with a great deal of success in various FRET studies (Itoh et al., 2002; Kraynov et al., 2000; Ng et al., 2001; Verveer et al., 2000).

The selection of effective donor and acceptor fluorophores for use in FRET experiments is essential and choices should be governed by the degree to which the emission and excitation spectra of the two fluorophores overlap. EGFP and Cy3 provide one of the most popular choices for donor and acceptor protein labelling and have been used extensively in FRET studies (Ng et al., 2001; Verveer et al., 2000). ECFP and EYFP have proved to be effective FRET pairs for the examination of intramolecular events such as protein folding and cleavage as they can be directly fused to the N- and C- termini of the studied protein. Any signalling events that cause protein folding bring the ECFP and EYFP components of the fusion protein into close proximity and hence increase the probability of FRET (Itoh et al., 2002; Ting et al., 2001). Conversely, protein cleavage that disrupts the close proximity of two fluorescent components within a single molecule can be detected by a loss of the FRET signal (Mahajan et al., 1999).

3.1.14 Microscopy-based techniques for FRET detection

A number of elegant microscopy-based techniques have now been developed that permit the analysis of FRET. Sensitised emission, acceptor photobleaching, and donor photobleaching based techniques as well as fluorescence lifetime imaging microscopy have all provided successful methods of monitoring FRET interaction in live and fixed cell specimens.

Sensitised emission: The sensitised emission technique is both conceptually and practically the most straightforward method of monitoring FRET. The technique relies on the principle that, in the absence of acceptor excitation light, acceptor emission will only occur if a proximal excited donor fluorophore is present. Consequently, by selectively exciting the donor fluorophore and simultaneously monitoring the emission of the acceptor, FRET interactions can be elucidated. Sensitised emission-based techniques are susceptible to complications associated with fluorophore concentrations and channel cross-talk. However, if the appropriate measures are taken to compensate for these complications then this technique can provide a very powerful and relatively straightforward means of monitoring biochemical interactions in living cells. Sensitised emission has proved popular due to its relatively simple implementation (the technique can be achieved using a conventional wide-field fluorescent microscope), and as a consequence has provided many new insights into the dynamics of molecular interactions in living cells (Kraynov et al., 2000; Mahajan et al., 1999; Mas et al., 2000).

Acceptor photobleaching: Whereas the sensitised emission technique monitors the effects of FRET on acceptor emission, the acceptor photobleaching technique monitors the effects of FRET on donor emission (Mas et al., 2000). This technique, generally implemented on a laser scanning confocal microscope, involves the selective Photobleaching of acceptor fluorophore within a defined region of the sample using high-intensity excitation light. Any increase in donor fluorescence within the photobleached region will reflect a rebalance of non-radiative to radiative energy dissipation due to FRET loss. Photobleaching of the acceptor fluorophore therefore results in the dequenching of donor fluorescence emission.

This technique provides a more quantitative approach to FRET analysis when compared to the sensitised emission technique as pre-bleach donor intensities can be compared to their post-bleach values. The major disadvantage of the acceptor photobleaching method is that it often requires long photobleaching times and high-energy excitation light, and as a consequence can prove impractical for live cell imaging experiments. Where possible, it is desirable to combine both sensitised emission and acceptor photobleaching techniques as each provides an independent evaluation of FRET. The principles of acceptor photobleaching are summarized in Figure 29, page 19.

Photobleaching digital imaging microscopy (pbDIM): A microscopy technique that relies on donor fluorophore photobleaching as opposed to acceptor photobleaching as a means of measuring FRET is photobleaching digital imaging microscopy (pbDIM)(Bastiaens and Squire, 1999; Gadella and Jovin, 1995). The pbDIM technique relies on the principle that the photobleaching kinetics of a donor fluorophore is altered when complexed with acceptor. Photobleaching involves a chemical alteration in the excited-state fluorophore that results in an irreversible loss of the molecule's fluorescence properties. Only fluorophores in the excited state are prone to such photochemical reactions. Furthermore, the probability of irreversible photodamage increases with time spent in the excited state. FRET acts to reduce the time that the donor fluorophore remains in the excited state by draining energy from the molecule. In doing so FRET also reduces the probability of donor fluorophore photobleaching. Therefore, FRET protects the donor fluorophore from photobleaching and as a consequence results in a prolonging of photobleaching times for only those donor fluorophores complexed with acceptor. Uncomplexed donor fluorophores will exhibit their

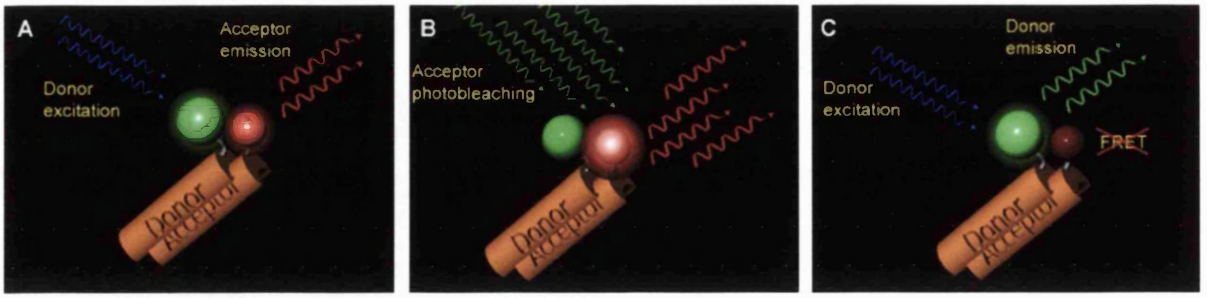

Figure 29. Analysis of FRET by acceptor photobleaching

(A) When proteins coupled to separate donor and acceptor fluorophores associate, excitation of the donor can result in FRET. (B) In the 'acceptor photobleaching' technique FRET is measured by the selective photobleaching and therefore destruction of the acceptor fluorophore using high intensity acceptor excitation light. This removes the potential sink for donor excitation energy, and upon donor excitation FRET cannot occur. (C) Therefore donor excitation results in donor re-emission. FRET can be measured as the increase in donor fluorescence emission that results as a consequence of acceptor photobleaching.

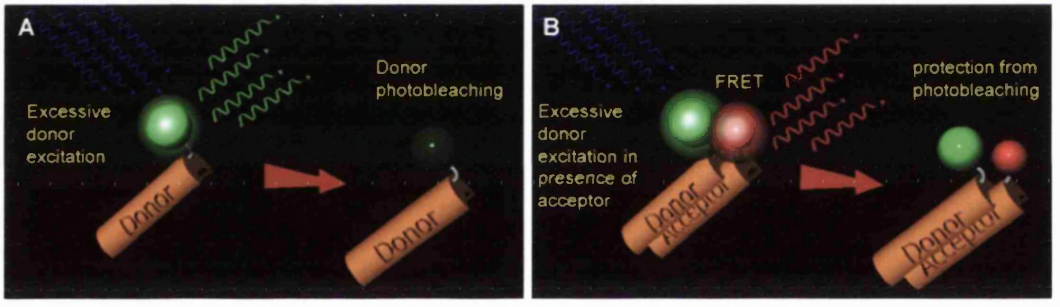

Figure 30. Analysis of FRET by donor photobleaching

(A) The longer a fluorophore remains in the excited state the more prone it becomes to irreversible photobleaching. (B) FRET reduces the average time a donor fluorophore remains in the excited state by transferring energy to the acceptor. As a consequence the donor fluorophore is less prone to photobleaching. Comparisons of donor photobleaching times that are recorded either in the presence or absence of an acceptor can, therefore, be used as a relative measure of FRET. Note that donor emission can still occur in the presence of an acceptor because FRET is a probabilistic event and not a certainty. Therefore FRET confers a degree of protection on donor photobleaching.

usual photobleaching kinetics. If any change is detected in the average photobleaching times of a donor fluorophore when measured both in the presence and absence of an acceptor that this can be taken to reflect the occurrence of FRET. The principles of donor photobleaching are summarized in Figure 30, page 19. That FRET acts to reduce the time that the donor fluorophore remains in the excited state is this basic underlying principle that enables fluorescence lifetime imaging to be applied to this field.

3.1.15 Fluorescence lifetime imaging microscopy (FLIM)

An alternative method of measuring FRET is provided by FLIM (Bastiaens and Squire, 1999; Wouters et al., 2001). FLIM enables FRET to be monitored in a quantifiable manner that is independent of fluorophore concentration while negating the necessity for photobleaching techniques. Furthermore, FLIM enables the high-resolution spatial mapping of FRET across an entire sample, a process that would be impractical using photobleaching alone. Thus, FLIM provides a non-invasive, highly sensitive means of quantifiably monitoring protein-protein interactions in both live and fixed cell specimens.

The fluorescence lifetime of a fluorophore is defined as the average duration the molecule remains in the excited state following photon absorption (Bastiaens and Squire, 1999). The lifetime of a donor fluorophore is a useful parameter to measure because it is sensitive to local environmental changes such as FRET interactions whilst insensitive to fluorophore concentration, a factor that can complicate techniques based on absolute intensity measurements. Two microscopy techniques have currently been developed that enable

fluorescent lifetimes to be measured and each is applicable to both wide-field and confocal imaging systems.

3.1.16 Time domain FLIM

The time domain technique uses pulsed excitation of the sample to induce pulsed emission of fluorescence (Bastiaens and Squire, 1999; Lee et al., 2001). The pulsed excitation of a population of a single species of fluorophore results in fluorescence emission that decays exponentially with time (Figure 31A, page 19). The lifetime of the fluorophore is derived from this decay curve and is defined as 1/e, which is the time taken for the intensity of fluorescence emission to decay to approximately 37 % of its initial value. Pulsed excitation is typically achieved using a solid-state ultra-fast femtosecond pulse-laser and subsequent fluorescent emission monitored using an appropriate detector. Both the width of the excitation pulse and the frequency of its generation are both important factors to be considered in time domain FLIM. It is essential that the width of the excitation pulse is far shorter than the lifetime of the imaged fluorophore to avoid overlap between excitation and emission events. If this is not ensured then excited fluorophores that emit photons during the earliest stages of fluorescence decay become susceptible to re-excitation by the tail of the lingering excitation pulse. This can initiate a second round of fluorescence decay that will overlap with, and thus obscure measurement of, the first. In addition, the time interval between excitation pulses should be of sufficient length to enable satisfactory decay of fluorescence emission. The typical frequency of pulse-lasers used in time domain FLIM is around 80 MHz, which provides an 80 ns pulse interval. The fluorescence lifetime of EGFP

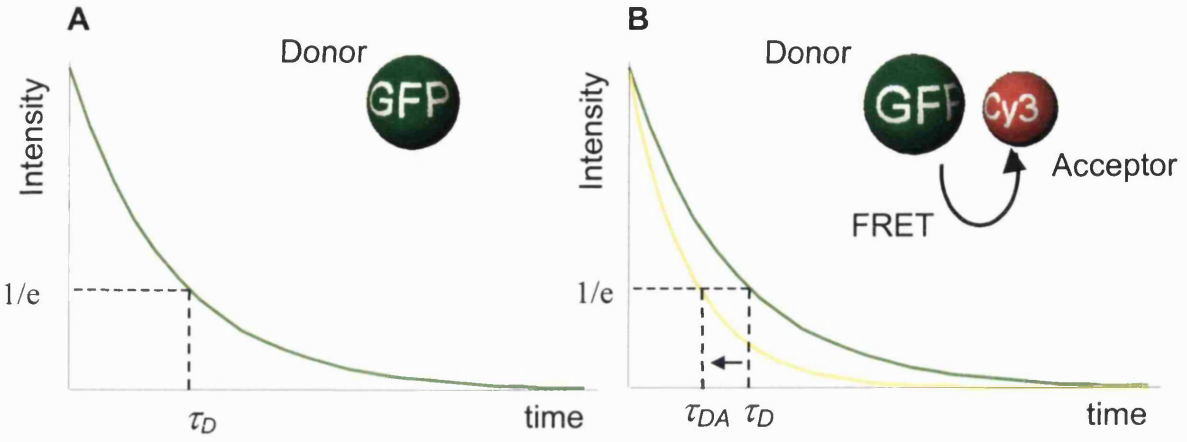

Figure 31. The characteristics of fluorescence emission

(A) The pulsed excitation of a population of a single species of donor fluorophore results in fluorescence emission that decays exponentially with time. The lifetime of the donor fluorophore (τ_D) can be derived from the curve of fluorescence decay and is defined as 1/e which is the time taken for the intensity of fluorescence to drop to approximately 37 % of its maximum value (1/e = 0.368). This lifetime value represents the average time that a fluorophore will remain in the excited state following photon absorption. (B) Upon interaction with acceptor the lifetime of the donor fluorophore falls to τ_{DA}. Thus, the interacting donor population will exhibit a sharper profile of fluorescence decay than that of the non-interacting population.

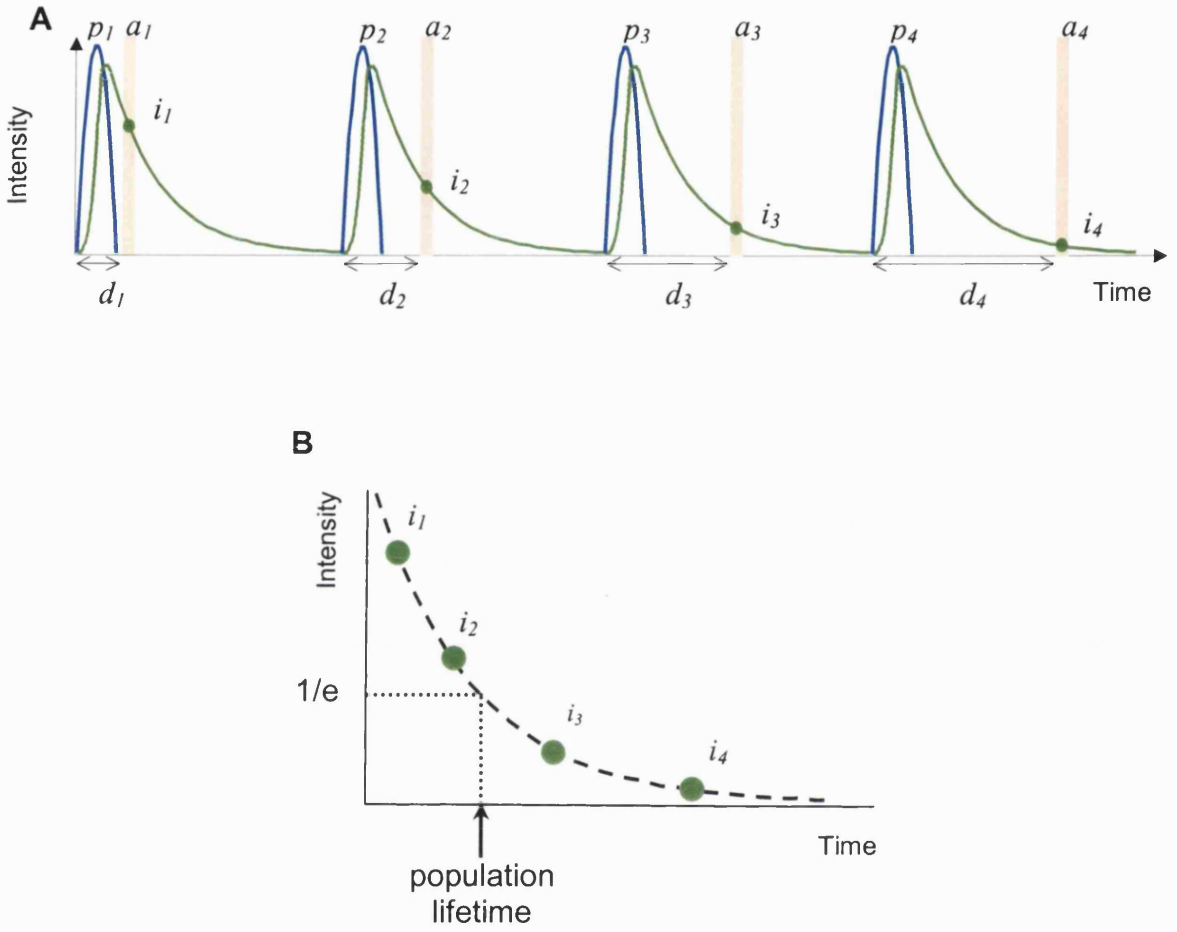

Figure 32. Time domain FLIM based on time-gated image acquisition

Time-gated imaging can be utilised as a means of reconstructing the profile of fluorescence emission of a pulse-excited fluorophore population. (A) Time-gated images (a_1 – a_4) of extremely short exposure time (approximately 120 ps) are acquired at increasing delays (d_1 – d_4) following sequential pulses of excitation light (p_1 – p_4). The intensity of fluorescence emission decays exponentially with time and the rapid, gated acquisitions sample the intensity of decay over increasing time points (i_1 – i_4). (B) Intensity values recorded at increasing time points following sample excitation can be used to reconstruct the exponential curve of fluorescence emission. This permits the subsequent derivation of the fluorescence lifetime of the fluorophore population (as defined by 1/e).

is typically around 2.2 ns when expressed in mammalian cells, and so the degree of fluorescence decay required to derive this value can occur easily within the 80 ns time frame provided.

Two methods have currently been developed that enable the fluorescence decay characteristics of a pulse-excited fluorophore population to be determined. In the first method described by Benny Lee and co-workers, the exponential decay of fluorescence emission is determined by acquiring a series of time-gated images of increasing delay between sequential excitation pulses (Lee et al., 2001). The relative difference between intensity values acquired at each time point can be used to reconstruct the exponential decay curve of fluorescence emission. The fluorescence lifetime of the fluorophore population can then be derived from this curve (Figure 32, page 19).

The Second method is based on time correlated single photon counting (TCSPC) and is applied in this study. In this method the time taken for individual photons to arrive at a detector is measured following the pulsed excitation of the sample. The arrival times of many thousands of photons are measured and this information then used to directly reconstruct the profile of fluorescence decay (Figure 33, page 19). Single photon counting requires extremely sensitive detection equipment and precise control of the excitation source intensity. The energy provided by the excitation pulse is attenuated to such a degree that the probability of detecting a single emitted photon following sample excitation is one in ten (i.e. $p = 0.1$). When a photon is detected the time delay between its arrival at the detector and the generation of the preceding excitation pulse is recorded. This process is repeated many times

to generate a large data set of photon delay (Figure 33A). The exponential decay curve of fluorescence emission can be constructed by plotting the frequencies of the various photon delay times. Thus the fluorescent lifetime of the fluorophore population can be derived (Figure 33B). If no photon is detected between two consecutive excitation pulses (as in the majority of cases) then no value is recorded. The relatively low probability of photon detection is necessary to ensure that only discrete photons are monitored at the detector. The likelihood of multiple photon recordings between consecutive excitation pulses is low. However, when more than one discrete photon is detected then only the time delay to the last photon is recorded.

Analysis of FRET using time domain FLIM: When a proportion of a donor fluorophore population is complexed with acceptor then it can be said that two exponential decay profiles exist for donor fluorescence emission; one that defines the emission profile of the uncomplexed population, and the other that defines the emission profile of the complexed/FRET population. The dipole interactions between donor and acceptor fluorophores modify the donor excitation kinetics such that if photon emission does occurs it will do so more rapidly than would otherwise be expected in the absence of acceptor. A donor fluorophore will thus either undergo rapid photon emission or non-radiative energy transfer. Consequently, the FRET population will exhibit an emission profile that decays more rapidly than the uncomplexed population resulting in a relative reduction in its fluorescence lifetime (Figure 31B). A bi-exponential model of decay will therefore represent the fluorescence emission of a mixed population of both interacting and non-interacting donor fluorophores. By fitting such a model to the acquired image data, the respective

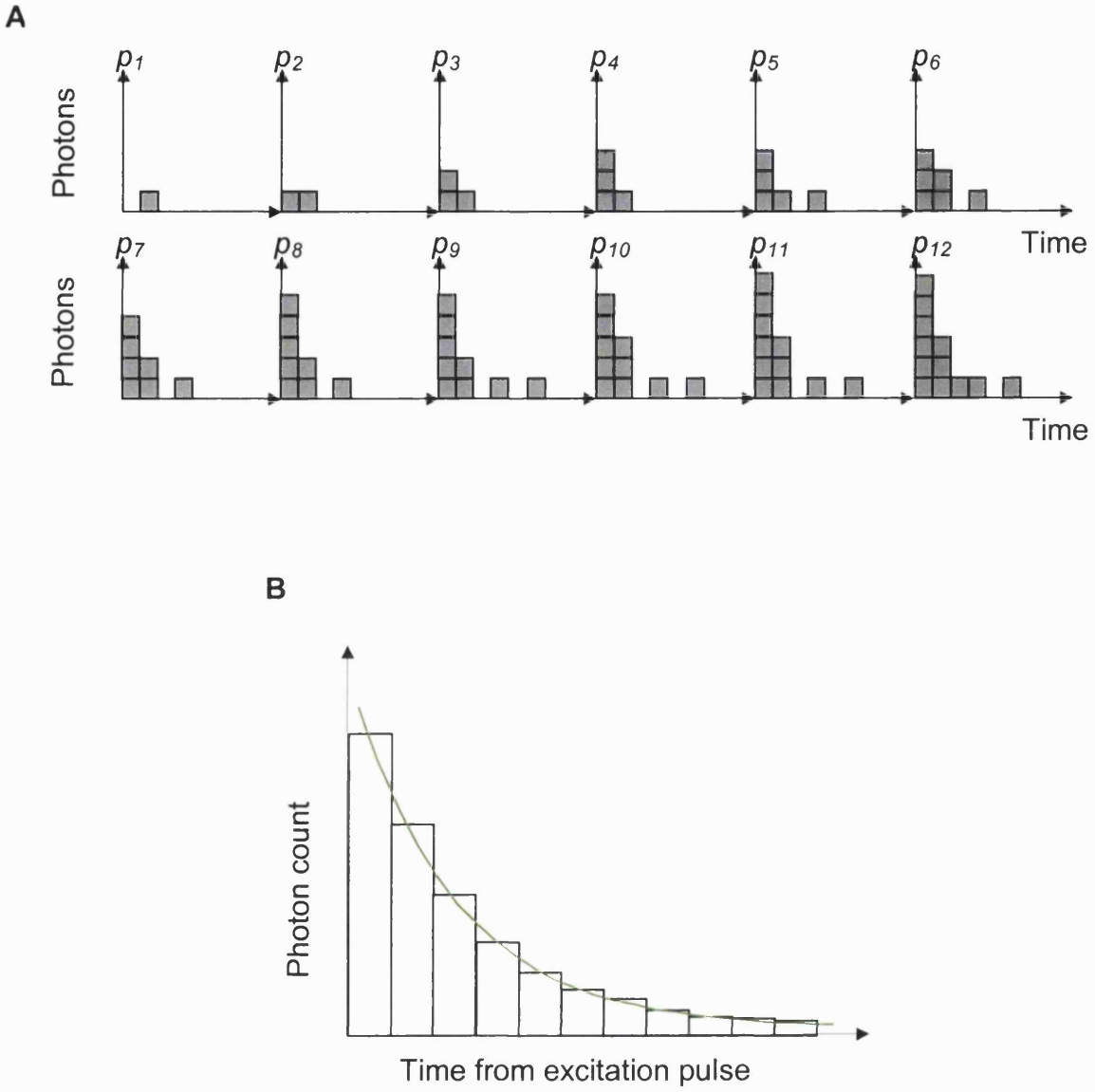

Figure 33. Time domain FLIM based on single photon counting

Single photon counting can be used as a means of reconstructing the profile of fluorescence emission of a pulse-excited fluorophore population. (A) One photon is counted per excitation pulse and its delay time scored. The process is repeated over sequential pulses ($p_1 - p_{12}$) until sufficient data exists (B) to reconstruct the exponential decay curve of fluorescence emission. The fluorescence lifetime is then derived from the curve. The degree to which the curve represents the actual exponential decay of fluorescence emission depends on the number of time bins to which photon delay times can be assigned.

lifetimes of the interacting and non-interacting fractions of the fluorophore population can be determined.

3.1.17 Frequency domain FLIM

Frequency domain FLIM involves the phase-sensitive imaging of fluorescence emission to determine the lifetime of the fluorophore population (Lakowicz et al., 1992). In this technique the continuous hi-frequency modulation of the excitation light is used to modulate the intensity of fluorescence emission (Figure 34A, page 19). The frequency of intensity modulation is the same for both the excitation light and fluorescence emission but differences exist between their phase and relative modulation depth (Figure 34B). These differences are determined by the fluorescent lifetime of the fluorophore and can be used as independent parameters for its derivation (Bastiaens and Squire, 1999). Calculation of the phase and modulation lifetimes (τ_φ and τ_m respectively) requires the acquisition of a series of homodyne, phase-shifted images in an attempt to map the phase and modulation characteristics of fluorescence emission (i.e. recreate the sinusoidal curve of fluorescence emission). To achieve this the sensitivity of the detector is modulated over the course of an exposure. The frequency of the detector modulation is the same as that of the modulated excitation light and initially they are in phase. However, over the course of sequential exposures, the phase of the detector sensitivity is shifted by defined increments. The intensity of the signal produced by the detector reflects the degree of phase shift between the modulated detector sensitivity and the sinusoidal curve of fluorescence emission. When they are exactly in phase a strong sinusoidal signal is generated by the detector. When they are

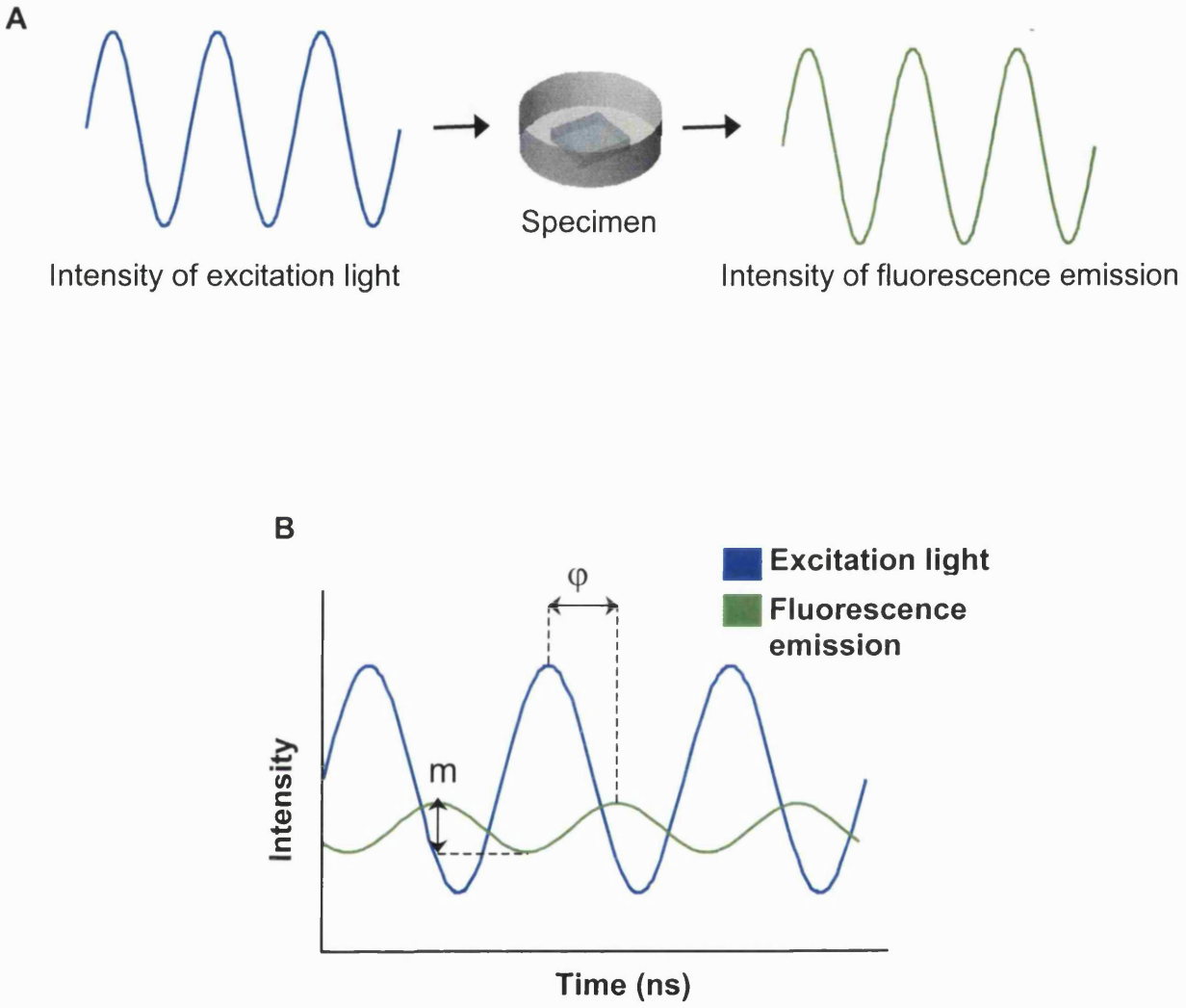

Figure 34. Frequency domain FLIM

Principles of frequency domain FLIM. (A) The intensity of the excitation light is modulated at a fixed frequency. The resulting intensity of fluorescence emission is modulates at the same frequency as the excitation light. (B) A phase shift, φ, is, however, introduced between the excitation light and the fluorescence emission due to the time the fluorophore remains in the excited state before photon emission. Both the degree of phase shift and the relative modulation depth, m, of fluorescence emission are determined by the fluorescence lifetime of the molecule.

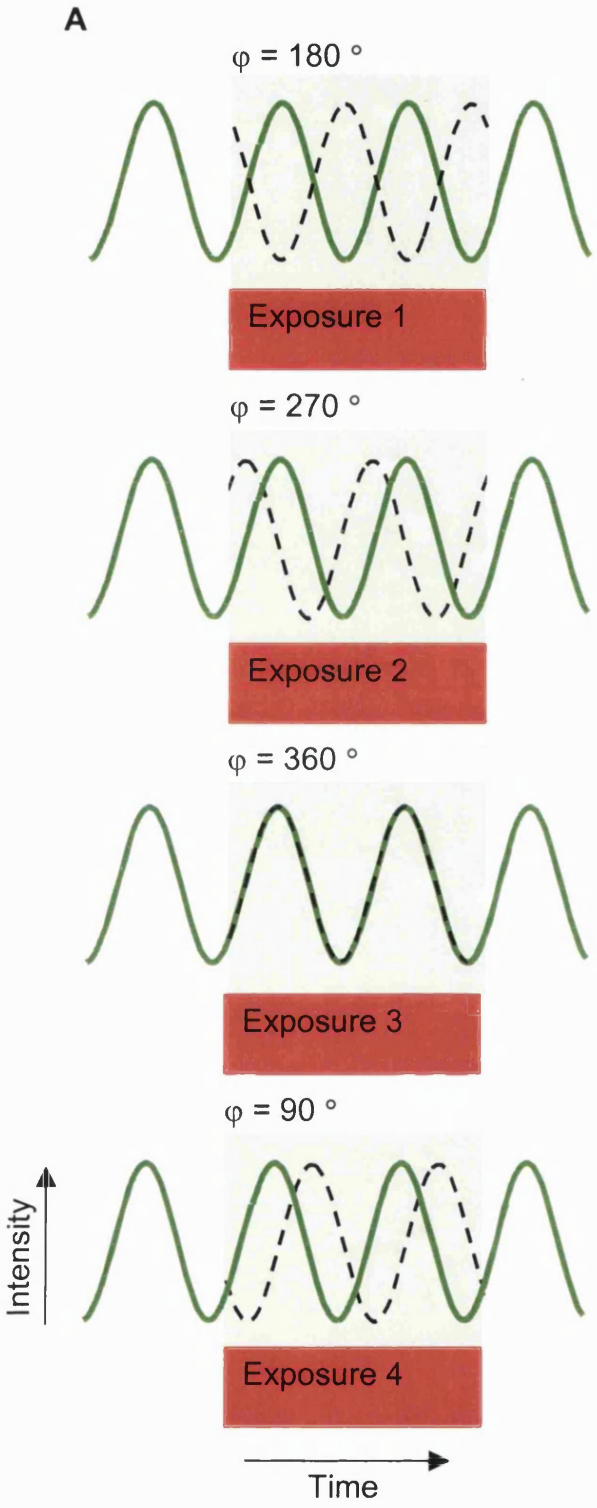

Figure 35. Phase sensitive imaging

(A) The sensitivity of the detector is modulated over the course of an exposure (dotted black line), and the phase of this modulation is shifted over sequential exposures. As the modulated sensitivity of the detector and fluorescence emission come into phase the resulting signal becomes greater (exposure 1 – 3, I = Integrated intensity). The signal is greatest when they are exactly in phase (exposure 3). The signal then weakens as the modulated detector sensitivity and fluorescence emission move out of phase once more (exposure 4). (B) The relative difference in the intensity of pixels taken from a series of phase-sensitive acquisitions can be used to reconstruct the sinusoidal curve of fluorescence emission. I_1 - I_4 represent the respective integrated intensities of exposures 1 – 4 in (A).

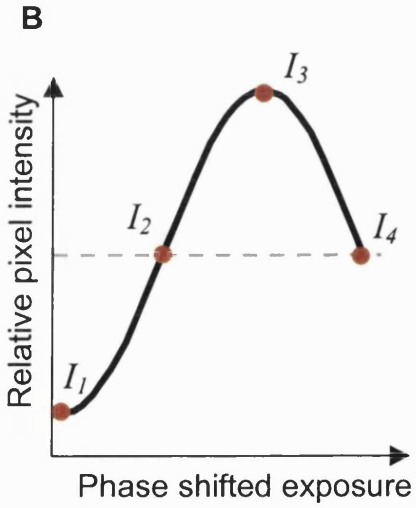

completely out of phase (i.e. shifted by 180 °) the peak intensity of fluorescence emission coincides with low detector sensitivity and only a weak signal is generated (Figure 35A). The output signal produced by the detector is integrated over the course of an exposure to generate a single intensity value for each pixel within an image. When the detector and fluorescence emission are in phase bright pixel intensities are recorded, when they are out of phase low intensities are recorded. The relative differences in pixel intensities from a range of phase-shifted images can thus be used to reconstruct the sinusoidal curve of fluorescence emission (Figure 35B). The reconstructed sinusoidal curve of fluorescence emission can then be compared to that of the excitation light, enabling differences in phase and modulation depth to be calculated and hence the derivation of fluorescent lifetimes.

One of the main advantages of frequency domain FLIM over the time domain method is that the former does not require ultra fast timing devices and expensive femto-second pulse lasers. The excitation source can be provided by a conventional and relatively cheap continuous wave laser in conjunction with acousto-optical modulators. Therefore frequency domain FLIM provides a relatively cheap alternative to the time domain approach. However, disadvantages arise from a loss of image resolution incurred by the necessary use of image intensifiers and the complexity of the mathematics involved in the extraction of lifetimes from image data.

Analysis of FRET using frequency domain FLIM: Lifetime is a function of the phase shift and modulation depth of fluorescence emission. Short lifetimes are characterized by relatively small shifts in phase and relatively large modulation depths. The small phase shift

is due to the relatively rapid re-emission of the excited fluorophore population while the large modulation depth is due to the resulting steep profile of fluorescence decay. Long lifetimes are characterized by large phase shifts and small modulation depths due to the relatively slow re-emission of the excited fluorophore population and the resulting shallow profile of fluorescence decay. FRET therefore results in a reduction in the phase shift and an increase in the modulation depth of the fluorescence emission of a donor fluorophore population as the fluorescence lifetime is reduced (Figure 36, page 19). Therefore any donor fluorophore population undergoing FRET will yield lower values for τ_φ and τ_m than would otherwise be expected in the absence of acceptor. The intensity of fluorescence emission is also less for a donor fluorophore population complexed with acceptor, as only a fraction of the population will undergo re-emission.

3.1.18 The application of FLIM in cell biology

The advantage of the application of techniques such sensitised emission, acceptor photobleaching, and pbDIM to FRET analysis is that they are relatively simple to implement and can be achieved using a conventional confocal microscope system without the requirement of any additional modification. Therefore they provide a relatively cheap and simple method of imaging FRET. The measurement of fluorescent lifetimes, however, requires complex and highly sensitive imaging equipment incorporated into purpose-built microscope systems. The expense of ultra-fast laser systems, picosecond accuracy timing devices, highly sensitive fluorescence detectors and the considerable expertise required for the assembly of such equipment into a functional FLIM system has, until relatively recently,

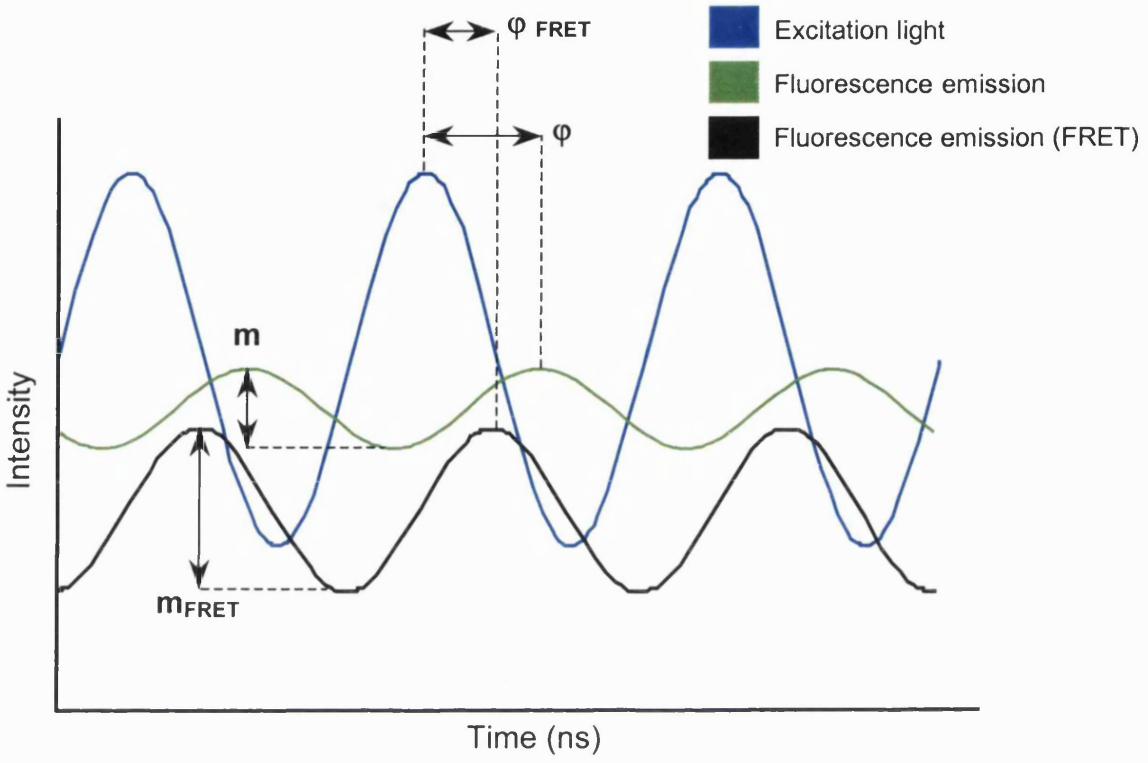

Figure 36. Effects of FRET on modulated fluorescence emission

In the absence of acceptor the modulated excitation of the sample results in modulated fluorescence emission of the same frequency but with a shift in phase of φ and a modulation depth of m. A sub-population of fluorophore interacting with acceptor (the FRET population) will exhibit a reduced phase shift of φ_{FRET} and an increased modulation depth of m_{FRET}. The intensity of fluorescence emission of the interacting donor population is reduced compared to that of the non-interacting population since a proportion of the excited fluorophores undergo FRET and therefore do not re-emit.

resulted in the fairly limited application of this technology in the cell biology field. However, the recent emergence of commercial FLIM systems on the market and the development of modules that integrate the complex electronics required for lifetime measurements onto a single circuit board effectively mean that the barriers to this once rather esoteric field no longer apply. As a consequence interest in the application of FLIM as a method of measuring FRET is expanding at a considerable rate. In this study both TCSPC and frequency domain techniques have been applied to the study of protein-protein interactions in both live and fixed cell specimens. TCSPC time domain FLIM was used for the high spatial resolution imaging of N-WASP/Cdc42 and N-WASP/p16 complex formation in single fixed cell specimens, while frequency domain FLIM was largely used to monitor the activation dynamics of Cdc42 through its interaction with PAK1 in living cells.

3.1.19 Study Aims

The aim of this study was to investigate the mechanisms of chemotaxis in cancer cells using the T15 rat sarcoma cell line as a model. The Dunn direct viewing chemotaxis chamber was used to assess the chemotaxis of cells subjected to various treatments. Microinjection was used to introduce cDNA constructs encoding EGFP fusions of various polarity proteins and their mutant variants into cells, and multi-channel digital time-lapse microscopy subsequently used to assess the effects of expressed proteins on the long-term chemotaxis and motility of these cells. The interactive tracking of cells from acquired film sequences was carried out to generate cell trajectories for subsequent statistical processing, enabling a quantitative analysis of cell behaviour. Specially developed Mathematica notebooks were also used to extract fluorescence data from multi-channel film sequences, enabling an analysis of the effects of varying levels of protein expression on cell motility.

Additionally, the newly developed FLAP technique was used to directly monitor actin dynamics in cultured sarcoma cells. The chief aim of FLAP studies was to compare the actin dynamics of the highly metastatic and motile T15 sarcoma cell line to that of the related but non-metastatic K2 cell line in an attempt to assess whether differences in the motile behaviour of these cells were reflected at the level of the cytoskeleton. FLAP studies were performed in collaboration with Graham Dunn, Mark Holt, and Daniel Soong of the Randall Centre, King's College London.

Finally FLIM/FRET studies were also performed in order to monitor the interaction of Cdc42 with its effector proteins PAK1 and N-WASP in intact cells in an attempt to ascertain the

spatiotemporal relationships of signalling molecules involved in the regulation of actin dynamics. Cdc42/effector interactions were studied in the NIH 3T3 mouse fibroblast cell line. FLIM/FRET studies were performed in collaboration with Tony Ng and Maddy Parsons of the Randall Centre, King's College London, and Simon Ameer-Beg and Borivoj Vojnovic of the Advanced Technology Development Group, Gray Cancer Institute.

3.2 METHODS

3.2.1 Large-scale preparation of plasmid DNA stocks

Plasmid DNA stocks were prepared from transformed bacterial cultures. Chemically competent *E.Coli* (Top 10, Invitrogen) were transformed with 20 ng plasmid DNA by heatshock at 50 °C for 45 seconds. Transformed bacteria were then incubated in SOC medium for 1 hour at 37 °C on a rotary shaker to establish antibiotic resistance. 100 µl of each bacterial culture was then spread on a freshly prepared sterile agar plate containing the relevant antibiotic (either 100 µg/ml Ampicillin or 50 µg/ml Kanamycin (Sigma)). The plates were then sealed with parafilm, inverted and incubated at 37 °C over night. A single isolated bacterial colony was selected from the plate and grown for 6 hours in 5 ml of L-Broth containing the relevant concentration of antibiotic. 500 µl of bacterial culture was then transferred to 200 ml of L-Broth/antibiotic solution and incubated at 37 °C on a rotary shaker to enable large-scale culture growth over night.

Bacteria cultures were pelleted via centrifugation at 4,000 rpm for 10 min using a Beckman centrifuge and plasmid DNA then isolated using the QIAfilter plasmid Maxi kit (Qiagen Cat: 12263) according to the manufacture's protocol. Briefly, bacterial pellets were resuspended in 50 mM TRIS, 100 mM EDTA, 10 mM 100 µg/ml RNAse, pH 7.5 solution before alkaline lysis in 0.2 M NaOH, 1 % SDS. Subsequent addition of 1.32 M K-Acetate, pH 4.8 was used to re-nature plasmid DNA and to precipitate proteins and genomic DNA. The aqueous and insoluble phases were then separated using the filter syringes provided. Plasmid DNA was then isolated upon addition of the aqueous sample to DNA-binding columns. The solution was allowed to pass through the column via gravity flow. The immobilized DNA was

washed twice by the addition of 80 % ethanol and finally eluted in 10 mM Tris-Cl, pH 8.5. DNA precipitation and isolation involved the addition of 7.5 volumes of isopropanol and subsequent centrifugation at 11,000 rpm for 30 min. The DNA pellet was washed in 80 % cold ethanol before re-centrifugation and finally solubilisation in Tris-EDTA buffer. DNA concentration and purity was assessed via analysis of UV absorbance at 260 nm and 280 nm respectively. In all cases the final DNA concentration was then adjusted to produce 0.5 μg/μl plasmid stocks.

3.2.2 Gel electrophoresis

Gel electrophoresis, used for the analysis and isolation of cDNA constructs and fragment, was conducted using a Hoefer HE 33 mini sub gel tank (Pharmacia Biotech) and voltage regulated power pack (BioRad). TAE running buffer (40mM TRIS-Acetate ,10 mM EDTA, pH 8.3) was used throughout. Plasmids, digested cDNA fragments, and PCR products were all resolved on 1 % agarose/TAE gels supplemented with 100 μg/ml Ethidium Bromide (BDH). In cases where DNA extraction was subsequently required gels were formed from a mixture of agarose and low gelling temperature agarose at a ratio of 2:1. Loading buffer (0.25 % bromophenol blue, 0.25% Xylene cyanol, and 30 % glycerol) was added to samples to facilitate gel loading and to enable the progress of DNA separation to be monitored. All gels were run for 60 min at constant voltage of 60 V. Resolved DNA was visualized using a UV transilluminator. 1 kb and 100 bp DNA ladders (Invitrogen) were run in parallel with all samples to enable the approximate size of DNA fragments to be determined.

3.2.3 Polymerase Chain Reaction (PCR)

PCR was used to amplify cDNA fragments encoding proteins of interest from template plasmid DNA and also to incorporate appropriate 5' and 3' restriction sites for subsequent in-frame ligation into the EGFP-C1 cloning vector for the generation of N-terminal EGFP fusions. PCR reactions were carried out using the temperature resistant DNA proof-reading polymerase deep VENT (New England Biolabs). 50 picomol of each primer, 2.5 mM of each nucleotide, 50 ng of template plasmid DNA, and 1U enzyme were used per reaction. All reactions were performed using an automated PTC-200 Peltier thermocycler (MJ Research) using the following amplicification reaction: an initial denaturing step at 95 °C for 5 min followed by 30 cycles of denaturing at 95 °C for 60 s, re-annealing at 50 °C for 60 s, and primer extension at 72 °C for 2 min. A final extension step was performed at 72 °C for 5 min before reaction termination.

Amplified PCR fragments were purified using the StrataPrep PCR purification kit (Stratagene, Cat: 400771). Methods were in accordance with the manufacture's protocol. Briefly, an equal volume of the provided DNA binding solution was added to the PCR reaction product and the resulting mixture added to a DNA binding column to enable DNA isolation via centrifugation at 14,000 rpm for 30 sec. The DNA, immobilised on the binding column, was then washed once by the addition of 75 % ethanol and repeated centrifugation. DNA was then eluted from the column following the addition of 10 mM Tris-Cl, pH 8.5 and re-centrifugation.

3.2.4 Restriction digestion and ligation of cDNA

Plasmid DNA was digested using the relevant restriction enzymes and associated buffers in accordance with the manufacture's protocol (New England Biolabs). Briefly, 1 μg of DNA was digested by 1U of enzyme for 1 hour at 37 °C in the relevant buffer. All reactions were supplemented with 1 % BSA carrier protein. When multiple digestions were required, the most compatible enzyme buffer was selected. Purified PCR products were digested in the absence of BSA or enzyme buffer as the elution buffer was sufficient for efficient enzyme digestion. Digestion reactions were terminated following the addition of loading buffer, and all DNA fragments subsequently resolved, isolated, and purified using gel electrophoresis and gel extraction.

Purified, digested plasmid DNA and PCR products were ligated at an approximate concentration ratio of 1:3 (vector:insert). DNA ligation reactions were performed over night at 4 °C using 1U T4-DNA ligase and appropriate buffer (New England Biolabs). Prior to ligation digested plasmids were treated with 1U alkaline phosphatase (Roche) for 5 min to cleave 5' phosphates and therefore prevent self-ligation.

3.2.5 Gel extraction

Digested cDNA fragments and PCR products were isolated for gels and purified using the QIAquick gel extraction kit (Qiagen, Cat: 28704). Methods were in accordance with the manufacture's protocol. Briefly, resolved fragments were excised from gels using a scalpel

and solubilised at 70 °C for 5 min in a guanidine hydrochloride/isopropanol solution. Solubilised products were then loaded into DNA binding columns to enable DNA isolated via centrifugation at 14,000 rpm for 1 min. Columns were then washed twice via the addition 80 % ethanol and repeated centrifugation. DNA was finally eluted from columns via the addition of 10mM Tris-Cl, pH 8.5 and re-centrifugation. Isolated and purified DNA fragments were used immediately in all ligation reactions due to their relatively unstable nature in linear form.

3.2.6 DNA sequencing

All DNA sequencing was performed via PCR-cycle sequencing (Big-Dye terminator system, PE Applied Biosystems) and analysed on an ABI 377 automated sequencer (PE Applied Biosystems). Automated sequencing was conducted in-house by the cancer research UK sequencing department.

Primers were designed for the sequencing of cDNA fragments inserted into the multiple cloning site of the EGFP-C1 vector as follows; 5'-CGGCATGGACGAGC, 3'-GCTGCCATGGCGCCC. Sequencing PCR reactions were conducted using a Peltier thermocycler. Each reaction contained 500 ng plasmid DNA, 3.2 picomols of primer, and the BDT terminator reaction mix. An annealing temperature of 46 °C and 53 °C was used for 5' and 3' primers respectively. Before sequencing PCR reactions were purified to remove unincorporated fluorescent nucleotides. Briefly, DNA was precipitated by incubation in 80 % ethanol, 37 mM Sodium Acetate, pH 4.5 for 30 min at room temperature. DNA was then

pelleted via centrifugation at 14,000 rpm for 20 min, then resuspended in 70 % ethanol and incubated at room temperature for a further 15 min. Finally DNA was repelleted via centrifugation for 5 min, the supernatant discarded, and the resulting pellet left to air dry for 20 min prior to sequence analysis.

3.2.7 Generation of EGFP/ECFP/EYFP fusion constructs

This section describes how the different fluorescent-fusion constructs used in this study were generated. Only those constructs specifically made for use in this study are described in detail. Many other constructs used in this study were obtain from other sources: EGFP-PAK1(wt), Myc-PAK1(wt), Myc-Cdc42(T17N), Myc-Cdc42(wt), and HA-Cdc42(wt) were kindly provided by Tony Ng. FLAG-Cdc42b(wt), FLAG-Cdc42(T17N), HA-Tc10(wt), and HA-Tc10(T31N) were kindly provided by Anne Ridley. EGFP-N-WASP(wt) and Myc-p16 were kindly provided by Laura Machesky. EGFP-N-WASP(ΔVCA) was kindly provided by Markus Zetle. EGFP-N-WASP(H211D) was kindly provided by Marion Peter. EGFP-βActin was kindly provided by John Copeland.

EGFP-Cdc42: Wild type human Cdc42b (brain isoform) was amplified by PCR from a human Cdc42b template plasmid, FLAG-Cdc42b(wt)/CMV5. PCR primers were designed to insert a flanking inframe 5' *Bgl*II restriction site and 5-glycine flexible linker, and downstream 3' *Eco*RI restriction site for insertion into the pEGFP-C1 vector (ClonTech, Cat: 6084-1). Primer designs were as follows:

5'-GCGAGATCTGGCGGGGGAGGAGGTATGCAGACAATTAAGTGTGTTGTTGTGG GCGATGGTGCT.

3'-CGCCGAGAATTCTTAGAATATACAGCACTTCCTTTTGGG.

The dominant negative variant (T17N) of the human placental isoform of Cdc42 was amplified by PCR from a human Cdc42p(T17N) template plasmid, FLAG-Cdc42b(T17N)/CMV5. Brain and placental isoforms of human Cdc42 only differ within the C-terminal region of the protein and thus the same 5' primer could be used in amplification reactions involving templates of either protein. A separate 3' primer was, however, required for the amplification of Cdc42p(T17N) and was as follows:

3'-CGCCGAGAATTCTCATAGCAGCACACACCTGCGGCTCTT.

Cdc42b(wt) and Cdc42p(T17N) PCR products were subjected to restriction digestion with *Bgl*II and *Eco*RI and ligated into the pEGFP-C1 vector cut with the same enzymes. Ligation products were transformed into *E.*coli and individual colonies subsequently selected for restriction digestion and sequence analysis to verify whether PCR and ligation steps were successful. This resulted in the generation of EGFP-Cdc42b(wt) and EGFP-Cdc42p(T17N) fusion constructs.

Wild-type and dominant negative variants of both EGFP-Cdc42 isoforms were then generated by a subsequent cross-ligation step: An internal and unique EcoRV restriction site within in the sequence of both the brain and the placental isoform of Cdc42 and upstream of the C-terminal region of sequence divergence enabled the C-teminal portion of each Cdc42 isoform to be swapped between wild-type and dominant neagative variants. EGFP-Cdc42b(wt) and EGFP-Cdc42p(T17N) plasmids were both digested with *Eco*RV and *Eco*RI, and the resulting C-terminal fragments then cross-ligated into the similarly digested parent plasmid of the other isoform. Ligation products were transformed into *E.*coli and

individual colonies subsequently selected for restriction digestion to confirmed the success of cross-ligation. The placental isoform of Cdc42 is ubiquitously expressed while expression of the brain isoform is restricted to neuronal tissue. Consequently only the wild type and dominant negative variants of the placental isoform of Cdc42 were used in subsequent experimental assays which all involved cell lines of mesenchymal origin. Therefore, Cdc42p will from now on be referred to as merely Cdc42.

EGFP-Tc10: The wild type and the dominant negative variant (T31N) of human Tc10 were amplified by PCR from the template plasmids HA-Tc10(wt)/KH3 and HA-Tc10(T31N)/KH3 respectively (Kind gifts from Anne Ridley). PCR primers were designed to insert a flanking in-frame 5' *BspE*I restriction site and 5-glycine flexible linker, and downstream 3' *Eco*RI restriction site for insertion into pEGFP-C1. Primer designs were as follow:

5'-GGCCGGAGGGGGCGGAGGTATGCCCGGAGCCGGCCGCAGCAGC.

3'-CCGAATTCTCATAGCAGCACACACCTGCGGCTCTTCTTCGG.

PCR products were subjected to restriction digestion with *BspE*I and *Eco*RI and ligated into the pEGFP-C1 vector cut with the same enzymes. Ligation products were transformed into *E.*coli and individual colonies subsequently selected for restriction digestion and sequence analysis. This resulted in the generation of EGFP-Tc10(wt) and EGFP-Tc10(T31N) fusion constructs.

EGFP-PAK1 truncation mutants: A PAK1 truncation sequence encoding amino acids 83 - 149 of the autoregulatory domain, the region which binds to the kinase domain of the protein in the autoinhibited state, was generated by PCR from the template plasmid

EGFP-PAK1(wt) (A king gift from Tony Ng) using the following primers: 5' – TTTCCGGAGGCGGTGGAGGAGGTCACACAATTCATGTCGGTTTTGATGCTGTCA CAGGGGAGTTTACGGG.

3' - CCGAATTCTTATGACTTATCTGTAAAGCTCATGTATTTCTGGC.

A truncation sequence encoding amino acids 1 – 149 and therefore including both the autoregulatory domain and the additional amino terminus of the protein were generated from the same template using the alternative 5' primer:

5'–TTTCCGGAGGCGGTGGAGGAGGTATGTCAAATAACGGCCTAGACATTCAAG ACAAACCCCCAGCCCCTCCG.

For both truncation constructs the PCR primers were designed to insert a flanking in-frame 5' *BspE*I and 6-glycine linker, and downstream *EcoR*I restriction sites for subsequent ligation into pEGFP-C1. PCR products were digested with *Bsp*EI and *Eco*RI and ligated into the similarly cut pEGFP-C1 vector. Ligation products were transformed into *E*coli and isolated clones selected for plasmid DNA amplification and subsequent verification of inserts via restriction digestion and sequence analysis. This resulted in the generation of EGFP-PAK1(83 - 149) and EGFP-PAK1(1 - 149) fusion constructs. All primers described in this section were generated in-house by the Cancer Research UK oligo-synthesis department.

ECFP-β-actin and EYFP-β-actin: Separate constructs encoding ECFP and EYFP amino teminal fusions of βactin were generated by directly cross-ligating a β-actin fragment from an EGFP-β-actin construct (in pEGFP-C1, a kind giflt from John Copeland) into the respective restriction sites of pECFP-C1 and pEYFP-C1 using *BamHI*/*Hind*III restriction digestion.

3.2.8 Cell Culture

The T15 and K2 rat sarcoma cell lines were kind gifts from Pavel Vesely, Institute of Molecular Genetics, Academy of Sciences of the Czech Republic. Cells were cultures in Hanks Minimum Essential Medium (HMEM) supplemented with 10 % batch-tested Bovine Serum (BS) (Serum Medium Laborbedarf), 0.09 % sodium bicarbonate (Sigma), 3.8 mM L-Glutamine, 2.1 mM Glucose, and Phenol Red pH indicator. The Swiss 3T3 mouse fibroblast cell line was grown in (DMEM) supplemented with 10% FCS, 1.6% L-Glutamine, 5 mM Glucose, and 100 U/μg/ml penicillin- streptomycin, and Phenol Red pH indicator.

Adherent T15, K2, and Swiss 3T3 cell cultures were grown and maintained as described for NIH 3T3 cell lines (see cell culture 2.2.1, page 19). However, T15 and K2 cultures were maintained in humidified incubator with 5 % ambient CO_2, not 10 % as described previously.

3.2.9 Preparation of coverslips

18 mm × 18 mm, thickness no. 1.5 glass coverslips were prepared for use in random walk, chemotaxis, and fixed-cell FRET/FLIM assays. Coverslip dimensions were primarily chosen for their compatibility with the Dunn chemotaxis chamber and to enable the optimal microscopic imaging of cells at both low and high magnification (the majority of modern microscope objectives are optimised for use with 170 μm thick (no. 1.5) glass coverslips).

Coverslip cleaning: Coverslips were thoroughly washed prior to tissue culture use: coverslips were placed in Teflon coverslip racks (molecular probes) and immersed in a mixture of 60 %

concentrated HCl, 40 % ethanol (95 % pure) for 2 hrs. Racks were subsequently removed from the acid/alcohol mixture and immersed in ddH_2O for three sequential 10 min washes. Coverslips were then stored under 70 % ethanol until required. Immediately before use coverslips were dried mechanically using an air hose with fitted ployVENT^{TM} 200 nm pore filter (Whatman). Passive evaporation was not permitted as a method of drying as this often resulted in the formation of residue on the coverslip surface.

Coverslip etching: In cases where cell cultures were prepared for microinjection and subsequent analysis in chemotaxis experiments, coverslips were marked to facilitate the relocation of the microinjected cells. When correctly assembled the Dunn chemotaxis chamber permits the observation of cells within only a small central region of the coverslip approximately 2 mm × 2 mm in area. To ensure microinjected cells could be observed within the chamber the central region of each coverslip was marked with a 'window' pattern, and cells only microinjected within this area. A manually controlled *xy* stage with graduated axes and a fitted diamond objective was used to accurately etch the window pattern into the centre of each coverslip.

3.2.10 Application of the Dunn chemotaxis chamber

Preperation of subconfluent cultures: Cells were plated on washed, pre-etched coverslips placed in 35 mm sterile plastic tissue culture dishes (Corning) containing 3 ml of the appropriate culture medium for the cell type used. Freshly trypsonised T15 rat sarcoma cells, NIH 3T3, and Swiss 3T3 fibroblasts were plated at 5×10^3, 2×10^3 and 1×10^4 cells per dish respectively. Coverslips were placed in dishes such that cells would be plated onto the

reverse surface to that of the scratched markings: many cell types are known to exhibit contact guidance *in vitro*, preferentially aligning and migrating along linear surface markings (Stepien et al., 1999). Since chemotaxis was the subject of investigation it was essential to minimize the influence of other environmental factors capable of influencing the direction of cell migration. Dishes were briefly shaken in a horizontal figure-of-eight pattern to facilitate the even spreading of cells before returning to the incubator.

Nuclear microinjection: T15 rat sarcoma cells were transferred to serum reduced (0.5 % BS), phenol red free culture medium three hours prior to microinjection and six hours prior to Dunn chamber assembly. Swiss fibroblasts were transferred to full serum (10 % FCS), phenol red free culture medium supplemented with 20 mM HEPES, pH 7.5 prior to microinjection to compensate for the usual CO_2 requirements.

Cells positioned within the central etched region of a coverslip were located on the microscope by focusing on the lower coverslip surface, detecting the etches, and then refocusing through the coverslip onto the cells. A group of evenly spaced cells within the etched region was selected and approximately every other cell microinjected in the nucleus. Expression constructs encoding EGFP fusions of proteins of interest were all microinjected at a concentration of 0.05 μg/μl. Cells were allowed 3 hours to express microinjected constructs before coverslips were assembled onto Dunn chemotaxis chambers. For detailed description of the microinjection system see: nuclear microinjection 2.2.2, page 19.

Preparation of growth factors: Lyophilized recombinant rat PDGF-BB (Sigma) and recombinant human IGF-1 (PeproTech) were reconstituted in ddH_2O adjusted to pH 7.0 and supplemented with 0.1 mg/ml BSA (Sigma) carrier protein to a concentration of 50 µg/µl and stored as separate 20 µl stock aliquots at –20 °C until required.

Aliquots containing culture medium with and without growth factors were prepared for Dunn chamber assembly. For T15 rat sarcoma cells reduced serum (0.5 % BS), phenol red free culture medium was used throughout. Immediately prior to chamber assembly growth factors were added to culture medium to a final concentration of 60 ng/ml PDGF-BB, 80 ng/ml IGF-1. For Swiss and NIH 3T3 fibroblasts full serum (10 % FCS), phenol red free medium supplemented with 20 mM HEPES adjusted to pH 7.5 was used throughout. PDGF-BB alone provided the chemotactic stimulus for Swiss and NIH 3T3 fibroblasts and was added to culture medium to a final concentration of 100 ng/ml.

Chamber assembly: Assembly of the Dunn chemotaxis chamber (Weber Scientific International) is summarized in Figure 37, page 19, and is described in detail here. The outer and inner wells of the chemotaxis chamber were flooded with culture medium before inverting the glass coverslip with adherent cells carefully onto the chamber using forceps. Care was taken to prevent bubbles from forming between the underside of the coverslip and the inner and outer wells. The volume of culture medium was sufficient to allow the coverslip to float above the surface of the chamber enabling it to be repositioned with the fingertips without crushing the cells. In cases where microinjected cells were present, a microscope with a fluorescent lamp was used to detect the fluorescent cells and carefully

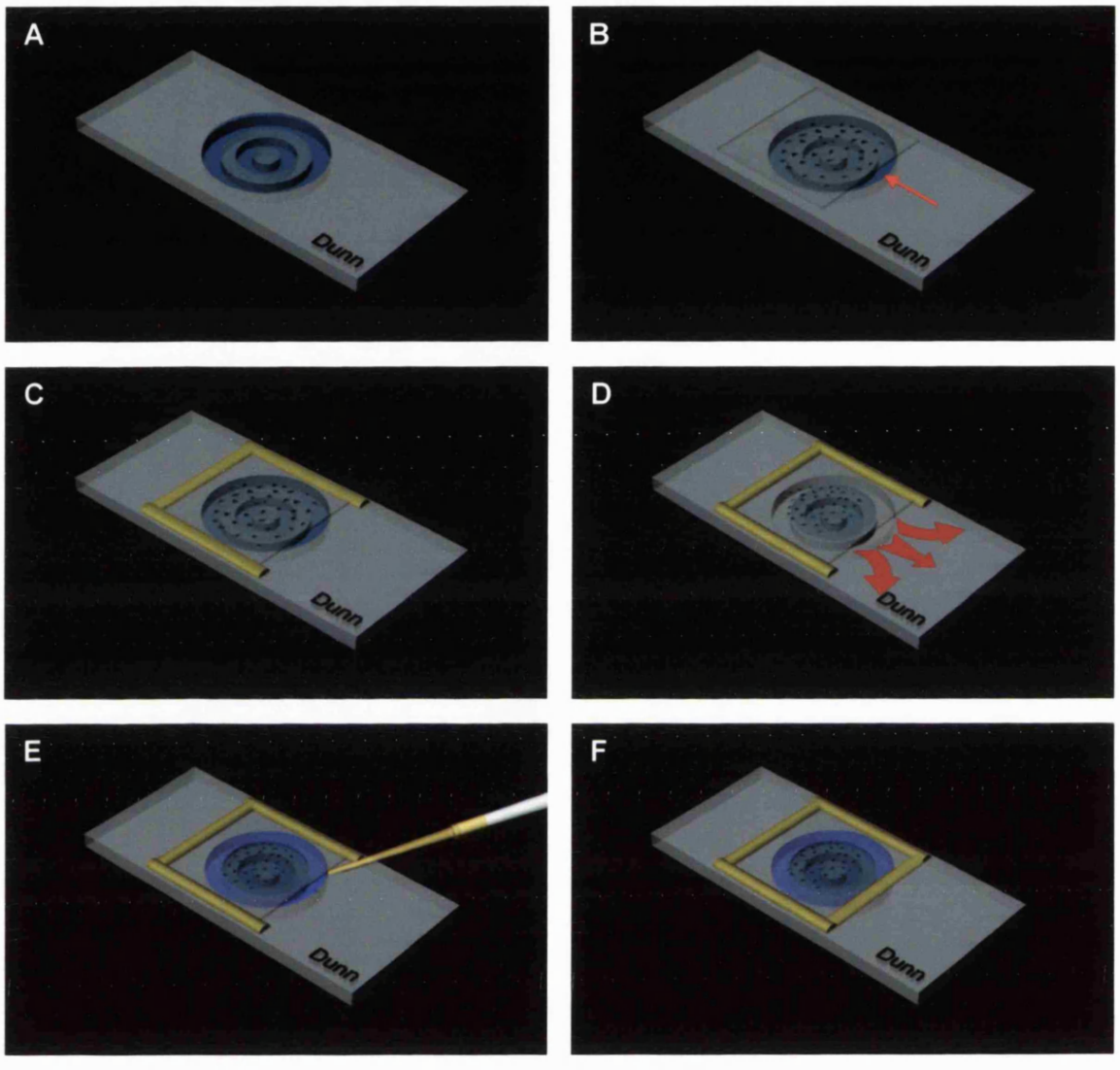

Figure 37. Assembly of the Dunn chemotaxis chamber

Procedure for assembling the Dunn chemotaxis chamber. (A) The central region of the chamber was flooded with culture medium. (B) The coverslip with adherent cells was then inverted and lowered onto the chamber. The coverslip was positioned such that a small filling slit was left at one end of the outer well (arrow). Tissue paper was used to carefully dry the edges of the coverslip so that it lay flush against the surface of the chamber. (C) The coverslip was then sealed to the chamber using the hot wax mixture. At this stage the edge that formed the filling slit was not sealed. (D) Tissue paper was used to draw medium out from the outer well. (E) The outer well was washed once with fresh medium and the chemoattractant then applied using a pipette. (F) The edge of the filling slit was dried and finally sealed with hot wax mixture.

position them over the annular platform, roughly parallel to the outer well. If the fluorescent cells had been microinjected within the central 2 mm × 2 mm etched area of the coverslip then the coverslip would be positioned such that a thin section of the outer well remained exposed at the opposite end of the chamber. This exposed region formed the 'filling slit' that enabled access to the outer well for the addition of culture medium containing the chemoattractant. The sides of the coverslip were gently dried using sterile tissue paper, taking care not to press down on the region suspended over the inner and outer wells as this could easily result in crushing the cells. Furthermore it was essential to avoid moving the coverslip after the fluorescent cells had been positioned over the annular platform. Once the coverslip perimeter was dry it was sealed to the chamber using a hot wax sealing mixture consisting of a 1:1:1 ratio of paraffin wax (Fischer Scientific), beeswax (Acros Organics), and petroleum jelly (Fischer Scientific) mixed and heated to 60 °C. The sealing mixture was applied using a paintbrush. The coverslip edge that formed the filling slit was not sealed at this stage. Medium within the outer well of the chemotaxis chamber was drawn out by applying sterile tissue paper to the edge of the filling slit. Suction pressure prevented the removal of medium from within the diffusion gap and the central well. The outer well was then washed once by the re-addition of fresh culture medium using an Eppendorf pipette. This was done to remove any factors released from crushed cells at the chamber perimeter that could have potentially influenced the behaviour of cells under observation. The fresh medium was then removed with tissue paper in the same way, and the culture medium containing the chemoattractant then applied. The edge of the filling slit was then carefully dried and finally sealed with the hot wax sealing mixture.

Recording of cell behaviour: Digital time-lapse microscopy was used to record cell behaviour in all Dunn chamber chemotaxis experiments. Cells were imaged on either a Zeiss Axiovert TV 135 (Carl Zeiss) or a Nikon Diaphot (Nikon) inverted microscope. The specifications of the Zeiss microscope are described in: time-lapse microscopy 2.2.3, page 19. As with the Zeiss system the Nikon microscope was optimised for the multi-channel time-lapse recording of live mammalian cells in culture. The microscope was fitted with tungsten and mercury lamps, separate bright field and fluorescence shutters (Uniblitz), a shutter controller (Ludle), and a sensitive CCD camera (Orcar ER, Hamamatsu). Peripheral devices were under the control of acquisition manager software. A filter block containing appropriate excitation and emission filters and a dichromatic mirror enabled the visualization of EGFP fluorescence (Omega, FX100-2 Alpha Vivid). The microscope was positioned on an optical table isolator and housed in a Perspex environment chamber accurately maintained at 37 °C.

The chemotaxis chamber was inverted and placed on the microscope in a conventional slide holder and positioned so that the diffusion gap was directly above the objective. The image acquisition software was then used to select a suitable observation field within the diffusion gap that contained the majority of the fluorescent cells. The innermost annular edge of the outer well was positioned at the top of the computer screen by rotating the CCD camera, thus aligning the chemotactic gradient with the vertical axis of the image. The chamber was then left to stand in the microscope for 20 min to allow the temperature to equilibrate and the focus to settle. In cases where microinjected cells were not studied a suitable field of evenly

spaced cells above the diffusion gap and furthest from the filling slit was selected for observation.

Low magnification multi-channel digital time-lapse microscopy was used to monitor cell behaviour in the chemotactic gradient over a 16-hour period. Sequential phase contrast and EGFP fluorescence images were acquired every 5 min using either a ×10 NA 0.3 or ×20 NA 0.5 phase contrast objective. A total of 200 time points were acquired resulting in films of 1000 minutes duration (~16.7 h).

3.2.11 Application of the random walk chamber

Preperation of subconfluent cultures: Freshly trypsonised NIH 3T3 fibroblast were plated on pre-washed coverslips placed in 35 mm sterile plastic tissue culture dishes containing 3 ml of the appropriate culture medium. The large central region of the coverslip available for imaging in the random walk chamber meant that cells could be microinjected across a far greater area than in chemotaxis experiments and therefore coverslip etching was not required.

Nuclear microinjection: NIH 3T3 fibroblasts were transferred to 10 % FCS, phenol red-free culture medium supplemented with 20 mM HEPES prior to microinjection. Groups of subconfluent, evenly spaced cells within a central region of the coverslip were located on the microscope and microinjected in the nucleus with expression constructs encoding the EGFP fusion protein of interest. All constructs were microinjected at a concentration of 0.05 μg/μl. Following microinjection the culture medium was replaced with fresh tissue culture medium and cells subsequently returned to the incubator to express microinjected constructs. Cells

were allowed 3 hours to express microinjected constructs before coverslips were assembled onto random walk chambers. For detailed description of the microinjection system see: nuclear microinjection, methods 2.2.2, page 19.

Chamber assembly: The random walk chamber was designed and manufactured in-house by Colin Gray. Assembly of the chamber is described here and summarized in Figure 38, page 19. The central well of the random walk chamber was flooded with culture medium (10 % FCS, phenol red free) and the coverslip then inverted and lowered carefully onto the chamber using forceps. Care was taken to ensure bubbles did not form between the underside of the coverslip and the central chamber well. Sterile tissue paper was used to dry the edges of the coverslip, which was positioned so that it completely covered the central well of the chamber. Hot wax mixture was then used to seal the coverslip to the chamber.

Recording of cell behaviour: Digital time-lapse microscopy was used to record the behaviour of NIH 3T3 fibroblasts in all random walk experiments. All experiments were conducted on the same Nikon Diaphot inverted microscope additionally used during chemotaxis experiments (*see section 3.2.10, page 19*). For random-walk experiments the microscope had been additionally modified to enable multi-field imaging. The addition of a motorised, multi-position stage (Marzhauser) and motorised focus (Piezo) enabled multiple fields within up to three different chambers to be acquired automatically on the same Nikon microscope. The system therefore provided a relatively hi-throughput assay for the study of cell motility.

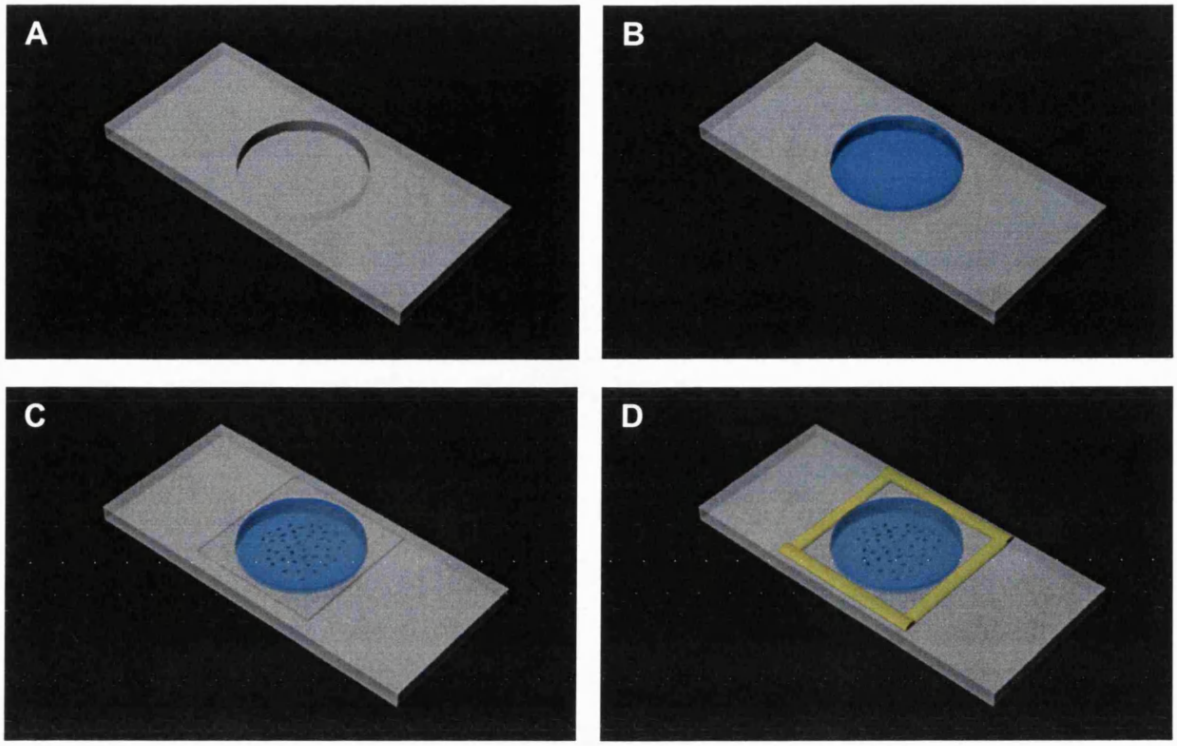

Figure 38. Assembly of the random walk chamber

Procedure for assembling the random walk chamber. The central region of the chamber (A) was flooded with culture medium (B). (C) A coverslip with adherent cells was then inverted and lowered carefully over the flooded area using forceps. The coverslip was positioned so that it completely covered the central well. Tissue paper was then used to carefully dry the coverslip edges so that that it lay flush against the surface of the chamber. (D) Hot wax mixture was then used to seal the coverslip to the chamber.

Random walk chambers (up to a maximum of 3) were inverted and positioned on the microscope in a multiple slide holder. Care was taken to ensure chambers were clamped securely within the holder to prevent observation fields from wandering during the operation of the motorised stage. Two separate observation fields containing fluorescent cells were selected within each chamber. Selected fields were spaced sufficiently far apart to minimize the risk of imaging the same cells within more that one field. The co-ordinates and focus positions of each observation field were stored by the acquisition software. Chambers were then left for 20 min to allow temperature to equilibrate and focus to settle. Sequential phase contrast and EGFP fluorescence images were then acquired for each observation field every 5 min over a 16 hour period using a ×10 NA 0.3 phase contrast objective.

3.2.12 Analysis of cell motility

Interactive cell tracking: Image analysis software (Tracker, Kinetic Imaging) was used to interactively track migrating cells from acquired film sequences to generate cell trajectories for the subsequent statistical analysis of cell behaviour (Figure 39, page 19). Interactive tracking involved the use of the mouse pointer to mark the positions, stored as a single image coordinates, of individual cells over consecutive frames of an entire film sequence. The centroid of a cell was taken to represent its position. Where multi-channel imaging had been used to identify fluorescent cells within an experiment, the phase contrast and fluorescent channels were merged to enable the identification of microinjected cells during the tracking process. Additional characteristics of a migrating cell could also be stored along with its cell trajectory data enabling the identification of microinjected cells during the later stages of data

analysis. Cell trajectories from an individual film were stored in a single text file in a format that could be interpreted by Mathematica notebooks developed within the laboratory for the analysis of cell behaviour.

Evaluation of chemotaxis: Purpose written Mathematica notebooks were used for the statistical analysis of cell trajectory data. To evaluate the chemotactic response of a cell population, individual cell trajectories were generated via the interactive tracking of film sequences as described. Cell trajectories were then shifted to a common origin (Figure 40A, page 19) and each converted to a single angle that represented the direction of cell movement. The angle, and thus the direction of cell movement was determined upon the cell reaching a virtual horizon defined as the maximum distance from the common origin achieved by 75 % of the cell population (Figure 40B). Cell directions were subsequently processed by statistics of directional data to test for significance of unimodal clustering using the Rayleigh test (Zicha et al., 1997). Cell directions were collectively represented by circular histograms with the height of individual segments representing the number of cells migrating in a given direction (Figure 40C). In cases where the unimodal clustering of cell directions was significance ($p < 0.05$) the mean direction of cell movement (θ) was represented by a red arrow and the associated 95 % confidence interval as a green pie wedge.

Data generated from chemotaxis experiments represented hierarchical structures and therefore the unbiased comparison of different treatment groups required the application of ANOVA. As ANOVA has not been developed for the comparison of circular data an alternative method of representing chemotaxis was required in order to compare cells from

different treatment groups with controls. Therefore, relative cell displacement in the direction of the chemotactic gradient was used as an alternative means of evaluating the chemotactic response. Upon reaching the virtual horizon both the total displacement *horizon*, represented in absolute terms, and the vertical displacement Δy of the cell were determined (Figure 40B). A relative value of cell displacement, independent of cell speed, could then be derived by the equation $\Delta y/horizon$. An abundance of positive displacement values would indicate a tendency for cells to migrate in the direction of the chemotactic gradient, while an even mixture of positive and negative values would represent movement that was indifferent to gradient direction.

Evaluation of cell speed: The generation of cell trajectory data also provided a means of evaluating cell speed. Mathematica algorithms were written to calculate the speed of individual cells over the course of film sequences. ANOVA was then used to process speed data and test for significances between control and treatment groups. Speed data for an entire treatment group was represented as a box-and-whisker chart with boxes spanning 50 % of the data and whiskers spanning 80 % of the data.

Evaluation of persistence: Individual cell persistences were calculated as a function of net and total cell displacement derived by the equation: persistence = net displacement/total displacement. The persistence of an individual cell was represented by a single value between 0 and 1: a persistence value that tended to 1 reflected highly persistent movement, indicating that the cell rarely deviated from its path over time. A persistence value that tended to 0 reflected poor persistence of movement, indicating that the cell altered direction frequently. Only those cells that remained within a film sequence for longer than 50 % of the

total film length (i.e. 500 min) were selected for subsequent persistence analysis. Selected cell trajectories were then cropped to equal lengths of 500 min before subsequent calculation of persistence values. Relatively long trajectories were selected for the calculation of persistence values in order to suppress the effects of 'noise' contributed by individual data points. However, the selection of only those trajectories that spanned the entire length of film sequences was undesirable because insufficient cell numbers would remain to provide a meaningful analysis. Trajectories that spanned 50 % of the total film length therefore provided a suitable compromise. ANOVA was used to process persistence values and test for significances between control and treatment groups. Persistence data for an entire treatment group was represented as a box-and-whisker chart, with circles representing median values, and boxes spanning 50 % and whiskers spanning 80 % of the data. The method of evaluating persistences is similar to that previously used by others to measure directionality and chemotaxis (Allan and Wilkinson, 1978; Vesely et al., 1987).

3.2.13 Intensity analysis

Specialised image processing software was developed in Mathematica that enabled the intensities of fluorescent cells to be extracted from film sequences, permitting an assessment of the effects of varying levels of protein expression on the speed of cell motility. Prior to image processing in Mathematica, imaging software (Acquisition Manager, Kinetic Imaging) was used to generate film sequences consisting of only those images acquired in the EGFP fluorescent channel during chemotaxis experiments. Image data was then normalised prior to the extraction of cell intensities.

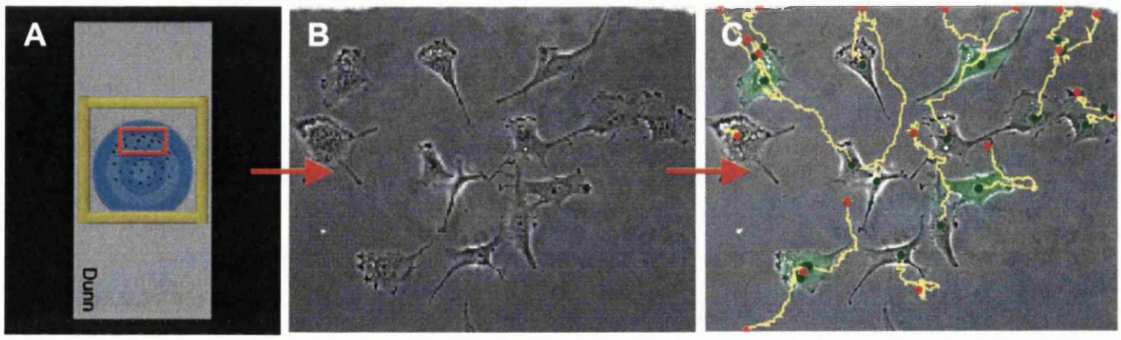

Figure 39. Interactive tracking of film data

Computer assisted tracking was used to generate cells trajectories from acquired film sequences. (A) The orientation of the field of view with respect to the chemotaxis chamber is indicated by the red box. (B) The top of the image represents the inner edge of the outer well and hence the source of the chemotactic gradient. (C) In experiments where fluorescence imaging had also been used phase contrast and EGFP fluorescence channels were overlaid in order to facilitate the identification of fluorescent cells. Cells were then tracked over the course of a film sequence in order to generate individual cell trajectories. Green and red circles represent the first and final positions of cell trajectories respectively.

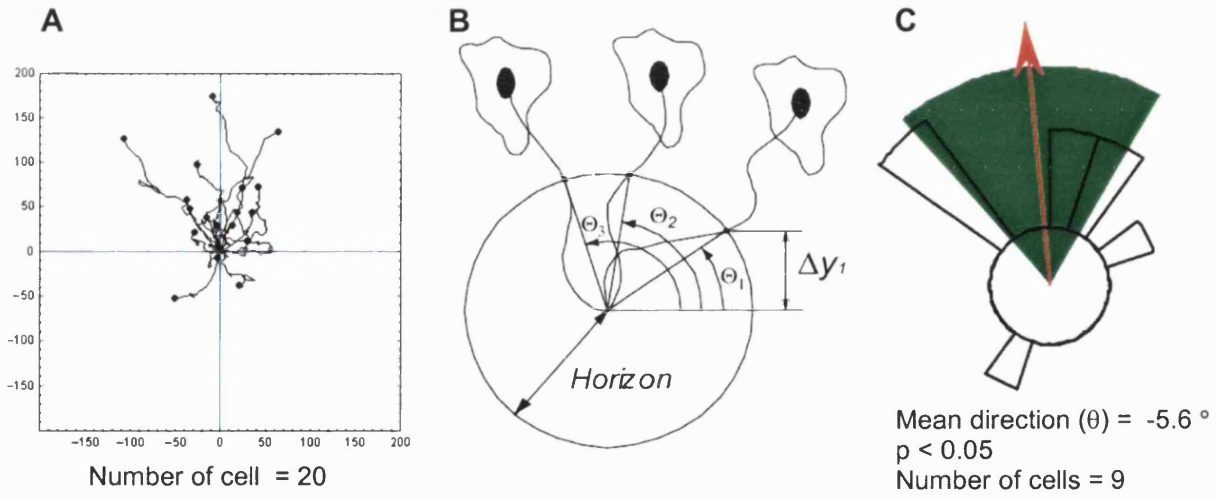

Figure 40. The evaluation of chemotaxis

(A) Cell trajectories generated from the interactive tracking of film data were shifted to a common origin (axes units are μm). (B) Individual trajectories were then converted to single angular directions upon cells reaching a virtual horizon. (C) Angular directions calculated for multiple cells are presented as circular histograms. Where significant unimodal clustering of angles exists the mean direction (θ) of cell migration and the associated 95 % confidence interval are shown. Relative cell displacement in the direction of the gradient is calculated as Δy/Horizon and is used for the evaluation of the chemotactic response by ANOVA. Example data are taken from the film in Figure 39.

Normalisation of image data: Chemotaxis experiments were conducted on microscopes with differing lamp, filter, and optical specifications. Furthermore, exposure times for the acquisition of fluorescent images often differed between experiments, while small fluctuations in the intensity of the excitation light meant that over the time course of a film image intensity values could vary. Therefore, before cell intensities could be extracted from images a degree of normalization was required to enable the inter-comparison of film data. When the total area of fluorescent objects within an image is small in comparison to the entire image area the modal pixel value typically represents the level of background noise. The low magnification imaging of subconfluent populations of fluorescent cells provides one such example of a low fluorescence area-to-total image area ratio. When camera exposure times are high and cell expression levels low there is a high degree of background noise and consequently modal values are large. Conversely, when exposure times are low and expression levels high, modal values are small. Therefore, prior to the extraction of cell intensities, the modal pixel value for each image was subtracted from all other image pixels values providing a mechanism for the normalization of fluorescence intensity.

Extraction of cell intensities: Cell trajectories previously obtained from the interactive tracking of film data were used to identify the positions of fluorescent cells over consecutive frames of a film sequence. For each image a circular boundary with a 30-pixel radius was defined around each cell coordinate and the total intensity of pixels contained within this region then calculated. The resulting value was taken to represent total cell intensity for that time point. In the majority of cases the total fluorescent area of a cell was contained entirely

within the region defined by the boundary. In cases where the boundaries of neighbouring cells overlapped intensity values were ignored. For a single film sequence total intensity values for all fluorescent cells were recorded for all time points and then stored in a text file in a format that could be interpreted by Mathematica notebooks for subsequent data analysis.

Analysis of intensity data: Cell intensity data was processed in Mathematica to analyse the effects of various levels of protein expression on cell speed. For each treatment group increasing levels of protein expression, represented by increasing fluorescence intensities were plotted against variations in cell speed. Cell speeds, calculated at hourly intervals, were sorted according to their associated intensity values. Speed data for a single treatment group was partitioned into six separate bins of increasing fluorescence intensity and represented as box-and-whisker charts. The hierarchical structure of the data set was maintained throughout enabling significant differences between the speed values of different intensity bins of the same and different treatment groups to be evaluated using ANOVA.

Practical imitations: The subtraction of modal intensities provided a degree of data normalization that better justified the inter-comparison of film data. However, there were some limitations to this approach. Although camera sensitivities were similar between microscopes they were not identical, and thus separate cameras would yield slightly differing modal values for an identical image. Furthermore, in cases where pixel saturation occurred, modal subtraction no longer provided a meaningful method of normalization. However, limitations aside, this approach did provide useful insights into the effects of varying expression levels of EGFP fusion proteins on rat sarcoma cell motility. The Mathematica

routines developed for the extraction of cell intensities can be found in: Appendices 5.2, page 19.

3.2.14 FLAP

Preparation of cell cultures and nuclear microinjection: Subconfluent cultures of T15 or K2 sarcoma cells were prepared as described in section 3.2.10, page 19 although coverslip etching was not required. Cells were transferred to 10 % BS, phenol red free culture medium three hours prior to microinjection and six hours prior to assembly of random walk chambers. A patch of subconfluent cells within the centre of each coverslip was selected and individual cells microinjected in the nucleus with a mixture of EGFP-β-actin and EYFP-β-actin plasmid DNA. Constructs were microinjected at a concentration of 0.1 μg/μl each. Cells were returned to the incubator and allowed 3 hours to express fluorescent proteins before assembly into the random walk chamber as described in section 3.2.11, page 19.

Confocal microscopy: All images were recorded using the same inverted laser scanning confocal microscope (Zeiss LSM 510) equipped with a 63 × NA 1.4 oil objective. The body of the microscope rested on an anti-vibration optical isolation table and was housed within a Perspex environmental chamber (built in-house) accurately maintained at 37 °C. The CFP and YFP channels used the 458 nm and 514 nm lines of an argon laser for excitation. A 545 nm dichromatic mirror was used to split the two emission channels, followed by a band-pass 475-525 nm filter for the ECFP channel and a long pass 530 nm filter for the EYFP channel. The pinhole for each channel was set such that the thickness of the optical slice was indicated as 300 nm by the LSM 510 software. Each image line was scanned twice at the

highest scan rate (0.64 μs/pixel) using multi-tracking mode, first by the 514 nm laser line and then by the 458 laser line.

Prior to imaging a thin, rectangular bleach region was defined over an appropriate region of the selected cell using the LSM 510 software. Bleach regions were always aligned lengthwise with respect to the horizontal plane of the image as this maximised the scanning rate. The gain and offset for each fluorescence channel were optimised so that the two images closely matched without saturation. The time-lapse mode of the LSM 510 software was used to collect sequential images and also to photobleach the pre-defined region. Usually three pre-bleach images were acquired before photobleaching using the 514 laser line at maximum excitation (1.32 mW) for 3 – 15 s in order to selectively photobleach EYFP within the defined region. After photobleaching the time-lapse sequence was automatically resumed.

Image processing: All image processing was performed in Mathematica using specially developed software (written and provided by Graham Dunn). For each recorded time point FLAP ratio signals were calculated as:

$$\frac{(I_{CFP} \times I_{YFP})}{I_{CFP}}$$

Where I_{CFP} and I_{YFP} represents the intensity of *ECFP* and *EYFP* at each image pixel. As the *ECFP* and *EYFP* channels are carefully matched prior to imaging, I_{CFP} values are taken to represent the expected I_{YFP} values for *EYFP* at each image pixel if bleaching had not taken

place. Therefore the reference fluorophore provides a means of determining the proportion of the total *EYFP* molecules within a pixel that have been bleached.

3.2.15 Preparation of fixed cell specimens for FLIM/FRET analysis

Preparation of cell cultures and nuclear microinjection: Subconfluent cell cultures of NIH 3T3 were prepared by plating 2×10^3 freshly trypsonised cells onto washed, un-marked coverslips placed in 35 mm sterile plastic tissue culture dishes containing 3 ml of tissue culture medium. Cells were allowed to grow for three days before experimentation. NIH 3T3 fibroblast cultures were transferred to 10 % FCS phenol red free medium supplemented with 20 mM HEPES immediately prior to microinjection. A patch of evenly spaced cells situated within the centre of the coverslip was selected and approximately 20-30 cells microinjected in the nucleus. Following completion of microinjection the medium was replaced with fresh tissue culture medium and the cells returned to the incubator. Cells were allowed 4 hours to express microinjected constructs before subsequent fixation and immunocytochemistry. Constructs encoding full-length EGFP-N-WASP(wt) and either myc-Cdc42(wt) or myc-p16 were co-microinjected at a concentration of 0.05 μg/μl and 0.10 μg/μl respectively to produce a donor/acceptor ratio of 1:2. In cases where HA-Cdc42(wt) was co-microinjected with EGFP-N-WASP(wt or H211D) and Myc-p16, constructs were microinjected at a ratio of 1:2:2 for EGFP-N-WASP, Myc-p16, and HA-Cdc42 respectively.

Immunocytochemistry: Cells were fixed in 4 % paraformaldehyde (sigma) for 15 min, washed 3 × with PBS and then permeabilised for 4 min with 0.1 % Triton-X 100. Following permeabilisation cells were washed 3 × with PBS before a 10 min treatment with 1 % sodium

borohydride (Sigma). 3 additional washes with PBS followed before a 20 min treatment with a 1 % BSA blocking solution. A 2 h incubation with the Cy3-conjugated 9E10 anti-Myc monoclonal antibody (Cy3-mAb) (1:60 dilution from 1 mg/ml stock, a gift from Tony Ng) then followed in order to label expressed Myc-tagged proteins. Three subsequent washes with 1 % BSA solution, followed by an additional 3 washes 10 min later were performed to remove any unbound antibody. In cases where either giantin or HA-Cdc42(wt) labelling was additionally required cells were incubated with primary antibodies (1:100 dilution from stock) for 30 min. Giantin was labelled using a rabbit monoclonal anti-giantin antibody (a kind gift from Dr. David Shima), and HA-Cdc42(wt) labelled using the 12CA5 mouse anti-HA monoclonal antibody (developed in house by the Cancer Research UK monoclonal antibody department). Samples were then washed as described and then incubation with the appropriate secondary antibody (1:200 dilution from stock) for an additional 30 min; either Cy5-donkey anti-rabbit or Cy5-donkey anti-mouse (Jackson ImmunoResearch Laboratories cat no. 711-175-152 & 715-175-150 respectively) for anti-giantin and anti-HA-Cdc42(wt) respectively. After a final wash coverslips were then mounted on glass slides in a Mowiol/anti-fade mountant. Samples were covered to protect from ambient light and allowed to set over night at room temperature.

3.2.16 Preparation of live cells for FLIM/FRET experiments

Preparation of cell cultures and microinjection: Subconfluent cell cultures of NIH 3T3 fibroblasts for use in live-cell FRET/FLIM assays were prepared by plating 2×10^3 freshly trypsonised cells onto 35 mm glass-bottomed microwell dishes containing 3 ml of tissue culture medium. Cells were allowed to grow for three days before experimentation. Nuclear

microinjection was carried out as described for fixed cell experiments (see section 3.2.15, page 19). Constructs encoding EGFP-Cdc42(wt) and myc-PAK1(wt) were co-microinjected at a concentration of 0.05 μg/μl and 0.10 μg/μl respectively to achieve a donor/acceptor concentration ratio of 1:2. Cells were allowed to express constructs for 4 hours. EGFP-Cdc42(wt) expressing cells were then relocated and microinjected in the cytoplasm with the Cy3-mAb against Myc-PAK1. Antibody was microinjected at a concentration of 1 mg/ml. The microinjection system used was optimised for the low level detection of fluorescence: see cytoplasmic microinjection 2.2.2, page 19. Cells were returned to the incubator and allowed 30 min to recover from cytoplasmic microinjection. Care was taken to ensure that some EGFP-Cdc42(wt) expressing cells were left uninjected to provide control lifetimes for EGFP in the absence of acceptor.

3.2.17 Time domain FLIM

TCSPC based FLIM was performed to measure FRET between donor EGFP-N-WASP(wt) and a Cy3-mAb against either myc-Cdc42(wt) or myc-p16(wt) in order to determine where N-WASP/Cdc42 and N-WASP/Arp2/3 activation complexes formed within the cells respectively.

The hybrid multiphoton TCSPC FLIM system: A hybrid system incorporating multiphoton imaging with TCSPC was utilized to enable the three-dimensional, high-resolution fluorescence lifetime imaging of the biological sample. The system was developed by Dr. Simon Ameer-Beg and Dr. Borivoj Vojnovic of the Advanced Technology Development Group, Gray Cancer Institute, Mount Vernon Hospital. Centring around an inverted

microscope (Nikon TE200), the system was assembled on an optical bench (Melles Griot). A solid-state-pumped YVO_4 Millenia X 10W/modelocked Tsunami titanium:sapphire pulse laser (Spectra Physics) provided the excitation source, which was tunable over a 690 – 1000 nm range. The laser was tuned to 900 nm to enable two-photon excitation of 450 nm at the focal point. A mercury arc lamp mounted on the epi-illumination port of the microscope enabled the fluorescent sample to be located prior to image acquisition while an adjustable mirror allowed the excitation light source to be alternated between the lamp and the laser. A beam splitter positioned in the optical path of the laser launched the excitation light into both a photosensitive diode, and a Bio-Rad MRC 1024 scanhead mounted on a side port of the microscope. The scanhead controlled the scanned excitation of the sample while the photosensitive diode monitored the occurrence of excitation pulses to enable time-correlated photon counting measurements. The scanhead was controlled via an OS2 Bio-Rad PC. Fluorescence emission from the excited sample was collected via a high-magnification, high-numerical aperture objective lens (Nikon CF160 ×40, NA 1.3, Plan Fluor) and directed onto three in-house developed non-descanned detectors and a photomultiplier tube (PMT) (Hamamatsu R7401-P). The non-descanned detection of fluorescence and the use of a high numerical aperture lens greatly enhanced the fluorescence detection efficiency of the system. The PMT enabled single photon events to be monitored by the time-correlation hardware. A PMT is a vacuum device consisting of a photocathode, a series of dynodes (amplifying stages), and an output anode. Photon impact at the photocathode surface generates an electron burst that is amplified exponentially along the length of the tube resulting in a short pulse of current at the anode output. The anode output was linked to an SPC700 module (Becker-Hickl) that handled the calculation of photon delay times required for fluorescence

lifetime imaging. The excitation source was attenuated so that a single excitation pulse would result in photon detection in only 1 in 10 instances. The ultra-fast timing capability of the SPC700 module then monitored the time between photon detection and the next excitation pulse. Two constant fraction discriminators (CFD) within the SPC700 module monitored excitation and emission pulses, one linked to the PMT and the other to the photosensitive diode. Upon detection of an emitted photon the PMT sent a start pulse to the first CFD triggering the internal clock, upon detection of the next excitation pulse the photosensitive diode sent a stop pulse to the second CFD stopping the clock. A time-to-amplitude converter (TAC) measured the delay times between emission and excitation events recorded by the CFDs with picosecond accuracy and stored the information in a large histogram memory. The system also simultaneously monitored the position of the scanning excitation light so that photon delay times were attributed to the appropriate pixel coordinate within the scanned image. As the sample was scanned and photon counts accumulated, a three-dimensional image of the scanned area was stored in memory consisting of an array of pixels, each containing a complete fluorescence decay function. This information was finally off-loaded onto a PC for lifetime calculations. The system enabled accurate fluorophore lifetime calculations to be made within the 0.5 – 5 ns range. The system set-up is summarized in Figure 41, page 19.

Note that for TCSPC measurements, delay times were measured in the reverse order to that explained in the introduction; i.e. the time from fluorescence emission to the next excitation pulse was measured as supposed to the time from fluorescence emission to the preceding excitation pulse as described in the introduction. This is because it is far more logical to

describe TCSPC in the context of related excitation and emission events. The principle, however, remains the same.

Evaluation of fluorescence lifetimes: The proportion of interacting and non-interacting donor fluorophores within each pixel of an image was calculated to provide a fluorescence lifetime map of the specimen. The exponential decay kinetics of the interacting and non-interacting fluorophore populations are distinct, with the lifetime of the interacting population defined by the equation:

$$\tau_{fret} = \tau_d \left(\frac{r}{R_0} \right)^6$$

Where R_0 is a constant and represents the Förster radius, τ_d the donor fluorophore lifetime in the absence of acceptor, and r the separation distance between the donor and acceptor fluorophores within the FRET pair. Since, in reality, a continuous distribution of values for r should exist, as the separation distances between donor and acceptor fluorophores are not identical from one FRET pair to another, each data set for a given pixel should be composed of an ensemble of fluorescent lifetimes. However, the application of a model that considers multiple lifetimes and thus multiple exponential decay profiles is impractical, requiring complex mathematics and formidable photon data sets in order to achieve reliable results. It was therefore assumed that two lifetime components existed, one that represented the interacting/FRET population, and one that represented the non-interacting population. Therefore, in order to determine the fluorescence lifetimes of the interacting and non-interacting donor fluorophore populations a bi-exponential decay model was applied to the data:

$$I(t) = I_0 \left[A_1 \, Exp\left(\frac{-t}{\tau_1}\right) + A_2 \, Exp\left(\frac{-t}{\tau_2}\right) \right]$$

I represent the intensity at any given time point t along the fluorescence decay curve. I_0 represents the maximum intensity (highest integrated photon count) for the brightest pixel within the three-dimensional image. τ_1 and τ_2 represent the lifetimes of the interacting and non-interacting populations at each pixel and A_1 and A_2 their respective fractional proportions.

Prior to the calculation of lifetimes image data sets were deconvolved to compensate for the instrumental response of the system. The instrumental response is a function of the accuracy of the SC700 TCSPC module and the inherent delay of the PMT and was established using a well-defined fluorophore of known lifetime. The bi-exponential model was then applied to the corrected data sets and the two lifetime components then derived. The method of image processing was a follows: initially a 9 × 9 pixel integrating filter was applied across the image, pooling photon counts from each 81-pixel matrix in order to create a sufficiently large data set for an accurate determination of the average lifetime for both interacting and non-interacting components at each image pixel while sacrificing image resolution. The bi-exponential fit was applied to the integrated data set and average lifetimes then determined for the interacting and non-interacting populations. To restore image resolution while still

benefiting from the accuracy of large integrated data sets, the relative fractions of the two lifetime components (A_1 and A_2) were then evaluated on a pixel-by-pixel basis while fixing the two lifetime values (τ_1 and τ_2) determined for the associated 9×9 integrating filter. Normalization of the image data then enabled the relative concentration of FRET species (RCFS) within each pixel to be determined:

$$RCFS^{i,j} = \frac{I^{i,j} A_1{}^{i,j}}{I_{max}}$$

Where I is the time integrated photon count at pixel i,j (i.e. the total pixel intensity), A_1, the interacting fraction at pixel i,j (i.e. the proportion of all donor fluorophore within the pixel undergoing FRET), and I_{max} the time integrated photon count for the brightest pixel within the image (thus normalising each pixel value across the image). Thus a map illustrating the relative abundance of the interacting donor fluorophore population could be constructed for each image, revealing regions of Cdc42/N-WASP or N-WASP/Arp2/3 interaction. Both raw data lifetime maps and RCFS maps are presented in this study.

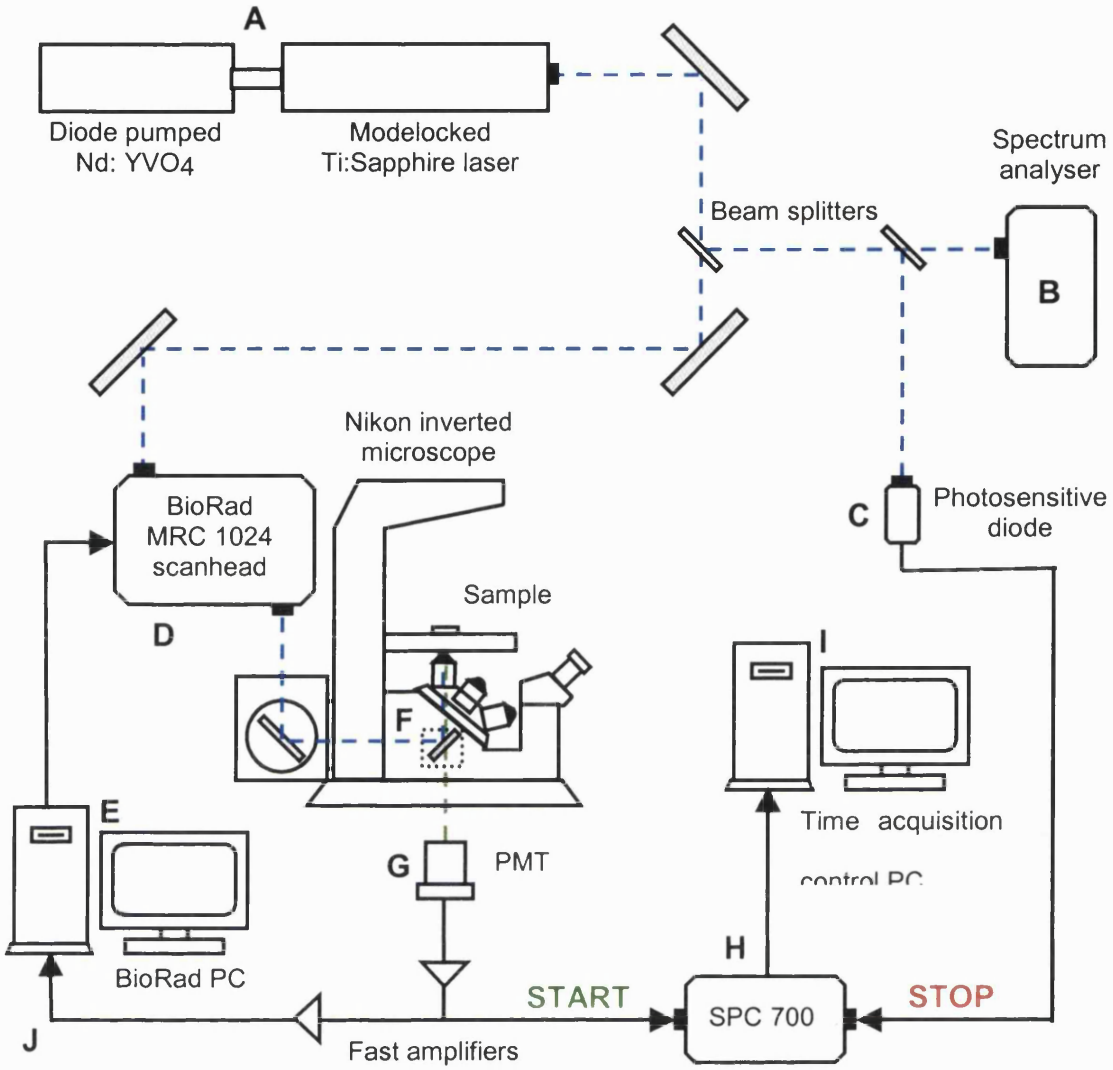

Figure 41. Schematic of the multiphoton TCSPC FLIM system setup

(A) The excitation source was provided by a high frequency 100 fs, 82 MHz modelocked Ti:sapphire pulse laser fed by a continuous wave YVO_4 laser. (B) The excitation light was directed via mirrors and beam splitters to a spectrum analyser (B), a photosensitive diode (C), and the BioRad MRC 1024 scanhead (D). The scanhead enables the scanned excitation of the sample and was under the control of a BioRad PC (E). A dichroic mirror enabled the separation of excitation and emission light following sample excitation (F) Fluorescence light was directed onto non-descanned detectors and a photomultiplier tube (G). Output signals from both the PMT and the photosensitive diode were passed to separate CFD inputs in the SPC 700 Becker & Hickl FLIM module (H). The picosecond accurate TAC within the module calculated the time delay between input signals from the PMT and photosensitive diode respectively. The SPC 700 module was controlled by a separate PC to that of the scanhead (I). Synchronized communication between the SPC 700 module and the scanhead enabled photon counts to be attributed to the correct region within the scanned image (J).

3.2.18 Frequency domain FLIM

Frequency domain FLIM was performed to monitor FRET in both live and fixed cell specimines. In live cell specimens frequency domain FLIM was used to monitor the activation dynamics of Cdc42 through its interaction with PAK1 in a manner analogous to that previously used for the analysis of Rac1 activation by others (Kraynov et al., 2000). In live cell experiments EGFP-Cdc42(wt) provided the donor while Myc-PAK1 targeted by Cy3-mAb subsequently microinjected into the cell cytoplasm provided the acceptor.

The Frequency Domain FLIM system: A purpose built frequency domain system was used to monitor FRET interactions in both live and fixed cell specimens. The system was constructed by Anthony Squire and Philippe Bastiaens, Department of Biophysics, Cancer Research UK. A comprehensive description of the system design and the mathematical algorithms required for the extraction of lifetimes from image data has been described previously (Squire and Bastiaens, 1999). However, the principle features of the system are described here.

The system centred around a Zeiss Axiovert TV 135 inverted microscope (Carl Zeiss) housed within a Perspex environmental chamber (built in-house) accurately maintained at 37 °C enabling experiments to be performed on live cells. The microscope, optics and laser rested on an optical isolation table (Melles Griot). The hi-frequency modulation of the excitation light was achieved using a conventional, continuous wave Argon/Krypton laser (Coherent Innova 70C Spectrum) in conjunction with a temperature controlled 80 MHz resonance acousto-optic modulator (AOM) (Intra-Action Corp.). When a voltage was passed across the AOM the internal crystal oscillated at a pre-defined frequency. When the excitation beam

passed through the oscillating crystal dispersions of the same frequency were generated in the emitted beam, which were subsequently manifested as intensity oscillations at the image plane, thus providing sinusoidally modulated excitation light. The AOMs generated excitation light of a constant oscillation frequency of 80.224 MHz and were regulated by two high-frequency synthesizers (Marconi, Cat: 2023) that provided a highly stable, phase-locked sinusoidal voltage source. A rotating ground glass disc placed in the optical path of the excitation beam was used to remove the coherence properties of the laser beam in order to remove problems associated with laser speckle at the sample. Donor EGFP excitation was achieved using the 488 nm line of the laser, and the resultant fluorescence collected by a high numerical aperture lens (Zeiss Plan Apo, NA 1.4, × 100 oil objective). The collected light was directed via a 505 long-pass dichroic mirror (Chroma) and a 514/10 nm band-pass emission filter (Lys & Optic) onto an image intensifier (Hamamatsu Cat: C5825) consisting of a photocathode, multichannel plate, and phosphor screen. Light from the phosphor screen was then projected directly onto a CCD camera (Photometrix Quantix) via a telescopic lens. The principle purpose of the image intensifier was to enhance the signal of the fluorescence emission: as fluorescent light hit the photocathode it generated an electron burst that was passed through the multichannel plate for electron amplification. The resulting cascade of electrons bombarded a phosphor screen, the light from which was projected onto the CCD camera. This process results in the rapid amplification of the fluorescence signal while sacrificing image resolution.

The sensitivity of the detector, also under the control of the high-frequency synthesizers, was modulated at the same frequency as the excitation light to enable homodyne phase sensitive

imaging. Modulation of the detector sensitivity was achieved by varying the voltage across the photocathode of the image intensifier. An adjustable mirror enabled the excitation light source to alternate between the laser and a 100 W mercury lamp (Zeiss) coupled to the epi-illumination port of the microscope. Use of the mercury lamp facilitated the location of fluorescent cells prior to imaging. A 565 nm long-pass dichromatic mirror and 610/75 nm long pass emission filter (Omega) also permitted Cy3 fluorescence images to be acquired in combination with the mercury lamp, enabling confirmation of the presence of acceptor in imaged specimens. Peripheral devices were under the control of a Macintosh 8600 PowerPC and image acquisition software (IPLab Spectrum, Signal Analytics Corp.). The system set-up is summarized in Figure 42, page 19.

Evaluation of fluorescence lifetimes: A series of 16 homodyne phase sensitive images were taken per lifetime measurement to enable an accurate reconstruction of the sinusoidal curve of fluorescence emission. The image acquisition software was also responsible for the on line processing of image data for the derivation of τ_φ and τ_m lifetimes. Briefly, data was processed as follows: a threshold mask was applied to each image in order to extract cell pixel values while discarding background noise. A Fourier series was applied to the data set in order to deconstruct the fluorescence emission into its individual sinusoidal components. Phase and modulation values could then be calculated from the comparison of excitation and emission curves. The τ_φ and τ_m lifetimes for each image pixel could then be derived from phase and modulation calculations via the following equations:

$$\tau_{\varphi} = \frac{1}{\omega} \tan(\varphi) \qquad \tau_m = \frac{1}{\omega} \times \sqrt{\frac{1}{m^2} - 1}$$

Where φ and m represent the phase and modulation depth respectively and ω represents the angular frequency of the modulation (i.e. $\omega = 2\pi \times$ modulation frequency).

The measurement of τ_{φ} and τ_m provided independent evaluations of the fluorescence lifetime at each image pixel. Lifetime data was displayed either as cell lifetime maps or by plotting all τ_{φ} pixel values against all corresponding τ_m values in order to generate scatter plots of cell lifetimes for each image. For lifetime maps each image pixel represented an average of the τ_{φ} and τ_m pixel values.

Cells imaged in the absence of acceptor were used to derive a single control lifetime for the donor fluorophore, τ_D, calculated as the mean lifetime of all image pixels within the cell. This control lifetime values was then fixed and used to calculate the efficiency of FRET in images of cells where both donor and acceptor fluorophores were present:

$$Efficiency = 1 - \frac{\tau_{DA}{}^{i,j}}{\tau_D}$$

Where τ_D is the fixed lifetime value for the donor fluorophore in the absence of acceptor and τ_{DA} the average fluorescence lifetime of the donor fluorophore in the presence of acceptor at image pixel i,j.

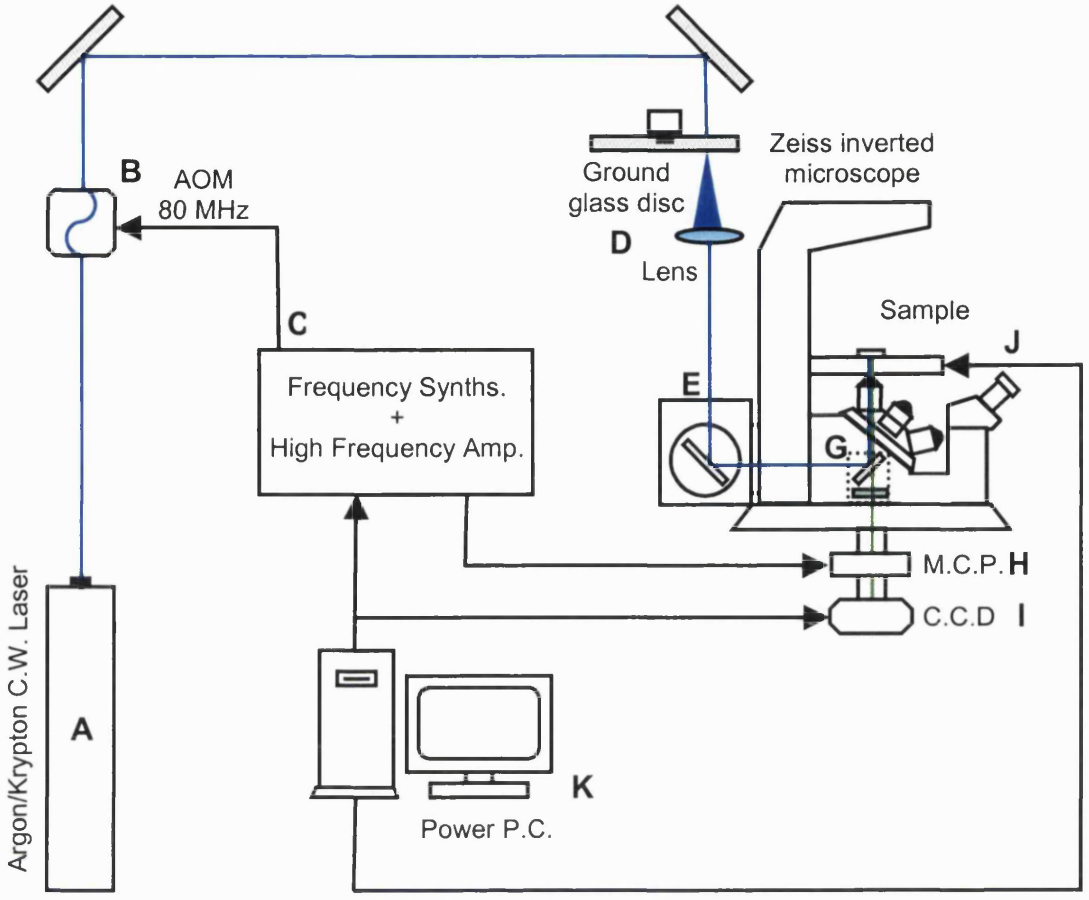

Figure 42. Schematic of the frequency domain FLIM system setup

(A) The excitation source was provided by the 488 nm emission line of an Argon/Krypton gas laser. (B) The excitation light was passed through an 80 MHz resonating AOM to generate a sinusoidally modulated excitation beam. (C) Two frequency synthesizers and a high voltage amplifier accurately controlled the frequency of modulation. The high coherent properties of the excitation light were removed by passing the beam through a rotating ground glass disk and reconverging the scattered light with a high NA lens. The excitation light was then launched into the epi-illumination port of the inverted microscope. (G) A dichroic mirror and emission filter separated the excitation and emission light following sample excitation. Fluorescence light was subsequently directed onto a multichannel plate (H), the gain of which was modulated enabling homodyne phase sensitive imaging using a CCD camera (I). An automated multi-position stage enabled the rapid high magnification imaging of multiple cells during a single experiment (J). Peripheral devices were controlled by a Macintosh PowerPC (k). This diagram is based on a simplified version of that previously published (Squire and Bastiaens, 1999).

3.3 RESULTS

In this study expression constructs encoding EGFP fusions of dominant negative Cdc42, Tc10, N-WASP, and PAK1 were introduced into cells using nuclear microinjection in order to investigate the role of their endogenous counterparts in the chemotaxis and motility of T15 rat sarcoma cells. Expression constructs encoding EGFP fusions of wild-type proteins were also used to determine whether effects seen with inhibitory proteins were the specific consequence of the dominant negative properties conferred by their mutations.

Much of our understanding of GTPase function has greatly profited from the identification, through mutational analysis, of functional variants that exhibit alterations in guanine nucleotide binding and hydrolysing efficiencies (Bishop and Hall, 2000). Single amino acid changes in the guanine nucleotide binding pocket of Cdc42, Tc10, and other GTPases have provided dominant negative and constitutively active mutant variants of these proteins that have been of great use in the study of GTPase related signalling. The introduction of the single amino acid change T17N in Cdc42 confers a dominant negative function by locking the protein in the GDP bound state. In this study this dominant negative variant, Cdc42(T17N) along with a similar Tc10 variant Tc10(T31N), were used to elucidate the role of the respective endogenous proteins in the chemotaxis of rat sarcoma cells. Truncated mutations of WASP family proteins that lack the VCA region within the carboxyl-terminus of the molecule have provided an effective means of disrupting WASP-mediated signalling to the cytoskeleton (Frischknecht et al., 1999). Deletion of the VCA region prevents the recruitment of the Arp2/3 complex following protein activation, thus preventing actin nucleation and subsequent filament assembly. The amino-terminus of the protein remains

intact and thus competes with endogenous protein for activation by upstream regulators. The N-WASP truncation mutant N-WASP(ΔVCA) was used in this study to disrupt the function of the endogenous protein. Mutations in PAK1 that render the kinase domain inactive and PAK1 fragments that consist of portions of the autoregulatory sequence have proved effective in inhibiting the kinase dependent signalling of this molecule (Kiosses et al., 1999; Zhao et al., 1998). In this study two alternative truncation mutants were used in order to inhibit endogenous PAK1 function. The first consisted of amino acids 83 - 149 of the autoregulatory sequence, the region of the protein responsible for masking the kinase domain when in the autoinhibited state. The second consisted of amino acids 1 – 149 and therefore contained both the autoinhibitory sequence and the remaining N-terminal portion of the protein, enabling additional membrane localization and GTPase binding.

Nuclear microinjection provided the main tool for introducing exogenous expression constructs into cells. Dunn chamber chemotaxis assays were performed to evaluate the directional response and motility of subconfluent cultures of serum starved T15 rat sarcoma cells expressing microinjected constructs. The addition of a mixture of PDGF-BB and IGF-1 to the outer well of the chemotaxis chamber provided the chemotactic signal. For each experiment a suitable field of cells situated directly in the diffusion gap of the chemotaxis chamber and containing both expressing and non-expressing cells was selected for low magnification (10 × or 20 ×) observation via digital time-lapse microscopy. Sequential phase contrast and EGFP fluorescence images were acquired at 5 min time-lapse intervals and cells were filmed for a duration of 16 hours. The interactive tracking of acquired film sequences was used to generate cell trajectories for the subsequent statistical analysis of cell behaviour.

The trajectories of fluorescent cells from each treatment group were compared to those of control cells expressing EGFP vector alone to assess the effects of the various expressed proteins on the chemotaxis, speed, and persistence of cell movement.

Please note that while the effects of different treatments are considered and discussed separately in this chapter, graphically they are often presented together for ease of comparison.

3.3.1 Characterisation of T15 sarcoma cells in stable gradients of PDGF-BB/IGF-1

A total of 75 chemotaxis experiments were conducted to assess the role of various polarity proteins in the chemotaxis and motility of T15 rat sarcoma cells. Non-expressing cells were included in the observation field of all recordings to provide an internal control for chemotaxis. The data acquired from non-expressing cell populations from all 75 chemotaxis experiments enabled a detailed analysis of the behavioural characteristics of the T15 rat sarcoma cell line in PDGF-BB/IGF-1 gradients. Subconfluent cultures of T15 sarcoma cells were previously shown to exhibit chemotaxis in mixed gradients of PDGF-BB (60 ng/ml) and IGF-1 (80 ng/ml) as assessed using the Dunn direct viewing chemotaxis chamber (Zicha et al., 1991). The analysis of cell trajectories generated from the interactive tracking of 1959 non-expressing cells from 75 chemotaxis experiments performed in this study reconfirmed this finding. T15 sarcoma cells exhibited a strong chemotactic response (Figure 43A, page 19) as confirmed by the significant unimodal clustering of cell directions towards the source of the chemoattractant (Rayleigh test, $p < 0.001$). The chemotactic response of cells was apparent over the entire course of experiments, and was maximal approximately 5 hours

following the commencement of filming (Figure 43B). Cell populations also revealed a distinctive speed profile over the course of experiments. Cell speed typically increased over the initial stages of the time-course, reaching a peak after approximately 5 hours, and then finally tailing off after a period of approximately 8 hours (Figure 43C). T15 sarcoma cells exhibited a mean speed of 14.3 μm/h in PDGF-BB/IGF-1 gradients.

Although a consistent tissue culture technique was adopted to achieve reproducible cell densities between chemotaxis experiments, some variation between cultures was unavoidable. Furthermore, local variations in cell density within a single culture were difficult to control. As a consequence, variations in cell number existed between the observation fields of different chemotaxis experiments. Density is known to influence the speed of motility of a number of different cell types (Abercrombie, 1970). It was therefore important to assess whether the range of cell densities observed was sufficiently large to significantly alter the behaviour of cell populations between experiments. This was of importance as cell speed was one of the aspects of cell behaviour that was under investigation. ANOVA revealed that no such significance existed (Figure 43D). Consequently the range of cell densities within which chemotaxis experiments were conducted was not in its self an influential factor on cell speed.

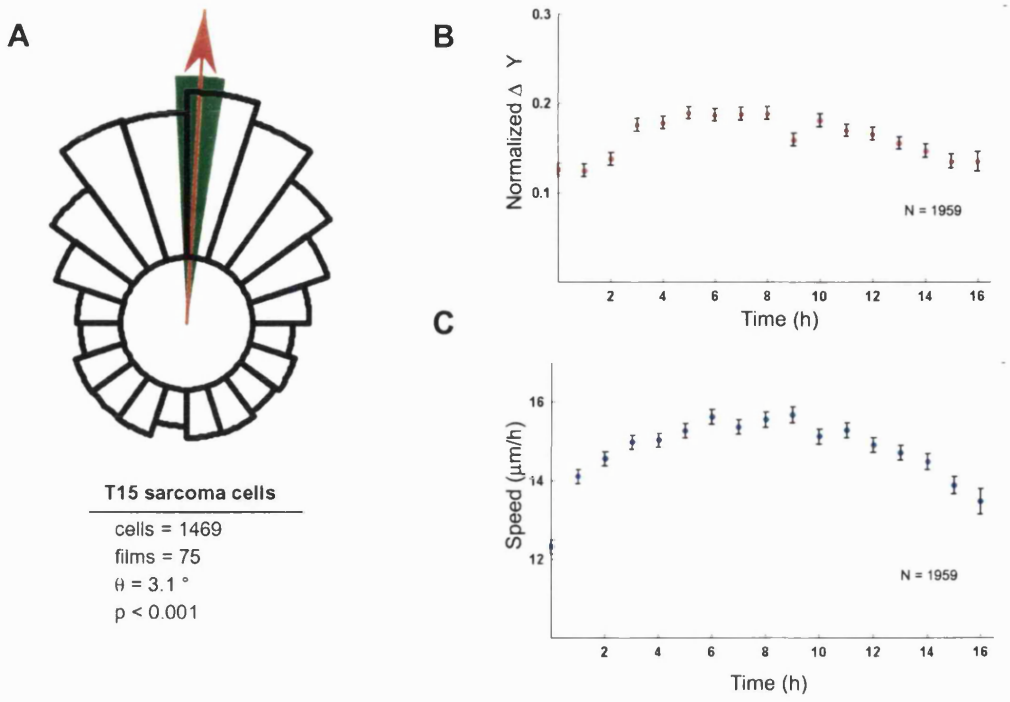

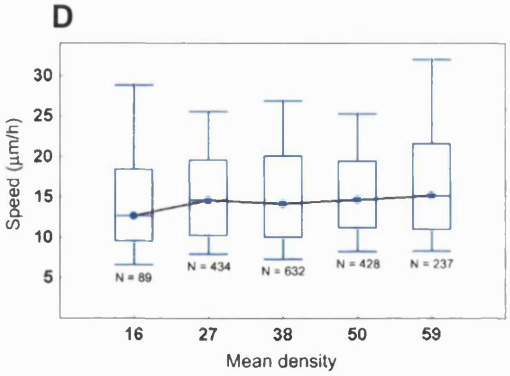

Figure 43. The chemotaxis and motility of sarcoma cells

Summary of the chemotaxis and motility of T15 sarcoma cells recorded in gradients of PDGF-BB (80 mg/ml) and IGF-1 (60 ng/ml) using the Dunn chemotaxis chamber. The data were derived from the analysis of non-fluorescent cell populations from a total of 75 chemotaxis experiments. (A) Circular histogram revealing the strong chemotactic response of the T15 sarcoma cells in PDGF-BB/IGF-1 gradients, as demonstrated by the highly significant unimodal clustering of cell directions toward the source of the chemotactic stimulus. (B) Graph illustrating the relative displacement of the cell population in the chemotactic gradient over the course of experiments. Relative displacement is calculated as ΔY/horizon (see methods 3.2.12, page 19) and is presented at hourly intervals. Positive values indicate the preferential migration of cells towards the source of the chemotactic stimulus. (C) Graph illustrating the speed profile of sarcoma cells over the course of the 16-hour filming period. (D) Box and whisker chart summarising the speed of cells from populations of increasing densities. The data set spans the full range of cell densities observed for all 75 chemotaxis experiments performed. Individual experiments were partitioned into groups of increasing cell density and assessed by ANOVA to determine whether significances existed between the cell speeds of the different density groups. No significance difference existed over the range of cell densities observed (n.s., ANOVA). Circles represent median values while boxes span 50 %, and whiskers span 80 % of the data within each group.

3.3.2 Effects of EGFP expression on sarcoma cell motility

The application of EGFP as a means of fluorescently labelling proteins for use in live cell imaging experiments requires that the toxicity of the fluorophore be assessed for the cell line in question. Deleterious effects on cell behaviour that result as a consequence of the over-expression and/or photo-toxicity of the protein may render the fluorophore unsuitable for a particular cell system.

T15 sarcoma cells expressing EGFP were assayed in the Dunn chemotaxis chamber to determine any possible effects that expression of the fluorophore alone may have on cell behaviour. The speed and directionality of 131 EGFP expressing cells from 10 independent chemotaxis experiments were analysed. The non-expressing cells within the same experimental group were used as a comparative control. Differences in speed and directionality between the expressing and non-expressing cell populations were assessed using ANOVA.

EGFP expression was not found to have a significant effect on either the speed or directionality of T15 sarcoma cells. Cells from both the expressing and non-expressing populations exhibited strong chemotactic responses in PDGF-BB/IGF-1 gradients (Figure 44 A & B, page 19). See also the representative filmstrip in Figure 45A, page 19. The fluorescent cells can clearly be seen to migrate towards the outer well of the chemotaxis chamber. No significant difference existed between the chemotactic response of the expressing and non-expressing cell populations as assessed by ANOVA.

It was hypothesized that any toxic effects associated with EGFP expression would most likely be manifested as an impairment of cell motility. However, EGFP expression did not have a noticeable effect on the speed of cell motility (see trajectory plots Figure 44 C & D). The ANOVA comparison of the speeds of non-expressing and expressing cells confirmed that EGFP expression did not confer a significant inhibitory effect on the speed of sarcoma cell motility Figure 44E. Observations of individual films also indicated that there was no obvious effect of EGFP expression on cell viability although this was not assessed statistically.

EGFP fusion provided a useful means of assaying the effects of various proteins on the long-term motile behaviour of T15 sarcoma cells in live cell imaging experiments. The fluorescent protein alone had no effect on cell directionality and speed and thus provided a useful base-line control when analysing the effects of other EGFP fusion proteins on these aspects of cell behaviour.

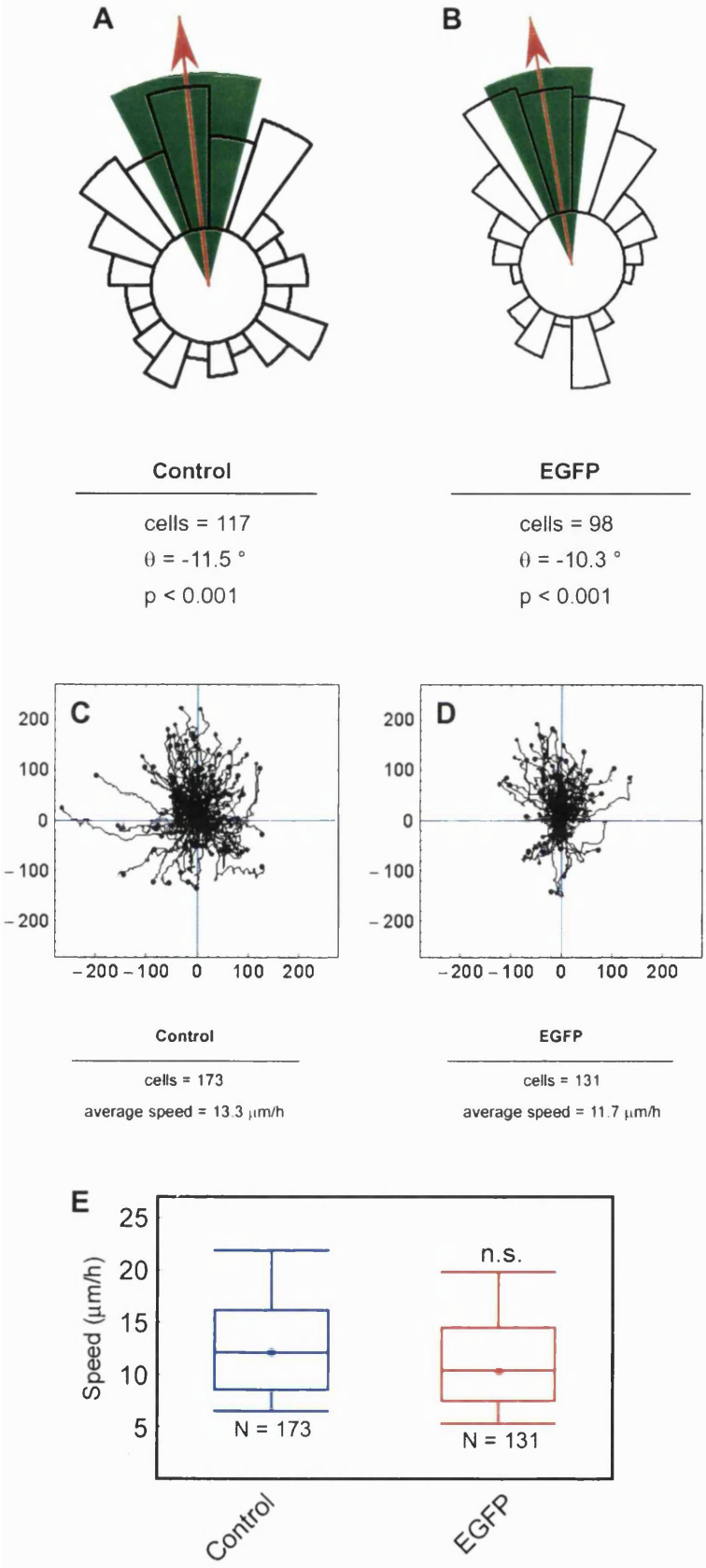

Figure 44. Effects of EGFP expression on sarcoma cell motility

Circular histograms, trajectory plots, and box and whisker charts demonstrating the effects of EGFP expression on the chemotaxis and motility of sarcoma cells. Figures summarise data obtained from the interactive tracking of cells from 10 independent chemotaxis experiments. (A & B) Circular histograms demonstrating the directional response of non-expressing and EGFP expressing cells respectively. Both control and EGFP expressing cells exhibited strong chemotactic responses in PDGF-BB/IGF-1 gradients. EGFP expression did not significantly alter the chemotaxis of cells (ANOVA, n.s.). (C & D) Trajectory plots for non-expressing and EGFP expressing cells respectively revealing the individual paths, shifted to a common origin, of cells over the course of chemotaxis experiments. The paths of both non-expressing and EGFP expressing cells tended towards the source of the gradient (top of plot) over the course of experiments. EGFP expression did not visibly suppress cell movement. Axes units are in microns. Filled circles denote the final position of cells. (E) Box and whisker plots summarising the mean speeds of non-expressing (control) and EGFP expressing sarcoma cells over the course of chemotaxis experiments. EGFP expression did not significantly impair cell speed (ANOVA, n.s.). Circles represent median values while boxes span 50 %, and whiskers span 80 % of the data within each group.

3.3.3 Cdc42 and Tc10 are implicated in the motility but not the chemotaxis of T15 rat sarcoma cells

Cdc42 function has previously been shown to be essential for the chemotaxis of certain cells of the mammalian immune system including macrophages and T lymphocytes (Allen et al., 1998; Haddad et al., 2001). It was therefore hypothesized that this protein would be of similar importance in the chemotaxis of the T15 rat sarcoma cell line. To determine the role of Cdc42 in the chemotaxis of T15 rat sarcoma cells an EGFP fusion of the dominant negative variant Cdc42(T17N) was microinjected into cells and cell behaviour subsequently assessed using the Dunn chemotaxis chamber. Figure 45B, page 19 is an image sequence from a representative film demonstrating the directional response of EGFP-Cdc42(T17N) expressing cells recorded in the chamber. The analysis of 57 cells from 7 independent cultures revealed that EGFP-Cdc42(T17N) had no significant effect on the chemotaxis of T15 sarcoma cells, with cells exhibiting a strong directional response in gradients of PDGF-BB/IGF-1 (Figure 47B, page 19). No significant difference existed between the chemotactic response of EGFP-Cdc42(T17N) expressing cell and control cells expressing EGFP alone as confirmed by ANOVA (Table 4, page 19). Expression of wild-type protein also had no effect on chemotaxis (Figure 48B, page 19). EGFP-Cdc42(wt) expressing cells could clearly be seen to migrate towards outer well of the chemotaxis chamber (see representative film sequence Figure 46B, page 19) and no significant difference existed between the directional response of these cells and controls (Table 4). In all cases the non-expressing cell populations provided inbuilt controls for chemotaxis, confirming that effective chemotactic gradients had established during individual experiments, see Figure 49, page 19 (dominant negative experiments) and Figure 50, page 19 (wild-type experiments).

The expression of dominant negative Cdc42 did, however, affect the speed of T15 rat sarcoma cell motility. EGFP-Cdc42(T17N) expressing cells were capable of detecting and translocating towards the source of the chemotactic gradient but they did so more slowly than the surrounding, non-expressing cells (this is clear from the image sequence in Figure 45B). Cells exhibited a 25 % reduction in speed when compared to EGFP control cells. Trajectory plots illustrating the individual paths taken by cells during the course of experiments demonstrate effectively the suppressive effects that Cdc42 inhibition had on the speed of cell motility (Figure 51B, page 19). Plots reveal that the paths of EGFP-Cdc42(T17N) expressing cells were visibly suppressed compared to those of EGFP control cells (Figure 51, compare B with A). The significance of the speed reduction was confirmed by ANOVA ($p < 0.01$) (Figure 53A, page 19 & Table 5, page 19). Expression of the wild-type protein had no significant effect on cell speed (Figure 53B & Table 5), confirming that the reduction in speed was specific to the dominant negative mutation and not a consequence of toxicity associated with an increased presence of Cdc42 protein *per se*. Note how the trajectories of EGFP-Cdc42(wt) expressing cells were similar to those of control cells expressing EGFP alone (Figure 52, compare B with A. See also example film sequence, Figure 46B & A).

As Cdc42 was not required for the chemotaxis of T15 rat sarcoma cells it was possible that the closely related GTPase Tc10 was of more importance in regulating chemotactic behaviour in this particular cell line. Tc10 shares many down-stream signalling target with Cdc42 and has been shown to induce long filopodia-like formations when over-expressed in

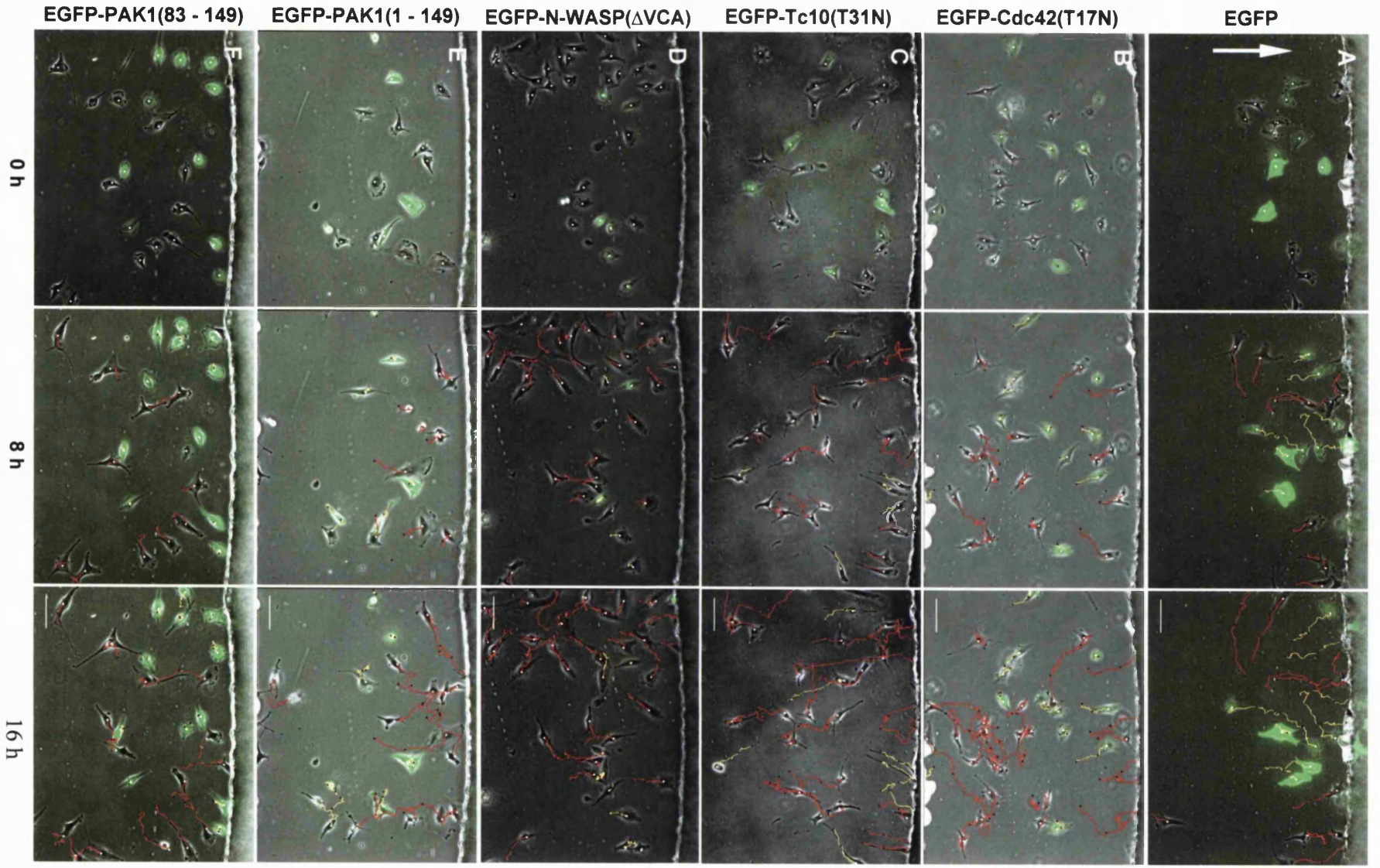

Figure 45. *Figure legend overleaf.*

Figure 45. (previous page) Film sequences of migrating sarcoma cells expressing inhibitory constructs

Image sequences from chemotaxis experiments demonstrating the behaviour of T15 sarcoma cells in gradients of PDGF-BB (80 ng/ml)/IGF-1(60 ng/ml) following microinjection and expression of various inhibitory constructs fused to EGFP. Each image sequence is derived from a representative film for a given treatment group and represent 0, 8 and 16-hour time points. Images are composites of overlaid phase contrast and EGFP fluorescence channels allowing the simultaneous observation of both expressing and non-expressing cells. Cells were microinjected with expression constructs encoding either EGFP control (A), EGFP-Cdc42(T17N) (B), EGFP-Tc10(T31N) (C), EGFP-N-WASP(ΔVCA) (D), EGFP-PAK1(1 – 149) (E), or EGFP-PAK1(83 – 149) (F). Yellow trajectories illustrate the individual paths of cells expressing fluorescent proteins, while red trajectories represent those of the non-expressing cells. White filled circles illustrate the current position of each cell for the image shown. In all experiments the camera was rotated so that the outer well was positioned at the top of each image. Consequently the direction of increasing growth factor concentration runs from the bottom to the top of each image, as represented by the white arrow in the first image of the first sequence. Scale bar = 100 μm.

Figure 46. (overleaf) Film sequences of migrating sarcoma cells expressing wild type constructs

Image sequences from chemotaxis experiments demonstrating the behaviour of T15 sarcoma cells in gradients of PDGF-BB (80 ng/ml)/IGF-1 (60 ng/ml) following microinjection and expression of various wild-type constructs fused to EGFP. Cells were microinjected with expression constructs encoding either EGFP control (A), EGFP-Cdc42(wt) (B), EGFP-Tc10(wt) (C), EGFP-N-WASP(wt) (D), or EGFP-PAK1(wt) (E). Time intervals, image compositions, orientation of the chemotactic gradient, and scales are the same as for Figure 45.

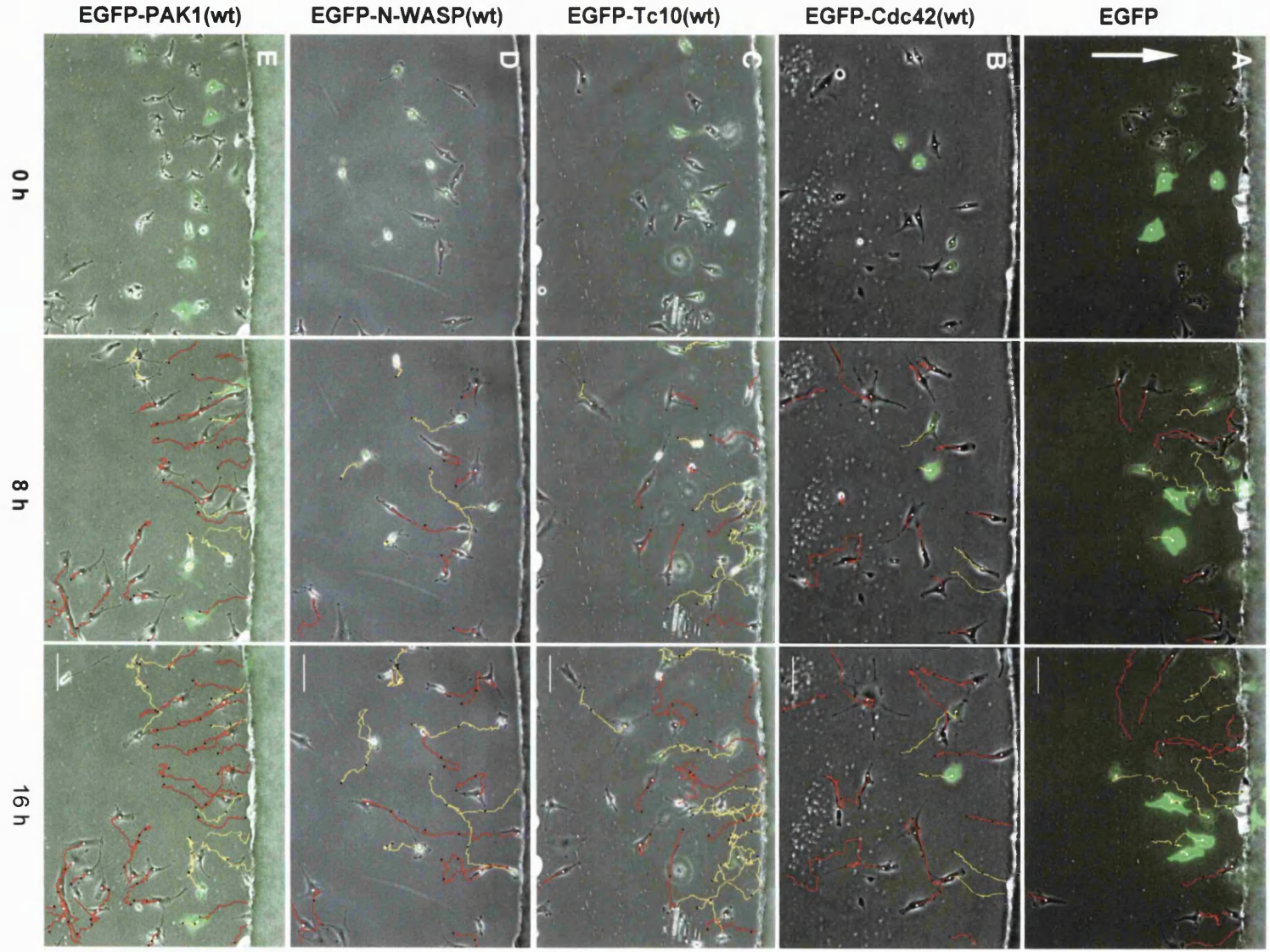

Figure 46. *Figure legend on preceding page.*

fibroblast cell lines, a phenotype often associated with Cdc42 expression (Neudauer et al., 1998). Furthermore, Tc10 has been implicated in control of axonal outgrowth in neurons (Abe et al., 2003), and is therefore an important regulator of cell polarity in other mammalian systems.

Expression of an EGFP fusion of the dominant negative Tc10 variant, Tc10(T31N), had no effect on the chemotaxis of T15 sarcoma cells. The analysis of 35 cells from 5 independent cultures revealed that EGFP-Tc10(T31N) expressing cells could exhibit a strong chemotactic response in PDGF-BB/IGF-1 gradients (see representative film sequence in Figure 45C, page 19). A significant chemotactic response was confirmed for cells expressing both dominant negative and wild-type proteins (Figure 47C, page 19 & Figure 48C page 19 respectively). EGFP-Tc10(T31N) expression did, however, impair cell speed (Figure 53A, page 19). Interestingly the degree of speed inhibition was comparable to that associated with the inhibition of Cdc42 (25 % reduction). Again, the reduction in speed was specific to the dominant negative variant of the protein and was significant compared to the speed of control cells (Table 5, page 19). As with cells expressing EGFP-Cdc42(T17N), the trajectories of EGFP-Tc10(T31N) expressing cells appeared suppressed compared to those of control cells (Figure 51 compare C & A, page 19). Interestingly, the expression of EGFP-Tc10(wt) significantly enhanced the speed of cell motility (Figure 53B & Table 5). Endogenous Tc10 expression levels may therefore present a limiting factor in the speed of T15 rat sarcoma cell motility.

3.3.4 N-WASP is implicated in the motility but not chemotaxis of T15 rat sarcoma cells

The WASP-family proteins represent key regulators of actin dynamics, providing mechanisms for the control of *de novo* actin polymerisation through their interaction with the Arp2/3 complex (Takenawa and Miki, 2001). Hematopoeitic WASP is an essential requirement of macrophage and T lymphocyte chemotaxis (Haddad et al., 2001; Zicha et al., 1998), while N-WASP is essential for axonal outgrowth in hippocampal neurons (Banzai et al., 2000). N-WASP presents a target for upstream regulation by both Cdc42 and Tc10, and induces morphological structures commonly associated with the activation of these regulators (Miki et al., 1998; Neudauer et al., 1998). N-WASP is therefore likely to play a significant role in the latter stages of GTPase-mediated receptor signalling to the cytoskeleton.

Although dominant negative constructs of Cdc42 and Tc10 were unable to abolish the chemotaxis of T15 rat sarcoma cells this may have reflected a degree of functional redundancy between the two proteins. It is conceivable that either could adopt the role of the other in transducing signals to the cytoskeleton through interactions with their mutual targets including N-WASP and PAK1. If N-WASP represented a point of convergence in Cdc42 and Tc10 signalling pathways it was important to examine whether this protein was implicated in the regulation of chemotaxis in sarcoma cells.

In order to assess the role of N-WASP in the chemotaxis of T15 sarcoma cells expression constructs encoding an EGFP fusion of either the wild-type protein or the dominant negative truncation mutant, N-WASP(ΔVCA), were microinjected into cells and cell behaviour subsequently assessed in the Dunn chemotaxis chamber. Expression of EGFP-N-WASP(ΔVCA) did not abolish the chemotaxis of T15 rat sarcoma cells. The

analysis of 29 cells from 7 independent cultures revealed that EGFP-N-WASP(ΔVCA) expressing cells could exhibit chemotaxis in PDGF-BB/IGF-1 gradients (Figure 47D, page 19). No significant difference existed between the chemotactic response of these cells and control cell expressing EGFP alone (Table 4, page 19). Expression of the dominant negative protein did, however, significantly impair motility resulting in an approximate 40 % reduction in cell speed when compared to controls (Figure 53A, page 19 & Table 5, page 19). The poor motility of these cells is particularly apparent in the example film sequence shown in Figure 45D, page 19.

Although no discernible effects on cell morphology resulted from expression of the dominant negative N-WASP truncation mutant, expression of the wild-type protein resulted in cell rounding and the extension of long spindle-like lamellipodia (see example film sequence Figure 46D). These morphological changes were associated with enhanced motile behaviour and cells exhibited significantly higher speeds than controls (Figure 53B & Table 5). This is particularly apparent from the EGFP-N-WASP(wt) trajectory plot, which reveals the extended cell paths of individual highly motile cells (Figure 52D, page 19, compare with EGFP control Figure 52A). It is therefore possible that endogenous levels of N-WASP protein may present a limiting factor in the determination of cell speed, as has been suggested for Tc10. Although expression of EGFP-N-WASP(wt) had profound effects on cell morphology and motility, the chemotactic responses of these cells were unaffected (Figure 48D, page 19). Therefore N-WASP expression constructs induced changes in cell behaviour that were not dissimilar to those of its upstream regulator Tc10.

3.3.5 PAK1 is essential for both the chemotaxis and efficient motility of T15 rat sarcoma cells

PAK1 is a known regulator of cell morphology and polarity in a number of eukaryotic cells systems, coordinating changes through its influence on the actin cytoskeleton. Studies conducted using the Boyden chamber have identified PAK1 kinase activity as important for both the efficient haptotaxis of fibroblasts on immobilized collagen gradients, and the chemokine-driven chemotaxis of HEK cells (Sells et al., 1999; Wang et al., 2002). PAK1 therefore provides an obvious candidate for study in the chemotaxis of the T15 rat sarcoma cell line.

Two truncation mutants were generated in order to disrupt PAK1 signalling within cells: the EGFP-PAK1(83 – 149) fragment which consisted of the kinase domain-binding portion of the autoregulatory sequence, and the EGFP-PAK1(1 – 149) fragment which consisted of the kinase domain-binding fragment and the amino terminal region required for membrane targeting and GTPase binding. Expression of these truncation mutants had a profound effect on both the directionality and speed of cell migration. EGFP-PAK1(1 – 149) greatly impaired the chemotactic response of cells as demonstrated by the loss of significance in the unimodal clustering of cell directions toward the gradient source (Figure 47E, page 19). A significant difference existed between the directional responses of EGFP-PAK1(1 – 149) expressing cells and control cells expressing EGFP alone, confirming that chemotaxis had been abolished (Table 4, page 19). The example film sequence in Figure 45E clearly demonstrates the reduced tendency for these cells to move toward the outer well of the chemotaxis chamber.

Expression of PAK1(83 – 149) also seemed to abolish the chemotactic response of T15 sarcoma cells (Figure 47F). However, a significant difference between the chemotactic responses of EGFP-PAK1(83 – 149) expressing cells and controls was not detectable by ANOVA (Table 4). It is therefore possible that the effects of the 83 – 149 truncation mutant on cell directionality were not as severe as those of the membrane targeted fragment. Note that the non-expressing cells from both the EGFP-PAK1(1 - 149) and EGFP-PAK1(83 - 149) treatment groups exhibited strong chemotactic responses during experiments (Figure 49 E & F, page 19), demonstrating that loss of chemotaxis observed in the fluorescent cell population was a specific consequence of the expressed proteins.

The effect of EGFP-PAK1(83 – 149) expression on cell motility was profound leading to a 40 % reduction in cell speed (Figure 53A, page 19, Table 5 & page 19). Protein expression also had a profound effect on cell morphology, resulting in cell spreading and a loss of polarity. Note the relatively spread and symmetrical morphology of fluorescent cells in the example film sequence in Figure 45F. Note also the poor translocation of these cells over the course of the time-lapse recording. The comparison of the trajectories of cells expressing EGFP-PAK1(83 - 149) with those of cells expressing EGFP alone demonstrates effectively the profound inhibitory effect that this PAK1 mutant had on the speed of cell motility (compare Figure 51F with Figure 51A, page 19).

Expression of EGFP-PAK1(1 - 149) was also found to significantly impair the speed of cell motility (Figure 53A), but to a lesser degree than the 83 – 149 truncation mutant (~30 % reduction). Loss of cell polarity was also often associated with expression of the 1 - 149

mutant although, interestingly, this seemed to result from cell contraction and rounding rather than spreading. In many cases cell contraction was only transient and subsequent re-spreading could be observed after a number of hours.

The intensity of EGFP-PAK1(wt) expression often diminishes over the course of chemotaxis experiments (see intensity analysis, section 3.3.7, page 19), suggesting a down regulation in protein expression. It was therefore more difficult to discern the effects of the wild-type protein on cell behaviour. Notwithstanding, the analysis of cells expressing the wild-type protein did not reveal any significant change in the chemotactic response or the speed of motility (Figure 48E, page 19 & Figure 53B).

PAK1 signalling was, therefore, essential for the efficient PDGF-BB/IGF-1 driven chemotaxis of T15 rat sarcoma cells. Although a known target of both Cdc42 and Tc10, the activities of these proteins were not essential for PAK1 mediated chemotaxis. Furthermore, although Cdc42, Tc10, and N-WASP all contributed to the motile response of T15 rat sarcoma cells PAK1 was the greatest single contributor to cell motility. PAK1 is therefore a essential polarity and motility protein in rat sarcoma cells.

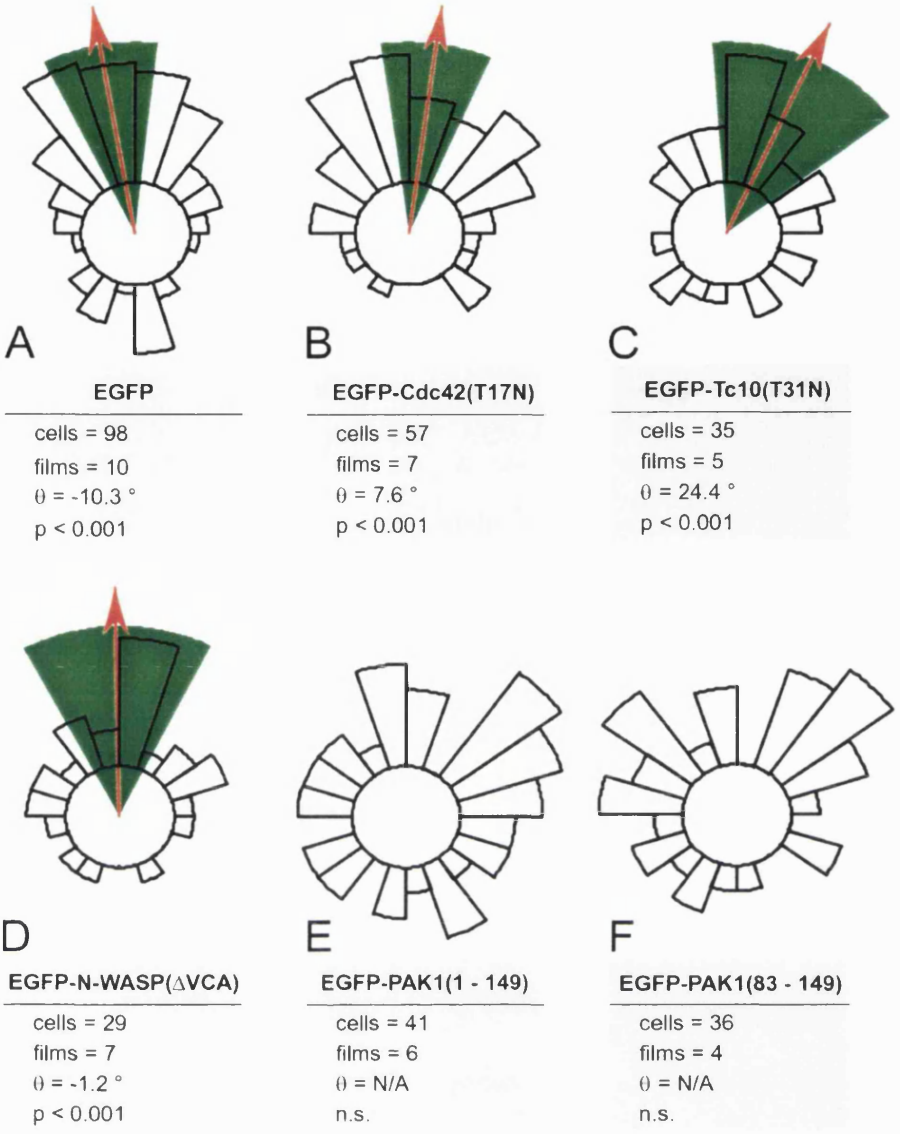

Figure 47. Effects of dominant negative treatments on the directionality of sarcoma cells

Circular histograms demonstrating the chemotactic responses of T15 rat sarcoma cells from EGFP control and dominant-negative treatment groups towards a combination of PDGF-BB (60 ng/ml) and IGF-1 (80 ng/ml). Cells expressing either EGFP control (A) or EGFP fusions of dominant-negative Cdc42 (B), Tc10 (C), or N-WASP (D) all exhibited strong chemotaxis. However, chemotaxis was abolished in cells expressing EGFP fusions of PAK1 truncation mutants (E & F). PAK1 was, therefore, necessary for the efficient chemotaxis of these cells. Cells were considered to have exhibited a chemotactic response upon detection of a significant unimodal clustering of cell directions oriented towards the source of the chemotactic stimulus (North with respect to each histogram). Significances were determined using the Rayleigh test for the statistical analysis of circular data sets (p values shown). When significant clustering is observed the mean cell direction (θ) is indicated by an arrow. A mean cell direction of 0° is directed exactly at the source of the gradient. Data for each treatment group are pooled from a number of films as indicated.

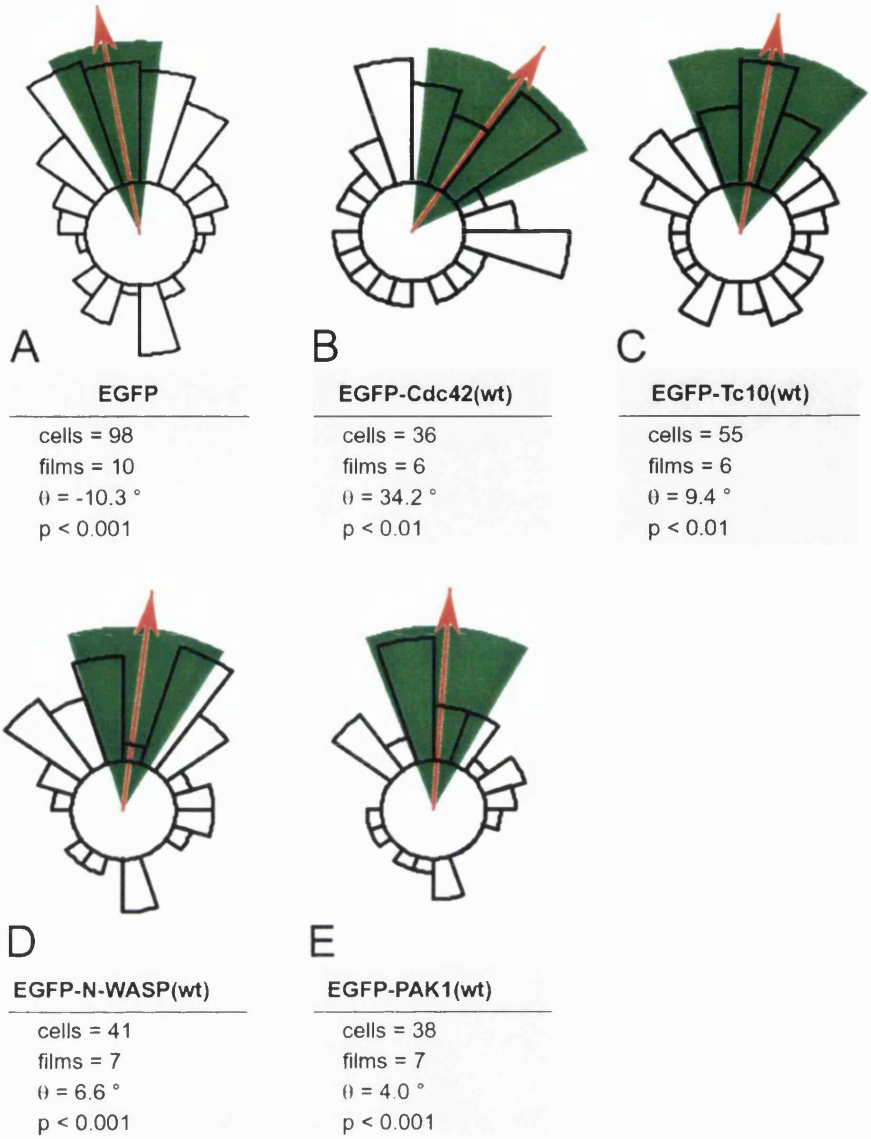

Figure 48. Effects of wild-type treatments on the directionality of sarcoma cells

Circular histograms demonstrating the chemotactic responses of T15 rat sarcoma cells from EGFP control and wild-type treatment groups toward a combination of PDGF-BB (60 ng/ml) and IGF-1 (80 ng/ml). Cells expressing either EGFP control (A) or EGFP fusions of wild-type Cdc42 (B), Tc10 (C), N-WASP (D), and PAK1 (E) all exhibited strong chemotactic responses as determined by the significant unimodal clustering of cell directions towards the source of the chemotactic stimulus. Data for each treatment group is pooled from a number of films. An explanation of the circular histogram is provided in Figure 47.

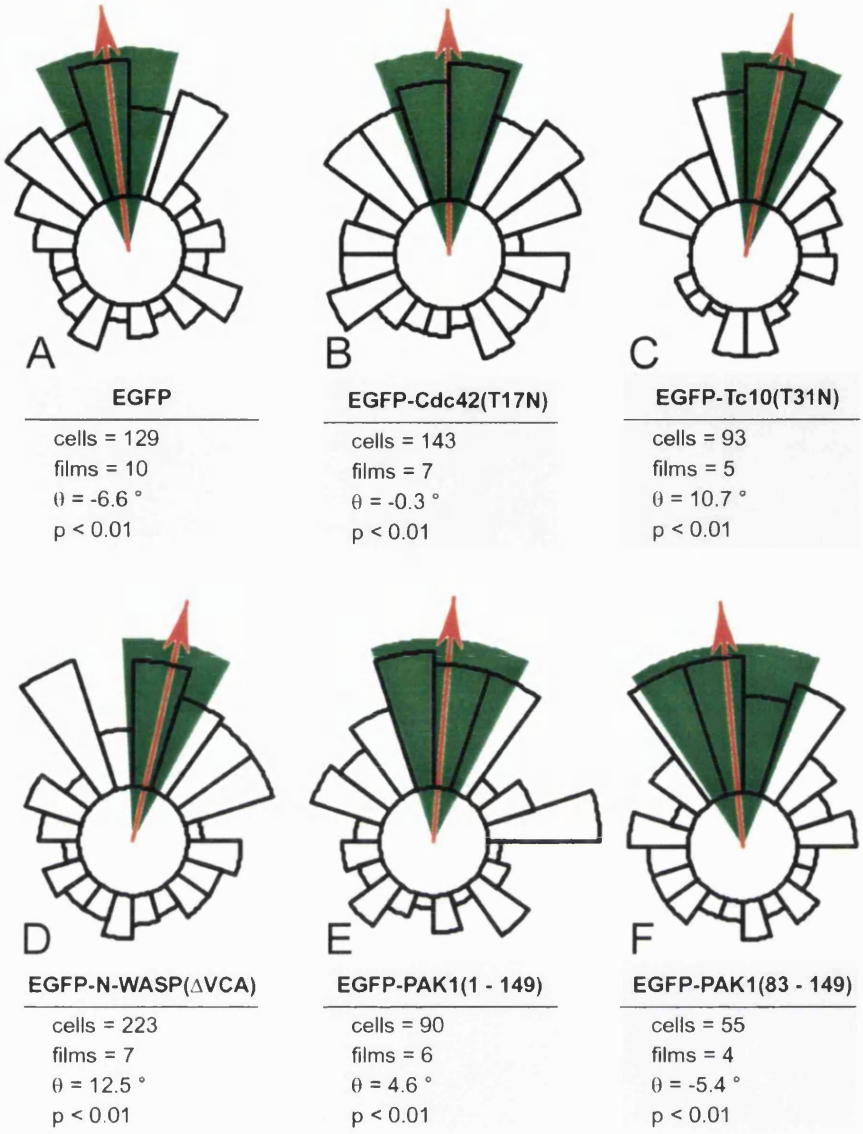

Figure 49. The chemotactic responses of non-expressing cells from dominant negative treatment groups

Circular histograms demonstrating the chemotactic responses of non-expressing T15 rat sarcoma cells from EGFP control and dominant-negative treatment groups. The non-expressing cell populations within all treatment groups provided a control for chemotaxis. Individual circular histograms represent non-expressing cells from EGFP control (A), EGFP-Cdc42(T17N) (B), EGFP-Tc10(T31N) (C), EGFP-N-WASP(ΔVCA) (D), EGFP-PAK1(1 - 149) (E), and EGFP-PAK1 (83 – 149) (F) treatment groups. Cells exhibited strong chemotactic responses in all cases as determined by the significant unimodal clustering of cell directions towards the source of the chemotactic stimulus. Therefore effective chemotactic gradients established during experiments. Data for each treatment group is pooled from a number of films. An explanation of the circular histogram is provided in Figure 47.

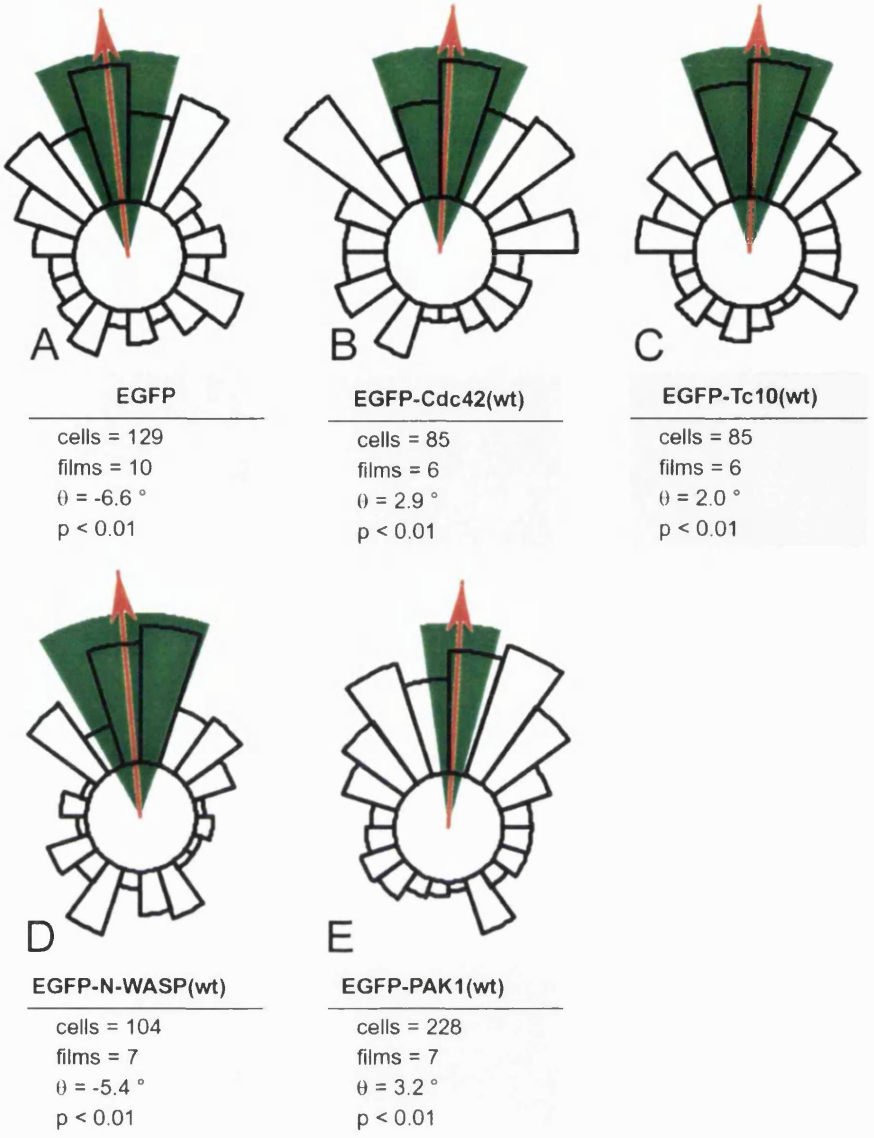

Figure 50. The chemotactic responses of non-expressing cells from wild type treatment groups

Circular histograms demonstrating the chemotactic responses of non-expressing T15 rat sarcoma cells from EGFP control and wild-type treatment groups. Individual circular histograms represent non-expressing cells from EGFP control (A), EGFP-Cdc42(wt) (B), EGFP-Tc10(wt) (C), EGFP-N-WASP(wt) (D), and EGFP-PAK1(wt) (E) treatment groups. Cells from all treatment groups exhibited strong chemotactic responses as determined by the significant unimodal clustering of cell directions towards the source of the chemotactic stimulus. Therefore effective chemotactic gradients established during experiments. Data for each treatment group is pooled from a number of films. An explanation of the circular histogram is provided in Figure 47.

Summary of normalised cell displacement in the gradient

Treatment	Number of films	Number of cells	Mean normalised displacement	Standard Error	Sig. (ANOVA)
EGFP-Cdc42(wt)	6	33	0.41	0.14	**n.s.**
EGFP-Cdc42(T17N)	7	54	0.56	0.05	**n.s.**
EGFP-Tc10 (wt)	6	51	0.36	0.14	**n.s.**
EGFP-Tc10 (T31N)	5	33	0.44	0.17	**n.s.**
EGFP-N-WASP(wt)	7	36	0.37	0.12	**n.s.**
EGFP-N-WASP(ΔVCA)	7	26	0.47	0.10	**n.s.**
EGFP-PAK1(wt)	7	35	0.45	0.16	**n.s.**
EGFP-PAK1(1-149)	6	37	0.17	0.07	**
EGFP-PAK1(83-149)	4	35	0.34	0.09	**n.s.**
EGFP	10	91	0.56	0.07	**n.s.**
	65	**431**			

Table 4. Numerical summary of the chemotactic responses of sarcoma cells

Summary of effects of the expression of various EGFP-fusion proteins on the chemotaxis of sarcoma cells. In order to apply ANOVA to experimental data chemotaxis was also measured as the normalised displacement of cells relative to the direction of the chemotactic gradient, ΔY/horizon (see methods 3.2.12, page 19). The mean normalised displacement represents the mean of all normalised displacement values derived for all cells within a specific treatment group. A mean normalised displacement value of 1 would reflect the migration of a cell population exactly towards the source of the chemotactic stimulus for the full duration observed, while negative values would reflect the tendency of cells to migrate away from the chemotactic stimulus. A value of 0 would reflect the absolute indifference of the cell population to the presence of a chemotactic stimulus. The EGFP expressing control cell population exhibited a mean normalised displacement value of 0.56, indicating that approximately 50 % of cell movement was directed towards the source of the chemotactic gradient (i.e. towards the outer well of the chemotaxis chamber). Only the EGFP-PAK1 (1 – 149) inhibitory construct had a significant effect ($p < 0.01$ ANOVA) on the chemotaxis of T15 sarcoma cells when compared to the EGFP control group.

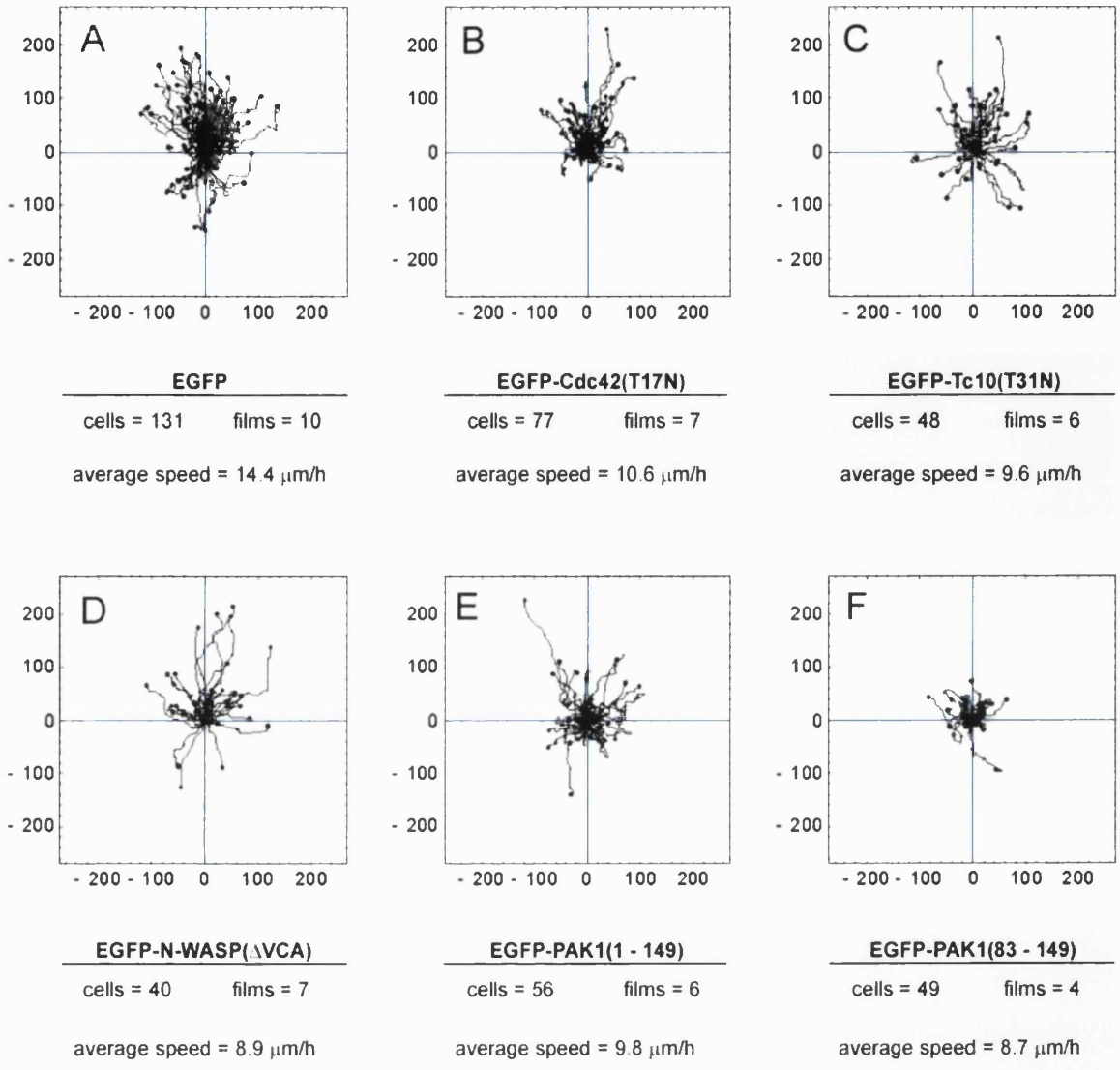

Figure 51. Trajectories of sarcoma cells expressing dominant negative constructs

Cell trajectory plots illustrating the individual paths of T15 rat sarcoma cells over the course of chemotaxis experiments. Trajectories are shifted to a common origin and represent the paths of cell expressing either EGFP control (A), EGFP-Cdc42(T17N) (B), EGFP-Tc10(T31N) (C), N-WASP(ΔVCA) (D), EGFP-PAK1(1 – 149) (E), or EGFP-PAK1 (83 – 149) (F). Trajectories appear suppressed where treatments impaired cell speed. This is most apparent for EGFP-Cdc42(T17N), EGFP-PAK1(1 - 149), and EGFP-PAK1(83 - 149) treatment groups where reductions in speed were highly significant. The source of the gradient is positioned at the top of each plot. Axes units are in microns. Trajectories for each treatment group are pooled from a number of films.

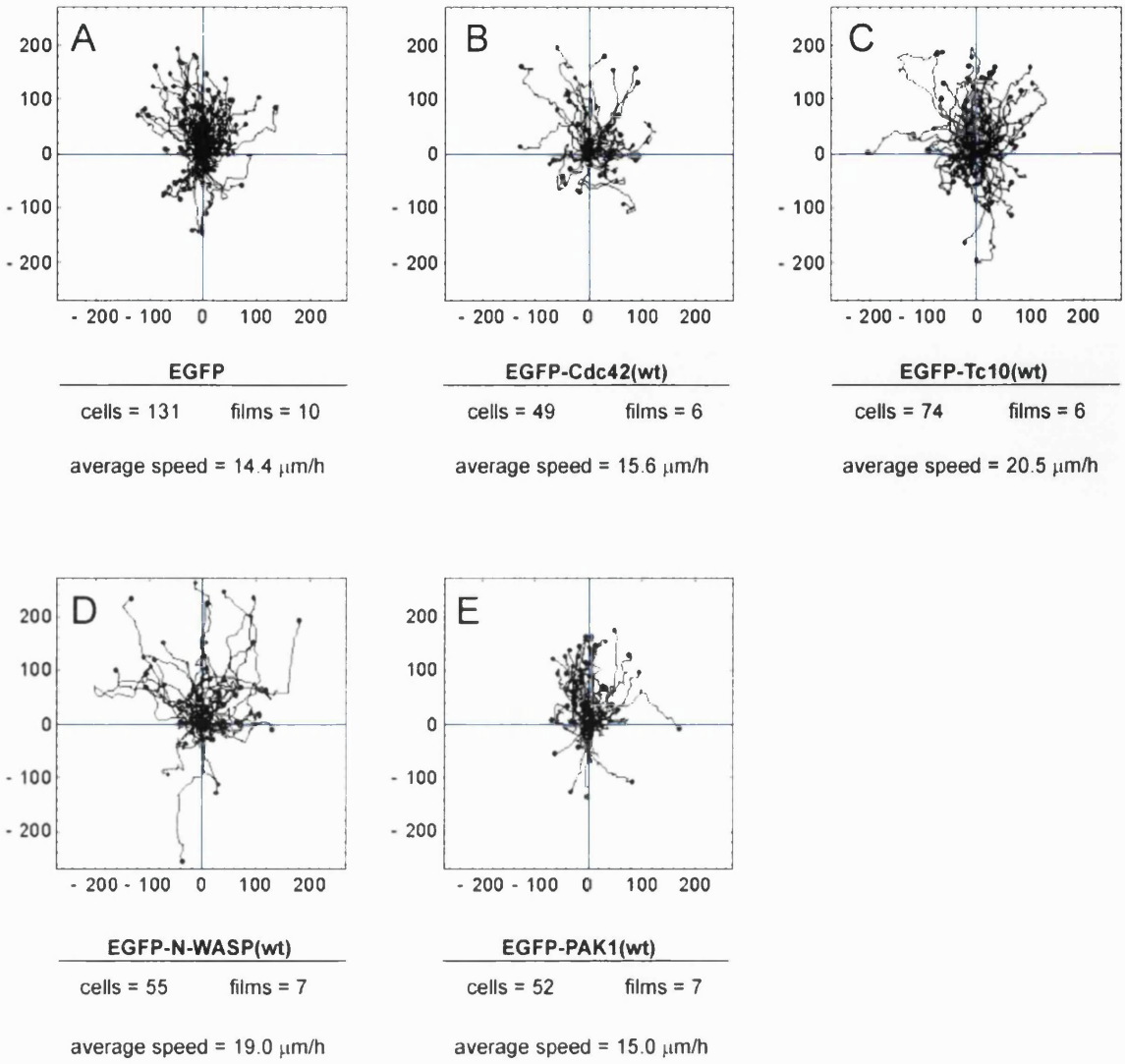

Figure 52. Trajectories of sarcoma cells expressing wild type constructs

Cell trajectory plots illustrating the individual paths of T15 rat sarcoma cells over the course of chemotaxis experiments. Individual plots represent cells expressing EGFP control (A), EGFP-Cdc42(wt) (B), EGFP-Tc10(wt) (C), EGFP-N-WASP(wt) (D), and EGFP-PAK1(wt) (E). Unlike the dominant negative constructs, expression of wild-type constructs had no deleterious effect on the speed of cell motility. Tc10 and N-WASP expression significantly enhanced the speed of cell motility (C & D). This is particularly apparent from the elongated paths of cells from the EGFP-N-WASP(wt) treatment group (D). The source of the gradient is positioned at the top of each plot and axes units are in microns. Trajectories for each treatment group are pooled from a number of films.

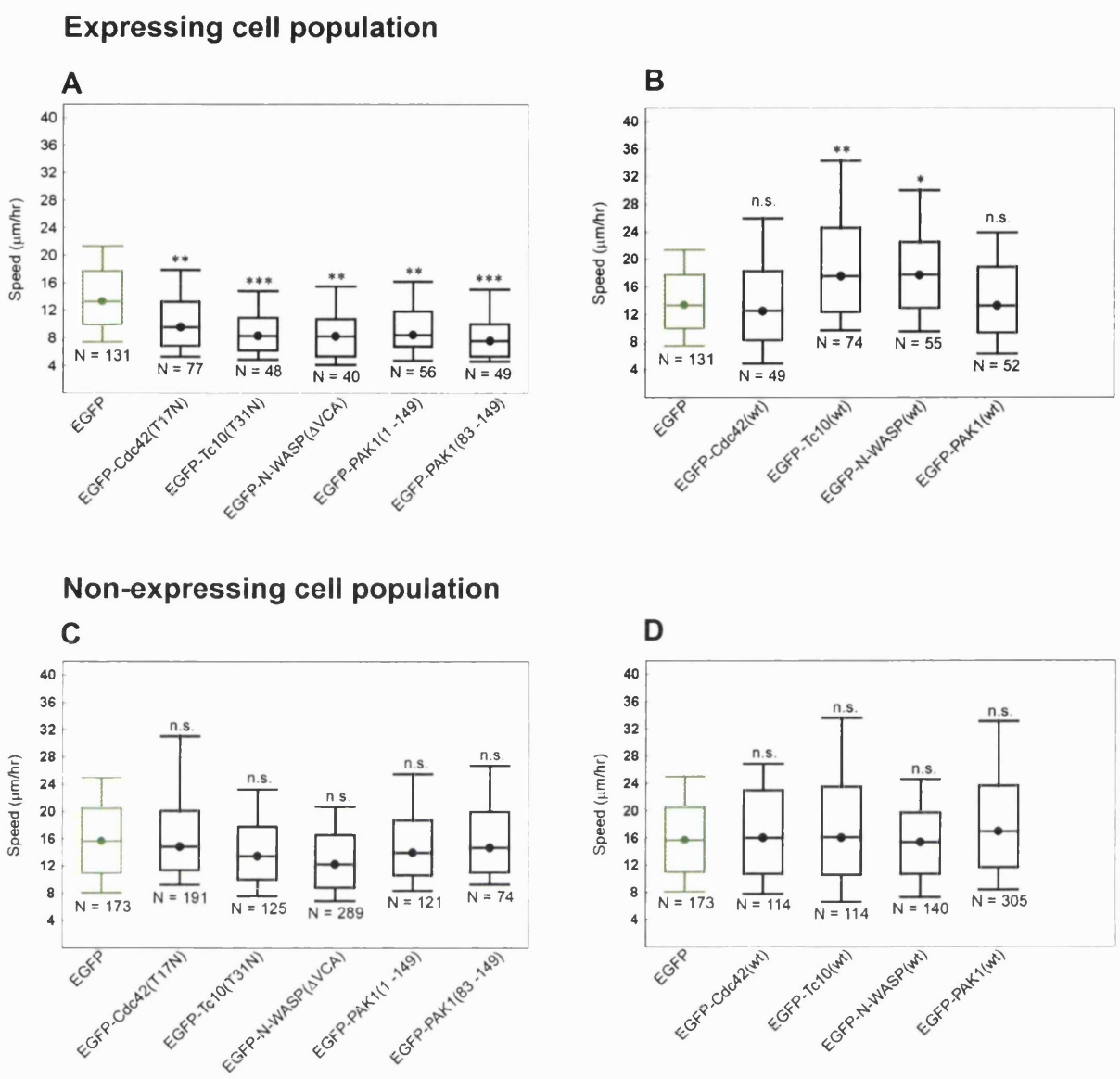

Figure 53. Box and whisker charts summarising the speed of sarcoma cell motility

Box and whisker charts summarising the effects of dominant negative (A) and wild-type (B) treatments on the speed of T15 sarcoma cell motility. Expression of dominant negative Cdc42, Tc10, N-WASP, and PAK1 constructs all resulted in a significant reduction in cell speed, indicating that all signalling molecules studied were important for efficient cell motility. Speed reductions were not observed following the expression of wild-type proteins. Indeed the expression of wild-type Tc10 and N-WASP constructs significantly enhanced cell speed ($p < 0.01$, $p < 0.05$ respectively). Charts (C & D) summarise the speed of the non-expressing cell populations from dominant-negative and wild-type treatment groups respectively. Significances were derived from the statistical comparison of each treatment group with the EGFP control group (green) using ANOVA. Likewise, the non-expressing cell populations from each treatment group were compared to the non-expressing cells of the EGFP control group. Circles represent median values while boxes span 50 %, and whiskers span 80 % of the data within each group.

Summary of cell speed

Treatment	Number of films	Number of cells	Mean Speed (µm/h)	Standard Error	Sig. (ANOVA)
EGFP-Cdc42(wt)	6	49	15.6	1.71	n.s.
EGFP-Cdc42(T17N)	7	77	10.6	0.55	**
EGFP-Tc10 (wt)	6	74	20.5	1.44	**
EGFP-Tc10 (T31N)	5	48	9.6	0.69	***
EGFP-N-WASP(wt)	7	55	19.0	1.02	*
EGFP-N-WASP(ΔVCA)	7	40	8.9	0.66	**
EGFP-PAK1(wt)	7	52	15.0	1.00	n.s.
EGFP-PAK1(1-149)	6	56	9.8	0.57	**
EGFP-PAK1(83-149)	4	49	8.7	0.63	***
EGFP	10	131	14.4	0.58	n.s.
	65	**631**			

Table 5. Numerical summary of sarcoma cell speed

Summary of the effects of the expression of various inhibitory constructs on the speed of sarcoma cells motility. All inhibitory constructs significantly impaired the speed of cell motility, with the most dramatic reductions obtained with the expression of the PAK1 kinase inhibitory fragment EGFP-PAK1 (83 – 149) ($p < 0.001$, ANOVA). Wild-type constructs did not impair cell motility confirming that reductions in speed were the consequence of specific dominant negative mutations or truncations and not the mere consequence of excessive protein overexpression. Indeed, expression of wild-type N-WASP and Tc10 actually resulted in an increase in the speed of cell motility ($p < 0.05$, $p < 0.01$ ANOVA respectively). The table indicates the number of experiments (films) and cells comprising each treatment group, the mean and standard error of cell speed for each group, and the significance of changes in cell speed conferred by protein expression. Significances were obtained from the statistical comparison of each treatment group with the EGFP control group using ANOVA. Red stars indicate significant reductions in speed while blue stars indicate significant increases. (1 star, $p < 0.05$; 2 stars, $p < 0.01$; 3 stars $p < 0.001$)

3.3.6 PAK1 regulates persistence of cell movement

PAK1 kinase activity has previously been implicated in the control of cell persistence (Sells et al., 1999). Therefore, it was hypothesized that the loss of directionality associated with PAK1 inhibition may in part have been a consequence of a fall in the persistence of cell movement: any factor that reduces the persistence of a motile cell is also likely to impair the cell's chemotactic ability as frequent turning frustrates the attempts of the cell to reach the chemoattractant source. Although PAK1 had previously been implicated in the regulation of persistence, attempts were not made to quantify or statistically assess the changes observed. In this study the trajectories of cells expressing PAK1 truncation mutants, as well as the various other proteins studied, were analysed to assess the effects of these treatments on the persistence of cell movement.

Cells from the control population expressing EGFP vector alone exhibited a wide range of persistences, reflecting the high degree of heterogeneity inherent within the normal cell population (Figure 54 A – D, page 19). However, expression of the inhibitory PAK1 constructs EGFP-PAK1(1 – 149), and EGFP-PAK1(83 – 149) significantly increased the frequency of poorly persistent cells within the population (Figure 55A, page 19). This was most notable following expression of the 83 – 149 truncation mutant (see also example trajectories of poorly persistent EGFP-PAK1(83 - 149) expressing cells Figure 54 E & F). The disruption of cell polarity associated with the expression of either of these inhibitory constructs was likely to account for the reduced persistence seen in these cells. Loss of persistent cell movement was, in turn, likely to underlie the impaired chemotactic ability of these cells. Expression constructs encoding dominant negative Cdc42, Tc10, and N-WASP,

and all wild-type proteins had no significant effect on the persistence of cell movement (Figure 55 A & B).

3.3.7 Effects of varying levels of EGFP-fusion protein expression on cell speed

Intensity analysis was performed to determine the effects of varying levels of protein expression on the speed of sarcoma cell motility. It was apparent from chemotaxis experiments that the different EGFP-fusion constructs microinjected into cells expressed with varying degrees of efficiency; while proteins such as EGFP and EGFP-PAK1(83 – 149) were continuously and often highly expressed, others such as EGFP-PAK1(wt) and wild-type and dominant negative variants of N-WASP were down regulated over the course of experiments (Figure 56, page 19). Figure 57 & Figure 58 (pages 19 & 19) are representative image sequences from PAK1(83 – 149) and EGFP-N-WASP(wt) experiments that have been processed in order to extract individual cell intensities. Image sequences highlight differences in both the efficiency and profile of protein expression that existed between the two expression constructs. It was therefore of importance to determine the relationship between cell intensity and speed. The primary aim was to determine whether reductions in speed associated with certain treatments were observable across a range of expression levels or whether they were only detectable in the highest expressing cells within an experimental group, a finding that could point towards non-specific protein toxicity accounting for such motile changes. Furthermore it was essential to establish whether differences existed between the speeds of cells expressing different proteins when compared at similar expression levels. This was particularly important in cases where wild-type and dominant negative variants of the same protein exhibited different expression efficiencies.

Figure 54. *(Figure legend on following page).*

EGFP

High persistence

A

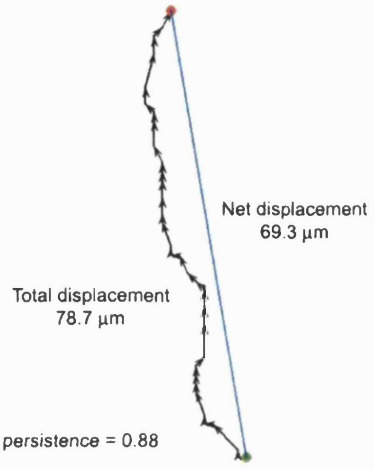

B

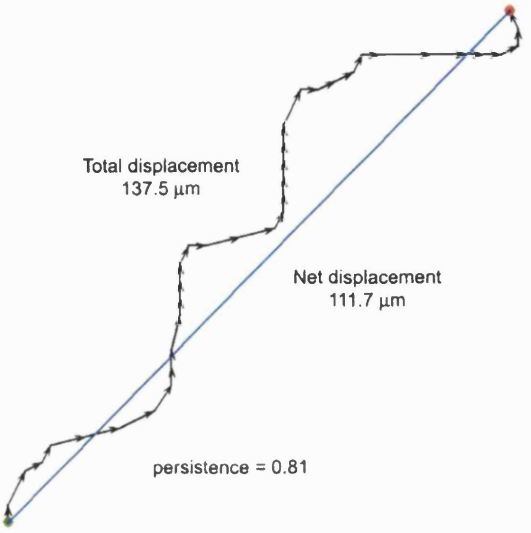

Low persistence

C

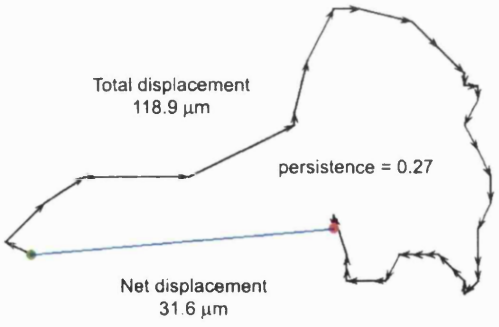

D

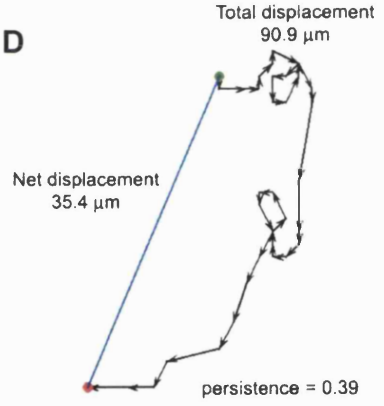

EGFP-PAK1(83 – 149)

Low persistence

E

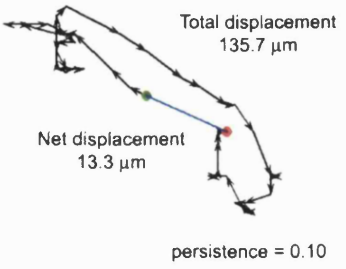

F

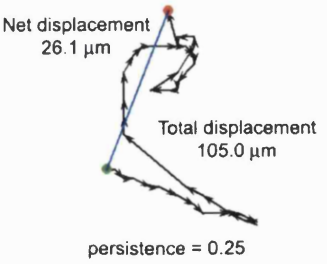

Figure 54. Cell trajectories demonstrating the persistence of sarcoma cell motility (preceding page)

Trajectories and associated persistence calculations for example cells selected from EGFP control (A – D) and EGFP-PAK1 (83-149) (E & F) treatment groups. Individual cells from the control cell population exhibited a wide variety of persistences, ranging from highly persistent (A & B) to poorly persistent (C & D) movement. However, EGFP-PAK1 (83 –149) expressing cells consistently exhibited poorly persistent cell movement (E & F). Sequentially linked black arrows illustrate the path of a single cell over a 500 min time course. Individual arrows indicate both the direction and extent of cell displacement over a single 10 min time interval. Total cell displacement is derived from the sum of the lengths of all these 10 min displacements. Blue lines indicate net cell displacement over the 500 min time-course with green and red circles representing initial and final cell positions. Cell persistence is derived from net and total cell displacement values via the equation: persistence = net displacement/total displacement. Values close to 1 represent highly persistent movement while values close to 0 represent only poorly persistent movement. Only cell trajectories comprising of greater than 50 data points (50 % of the length of the entire film sequence) were selected for subsequent persistence analysis. Trajectories were cropped to equal lengths before the calculation of cell persistences.

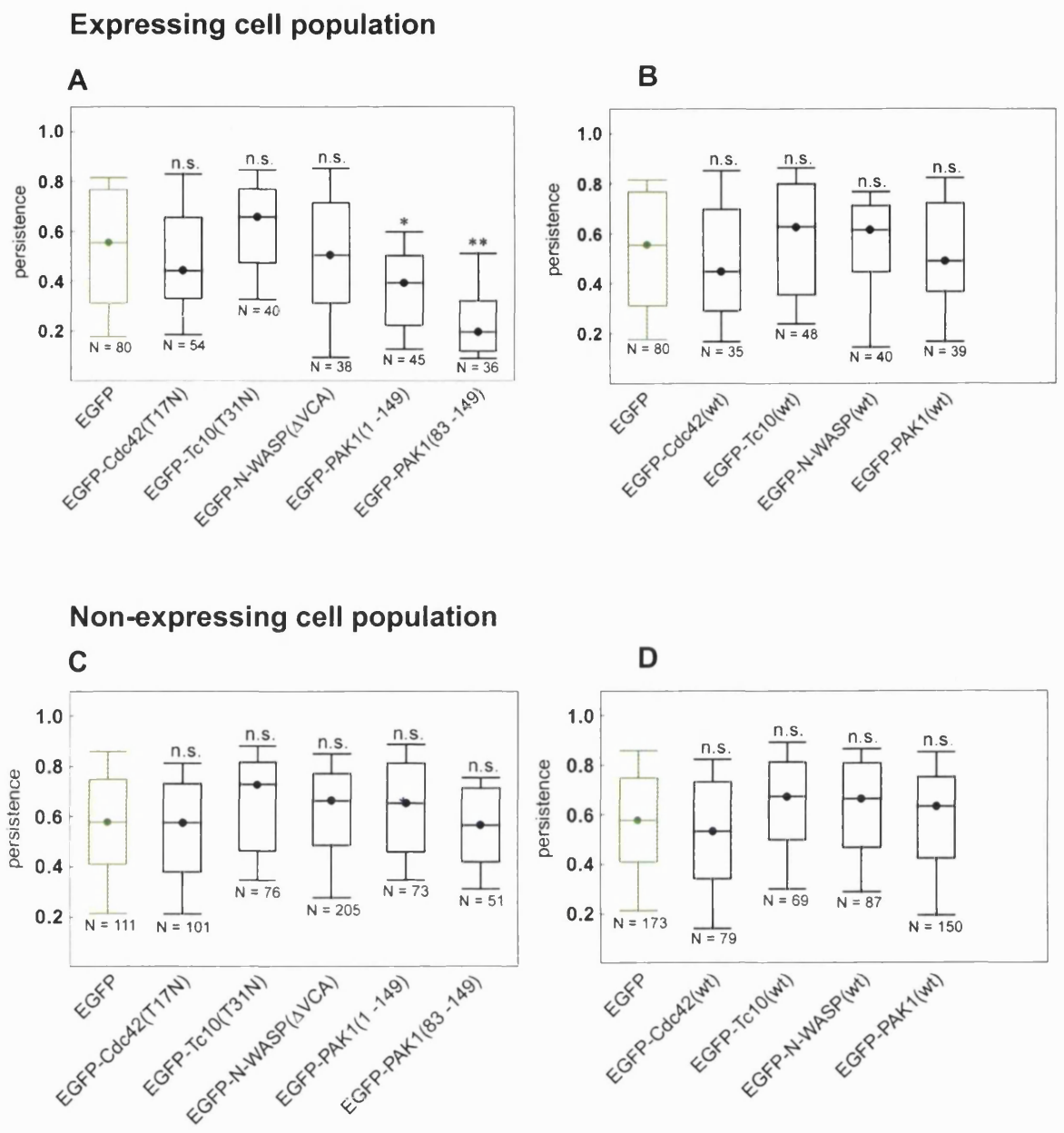

Figure 55. Box and whisker charts summarising the persistence of sarcoma cell motility

Box and whisker charts summarising the range of cell persistence values calculated for cells expressing dominant negative (A) and wild-type (B) constructs. Significances were derived from the ANOVA comparison of individual treatment groups with the EGFP control group. Expression of EGFP-PAK1(1 – 149) and EGFP-PAK1(83 – 149) resulted in a significant reduction in the persistence of cell movement ($p < 0.05$, $p < 0.01$ respectively). Expression of EGFP-Cdc42(T17N), EGFP-Tc10(T31N), and EGFP-N-WASP(ΔVCA) inhibitory constructs, and the expression of all wild-type constructs had no significant effect on the persistence of cell movement. Persistence values did not vary significantly between the non-expressing cells of each treatment groups and the non-expressing cells of the EGFP control group (C & D, dominant negative and wild-type treatment groups respectively).

Individual cell intensities and corresponding cell speeds were extracted from the fluorescence images of multi-channel film sequences using purpose written image-processing algorithms developed in Mathematica. Varying levels of protein expression were then compared with associated changes in cell speed. For a detailed explanation of the methods used to extracting cell intensities from image sequences see methods 3.2.13, page 19. A high degree of variation in protein expression was found between the different EGFP fusion proteins studied. Highest levels of expression were observed in control cells expressing EGFP alone. However, across the broad range of cell intensities observed for this treatment group there was no significant correlation between protein expression and speed (Figure 59, page 19). Therefore expression of EGFP alone had no deleterious effect on cell motility.

Intensity analysis revealed that at the lowest levels of expression none of the dominant negative proteins studied had a significant inhibitory effect on cell speed (Figure 60, page 19, comparison of cell speeds within the lowest intensity bin of each treatment group with the lowest bin of the EGFP control group). However, low levels of wild-type Tc10, N-WASP, and PAK1 expression did seem to enhance the speed of cell motility (Figure 61, page 19). At increasing intensities of expression dominant negative constructs had a dramatic and sudden inhibitory effect on speed. This was most noticeable for dominant negative Cdc42, Tc10, and PAK1 (Figure 60). Importantly, this sudden fall in speed was not seen for many of the wild-type proteins studied, suggesting that the inhibition of cell speed observed following the expression of dominant negative proteins was the consequence of the specific mutations that these proteins conferred. However, at higher levels of expression there was the suggestion that some wild-type proteins may have conferred an inhibitory effect on cell speed. Indeed,

higher levels of EGFP-PAK1(wt) expression did significantly impair cell speed. It is important to note, however, that the inhibitory effects conferred by the dominant negative PAK1 truncation mutants were noticeable at far lower expression levels than those associated with the wild-type protein. A gradual but persistent decline in speed was also associated with increasing levels of EGFP-N-WASP(wt) expression. However, much of this decline was likely to be associated with a loss of the enhancing effects that this protein initially had on cell speed.

Although not significant, expression of EGFP-Cdc42(wt) did appear to suppress cell speed over a range of intensities, and differences between the speed-intensity relationship of wild-type and dominant negative Cdc42 expressing cells were less striking than with the other proteins studied. It is therefore possible that an inhibition of speed associated with EGFP-Cdc42(wt) expression may have been revealed from the assessment of larger data sets. However, dominant negative Cdc42 did have a significant effect on cell speed, which was apparent across a range of expression levels.

Intensity analysis revealed that, at comparable intensities, dominant negative proteins appeared to suppress cell speed far more efficiently than wild-type proteins. Indeed, at low levels of expression some wild-type proteins actually seemed to enhance cell speed. It can therefore be concluded with confidence that the inhibition of cell speed, seen in chemotaxis experiments following the expressing of various dominant negative constructs, occurred as a result of the specific inhibitory mutations that these proteins conferred and not as a consequence of non-specific toxicity associated with accumulating levels of exogenous protein.

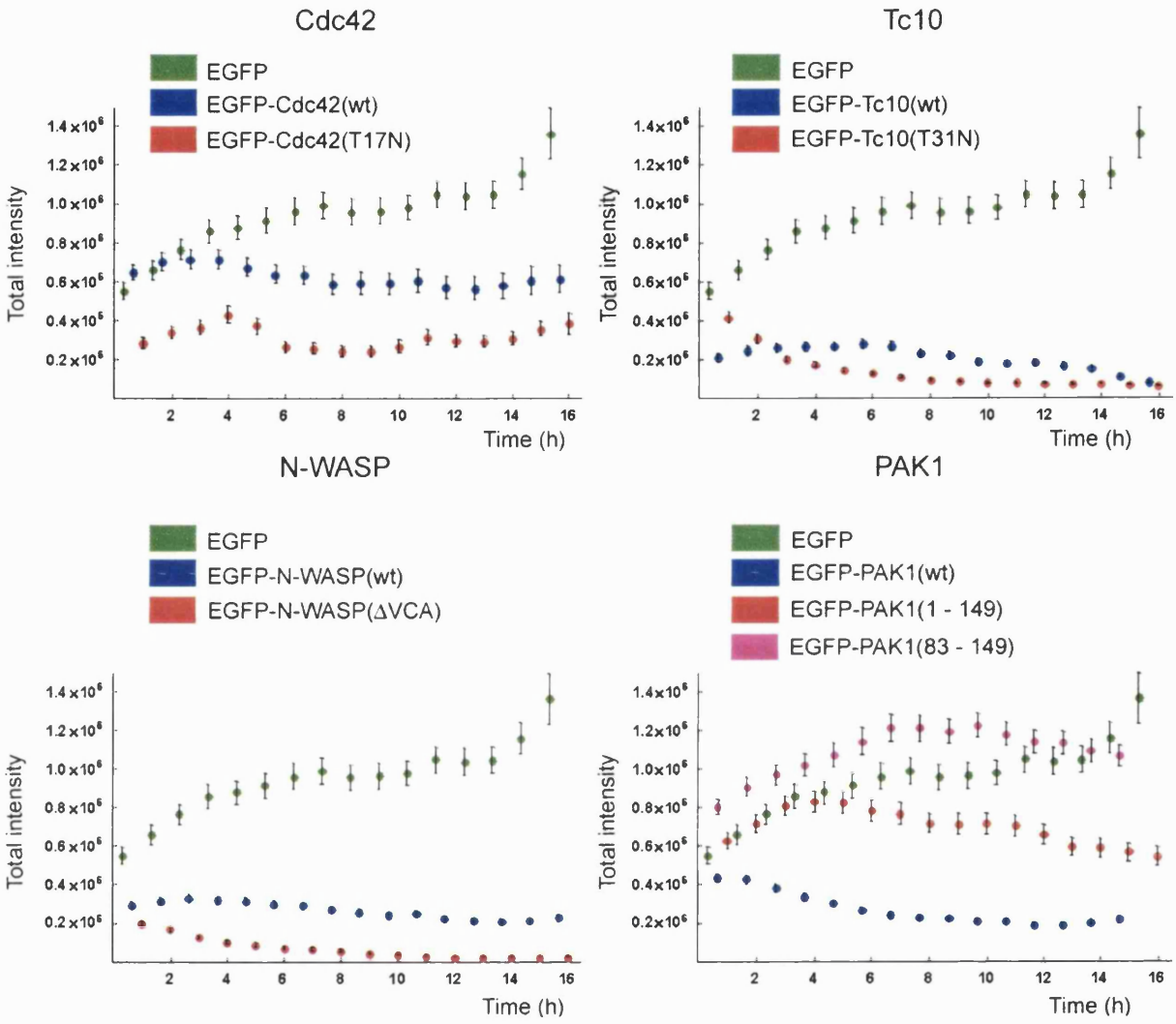

Figure 56. The expression profile of EGFP fusion proteins

Plots demonstrating the differing efficiencies with which EGFP fusion constructs were expressed over the course of chemotaxis experiments, as measured by changes in the total fluorescence intensity of expressing cells. Individual cell intensities were extracted from the fluorescence images of multi-channel film sequences using purpose written image-processing routines developed within Mathematica. Each plot summarises the mean intensity of expression, calculated at hourly intervals, of all cells within a single treatment group. The different constructs studied exhibited a wide range of expression efficiencies. Intensity values are measured in arbitrary units.

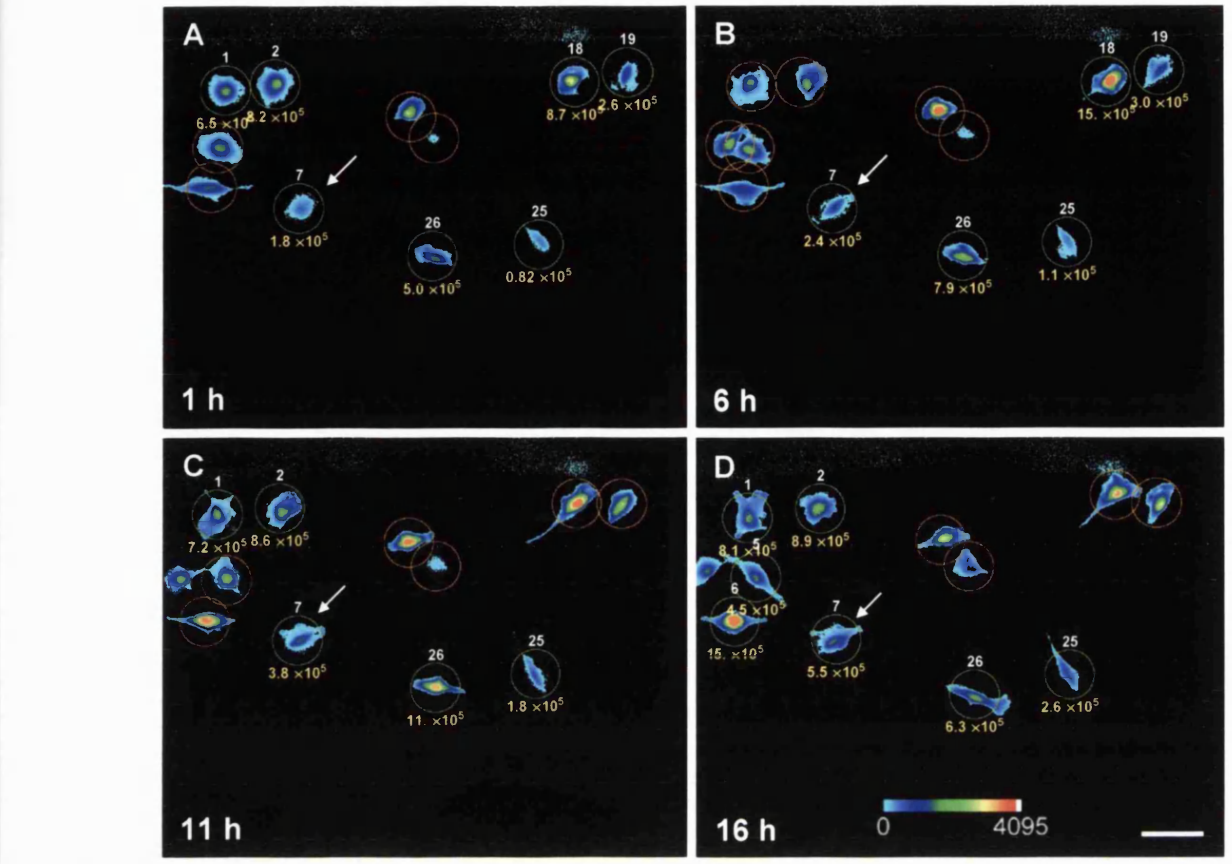

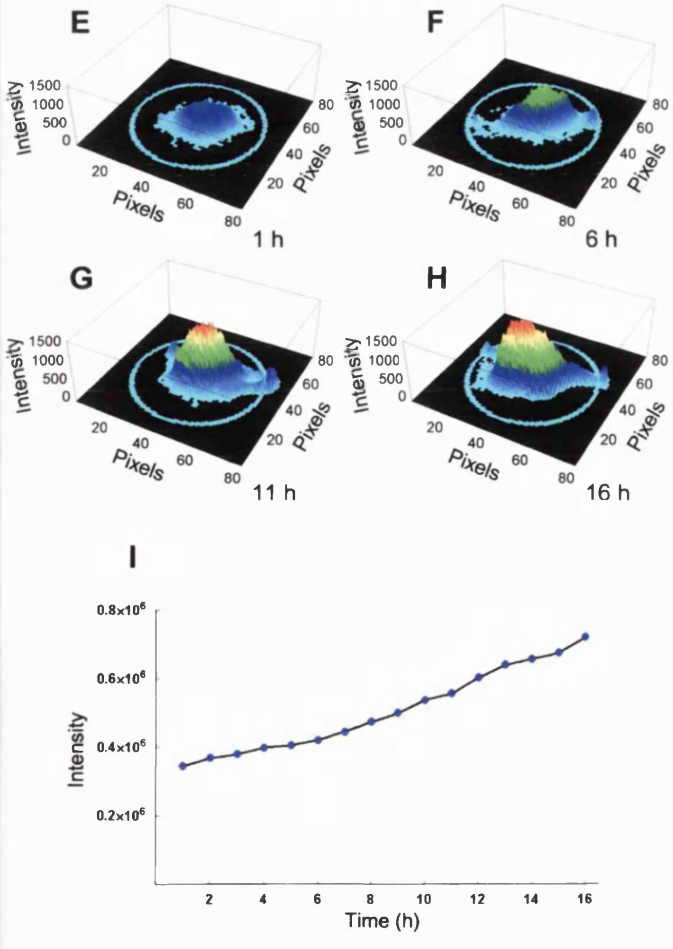

Figure 57. Extraction of cell intensities from an EGFP-PAK1(83 – 149) film sequence

Images (A – D) show EGFP-PAK1(83 - 149) expressing cells and their corresponding boundaries used for the extraction of intensities. Images represent 5-hour time points from the same film sequence. The total intensity of a cell was calculated as the sum of all pixel values contained within its associated boundary. When cell boundaries overlapped intensity values were ignored (orange boundaries). White numbers indicate cell number, defined by the order within which the cell was tracked. Yellow numbers indicate the total intensity value for a cell at a given time point. (E – H), three-dimensional representation of cell 7 from (A - D) (white arrow). Cell intensity increased continuously over time. Plot I, Total intensity of cell 7 over the course of the entire film sequence (intensities partitioned into hourly bins). Images are displayed in pseudocolour.
Scale bar = 100 μm.

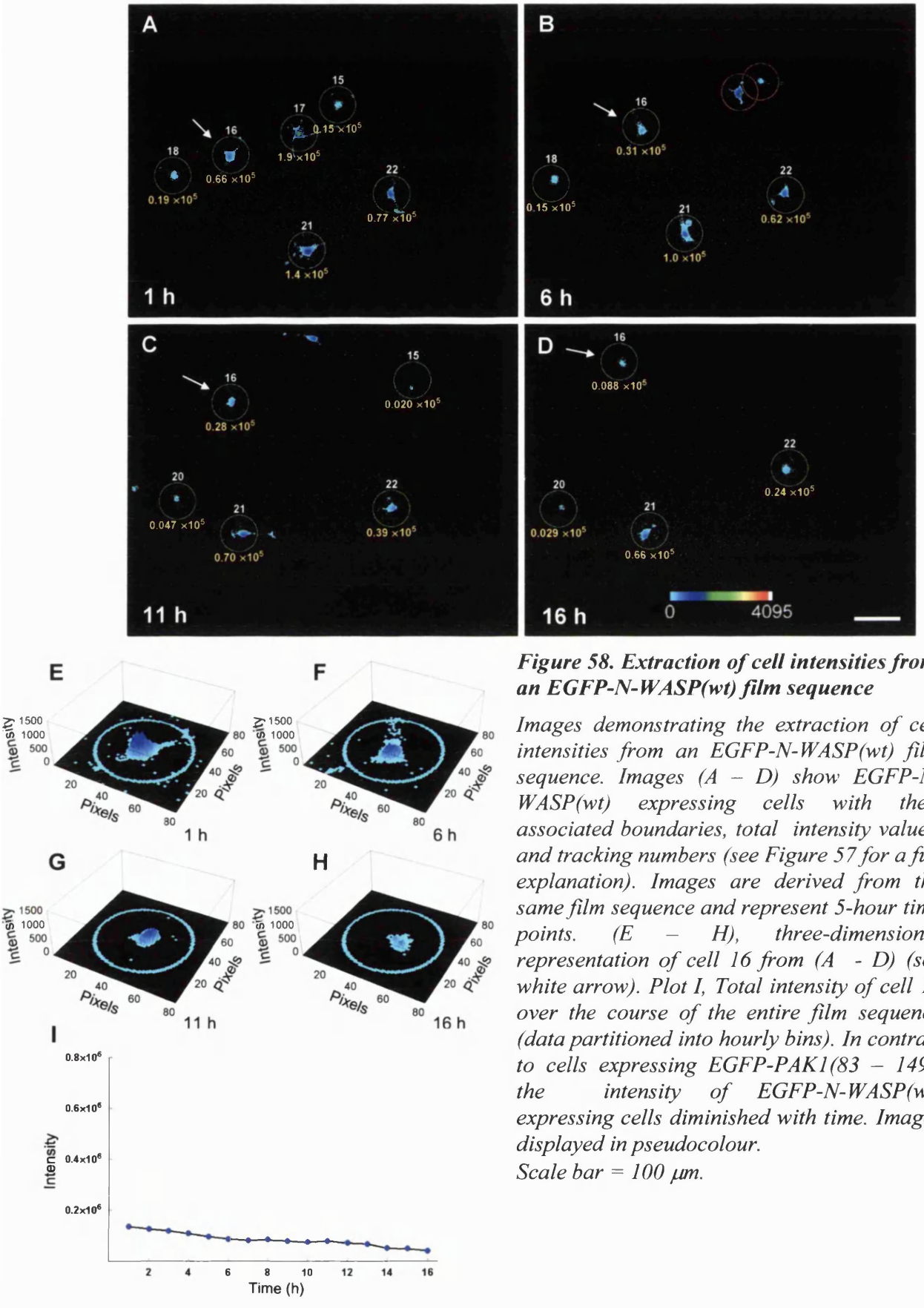

Figure 58. Extraction of cell intensities from an EGFP-N-WASP(wt) film sequence

Images demonstrating the extraction of cell intensities from an EGFP-N-WASP(wt) film sequence. Images (A – D) show EGFP-N-WASP(wt) expressing cells with their associated boundaries, total intensity values, and tracking numbers (see Figure 57 for a full explanation). Images are derived from the same film sequence and represent 5-hour time points. (E – H), three-dimensional representation of cell 16 from (A - D) (see white arrow). Plot I, Total intensity of cell 16 over the course of the entire film sequence (data partitioned into hourly bins). In contrast to cells expressing EGFP-PAK1(83 – 149), the intensity of EGFP-N-WASP(wt) expressing cells diminished with time. Images displayed in pseudocolour.
Scale bar = 100 μm.

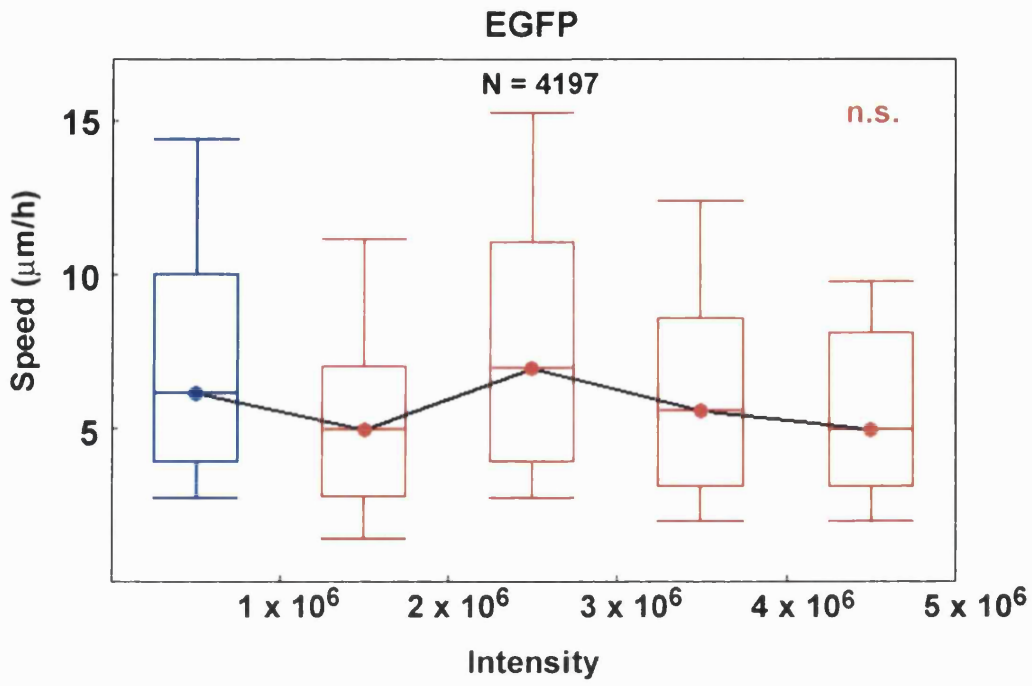

Figure 59. Effects of increasing EGFP expression on cell speed

Box and whisker charts demonstrating the effects of increasing levels of EGFP expression of the speed of sarcoma cell motility. Individual cell intensities and corresponding cell speeds were extracted from the fluorescence images of EGFP film sequences at hourly intervals using specially developed Mathematica software. In the above charts cell speeds are partitioned into data bins of increasing intensity. Each intensity bin spans 1×10^6 arbitrary intensity units. No obvious reduction in speed was associated with increasing levels of EGFP expression. The ANOVA comparison of the lowest intensity bin (blue) with all other intensity bins (red) did not reveal significance, indicating that higher levels of expression did not impair motility. N = number of intensity data points. Charts summarises data from 7 films.

Figure 60.

Figure legend on following page.

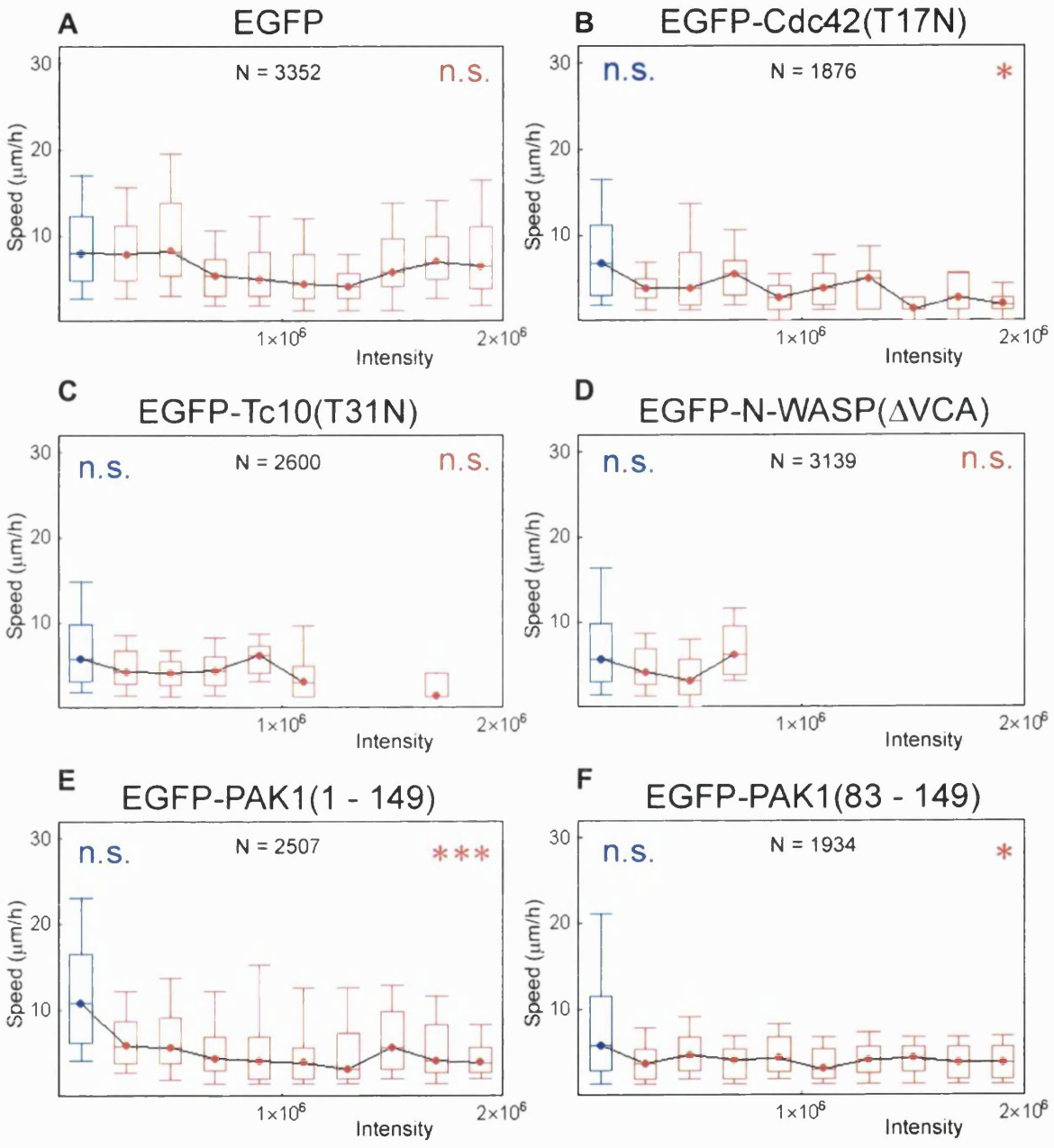

Figure 60. Cell speed and the intensity of expression of dominant negative proteins (previous page)

Box and whisker charts demonstrating the effects of increasing levels of expression of various dominant-negative proteins on the speed of sarcoma cell motility. Individual cell intensities and corresponding cell speeds were extracted from the fluorescence images of chemotaxis film sequences at hourly intervals. Charts represent data from EGFP control, EGFP-Cdc42(T17N), EGFP-Tc10(T31N), EGFP-N-WASP(ΔVCA), EGFP-PAK1(1 – 149), and EGFP-PAK1(83 – 149) treatment groups (A – F respectively). Cell speeds are partitioned into data bins of increasing intensity and are represented as box and whisker plots. The lowest intensity bin for each treatment group is displayed in blue, all other intensity bins are in red. Blue significance values are derived from the ANOVA comparison of the lowest intensity bin of each group with the lowest bin of the EGFP control group. Red significances represent the comparison of the lowest intensity bin with all other intensity bins within the same group. N = total number of intensity data points representing a given treatment group. Charts summarises data from a number of films.

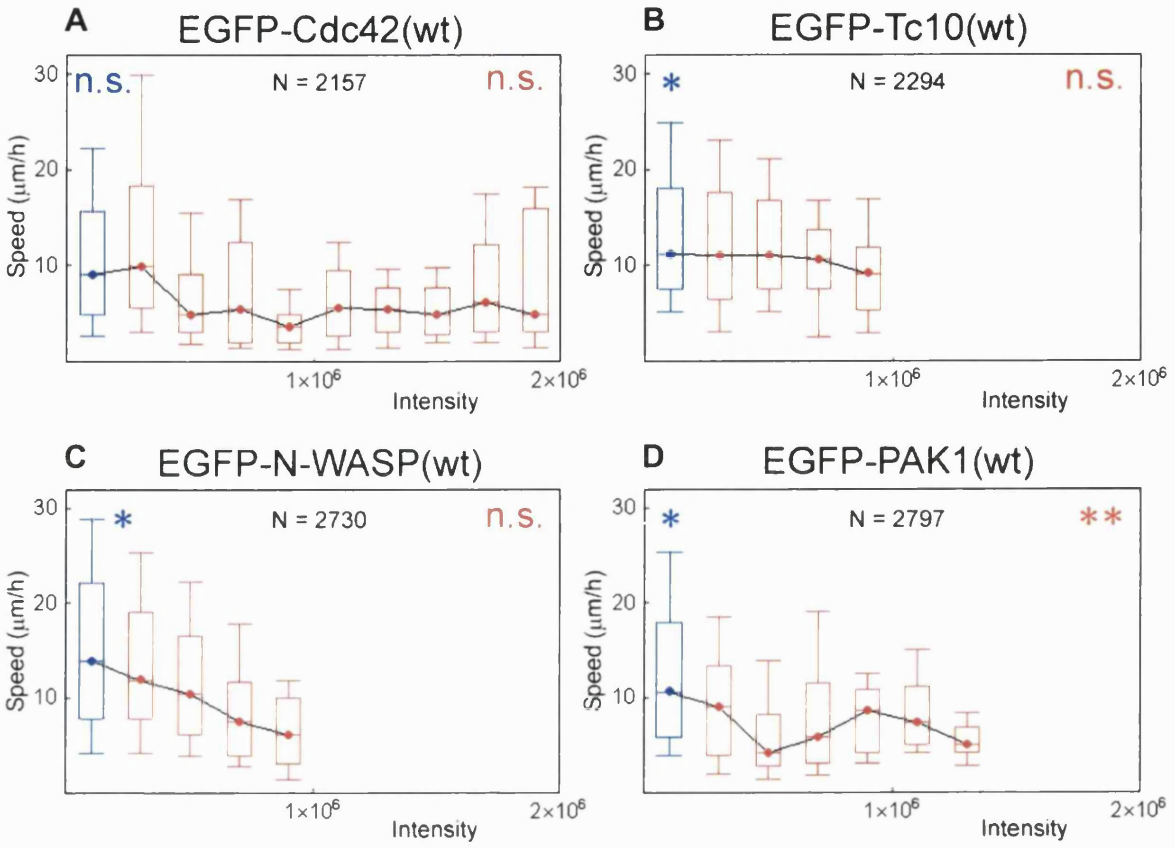

Figure 61. Cell speed and the intensity of expression of wild type proteins

Box and whisker charts demonstrating the effects of increasing levels of expression of various wild-type proteins on the speed of sarcoma cell motility. Charts represent data from EGFP-Cdc42(wt), EGFP-Tc10(wt), EGFP-N-WASP(wt), and EGFP-PAK1(wt) treatment groups (A – D respectively). Speeds within the lowest intensity bin of each treatment group are compared to those of the lowest bin of the EGFP treatment group. For a full description of the method of data presentation and statistical comparisons see Figure 60. N = total number of intensity data points representing a given treatment group. Charts summarise data from a number of films.

3.3.8 Cdc42 function in fibroblast chemotaxis and motility

Given the importance of Cdc42 function in the polarity and chemotaxis of a number of mammalian cell types it was somewhat surprising to find that it was of little importance in the PDGF-BB/IGF-1 driven chemotaxis of T15 rat sarcoma cells. However, sarcoma cells are transformed fibroblasts and therefore do not represent true fibroblasts but fibroblast-like cells. It was therefore important to establish whether Cdc42 function was in general of no importance in the chemotaxis of fibroblasts or whether this was a property unique to the T15 cell line. Consequently, established fibroblast cell lines were also used to investigate the role of Cdc42 function in chemotaxis and motility.

3.3.9 Swiss and NIH 3T3 fibroblasts exhibit chemotaxis in PDGF-BB gradients

Dunn chamber chemotaxis assays were performed to assess the long-term chemotactic potential of Swiss and NIH 3T3 fibroblasts exposed to gradients of PDGF-BB, an established fibroblast chemoattractant (Seppa et al., 1982). Both Swiss and NIH 3T3 fibroblasts exhibited chemotaxis in gradients of PDGF-BB (100 ng/ml) as confirmed by the significant unimodal clustering of cell directions toward the chemoattractant source (Figure 62, B & F, page 19). The directional responses of cells in the absence of growth-factor gradients were essentially random (Figure 62, A & E). However, it was clear from the observation of individual film sequences that the chemotactic response of the Swiss 3T3 cell line was far more dramatic than that of the NIH 3T3 cell line; a noticeable proportion of the NIH cell population within each experiment did not seem to respond to the chemotactic stimulus. Indeed, although the chemotactic response of NIH 3T3 cells was significant it was less so

than that of Swiss 3T3 cells (Rayleigh test, $p < 0.05$ and $p < 0.001$ respectively). Note also the more striking accumulation of cell trajectories in the direction of the gradient in the case of the Swiss 3T3 cell line (Figure 62 compare D with H). Interestingly, PDGF-BB stimulation did not appear to enhance the speed of cell motility, possibly a consequence of the high serum background in which experiments were conducted (Figure 63, page 19). Due to the low throughput nature of Dunn chamber chemotaxis assays, a large number of experiments were required to accumulate sufficient data sets for meaningful statistical analysis. Therefore it was decided that only the Swiss 3T3 cell line would be used for the further investigation of Cdc42 function in fibroblast chemotaxis, as the effects of treatments on the chemotaxis of NIH 3T3 cells would be difficult to establish against an intrinsically heterogeneous background of cell behaviour.

3.3.10 Swiss 3T3 fibroblasts exhibit Cdc42 independent chemotaxis

Subconfluent cultures of Swiss 3T3 fibroblasts were microinjected with expression constructs encoding either EGFP or EGFP-Cdc42(T17N) and assessed in the Dunn chemotaxis chamber for their ability to chemotax. Figure 64 A & B, page 19 are representative film sequences of Swiss 3T3 cells expressing EGFP and EGFP-Cdc42(T17N) respectively. It is apparent from these films that cells expressing either of these constructs demonstrated efficient chemotaxis in PDGF-BB gradients. The analysis of cell trajectories from four independent experiments confirmed that EGFP-Cdc42(T17N) expressing cells exhibited normal chemotaxis (Figure 65A, page 19). This finding was consistent with that of the T15 sarcoma cell line suggesting that Cdc42 is of no importance in the chemotaxis of fibroblast-like cells. Although EGFP-Cdc42(T17N) expression did appear to reduce cell

speed and although the paths of expressing cells appeared suppressed compared to those of control cells expressing EGFP alone (Figure 65B), these findings were not significant (Figure 65C).

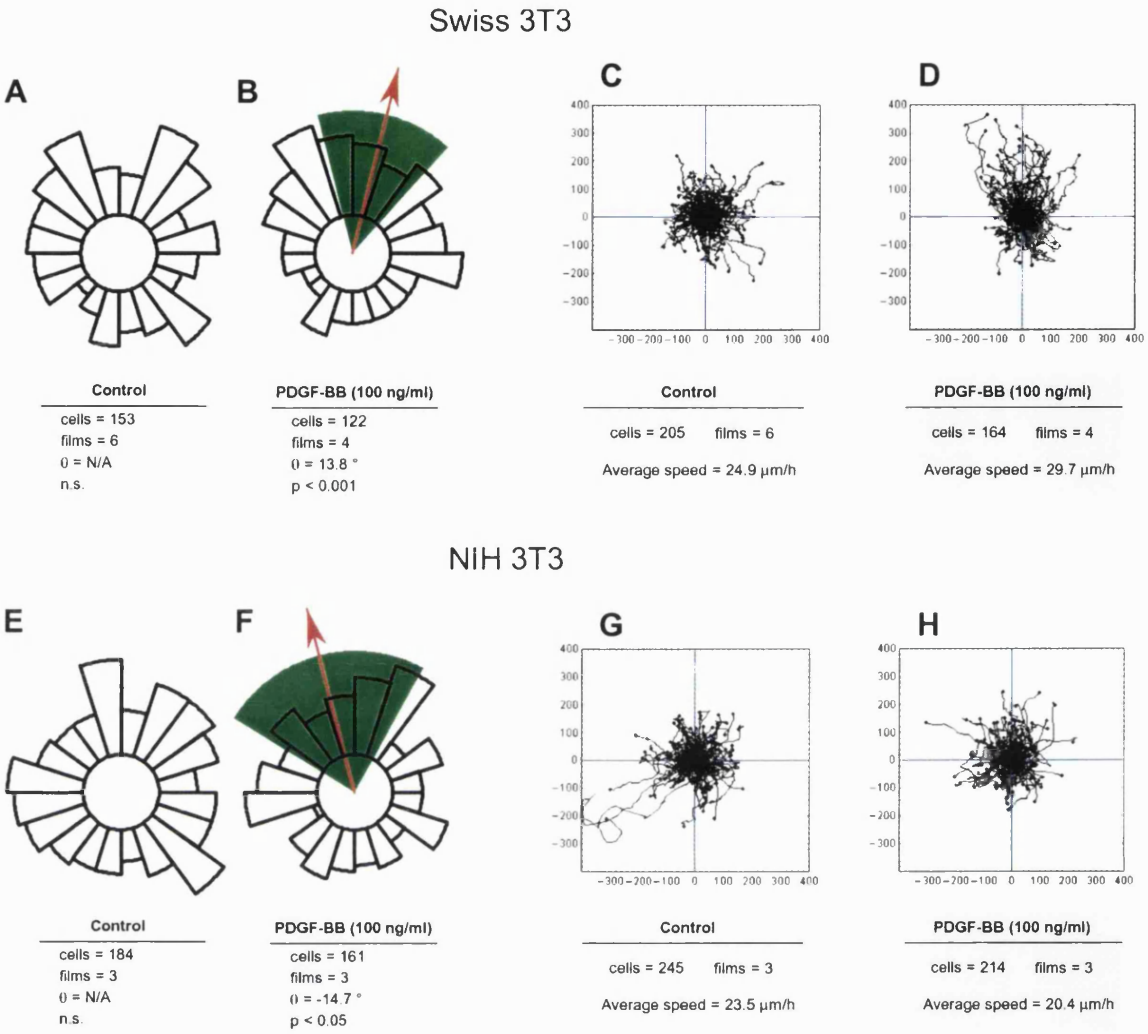

Figure 62. The chemotaxis of Swiss and NIH 3T3 fibroblasts

Circular histograms and trajectory plots demonstrating the chemotactic responses and motile behaviour of Swiss and NIH 3T3 fibroblasts either in the absence (A, C, E, & G) or in the presence (B, D, F, & H) of a PDGF-BB (100 ng/ml) gradient. Both Swiss and NIH 3T3s exhibited significant chemotaxis in PDGF-BB gradients as confirmed by the significant unimodal clustering of cell directions towards the source of the chemoattractant (B & F respectively). No significant directional response was observed when growth factors were omitted from the outer well of the chemotaxis chamber (A & E). Although both cell lines demonstrated significant chemotaxis in PDGF-BB gradients, Swiss 3T3 appeared to exhibit the strongest response (Rayleigh test $p < 0.001$). This is especially apparent from the trajectory plots: the clustering of cell paths towards the chemoattractant source was far more apparent for the Swiss 3T3 cell line (compare D, Swiss with H, NIH). The paths of control cells were not significantly clustered in any one direction (C & G).

Figure 63. The effects of PDGF-BB on fibroblast motility

Box and whisker plots summarising the speed of Swiss 3T3 and NIH fibroblast cells either in the presence or absence of a PDGF-BB gradient (100 ng/ml). Plots summarise data pooled from a number of experiments. No significant difference in speed existed between control cells and those exposed to PDGF-BB gradients for either of the fibroblast cell lines studied (n.s. ANOVA).

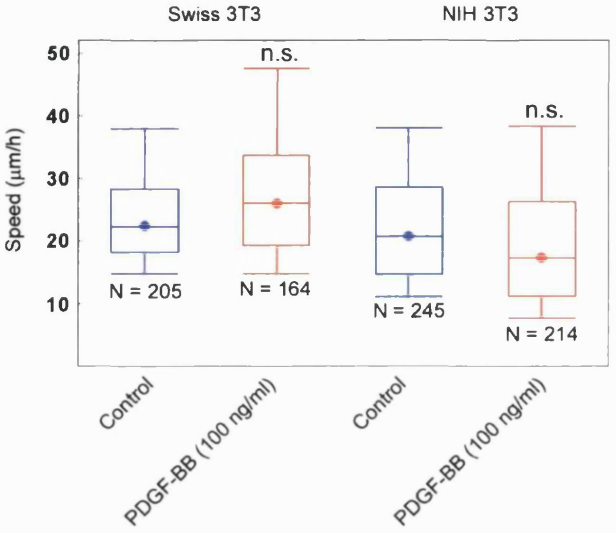

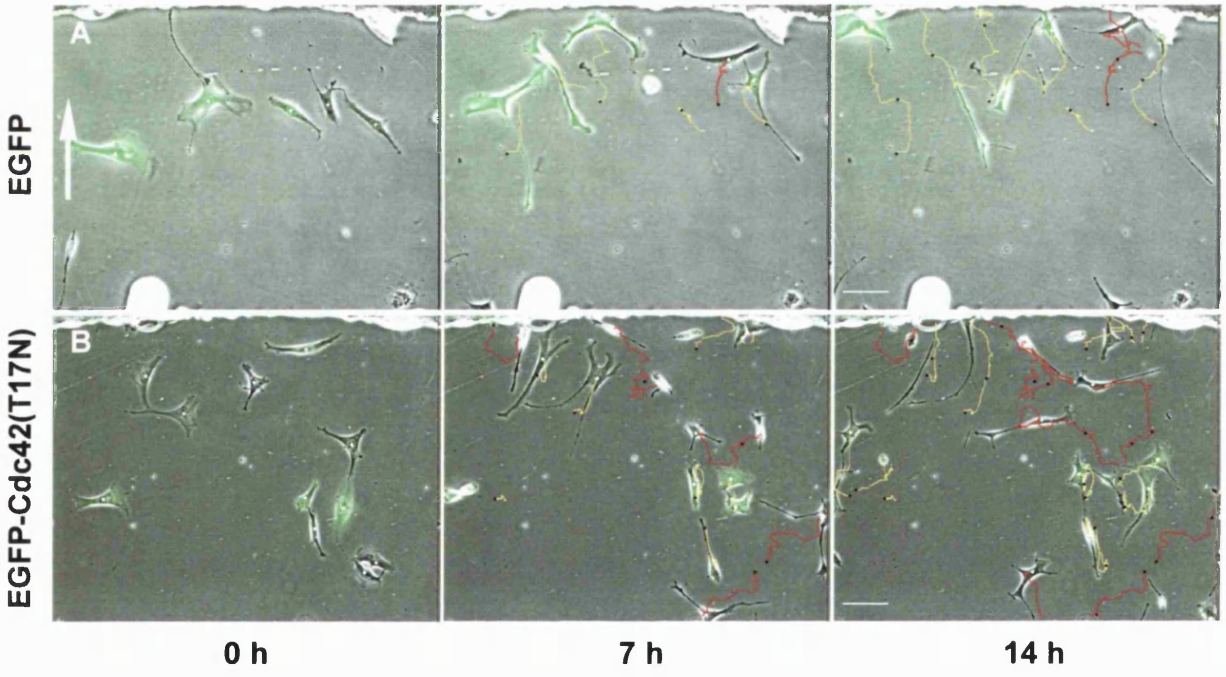

Figure 64. Film sequences of chemotaxing Swiss 3T3 fibroblasts

Representative image sequences from films demonstrating the chemotaxis of Swiss 3T3 fibroblasts expressing either EGFP control or EGFP-N17Cdc42(T17N) (A & B respectively). Images for each sequence represent 0 h, 7 h, and 14 h time points. Track colours and image compositions are as previously described (see Figure 45, page 197). The direction of increasing growth factor concentration runs from the bottom to the top of each image, as represented by the white arrow in the first image of the EGFP sequence. Scale = 100 µm.

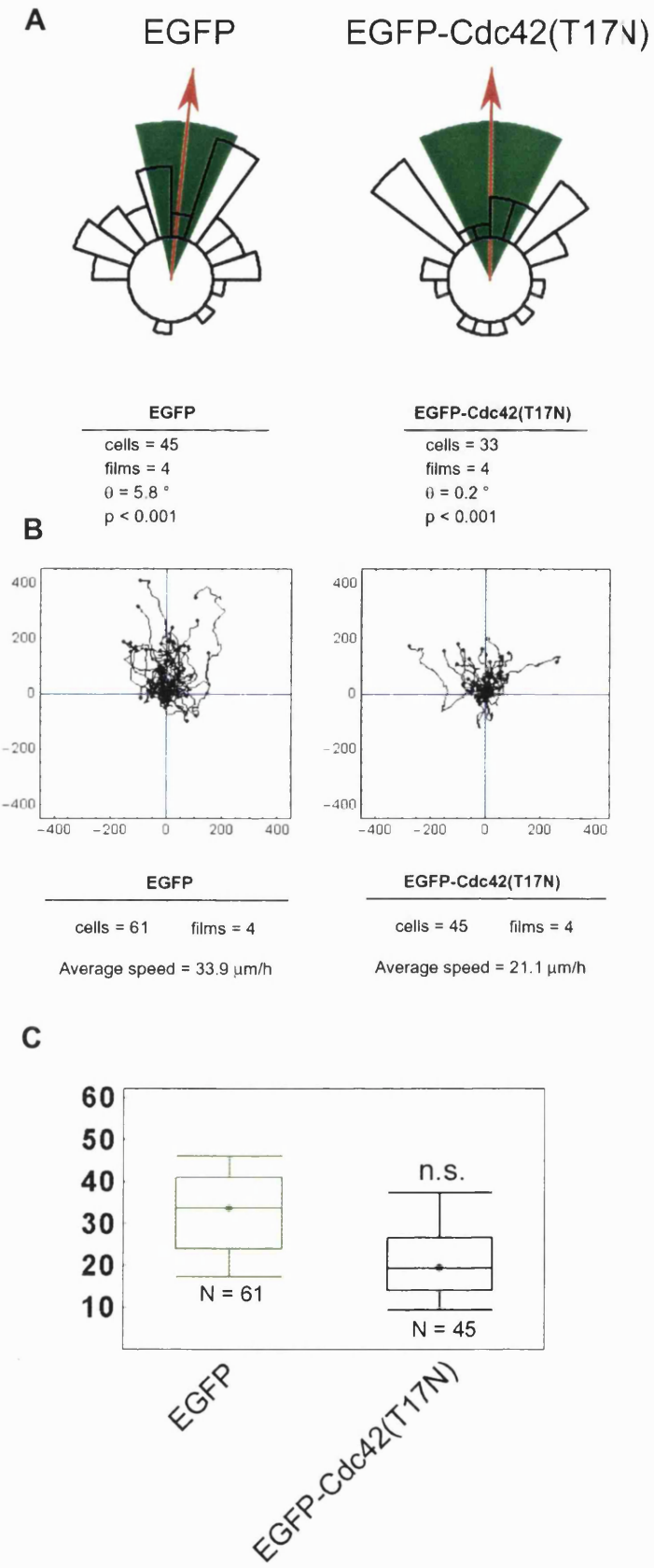

Figure 65. Swiss 3T3 fibroblasts exhibit Cdc42 independent chemotaxis

Circular histograms (A), trajectory plots (B), and box and whisker charts (C) summarising the effects of EGFP and EGFP-Cdc42(T17N) expression on the chemotaxis and motility of Swiss 3T3 fibroblasts. Inhibition of Cdc42 had no effect on Swiss 3T3 chemotaxis, consistent with findings for the T15 sarcoma cell line. Interestingly a significant reduction in cell speed was not observed following Cdc42 inhibition (C) (n.s. ANOVA). However, this may reflect the relatively small data sets analysed. Histograms and plots summarise data obtained from four separate experiments for each treatment group.

3.3.11 Cdc42 is required for the efficient motility of NIH 3T3 fibroblasts

Although the chemotactic response of NIH 3T3s was somewhat less efficient than that of Swiss 3T3s, this was not the consequence of poor cell motility *per se*. Indeed, both NIH and Swiss 3T3 fibroblasts were more motile than the previously studied T15 cell line. As Cdc42 had previously been implicated in the motility of the T15 cell line, and since there was a suggestion that it may also be of importance in the motility of Swiss 3T3s, 'random walk' experiments were conducted to investigate the role of Cdc42 in the motility of NIH 3T3 fibroblasts. When chemotaxis is not the subject of investigation the random-walk chamber provides a far more desirable method of assessing cell motility than the Dunn chemotaxis chamber. Technically, the random walk chamber is far simpler to assemble, as the precise positioning of fluorescent cells within the chamber is not a requirement. Furthermore, when combined with automated multi-field imaging, multiple fields of fluorescent cell can be viewed within a single chamber enabling greater sample numbers to be obtained from individual cultures. Thus, the random-walk assay permits the accumulation of far larger data samples than the Dunn chemotaxis chamber within the same time frame.

NIH 3T3 fibroblasts were microinjected with expression constructs encoding either EGFP control, or EGFP fusions of either wild-type or dominant negative Cdc42. Cells were permitted 3 hours to express the microinjected constructs before assembly into random walk chambers. Low magnification (10 ×) multi-field/multi-channel digital time-lapse microscopy was then used to assess the behaviour of expressing and non-expressing cells within multiple fields of random walk chambers over the course of 16 hours using a single microscope.

NIH 3T3 cultures were observed to grow at far greater rates than Swiss 3T3 or T15 cultures. As a consequence it became difficult to interactively track cells during the latter stages of film sequences as frequent cell collisions obscured the paths of individual cells. Therefore it was decided to only track and analyse cell behaviour over the first 8 hours of film sequences. Figure 66, page 19 illustrates the paths of expressing cells over the first 8 hours of random walk experiments. The trajectories of EGFP-Cdc42(T17N) expressing cells were visibly suppressed when compared to those of cells expressing EGFP control or wild-type protein (Figure 66 A - C). EGFP-Cdc42(T17N) expression significantly impaired cell speed (Figure 67, page 19) confirming the importance of the endogenous protein in fibroblast motility, a finding that is in agreement with observations made by others (Nobes and Hall, 1999). Expression of EGFP-Cdc42(wt) had no significant effect on NIH 3T3 motility.

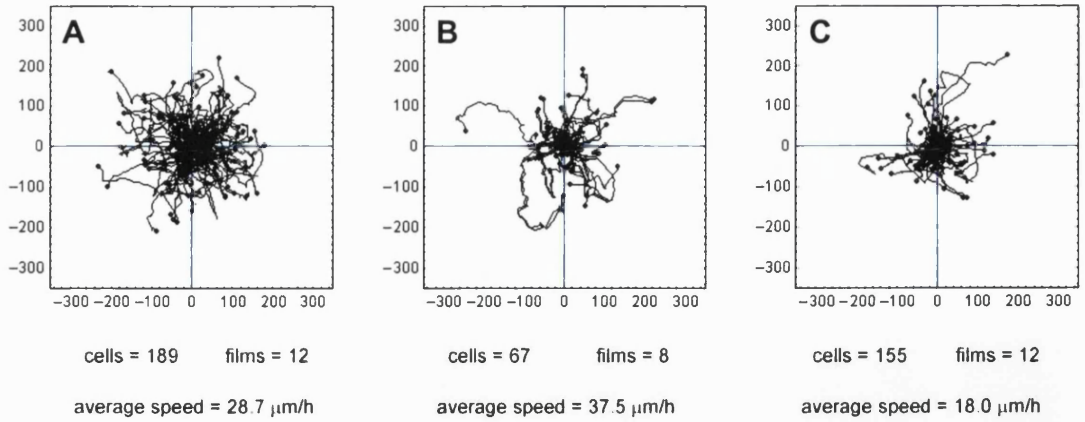

Figure 66. Cell trajectories of NIH 3T3s expressing wild type or dominant negative cdc42

Cell trajectory plots illustrating the individual paths of NIH 3T3 fibroblasts recorded in 'random walk' experiments. Cells were microinjected with cDNA constructs encoding either EGFP control (A), EGFP-Cdc42(wt) (B), or EGFP-Cdc42(T17N) (C). Each plot represents data pooled from a number of films. Trajectories represent the first 8 hours of 16-hour film sequences. Axes units represent distance in microns from the common origin.

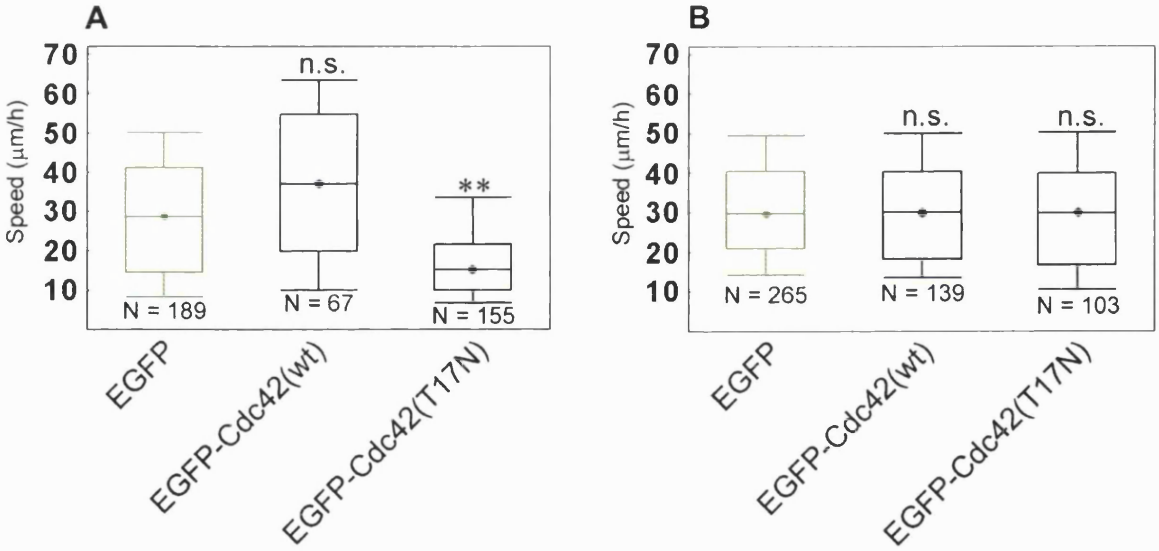

Figure 67. Box and whisker charts summarising the speed of NIH 3T3 motility

Box and whisker charts summarising the speed of NIH 3T3 fibroblast motility for EGFP control, EGFP-Cdc42(wt), and EGFP-Cdc42(T17N) treatment groups. Summaries of cell speeds for both the expressing (A) and non-expressing (B) cell populations within each treatment group are shown. N represents the total number of cells recorded for each treatment group while significances, derived from the ANOVA comparison of each treatment group with the EGFP control group, are displayed at the top of each chart. Speeds were derived from trajectories obtained via the interactive tracking of cells over the first 8 hours of 16-hour film sequences. Expression of EGFP-Cdc42(T17N) resulted in a significant reduction in cell speed (ANOVA, $p < 0.01$).

3.3.12 FLAP reveals distinct patterns of actin dynamics in sarcoma cells

FLAP experiments were conducted in order to examine the actin dynamics of metastatic T15 and non-metastatic K2 sarcoma cells ectopically expressing ECFP and EYFP fusions of β-actin. It was immediately apparent from the subcellular localisation of fluorescent β-actin that a great deal of heterogeneity could exist between the cytoskeletal organisations of different cells within the same tissue culture. However, in general T15 cells were highly polarised and typically showed very few high order actin structures (Figure 68A, page 19), while K2 cells were generally well spread and often exhibited many stress fibres (Figure 70A, page 19). FLAP studies revealed that these two major phenotypes were often associated with dramatically different actin dynamics.

Figure 68 shows images taken from an example T15 sarcoma cell FLAP experiment. Images (A, C, & E) represent overlays of ECFP-β-actin (red) and EYFP-β-actin (green) fluorescence channels. In (A) the images appear yellow due to the perfect co-localisation of the two subpopulations of differentially labelled β-actin molecules. A narrow strip of EYFP-β-actin was selected across the leading edge of the cell for photobleaching (indicated by the purple box) in order to assess the subsequent dynamics of the photolabelled β-actin molecules. (A) was acquired prior to bleaching while (C & E) were acquired at increasing time points following the bleaching event. Note the loss of the EYFP signal within the defined bleach region in image (C), which was acquired immediately after the photobleaching event (the image time stamp is defined as 0 s to indicate the first image acquired post-photobleaching). Images (B, D, & F) represent FLAP ratio images and are calculated as 1 minus the ratio of target (EYFP) to reference fluorophore (ECFP) intensity. Each pixel value within a FLAP

ratio image represents the relative concentration of bleached EYFP-β-actin molecules, expressed as a fraction of total number of expected EYFP-β-actin molecules (bleached and unbleached) at that location. (D & F) indicate the subsequent distribution of photolabelled actin molecules at increasing time points following the photobleaching event. The FLAP ratio images reveal that EYFP-β-actin molecules bleached within the narrow strip rapidly accumulate at regions of protrusion at the leading edge of the cell (D, purple arrows). The time taken to bleach the strip was 1.8 s and then image (D) was then acquired 2 s later. Photolabelled actin had therefore managed to accumulate within the very leading edge of the cell within an extremely short period of time. Indeed, the most distant point at which photolabelled β-actin accumulation can be observed lies 12 μm from the top of the bleach strip. It has been estimated that this actin would be required to translocate at a speed of at least 6 μm/s in order to cover this distance within this time interval. As this speed is greater than that which could be achieved by the diffusion of actin alone (based on diffusion modelling performed by Graham Dunn) this suggests that a mechanism of active transport may be involved in delivering actin to sites of active protrusion. It is also interesting to note from this image that photolabelled actin within the bleach region tended to persist longest within the cell cortex, indicating that a less mobile pool of actin existed within these regions. Image F represents an image acquired 60 s following the initial bleaching event and demonstrates that the photolabelled actin has almost completely dispersed from the photobleached region indicating the highly dynamic nature of actin within this cell.

Figure 69, page 19 shows FLAP ratio images from another T15 sarcoma cell experiment where the time-lapse interval between sequential acquisitions was far lower than for

Figure 68. Again the photolabelled actin rapidly and preferentially accumulated within the leading edge of the cell (purple arrows). In contrast relatively little actin was found to disperse below the bleach strip. Over time photolabelled β-actin appeared to flow radially towards the cell body from the leading edge (white arrows). The persistence of photolabelled β-actin within this region suggests that it had become incorporated into filaments and was undergoing retrograde flow.

In contrast to the highly polarised morphology of T15 cells, the K2 cells were often well spread and dense with stress fibres. In these cells actin appeared to be far less dynamic. Figure 70 shows images taken from an example K2 FLAP experiment and the time points shown are comparable to those for Figure 68. A thin strip of EYFP-β-actin was bleached across the cell, perpendicular to the orientation of the underlying stress fibres. Within this region β-actin was found to be highly stable and initially no significant dispersal of the photolabelled actin was observed following the bleach event. Even after a minute had elapsed the highest relative concentration of photolabelled actin was still confined to the bleach strip indicating the relatively un-dynamic nature of β-actin within these structures. The FLAP technique therefore revealed some distinct differences in the underlying actin dynamics of T15 and K2 sarcoma cells.

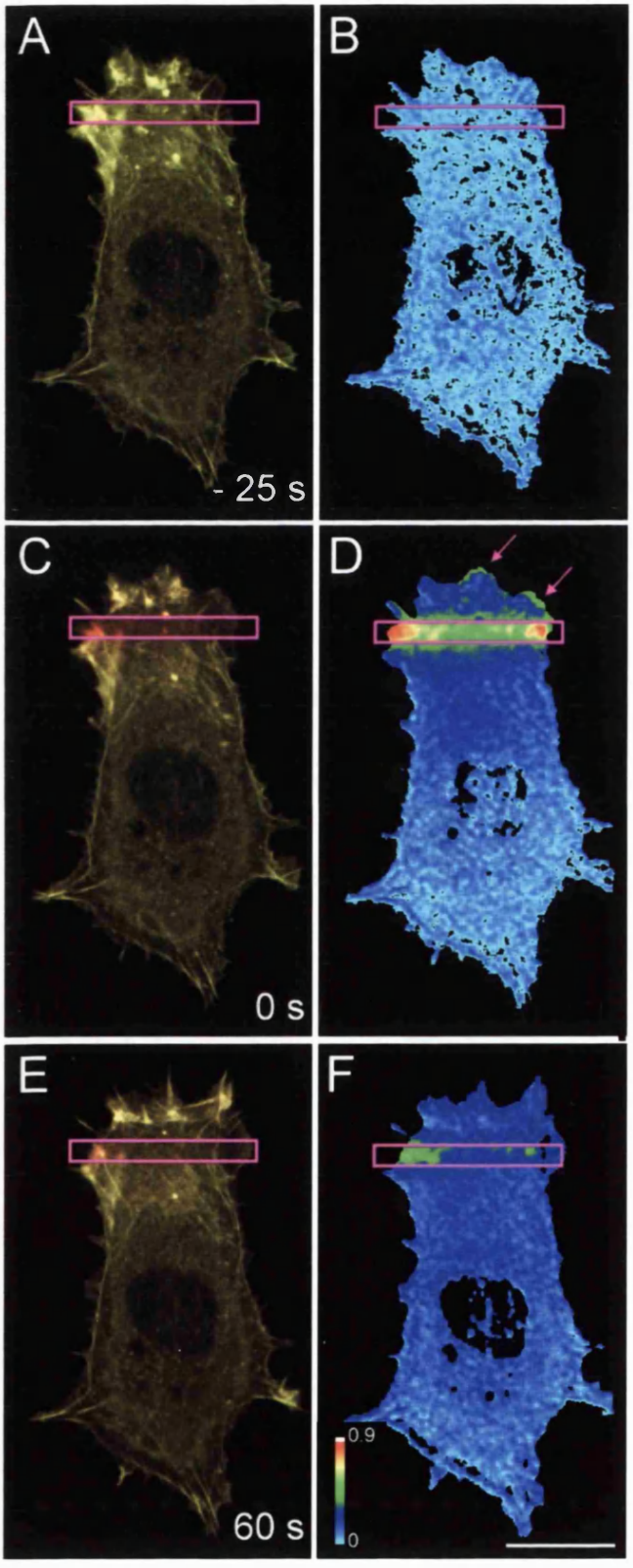

Figure 68. Actin dynamics in the leading edge of a T15 sarcoma cell

Images taken from an example T15 FLAP experiment. Images (A,C, & E) represent overlays of ECFP-β-actin and EYFP-β-actin fluorescence. The purple box indicates the strip across the leading edge of the cell selected for the photobleaching of EYFP-β-actin. Time stamps indicate time relative to the acquisition of the first image post photobleaching. Images (B, D, & F) represent processed FLAP ratio images for (A, C, & E) respectively. Pixel values from ratio images represent 1 minus the ratio of target (EYFP) to reference fluorophore (ECFP) intensity. Purple arrows highlight the accumulation of photolabelled β-actin at the tips of the leading edge of the cell. Scale bar = 20 μm.

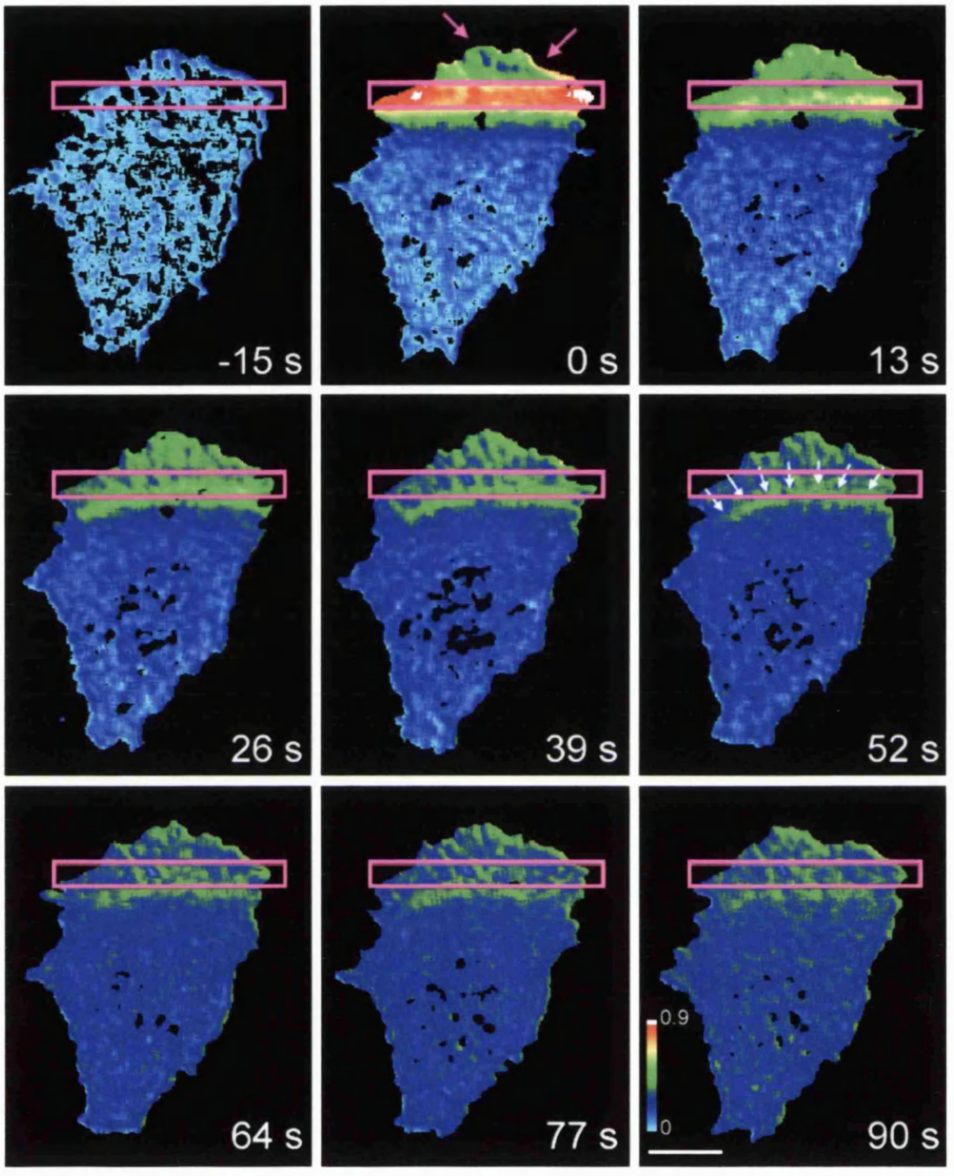

Figure 69. High temporal resolution imaging of actin dynamics in a T15 sarcoma cell

FLAP ratio images calculated for a T15 FLAP experiment where image acquisition was rapid. The purple box indicates the region selected for the selective photobleaching of EYFP-β-actin and time stamps indicate time relative to the acquisition of the first image post photobleaching. Purple arrows in time frame 0 s highlight the accumulation of photolabelled actin within the tips of the leading edge immediately after the bleaching event. The relatively long duration with which photolabelled actin persisted within the leading edge suggests the incorporation of photolabelled β-actin into filaments. White arrows in time frame 52 s indicate the direction of retrograde flow of photolabelled β-actin. Scale bar = 10 μm.

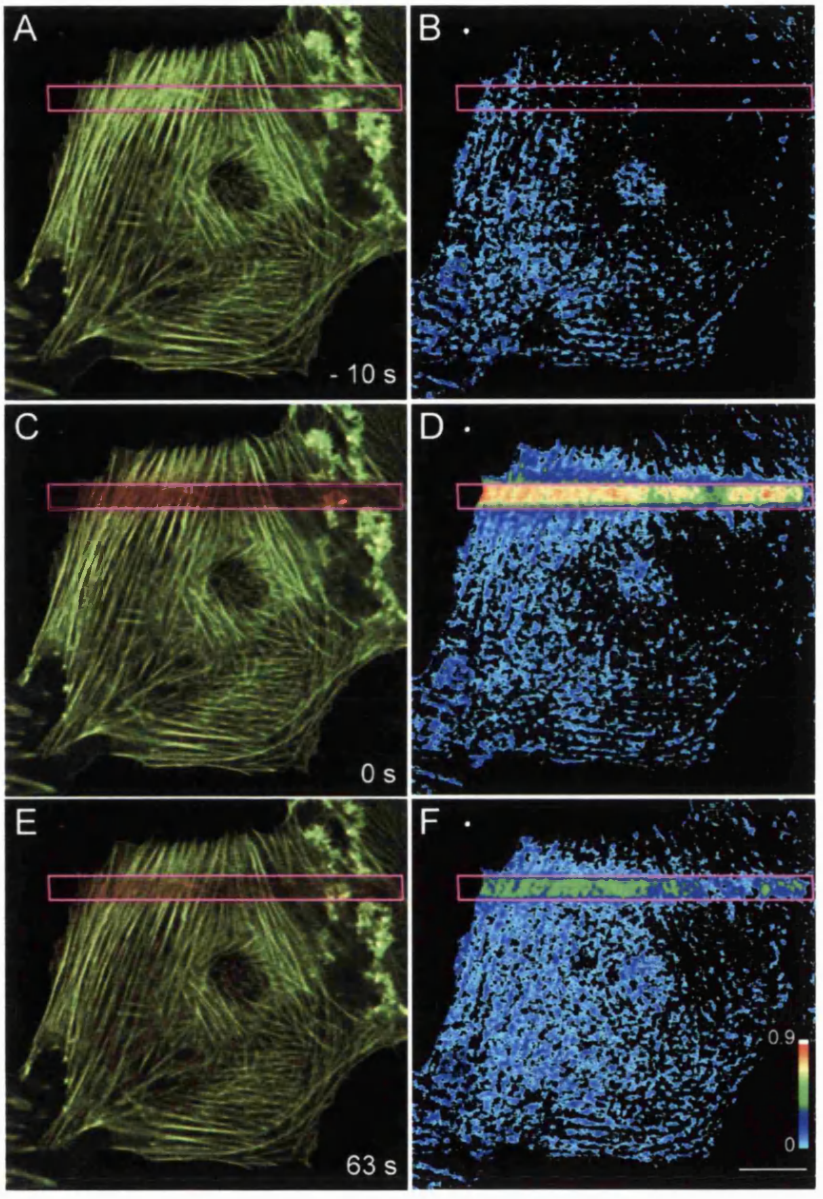

Figure 70. Actin dynamics in a K2 sarcoma cell

Images taken from an example K2 FLAP experiment. Images (A,C, & E) represent overlays of ECFP-β-actin and EYFP-β-actin fluorescence. Images (B, D, & F) represent FLAP ratio images for (A, C, & E) respectively. The purple box indicates the strip selected for the selective photobleaching of EYFP-β-actin. Time stamps indicate time relative to the acquisition of the first image post photobleaching. Unlike their T15 counterparts, K2 cells were often dense with stress fibres. In this example the bleach strip was oriented perpendicular to the underlying stress fibres. Photolabelled β-actin within these structures appeared to be highly stable. Scale bar = 20μm.

3.3.13 Studying Cdc42-related signalling pathways in single cells

Ultimately, an unequivocal confirmation of the precise signalling mechanisms involved in the regulation and control of cell polarity and motility must come from biochemical studies performed in intact living cells. A clear understanding of how protein interactions orchestrate the formation of the complex and highly organized actin ultrastructures that drive changes in cell morphology is a formidable challenge and requires that the relevant signalling components be studied within the context of their natural subcellular environment.

In an attempt to understand more clearly the spatiotemporal dynamics of Cdc42 signalling FLIM/FRET-based studies were conducted to monitor Cdc42/effector interactions *in situ*. Both N-WASP and PAK1 represent key effector targets in the Cdc42-dependent remodelling of the actin cytoskeleton and therefore these proteins provided the main focus of this study. Interactions between N-WASP and the p16 subunit of the Arp2/3 complex were also examined in an attempt to reconstruct a picture of the subcellular localisation of Cdc42/N-WASP/Arp2/3 complex formation, and therefore reveal potential sites of Cdc42-dependent actin polymerisation *in situ*. FLIM based on multiphoton TCSPC imaging was used to reveal the subcellular localisation of Cdc42/N-WASP and N-WASP/Arp2/3 complex formation. Single photon excitation TCSPC and frequency domain FLIM, which sample the entire thickness of the cell as opposed to single optical sections, were used in parallel to provide a more robust, but less spatially informative, analysis of FRET. In all cases FRET was monitored between donor EGFP-N-WASP and a Cy3-conjugated anti-Myc 9E10 monoclonal acceptor antibody (Cy3-mAb) targeted against either Myc-Cdc42 or Myc-p16.

The frequency-domain system, based on a wide field microscope set-up, enabled relatively fast image acquisition in comparison to the time-domain method, which was based on laser scanning of the sample. The relatively rapid acquisition times afforded by this system were exploited for the development of an assay that enabled the dynamics of Cdc42/PAK1 interactions to be monitored live cells. The association of Cdc42 with PAK1 was largely used as an assay to monitor the temporal activation dynamics of Cdc42 *in situ* as opposed to determining the precise localisation of Cdc42/PAK1 complexes within cells, since the system traded spatial resolution for rapid acquisition. For live cell experiments nuclear microinjection was used to introduce expression constructs encoding EGFP-Cdc42 donor and Myc-PAK1 into cells while the additional cytoplasmic microinjection of Cy3-mAb enabled expressed Myc-PAK1 to be subsequently labelled with acceptor. EGF was chosen as the stimulus for live cell experiments because it is one of the few proposed physiological stimulants of N-WASP activity (Vetterkind et al., 2002). All experiments were conducted using the highly motile NIH 3T3 fibroblast cell line.

3.3.14 N-WASP associates constitutively with Cdc42 in NIH 3T3 fibroblasts

Much of our current understanding of N-WASP signalling and activation dynamics has come from biochemical analysis involving the *in vitro* reconstitution of the minimal molecular components required for N-WASP activation and subsequent actin polymerisation. Such studies have provided valuable insight into the underlying mechanisms of N-WASP activation. However, these techniques cannot provide crucial information concerning the dynamics of N-WASP signalling *in situ*. In an attempt to elucidate where and when

N-WASP/Cdc42 complex formation occurs in cells multiphoton TCSPC-based FLIM was used to monitor FRET between ectopically expressed donor EGFP-N-WASP(wt) and Myc-Cdc42(wt) labelled with Cy3-mAb acceptor in fixed NIH 3T3 fibroblasts.

EGFP-N-WASP(wt)/Myc-Cdc42(wt) expressing cells were fixed, labelled with Cy3-mAb, and imaged on the Multiphoton TCSPC system. Imaging revealed that donor fluorescence lifetimes were reduced in the presence of acceptor labelling (Figure 71, page 19 compare C with D), indicating the occurrence of FRET. Interestingly, this demonstrated that EGFP-N-WASP(wt) could associate constitutively with Myc-Cdc42(wt) in unstimulated NIH-3T3 fibroblasts. The high-resolution imaging and optical sectioning afforded by multi-photon microscopy enabled a detailed analysis of the subcellular localisation of EGFP-N-WASP(wt)/Myc-Cdc42(wt) complexes. The relative concentration of FRET species, derived from the analysis of donor fluorescence lifetimes, was calculated for each pixel within an image. RCFS maps revealed that, in the majority of cells imaged, EGFP-N-WASP(wt)/Cy3-Myc-Cdc42(wt) complexes were largely confined to a perinuclear region (Figure 72A, page 19). Additional confocal analysis indicated that this region was likely to be either the Golgi apparatus or a compartment associated with this organelle as partial co-localisation was observed between EGFP-N-WASP(wt) and the Golgi marker giantin (Figure 72B). Rarely FRET could also be observed at the cell periphery, and in cases where expressing cells made contact FRET was also observed at cell junctions (Figure 73, page 19). The lifetime of EGFP in the absence of acceptor was typically around 2.2 ns (Figure 731, page 249) which is similar to the lifetime measurements obtained by others (2.4 ns - Pepperkok et al., 1999).

3.3.15 N-WASP/Cdc42 association is dependent on the nucleotide state of Cdc42

Since N-WASP and Cdc42 were found to associate constitutively in unstimulated cells it was important to determine whether this process was dependent upon the nucleotide state, and therefore activity, of Cdc42. Consequently, additional FLIM/FRET experiments using the frequency domain system were performed to assess the capacity of N-WASP to associate with both wild type and dominant negative forms of Cdc42. Although the frequency domain technique could not afford the same degree of spatial resolution provided by the multiphoton TCSPC technique, wide field imaging enabled lifetime values to be derived from the whole thickness of the cell as opposed to a singe optical section. As the aim of the study was to compare and contrast the relative efficiencies with which N-WASP could associate with wild type and dominant negative forms of Cdc42, the calculation of lifetime values from a greater cell volume was more desirable as it provided a more robust FRET analysis.

Unstimulated NIH 3T3 fibroblasts expressing either EGFP-N-WASP(wt)/Myc-Cdc42(wt) or N-WASP(wt)/Myc-Cdc42(T17N) were fixed and either labelled with Cy3-mAb acceptor or left unlabelled as a control for donor lifetime before subsequent imaging. In agreement with previous findings based on multiphoton TCSPC analysis, the frequency domain technique also revealed a constitutive association between EGFP-N-WASP(wt) and Myc-Cdc42(wt) in unstimulated cells (Figure 74, page 19). Scatter plots of pixel lifetime values pooled from a number of images revealed a clear reduction in both the τ_φ and τ_m lifetimes of EGFP-N-WASP(wt) when in the presence of Myc-Cdc42(wt) acceptor labelling (Figure 75, page 19). However, FRET was not detected between EGFP-N-WASP(wt) and the dominant negative

variant of Cdc42, Myc-Cdc42(T17N), indicating that these proteins could not interact in cells (Figure 76, page 19). This was further confirmed from the analysis of τ_φ and τ_m donor lifetime pixel values which did not vary for EGFP-N-WASP when either in the presence or absence of Myc-Cdc42(T17N) acceptor labelling (Figure 77, page 19). Interestingly, in the absence of Cdc42 association N-WASP was found to reside largely within the nucleus (compare Figure 74 A & C with Figure 76 A & C). This demonstrated that Cdc42 activation was required for the recruitment of N-WASP to the perinuclear environment.

3.3.16 N-WASP associates with Arp2/3 in the presence of Cdc42

Additional studies were performed in order to examine the effects of Cdc42 expression on the interaction of N-WASP with the Arp2/3 complex. NIH 3T3 fibroblasts were co-microinjected with expression constructs encoding EGFP-N-WASP(wt) and Myc-p16 and either with or without HA-Cdc42(wt). Cells were then fixed and either labelled with Cy3-mAb acceptor or left unlabelled as controls for donor lifetime before imaging using single photon TCSPC.

Analysis of donor fluorescence lifetimes revealed that EGFP-N-WASP(wt)/Myc-p16 association could only occur in the presence of HA-Cdc42 (Figure 78, page 19 compare C with G). Furthermore, co-expression of the GTPase binding deficient N-WASP mutant EGFP-N-WASP(H211D) with p16 did not result in a reduction in the donor lifetime even in the presence of HA-Cdc42 (Figure 78K), confirming that N-WASP/p16 association was Cdc42 dependent. Again, EGFP-N-WASP was largely confined to the nucleus in the absence of Cdc42 binding (Figure 78 compare A, B, I & J with E & F). As previous experiments

showed that N-WASP could only associate with the GTP-loaded, active form of Cdc42 these findings collectively suggest that a GTP-Cdc42/N-WASP/Arp2/3 complex could form *in situ*.

Additional multiphoton TCSPC imaging revealed that the highest relative concentration of FRET species for EGFP-N-WASP(wt) when co-expressed with Myc-p16 and HA-Cdc42(wt) was largely confined to the same perinuclear compartment observed for EGFP-N-WASP when co-expressed with Myc-Cdc42 (Figure 79, page 19). Again, confocal analysis revealed that this region often exhibited partial co-localisation with the Golgi apparatus, as determined from the Cy5-labelling of the Golgi marker giantin (Figure 79 D & G, F & I). FRET was rarely observed at the cell periphery (1 out of 8 fields imaged) and in cases where microinjected cells made contact FRET could also be observed at cell junctions. Therefore the subcellular localisation of EGFP-N-WASP/Arp2/3 complexes mirrored that found for N-WASP/Cdc42.

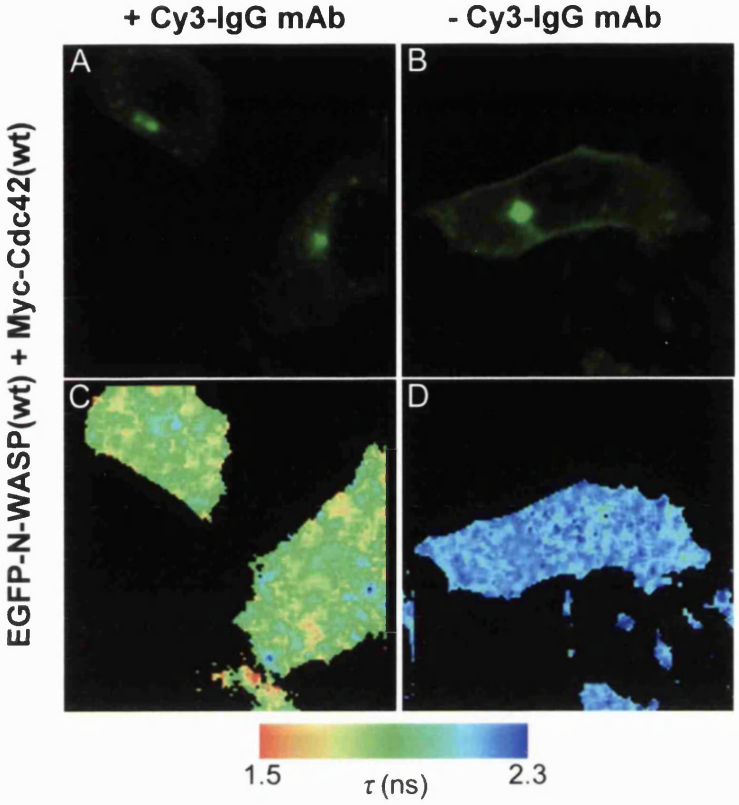

Figure 71. N-WASP/Cdc42 association in situ

Images of fixed NIH 3T3 fibroblasts acquired using the multiphoton, TCSPC system. Images represent donor fluorescence intensity (A & B) and associated lifetime maps (C & D) for cells expressing EGFP-N-WASP(wt) & Myc-Cdc42(wt), either in the presence (A & C) or absence (B & D) of Cy3-mAb acceptor labelling. Lifetime images are presented in pseudocolour, defined by the associated scale. The occurrence of FRET results in an overall shortening of pixel lifetimes. Images processed by Tony Ng.

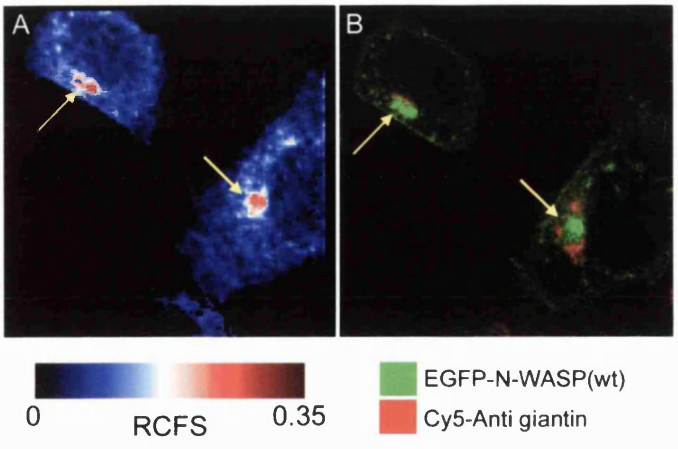

Figure 72. The localisation of N-WASP/Cdc42 association in situ

RCFS map and confocal image of the cells displayed in Figure 71, (A & C). The RCFS map reveals the relative concentration of donor fluorophore undergoing FRET within each image pixel (A). (B) represents a confocal section taken through the equatorial plane of the cells and demonstrates the partial co-localization of EGFP-N-WASP(wt) with the Golgi marker Giantin, labelled with a Cy5-mAb (yellow arrows). For the majority of cells images (7 of 10 fields of view), EGFP-N-WASP(wt)/Myc-Cdc42(wt) interaction was predominantly confined to this region (A & B yellow arrows). Images processed by Tony Ng.

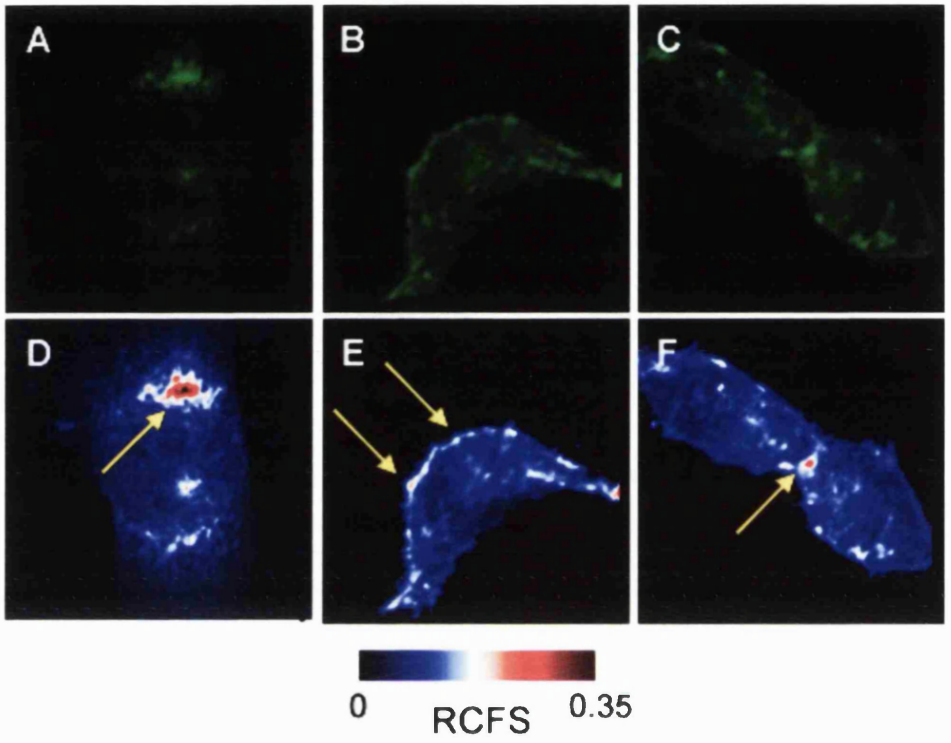

Figure 73. Differing patterns of N-WASP/ Cdc42 localisation in situ

Multiphoton donor fluorescence images (A – C) and associated RCFS maps (D – F) demonstrating the various subcellular regions in which EGFP-N-WASP/Myc-Cdc42 complexes were detected in fixed NIH 3T3 fibroblasts. Images represent single optical sections taken through the equatorial plane of the cell. FRET was most commonly observed in the perinuclear region (D). More rarely FRET was also observed at the cell periphery (E) and, in cases where microinjected cell made contact, also at cell junctions (F). Images represent 3 of 10 fields of view acquired. Arrows highlight regions where the relative concentration of FRET species was greatest. Images processed by Tony Ng.

Figure 74. N-WASP/Cdc42 association measured by frequency domain FLIM

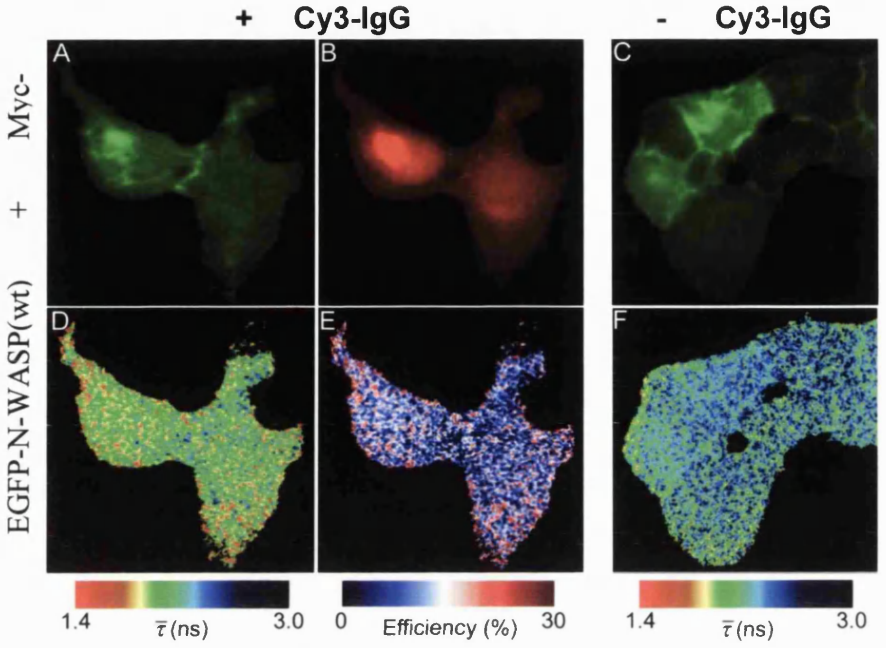

Images of fixed NIH 3T3 fibroblasts acquired using the frequency domain FLIM system. Images represent cells expressing EGFP-N-WASP(wt) and Myc-Cdc42(wt) either in the presence (A, B, D & E) or absence (C & F) of Cy3-mAb acceptor labelling. A and B are wide-field images and show EGFP-N-WASP(wt) and Cy3-mAb labelled Myc-Cdc42(wt) fluorescence respectively indicating the presence of both donor and acceptor fluorophores within the cells. D is the associated lifetime map of donor fluorescence where each pixel value is an average, τ, of independently derived τ_φ and τ_m lifetimes. E is a map of FRET efficiency indicating the extent to which FRET occurred within the cell. C and F are control images of a group of EGFP-N-WASP(wt)/Myc-Cdc42(wt) expressing cells where acceptor labelling had been omitted. C is a wide-field image showing EGFP-N-WASP(wt) fluorescence and F, the associated donor lifetime map. Average donor pixel lifetime values were reduced when Cy3-mAb acceptor labelling was present compare (D with F). Pseudocoulred images are defined by their accompanying scales. Images processed by Tony Ng.

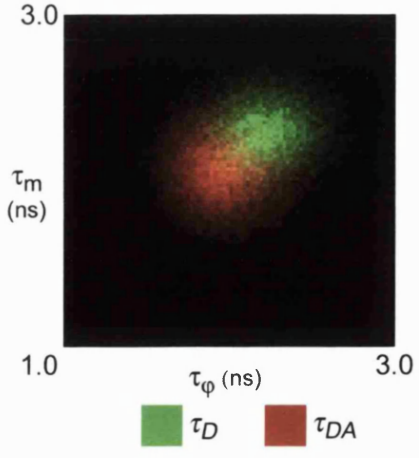

Figure 75. Lifetime scatter plots for N-WASP in the presence of Cdc42(wt) acceptor

Scatter plots of τ_φ and τ_m donor lifetime pixel values from images of cells expressing EGFP-N-WASP(wt)/Myc-Cdc42(wt) either in the presence (τ_{DA}) or absence (τ_D) of Cy3-mAb acceptor labelling. Associated τ_φ and τ_m lifetime valued calculated for each pixel within an image are plotted against one another. Each cluster of values represents lifetime plots pooled from a number of images (N = 16 and N = 9 for τ_D and τ_{DA} respectively). FRET results in a fall in both τ_φ and τ_m lifetime values and is therefore seen as a relative downward diagonal shift in the τ_{DA} values compared to that of τ_D.

Figure 76. N-WASP/Cdc42(T17N) association measured by frequency domain FLIM

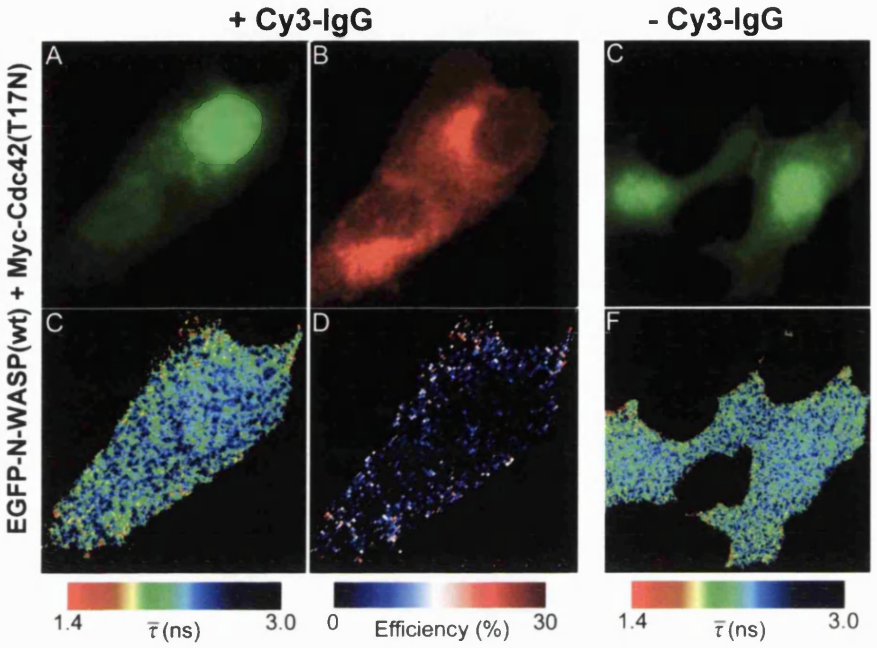

Images of fixed NIH 3T3 fibroblasts acquired using the frequency domain FLIM system. Images represent cells expressing EGFP-N-WASP(wt) and Myc-Cdc42(T17N) either in the presence (A, B, D & E) or absence (C & F) of Cy3-mAb acceptor labelling. Images A, B, D & E represent the same group of EGFP-N-WASP(wt)/Myc-Cdc42(T17N) expressing cells in the presence of acceptor labelling, while images C and F are of EGFP-N-WASP(wt)/Myc-Cdc42(T17N) expressing cells where acceptor labelling has been omitted. Image panels are as described for Figure 74. The lifetime of the donor fluorophore remains unchanged when either in the presence (C) or absence (F) of acceptor labelling, therefore demonstrating the inability of N-WASP to interact with the dominant negative form of Cdc42. Images processed by Tony Ng.

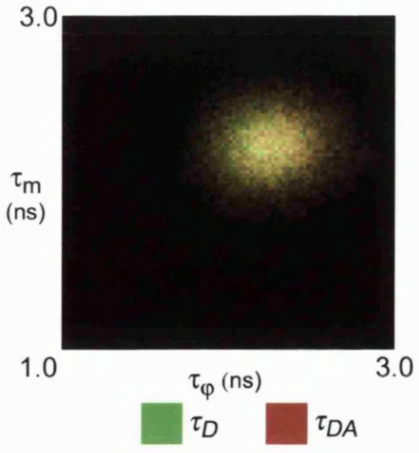

Figure 77. Lifetime scatter plots for N-WASP in the presence of Cdc42(T17N) acceptor

Scatter plots of τ_φ and τ_m donor lifetime pixel values from images of cells expressing EGFP-N-WASP(wt)/Myc-Cdc42(T17N) either in the presence (τ_{DA}) or absence (τ_D) of Cy3-mAb acceptor labelling. Individual τ_φ and τ_m pixel lifetime values are plotted against one another and each scatter represents pixel from a number of images (N = 16 and N = 9 for τ_D and τ_{DA} respectively). No discernable diagonal shift is seen between τ_{DA} and τ_D values, indicating an absence of FRET between donor EGFP-N-WASP(wt) and acceptor Cy3-mAb-Myc-Cdc42(T17N).

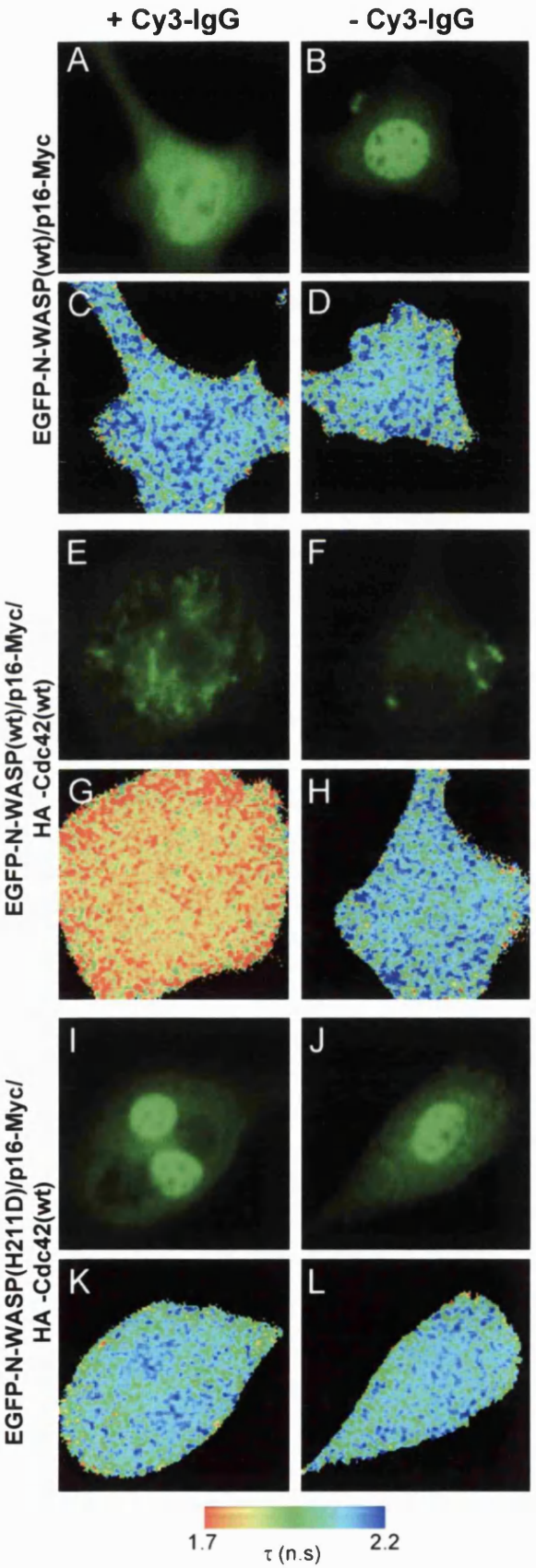

Figure 78. N-WASP/Arp2/3 association requires Cdc42

Images of fixed NIH 3T3 fibroblasts acquired using single-photon excitation, TCSPC. Panels A, B, E, F, I & J represent images of EGFP-N-WASP donor fluorescence while panels C, D, G, H, K & L represent their respective fluorescence lifetime maps. Cells were co-microinjected with constructs encoding either EGFP-N-WASP(wt) and Myc-p16 (A - D), EGFP-N-WASP(wt), Myc-p16 and HA-Cdc42(wt) (E - H), or EGFP-N-WASP(H211D), Myc-p16 and Cdc42-HA(wt) (I – L). Following fixation, cells were either labelled with Cy3-mAb targeted against the expressed p16 (left hand column) or left unlabelled as controls for donor fluorescence lifetime in the absence of acceptor (right hand column). All cells were also labelled with anti-HA Cy5-IgG in order to confirm Cdc42 expression. TCSPC was conduct using single photon excitation in order to acquire information from the entire thickness of the cell, therefore providing a more robust FRET analysis while sacrificing spatial resolution. A reduction in the lifetime of the donor when in the presence of Cy3-mAb acceptor is indicative of FRET (compare lifetime maps in the left column with those in the right). FRET between EGFP-N-WASP donor and Cy3-mAb-Myc-p16 acceptor was only observed when co-expressed with Cdc42 (G). Lifetime maps are in pseudocolour defined by the accompanying scale. Images processed by Tony Ng.

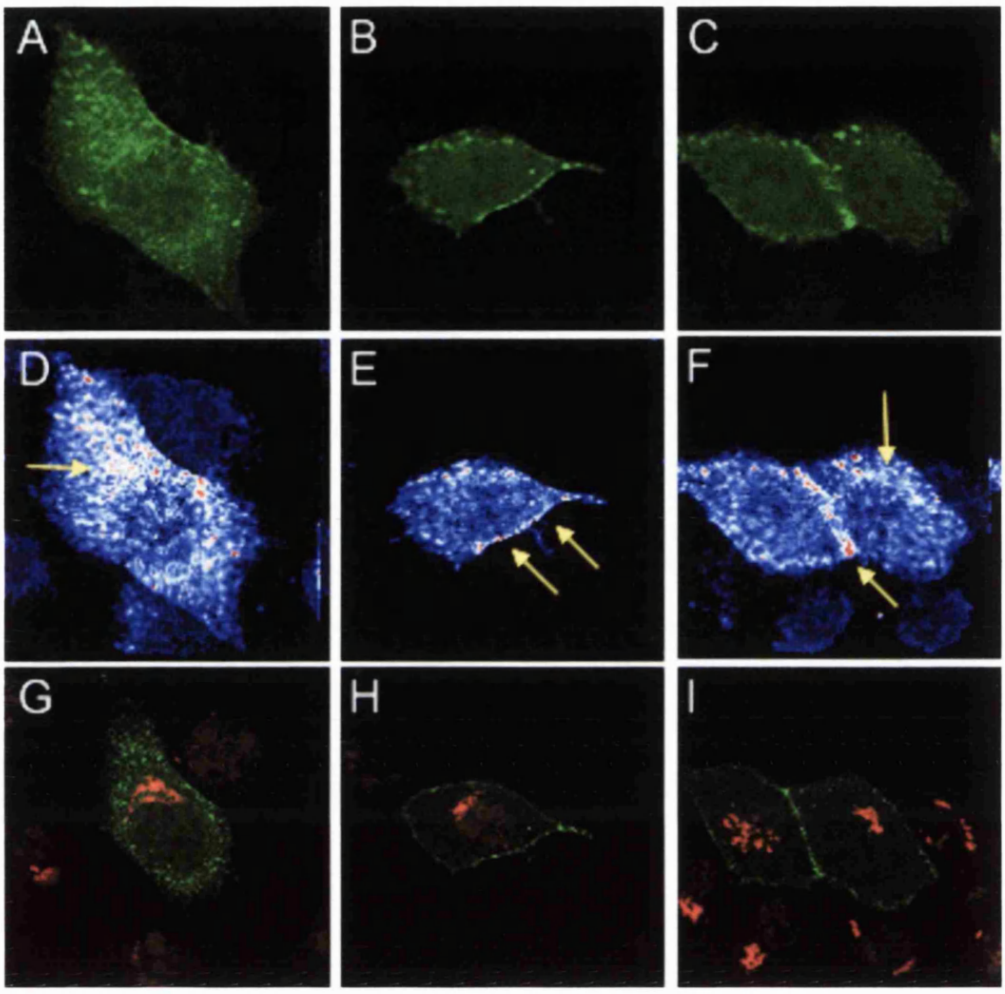

Figure 79. Localisation of N-WASP/Arp2/3 association in situ

Multiphoton donor fluorescence images (A – C), associated RCFS maps (D – F), and confocal sections (G – I) demonstrating the various subcellular regions in which EGFP-N-WASP/Arp2/3 complexes were detected in fixed NIH 3T3 fibroblasts. In addition to EGFP-N-WASP localisation (green) confocal images also show the location of the Golgi compartment as determined using a Cy5-anti giantin antibody (red). All images represent single optical sections taken through the equatorial plane of the cell. The subcellular localisation of N-WASP/Arp2/3 association mirrored that seen for N-WASP/Cdc42. FRET was most commonly observed in the perinuclear region (D), which showed partial co-localisation with the Golgi marker giantin (G). More rarely FRET was also observed at the cell periphery (E) and at cell junctions (F). Images represent 3 of 8 fields of view acquired. Arrows highlight regions where the relative concentration of FRET species was greatest. Images processed by Tony Ng.

3.3.17 EGF stimulates Cdc42 activation and association with PAK1

It was important to establish whether Cdc42 activation could be detected following the administration of physiological stimulants to NIH 3T3 cultures using FLIM/FRET analysis. Given that Cdc42 could interact constitutively with N-WASP in unstimulated NIH 3T3 fibroblasts, the activation dynamics of Cdc42 was studied through its ability to associate with PAK1. Live cell FLIM/FRET experiments were designed to investigate whether growth-factor stimulation could induce Cdc42/PAK1 association *in situ*.

A duel microinjection-frequency domain FLIM/FRET assay was developed for detecting the active GTP-bound form of EGFP-Cdc42(wt) in living cells. NIH 3T3 fibroblasts were microinjected in the nucleus with expression constructs encoding EGFP-Cdc42(wt) and Myc-PAK1(wt), and following detection of EGFP fluorescence were then re-microinjected in the cytoplasm with Cy3-mAb before subsequent imaging on the frequency domain system. Cells were then stimulated with 100 ng/ml EGF and then imaged at increasing time points over a 45 min period. The technique was similar in principle to that previously used for the intensity-based FRET analysis of EGFP-Rac1 activation (Kraynov et al., 2000).

The stimulation of cells with 100 ng/ml EGF rapidly induced EGFP-Cdc42(wt)/Cy3-Myc-PAK1(wt) associated as determined by a reduction in the lifetime of the donor fluorophore (measured as an average of independently derived τ_φ and τ_m lifetime values). Figure 80, page 19 shows the time-course of Cdc42/PAK1 association in a single NIH 3T3 fibroblasts (N = 1 of 4 separate experiments). Although Cdc42 was found to associate constitutively with N-WASP *in situ* this was not generally the case for PAK1. Although basal levels of Cdc42/PAK1 association did vary to a degree between cells, EGF stimulation could enhance

this association. Increased FRET was detectable as soon as six minutes following cell stimulation and remained detectable for the entire period observed. No significant change in donor lifetime was seen for control cells during the course of experiments.

3.3.18 Cdc42/PAK1 association is dependent on the nucleotide state of Cdc42

Parallel FLIM/FRET assays using fixed cell specimens were conducted to establish whether EGF-induced Cdc42/PAK1 association was dependent on the nucleotide state of the GTPase. NIH 3T3 fibroblasts co-expressing either EGFP-Cdc42(wt)/Myc-PAK1(wt) or EGFP-Cdc42(T17N)/Myc-PAK1(wt) were stimulated with 100 ng/ml EGF for 16 min, fixed, and then either labelled with Cy3-mAb or left unlabelled as a control before subsequent FLIM analysis using the frequency domain system. The analysis of donor lifetimes revealed that only the wild-type form of Cdc42 could associate with PAK1 following growth factor stimulation (Figure 81 D & J, page 19). There was no apparent change in the lifetime of EGFP-Cdc42(T17N) in the presence of Myc-PAK1 acceptor labelling when compared to the unlabelled controls (Figure 81 compare F with R) following EGF stimulation. These findings provide evidence that Cdc42/PAK1 association depends on both EGF stimulation and the nucleotide state of Cdc42.

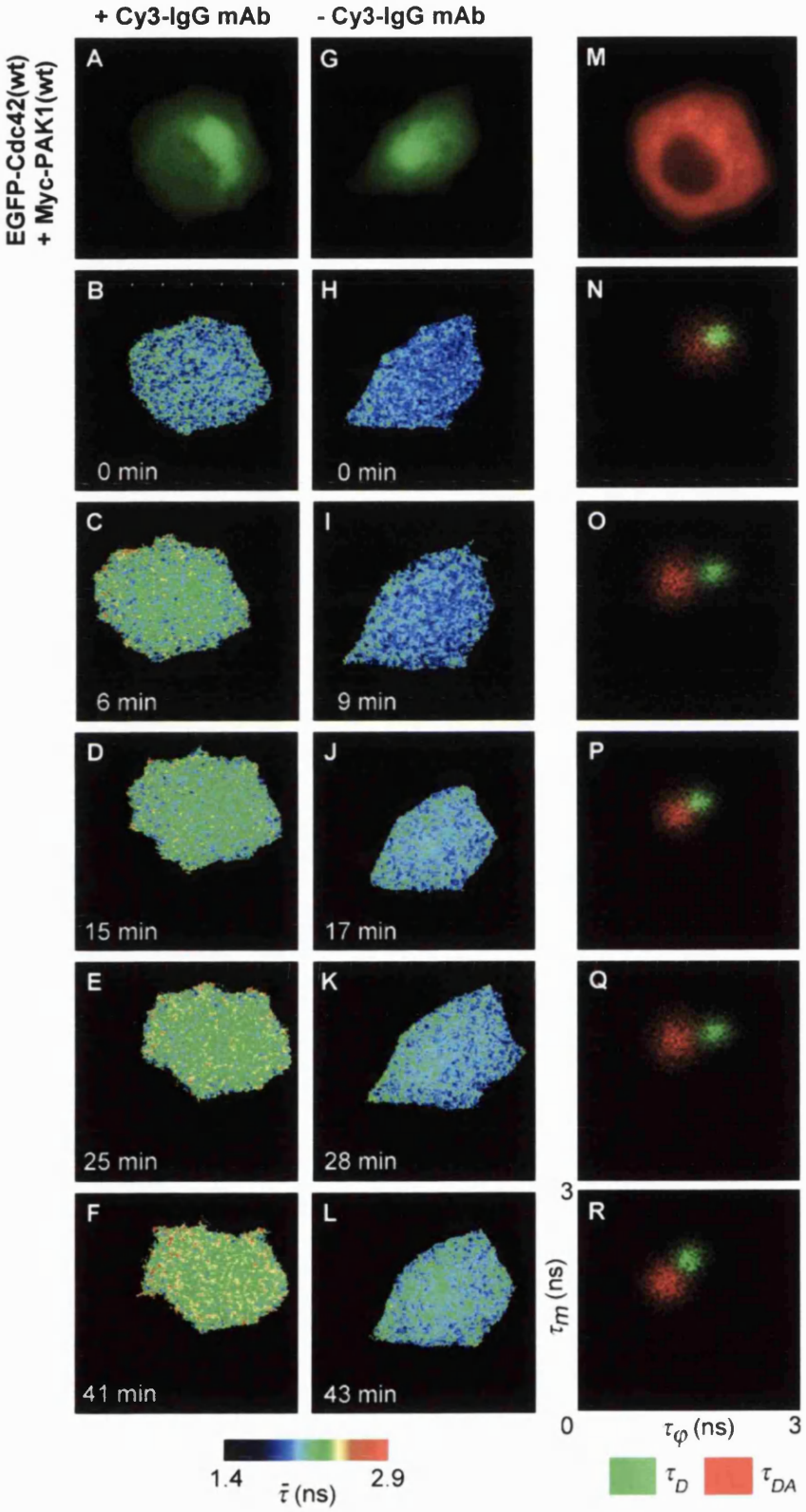
+ Cy3-IgG mAb
- Cy3-IgG mAb
EGFP-Cdc42(wt)
+ Myc-PAK1(wt)
A
G
M
B
0 min
H
0 min
N
C
6 min
I
9 min
O
D
15 min
J
17 min
P
E
25 min
K
28 min
Q
F
41 min
L
43 min
R
3
τ_m (ns)
0
τ_φ (ns)
3
1.4
$\bar{\tau}$ (ns)
2.9
τ_D
τ_{DA}

Figure 80. Imaging Cdc42 activation in living cells (previous page)

Wide field images, fluorescence lifetime maps and scatter plots from an example live cell FLIM/FRET experiment demonstrating the EGF dependent association of EGFP-Cdc42(wt) with Myc-PAK1(wt) in NIH 3T3 fibroblasts. EGFP-Cdc42(wt)/Myc-PAK1(wt) expressing cells were either microinjected in the cytoplasm with a Cy3-mAb against the Myc epitope of PAK1 or left uninjected to provide donor lifetime controls. (A & M) are wide field images of EGFP-Cdc42(wt) and Cy3-mAb fluorescence respectively, indicating the presence of both donor and acceptor fluorophores within the same cell. (G) is a wide field image of EGFP-Cdc42(wt) fluorescence taken from a control cell that was not microinjected with acceptor antibody. Image sequences (B – F) and (H – L) represent pseudocoloured lifetime maps of donor EGFP-Cdc42(wt) fluorescence for the Cy3-mAb microinjected cell and control cell respectively. Images were acquired at increasing time points following stimulation with 100 ng/ml EGF. Images (N – R) are the corresponding scatter plots of τφ and τm pixel lifetime values for (B – F) (τ_{DA}) and (H – L) (τ_D) respectively. The two cells shown were from the same experimental culture. Pseudocoloured lifetime and maps are defined by the lower scale. Images processed by Tony Ng.

Figure 81. The nucleotide state of Cdc42 is critical for PAK1 association (following page)

Wide field images, fluorescence lifetime maps and efficiency maps from fixed cell FLIM/FRET experiment demonstrating the dependency of EGF induced PAK1 targeting on the wild type form of Cdc42. (A, G, B & H) represent donor EGFP-Cdc42(wt) and acceptor Cy3-mAb/Myc-PAK1(wt) fluorescence images, and the donor fluorescence lifetime map, and FRET efficiency map for a representative EGFP-Cdc42(wt)/Myc-PAK1 expressing cell in the absence of EGF stimulation (0 min). (M & N) represent the donor EGFP-Cdc42(wt) fluorescence and lifetime map of a control cell at the same time point where acceptor labelling has been omitted. (C, I, D & J) as for (A, G, B & H) and (O & P) as for (M & N) but following 16 min stimulation with 100 ng/ml EGF. (E, K, F & L) represent donor EGFP-Cdc42(T17N) and acceptor Cy3-Myc-PAK1(wt) fluorescence images, and the donor lifetime map, and FRET efficiency map for an EGFP-Cdc42(T17N)/Myc-PAK1(wt) expressing cell following 16 min EGF stimulation. (Q & R) represent the donor fluorescence and lifetime map of the associated control. FRET is only noticeable between the wild-type form of EGFP-Cdc42 and Cy3-mAb-Myc-PAK1, and is dependent upon EGF stimulation. Pseudocoloured lifetime and efficiency maps are defined by the scales found below each relevant column. Images are of example cells taken from 1 of 5 independent measurements for each time point. Images processed by Tony Ng.

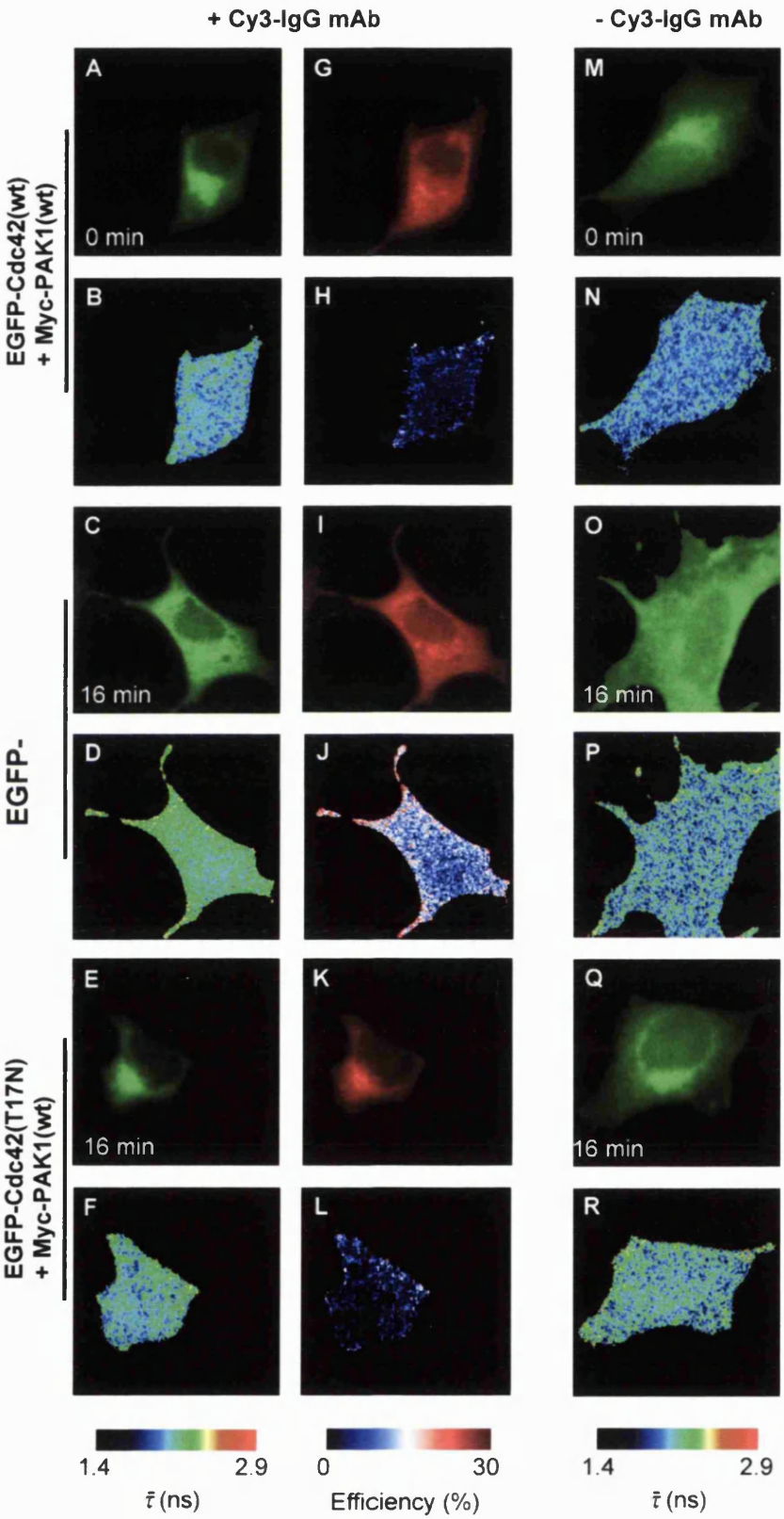
+ Cy3-IgG mAb
- Cy3-IgG mAb
EGFP-Cdc42(wt) + Myc-PAK1(wt)
EGFP-
EGFP-Cdc42(T17N) + Myc-PAK1(wt)
A
G
M
0 min
B
H
N
C
I
O
16 min
D
J
P
E
K
Q
16 min
F
L
R
1.4
2.9
τ (ns)
0
30
Efficiency (%)
1.4
2.9
τ (ns)

3.4 DISCUSSION

Chemotaxis is a basic but essential form of cell behaviour that is known to contribute to the development of numerous diseases including cancer metastasis. Tumour cells are known to preferentially chemotax towards growth factors and tissue extracts derived from organs that commonly represent their *in vivo* targets of metastasis (Hujanen and Terranova, 1985; Jacob et al., 1999), while growth factors associated with the vasculature are believed to guide tumour cells towards local blood vessels or lymphatics during the initial stages of intravasation (Wyckoff et al., 2000a; Wyckoff et al., 2000b). As the blood burden of trafficking tumour cells has been reported to correlate strongly with the frequency of metastases in target organs (Wyckoff et al., 2000a), intravasation is likely to provide a limiting step in the metastatic spread of certain cancers. Given the importance of chemotaxis in intravasation, elucidation of the molecular components responsible for regulating this behaviour is of significant interest to the cancer field. The identification of the key molecules that control the chemotaxis of cancer cells could prove useful in the development of therapeutic strategies for the treatment of metastatic disease. The rational development of drugs that block the ability of tumour cells to infiltrate the vasculature and lymphatics during intravasation, or the surrounding tissue of capillary beds within target organs during extravasation could significantly impair the process of cancer spread.

In this study the T15 rat sarcoma cell line, which exhibits high metastatic potential *in vivo* (Vesely et al., 1987), was used as a model for the study of metastatic cancer cell chemotaxis. PDGF-BB and IGF-1, two growth factors commonly associated with the vasculature and which are likely to be present in the tumour microenvironment *in vivo,* provided the

chemotactic stimulus. Cells were exposed to growth factor gradients using the direct viewing Dunn chemotaxis chamber and their resulting behaviour recorded using time-lapse microscopy. Microinjection was used to deliver expression constructs encoding EGFP fusions of wild type or dominant negative forms of the various proteins under investigation into cell nuclei in order to assess the effects of protein expression on both the chemotactic and motile behaviour of cells. The interactive tracking and subsequent statistical analysis of film data enabled changes in the directional response of cells to be assessed independently from changes in cell speed. Variations in both the efficiency and the profile of expression that existed between some of the different EGFP fusion proteins studied required the application of further analytical techniques to assess whether their differential effects on motility were still apparent at comparable levels of expression.

The proteins Cdc42, Tc10, N-WASP, and PAK1 provided the main focus of this study as previous reports have implicated them in the control of a range of polarity events in other mammalian cell models. However, the role of these proteins in the chemotaxis of cancer cells has previously not been assessed. A total of 75 individual chemotaxis experiments were conducted to analyse the role of these proteins in the chemotaxis of sarcoma cells. Findings from this study demonstrated that while Cdc42, Tc10, N-WASP, and PAK1 were all required for efficient cell motility only PAK1 was required for the chemotaxis of sarcoma cells in gradients of PDGF-BB and IGF-1. Inhibition of motility and/or chemotaxis was only associated with the dominant negative forms of the various proteins studied indicating that their inhibitory effects were a specific consequence of the mutations that these proteins

conferred. Wild type proteins did not inhibit motility or chemotaxis but in certain cases actually enhanced cell speed.

3.4.1 Cdc42, Tc10 and N-WASP regulate sarcoma cell motility but not directionality

That Cdc42 was not required for the chemotaxis of sarcoma cells was somewhat surprising as a number of independent reports have identified this protein as an essential mediator of chemotaxis in other cell systems. Cdc42 appears to be a common mediator of chemotaxis in cells of haematopoietic origin. Hadad and co-workers have shown that the SDF-1 driven chemotaxis of T lymphocytes is dependent upon Cdc42 function and that this process specifically requires the interaction of Cdc42 with its downstream effector WASP (Haddad et al., 2001). In agreement with these findings Allen and co-workers have shown that the CSF-1 induced chemotaxis of the Bac-1 macrophage cell line can be blocked following microinjection of the dominant negative Cdc42 variant, Cdc42(T17N) (Allen et al., 1998). The chemotaxis of primary macrophages towards CSF-1 is abolished in patients suffering from WAS, an immunodeficiency disorder associated with germline mutations in the WASP gene (Zicha et al., 1998). Independent studies have also shown that monocytes isolated from WAS patients fail to polarise and chemotax in response to gradients of either monocyte chemoattractant protein-1 (MCP-1) or macrophage inflammatory protein-1α (MIP-1α), two potent leukocyte chemoattractants (Badolato et al., 1998). Taken together these findings strongly implicate Cdc42/WASP dependent signalling in the chemotaxis of haematopoietic cells. Furthermore, while CSF-1 targets tyrosine kinase receptors, SDF-1, MCP-1 and MIP-1α bind serpentine receptors indicating that Cdc42/WASP pathways have the potential to integrate chemotactic signals originating from a variety of receptor types.

The Cdc42 independent chemotaxis of sarcoma cells in gradients of PDGF-BB/IGF-1 is a finding that may highlight a fundamental difference in the underlying mechanisms that regulate the chemotaxis of immune cells and certain tumour cells. In order to explore whether Cdc42 independent chemotaxis was a unique property of the T15 sarcoma cell line or whether it was a property shared by other cells of mesenchymal origin, the role of this protein was also assessed in the chemotaxis of untransformed fibroblasts. PDGF-BB alone was found to be a potent chemoattractant for the Swiss 3T3 fibroblast cell line when used in the Dunn chemotaxis chamber. Interestingly, the chemotactic response of the NIH 3T3 cell line, although significant, was far less pronounced. The Swiss 3T3 cell line was therefore selected in order to further assess the function of Cdc42 in the chemotaxis of untransformed fibroblasts. It was found that the expression of EGFP-Cdc42(T17N) had no significant effect on the chemotactic response of Swiss 3T3s suggesting that Cdc42 was of no importance in the growth factor mediated chemotaxis of fibroblasts and fibroblast-like cells.

Interestingly, Banyard and co-workers have previously reported that Cdc42 function is required for the Rat-1 fibroblast invasion of three-dimensional collagen gels containing PDGF-BB but not for the PDGF-BB induced chemotaxis of these cells as assessed using the Boyden chamber (Banyard et al., 2000). The latter finding would seem to be in agreement with observations made in this study. The authors' findings are important as they reveal how the significance of specific proteins implicated in the control of cell motility can dramatically alter with changes in the cellular environment. Three-dimensional collagen gels represent environments of far greater complexity than simple polycarbonate filters or planar surfaces

such as coverslips. As a consequence the molecular machinery employed by the cell in regulating movement in these markedly differing environments is likely to differ to some extent. Moreover, efficient matrix degradation and the dynamic regulation of adhesions to a three-dimensional extracellular environment are far more likely to be of significance in determining the success of cell migration through collagen gels when compared to cell migration on planar substrates. Although collagen gels are likely to provide a more physiologically relevant environment for the assessment of cell migration their complexity can prove problematic when attempting to dissect the role of various signalling molecules in only a single aspect of this behaviour.

Although Cdc42 function was not found to be of importance in the chemotaxis of sarcoma cells it was, however, necessary for efficient motility. While EGFP-Cdc42(T17N) expressing cells could detect, polarise and migrate towards the source of the chemoattractant they did so more slowly than control cells expressing EGFP alone. Similarly, the assessment of the random motility of NIH 3T3 fibroblasts also demonstrated that Cdc42 function was required for efficient motility in these cells. The observation that Cdc42 inhibition impairs the speed of fibroblast motility is in agreement with findings made by others. Nobes and co-workers have reported an approximate two-fold reduction in the rate at which rat embryonic fibroblasts can infiltrate the underlying substratum in wound healing assays following the ectopic expression of Cdc42(T17N) (Nobes and Hall, 1999). However, in keeping with observations made from chemotaxis experiments, the effects of Cdc42 function on fibroblast motility were in contrast to those that have been reported for macrophages. It is interesting to note that while in this study Cdc42 function was required for efficient sarcoma cell motility

and not chemotaxis, Cdc42 has been reported to be of no importance in macrophage motility despite the essential role of this protein in the chemotaxis of these cells (Allen et al., 1998). Fundamental differences are therefore likely to exist in the way in which cells of mesenchymal origin and cell of haematopoietic origin regulate their motile and chemotactic behaviour.

It was hypothesised that the related Rho GTPase Tc10 may have been of more importance than Cdc42 in the directionality of sarcoma cells given the many similarities that exist between these proteins and given that Cdc42 itself was not implicated in this process in this cell type. Although Cdc42 and Tc10 share many features in common including a high degree of sequence homology (Murphy et al., 1999), shared downstream targets (Abe et al., 2003; Neudauer et al., 1998), and their ability to remodel the actin cytoskeleton and generate similar morphological structures (Neudauer et al., 1998), the role of Tc10 in cell motility had previously not been assessed. Although predominantly expressed in skeletal muscle and adipose tissue where its primary function is in the regulation of insulin-induced glucose uptake (Chiang et al., 2001), Tc10 expression has also been detected in other cell types including fibroblasts and neurons (Drivas et al., 1990). Constitutively active variants of Tc10 can induce cytoskeletal changes similar to those associated with Cdc42 function (Neudauer et al., 1998) and inhibition of the endogenous protein has been reported to block axonal outgrowth in neuronal cells (Abe et al., 2003). Given the importance of Tc10 in the regulation of cytoskeleton and morphogenesis in other cell systems, it provided a logical candidate for study in the chemotaxis of sarcoma cells.

This study revealed that Tc10 was of no importance in the chemotaxis of sarcoma cells. However, Tc10 was required for efficient cell motility. Although findings were similar to those found for Cdc42 they were not identical. While dominant negative variants of Tc10 and Cdc42 both had inhibitory effects on sarcoma cell motility, the overexpression of wild-type Tc10 significantly enhanced cell speed, a finding that was not associated with the overexpression wild type Cdc42. This suggests that the availability of endogenous Tc10 could be a limiting factor in determining the speed of cell motility: while inhibition of the endogenous protein impairs cell motility, an increase in the availability of the protein enhances this process. This study therefore ascribes, for the first time, a role for Tc10 in the regulation of cell motility.

The inability of dominant negative mutants of either Cdc42 or Tc10 to inhibit the chemotaxis of sarcoma cells suggested that a GTPase/WASP-like pathway was unlikely to be responsible for regulating the growth factor-induced chemotaxis of fibroblast like cells. Therefore Cdc42/WASP signalling may form part of a specialised pathway that has specifically evolved to regulate the chemotactic behaviour of cells that exhibit significant motile and chemotactic behaviour *in vivo*. Cells of the immune system are required to respond rapidly and regularly to chemotactic signals that are generated as a result of infection and tissue trauma. The degree to which fibroblasts exhibit chemotaxis *in vivo* is less clear but is likely to be largely confined to times of wound repair and development. Although WASP expression is confined to cells of haematopoietic origin, the related protein N-WASP is ubiquitously expressed, regulating cytoskeletal rearrangement in a wide variety of cell types through its interaction with the Arp2/3 actin-nucleating complex (Takenawa and Miki, 2001). Although N-WASP

function has been the focus of a great deal of study over recent years this has largely been in the context of vesicular transport, morphogenesis, neurite outgrowth, and the intracellular motility of viral and bacterial pathogens. Conversely, little attention has been paid to the role of N-WASP in cell migration. However, recent reports by Yamaguchi and co-workers suggest that N-WASP may be implicated in the directional migration of at least certain cell types of non-haematopoietic origin (Yamaguchi et al., 2002). Of all the WASP-family members identified to data WASP and N-WASP are believed to be unique in their ability to be regulated by Cdc42. However, recent reports also indicate that N-WASP can be activated via phosphorylation events, possibly highlighting the existence of multiple modes of protein activation (Suetsugu et al., 2002). Consequently, findings from Cdc42/Tc10 experiments cannot alone preclude the involvement of an N-WASP signalling pathway in the chemotaxis of sarcoma cells.

Additional studies were performed in order to assess the role of N-WASP function in the chemotaxis of rat sarcoma cells. The inhibition or overexpression of N-WASP produced similar findings to those observed with Tc10. The ectopic expression of the dominant negative N-WASP truncation mutant EGFP-N-WASP(ΔVCA) impaired cell motility but had no effect on chemotaxis. Expression of the wild type protein, however, significantly enhanced the speed of cell motility. It is therefore possible that the changes in cell motility observed following the inhibition or overexpression of Tc10 may have reflected the downstream effects that this protein conferred on N-WASP function. However, the increased motility associated with the ectopic expression of wild type N-WASP was also associated

with an altered phenotype characterised by the formation of long thin lamellipodia-like extensions, a phenotype that was not observed following Tc10 overexpression.

Taken together the above findings rule out the involvement of a GTPase/N-WASP dependent signalling pathway in the PDGF-BB/IGF-1 chemotaxis of sarcoma cells. The extent to which these findings are specific to the chemoattractants and/or cell line used is unclear. However, findings from the Swiss 3T3s studies suggest that this may be a common feature of fibroblast chemotaxis, although such conclusions cannot be drawn without performing additional studies in these cells. Interestingly, recent reports implicate a role for N-WASP in the directed migration of epithelial cells (Yamaguchi et al., 2002). The authors report a mild but significant inhibition in the response of Madin-Darby canine kidney epithelial cells (MDCK) to gradients of hepatocyte growth factor (HGF) upon expression of a dominant negative N-WASP construct. It is possible therefore that N-WASP adopts a role in epithelial cell chemotaxis that is similar to that for WASP in cells of haematopoietic origin. Data from this study demonstrates that sarcoma cells require N-WASP for efficient cell motility but not chemotaxis. It is conceivable that a reduction in the speed of cell motility could equally account for the impaired response observed for MDCK cells in HGF gradients: the authors did not apply checkerboard analysis to their trans-well experiments and consequently cannot preclude changes in migration speeds accounting for the observations made. HGF is a potent motogen inducing cell scattering when applied to epithelial cell cultures *in vitro* (Ridley et al., 1995). Although the authors did not report a significant difference between the HGF induced scattering of cells over expressing either dominant negative or wild type forms of N-WASP, no attempt was made to evaluate the observations made or to assess the effects of

the different proteins on the speed of cell motility. An unequivocal confirmation that N-WASP regulates epithelial cell chemotaxis will therefore require additional studies.

Observations of film recordings and independent intensity analysis revealed that both EGFP-N-WASP(ΔVCA) and EGFP-N-WASP(wt) expression declined over the course of chemotaxis experiments. This suggested that protein expression was either being down regulated or that proteins were actively being degraded by the cell over time. It is interesting to note that Suetsugu and co-workers have recently reported that tyrosine phosphorylation of N-WASP results in both the activation and subsequent ubiquitin-mediated degradation of the protein in neurones (Suetsugu et al., 2002). However, the authors also found that when N-WASP was involved in the promotion of neurite outgrowth protein degradation was inhibited, resulting in an accumulation of the phosphorylated form of the protein. This suggests that when actively involved in actin assembly N-WASP is protected from degradation. As the initiation of actin assembly requires a functional VCA domain within the C-terminus of the molecule, the phosphorylation dependent activation of EGFP-N-WASP(ΔVCA) would not result in recruitment of Arp2/3 and therefore this truncation variant may be more prone to degradation than the full-length, wild type protein.

3.4.2 PAK1 regulates chemotaxis and motility in sarcoma cells

This study demonstrated unequivocally the dependence of sarcoma cell chemotaxis on the function of the serine/threonine kinase PAK1. PAK1 was found to regulate chemotaxis via a Cdc42 independent pathway that was also essential for efficient cell polarity and motility. Two separate PAK1 inhibitory mutants were developed in order to assess different aspects of

PAK1 signalling. The 1 – 149 fragment, which included the autoregulatory domain, the CRIB domain, and an upstream proline rich domain responsible for binding the adaptor proteins Nck and paxillin, was most effective at inhibiting the chemotactic response. Some loss of chemotaxis was also observed following expression of the autoregulatory fragment 83 – 149, although the potent inhibitory effects that this construct conferred on cell speed made an accurate assessment of directionality more difficult. A significant but less striking inhibition of motility was also associated with the expression of the 1 – 149 truncation mutant. While expression of the 1 – 149 fragment often resulted in cell contraction and rounding expression of the 83 – 149 fragment resulted in cell spreading and ruffling. Both constructs resulted in a significant reduction in the persistence of cell movement, which was likely to account, in part, for the loss of chemotaxis observed. The expression of full length, wild type PAK1 had no significant effect on cell behaviour confirming that loss of chemotaxis and impaired cell motility were specific for the mutant proteins used.

Findings from this study are in partial agreement with those made by others. Wang and coworkers report a role for PAK1 in the CXCL-1 dependent chemotaxis of human endothelial kidney cells (HEK-293) (Wang et al., 2002). However, the authors also report that PAK1 mediates HEK-293 chemotaxis in a Cdc42 independent manner, while in this study it was found that sarcoma cells exhibited Cdc42-independent chemotaxis. Therefore, although PAK1 may regulate chemotaxis in a variety of cell types the mode of its activation may exhibit a significant degree of cell-type specificity. The degree to which the findings reported by the authors specifically reflect the loss of HEK-293 chemotaxis as opposed to changes in the speed of cell motility is unclear. The authors used trans-well assays in order to

assess chemotactic behaviour without applying Zigmond-Hirsch checkerboard analysis in their study. As it is clear from findings in this study and others (Kiosses et al., 1999) that PAK1 can also significantly influence the speed of cell motility, the authors cannot preclude changes in cell speed alone accounting for the observations made in their study.

An indication that PAK1 may be of importance in the chemotaxis of fibroblasts is provided by Sells and co-workers who reported that the overexpression of a PAK1 construct deficient in kinase activity resulted in reduced persistence and impaired haptotaxis in NIH 3T3s (Sells et al., 1999). The reduction in persistence, characterised by an increased frequency in cell turning, was specific for the kinase deficient protein, while, in contrast, a constitutively active variant greatly enhanced the persistence of cell movement. The authors' findings are in agreement with those made in this study. Expression of both the 83 – 149 and the 1 – 149 PAK1 truncation mutants resulted in a significant reduction in the persistence of sarcoma cell motility. Loss of persistent movement provides one possible explanation for the loss of chemotaxis observed in sarcoma cells following PAK1 inhibition, as an increase in the frequency of turning will function to impede the progress of cells toward the source of a chemoattractant. In agreement with this Sells and co-workers also found that inhibition of PAK1 kinase activity impaired the haptotactic response of NIH 3T3s to immobilised collagen gradients, while constitutively active PAK1 enhanced this process.

Loss of persistence, and therefore the ability to chemotax efficiently, is likely to result from a loss of cell polarity control in the absence of PAK1 function. Expression of the 83 – 149 and the 1 – 149 PAK1 truncation mutants resulted in a dramatic loss of sarcoma cell polarity

resulting in cell spreading and cell contraction respectively. Sells and co-workers also identified abnormalities in cell morphology associated with PAK1 inhibition or activation, although their observations were notably different to those found in this study. The authors found that kinase-deficient PAK1 resulted in poor polarity control as cells often adopted a multi-lobed appearance, with many lamellapodia emanating from the cell surface simultaneously. In contrast, however, they found that expression of constitutively active PAK1 resulted in highly polarised cells with single broad leading-edge lamellapodia.

Although significant similarities exist between findings reported by Sells and co-workers and those made in this study, notable differences are also apparent. While PAK1 inhibitory constructs were found to significantly impair the speed of sarcoma cell motility in this study, Sells and co-workers found that overexpression of PAK1 in NIH 3T3 fibroblasts resulted in enhanced cell motility, irrespective of kinase activity. Consequently, the authors conclude that PAK1 regulates directionality and motility via separate kinase-dependent and kinase-independent mechanisms. However, this study strongly implicates a role for PAK1 kinase activity in sarcoma cell motility. Kiosses and co-workers have previously demonstrated a role for PAK1 kinase activity in the motility of human microvascular endothelial cells (HMEC-1) (Kiosses et al., 1999). The authors report an approximate 60 % reduction in cell speed following the inhibition of endogenous PAK1 with a kinase deficient/GTPase binding deficient PAK1 mutant. The reduction in cell speed was also associated with dramatic morphological changes including cell spreading and a loss of polarity. These finding are in complete agreement with those found in sarcoma cells following expression of the PAK1 83 – 149 truncation mutant. Furthermore, the authors also reported that the expression of a

GTPase binding deficient PAK1 mutant that was not deficient in its kinase activity had no significant effect on speed, therefore demonstrating that PAK1 kinase activity is required for efficient cell motility. Interestingly, Kiosses and co-workers also found that overexpression of a constitutively active PAK1 mutant also inhibited cell motility suggesting that, above all, proper regulation of PAK1 activity is required for efficient cell motility. As in this study, however, the authors did not report any effects on cell speed following overexpression of the wild type protein.

Kiosses and co-workers have mapped the region of PAK1 responsible for cell motility to the first 74 amino acids of the protein indicating that recruitment of PAK1 by adaptor molecules such as Nck and paxillin is essential for efficient cell motility. However, studies in sarcoma cells revealed that ultimately, kinase activity was required for efficient motility as the 83 - 149 fragment could also dramatically impair speed. An explanation that accommodates both these observations is that adaptor proteins are required to localise PAK1 appropriately to regions within the cell where kinase activity is then necessary to initiate further downstream signalling events. As the authors did not assess the role of PAK1 kinase activity independently of its capacity to be localised by adaptor proteins they cannot preclude the additional importance of kinase function in PAK1 dependent cell motility.

It is possible that the discrepancies in the findings made by Sells and co-workers and those found in this study and by Kiosses and co-workers may reflect differences in the experimental techniques employed. While microinjection was used to induce the transient expression of PAK1 constructs in both this study and those performed by Kiosses and co-

workers, permanent cell lines were used in studies performed by Sells and co-workers. Both techniques carry their advantages and disadvantages, which could have contributed to the conflicting observations made. If not carefully controlled, microinjection can result in excessive protein expression that can potentially have non-specific and often toxic effects on the cell. In turn, permanent cell lines can potentially suffer from alterations in gene expression that result from the long-term presence of the exogenous protein. However, it does seems likely that the inconsistencies reported are the product of the different cell types used as supposed to the differing techniques applied in their study. Firstly, Kiosses and co-workers also conducted microinjection studies in NIH 3T3s where no significant inhibition of cell motility was observed. Secondly, although microinjection did often result in high levels of protein expression in sarcoma cells in this study, additional intensity analysis revealed that dominant negative constructs could still confer their inhibitory effects at very low levels of expression. Although wild-type PAK1 did appear to have a slight inhibitory effect on cell speed at higher levels of expression this was far less striking than the effects associated with the dominant negative constructs at far lower levels of expression. Indeed, wild type PAK1 actually enhanced motility when expressed at low levels. Finally, across a broad range of intensities observed, EGFP expression alone was never found to have a significant inhibitory effect on sarcoma cell motility, indicating that non-specific deleterious effects associated with expression of the fluorophore were not a concern in this study.

The differences in morphology associated with the two separate PAK1 truncation mutants used in this study were likely to reflect the differential ways in which they conferred their effects on PAK1 signalling. The 83 – 149 truncation mutant, which specifically targets the

kinase domain of PAK1, dramatically impaired cell motility and induced cell spreading and loss of polarity. This finding clearly reflects the importance of PAK1 kinase activity in cell motility and polarity. While the 1 – 149 truncation mutant also impaired cell motility, it did so to a lesser degree. Furthermore, the loss of polarity conferred by this mutant was associated with cell rounding; possibly reflecting increased contractility or loss of adhesion. A number of possible explanations could account for these apparent discrepancies: PAK1 has been reported to phosphorylate and inactivate Myosin Light Chain Kinase (MLCK) upon activation, resulting in a down regulation of myosin activity (Sanders et al., 1999). Therefore inhibition of PAK1 could result in increased cell contractility as levels of phosphorylated myosin increase within the cell. However, this is unlikely to explain the phenotype associated with the expression of the 1 – 149 mutant as the 83 – 149 mutant would have also been expected to inhibit PAK1-dependent MLCK phosphorylation. Furthermore, in contrasting reports others have noted an increase in myosin phosphorylation following the expression of a constitutively active PAK1 variant, suggesting that in certain circumstances PAK1 activation can in fact promote myosin activity (Sells et al., 1999).

A more plausible explanation for the different morphologies observed is likely to stem from the additional capacity of the 1 – 149 mutant to bind adaptor proteins such as Nck and paxillin. As paxillin has been reported to localise PAK1 to focal adhesion in a manner that is independent of PAK1 kinase activity, it is possible that PAK1, independent of kinase function, is required for efficient adhesion. If an inability to efficiently localise endogenous PAK1 to sites of focal adhesion formation results in reduced adhesion to the substrate then such changes would only be associated with the expression of the 1 – 149 mutant. Loss of

adhesion could account for the cell rounding often associated with the expression of the 1 - 149 mutant in sarcoma cells.

The capacity of the 1 – 149 mutant to bind Nck could also provide an explanation for the loss of chemotaxis observed in sarcoma cells expressing this truncation mutant. Nck is recruited to activated tyrosine kinase receptors following growth factor stimulation where it functions as an adaptor molecule, localising other signalling proteins to sites of receptor activation. Nck is likely to play an important role in PAK1 related signalling during PDGF-BB/IGF-1 driven chemotaxis as this proteins has been shown to associate constitutively with PAK1 and also with the activated PDGF receptor (Lu et al., 1997). If sites of receptor activation provide the primary spatial information concerning the source of a chemoattractant, then the inhibition of Nck-dependent PAK1 receptor recruitment could result in a failure to transmit external spatial cues to the cytoskeleton in order to bring about appropriate morphological responses. This would effectively 'blind' the cell, rendering it incapable of responding to signalling gradients. Indeed, the *Dosophila* Nck homolog DOCKS has been directly implicated in the axonal pathfinding of photoreceptor neurones, thus already providing a link for Nck in the control of directionality in other cell systems (Garrity et al., 1996). Therefore, the role of a Nck-PAK1 pathway in the PDGF-BB/IGF-1 driven chemotaxis of sarcoma cells is favoured here. It should be noted that if Nck is important in relaying such spatial information from the extracellular environment into the cell then the capacity for the 1 – 149 fragment to inhibit the ability of Nck to associate with other putative targets cannot be ruled out as important for the chemotactic response of sarcoma cells. However, since the 83 – 149

mutant also had a noticeable, although, less dramatic inhibitory effect on the directional response of sarcoma cells it is likely that PAK1 is directly implicated in chemotaxis.

It is clear that an attempt to develop a global model that defines in general terms the role of PAK1 in the regulation of cell motility and polarity is unwise, as considerable inconsistencies exist in the literature that are likely to reflect the various cell types used. Findings from this study define a new role for PAK1 in the Cdc42 independent regulation of chemotaxis in sarcoma cells. PAK1 was also found to be essential for the efficient motility of sarcoma cells indicating the importance of this molecule in both directionality and speed. Additional studies will now be required to try and delinearise the signalling events downstream of PAK1 in an attempt to isolate, if possible, targets of PAK1 signalling that control motility and directionality respectively.

3.4.3 Analysis of fluorescence intensity in studying the effects of varying levels of protein expression on cell motility

One of the major shortcomings associated with transient expression techniques such as microinjection and transfection is their inability to effectively regulate protein expression. Non-specific and/or cytotoxic effects that can arise from excessive protein expression are of particular concern when protein expression is under the control of powerful viral promoters, which are often incorporated into modern expression cassettes. Moreover, when EGFP fusion is used as a means of detecting and studying the localisation of proteins, potential photo-toxic effects associated with the expression of the fluorophore present an additional hazard. As microinjection and transfection are used routinely as a means of assessing the effects of

various proteins on cell behaviour, it is essential that the physiologically relevant effects conferred by the expression of a protein are not confused with non-specific cytotoxic and/or phototoxic effects that are often associated with excessive expression. Furthermore, when the effects of a number of different expression constructs are assessed it is important to ensure that observations associated with individual treatments are not merely the consequence of their varying expression efficiencies. In an attempt to address these issues purpose written intensity analysis programs were written that enabled changes in the speed of cell motility to be correlated with changes in the intensity of expressed proteins fused to EGFP.

The various expression constructs used in this study exhibited a range of expression efficiencies. Although all dominant negative proteins conferred an inhibitory effect on cell speed while wild type proteins had no such effect, certain dominant.negative proteins were also found to exhibit far greater efficiencies of expression when compared with their wild type counterparts. It was therefore important to assess whether the inhibitory effects that dominant negative proteins conferred on cell speed were the consequence of their specific mutations or whether these effects were artefacts of excessive protein expression. Furthermore, it was important to determine whether differences conferred on the speed of cell motility could still be detected between dominant negative and wild type treatments when assessed at comparable levels of expression.

Intensity analysis revealed that phototoxicity associated with EGFP expression was not an issue in this study. Of all the expression constructs microinjected into cells, EGFP vector alone exhibited the greatest levels of expression. However, over the entire range of EGFP

expression levels observed no significant impairment of cell speed was detectable. Intensity analysis was also used successfully to determine the effects that PAK1 constructs conferred on cell speed at comparable levels of expression. This was of particular importance as dominant negative variants exhibited a far greater range of expression efficiencies than the wild type protein. However, intensity analysis revealed that dominant negative proteins conferred their inhibitory effects at all but the very lowest levels of expression, while the wild type protein only appeared to have an inhibitory effect at far higher levels. Furthermore, at lower levels of expression the wild type protein actually enhanced the speed of cell motility. Therefore intensity analysis permitted original observations and conclusions made from chemotaxis experiments regarding changes in cell motility to be viewed with confidence.

3.4.4 Imaging actin dynamics in metastatic and non-metastatic cells

The newly developed FLAP technique (Dunn et al., 2002) was applied in a comparative study of actin dynamics in the related T15 metastatic and K2 non-metastatic sarcoma cell lines. Others have previously reported significant differences in both the cytoskeletal architecture and motile behaviour between these two cell lines (Pokorna et al., 1994): it has been shown that T15 cells generally exhibit relatively few high order actin structures, are polarised and highly motile, while K2 cells are often well spread, dense with stress fibres, and only poorly motile in comparison. The development of the FLAP technique enabled the dynamics of differing actin structures to be explored within these cells.

FLAP studies revealed additional differences between these cells. Actin within T15 cells was often highly dynamic. In many cases ratiometric imaging revealed the rapid incorporation of photolabelled actin molecules into the leading edge of lamellapodia, indicating that actin was highly mobile in these motile cells. In contrast actin structures in K2 cells were often static as reflected by the poor mobility of photolabelled actin molecules within these cells.

3.4.5 Imaging Cdc42/N-WASP/Arp2/3 interactions in single cells

The development of microscopy techniques that enable the interactions of proteins to be monitored in single cells has been a valuable addition to the field of cell biology. FRET permits the non-invasive imaging of protein interactions *in situ*, providing valuable information regarding the spatiotemporal dynamics of signalling processes that otherwise cannot be discerned through more conventional biochemical techniques. In this study the application of multiphoton TCSPC and frequency domain FLIM techniques to the analysis of FRET has enabled the direct visualisation of protein interactions in single cells. Both techniques were applied successfully in the analysis of Cdc42 signalling in the NIH 3T3 fibroblast cell line. The high degree of spatial resolution afforded by multiphoton imaging enabled a detailed study of the subcellular localisation of Cdc42/N-WASP and N-WASP/Arp2/3 complexes in single fixed cells, while the relatively rapid acquisition times associated with frequency domain FLIM enabled the dynamics of Cdc42/PAK1 signalling to be assessed in living cells in response to growth factor stimulation.

This study revealed for the first time the subcellular localisation of Cdc42/N-WASP complexes in cultured mammalian cells. Cdc42 was found to associate constitutively with N-WASP in NIH 3T3 fibroblasts and complexes were observed to localise predominantly to a perinuclear region that partially co-localised with the Golgi apparatus. Interestingly, Cdc42/N-WASP complexes were rarely observed at the cell periphery. In the few cases where microinjected cells made contact, complexes were also found to localise to cell junctions. The localisation of N-WASP/Arp2/3 complexes was found to largely mirror that of Cdc42/N-WASP suggesting the formation of Cdc42/N-WASP/Arp2/3 ternary complexes at these sites. That Cdc42/N-WASP/Arp2/3 complexes were rarely observed at the cell periphery is of interest because it questions the importance of this pathway in peripheral actin assembly. Indeed these observations suggest that Cdc42/N-WASP/Arp2/3-regulated actin assembly is largely confined to a perinuclear/Golgi region in NIH 3T3 fibroblasts. This is consistent with findings by Luna and co-workers who have reported that Cdc42 regulates vesicular transport between the Golgi and Endoplasmic Reticulum in an N-WASP dependent manner (Luna et al., 2002). *In vitro* studies have revealed that Cdc42-dependent N-WASP activation requires the synergistic co-operation of $PI(4,5)P_2$ (Prehoda et al., 2000). The subcellular distribution and availability of $PI(4,5)P_2$ should therefore determine the capacity of Cdc42 to effectively activate N-WASP and initiate Arp2/3 recruitment. Given the importance of phosphoinositides in membrane trafficking (De Camilli et al., 1996) and given that various lipid kinases responsible for $PI(4,5)P_2$ synthesis are known to be present within the Golgi compartment (Jones et al., 2000), the appropriate conditions are likely to exist *in situ* that permit Cdc42/$PI(4,5)P_2$/N-WASP/Arp2/3 interaction at the Golgi membrane and/or at the membrane of Golgi related vesicles.

The absence of significant FRET at the cell periphery suggests that other WASP family members may be of more importance in regulating Arp2/3-dependent peripheral actin assembly in fibroblasts. These findings may seem to be inconsistent with those reported by Miki and co-workers who have demonstrated that N-WASP function is required for the Cdc42-dependent formation of filopodia, and therefore the formation of peripheral actin structures (Miki et al., 1998a). However, more recent reports indicate that, although N-WASP is capable of mediating Cdc42-dependent filopodia formation, it is also dispensable in this role since fibroblasts defective in N-WASP function are still capable of producing these structures (Lommel et al., 2001). The degree to which Cdc42/N-WASP/Arp2/3 signalling contributes to peripheral actin assembly may therefore depend upon on the cell type in question.

The abundance of Arp2/3 in the leading edge lamellapodia of motile cells suggests that this actin-nucleating protein is essential for peripheral cytoskeletal rearrangements and lamellapodia formation. The formation of lamellapodia and membrane ruffles has long been associated with the activation of the Rho GTPase Rac1 (Ridley et al., 1992). The recently identified WAVE proteins (Miki et al., 1998b), WASP family members that lie downstream of Rac and not Cdc42, therefore provide likely candidates for the regulation of Arp2/3-dependent actin assembly in the lamellapodia and cell periphery. It would therefore be of great interest to conduct additional studies in NIH 3T3s in order to elucidate, via FLIM/FRET analysis, the subcellular distribution of WAVE/Arp2/3 complexes and compare and contrast these findings with those already made for N-WASP/Arp2/3.

3.4.6 Imaging Cdc42 activation in single living cells

A live cell assay was developed that enabled FRET to be monitored in living cells allowing the dynamics of protein interactions to be observed over time. By microinjecting cells with expression constructs encoding EGFP-Cdc42 and Myc-PAK1 and then re-microinjecting the same cells with an antibody conjugated to an acceptor fluorophore which specifically targeted the Myc epitope of PAK1, FRET could be monitored between the donor and acceptor fluorophores in living cells. The presence of excess, unbound acceptor antibody could be ignored because only the fluorescence emission of the donor fluorophore was required for FRET analysis. This assay proved effective in the study of Cdc42/PAK1 interactions in living cells and is analogous in principle to that previously used by others to monitor the activation of Rac1 in living cells (Kraynov et al., 2000).

Although Cdc42/N-WASP association was largely constitutive in NIH 3T3 fibroblasts, Cdc42/PAK1 association could be induced following the administration of the physiological stimulant EGF to cell cultures. Live cell experiments revealed that EGF receptor activation resulted in a rapid association between Cdc42 and PAK1. This association occurred within 6 min of growth factor stimulation and was detectable for the full duration that cells were observed. The extent to which Cdc42 and PAK1 associated in unstimulated cells varied, possibly reflecting the differing degrees to which cells were stimulated by cytoplasmic microinjection. However, this study demonstrated that frequency domain FLIM could successfully be used to detect Cdc42 activation in single living cells following the administration of a physiological stimulus.

The ability to develop and apply techniques that enable specific protein interactions to be monitored over time in living cells is essential for a thorough understanding of the dynamic cellular processes that regulate cell morphology and motility. Although *in vitro* biochemical studies have proved instrumental in our understanding of the minimal essential components requires for actin assembly and disassembly, the precise way in which these components organise themselves within the cell is still unclear. An understanding of the spatiotemporal organisation of signalling events within the cell is likely to be the key to understanding how simple protein interactions can ultimately orchestrate the assembly of complex cytoskeletal structures that dictate cell morphology. By adopting techniques that permit the non-invasive study of protein interactions *in situ*, these questions can finally be addressed.

FLIM is likely to play an increasing role in the field of cell biology as the technology becomes more affordable. FLIM will continue to benefit from advances in both physics and bioengineering. Faster image acquisition times, greater detector sensitivities, and higher image resolution capabilities will all help to increase the amount of information that can be extracted from live cell imaging experiments while minimising exposure times and therefore photo-damage to the sample. The development of new biofluorescent probes with different spectral properties will increase the availability of suitable fluorophore pairs for FRET experiments, increasing the number of molecular interactions that can be studied simultaneously within a single cell. If such techniques can be coupled with methods that enable the expression of exogenous proteins to be tightly controlled then FLIM/FRET technology has the potential to revolutionise our understanding of the cell.

3.5 CONCLUSION

This study found that the polarity protein PAK1 was essential for both the efficient chemotaxis and motility of T15 rat sarcoma cells. While Cdc42, Tc10, and N-WASP were all necessary for efficient motility they were not required for the chemotaxis of these cells. The additional application of intensity analysis to experimental data permitted the different fluorescent fusion proteins studied to be assessed at comparable levels of expression. This minimised the likelihood that conclusions were drawn from significances that arose merely as a consequence of expression inconsistencies between the different proteins studied.

The fact that PAK1 regulated sarcoma cell chemotaxis via a Cdc42 independent pathway suggests that the mechanisms involved in the control of sarcoma cell chemotaxis are distinct from those employed by cells of haematopoietic origin, which depend upon both Cdc42 and WASP signalling. The possibility that distinct signalling pathways exist in the control of tumour cell and immune cell chemotaxis raises the prospect of establishing treatments that permit this behaviour to be inhibited in a cell-specific manner. The potential to develop therapies that could specifically impair the chemotactic ability of tumour cells without further compromising the immunity of the patient would be of great significance in the treatment of metastatic disease.

The newly developed FLAP technique was also successfully applied to the comparative study of actin dynamics in metastatic and non-metastatic sarcoma cells. Studies revealed that the actin cytoskeleton of metastatic T15 sarcoma cells was highly dynamic, with actin molecules rapidly translocating to the leading edge of protruding motile cells. In contrast the

cytoskeleton of the poorly motile and non-metastatic K2 cells was often largely static in comparison.

This study also demonstrated the successful application of both multiphoton TCSPC FLIM and frequency domain FLIM to fixed cell and live cell FRET imaging, respectively. While the multiphoton technique enabled the detailed high resolution analysis of the distribution of the FRET population within a single optical section of the sample, the faster acquisition times associated with the wide-field frequency domain technique enabled FRET to be monitored in living cells. Multiphoton TCSPC FLIM/FRET studies provided, for the first time, information concerning the subcellular localisation of Cdc42/N-WASP and N-WASP/Arp2/3 complex formation *in situ*, revealing that these associations primarily occurred within a perinuclear compartment. Wide field frequency domain FLIM/FRET studies demonstrated that the activation kinetics of Cdc42 could be monitored in single living cells following the administration of a physiological stimulus.

4 CONCLUDING REMARKS

The importance of light microscopy in the biomedical sciences has increased dramatically over the past decade. The development of digital time-lapse recording techniques allowing the flexible acquisition of fluorescence images in multiple channels and computer aided techniques that enable the post_acquisition processing and analysis of image data have all functioned to greatly increase the range of biological questions that can be answered through the use light microscopy techniques. Thus a transition has occurred which has seen light microscopy evolve from a technique simply enabling the high magnification observation of the biological sample into an effective tool for the quantitative analysis of specific aspects of cellular behaviour and subcellular molecular dynamics. The field is likely to continue to evolve at an ever-increasing rate; the next few years are likely to see a significant increase in the application of FLIM/FRET techniques as commercially available modules have now been developed that can be incorporated into conventional confocal microscope systems. In parallel to the technological advances that have greatly aided the light microscopy field novel ways of applying the technology are continuously being developed; for example, the development of single molecule speckle fluorescence on wide field systems and the development of FRAP, FLIP, and FLAP photobleaching technique on confocal microscope systems have all further widened the possible application of these technologies.

In this study microinjection in conjunction with multi-channel digital time-lapse microscopy and quantitative analysis of processed image data were successfully applied to the study of two markedly different aspects of cellular behaviour; gap junction mediated intercellular communication, and sarcoma cell motility and chemotaxis. When assessing the effects of

particular treatments on specific aspects of cell behaviour large data sets were required in order to accommodate for the inherent heterogeneity found within the cell population. Automated time-lapse acquisition greatly facilitated this process. The accumulation of large data sets and the subsequent application of appropriate statistical tests to the processed image data allowed a robust analysis to be performed, enabling significances to be derived that indicated the degree to which various treatments effected the different aspects of cell behaviour under investigation. When applying microscopy techniques to the study of cell behaviour care should be taken to ensure that the appropriate techniques for the quantification and statistical analysis of the acquired data are chosen. For instance a two tailed t-test could be used to evaluate the effects of different Cx31 mutations on the ability of cells to transfer dye as each culture represented an independent experiment and each experiment yielded a single value that defined the mean rate of dye transfer. On the other hand the analysis of the effects of different treatments of the motility and chemotaxis of sarcoma cells required the use of ANOVA for significance testing as cell trajectories generated from the interactive tracking of film sequences produced hierarchical data structures. This study, therefore, clearly demonstrates that quantitative light microscopy techniques can be applied successfully in the study of a diverse range of cell behaviour.

REFERENCES

Abe, T., Kato, M., Miki, H., Takenawa, T. and Endo, T. (2003). Small GTPase Tc10 and its homologue RhoT induce N-WASP-mediated long process formation and neurite outgrowth. J Cell Sci **116**, *155-68.*

Abercrombie, M. (1970). Contact inhibition in tissue culture. In Vitro **6**, *128-42.*

Adams, A. E., Johnson, D. I., Longnecker, R. M., Sloat, B. F. and Pringle, J. R. (1990). CDC42 and CDC43, two additional genes involved in budding and the establishment of cell polarity in the yeast Saccharomyces cerevisiae. J Cell Biol **111**, *131-42.*

Ahmad, A. and Hart, I. R. (1997). Mechanisms of metastasis. Crit Rev Oncol Hematol **26**, *163-73.*

Allan, R. B. and Wilkinson, P. C. (1978). A visual analysis of chemotactic and chemokinetic locomotion of human neutrophil leucocytes. Use of a new chemotaxis assay with Candida albicans as gradient source. Exp Cell Res **111**, *191-203.*

Allen, W. E., Zicha, D., Ridley, A. J. and Jones, G. E. (1998). A role for Cdc42 in macrophage chemotaxis. J Cell Biol **141**, *1147-57.*

Altevogt, B. M., Kleopa, K. A., Postma, F. R., Scherer, S. S. and Paul, D. L. (2002). Connexin29 is uniquely distributed within myelinating glial cells of the central and peripheral nervous systems. J Neurosci **22**, *6458-70.*

Aspenstrom, P. (1999). Effectors for the Rho GTPases. Curr Opin Cell Biol **11**, *95-102.*

Auerbach, R., Lu, W. C., Pardon, E., Gumkowski, F., Kaminska, G. and Kaminski, M. (1987). Specificity of adhesion between murine tumor cells and capillary endothelium: an in vitro correlate of preferential metastasis in vivo. Cancer Res **47**, *1492-6.*

Avraham, K. B. (2001). Inherited connexin mutations associated with hearing loss. Cell Commun Adhes **8**, *419-24.*

Badolato, R., Sozzani, S., Malacarne, F., Bresciani, S., Fiorini, M., Borsatti, A., Albertini, A., Mantovani, A., Ugazio, A. G. and Notarangelo, L. D. (1998). Monocytes from Wiskott-Aldrich patients display reduced chemotaxis and lack of cell polarization in response to monocyte chemoattractant protein-1 and formyl-methionyl-leucyl-phenylalanine. J Immunol **161**, *1026-33.*

Bailly, M., Wyckoff, J., Bouzahzah, B., Hammerman, R., Sylvestre, V., Cammer, M., Pestell, R. and Segall, J. E. (2000). Epidermal growth factor receptor distribution during chemotactic responses. Mol Biol Cell **11**, *3873-83.*

Baker, M. D. (2002). Electrophysiology of mammalian Schwann cells. Prog Biophys Mol Biol **78**, *83-103.*

Banyard, J., Anand-Apte, B., Symons, M. and Zetter, B. R. (2000). Motility and invasion are differentially modulated by Rho family GTPases. Oncogene **19**, *580-91.*

Banzai, Y., Miki, H., Yamaguchi, H. and Takenawa, T. (2000). Essential role of neural Wiskott-Aldrich syndrome protein in neurite extension in PC12 cells and rat hippocampal primary culture cells. J Biol Chem **275**, *11987-92.*

Bastiaens, P. I. and Squire, A. (1999). Fluorescence lifetime imaging microscopy: spatial resolution of biochemical processes in the cell. Trends Cell Biol **9**, *48-52.*

Beyer, E. C., Gemel, J., Martinez, A., Berthoud, V. M., Valiunas, V., Moreno, A. P. and Brink, P. R. (2001). Heteromeric mixing of connexins: compatibility of partners and functional consequences. Cell Commun Adhes 8, 199-204.

Bishop, A. L. and Hall, A. (2000). Rho GTPases and their effector proteins. Biochem J 348 Pt 2, 241-55.

Boerma, M., Forsberg, L., Van Zeijl, L., Morgenstern, R., De Faire, U., Lemne, C., Erlinge, D., Thulin, T., Hong, Y. and Cotgreave, I. A. (1999). A genetic polymorphism in connexin 37 as a prognostic marker for atherosclerotic plaque development. J Intern Med 246, 211-8.

Bokoch, G. M., Reilly, A. M., Daniels, R. H., King, C. C., Olivera, A., Spiegel, S. and Knaus, U. G. (1998). A GTPase-independent mechanism of p21-activated kinase activation. Regulation by sphingosine and other biologically active lipids. J Biol Chem 273, 8137-44.

Boyce, K. J., Hynes, M. J. and Andrianopoulos, A. (2001). The CDC42 homolog of the dimorphic fungus Penicillium marneffei is required for correct cell polarization during growth but not development. J Bacteriol 183, 3447-57.

Boyden, S. (1962). The chemotactic effects of mixtures of antibody and antigen on polymorphic leukocytes. J. Exp. Med. 115, 453-466.

Bray, D. (2001). Cell movements 2nd ed., Garland Publishing, New York.
Budrene, E. O. and Berg, H. C. (1991). Complex patterns formed by motile cells of Escherichia coli. Nature 349, 630-3.

Carbillon, L., Seince, N. and Uzan, M. (2001). Myometrial maturation and labour. Ann Med 33, 571-8.

Carystinos, G. D., Bier, A. and Batist, G. (2001). The role of connexin-mediated cell-cell communication in breast cancer metastasis. J Mammary Gland Biol Neoplasia 6, 431-40.

Chiang, S. H., Baumann, C. A., Kanzaki, M., Thurmond, D. C., Watson, R. T., Neudauer, C. L., Macara, I. G., Pessin, J. E. and Saltiel, A. R. (2001). Insulin-stimulated GLUT4 translocation requires the CAP-dependent activation of TC10. Nature 410, 944-8.

Chung, C. Y. and Firtel, R. A. (1999). PAKa, a putative PAK family member, is required for cytokinesis and the regulation of the cytoskeleton in Dictyostelium discoideum cells during chemotaxis. J Cell Biol 147, 559-76.

Cole, N. B., Smith, C. L., Sciaky, N., Terasaki, M., Edidin, M. and Lippincott-Schwartz, J. (1996). Diffusional mobility of Golgi proteins in membranes of living cells. Science 273, 797-801.

Common, J. E., Becker, D., Di, W. L., Leigh, I. M., O'Toole, E. A. and Kelsell, D. P. (2002). Functional studies of human skin disease- and deafness-associated connexin 30 mutations. Biochem Biophys Res Commun 298, 651-6.

Conroy, D. M. and Williams, T. J. (2001). Eotaxin and the attraction of eosinophils to the asthmatic lung. Respir Res 2, 150-6.

De Camilli, P., Emr, S. D., McPherson, P. S. and Novick, P. (1996). Phosphoinositides as regulators in membrane traffic. Science 271, 1533-9.

De Maio, A., Vega, V. L. and Contreras, J. E. (2002). Gap junctions, homeostasis, and injury. J Cell Physiol 191, 269-82.

Deans, M. R., Volgyi, B., Goodenough, D. A., Bloomfield, S. A. and Paul, D. L. (2002). Connexin36 is essential for transmission of rod-mediated visual signals in the mammalian retina. Neuron 36, 703-12.

Di, W. L., Monypenny, J., Common, J. E., Kennedy, C. T., Holland, K. A., Leigh, I. M., Rugg, E. L., Zicha, D. and Kelsell, D. P. (2002). Defective trafficking and cell death is characteristic of skin disease-associated connexin 31 mutations. Hum Mol Genet 11, 2005-14.

Di, W. L., Rugg, E. L., Leigh, I. M. and Kelsell, D. P. (2001). Multiple epidermal connexins are expressed in different keratinocyte subpopulations including connexin 31. J Invest Dermatol 117, 958-64.

Diestel, S., Richard, G., Doring, B. and Traub, O. (2002). Expression of a connexin31 mutation causing erythrokeratodermia variabilis is lethal for HeLa cells. Biochem Biophys Res Commun 296, 721-8.

Donaldson, P., Kistler, J. and Mathias, R. T. (2001). Molecular solutions to mammalian lens transparency. News Physiol Sci 16, 118-23.

Drivas, G. T., Shih, A., Coutavas, E., Rush, M. G. and D'Eustachio, P. (1990). Characterization of four novel ras-like genes expressed in a human teratocarcinoma cell line. Mol Cell Biol 10, 1793-8.

Dunn, G. A., Dobbie, I. M., Monypenny, J., Holt, M. R. and Zicha, D. (2002). Fluorescence localization after photobleaching (FLAP): a new method for studying protein dynamics in living cells. J Microsc 205, 109-12.

Eby, J. J., Holly, S. P., van Drogen, F., Grishin, A. V., Peter, M., Drubin, D. G. and Blumer, K. J. (1998). Actin cytoskeleton organization regulated by the PAK family of protein kinases. Curr Biol 8, 967-70.

Edwards, D. C., Sanders, L. C., Bokoch, G. M. and Gill, G. N. (1999). Activation of LIM-kinase by Pak1 couples Rac/Cdc42 GTPase signalling to actin cytoskeletal dynamics. Nat Cell Biol 1, 253-9.

Elfgang, C., Eckert, R., Lichtenberg-Frate, H., Butterweck, A., Traub, O., Klein, R. A., Hulser, D. F. and Willecke, K. (1995). Specific permeability and selective formation of gap junction channels in connexin-transfected HeLa cells. J Cell Biol 129, 805-17.

Etienne-Manneville, S. and Hall, A. (2002). Rho GTPases in cell biology. Nature 420, 629-35.

Evans, W. H., Martin, P. E. (2002). Gap Junctions: structure and function. Mol Membr Biol 19, 121-36.

Falk, M. (2002). Genetic tags for labelling live cells: gap junctions and beyond. Trends Cell Biol 12, 399-404.

Fidler, I. J. and Ellis, L. M. (1994). The implications of angiogenesis for the biology and therapy of cancer metastasis. Cell 79, 185-8.

Fidler, I. J. and Hart, I. R. (1982). Biological diversity in metastatic neoplasms: origins and implications. Science 217, 998-1003.

Frischknecht, F., Moreau, V., Rottger, S., Gonfloni, S., Reckmann, I., Superti-Furga, G. and Way, M. (1999). Actin-based motility of vaccinia virus mimics receptor tyrosine kinase signalling. Nature 401, 926-9.

Frost, J. A., Khokhlatchev, A., Stippec, S., White, M. A. and Cobb, M. H. (1998). Differential effects of PAK1-activating mutations reveal activity-dependent and -independent effects on cytoskeletal regulation. J Biol Chem 273, 28191-8.

Gadella, T. W., Jr. and Jovin, T. M. (1995). Oligomerization of epidermal growth factor receptors on A431 cells studied by time-resolved fluorescence imaging microscopy. A stereochemical model for tyrosine kinase receptor activation. J Cell Biol 129, 1543-58.

Garrity, P. A., Rao, Y., Salecker, I., McGlade, J., Pawson, T. and Zipursky, S. L. (1996). Drosophila photoreceptor axon guidance and targeting requires the dreadlocks SH2/SH3 adapter protein. Cell 85, 639-50.

Gillitzer, R. and Goebeler, M. (2001). Chemokines in cutaneous wound healing. J Leukoc Biol 69, 513-21.

Goldberg, G. S., Bechberger, J. F., Tajima, Y., Merritt, M., Omori, Y., Gawinowicz, M. A., Narayanan, R., Tan, Y., Sanai, Y., Yamasaki, H. et al. (2000). Connexin43 suppresses MFG-E8 while inducing contact growth inhibition of glioma cells. Cancer Res 60, 6018-26.

Gotta, M., Abraham, M. C. and Ahringer, J. (2001). CDC-42 controls early cell polarity and spindle orientation in C. elegans. Curr Biol 11, 482-8.

Gottfried, I., Landau, M., Glaser, F., Di, W. L., Ophir, J., Mevorah, B., Ben-Tal, N., Kelsell, D. P. and Avraham, K. B. (2002). A mutation in GJB3 is associated with recessive erythrokeratodermia variabilis (EKV) and leads to defective trafficking of the connexin 31 protein. Hum Mol Genet 11, 1311-6.

Haddad, E., Zugaza, J. L., Louache, F., Debili, N., Crouin, C., Schwarz, K., Fischer, A., Vainchenker, W. and Bertoglio, J. (2001). The interaction between Cdc42 and WASP is required for SDF-1-induced T-lymphocyte chemotaxis. Blood 97, 33-8.

Hall, A. (1998). Rho GTPases and the actin cytoskeleton. Science 279, 509-14.

Hart, I. R., Talmadge, J. E. and Fidler, I. J. (1981). Metastatic behavior of a murine reticulum cell sarcoma exhibiting organ-specific growth. Cancer Res 41, 1281-7.

Hashimoto, S., Tsubouchi, A., Mazaki, Y. and Sabe, H. (2001). Interaction of paxillin with p21-activated Kinase (PAK). Association of paxillin alpha with the kinase-inactive and the Cdc42-activated forms of PAK3. J Biol Chem 276, 6037-45.

Hill, C. E., Phillips, J. K. and Sandow, S. L. (2001). Heterogeneous control of blood flow amongst different vascular beds. Med Res Rev 21, 1-60.

Hing, H., Xiao, J., Harden, N., Lim, L. and Zipursky, S. L. (1999). Pak functions downstream of Dock to regulate photoreceptor axon guidance in Drosophila. Cell 97, 853-63.

Hujanen, E. S. and Terranova, V. P. (1985). Migration of tumor cells to organ-derived chemoattractants. Cancer Res 45, 3517-21.

Ito, A., Nakajima, S., Sasaguri, Y., Nagase, H. and Mori, Y. (1995). Co-culture of human breast adenocarcinoma MCF-7 cells and human dermal fibroblasts enhances the production of matrix metalloproteinases 1, 2 and 3 in fibroblasts. Br J Cancer 71, 1039-45.

Itoh, R. E., Kurokawa, K., Ohba, Y., Yoshizaki, H., Mochizuki, N. and Matsuda, M. (2002). Activation of rac and cdc42 video imaged by fluorescent resonance energy transfer-based single-molecule probes in the membrane of living cells. Mol Cell Biol 22, 6582-91.

Jacob, K., Webber, M., Benayahu, D. and Kleinman, H. K. (1999). Osteonectin promotes prostate cancer cell migration and invasion: a possible mechanism for metastasis to bone. Cancer Res 59, 4453-7.

Johnson, D. I. (1999). Cdc42: An essential Rho-type GTPase controlling eukaryotic cell polarity. Microbiol Mol Biol Rev 63, 54-105.

Jones, D. H., Morris, J. B., Morgan, C. P., Kondo, H., Irvine, R. F. and Cockcroft, S. (2000). Type I phosphatidylinositol 4-phosphate 5-kinase directly interacts with ADP-ribosylation factor 1 and is responsible for phosphatidylinositol 4,5-bisphosphate synthesis in the golgi compartment. J Biol Chem 275, 13962-6.

Kelsell, D. P., Di, W. L. and Houseman, M. J. (2001). Connexin mutations in skin disease and hearing loss. Am J Hum Genet 68, 559-68.

Kelsell, D. P., Wilgoss, A. L., Richard, G., Stevens, H. P., Munro, C. S. and Leigh, I. M. (2000). Connexin mutations associated with palmoplantar keratoderma and profound deafness in a single family. Eur J Hum Genet **8**, *141-4.*

Kiley, S. C., Parker, P. J., Fabbro, D. and Jaken, S. (1992). Hormone- and phorbol ester-activated protein kinase C isozymes mediate a reorganization of the actin cytoskeleton associated with prolactin secretion in GH4C1 cells. Mol Endocrinol **6**, *120-31.*

Kim, A. S., Kakalis, L. T., Abdul-Manan, N., Liu, G. A. and Rosen, M. K. (2000). Autoinhibition and activation mechanisms of the Wiskott-Aldrich syndrome protein. Nature **404**, *151-8.*

Kiosses, W. B., Daniels, R. H., Otey, C., Bokoch, G. M. and Schwartz, M. A. (1999). A role for p21-activated kinase in endothelial cell migration. J Cell Biol **147**, *831-44.*

Klein, C. A., Blankenstein, T. J., Schmidt-Kittler, O., Petronio, M., Polzer, B., Stoecklein, N. H. and Riethmuller, G. (2002). Genetic heterogeneity of single disseminated tumour cells in minimal residual cancer. Lancet **360**, *683-9.*

Koike, C., Watanabe, M., Oku, N., Tsukada, H., Irimura, T. and Okada, S. (1997). Tumor cells with organ-specific metastatic ability show distinctive trafficking in vivo: analyses by positron emission tomography and bioimaging. Cancer Res **57**, *3612-9.*

Kraynov, V. S., Chamberlain, C., Bokoch, G. M., Schwartz, M. A., Slabaugh, S. and Hahn, K. M. (2000). Localized Rac activation dynamics visualized in living cells. Science **290**, *333-7.*

Labruyere, E., Zimmer, C., Galy, V., Olivo-Marin, J. C. and Guillen, N. (2003). EhPAK, a member of the p21-activated kinase family, is involved in the control of Entamoeba histolytica migration and phagocytosis. J Cell Sci **116**, *61-71.*

Lakowicz, J. R. (1999). principles of fluorescence spectroscopy. Kluwer Academic.

Lakowicz, J. R., Szmacinski, H., Nowaczyk, K., Berndt, K. W. and Johnson, M. (1992). Fluorescence lifetime imaging. Anal Biochem **202**, *316-30.*

Lam, W. C., Delikatny, E. J., Orr, F. W., Wass, J., Varani, J. and Ward, P. A. (1981). The chemotactic response of tumor cells. A model for cancer metastasis. Am J Pathol **104**, *69-76.*

Lee, K. C., Siegel, J., Webb, S. E., Leveque-Fort, S., Cole, M. J., Jones, R., Dowling, K., Lever, M. J. and French, P. M. (2001). Application of the stretched exponential function to fluorescence lifetime imaging. Biophys J **81**, *1265-74.*

Lei, M., Lu, W., Meng, W., Parrini, M. C., Eck, M. J., Mayer, B. J. and Harrison, S. C. (2000). Structure of PAK1 in an autoinhibited conformation reveals a multistage activation switch. Cell **102**, *387-97.*

Libby, P. (2002). Atherosclerosis: the new view. Sci Am **286**, *46-55.*

Lippincott-Schwartz, J., Snapp, E. and Kenworthy, A. (2001). Studying protein dynamics in living cells. Nat Rev Mol Cell Biol **2**, *444-56.*

Lommel, S., Benesch, S., Rottner, K., Franz, T., Wehland, J. and Kuhn, R. (2001). Actin pedestal formation by enteropathogenic Escherichia coli and intracellular motility of Shigella flexneri are abolished in N-WASP-defective cells. EMBO Rep **2**, *850-7.*

*Lopez-Bigas, N., Olive, M., Rabionet, R., Ben-David, O., Martinez-Matos, J. A., Bravo, O., Banchs, I., Volpini, V., Gasparini, P., Avraham, K. B. et al. (2001a). Connexin 31 (GJB3) is expressed in the peripheral and auditory nerves and causes neuropathy and hearing impairment. Hum Mol Genet **10**, 947-52.*

*Lopez-Bigas, N., Rabionet, R., Arbones, M. L. and Estivill, X. (2001b). R32W variant in Connexin 31: mutation or polymorphism for deafness and skin disease? Eur J Hum Genet **9**, 70.*

*Lopez-Bigas, N., Rabionet, R., Martinez, E., Banchs, I., Volpini, V., Vance, J. M., Arbones, M. L. and Estivill, X. (2000). Identification of seven novel SNPS (five nucleotide and two amino acid substitutions) in the connexin31 (GJB3) gene. Hum Mutat **15**, 481-2.*

Lu, W., Katz, S., Gupta, R. and Mayer, B. J. (1997). Activation of Pak by membrane localization mediated by an SH3 domain from the adaptor protein Nck. Curr Biol 7, 85-94.

*Lu, W. and Mayer, B. J. (1999). Mechanism of activation of Pak1 kinase by membrane localization. Oncogene **18**, 797-806.*

*Luna, A., Matas, O. B., Martinez-Menarguez, J. A., Mato, E., Duran, J. M., Ballesta, J., Way, M. and Egea, G. (2002). Regulation of protein transport from the Golgi complex to the endoplasmic reticulum by CDC42 and N-WASP. Mol Biol Cell **13**, 866-79.*

*Machesky, L. M. and Gould, K. L. (1999). The Arp2/3 complex: a multifunctional actin organizer. Curr Opin Cell Biol **11**, 117-21.*

*Machesky, L. M. and Insall, R. H. (1999). Signalling to actin dynamics. J Cell Biol **146**, 267-72.*

*Mahajan, N. P., Harrison-Shostak, D. C., Michaux, J. and Herman, B. (1999). Novel mutant green fluorescent protein protease substrates reveal the activation of specific caspases during apoptosis. Chem Biol **6**, 401-9.*

*Mas, P., Devlin, P. F., Panda, S. and Kay, S. A. (2000). Functional interaction of phytochrome B and cryptochrome 2. Nature **408**, 207-11.*

*Martin, P. E., Blundell, G., Ahmad, S., Errington, R. J., Evans, W. H. (2001). Multiple pathways in the trafficking and assembly of connexion 26, 32 and 43 into gap junction intercellular communication channels. J Cell Sci **114**, 3845-55.*

*Miki, H., Sasaki, T., Takai, Y. and Takenawa, T. (1998a). Induction of filopodium formation by a WASP-related actin-depolymerizing protein N-WASP. Nature **391**, 93-6.*

Miki, H., Suetsugu, S. and Takenawa, T. (1998b). WAVE, a novel WASP-family protein involved in actin reorganization induced by Rac. Embo J 17, 6932-41.

*Montecino-Rodriguez, E. and Dorshkind, K. (2001). Regulation of hematopoiesis by gap junction-mediated intercellular communication. J Leukoc Biol **70**, 341-7.*

*Morley, S. M., Dundas, S. R., James, J. L., Gupta, T., Brown, R. A., Sexton, C. J., Navsaria, H. A., Leigh, I. M. and Lane, E. B. (1995). Temperature sensitivity of the keratin cytoskeleton and delayed spreading of keratinocyte lines derived from EBS patients. J Cell Sci **108 (Pt 11)**, 3463-71.*

*Muller, A., Homey, B., Soto, H., Ge, N., Catron, D., Buchanan, M. E., McClanahan, T., Murphy, E., Yuan, W., Wagner, S. N. et al. (2001). Involvement of chemokine receptors in breast cancer metastasis. Nature **410**, 50-6.*

*Murphy, G., Reynolds, J. J. and Hembry, R. M. (1989). Metalloproteinases and cancer invasion and metastasis. Int J Cancer **44**, 757-60.*

Murphy, G. A., Solski, P. A., Jillian, S. A., Perez de la Ossa, P., D'Eustachio, P., Der, C. J. and Rush, M. G. (1999). Cellular functions of TC10, a Rho family GTPase: regulation of morphology, signal transduction and cell growth. Oncogene **18**, *3831-45.*

Nelles, E., Butzler, C., Jung, D., Temme, A., Gabriel, H. D., Dahl, U., Traub, O., Stumpel, F., Jungermann, K., Zielasek, J. et al. (1996). Defective propagation of signals generated by sympathetic nerve stimulation in the liver of connexin32-deficient mice. Proc Natl Acad Sci U S A **93**, *9565-70.*

Nelson, R. D., Quie, P. G. and Simmons, R. L. (1975). Chemotaxis under agarose: a new and simple method for measuring chemotaxis and spontaneous migration of human polymorphonuclear leukocytes and monocytes. J Immunol **115**, *1650-6.*

Neudauer, C. L., Joberty, G., Tatsis, N. and Macara, I. G. (1998). Distinct cellular effects and interactions of the Rho-family GTPase TC10. Curr Biol **8**, *1151-60.*

Ng, T., Parsons, M., Hughes, W. E., Monypenny, J., Zicha, D., Gautreau, A., Arpin, M., Gschmeissner, S., Verveer, P. J., Bastiaens, P. I. et al. (2001). Ezrin is a downstream effector of trafficking PKC-integrin complexes involved in the control of cell motility. Embo J **20**, *2723-41.*

Nguyen, L., Rigo, J. M., Rocher, V., Belachew, S., Malgrange, B., Rogister, B., Leprince, P. and Moonen, G. (2001). Neurotransmitters as early signals for central nervous system development. Cell Tissue Res **305**, *187-202.*

Nicolson, G. L., Dulski, K. M. and Trosko, J. E. (1988). Loss of intercellular junctional communication correlates with metastatic potential in mammary adenocarcinoma cells. Proc Natl Acad Sci U S A **85**, *473-6.*

Nobes, C. D. and Hall, A. (1999). Rho GTPases control polarity, protrusion, and adhesion during cell movement. J Cell Biol **144**, *1235-44.*

Oviedo-Orta, E. and Evans, W. H. (2002). Gap junctions and connexins: potential contributors to the immunological synapse. J Leukoc Biol **72**, *636-42.*

Pal, J. D., Berthoud, V. M., Beyer, E. C., Mackay, D., Shiels, A. and Ebihara, L. (1999). Molecular mechanism underlying a Cx50-linked congenital cataract. Am J Physiol **276**, *C1443-6.*

Pal, J. D., Liu, X., Mackay, D., Shiels, A., Berthoud, V. M., Beyer, E. C. and Ebihara, L. (2000). Connexin46 mutations linked to congenital cataract show loss of gap junction channel function. Am J Physiol Cell Physiol **279**, *C596-602.*

Pauli, B. U., Schwartz, D. E., Thonar, E. J. and Kuettner, K. E. (1983). Tumor invasion and host extracellular matrix. Cancer Metastasis Rev **2**, *129-52.*

Pepperkok, R. Squire, A., Geley, S. Bastiaens, P., I. (1999). Simultaneous detection of multiple green fluorescent proteins in live cells by fluorescence lifetime imaging microscopy. Curr Biol **9**, *269-72.*

Perez Velazquez, J. L. and Carlen, P. L. (2000). Gap junctions, synchrony and seizures. Trends Neurosci **23**, *68-74.*

Podolin, P. L., Bolognese, B. J., Foley, J. J., Schmidt, D. B., Buckley, P. T., Widdowson, K. L., Jin, Q., White, J. R., Lee, J. M., Goodman, R. B. et al. (2002). A potent and selective nonpeptide antagonist of CXCR2 inhibits acute and chronic models of arthritis in the rabbit. J Immunol **169**, *6435-44.*

Pokorna, E., Jordan, P. W., O'Neill, C. H., Zicha, D., Gilbert, C. S. and Vesely, P. (1994). Actin cytoskeleton and motility in rat sarcoma cell populations with different metastatic potential. Cell Motil Cytoskeleton **28**, *25-33.*

Politz, J. C. *(1999). Use of caged fluorochromes to track macromolecular movement in living cells. Trends Cell Biol* ***9****, 284-7.*

Pollard, T. D. and Borisy, G. G. *(2003). Cellular motility driven by assembly and disassembly of actin filaments. Cell* ***112****, 453-65.*

Pollock, R. E. *(1999). Manual of Clinical Oncology* ***7th ed.****, Wiley-Liss, Inc., New York.*

Prehoda, K. E., Scott, J. A., Mullins, R. D. and Lim, W. A. *(2000). Integration of multiple signals through cooperative regulation of the N-WASP-Arp2/3 complex. Science* ***290****, 801-6.*

Rabionet, R., Lopez-Bigas, N., Arbones, M. L. and Estivill, X. *(2002). Connexin mutations in hearing loss, dermatological and neurological disorders. Trends Mol Med* ***8****, 205-12.*
Ridley, A. J. *(1996). Rho: theme and variations. Curr Biol* ***6****, 1256-64.*

Ridley, A. J., Comoglio, P. M. and Hall, A. *(1995). Regulation of scatter factor/hepatocyte growth factor responses by Ras, Rac, and Rho in MDCK cells. Mol Cell Biol* ***15****, 1110-22.*

Ridley, A. J., Paterson, H. F., Johnston, C. L., Diekmann, D. and Hall, A. *(1992). The small GTP-binding protein rac regulates growth factor-induced membrane ruffling. Cell* ***70****, 401-10.*

Ripps, H. *(2002). Cell death in retinitis pigmentosa: gap junctions and the 'bystander' effect. Exp Eye Res* ***74****, 327-36.*

Rojas, R., Ruiz, W. G., Leung, S. M., Jou, T. S. and Apodaca, G. *(2001). Cdc42-dependent modulation of tight junctions and membrane protein traffic in polarized Madin-Darby canine kidney cells. Mol Biol Cell* ***12****, 2257-74.*

Rook, A., Wilkinson, D., Ebling, F., Champion, R. and Burton, J. *(1998). Textbook of dermatology* ***6th ed.****, Blackwell Scientiffic, London.*

Rouach, N., Avignone, E., Meme, W., Koulakoff, A., Venance, L., Blomstrand, F. and Giaume, C. *(2002). Gap junctions and connexin expression in the normal and pathological central nervous system. Biol Cell* ***94****, 457-75.*

Rusciano, D. and Burger, M. M. *(1992). Why do cancer cells metastasize into particular organs? Bioessays* ***14****, 185-94.*

Sanders, L. C., Matsumura, F., Bokoch, G. M. and de Lanerolle, P. *(1999). Inhibition of myosin light chain kinase by p21-activated kinase. Science* ***283****, 2083-5.*

Saunders, M. M., Seraj, M. J., Li, Z., Zhou, Z., Winter, C. R., Welch, D. R. and Donahue, H. J. *(2001). Breast cancer metastatic potential correlates with a breakdown in homospecific and heterospecific gap junctional intercellular communication. Cancer Res* ***61****, 1765-7.*

Sells, M. A., Boyd, J. T. and Chernoff, J. *(1999). p21-activated kinase 1 (Pak1) regulates cell motility in mammalian fibroblasts. J Cell Biol* ***145****, 837-49.*

Sells, M. A., Knaus, U. G., Bagrodia, S., Ambrose, D. M., Bokoch, G. M. and Chernoff, J. *(1997). Human p21-activated kinase (Pak1) regulates actin organization in mammalian cells. Curr Biol 7, 202-10.*

Seppa, H., Grotendorst, G., Seppa, S., Schiffmann, E. and Martin, G. R. *(1982). Platelet-derived growth factor in chemotactic for fibroblasts. J Cell Biol* ***92****, 584-8.*

Serre-Beinier, V., Mas, C., Calabrese, A., Caton, D., Bauquis, J., Caille, D., Charollais, A., Cirulli, V. and Meda, P. *(2002). Connexins and secretion. Biol Cell* ***94****, 477-92.*

Severs, N. J., Rothery, S., Dupont, E., Coppen, S. R., Yeh, H. I., Ko, Y. S., Matsushita, T., Kaba, R. and Halliday, D. *(2001). Immunocytochemical analysis of connexin expression in the healthy and diseased cardiovascular system. Microsc Res Tech* ***52****, 301-22.*

Shreiber, D. I., Enever, P. A. and Tranquillo, R. T. *(2001). Effects of pdgf-bb on rat dermal fibroblast behavior in mechanically stressed and unstressed collagen and fibrin gels. Exp Cell Res* ***266****, 155-66.*

Simon, A. M. and Goodenough, D. A. *(1998). Diverse functions of vertebrate gap junctions. Trends Cell Biol* ***8****, 477-83.*

Simon, A. M., Goodenough, D. A., Li, E. and Paul, D. L. *(1997). Female infertility in mice lacking connexin 37. Nature* ***385****, 525-9.*

Smits, H. A., Rijsmus, A., van Loon, J. H., Wat, J. W., Verhoef, J., Boven, L. A. and Nottet, H. S. *(2002). Amyloid-beta-induced chemokine production in primary human macrophages and astrocytes. J Neuroimmunol* ***127****, 160-8.*

Sohl, G., Degen, J., Teubner, B. and Willecke, K. *(1998). The murine gap junction gene connexin36 is highly expressed in mouse retina and regulated during brain development. FEBS Lett* ***428****, 27-31.*

Squire, A. and Bastiaens, P. I. *(1999). Three dimensional image restoration in fluorescence lifetime imaging microscopy. J Microsc* ***193 (Pt 1)****, 36-49.*

Stepien, E., Stanisz, J. and Korohoda, W. *(1999). Contact guidance of chick embryo neurons on single scratches in glass and on underlying aligned human skin fibroblasts. Cell Biol Int* ***23****, 105-16.*

Stowers, L., Yelon, D., Berg, L. J. and Chant, J. *(1995). Regulation of the polarization of T cells toward antigen-presenting cells by Ras-related GTPase CDC42. Proc Natl Acad Sci U S A* ***92****, 5027-31.*

Strohmeyer, R. and Rogers, J. *(2001). Molecular and cellular mediators of Alzheimer's disease inflammation. J Alzheimers Dis* ***3****, 131-157.*

Suetsugu, S., Hattori, M., Miki, H., Tezuka, T., Yamamoto, T., Mikoshiba, K. and Takenawa, T. *(2002). Sustained activation of N-WASP through phosphorylation is essential for neurite extension. Dev Cell* ***3****, 645-58.*

Suzuki, H. *(2000). Cellular mechanisms of myogenic activity in gastric smooth muscle. Jpn J Physiol* ***50****, 289-301.*

Takenawa, T. and Miki, H. *(2001). WASP and WAVE family proteins: key molecules for rapid rearrangement of cortical actin filaments and cell movement. J Cell Sci* ***114****, 1801-9.*

Tanabe, K., Tachibana, T., Yamashita, T., Che, Y. H., Yoneda, Y., Ochi, T., Tohyama, M., Yoshikawa, H. and Kiyama, H. *(2000). The small GTP-binding protein TC10 promotes nerve elongation in neuronal cells, and its expression is induced during nerve regeneration in rats. J Neurosci* ***20****, 4138-44.*

Ting, A. Y., Kain, K. H., Klemke, R. L. and Tsien, R. Y. *(2001). Genetically encoded fluorescent reporters of protein tyrosine kinase activities in living cells. Proc Natl Acad Sci U S A* ***98****, 15003-8.*

*Trosko, J. E. and Chang, C. C. (2001). Mechanism of up-regulated gap junctional intercellular communication during chemoprevention and chemotherapy of cancer. Mutat Res **480-481**, 219-29.*

*Vadlamudi, R. K., Li, F., Adam, L., Nguyen, D., Ohta, Y., Stossel, T. P. and Kumar, R. (2002). Filamin is essential in actin cytoskeletal assembly mediated by p21-activated kinase 1. Nat Cell Biol **4**, 681-90.*

*Verveer, P. J., Wouters, F. S., Reynolds, A. R. and Bastiaens, P. I. (2000). Quantitative imaging of lateral ErbB1 receptor signal propagation in the plasma membrane. Science **290**, 1567-70.*

Vesely, P., Chaloupkova, A., Urbanec, P., Urbancova, H., Bohac, L., Krchnakova, E., Franc, F., Sprincl, L., Vousden, K., Moss, R. et al. (1987). Patterns of in vitro behaviour characterizing cells of spontaneously metastasizing K2M rat sarcoma. Folia Biol (Praha) 33, 307-24.

Vetterkind, S., Miki, H., Takenawa, T., Klawitz, I., Scheidtmann, K. H. and Preuss, U. (2002). The rat homologue of Wiskott-Aldrich syndrome protein (WASP)-interacting protein (WIP) associates with actin filaments, recruits N-WASP from the nucleus, and mediates mobilization of actin from stress fibers in favor of filopodia formation. J Biol Chem 277, 87-95.

*Wang, D., Sai, J., Carter, G., Sachpatzidis, A., Lolis, E. and Richmond, A. (2002a). PAK1 kinase is required for CXCL1-induced chemotaxis. Biochemistry **41**, 7100-7.*

*Wang, W., Wyckoff, J. B., Frohlich, V. C., Oleynikov, Y., Huttelmaier, S., Zavadil, J., Cermak, L., Bottinger, E. P., Singer, R. H., White, J. G. et al. (2002b). Single cell behavior in metastatic primary mammary tumors correlated with gene expression patterns revealed by molecular profiling. Cancer Res **62**, 6278-88.*

*Wilkinson, P. C. (1987). Leucocyte locomotion: behavioural mechanisms for accumulation. J Cell Sci Suppl **8**, 103-19.*

Wouters, F. S., Verveer, P. J. and Bastiaens, P. I. (2001). Imaging biochemistry inside cells. Trends Cell Biol 11, 203-11.

*Wyckoff, J. B., Jones, J. G., Condeelis, J. S. and Segall, J. E. (2000a). A critical step in metastasis: in vivo analysis of intravasation at the primary tumor. Cancer Res **60**, 2504-11.*

*Wyckoff, J. B., Segall, J. E. and Condeelis, J. S. (2000b). The collection of the motile population of cells from a living tumor. Cancer Res **60**, 5401-4.*

*Xia, J. H., Liu, C. Y., Tang, B. S., Pan, Q., Huang, L., Dai, H. P., Zhang, B. R., Xie, W., Hu, D. X., Zheng, D. et al. (1998). Mutations in the gene encoding gap junction protein beta-3 associated with autosomal dominant hearing impairment. Nat Genet **20**, 370-3.*

*Xiang, Y., Li, Y., Zhang, Z., Cui, K., Wang, S., Yuan, X. B., Wu, C. P., Poo, M. M. and Duan, S. (2002). Nerve growth cone guidance mediated by G protein-coupled receptors. Nat Neurosci **5**, 843-8.*

*Yamaguchi, H., Miki, H. and Takenawa, T. (2002). Neural Wiskott-Aldrich syndrome protein is involved in hepatocyte growth factor-induced migration, invasion, and tubulogenesis of epithelial cells. Cancer Res **62**, 2503-9.*

*Yamaguchi, T., Chattopadhyay, N., Kifor, O., Butters, R. R., Jr., Sugimoto, T. and Brown, E. M. (1998). Mouse osteoblastic cell line (MC3T3-E1) expresses extracellular calcium (Ca2+o)-sensing receptor and its agonists stimulate chemotaxis and proliferation of MC3T3-E1 cells. J Bone Miner Res **13**, 1530-8.*

*Zhao, Z. S., Manser, E., Chen, X. Q., Chong, C., Leung, T. and Lim, L. (1998). A conserved negative regulatory region in alphaPAK: inhibition of PAK kinases reveals their morphological roles downstream of Cdc42 and Rac1. Mol Cell Biol **18**, 2153-63.*

Zicha, D., Allen, W. E., Brickell, P. M., Kinnon, C., Dunn, G. A., Jones, G. E. and Thrasher, A. J. *(1998). Chemotaxis of macrophages is abolished in the Wiskott-Aldrich syndrome. Br J Haematol* ***101****, 659-65.*

Zicha, D., Dobbie, I. M., Holt, M. R., Monypenny, J., Soong, D. Y., Gray, C. and Dunn, G. A. *(2003). Rapid actin transport during cell protrusion. Science* ***300****, 142-5.*

Zicha, D., Dunn, G. and Jones, G. *(1997). Analyzing chemotaxis using the Dunn direct-viewing chamber. Methods Mol Biol* ***75****, 449-57.*

Zicha, D. and Dunn, G. A. *(1995). Are growth factors chemotactic agents? Exp Cell Res* ***221****, 526-9.*

Zicha, D., Dunn, G. A. and Brown, A. F. *(1991). A new direct-viewing chemotaxis chamber. J Cell Sci* ***99 (Pt 4)****, 769-75.*

Zigmond, S. H. *(1988). Orientation chamber in chemotaxis. Methods Enzymol* ***162****, 65-72.*

Zigmond, S. H. and Hirsch, J. G. *(1973). Leukocyte locomotion and chemotaxis. New methods for evaluation, and demonstration of a cell-derived chemotactic factor. J Exp Med* ***137****, 387-410.*

Ziman, M., Preuss, D., Mulholland, J., O'Brien, J. M., Botstein, D. and Johnson, D. I. *(1993). Subcellular localization of Cdc42p, a Saccharomyces cerevisiae GTP-binding protein involved in the control of cell polarity. Mol Biol Cell* ***4****, 1307-16.*

5 APPENDICES

5.1 MATHEMATICA ROUTINES FOR THE QUANTITATION OF DYE TRANSFER

MAIN PROGRAM BODY

```
Install["path\\BINARY30.exe"];
<< "path\\ReadTIFFpackageLSM.m";
Needs["Statistics`DataManipulation`"]

dirpath = "ImagePath"
imageFiles = FileNames["*.tif", dirpath]
celFiles = FileNames["*.cel", dirpath]

Do[
      Clear[data];
      Clear[frameValues];
      frameValues = {};
      Print["FILE -> " <> imageFiles[[filesProgress]]];

Do[

//Load Image File

  Clear[imageData];
  Clear[displacements];
  Clear[total];
  Clear[pixelValue];
  imageData =
    Flatten[{ReadTIFFg[imageFiles[[filesProgress]],  report -> False,
ignoreNonBaseline -> False, pageNumber -> progress]}, 1];

//Bin image 4 × 4

Do[
    Do[
      imageData[[lineNumber]] =
          Flatten[Partition[imageData[[lineNumber]],4] /.
            {w_, x_, y_, z_}:>(w + x + y + z)/4 // N, 1];
      , {lineNumber, Length[imageData]}];

    imageData = Transpose[imageData];
    , {twice, 2}];

// Threshold image

imageThreshold = extractThreshold[imageData];
imageData = imageData /. gv_Real :>
If[gv < imageThreshold, 0, If[gv < 4095, gv - imageThreshold, 4095]];
```

```
//Calculate pixel displacements

cellx = Round[cells[[filesProgress, 1]]/4];
celly = Round[cells[[filesProgress, 2]]/4];
celly = Length[imageData] - celly;

displacements = Transpose[Table[
Sqrt[(cellx - pixelX)^2 + (celly - pixelY)^2] // N, {pixelX,
Length[imageData[[1]]]}, {pixelY, Length[imageData]}]];


//Calculate NMD

pixelValue = (Flatten[displacements]* Flatten[imageData ]);
total = (Plus @@ pixelValue)/(Plus @@ Flatten[imageData]);
Print["now processing -> sequnece " <> ToString[filesProgress] <> " frame
" <> ToString[progress] <> " value -> " <> ToString[total]];
AppendTo[frameValues, total];

, {progress, 3, 300, 3}];


// Plot NMD values and save to file

ListPlot[frameValues, PlotJoined -> True, PlotStyle -> RGBColor[0,1,0]];

outputFileName2 = dirpath <>
StringDrop[StringDrop[imageFiles[[filesProgress]],
StringLength[dirpath]], -4] <> ".dye";

outputFile2 = OpenWrite[outputFileName2];
Write[outputFile2, frameValues];
Close[outputFile2];

, {filesProgress, Length[imageFiles]}];

Print["done."];

// END
```

PROGRAM FUNCTIONS

FUNCTION: AUTOMATIC THRESHOLD

```
Clear[extractThreshold];
extractThreshold[imageData_] :=
Module[{histoData, data, quadruples},

histoData = histogram[Flatten[imageData]] // N;
data = Drop[histoData,
      Position[histoData,Max[Transpose[histoData][[2]]]][[1, 1]]];

quadruples = Partition[
      Partition[Transpose[data][[2]], 2, 1] /. {x1_, y1_}
      :> x1 - y1, 7, 1];

quadruples = Sort /@ quadruples;
data[[Position[quadruples,
      Cases[quadruples, {a_, b_, ___} /;
      a < 0 && b < 0][[1]]][[1, 1]] + 2, 1]]
];
```

Note: this function additionally calls the histogram function that is defined in section 5.2.

5.2 MATHEMATICA ROUTINES FOR THE EXTRACTION OF CELL INTENSITIES

MAIN PROGRAM BODY

```
Install["path\\BINARY30.exe"];
<< "path\\ReadTIFFpackageLSM.m";
Needs["Statistics`DataManipulation`"]

dirpath = "ImagePath"
imageFiles = FileNames["*.tif", dirpath]
celFiles = FileNames["*.cel", dirpath]

boundryRadius = 30;
      Do[
      imageName1 = StringDrop[StringDrop[imageFiles[[currentFile]],
      Take[StringPosition[imageFiles[[currentFile]], "\\"], -1]
      [[1, 2]]], -4
      ];

// Prepare output file

currentFileName = "data output path\\" <> imageName1 <> ".int";
outputFile = OpenWrite[currentFileName];
Write[
outputFile, {FRAME, CELL, {x, y}, MODE, TOTAL_INTENSITY,
INTENSITY_AREA}];
Close[outputFile];

filmLength = Max[ReadList[celFiles[[currentFile]]] /.
{c_Integer, f_, {x_, y_, p_}} -> f];
Print["Film Length - > ", filmLength];

oldData = {};

Do[
   Print["Round -> ", round];

// Load image file

      imageData = getImage[currentFile, round];
      hisData = histogram[Flatten[imageData],
      numberOfBins -> 4096];
      modalValue = hisData[[Position[hisData, Max[hisData /.
      {x_, y_} -> y]][[1, 1]]]][[1]];


// Threshold image

      imageData = imageData - modalValue;
      imageData = imageData /. gv_Real :>  If[gv < 0, 0, gv];
      currentFrame = getCellPositions[currentFile, round];
      Print["Cells in frame -> ", Length[currentFrame]];
```

```
      If[round > 1,
      lastFrame = getCellPositions[currentFile, round - 1];];
      frameData = {}; cellData = {}; nextOldData = {};
Do[
      image = imageData;
      intensityValues = {};

// Generate cell boundaries

      boundry = cellBoundry[turn, boundryRadius, currentFrame];
      Do[image[[boundry[[i]][[1]], boundry[[i]][[2]]]] = 4096
      ,{i, Length[boundry]}];

// extract cell intensities

      Do[
          pixelIntensities = getRowValues[image, i];
          AppendTo[intensityValues, pixelIntensities];
      ,{i, Dimensions[image][[1]]}];
intensityValues = Flatten[intensityValues];
intensityValues = Delete[intensityValues, Position[intensityValues,0]];
totalIntensity = Round[Plus @@ Flatten[intensityValues] // N];

// Reject values where cell boundaries overlap

rejectCell = rejectionTest[currentFrame, turn];
Print[rejectCell];
AppendTo[nextOldData, {currentFrame[[turn]][[2]], totalIntensity}];
cellData = {currentFrame[[turn]][[1]], currentFrame[[turn]][[2]],
            {currentFrame[[turn]][[3]], currentFrame[[turn]][[4]]},
            modalValue, totalIntensity, Length[intensityValues]};
If[rejectCell != True, AppendTo[frameData, cellData]];
Print[modalValue, " ", totalIntensity];
, {turn, Length[currentFrame]}
];

// Save data to file

outputFile = OpenAppend[currentFileName];
Write[outputFile, frameData]; Close[outputFile];
oldData = nextOldData;
Print["last analyses; round = ", round, " currentFile = ",
currentFile];
, {round, filmLength}],

{currentFile, 1, Length[imageFiles]}
];
Print["done."];

// END
```

PROGRAM FUNCTIONS

FUNCTION: LOAD IMAGE

```
Clear[getImage];
getImage[localFile_, localRound_] :=
Module[{localImageData},

localImageData = Flatten[{ReadTIFFlsm[imageFiles[[localFile]],
report -> False, ignoreNonBaseline -> False, subImage -> 0,
pageNumber -> localRound]}, 1];
localImageData
];
```

FUNCTION: GENERATE IMAGE HISTOGRAM

```
Clear[histogram];
histogram[data_List, opts___] :=
Module[{ymin, ymax, dy, datfreq, xp, k = 0, dat, xpos, plotFreq, xfact,
      nbins, numberOfBins},

nbins = numberOfBins /. {opts} /. numberOfBins -> 700;
ymin = Min[data]; ymax = Max[data];
dy = ((ymax - ymin) + (ymax - ymin)*1./(100*nbins))/nbins;
ymin = ymax - nbins*dy;
Frequencies[data /. y_ :> Ceiling[(y - ymin)/dy]] /. {x_,y_} :>
      {ymin + dy*y - dy/2, x}
];
```

FUNCTION: EXTRACT CELL POSITIONS

```
Clear[getCellPositionsNew];
getCellPositionsNew[localFile_, localRound_] :=
Module[{localCurrentFrame, cells},

cells = ReadList[celFiles[[localFile]]];
pathCells = Cases[cells, {c_, f_, {x_, y_, p_}} /; p >= 16 -> c];
pathCells = Cases[cells, {c_, f_, {x_, y_, p_}} /;
      MemberQ[pathCells, c]];

localCurrentFrame = pathCells /.
      {c_, f_, {x_, y_, p_}} /; f == localRound -> {f, c, x,
              Dimensions[imageData][[1]] - y};

localCurrentFrame = Cases[localCurrentFrame, {f_, c_, x_, y_}];
localCurrentFrame = Cases[localCurrentFrame, {f_, c_, x_, y_} /;
       x - 35 > 0 && x + 35 < Dimensions[imageData][[2]] && y - 35 > 0 &&
      y + 35 < Dimensions[imageData][[1]]];

localCurrentFrame
];
```

FUNCTION: GENERATE CELL BOUNDARYS

```
Clear[cellBoundry];
cellBoundry[cellNumber_Integer, boundryRadius_Integer, localCurrentFrame_]
:=
Module[{drawCircle, locali},

drawCircle = Table[{Round[localCurrentFrame[[cellNumber]][[4]] +
      boundryRadius*Cos[theta]],
      Round[localCurrentFrame[[cellNumber]][[3]] +
      boundryRadius*Sin[theta]]}, {theta, 0, 2*Pi, .01}];

drawCircle
];
```

FUNCTION: EXTRACT CELL INTENSITIES

```
Clear[getRowValues];
getRowValues[localImage_, iterator_] :=
Module[{circlePositions, circlePositionsTemp,
      localIntensityValues, locali},

circlePositions = Position[localImage[[iterator]], 4096];
circlePositionsTemp = Partition[Flatten[circlePositions], 2, 1];
circlePositionsTemp =
      Table[Subtract @@ Reverse[circlePositionsTemp[[locali]]], {locali,
      Length[circlePositionsTemp]}];
If[Max[circlePositionsTemp] > 2,
      circlePositionsTemp =
      Flatten[Position[circlePositionsTemp, x_ /; x > 1]];
      circlePositionsTemp =
      Flatten[{Take[circlePositions, circlePositionsTemp],
      Take[circlePositions, circlePositionsTemp + 1]}];
      localIntensityValues =
      Drop[Drop[Take[
      localImage[[iterator]], circlePositionsTemp],1], -1];,
      localIntensityValues = {0}; localIntensityValues
];

localIntensityValues
];
```

FUNCTION: REJECT CELLS WITH OVERLAPPING BOUNDARYS

```
Clear[rejectionTest];
rejectionTest[currentFrameLocal_, turnLocal_] := Module[{rejectionValues,
        tempCurrentFrame, locali, localj,allCells, pixelIntensitiesLocal,
        rejectCellLocal},

rejectionImage = image;
rejectionValues = {};
tempCurrentFrame = Drop[currentFrameLocal, {turnLocal, turnLocal}];

      Do[
            allCells = cellBoundry[localj,
            boundryRadius, tempCurrentFrame];
            Do[
                  rejectionImage[[allCells[[locali]][[1]],
                  allCells[[locali]][[2]]]] = 5000.
            ,{locali, Length[allCells]}];
      ,{localj, Length[tempCurrentFrame]}];

allCells = cellBoundry[turnLocal, boundryRadius, currentFrameLocal];

      Do[
            rejectionImage[[allCells[[locali]][[1]],
            allCells[[locali]][[2]]]] = 4096
      , {locali, Length[allCells]}];

      Do[
            pixelIntensitiesLocal = getRowValues[rejectionImage, locali];
            AppendTo[rejectionValues, pixelIntensitiesLocal];
      , {locali, Dimensions[rejectionImage][[1]]}];

rejectionValues = Flatten[rejectionValues];
rejectionValues = Delete[rejectionValues, Position[rejectionValues, 0]];
Print["cell -> ", turnLocal];

If [Length[Cases[rejectionValues, localx_Real /; localx == 5000.]] > 0,
        Print["Rejected -> Yes"];
        rejectCellLocal = True;
        ,
        Print["Rejected -> No"];
        rejectCellLocal = False
];
rejectCellLocal
];
```

5.3 LIST OF MANUFACTURERS

Amersham Biosciences UK Limited, Pollards Wood, Nightingales Lane, Chalfont, St.Giles, Bucks HP8 4SP, UK

Becker & Hickl GmbH, Nahmitzer, Damm 30D-12277, Berlin, Tel: +49 (30) 787 56 32, E-mail: info@beckl-hicker.com

BDH Laboratory Supplies, Poole, Dorset BH15 1TD, UK, Tel: 01202 660444

Clontech, 1020 East Meadow Circle, Palo Alto, CA 94303-4230, USA

Eppendorf AG, Barkhausenweg 122339, Hamburg Germany, Tel: ++ 49 40 53 8010

Hamamatsu Photonics UK Ltd., Lough Point, 2 Gladbeck Way, Windmill Hill, Enfield, Middlesex EN2 7JA, UK, Tel: 020 8367 3560, Fax: 020 8367 6384, E-mail: info@hamamatsu.co.uk

Kinetic Imaging Ltd, 1 Orchard Place, Nottingham Business Park, Nottingham NG8 6PX, UK, Tel: 0115 973 9027, Fax: 0115 973 9021, E-mail: info@kinetic-mail.co.uk

Märzhäuser Wetzlar GmbH & CO KG, In der Murch 15, 35579 Wetzlar-Steindorf, Germany, Tel: +49-6441-91160, Fax: +49-6441-911640 E-mail: info@marzhauser.com

MatTek, 200 Homer Ave., Ashland, MA 01721, USA, Tel.: 508-881-6771, Fax: 508-879-1532

Molecular Probes Inc., 4849 Pitchford Ave., Eugene, OR 97402 9165, USA, Tel: +1 541 465 8300, Fax: +1 541 344 6504

Nikon instruments, 380 Richmond Road, Kingston upon Thames, Surrey KT2 5PR, UK, Tel: +44-20-8541-4440, Fax: +44-20-8541-4584, E-mail: www.ave.nikon.co.jp

Sigma-Aldrich Company Ltd., The Old Brickyard, New Road, Gillingham, Dorset SP8 4XT, Tel: +44 800 717181

Spectra-Physics GmbH, Guerickeweg 7, D-64291 Darmstadt, Germany, Tel: ++44 (0) 1442-258100, Fax: ++44 (0) 1442-268538, E-mail; www.spectraphysics.com

Weber Scientific Int. Ltd., 40 Udnet Park Rd, Teddington, Middlesex TW11 9BG, UK, Tel: +44-281-9776330, Fax: +44-281-9434224

Zeiss, Carl Zeiss Ltd., PO Box 78, Woodfield Road, Welwyn Garden City, Herts AL7 1LU, UK, Tel: 01707 871200, Fax: 01707 330237

5.4 AUTHOR PUBLICATIONS

Zicha, D., Dobbie, I. M., Holt, M. R., Monypenny, J., Soong, D. Y., Gray, C. and Dunn, G. A. (2003). Rapid actin transport during cell protrusion. *Science* **300**, 142-5.

Di, W. L.*, Monypenny, J.*, Common, J. E., Kennedy, C. T., Holland, K. A., Leigh, I. M., Rugg, E. L., Zicha, D. and Kelsell, D. P. (2002). Defective trafficking and cell death is characteristic of skin disease-associated connexin 31 mutations. *Hum Mol Genet* **11**, 2005-14.

Dunn, G. A., Dobbie, I. M., Monypenny, J., Holt, M. R. and Zicha, D. (2002). Fluorescence localization after photobleaching (FLAP): a new method for studying protein dynamics in living cells. *J Microsc* **205**, 109-12.

Ng, T., Parsons, M., Hughes, W. E., Monypenny, J., Zicha, D., Gautreau, A., Arpin, M., Gschmeissner, S., Verveer, P. J., Bastiaens, P. I. et al. (2001). Ezrin is a downstream effector of trafficking PKC-integrin complexes involved in the control of cell motility. *Embo J* **20**, 2723-41.

Holt, M. R., Soong, D. Y., Monypenny, J., Dobbie, I. M., Zicha, D. and Dunn, G. (in press). Using bioprobes to follow protein dynamics in living cells. In *Cell Motility: from molecules to organisms*, (ed. A. Ridley, P. Clark and M. Peckham), Wiley & Sons.

Published abstracts

Monypenny, J. (2000). Investigating the role of the Rho family of GTPases in the chemotaxis of cancer cells. *Acta Medica (Hradec Králové)* **43**, 161.

*Join first authors

Rapid Actin Transport During Cell Protrusion

Daniel Zicha,[1] Ian M. Dobbie,[2] Mark R. Holt,[3] James Monypenny,[1] Daniel Y. H. Soong,[3] Colin Gray,[1] Graham A. Dunn[3]*

Transformed rat fibroblasts expressing two variants of green fluorescent protein, each fused to β-actin, were used to study actin dynamics during cell protrusion. The recently developed FLAP (fluorescence localization after photobleaching) method permits the tracking of one fluorophore after localized photobleaching by using the other as a colocalized reference. Here, by visualizing the ratio of bleached to total molecules, we found that actin was delivered to protruding zones of the leading edge of the cell at speeds that exceeded 5 micrometers per second. Monte Carlo modeling confirmed that this flow cannot be explained by diffusion and may involve active transport.

Understanding actin dynamics in the leading lamellae of cultured fibroblasts has long been considered the key to understanding cell locomotion. Recent studies have unraveled an intricate underlying biochemistry, including the role of the Arp2/3 complex in actin polymerization and the role of cofilin in depolymerization (*1*, *2*). They have provided mechanistic explanations for the polymerization of actin during the protrusion of thin veil-like lamellipodia (ruffles) at the leading margin of the cell and for the constant rearward flow of polymerized actin (F-actin) at a rate of 1 to 2 μm/min away from the margin (*1*, *3*). Advances in single-molecule speckle fluorescence have allowed the lifetimes of actin molecules in filaments to be studied and have revealed that, although the rate of actin polymerization is promoted within 1 μm of the leading edge, both polymerization and depolymerization occur at a high rate during the rearward flow of F-actin (*3*).

In contrast, the equally crucial question of how actin monomer (G-actin) returns to the leading edge has received little attention beyond the assumption that it happens by diffusion (*1*). We report an extension of the fluorescence localization after photobleaching (FLAP) method that may shed light on the mechanism of this process. Highly malignant transformed rat fibroblasts of the T15 line were chosen for this study because they show very active lamellipodial protrusion but

[1]Light Microscopy, Cancer Research UK, Lincoln's Inn Fields Laboratories, London WC2A 3PX, UK. [2]Genome Stability Laboratory, Department of Biochemistry, National University of Ireland, Galway, Ireland. [3]The Randall Centre, New Hunt's House, Guy's Campus, King's College London, London SE1 1UL, UK.

*To whom correspondence should be addressed. E-mail: graham.a.dunn@kcl.ac.uk

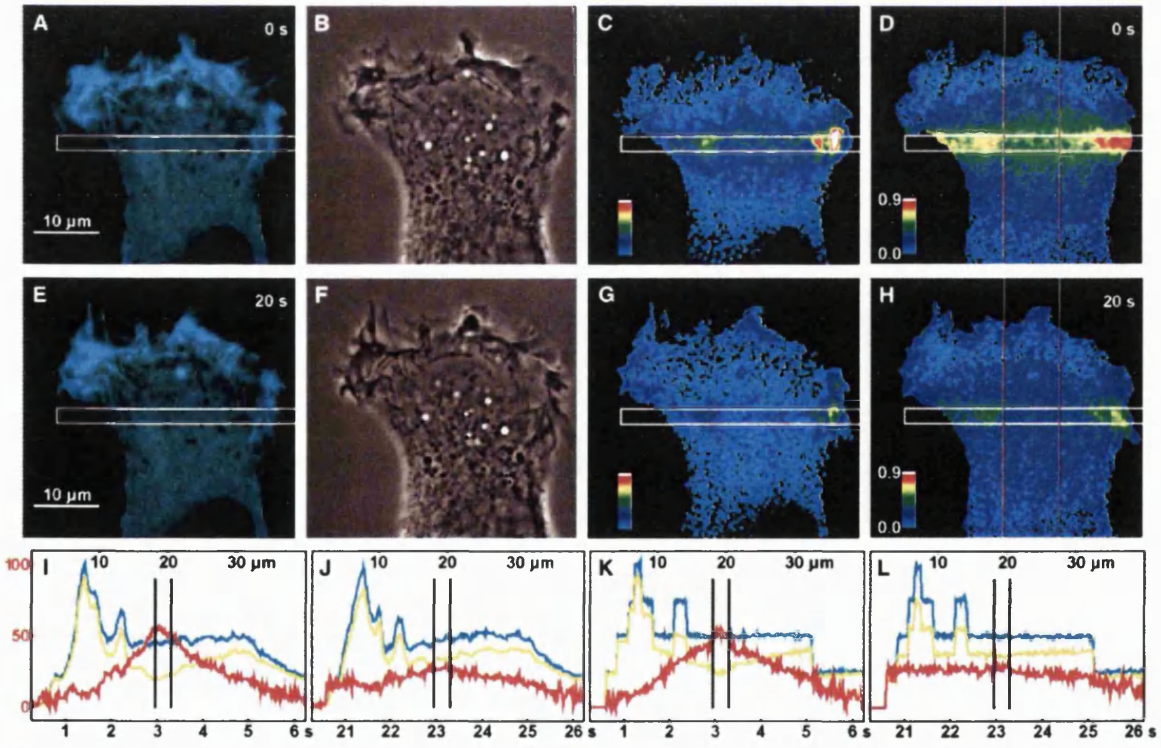

Fig. 1. (**A** to **H**) Eight scanning confocal images of the leading lamella of a T15 cell scanned from top to bottom immediately after a strip (white box) was photobleached for 4 s (A to D) and scanned again 20 s later (E to H). (A) and (E), CFP fluorescence images; (B) and (F), phase contrast images; (C) and (G), absolute FLAP images; (D) and (H), FLAP ratio images. (**I** and **J**) Traces of CFP- and YFP-actin (cyan and yellow, respectively) and the FLAP ratio signal (red) integrated across a narrow central band [gray lines in (D) and (H)] immediately after bleaching (I) and 20 s later (J). Vertical parallel lines indicate the bleach zone, and the horizontal axis is calibrated for both distance and time of scan progress after the end of bleaching. (**K** and **L**) Diffusion of G-actin along the *y* axis of the cell immediately after bleaching (K) and 20 s later (L) is modeled with a diffusion coefficient of 6 $\mu m^2/s$, an F-actin/G-actin ratio of 0.1, and a half-life of F-actin of 20 s. Composite images simulate the progress of scanning. Details of laser scanning microscopy with a Zeiss LSM 510 and of the cDNA constructs used for nuclear microinjection are as given in (*4*, *5*).

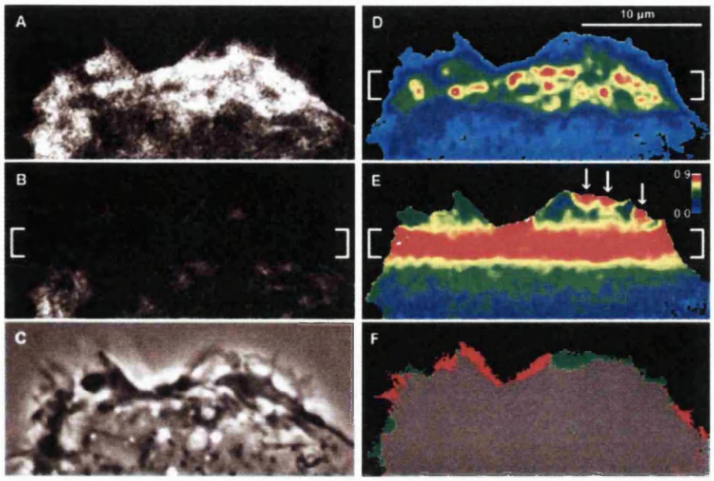

Fig. 2. Six images of the same T15 cell as in Fig. 1, scanned from top to bottom immediately after a strip (white brackets) was photobleached for 4 s, showing (**A**) CFP-actin, (**B**) YFP-actin, (**C**) phase contrast, (**D**) absolute FLAP, (**E**) FLAP ratio, and (**F**) a diagram of protrusion (green) and retraction (red) of the cell margin constructed from two thresholded CFP images acquired immediately before and after bleaching. The CFP and YFP images are shown in gray scale for comparison with each other. White arrows in the FLAP ratio image (E) indicate regions of strongly labeled actin at the leading edge.

few high-order actin structures such as stress fibers (Fig. 1, B and F). The yellow fluorescent protein (YFP) target fluorophore was photobleached in a narrow strip across the leading lamella of a T15 cell and analyzed with both absolute and ratio FLAP methods (Fig. 1). Absolute FLAP images (Fig. 1, C and G) were derived from the difference between the images of the target fluorophore and the reference fluorophore, cyan fluorescent protein (CFP) (*4*). FLAP ratio images (Fig. 1, D and H) were calculated as 1 minus the ratio of target to reference fluorophore intensity (*5*). Although the absolute FLAP images give the expected number of bleach-labeled YFP-actin molecules at each pixel location, the FLAP ratio images express this number as a fraction of the total YFP-actin molecules at that location. Thus, the FLAP ratio signal enabled us to track the dispersal of the bleach-labeled actin through regions of differing actin density (Fig. 1, C and D).

In images scanned immediately after the 4-s bleach period, the central region of the bleach strip showed a rapid dispersal of the

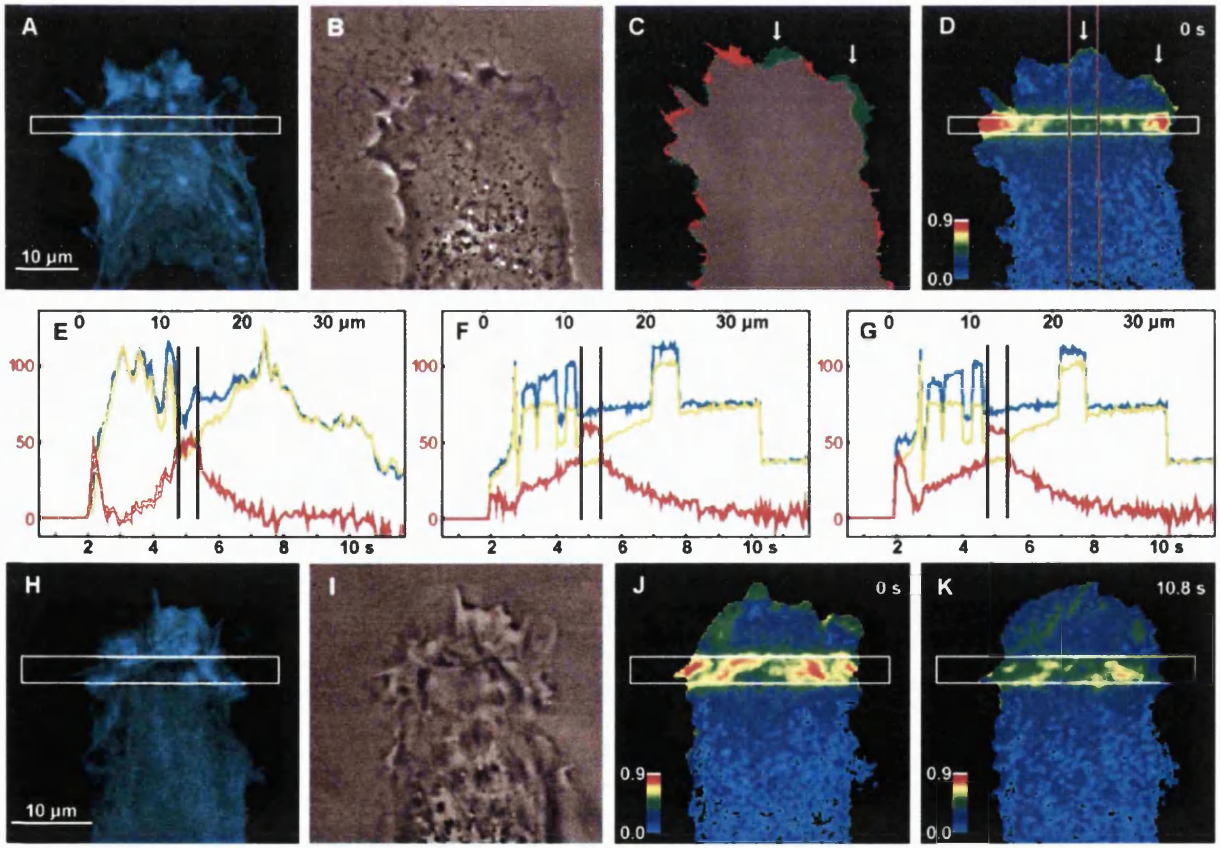

Fig. 3. Images of two T15 cells scanned immediately after a strip (white box) was photobleached for 1.8 s (**A** to **D**) or 1.7 s (**H** to **J**) and of the last cell scanned again 10.8 s later (**K**), showing CFP-actin (A and H), phase contrast (B and I), protrusion and retraction (C), and FLAP ratio (D, J, and K). White arrows indicate coincidence between regions of profusion (C) and regions of highly labled actin (D). (**E**) Signal traces as in Fig. 1 are integrated between the gray lines in (D) immediately after bleaching. (**F**) Diffusion of G-actin along the *y* axis of the cell is modeled with a diffusion coefficient of 5.65 $\mu m^2/s$, an F-actin/G-actin ratio of 0.8, and an F-actin half-life of 4 s together with protrusion and trapping of G-actin at the leading edge. (**G**) The final model further incorporates a forward drift at 6 μm/s of 6% of total G-actin; all other parameters are as in (F).

FLAP ratio signal into the surrounding lamella, whereas the lateral regions showed a much more persistent signal (Fig. 1D). We used a Monte Carlo model of diffusion during photobleaching (Fig. 1, K and L) to estimate that the bleach-labeled G-actin in the central region (Fig. 1, I and J) had a diffusion coefficient of 5.65 $\mu m^2/s$ (supporting online text). This is consistent with a published estimate of 5.8 $\mu m^2/s$ for G-actin in cytoplasm derived from fluorescence recovery after photobleaching (FRAP) measurements (*6*). Our best-fit model incorporated nondiffusible F-actin with an F-actin/G-actin ratio of 0.1. An F-actin half-life of less than 20 s was required to mimic the dispersal of the signal (Fig. 1, J and L), which is comparable with an estimate of 30 s for the half-life of actin filaments in the broad leading lamellipodium of *Xenopus* fibroblasts (*3*). When the same cell was bleached closer to the leading edge a few minutes later (Fig. 2), the dispersal of the FLAP ratio signal was slow (Fig. 2E) and comparable to that in the lateral regions of the bleach zone in Fig. 1. This indicates that a continuous band of relatively stable actin, about 5 to 7 μm wide, extended around the peripheral zone of the leading lamella.

The most noticeable feature, however, was the sudden appearance of strongly labeled actin at discrete regions of the leading edge (Fig. 2E, arrows). The maximum time available for these YFP-actin molecules to become photobleached and then to migrate to the leading edge was 5 s. The high signal also indicates that these molecules probably polymerized at the leading edge. A diagram of protrusion and retraction of the leading margin during a 15-s interval (Fig. 2F) revealed that the discrete zones of highly labeled actin were confined to a region in which the margin was actively protruding.

To analyze whether this rapid translocation of actin to the leading edge during protrusion could be due solely to molecular diffusion, we assumed that the diffusion coefficient of G-actin was again 5.65 $\mu m^2/s$, although there is much more F-actin obstructing diffusion in the frontal zone. However, the effect of obstruction is probably slight: It has been estimated that a reticular network must occlude 90 to 97% of diffusion space in order to reduce diffusion by 39 to 60% (*7*).

In an example of the furthest distance over which we have observed rapid translocation, highly labeled actin (Fig. 3D, arrows) reached the edge 2 s after bleaching a strip 12 μm away for 1.8 s, giving an estimated speed of translocation of around 6 μm/s. Again, the protrusion-retraction diagram (Fig. 3C, arrows) showed a good correlation between the appearance of actin at the edge and active protrusion. A diffusion model required an F-actin/G-actin ratio of 0.8 and a half-life of F-actin of 4 s in order to model the dispersion of actin within the lamella, although this model showed no elevated FLAP ratio signal at the leading edge (supporting online text). We obtained a slightly elevated signal at the leading edge (Fig. 3F), although not nearly as high as in the real cell (Fig. 3E), by incorporating protrusion into the model and by simulating the conversion of G-actin to F-actin within 0.4 μm of the edge. Only 15.9% of the YFP molecules in the whole cell were bleached, and in the model the edge signal never rose much above 20%, no matter how long it was run, indicating that molecular diffusion could not account for the observed signal of 40% at the leading edge regardless of diffusion coefficient. In order to obtain an adequate fit to observed data, we incorporated active transport of actin into the model (Fig. 3G). This was done by biasing the diffusion of a subpopulation of G-actin (6% of total G-actin) to give a forward drift velocity of 6 μm/s superimposed on diffusion (supporting online text). A further experiment showed that the labeled actin newly incorporated into the leading edge migrated rearward (Fig. 3, J and K). The fact that this actin did not disperse rapidly indicates that it was polymerized.

A biochemical analysis revealed that the rapid recruitment of actin to the leading edge was abolished by treatment with 5 μM of the actin filament–stabilizing drug jasplakinolide for 20 min before bleaching (Fig. 4, A to C). After treatment, the bleach zone showed a highly persistent FLAP ratio signal with little decay after nearly 12 min (Fig. 4C), whereas normally the signal was uniformly dispersed throughout the cell after 2 to 3 min. Depletion of adenosine triphosphate with 6 mM 2- deoxyglucose plus 1 μM antimycin for 20 to 40 min suppressed ruffling activity and also abolished the rapid actin recruitment (Fig. 4, D to F). In contrast, treatment with the myosin light chain kinase (MLCK) inhibitor ML-7 (1 μM) (Fig. 4, G to I) or with the Rho-associated kinase (ROCK) inhibitor Y-27632 (10 μM) for 1 to 2 hours (Fig. 4, J to L) did not inhibit ruffling. Even so, there was no sign of rapid actin translocation to the leading edge in either case (Fig. 4, I and L). The

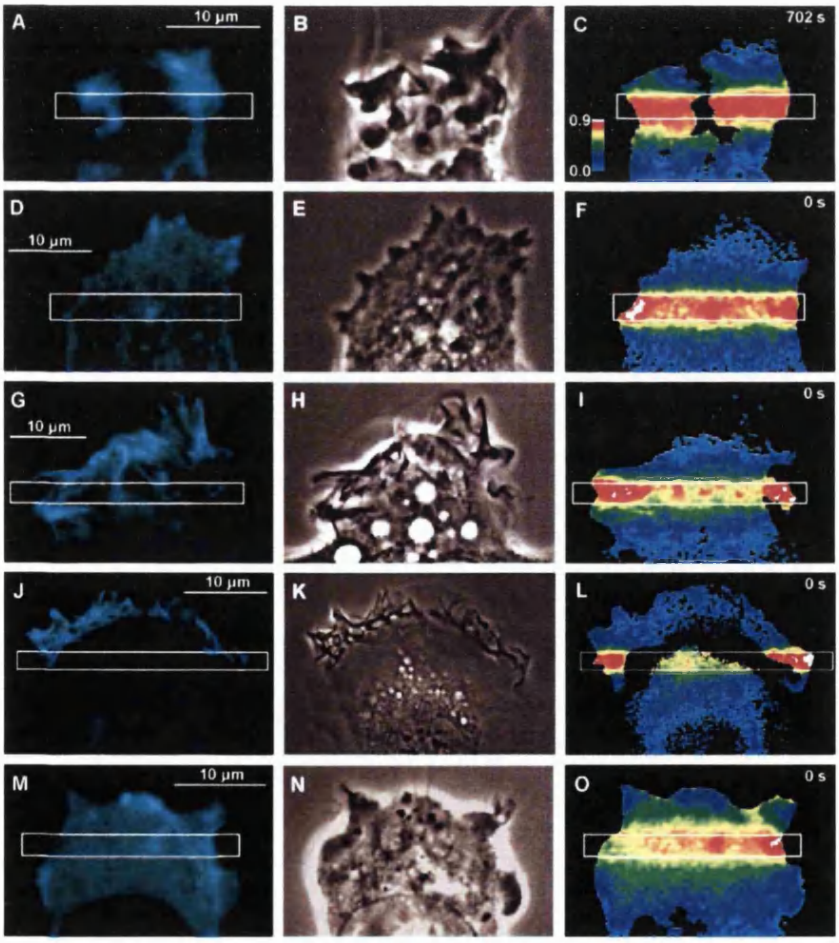

Fig. 4. CFP-actin (left), phase contrast (center), and FLAP ratio images (right) under different treatments with metabolic inhibitors: (**A** to **C**) 5 μM jasplakinolide; (**D** to **F**) 6 mM 2-deoxyglucose and 1 μM antimycin; (**G** to **I**) 1 μM ML-7; (**J** to **L**) 10 μM Y-27632; and (**M** to **O**) 500 nM nocodazole. Each FLAP ratio image is marked with the time after the end of bleaching that scanning was started.

ML-7 treatment but not the Y-27632 treatment significantly suppressed the speed of cell motility, measured as 5-min displacements, in analysis of variance tests versus the control [control: 1.32 ± 0.08 μm (mean ± SEM), $n = 41$ cells; ML-7 treatment: 1.11 ± 0.07 μm, $n = 42$ cells, $P < 0.05$; Y-27632 treatment: 1.49 ± 0.07 μm, $n = 41$ cells, not significant] (*5*). Finally, treatment with 500 nM nocodazole for 30 min (Fig. 4, M to O) led to the complete disruption of cytoplasmic microtubules and, although ruffling activity was changed in character (Fig. 4N), there were indications that labeled actin was still rapidly recruited to the leading edge (Fig. 4O).

In summary, we found that actin polymerized during protrusion of the leading edge can be recruited within 2 to 3 s from a region that extends up to 15 μm behind the edge. This process is too rapid to be explained by diffusion of G-actin and must involve some form of active transport. It requires G-actin, adenosine triphosphate, and active protrusion but not intact microtubules. The effects of MLCK inhibition indicate that myosin function is required for rapid actin transport, although not for ruffling. The similar effects of ROCK inhibition further suggest that the required myosin is activated by Rho and is probably nonmuscle myosin II.

We conclude that G-actin is not carried rapidly to the leading edge by microtubule-based motors or by motor proteins of the myosin superfamily. Myosin II is unlikely to transport actin directly, but it is needed for contraction of the cell body. This could generate a pressure gradient leading to a hydrodynamic flow that carries G-actin with it. The flow would be directed toward sites of reduced pressure that may occur where the cell margin is expanding rapidly. Such rapid expansion might occur passively at sites of cortical weakness or actively where polymerizing actin is pushing the membrane outward (*1*). Pressure-driven flow through gels can result in channeling, and there is some evidence for this in the figures. Retraction of the cell margin may occur by Rho-dependent contraction (*8*), in which case the mechanism we propose could account for a reported positive correlation between rates of protrusion and retraction (*9*). Rapid actin transport is not required for cell locomotion or for ruffling, which is thought to be regulated by Rac (*10*), but it may determine sites of protrusion and thus participate in signal-mediated cell polarity and directed locomotion. Our view is that hydrodynamic flow supplies actin from sites of high depolymerization to sites of rapid protrusion where diffusion alone is inadequate.

References and Notes

1. T. D. Pollard, L. Blanchoin, R. D. Mullins, *Annu. Rev. Biophys. Biomol. Struct.* **29**, 545 (2000).
2. D. Pantaloni, C. Le Clainche, M. F. Carlier, *Science* **292**, 1502 (2001).
3. N. Watanabe, T. J. Mitchison, *Science* **295**, 1083 (2002).
4. G. A. Dunn, I. M. Dobbie, J. Monypenny, M. R. Holt, D. Zicha, *J. Microsc.* **205**, 109 (2002).
5. Materials and methods are available as supporting material on *Science* Online.
6. J. L. McGrath, Y. Tardy, C. F. Dewey Jr., J. J. Meister, J. H. Hartwig, *Biophys. J.* **75**, 2070 (1998).
7. B. P. Olveczky, A. S. Verkman, *Biophys. J.* **74**, 2722 (1998).
8. R. A. Worthylake, S. Lemoine, J. M. Watson, K. Burridge, *J. Cell Biol.* **154**, 147 (2001).
9. G. A. Dunn, D. Zicha, *J. Cell Sci.* **108**, 1239 (1995).
10. A. J. Ridley, H. F. Paterson, C. L. Johnston, D. Diekmann, A. Hall, *Cell* **70**, 401 (1992).

11. Supported by Medical Research Council (UK) Programme grant G0300046-64953 (G.A.D.). We thank P. Jordan and P. Fraylich for technical assistance.

Supporting Online Material

www.sciencemag.org/cgi/content/full/300/5616/142/DC1
Materials and Methods
Supporting Text
Figs. S1 to S8
References and Notes

3 January 2003; accepted 21 February 2003

Forces for Morphogenesis Investigated with Laser Microsurgery and Quantitative Modeling

M. Shane Hutson,[1] Yoichiro Tokutake,[1] Ming-Shien Chang,[1]* James W. Bloor,[2]† Stephanos Venakides,[3] Daniel P. Kiehart,[2]‡§ Glenn S. Edwards[1]‡§

We investigated the forces that connect the genetic program of development to morphogenesis in *Drosophila*. We focused on dorsal closure, a powerful model system for development and wound healing. We found that the bulk of progress toward closure is driven by contractility in supracellular "purse strings" and in the amnioserosa, whereas adhesion-mediated zipping coordinates the forces produced by the purse strings and is essential only for the end stages. We applied quantitative modeling to show that these forces, generated in distinct cells, are coordinated in space and synchronized in time. Modeling of wild-type and mutant phenotypes is predictive; although closure in *myospheroid* mutants ultimately fails when the cell sheets rip themselves apart, our analysis indicates that β_{PS} integrin has an earlier, important role in zipping.

Dorsal closure, an essential stage of *Drosophila* embryogenesis, has been extensively studied (*1–7*). However, an understanding of the cellular and molecular mechanisms that generate force and drive tissue dynamics in this process has been elusive. The quantitative and predictive capabilities of physical modeling (*8–11*) now offer a powerful set of tools to address this problem. The dynamics of dorsal closure can be visualized in living embryos with the use of green fluorescent protein (GFP) transgenes that label the actin cytoskeleton (Fig. 1A) (*12–14*). In the early stages of closure, the dorsal surface of the embryo is covered by large, flat polygonal cells of the amnioserosa. The rest of the embryo is covered by cells of the lateral and ventral epidermis which are smaller and cuboidal to columnar in shape. The visible area of the amnioserosa is shaped roughly like a human eye, with a wide central section that tapers to canthi, the corners of the eye (Fig. 1A). A single row of amnioserosa cells is tucked under the lateral epidermis throughout closure (*12*). Where these cell sheets overlap, the most dorsal row of lateral epidermis cells comprises a third distinct tissue known as the leading edge of the lateral epidermis (*12*, *15*, *16*). The cells of the leading edge on each flank of the embryo contain an actin-rich supracellular "purse string" (*4*, *6*, *12*). In addition, these cells extend dynamic fingerlike filopodia, ~10 μm in length (*13*). At the canthi, pairs of these filopodia can span the gap between opposing leading edges. As dorsal closure progresses, each structure changes (*6*, *12*): Cells of the lateral epidermis stretch toward the dorsal midline, the supracellular purse strings contract along their length, and the cells of the amnioserosa actively and asymmetrically change shape as their apical surfaces contract. Concomitant with these movements, the two flanks of the lateral epidermis are zipped together as filopodia and lamellipodia from opposing leading edges interdigitate to form a seam (*13*, *17*, *18*). The bulk of closure requires ~2 to 3 hours.

Dorsal closure has previously been examined through mechanical, laser, and genetic perturbations. Laser-ablation experiments

[1]Department of Physics and Free Electron Laser Laboratory, [2]Department of Biology, [3]Department of Mathematics, Duke University, Durham, NC 27708, USA.

*Present address: School of Physics, Georgia Institute of Technology, Atlanta, GA 30332, USA.
†Present address: Research School of Biosciences, University of Kent, Canterbury, Kent CT2 7NJ, UK.
‡These authors contributed equally to this work.
§To whom correspondence should be addressed. E-mail: dkiehart@duke.edu (D.P.K.); edwards@fel.duke.edu (G.S.E.)

Human Molecular Genetics, 2002, Vol. 11, No. 17 2005–2014

Defective trafficking and celi death is characteristic of skin disease-associated connexin 31 mutations

Wei-Li Di[1,†], James Monypenny[2,†], John E.A. Common[1], Cameron T.C. Kennedy[3], Katalin A. Holland[1], Irene M. Leigh[1], Elizabeth L. Rugg[1], Daniel Zicha[2] and David P. Kelsell[1,*]

[1]Centre for Cutaneous Research, Barts and the London School of Medicine and Dentistry, Queen Mary, University of London, Whitechapel, London E1 2AT, UK, [2]Light Microscopy, Cancer Research UK, London Research Institute, Lincoln's Inn Fields Laboratories, London WC2A 3PX, UK and [3]Bristol Dermatology Centre, Bristol Royal Infirmary, Bristol BS2 8HW, UK

Received April 16, 2002; Revised June 20, 2002; Accepted June 22, 2002

Distinct germiine mutations in the gene (*GJB3*) encoding connexin 31 (Cx31) underlie the skin disease erythrokeratoderma variabiis (EKV) or sensorineural hearing loss with/without peripheral neuropathy. Here we describe a number of functional analyses to investigate the effect of these different disease-associated Cx31 mutants on connexon trafficking and interceliular communication. Immunostaining of a biopsy taken from an EKV patient harbouring the R42P mutation revealed sparse epidermal staining of Cx31, and, when present, it had a perinuclear localization. Transfection and microinjection studies in both keratinocytes and fibroblast celi lines also demonstrated that R42P and four other EKV-associated mutant Cx31 proteins displayed defective trafficking to the plasma membrane. The deafness/neuropathy only mutant 66delD had primarily a cytoplasmic localization, but some protein was visualized at the plasma membrane in a few transfected cells. Both 66delD- and R32W-Cx31/EGFP proteins had significantly impaired dye transfer rates compared to wiid-type Cx31/EGFP protein. A striking characteristic feature observed with the dominant skin disease Cx31 mutations was a high incidence of cell death. This was not observed with wild-type, R32W 66delD Cx31 proteins. in conclusion, we have identified some key cellular phenotypic differences with respect to disease-associated Cx31 mutations.

INTRODUCTION

Gap junctions provide a mechanism of synchronized cellular response to a variety of intercellular signals by regulating the diffusion of small molecules (<1 kDa) such as metabolites and ions between the cytoplasm of adjacent cells (1). Connexins are the major proteins of gap junctions and are encoded by a large gene family (2). All connexins have four transmembrane domains and two extracellular loops with the N- and C-termini located in the cytoplasm. Each connexin assembles into hexameric hemichannels (termed connexons) in the endoplasmic reticulum and are then transported into the lipid bilayer of the plasma membrane. A connexon then docks with a connexon of an adjacent cell to form a dodecameric aqueous channel. These intercellular channels, cluster in the cell to form the gap junctions. Connexons can form either homotypic or heterotypic channels, with various channel types having distinct molecular permeabilities (3,4).

The epidermis is a stratified squamous epithelium comprising predominantly keratinocytes. The keratinocyte undergoes a process of terminal differentiation resulting in a stratum corneum, the critical component for barrier function. There are abundant gap junctions and connexin proteins in the epidermis (5). We have recently shown that at least 10 connexin proteins are expressed in the human epidermis, with the junctional composition and cellular localization changing during keratinocyte differentiation (6). Compelling evidence for a key role for connexins in epidermal biology has come from the association of mutations in four connexins with hyperproliferative skin disorders (7–10). These genetic studies demonstrate that intercellular communication via gap junctions is an important mechanism by which the normal epidermis develops and differentiates.

One such skin disease is erythrokeratoderma variabilis (EKV), in which a number of mutations in the gene encoding Cx31 have been demonstrated (7,11,12). EKV presents as a diffuse thickening of the palmoplantar epidermis, symmetrically distributed fixed hyperkeratotic plaques and transient erythematous areas (13). Both the hyperkeratosis and erythematous patches can be triggered by trauma to the skin, temperature

*To whom correspondence should be addressed. Tel: +44 2078827167; Fax: +44 2078827171; Email: kelsell@cancer.org.uk
†The authors wish it to be known that, in their opinion, the first two authors should be regarded as joint First Authors.

changes, UV exposure and emotional stress. Like Cx26 and Cx30 (reviewed in 14), dominant Cx31 mutations have also been described associated with hearing loss with no epidermal manifestations (15). Adding further complexity to the biology of Cx31 and its role in disease is the recent identification of another dominant *GJB3* mutation, 66delD, segregating in a family with peripheral neuropathy and sensorineural hearing loss (16). Though recessive *GJB3* mutations have been associated with hearing loss (17), more recently the L34P mutation in *GJB3* has been shown to underlie a recessive form of the skin disease EKV (18). Thus the spectrum of *GJB3* mutations described to date results in a variety of genetic disorders.

Human genetic disease studies suggest that different *GJB3* mutations have distinct effects on the Cx31 protein in terms of epidermal differentiation, auditory transduction and peripheral neuronal function. Here, we demonstrate genotype–phenotype differences at the cellular level and identify cell death as a common mechanism linked with EKV-associated Cx31 mutations.

RESULTS

Perinuclear localization of Cx31 in EKV-affected epidermis

Cx31 is expressed in late keratinocyte differentiation, localizing at gap junctions in the stratum granulosum of epidermis (Fig. 1A) (6). To look at the effect of an EKV-associated mutation on Cx31 localization, immunocytochemistry using a polyclonal Cx31 antibody was performed on frozen tissue sections taken from an EKV patient heterozygous for the R42P mutation in *GJB3* (11). The majority of Cx31 staining in the patient's epidermis was perinuclear, with little punctate staining observed (Fig. 1C). These *in vivo* data indicate that R42P effects the trafficking of Cx31 to the plasma membrane and also possibly reduces the expression level of Cx31 in keratinocytes. These two observations also indicate that R42P can dominantly disrupt the trafficking of wild-type Cx31, which is in agreement with its autosomal dominant mode of inheritance. From the antibodies available, the R42P in Cx31 does not appear to effect the expression and localization of other epidermally expressed connexins, including Cx26, Cx30, Cx30.3 and Cx43 (data not shown).

Localization of mutant Cx31-EGFP

To investigate the localization of other mutant forms of Cx31, we examined the cellular localization of wild-type (WT) Cx31/EGFP and various mutant Cx31/EGFP 24 hours post-transfection (Table 1). Cells expressing WT-Cx31/EGFP showed punctate staining and aggregation at the plasma membrane, especially in regions of cell–cell contact (Fig. 2A, B and I). In contrast, none of the mutant clones formed membrane-associated aggregates. As with the keratinocytes endogenously heterozygous for R42P, the R42P-Cx31/EGFP was cytoplasmic and had a perinuclear protein localization in expressing cells (Fig. 2C and J). Similar to R42P-Cx31/EGFP, the other mutant Cx31 proteins associated with EKV—C86S-Cx31/EGFP, G12R-Cx31/EGFP and G12D-Cx31/EGFP—also had a cytoplasmic localization (Fig. 2D, E and F). Immunocytochemistry for the keratin and actin filaments in transfected NEB1 cells using keratin LP34 antibody and a β-actin antibody confirmed a cytoplasmic location for these mutant proteins and also revealed an intact keratin and actin filament network among those cells expressing either wild-type or mutant Cx31/EGFP. Another intriguing phenotype was observed for all of the EKV-associated Cx31/EGFP mutants: many of the transfected cells became rounded, detached and died. This suggested that these skin disease-associated mutant Cx31 proteins were inducing cell death.

A slightly different cellular distribution was observed for the mutant Cx31 associated with peripheral neuropathy and hearing impairment. Though the majority of 66delD-Cx31/EGFP was cytoplasmic (Fig. 2G), some punctate staining at the plasma membrane was observed. Another distinct localization was observed for R32W-Cx31/EGFP, a rare polymorphic variant of *GJB3* with no identified disease association, which showed a punctate staining pattern, but with no detectable aggregation at the plasma membrane between R32W-Cx31/EGFP-expressing cells (Fig. 2H). In contrast to the EKV-associated Cx31/EGFP mutants, cells transfected with these mutant constructs exhibited the normal wild-type cell culture phenotype with no increased levels of cell death.

Dye transfer studies of WT-Cx31/EGFP, R32W-Cx31/EGFP and 66delD-Cx31/EGFP

Prior to performing the microinjection dye transfer studies, immunocytochemistry using a panel of connexins—Cx26, 30, 31, 32, 40, 43 and 45—was performed on both human NEB1 keratinocyte-derived cells and the murine NIH 3T3 fibroblast cells. Immunostaining analysis in NEB1 cells showed low levels of Cx26, 30, 32, 40, 43 and 45, but abundant Cx31 expression with an irregular distribution. NIH 3T3 cells have previously been shown to express Cx43 (19), and, in addition, we found the expression of a number of other connexins, including Cx31 (data not shown). This indicates that both cell lines used in this study express a number of connexins endogenously.

WT-Cx31/EGFP-expressing NEB1 cells exhibited an enhanced rate of dye transfer compared with non-transfected cells. Dye transferred most rapidly through adjoining fluorescent cells when compared to their non-fluorescent neighbours (Figs 3A–D and 6). However, the extent to which dye transferred between adjoining fluorescent cells varied widely between experiments, possibly reflecting a difference in expression levels of endogenous protein or channel activity states between cells in the local population. Indeed, a similar variation in dye transfer efficiency could also be seen in the uninjected cell population, with some cells exhibiting a significant ability to transfer dye while others showed only poor transfer rates. These experiments were also performed in NIH 3T3 fibroblasts. Though these cells express endogenous Cx31 and other connexins, basal dye transfer levels were poor, with dye rarely propagating further than those cells directly in contact with the injected cell. In dramatic contrast, however, dye rapidly propagated through the WT-Cx31/EGFP-expressing population (Fig. 6). The steady rate at which dye transferred through Cx31-expressing cells suggests that channels exhibited similar activity states and that endogenous

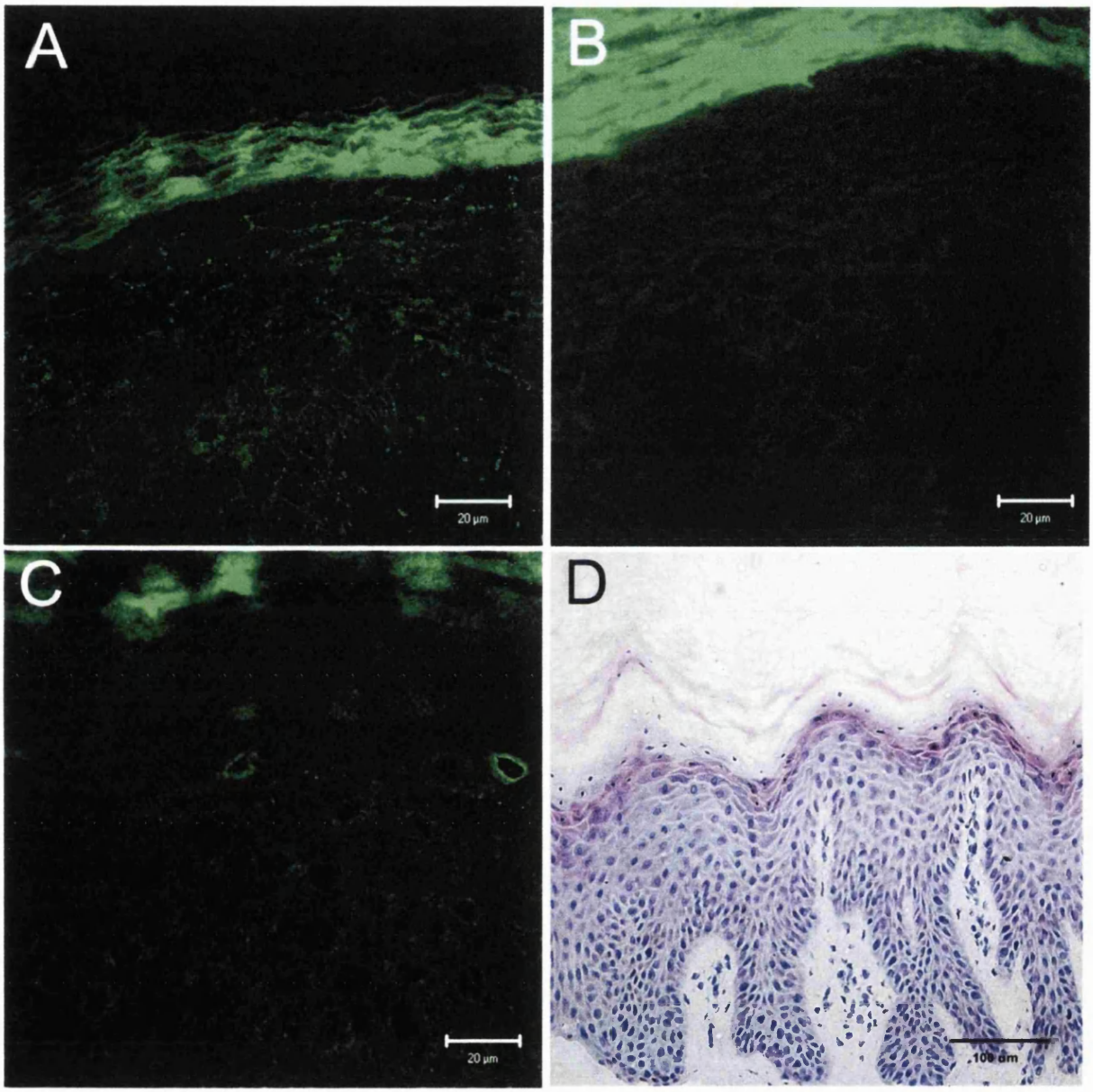

Figure 1. Cx31 localization in normal and EKV epidermis. (**A**) Palm epidermis from an individual with wild-type *GJB3*. Note the evenly distributed punctate membranous pattern of Cx31 in the stratum granulosum. (**B**) Control immunostaining of normal palm epidermis without specific primary Cx31 antibody. Non-specific staining is seen in the stratum corneum. (**C**) Lesional epidermis from an individual with EKV heterozygous for R42P in *GJB3*. Note the sparse and perinuclear Cx31 immunostaining in the stratum granulosum. (**D**) Haematoxylin and eosin staining of lesional epidermis from the same EKV patient as in (C).

protein levels were sufficiently low not to influence the effects of the exogenous protein.

Unlike WT-Cx31/EGFP, the expression of 66delD-Cx31/EGFP did not significantly enhance the rate of dye transfer in either NEB1 cells (Figs 3I-L and 6) or NIH 3T3 fibroblasts (Fig. 6), indicating that the mutant form cannot form functional channels. In addition, R32W-Cx31/EGFP also did not form functional channels. Expression of R32W-Cx31/EGFP in NEB1 cells did not elevate dye transfer rates above basal levels (Figs 3E–H and 6), and little or no dye transfer was observed in fibroblasts (Fig. 6). R32W in *GJB3* has been reported as a polymorphism with no proven disease association (20,21). However, we have hypothesized that it may have a modifying effect with respect to epidermal disease severity or hearing loss when associated with other connexin mutations. This has been debated further (22). Our data show that R32W does not form

functional intercellular channels and has impaired dye transfer, suggesting that it is a non-functional variant of *GJB3*.

Microinjection studies of R42P-Cx31/EGFP- and C86S-Cx31/EGFP-induced cell death

From our transfection studies, expression of R42P-, C86S-, G12R- and G12D-Cx31/EGFP in NEB1 cells resulted in increased cell death. This phenomenon did not appear in cells transfected or microinjected with WT-, 66delD- and R32W-Cx31/EGFP constructs. Using a combination of microinjection and digital time-lapse microscopy, we investigated further the cellular phenotypes for two of the skin disease-associated Cx31 mutants, R42P-Cx31/EGFP and C86S-Cx31/EGFP. Interestingly, R42P-Cx31/EGFP exhibited two distinctive cellular phenotypes. The first was an immediate change in cell morphology, including extensive cell blebbing and nuclear shrinkage, phenotypes associated with cell death (Fig 4A and B). Cells poorly adhered to the substrate and were difficult to microinject. In cases where microinjection was successful, dye did not transfer to neighbouring cells but merely leaked out from the cell. Cells also showed positive nuclear labeling with propidium iodide, suggesting a disrupted plasma membrane (Fig. 4C and D). As with the other localization studies described previously, R42P-Cx31/EGFP had a perinuclear localization. The second phenotype was similar to that of uninjected cells, with some protein present at the plasma membrane, and no cell death (Fig. 6). As with R42P-Cx31/EGFP, C86S-Cx31/EGFP-expressing NEB1 cells also exhibited two major phenotypes; those that showed profound blebbing and nuclear shrinkage, and those that were similar to the uninjected cell population. The blebbing phenotype corresponded with positive nuclear labelling with propidium iodide (Fig. 4E and F). Initially, dye transfer was occurring through fluorescent cells, but as the cells changed morphology, the dye leaked out of the cell, as for R42P-Cx31/EGFP. In the phenotype where membrane integrity remained intact throughout, the protein showed both vesicular localization and, to some degree, punctate membrane localization, although not as striking as is seen with the wild-type protein. Indeed, dye transfer did seem to propagate preferentially through the C86S-Cx31/EGFP-expressing cells associated with this second phenotype when compared to the surrounding non-fluorescent cell population (Fig. 6). This 'normal' phenotype was not observed in NIH 3T3 cells for either R42P-Cx31/EGFP or C86S-Cx31/EGFP (Fig. 6).

Table 1. Genotype and phenotype of mutated Cx31

Mutation	Phenotype	Primers for SDM[a]	References
R42P	EKV	Used genomic DNA from patient	11
G12R	EKV	GGCCCTACTGAGCCGTGTGA ACAAGTACTC	7
G12D	EKV	GGCCCTACTGAGCGATGT GAACAAGTACTC	7
C86S	EKV	CTCATCTTCGTCACAAGCC CCTCGCTGCTG	7
66delD	Neuropathy and hearing loss	GCACCAACGTCTGCTAC (codon deleted) ACTA CTTCCCCATC	16
R32W	Of unknown disease significance	GGTGTTCGTCTTCTGGGTGC TGGTATACG	20,21

[a]The mutated site is bold and mutated or deleted codon underlined.

DISCUSSION

From immunocytochemical analysis of affected epidermis from an EKV patient harbouring the R42P mutation in Cx31 and studies using a R42P-Cx31/EGFP construct, a cytoplasmic localization of the mutant protein was revealed. Previously, we had described no obvious structural abnormalities in the skin biopsy from this patient (11). In particular, gap junctions were still present in different epidermal layers, with no observable gross abnormalities by light microscopy and electron microscopy. We speculated that one possible mechanistic effect of the R42P mutation in *GJB3* on connexin 31 would be to alter gating polarity, resulting in defective channel formation and regulation. Another hypothesis was that the substitution of arginine 42 by proline would have a wider structural destabilization effect on connexon formation. The functional data described in this study would support the latter mechanism, due to a cytoplasmic localization of the protein with undetectable Cx31 protein at the plasma membrane. Surprisingly, all the other EKV-associated Cx31 mutant proteins assayed also displayed trafficking defects with retention in the cytoplasm, suggesting that this is a common cellular phenotype. It is possible that these particular Cx31 mutant proteins may also disrupt the assembly of other connexon types in the Golgi and endoplasmic reticulum (ER). From immunocytochemistry of epidermis from an EKV patient harbouring the R42P mutation in Cx31, no obvious alterations in the localization and distribution of other connexins were observable.

All the other EKV-associated Cx31 mutants also displayed the same trafficking defects as R42P and had a cytoplasmic localization. Previously, specific mutations in Cx32 have also been shown to have trafficking defects accumulating in the cytoplasm and also within the Golgi apparatus (23,24). Interestingly, one of these Cx32 mutations is G12S. This is the same conserved residue mutated in Cx31 (G12R and G12D), and these Cx31 mutants also display similar trafficking defects. These data suggest that this residue in the N-terminus of connexins is important for the correct folding of the connexin and/or its assembly into connexons. A disruptive conformational change for the EKV mutations R42P and C86S in Cx31 that lie adjacent to or within transmembrane domains, respectively, may also lead to retention in the cytoplasm and possibly the Golgi apparatus/ER.

The other characteristic feature associated with the EKV Cx31 mutants was increased cell death, particularly striking in the NIH 3T3 cells. Although the mechanism of cell death is not known, it could possibly relate to increased intracellular Ca^{2+} and/or plasma membrane disruption. Evidence from the microinjection experiments indicated that the plasma membrane was very 'leaky' in the two EKV-associated Cx31 mutants investigated. From the microinjection studies for R42P- and C86S-Cx31/EGFP in the keratinocyte cell line, two cellular phenotypes were observed. Predominantly, these mutants induced blebbing and cell death. However, some microinjected cells did not die. This difference in the cellular processing of the microinjected mutant Cx31 constructs could

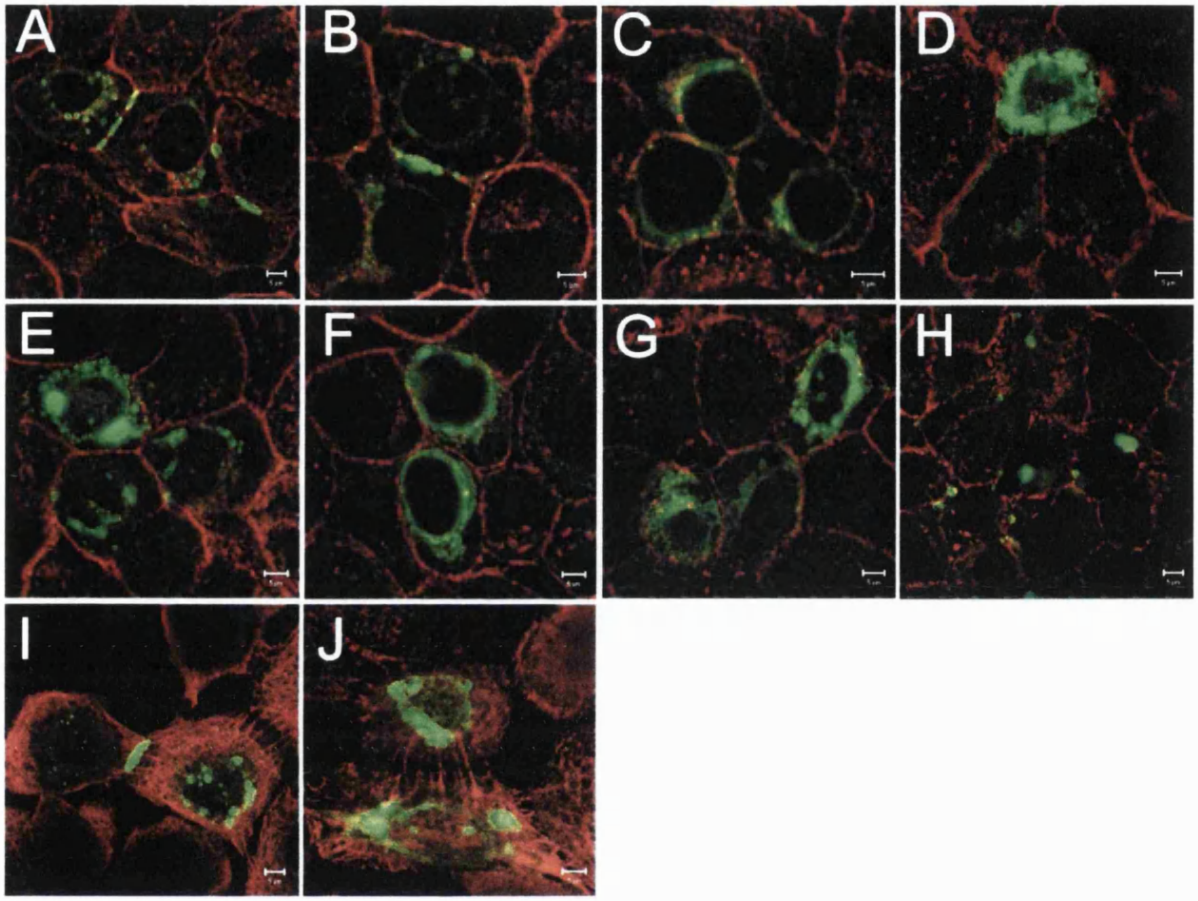

Figure 2. Localization studies in NEB1 keratinocytes transfected with (**A** and **B**) WT-Cx31/EGFP, (**C**) R42P-Cx31/EGFP, (**D**) C86S-Cx31/EGFP, (**E**) G12R-Cx31/EGFP, (**F**) G12D-Cx31/EGFP, (**G**) 66delD-Cx31/EGFP, (**H**) R32W-Cx31/EGFP, (**I**) WT-Cx31/EGFP and (**J**) R42P-Cx31/EGFP. Green fluorescence indicates the EGFP fusion connexin protein. Red fluorescence shows β-actin (A–H) and keratin filaments I, J). Note the conspicuous aggregation of wild-type Cx31 at the plasma membrane between the cells. In contrast, the majority of the mutant Cx31/EGFP proteins, e.g. R42P-Cx31/EGFP, were cytoplasmic, with less apparent membrane localization. Note the appearance of an intact keratin filament network.

be related to the inherent variability in different cell populations. For example, in the NEB1 keratinocytes, it could relate to the variable expression of endogenous connexins and/or the differentiation status of different cell populations. Further studies are in progress to understand why these two different *in vitro* cell phenotypes occur and if this variable processing is dependent on the cellular background. These studies may help to explain further the genotype–phenotype correlation of Cx31 and other connexin mutations.

The 66delD mutation is associated with a dominant syndrome of hearing loss and peripheral neuropathy (16). The localization studies and dye transfer experiments support the deleterious nature of this mutation with respect to Cx31 channel formation (Fig. 2G and 6). Interestingly, 66delD in Cx31 affects the same residue mutated in Cx26, D66H, which associates with Vohwinkel's syndrome: palmoplantar keratoderma and mild–moderate hearing loss (8,20). Like 66delD-Cx31/EGFP, D66H-Cx26 has defective trafficking with primarily a cytoplasmic localization (25).

Though R32W-Cx31/EGFP could traffic to the plasma membrane, it never formed large aggregates of protein that are indicative of connexon channels, and was unable to transfer dye efficiently. Previously, it has been shown that, for Cx43, the formation of plaques is a requirement for intercellular communication as measured by dye-coupling experiments (26). R32W in *GJB3* results in a substitution of a highly conserved arginine residue in the first transmembrane domain of the Cx31 protein and appears to be a relatively rare coding polymorphism (22). We have investigated further its prevalence in a number of ethnic control populations. R32W was found in a heterozygous form in 3% of Irish, 0.7% of Afro-Caribbeans and 2.5% of Asians. In all control samples tested ($n = 364$), the overall allele frequency was 1.9%. As no R32W homozygotes were detected, it is still plausible that it is a recessive *GJB3* allele. However, it has been demonstrated that L34P in *GJB3* and M34T in *GJB2*, which both occur in the first transmembrane domain, are recessive alleles underlying EKV and mild–moderate hearing loss, respectively (18,27,28). As our functional data suggest that R32W has a

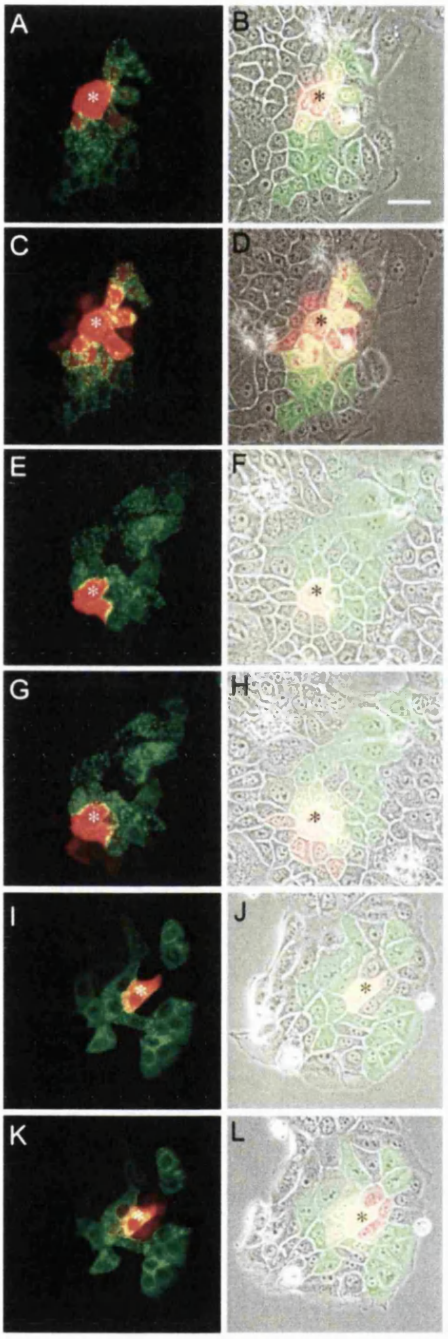

Figure 3. Dye transfer analysis using Alexa 568 in NEB1 cells microinjected with Cx31/EGFP fusion constructs. Images show green (EGFP)/red (Alexa568) fluorescence overlays without phase contrast (left column) and with phase contrast (right column) to indicate surrounding uninjected cells. NEB1 cells are expressing, WT-Cx31/EGFP (**A**)–(**D**), R32W-Cx31/EGFP (**E**–**H**), and 66delD-Cx31/EGFP (**I**)–(**L**). Images (A), (B), (E), (F), (I) and (J) represent the first time point of the time-lapse sequences, and the remaining images were acquired 33 min later. Note the efficient dye transfer between WT-Cx31/EGFP-expressing cells but reduced transfer between cells expressing R32W-Cx31/EGFP and 66delD-Cx31/EGFP. Asterix indicates the cell microinjected with Alexa 568 dye. Scale bar 50 μm.

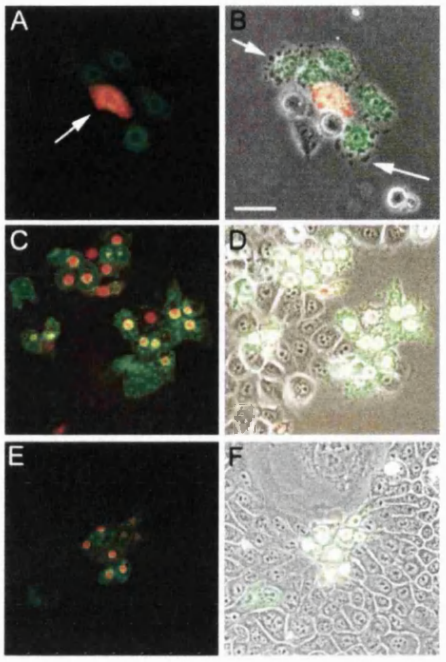

Figure 4. Illustration of the induction of cell death following the microinjection of R42P-Cx31/EGFP and C86S-Cx31/EGFP constructs in NEB1 cells. (**A** and **B**) show Green (EGFP)/red (Alexa568) fluorescence overlays without phase contrast (left column) and with phase contrast (right column). (**C**–**F**) Green (EGFP)/red (propidium iodide) fluorescence overlays without phase contrast (left column) and with phase contrast (right column). NEB1 cells express R42P-Cx31/EGFP in (A)–(D) and C86S-Cx31/EGFP in (E)–(F). Note the blebbing phenotype (examples of blebs indicated by arrows), the nuclear shrinkage and the intense nuclear propidium iodide staining showing cell death. Scale bar 50 μm.

deleterious effect on Cx31 plaque formation and dye transfer, we postulate that homozygosity for R32W may result in a, as yet unknown, recessive disease phenotype. Further genetic studies and analyses need to be performed to assess a possible disease association of this Cx31 variant.

In summary, our *in vivo* and *in vitro* data demonstrate that R42P in Cx31 prevents the trafficking of the protein to the membrane. This abnormal localization appears to lead to cell death. Our *in vitro* data indicate that trafficking defects and cell death are common mechanisms of mutant Cx31 associated with EKV. It is not clear how these two cellular phenotypes associate with the hyperkeratosis seen in the patients. It is possibly related to the loss of Cx31-mediated intercellular communication during terminal keratinocyte differentiation and/or the induction of cell death invoking a wound-healing response in surviving keratinocytes, leading to hyperproliferation. In addition, the transient nature of the erythemous plaques may correspond to the differential effects of the EKV-associated mutations in different keratinocyte populations. These data suggest that trafficking defects represent a common feature of epidermal disease-associated connexin mutations and constitute a step towards understanding the intriguing genotypes-phenotypes produced due to β-connexin mutations. The nature of the mechanism of cell death associated with the skin disease Cx31 mutants remains to be elucidated.

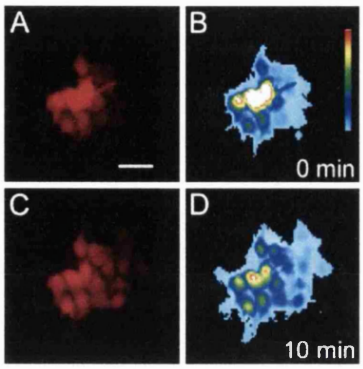

Figure 5. Processing of red fluorescence images (**A** and **C**) for calculations of normalized mean distance of Alexa 568 dye transfer in NIH 3T3 cells expressing WT-Cx31/EGFP. A and B represent time point 0 min; C and D 30 min. **B** and **D** show post-processed pseudocoloured images used for mean dye distance calculations. Scale bar 50 μm. Minimum intensity in the pseudocolour scale bar is represented in blue, and maximum intensity in white.

MATERIALS AND METHODS

Tissue processing and cell culture

Skin biopsy material was obtained and processed from a consenting individual with EKV who is heterozygous for an arginine-to-proline substitution in codon 42 (R42P) in connexin 31 (Cx31) (11). The biopsy was immediately snap-frozen in liquid nitrogen and stored at −70°C for immunocytochemical analysis. This study has ethical approval.

NEB1 cells, which were immortalized from normal keratinocytes by HPV16 (29), were cultured in 3 : 1 Dulbecco's modified eagle's medium (DMEM) F12 medium, supplemented with 10% fetal calf serum (FCS), 0.4 μg/ml hydrocortisone, 5 μg/ml insulin, 10 ng/ml epidermal growth factor, 10×10^{-10} M choleratoxin, 5 μg/ml transferrin, 2×10^{-11} M lyothyronine and 100 U/100 μg/ml penicillin–streptomycin. NIH 3T3 cells (murine fibroblast cells) were cultured in DMEM, supplemented with 10% FCS and 100 U/100 μg/ml penicillin–streptomycin. After reaching confluence, cells were plated on 35 mm glass-bottom microwell dishes (MatTek, Ashand, MA, USA) for microinjection or 13 mm coverslips for transfection and immunocytochemistry.

Immunofluoresence staining and confocal microscopy

Immunofluorescence staining was performed in frozen tissue sections (6 μm thickness) and fixed cells using methods previously described (6). The following connexin antibodies were used: monoclonal anti-mouse Cx26 (dilution 1 : 100; Zymed, San Francisco, CA, USA), polyclonal rabbit anti-mouse Cx30 (dilution 1 : 100; Zymed), polyclonal rabbit anti-human Cx31 [dilution 1 : 100 (6)], monoclonal anti-rat Cx32 (dilution 1 : 100; Zymed), polyclonal rabbit anti-mouse Cx40 (dilution 1 : 100; Alpha Diagnostic, San Antonio, TX, USA), monoclonal anti-rat Cx43 (dilution 1 : 100; Zymed) and polyclonal rabbit anti-mouse Cx45 (dilution 1 : 50; Alpha Diagnostic). Keratin filaments were stained with monoclonal pan-keratin antibody LP34 (30), and actin filaments were stained with monoclonal anti-mouse β-actin (Sigma, Poole, Dorset, UK). Briefly, cells were fixed with 4% paraformaldehyde for connexin antibody staining, 100% methanol for β-actin staining and 50 : 50 acetone/methanol for the pan-keratin antibody. Sections were then rinsed with phosphate-buffered saline (PBS) and incubated in PBS containing 3% rabbit or goat serum and 0.1% Triton X-100 (Sigma) for 10 min at room temperature. After rinsing, the slides were incubated in a humidified chamber at 37°C for 2 h with primary antibody. Following several rinses with PBS, sections were incubated in the dark for 1 h at room temperature with fluorescein isothiocyanate (FITC)-conjugated rabbit anti-mouse IgG or goat anti-rabbit IgG (Molecular Probes, Oregon, USA) diluted 1 : 100. After rinsing with PBS, the sections were mounted in mowiol reagent containing 10% mowiol D-488 (Calbiochem, Nottingham, UK), 25% glycerol and 2.5% 1.4-diazabicyclo[2.2.2] octane (Sigma) in 50 mM Tris-HCl, pH 8.5. Images were recorded using a Zeiss LSM510 laser scanning confocal microscope (Carl Zeiss) and processed using Adobe Photoshop 6.

Construction of chimeric Cx31/EGFP

PCR was carried out on wild-type (WT) human genomic DNA. The open reading frame of WT-Cx31 was fused in-frame to the N-terminus of enhanced GFP (EGFP) by a two-step cloning procedure. First, the authentic connexin stop codon was changed from TGA to GGA by PCR using the primers with a restriction site sequence *Sac*II, 5′-GCCCCGCGGATGGACTGGAAGACACTC-3′ for forward and 5′-GCCCCGCGGCTCCGATGGGGGTCAGGTT-3′ for reverse, and was cloned directly into a TA cloning vector, pGEM-T (Promega, Southampton, UK). Second, the *Sac*II fragment of Cx31 from pGEM-T/Cx31 was further cloned into pEGFP-N3 vector (Clontech, Hampshire, UK). R42P mutant Cx31 gene was generated from patient genomic DNA using the primers with restriction site sequences *Hind*III and *Sal*I, 5′-GCGAAGCT TATGGACTGGAAGACACTC-3′ for forward and 5′-GCGG TCGACTCCGATGGGGGTACGGTT-3′ for reverse. The PCR product was directly cloned into pEGFP vector. In this orientation, the EGFP was at the C-terminus of the WT-Cx31 and R42P-Cx31 protein and the stop codon was altered to allow 'read through' and expression of the EGFP protein. All positive clones were identified by restriction enzyme analysis and automated DNA sequencing to determine that there were no 'introduced' nucleotide errors in both clones.

Site-directed mutagenesis (SDM)

The five other Cx31 mutations were independently introduced into WT-Cx31/EGFP by SDM. Their abbreviations, clinical phenotypes and the primers used for SDM are listed in Table 1. The WT-Cx31/EGFP sequence was converted using the Quickchange Site Directed Mutagenesis kit (Stratagene, La Jolla, CA, USA) according to the manufacturer's instructions. Briefly, PCR reactions using overlapping primers containing the base pair change were carried out using the supercoiled double-stranded DNA from pWT-Cx31/EGFP as a template. Then, the products were directly transformed into competent JM109 *E. coli* (Clontech) and several colonies were selected and sequenced. Colonies with the correct base change and no other additional mutations were selected for subsequent study.

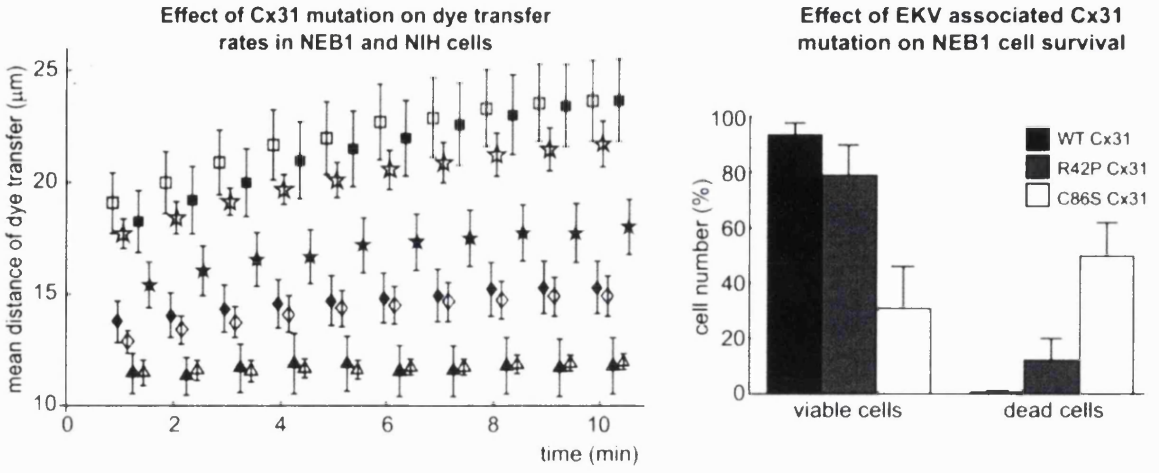

Cell Line	Cx31 mutation	Number of films	Mean rate of dye transfer (μm/hr)	Standard error	Two sided t-test p value	Number of cells scored	Cell Death (%)	ANOVA p value
		Dye Transfer Analysis				Cell Death Analysis		
NEB1	Wild-Type □	10	10.06	1.92	-	212	0.4	-
	C86S ☆	4	8.80	1.02	n.s.	207	49.8	$p < 0.01$
	R42P ★	5	5.38	0.79	$p < 0.05$	334	11.9	n.s.
	R32W ◆	8	3.47	0.65	$p < 0.01$	No apparent cell death		
	66delD ◇	5	4.39	1.03	$p < 0.05$			
NIH 3T3	Wild-Type ■	11	11.98	1.50	-			
	R32W ▲	7	0.62	1.46	$p < 0.001$			
	66delD △	5	1.02	0.97	$p < 0.001$			
	C86S	N/A	N/A	N/A	N/A	All cells die		
	R42P	N/A	N/A	N/A	N/A			

Figure 6. Summary of dye transfer and cell death in NEB1 and NIH 3T3 cells expressing different Cx31 mutations. Top left plot shows time courses of normalized mean dye transfer distances represented by mean values (points) and standard errors of sample mean (bars) for groups of experiments with NEB1 cells expressing WT-Cx31/EGFP (open box), C86S-Cx31/EGFP (open star), R42P-Cx31/EGFP (filled star), R32W-Cx31/EGFP (filled diamond), and 66delD-Cx31/EGFP (open diamond), and NIH 3T3 cells expressing WT-Cx31/EGFP (filled box), R32W-Cx31/EGFP (filled triangle) and 66delD-Cx31/EGFP (open triangle). The top right bar chart presents means and standard errors of relative incidence of viability and death found in NEB1 cells expressing the EKV-associated Cx31 mutations R42P and C86S. Propidium iodide-negative cells with absence of nuclear shrinkage were scored as viable, and propidium iodide-positive cells as dead. The bottom table overviews the numerical representation and statistical significances of the effects of different Cx31 mutations on both the rate of dye transfer and cell survival in NEB1 and NIH 3T3 cells. The mean dye transfer rate for each treatment is calculated as the mean slope of the linear regression of the dye transfer distance time courses and expressed in micrometres per hour. The *P*-values represent significances of differences in dye transfer rates or incidence of cell death between cells expressing the relevant Cx31 mutation as compared to the WT protein.

Transfection with Cx31/EGFP fusion constructs

NEB1 cells were transfected with the pWT-Cx31/EGFP and each of the mutated pCx31/EGFP constructs using Transfast (Promega). Cells ($0.5–1 \times 10^5$/13 mm coverslip) were transfected with 0.5 μg of plasmid DNA in 1 : 2 Transfast reagent. Twenty-four hours post-transfection, cells were fixed with 4% buffered paraformaldehyde for the intracellular localization analysis and immunofluorescence staining.

Nuclear microinjection of Cx31/EGFP fusion constructs

NEB1 keratinocytes and NIH 3T3 fibroblasts were seeded in MatTek dishes and allowed 3 days to grow to near confluency. Culture medium for microinjection and imaging was supplemented with 20 mM HEPES. A transjector and micromanipulator (Eppendorf) mounted on a Zeiss Axiovert 135 TV inverted microscope (Carl Zeiss) were used for microinjection of plasmid DNA–EGFP fusion constructs. Groups of adjacent cells in a culture were injected with one of the constructs at a concentration of 0.05 μg/μl to create tight patches of fluorescent cells. Cells were allowed 4–5 h to express the proteins.

Measurement of dye transfer rate

For all dye transfer experiments, patches of fluorescent cells were identified and single cells close to the patch perimeter were microinjected in the cytoplasm with 2 mM Alexa 568 dye (Molecular Probes). The occurrence of dye transfer between adjacent cells was determined using digital time-lapse

microscopy. Cells were both microinjected and imaged on the inverted microscope mounted with the micromanipulator and transjector. Images were acquired every 20 s in three separate channels (phase contrast, EGFP fluorescence, and Alexa 568 fluorescence) using a 20 × NA 0.5 objective, an Orca ER CCD camera (Hammamatsu) and a multiple dichroic in conjunction with motorized excitation and emission filter wheels (Sutter Instruments). Image acquisition was controlled using Acquisition Manager (Kinetic Imaging). The exposure time for the Alexa 568 channel was kept constant between all time-lapse experiments shown. The microscope body was housed in a Perspex environment chamber accurately maintained at 37°C, and the cells were enclosed within a glass-topped, steel humidity chamber upon completion of cytoplasmic microinjection. The time elapsed from microinjection of dye to commencement of image acquisition was approximately a minute.

Fluorescence images of the Alexa 568 dye were cropped, binned to a pixel size of 2.6 × 2.6 μm and automatically thresholded (Fig. 5). The site of dye microinjection was interactively marked using a mouse pointer, and normalized mean distance of dye transfer was calculated as $\mathrm{NMD}(t) = \sum I_{xyt} d_{xyt} / \sum I_{xyt}$ for each frame in the sequence. I_{xyt} is the intensity of an image pixel (x,y) at time t, and d_{xyt} is the distance of the pixel (x,y) from the site of dye microinjection. NMD(t) data evaluated for the initial 10 min of a recording were subjected to a linear regression analysis, and the slope of the regression function was taken as the rate of the dye transfer for the particular sequence. Significances of differences in the rate of the dye transfer between groups of sequences were evaluated by two-sided t-test. Image processing, regression analysis and statistical tests were performed in Mathematica (Wolfram Research) using specially developed software.

Determination of cell death

Cells microinjected with the expression Cx31/EGFP fusion constructs were incubated for 5 h and then treated with 0.5 μg/ml of the membrane-impermeable dye propidium iodide. After 10 min, images were acquired in phase-contrast, red and green fluorescence. Dead cells (propidium iodide positive) and viable cells (propidium iodide negative and absence of nuclear shrinkage) were counted. Data were expressed as percentages of total cells scored and tested for significant differences by analysis of variance (ANOVA).

REFERENCES

1. Pitts, J.D. (1998) The discovery of metabolic co-operation. *Bioessays*, **20**, 1047–1051.
2. Simon, A.M. and Goodenough, D.A. (1998) Diverse functions of vertebrate gap junctions. *Trends Cell Biol.*, **8**, 477–483.
3. Goldberg, G.S., Lampe, P.D. and Nicholson, B.J. (1999) Selective transfer of endogenous metabolites through gap junctions composed of different connexins. *Nat. Cell. Biol.*, **1**, 457–459.
4. Niessen, H., Harz, H., Bedner, P., Kramer, K. and Willecke, K. (2000) Selective permeability of different connexin channels to the second messenger inositol 1,4,5-trisphosphate. *J. Cell Sci.*, **113**, 1365–1372.
5. Salomon, D., Masgrau, E., Vischer, S., Ullrich, S., Dupont, E., Sappino, P., Saurat, J.H. and Meda, P. (1994) Topography of mammalian connexins in human skin. *J. Invest. Dermatol.*, **103**, 240–247.
6. Di, W.L., Rugg, E.L., Leigh, I.M. and Kelsell, D.P. (2001) Multiple epidermal connexins are expressed in different keratinocyte subpopulations including connexin 31. *J. Invest. Dermatol.*, **117**, 958–964.
7. Richard, G., Smith, L.E., Bailey, R.A., Itin, P., Hohl, D., Epstein, E.H. Jr., DiGiovanna, J.J., Compton, J.G. and Bale, S.J. (1998) Mutations in the human connexin gene *GJB3* cause erythrokeratodermia variabilis. *Nat. Genet.*, **20**, 366–369.
8. Maestrini, E., Korge, B.P., Ocaña-Sierra, J., Calzolari, E., Cambiaghi, S., Scudder, P., Hovnanian, A., Monaco, A. and Munro, C. (1999) A missense mutation in connexin26, D66H, causes mutilating keratoderma with sensorineural deafness (Vohwinkel's syndrome) in three unrelated families. *Hum. Mol. Genet.*, **8**, 1237–1243.
9. Lamartine, J., Munhoz Essenfelder, G., Kibar, Z., Lanneluc, I., Callouet, E., Laoudj, D., Lemaitre, G., Hand, C., Hayflick, S.J., Zonana, J. *et al.* (2000) Mutations in GJB6 cause hidrotic ectodermal dysplasia. *Nat. Genet.*, **26**, 142–144.
10. Macari, F., Landau, M., Cousin, P., Mevorah, B., Brenner, S., Panizzon, R., Schorderet, D.F., Hohl, D. and Huber, M. (2000) Mutation in the gene for connexin 30.3 in a family with erythrokeratodermia variabilis. *Am. J. Hum. Genet.*, **67**, 1296–1301.
11. Wilgoss, A., Leigh, I.M., Barnes, M.R., Dopping-Hepenstal, P., Eady, R.A., Walter, J.M., Kennedy, C.T. and Kelsell, D.P. (1999) Identification of a novel mutation R42P in the Gap junction protein beta-3 associated with autosomal dominant erythrokerato-derma variabilis. *J. Invest. Dermatol.*, **113**, 1119–1122.
12. Richard, G., Brown, N., Smith, L.E., Terrinoni, A., Melino, G., Mackie, R.M., Bale, S.J. and Uitto, J. (2000) The spectrum of mutations in erythrokeratodermias—novel and de novo mutations in *GJB3*. *Hum. Genet.*, **106**, 321–329.
13. Hohl, D. (2000) Towards a better classification of erythrokeratodermias. *Br. J. Dermatol.*, **143**, 1133–1137.
14. Kelsell, D.P., Di, W.L. and Houseman, M.J. (2001) Connexin mutations in skin disease and hearing loss. *Am. J. Hum. Genet.*, **68**, 559–568.
15. Xia, J.H., Liu, C.Y., Tang, B.S., Pan, Q., Huang, L., Dai, H.P., Zhang, B.R., Xie, W., Hu, D.X., Zheng, D. *et al.* (1998) Mutations in the gene encoding gap junction protein beta-3 associated with autosomal dominant hearing impairment. *Nat. Genet.*, **20**, 370–373.
16. Lopez-Bigas, N., Olive, M., Rabionet, R., Ben-David, O., Martinez-Matos, J.A., Bravo, O., Banchs, I., Volpini, V., Gasparini, P., Avraham, K.B. *et al.* (2001) Connexin 31 (*GJB3*) is expressed in the peripheral and auditory nerves and causes neuropathy and hearing impairment. *Hum. Mol. Genet.*, **10**, 947–952.
17. Liu, X.Z., Xia, X.J., Xu, L.R., Pandya, A., Liang, C.Y., Blanton, S.H., Brown, S.D., Steel, K.P. and Nance, W.E. (2000) Mutations in connexin31 underlie recessive as well as dominant non-syndromic hearing loss. *Hum. Mol. Genet.*, **9**, 63–67.
18. Gottfried, I., Landau, M., Glaser, F., Di, W.-L., Ophir, J., Mevorah, B., Ben-Tal, N., Kelsell, D.P. and Avraham, K.P. (2002) A mutation in *GJB3* is associated with recessive erythrokeratodermia variabilis (EKV) and leads to defective trafficking of the connexin 31 protein. *Hum. Mol. Genet.*, **12**, 1–6.
19. Saito, T., Schlegel, R., Andresson, T., Yuge, L., Yamamoto, M. and Yamasaki, H. (1998) Induction of cell transformation by mutated 16K vacuolar H+-atpase (ductin) is accompanied by down-regulation of gap junctional intercellular communication and translocation of connexin 43 in NIH3T3 cells. *Oncogene*, **17**, 1673–1680.
20. Kelsell, D.P., Wilgoss, A.L., Richard, G., Stevens, H.P., Munro, C.S. and Leigh, I.M. (2000) Connexin mutations associated with palmoplantar keratoderma and profound deafness in a single family. *Eur. J. Hum. Genet.*, **8**, 141–144.
21. Lopez-Bigas, N., Rabionet, R., Martinez, E., Banchs, I., Volpini, V., Vance, J. M., Arbones, M.L. and Estivill, X. (2000) Identification of seven novel SNPS (five nucleotide and two amino acid substitutions) in the connexin31 (*GJB3*) gene. *Hum. Mutat.*, **15**, 481–482.
22. Lopez-Bigas, N., Rabionet, R., Arbones, M.L. and Estivill, X. (2001) R32W variant in Connexin 31: mutation or polymorphism for deafness and skin disease? *Eur. J. Hum. Genet.*, **9**, 70.
23. Deschenes, S.M., Walcott, J.L., Wexler, T.L., Scherer, S.S. and Fischbeck, K.H. (1997) Altered trafficking of mutant connexin32. *J. Neurosci.*, **17**, 9077–9084.
24. Abrams, C.K., Oh, S., Ri, Y. and Bargiello, T.A. (2000) Mutations in connexin 32: the molecular and biophysical bases for the X-linked form of Charcot–Marie–Tooth disease. *Brain Res. Brain Res. Rev.*, **32**, 203–214.

25. Di, W.-L., Common, J.E.A. and Kelsell, D.P. (2002) Connexin 26 expression and mutation analysis in epidermal disease. *Cell Commun. Adhesion*, **8**, 415–418.
26. Bukauskas, F.F., Jordan, K., Bukauskiene, A., Bennett, M.V., Lampe, P.D., Laird, D.W. and Verselis, V.K. (2000) Clustering of connexin 43-enhanced green fluorescent protein gap junction channels and functional coupling in living cells. *Proc. Natl. Acad. Sci. USA*, **97**, 2556–2561.
27. Cucci, R.A., Prasad, S., Kelley, P.M., Green, G.E., Storm, K., Willcox, S., Cohn, E.S., Van Camp, G. and Smith, R.J. (2000) The M34T allele variant of connexin 26. *Genet. Test.*, **4**, 335–344.
28. Houseman, M.J., Ellis, L.A., Pagnamenta, A., Di, W.L., Rickard, S., Osborn, A.H., Dahl, H.H., Taylor, G.R., Bitner-Glindzicz, M., Reardon, W. *et al.* (2001) Genetic analysis of the connexin-26 M34T variant: identification of genotype M34T/M34T segregating with mild–moderate non-syndromic sensorineural hearing loss. *J. Med. Genet.*, **38**, 20–25.
29. Morley, S.M., Dundas, S., James, J., Brown, R.A., Sexton, C., Navsaria, H.A., Leigh, I.M. and Lane, E.B. (1995) Temperature sensitivity of the keratin cytoskeleton and delayed spreading of keratinocyte lines derived from EBS patients. *J. Cell Sci.*, **108**, 3463–3471.
30. Lane, E.B., Bártek, J., Purkis, P.E. and Leigh, I.M. (1985) Keratin antigens in differentiating skin. *Ann. N. Y. Acad. Sci.*, **455**, 241–258.

Journal of Microscopy, Vol. 205, Pt 1 January 2002, pp. 109–112
Received 26 October 2001; accepted 3 December 2001

SHORT COMMUNICATION

Fluorescence localization after photobleaching (FLAP): a new method for studying protein dynamics in living cells

G. A. DUNN*, I. M. DOBBIE†, J. MONYPENNY†, M. R. HOLT* & D. ZICHA†
*MRC Muscle and Cell Motility Unit, The Randall Centre, New Hunt's House, King's College London, London SE1 1UL, UK
†Light Microscopy, Imperial Cancer Research Fund, 44 Lincoln's Inn Fields, London WC2A 3PX, UK

Key words. Actin, cell motility, CFP, FLIP, fluorescence microscopy, FRAP, GFP, laser scanning confocal microscopy, photobleaching, YFP.

Summary

FLAP is a new method for localized photo-labelling and subsequent tracking of specific molecules within living cells. It is simple in principle, easy to implement and has a wide potential application. The molecule to be located carries two fluorophores: one to be photobleached and the other to act as a reference label. Unlike the related methods of fluorescence recovery after photobleaching (FRAP) and fluorescence loss in photobleaching (FLIP), the use of a reference fluorophore permits the distribution of the photo-labelled molecules themselves to be tracked by simple image differencing. In effect, FLAP is therefore comparable with methods of photoactivation. Its chief advantage over the method of caged fluorescent probes is that it can be used to track chimaeric fluorescent proteins directly expressed by the cells. Although methods are being developed to track fluorescent proteins by direct photoactivation, these still have serious drawbacks. In order to demonstrate FLAP, we have used nuclear microinjection of cDNA fusion constructs of β-actin with yellow (YFP) and cyan (CFP) fluorescent proteins to follow both the fast relocation dynamics of monomeric (globular) G-actin and the much slower dynamics of filamentous F-actin simultaneously in living cells.

Introduction

Transfection of cells with cDNA constructs containing the green fluorescent protein (GFP) gene has revolutionized the study of protein dynamics within living cells (Lippincott-Schwartz *et al.*, 2001; Misteli, 2001), yet its further development has been hampered by a lack of effective methods for activating the fluorescence in a localized manner. In particular, the well established technique of photo-decaging fluorescent probes to photo-label selected molecules (Theriot & Mitchison, 1992; McGrath *et al.*, 1998; Mitchison *et al.*, 1998) cannot be applied to fluorescent proteins directly expressed by the cells.

Recent approaches to solving this critical problem have centred on methods for photoactivating GFP directly, either to change its fluorescence spectra (Elowitz *et al.*, 1997) or to enhance its blue-excited fluorescence (Yokoe & Meyer, 1996). Unfortunately, the first method requires conditions of low oxygen concentration that are generally incompatible with maintaining physiological conditions in cell cultures, whereas the second merely enhances the signal and cannot provide unambiguous localization of photoactivated molecules.

Here we have taken a different approach based on the fact that GFP and its variants are well suited to photobleaching. The methods of FRAP and FLIP have been successfully applied to cells transfected with GFP fusion constructs (Cole *et al.*, 1996; White & Stelzer, 1999; Lippincott-Schwartz *et al.*, 2001; Reits & Neefjes, 2001) and have permitted the dynamics of the remaining unbleached molecules to be studied. Our proposed FLAP method is simply an extension of this approach, which allows continued tracking of the bleached molecules as well as the unbleached ones. This is achieved by tagging the molecules to be tracked with two different fluorophores and bleaching just one of them in a localized region of the cell. If care is taken to ensure accurate matching of the two signals before bleaching, the population of molecules exposed to bleaching is thereafter unambiguously identified as those in which the two signal strengths differ. Basic image processing can reveal the distribution of this population of photo-labelled molecules and an additional advantage over photoactivation methods is that information on the distribution of the unbleached molecules is also readily available.

Correspondence: Graham A. Dunn. E-mail: graham.a.dunn@kcl.ac.uk

For the FLAP method to work optimally, the two fluorophores should be excited together and imaged simultaneously. If the emission spectra overlap too much to be easily separated, a satisfactory compromise is to switch the two excitation channels line-by-line during a single frame scan using a confocal microscope equipped with acousto-optical tunable filters.

Materials and methods

Cell culture and microinjection

Transformed rat fibroblasts (a gift from Dr Pavel Vesely) were seeded on 18 × 18 mm coverslips in Hank's Minimum Essential Medium containing 10% bovine serum. DNA constructs were microinjected into cell nuclei using an Eppendorf Transjector and micromanipulator system mounted on a Zeiss Axiovert 35. Cells were ready for use after allowing 2–3 h for expression of the constructs.

DNA constructs

Separate constructs encoding yellow and cyan N-terminal fluorescent proteins were cloned from a β-actin construct (a gift from Dr John Copeland) using pECFP-C1 and pEYFP-C1 vectors (ClonTech, Palo Alto, CA, USA). They were co-injected at a concentration of 0.1 $\mu g\ \mu L^{-1}$ each.

Microscopy

Images were recorded using a laser scanning confocal microscope (Zeiss LSM 510) equipped with a 37 °C temperature-controlled hood and a 63 × Plan-Apochromat NA 1.4 pH 3 oil objective. The CFP and YFP channels used 458 nm and 514 nm lines of an argon laser for excitation and a phase contrast image was recorded simultaneously with the CFP channel. A 545 nm dichroic mirror was used to split the two emission channels, followed by a bandpass 475–525 nm filter for the CFP channel and a long pass 530 nm filter for the YFP channel. In each case the pinhole was set such that the optical slice was indicated as 3 μm by the LSM 510 software. Each image line was scanned twice at the highest scan rate (0.64 $\mu s\ pixel^{-1}$) using multi-tracking mode, first by the 514 nm laser line with the YFP channel detector active and then by the 458 nm laser line with the CFP detector and the transmission phase-contrast detector active. Alternatively, we have found that simultaneous imaging of CFP and YFP is possible using 458 nm illumination to excite both fluors.

Before starting a recording sequence, a rectangular image capture region and a much smaller bleach region (a strip 2 μm wide or a circle 3–10 μm diameter) were positioned on the selected cell. The gain and offset for each fluorescence channel were optimized so that the two images were closely matched without saturation. The time-lapse (bleach) mode of the Zeiss LSM510 was then used to collect sequential images. Five or 10 frames were collected, then the 514 nm laser line was used at maximum power (measured as 1.32 mW) to scan the bleach region for 3–15 s and the time-lapse sequence was resumed immediately afterwards.

Image processing

The image of the FLAP signal was obtained by subtracting the image of the photobleached fluor from that of the unbleached fluor. Smoothing of the two input images (5 × 5 pixel averaging) was used to reduce noise in the FLAP image. Fading of the two fluorophores was minimal and well balanced during the sequences shown here and was not compensated for, although compensation would be required if fading were rapid or unbalanced. Post-processing of the FLAP image consisted of thresholding to remove background pixel noise and mapping the grey levels onto a pseudocolour scale. The threshold level was chosen to reduce noise to an acceptable level in the pre-bleach FLAP images and then kept constant for all images in the sequence.

Results

After allowing the β-actin constructs to become expressed, confocal microscopy revealed that the two fluorophores were accurately co-localized within the cells and thus that the intensity difference – the FLAP signal – was close to zero throughout the image (Fig. 1(c) and (e)). Photobleaching the YFP in a narrow strip traversing the lamella of a transformed rat fibroblast (Fig. 1(a) and (b)) gave rise to a strong FLAP signal (Fig. 1d), which is shown encoded in pseudocolour (Fig. 1f). The selected cell had prominent microfilament bundles or stress fibres (Fig. 1a) and the FLAP signal revealed that a variety of dynamic activities were taking place. Immediately after bleaching, a diffuse low-level signal had uniformly filled the local cytoplasm of the cell but had not managed to pass the cell nucleus. A much stronger signal was confined to the microfilament bundles but even this had migrated along the bundles some 1–2 μm away from the nucleus and 2–3 μm towards the nucleus during the 4 s bleach period (Fig. 1f).

In order to confine our initial studies to simpler examples of actin dynamics, we concentrated on spot bleaching of three types of actin structure in cells lacking prominent stress fibres. We repeatedly observed three distinct patterns of behaviour of the FLAP signal during the 3–4 min subsequent to bleaching. If the bleach spot were located in a region of high actin concentration in the lamella of the cell (Fig. 2(a)–(c)), the FLAP signal usually showed rapid dispersal and, in the case of this particular cell, it had spread through most of the cytoplasm during the 8 s bleach period (Fig. 2a). Subsequently, the signal accumulated in another region of high actin concentration (Fig. 2b – arrow) and was little changed by 100 s after bleaching (Fig. 2c). Another pattern was revealed when the bleach spot was located in an active ruffling region at the leading edge (Fig. 2(d)–(f)). In this case there was little or no general

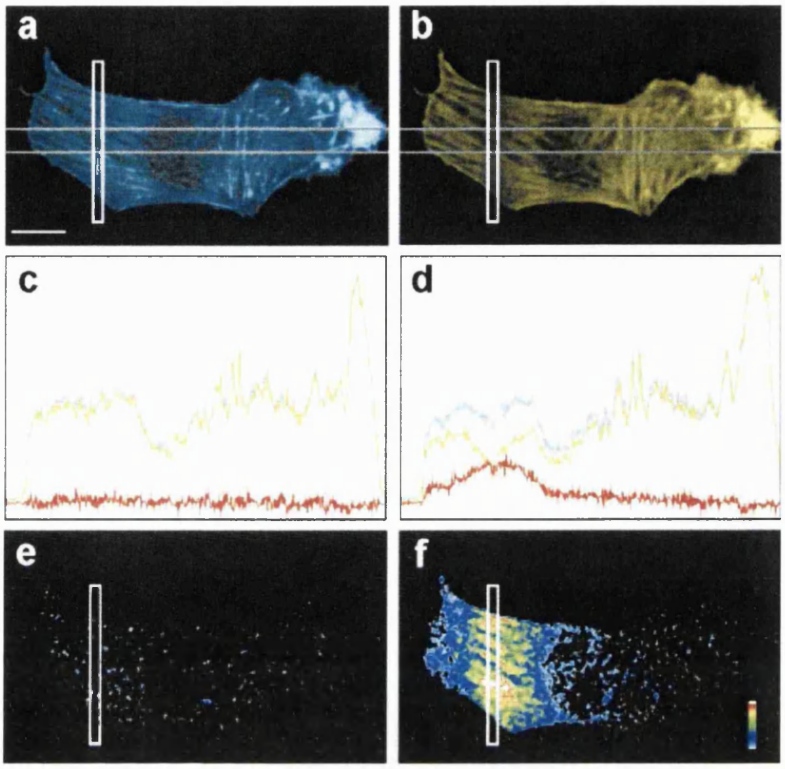

Fig. 1. Transformed rat fibroblast showing simultaneously acquired CFP (a) and YFP (b) images immediately after photobleaching the lamella in a narrow strip (white rectangle). Intensity profiles integrated between the grey lines before (c) and after (d) photobleaching show CFP (cyan), YFP (yellow) and FLAP (red) signals. The FLAP images corresponding to the profiles (c) and (d) are shown encoded in pseudocolour in (e) and (f). Bleach time 3.8 s. Scale bar 10 μm.

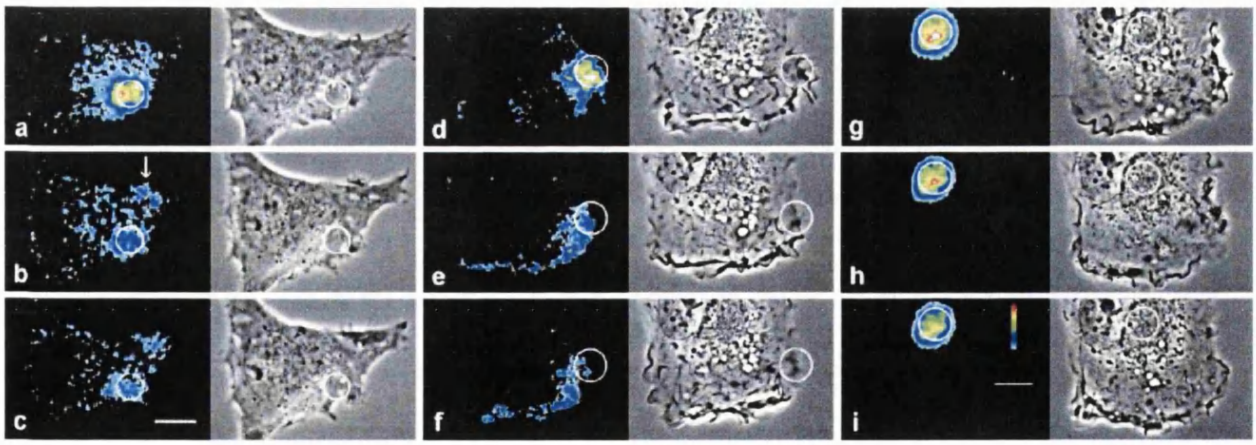

Fig. 2. Three image sequences show the FLAP image in pseudocolour (left panel) and phase-contrast image (right panel) at the following times after bleaching: 0 s (a, d and g), 50 s (b and e), 100 s (c, f and h) and 200 s (i). In these sequences the individual channels were acquired in multi-tracking mode. Bleach region shown as a circle in each image. Threshold level set to 8% of maximum signal. Bleach times 8.6 s (a) and 13.5 s (d and g). Scale bars 10 μm.

dispersal of the FLAP signal, although it had usually filled the local ruffle system immediately after bleaching (Fig. 2d). During the subsequent 50 s the signal migrated laterally, spreading into more distant ruffles along the leading edge (Fig. 2(e) and (f)) and tended to persist locally longer than in the first type of pattern. A third distinct pattern was associated with denser accumulations of expressed actin found often in the perinuclear region of the cell (Fig. 2(g)–(i)). When the same cell was targeted in this region, 10 min after the last sequence, the FLAP signal remained precisely localized on the bleach spot and showed no discernible dispersal and very little decay during the 4 min recorded sequence.

Discussion

It is apparent from these images that the FLAP method will prove useful for shedding light on the dynamics of actin as well as other proteins of the cytoskeleton. Other studies have shown that GFP and its variants, when tagged to actin, do not appear to affect significantly its polymerization or other interactions (Choidas *et al.*, 1998; Fischer *et al.*, 1998). The rapid initial diffusion of part of the signal in Figs 1(f) and 2(a) indicates that a considerable portion of the targets must have contained G-actin, possibly associated with an actin-binding protein such as profilin or β-thymosin. Our measurements indicate that the total signal, integrated over the cell, does not decay, although dispersal of the signal causes more of it to fall below the threshold. In the case of the second type of behaviour, the mobility of the FLAP signal is too slow for freely diffusing G-actin but probably too fast for crosslinked actin filaments. Thus, the relatively high mobility of the FLAP signal in ruffles may indicate freely mobile oligomeric actin filaments or it could be due to some form of G-actin that is not entirely free to diffuse, possibly because it is associated in some way with the membrane. The third type of behaviour suggests that the perinuclear actin is either sequestered and/or crosslinked, and this experiment also serves as a control to show that bleaching is truly confined to the defined bleach region when there is little or no translocation of the actin. It is interesting that the stress fibres shown by the cell in Fig. 1 are not as stable as this perinuclear actin, as a strong signal had migrated well outside the bleach region, along the filament bundles, immediately after bleaching. The questions raised by these observations will all require much more detailed studies of specific systems before they can be resolved. Longer recording periods will be needed to observe dynamic changes in the more stable regions of the cytoskeleton and faster sampling rates (with correspondingly reduced imaging regions) to follow the diffusion of G-actin.

Future improvements to the method will accrue from having both fluorophores on the same molecule and imaging both channels simultaneously. This would reduce fluorescence 'speckle' noise in the FLAP signal, thus increasing the signal-to-noise ratio and hence the sensitivity of the method. Although multi-tracking provides lower crosstalk between channels, we have shown that simultaneous imaging of CFP and YFP is possible using 458 nm illumination to excite both fluors (Fig. 1). Double constructs of GFP variants coupled by linker sequences have been made for fluorescence resonance energy transfer (FRET) studies (Pollok & Heim, 1999) and we are currently producing a CFP-YFP-actin construct. Although there is no evidence of FRET in the current study (there is no enhancement of the CFP signal when the YFP is bleached), CFP and YFP are known to be an efficient FRET pair when closely linked on the same molecule (Pollok & Heim, 1999). This may prove to be advantageous for FLAP if the FRET acceptor is the one chosen to be bleached: bleaching would then enhance the brightness of the donor and thus increase the FLAP signal.

Even when not using fluorescent proteins, FLAP may yet prove to have significant advantages over the method of caged fluorescent probes. It is much easier to implement on confocal or conventional fluorescent microscopes, it avoids exposing the cells to harmful UV irradiation, and it can reveal the distribution of all the fluorescent molecules – not only those that have been photolabelled. Directly coupled pairs of fluorescent dyes, chosen to have suitable FRET properties and well separated emission spectra for simultaneous imaging, could be specially synthesized for conjugation with biologically relevant molecules to be used in FLAP experiments. Synthetic dyes will have much greater versatility than fluorescent proteins for multichannel FLAP applications.

Acknowledgement

We thank Dr C. Gray (ICRF) for help with tissue culture and microinjection.

Supplementary material

Movies showing these behaviour patterns are available at the following web address: http://www.blackwell-science.com/products/journals/suppmat/JMS/JMS1007/JMS1007.htm.

References

Choidas, A., Jungbluth, A., Sechi, A., Murphy, J., Ullrich, A. & Marriott, G. (1998) The suitability and application of a GFP-actin fusion protein for long-term imaging of the organization and dynamics of the cytoskeleton in mammalian cells. *Eur. J. Cell Biol.* **77**, 81–90.

Cole, N.B., Smith, C.L., Sciaky, N., Terasaki, M., Edidin, M. & Lippincott-Schwartz, J. (1996) Diffusional mobility of Golgi proteins in membranes of living cells. *Science*, **273**, 797–801.

Elowitz, M.B., Surette, M.G., Wolf, P., Stock, J. & Leibler, S. (1997) Photoactivation turns green fluorescent protein red. *Current Biol.* **7**, 809–812.

Fischer, M., Kaech, S., Knutti, D. & Matus, A. (1998) Rapid actin-based plasticity in dendritic spines. *Neuron*, **20**, 847–854.

Lippincott-Schwartz, J., Snapp, E. & Kenworthy, A. (2001) Studying protein dynamics in living cells. *Nat. Rev. Mol. Cell Biol.* **2**, 444–456.

McGrath, J.L., Tardy, Y., Dewey, C.F., Jr, Meister, J.J. & Hartwig, J.H. (1998) Simultaneous measurements of actin filament turnover, filament fraction, and monomer diffusion in endothelial cells. *Biophys. J.* **75**, 2070–2078.

Misteli, T. (2001) Protein dynamics: implications for nuclear architecture and gene expression. *Science*, **291**, 843–847.

Mitchison, T.J., Sawin, K.E., Theriot, J.A., Gee, K. & Mallavarapu, A. (1998) Caged fluorescent probes. *Meth. Enzymol.* **291**, 63–78.

Pollok, B.A. & Heim, R. (1999) Using GFP in FRET-based applications. *Trends Cell Biol.* **9**, 57–60.

Reits, E.A.J. & Neefjes, J.J. (2001) From fixed to FRAP: measuring protein mobility and activity in living cells. *Nature Cell Biol.* **3**, E145–E147.

Theriot, J.A. & Mitchison, T.J. (1992) Comparison of actin and cell surface dynamics in motile fibroblasts. *J. Cell Biol.* **119**, 367–377.

White, J. & Stelzer, E.H. (1999) Photobleaching GFP reveals protein dynamics inside live cells. *Trends Cell Biol.* **9**, 61–65.

Yokoe, H. & Meyer, T. (1996) Spatial dynamics of GFP-tagged proteins investigated by local fluorescence enhancement. *Nature Biotechnol.* **14**, 1252–1256.

The EMBO Journal Vol. 20 No. 11 pp. 2723–2741, 2001

Ezrin is a downstream effector of trafficking PKC–integrin complexes involved in the control of cell motility

Tony Ng[1,2,3], Maddy Parsons[1], William E.Hughes[4], James Monypenny[5], Daniel Zicha[5], Alexis Gautreau[6], Monique Arpin[6], Steve Gschmeissner[7], Peter J.Verveer[8], Philippe I.H.Bastiaens[8] and Peter J.Parker[4]

[1]Richard Dimbleby Department of Cancer Research, St Thomas' Hospital, Lambeth Palace Road, London SE1 7EH, [2]Cell Biophysics Laboratory, [4]Protein Phosphorylation Laboratory, [5]Light Microscopy Laboratory and [7]Electron Microscopy Unit, Imperial Cancer Research Fund, 44 Lincoln's Inn Fields, London WC2A 3PX, UK, [6]Laboratoire de Morphogenese et Signalisation Cellulaires, UMR 144 CNRS/Institut Curie, 75248 Paris Cedex 05, France and [8]Cell Biology and Cell Biophysics Programme, EMBL, Meyerhofstrasse 1, D-69117 Heidelberg, Germany

[3]Corresponding author
e-mail: T.Ng@icrf.icnet.uk

T.Ng and M.Parsons contributed equally to this work

Protein kinase C (PKC) α has been implicated in β1 integrin-mediated cell migration. Stable expression of PKCα is shown here to enhance wound closure. This PKC-driven migratory response directly correlates with increased C-terminal threonine phosphorylation of ezrin/moesin/radixin (ERM) at the wound edge. Both the wound migratory response and ERM phosphorylation are dependent upon the catalytic function of PKC and are susceptible to inhibition by phosphatidylinositol 3-kinase blockade. Upon phorbol 12,13-dibutyrate stimulation, green fluorescent protein–PKCα and β1 integrins co-sediment with ERM proteins in low-density sucrose gradient fractions that are enriched in transferrin receptors. Using fluorescence lifetime imaging microscopy, PKCα is shown to form a molecular complex with ezrin, and the PKC-co-precipitated endogenous ERM is hyperphosphorylated at the C-terminal threonine residue, i.e. activated. Electron microscopy showed an enrichment of both proteins in plasma membrane protrusions. Finally, overexpression of the C-terminal threonine phosphorylation site mutant of ezrin has a dominant inhibitory effect on PKCα-induced cell migration. We provide the first evidence that PKCα or a PKCα-associated serine/threonine kinase can phosphorylate the ERM C-terminal threonine residue within a kinase–ezrin molecular complex *in vivo*.

Keywords: ERM/FLIM/migration/PKC/wound

Introduction

Of the protein kinase C (PKC) family of protein kinases, several isoforms including PKCα (Platet *et al.*, 1998), PKCδ (Kiley *et al.*, 1999) and PKCθ (Tang *et al.*, 1997) have been implicated in promoting a cell migratory phenotype. Recently, we and others have shown an enhancement of haptotactic cell motility/invasiveness following overexpression of PKCα (Ng *et al.*, 1999a; Sun and Rotenberg, 1999). The precise mechanism(s) by which the catalytic activity of PKC influences cell motility has yet to be defined but is likely to involve components of the focal complexes, the small GTPases (Rho, Rac and Cdc42) and actin cytoskeleton-binding proteins (reviewed by Zigmond, 1996). In MCF-7 breast cancer epithelial cells, the signal machinery that drives efficient cell migration towards extracellular matrix β1 integrin substrates is dependent upon the PKCα-catalysed recycling of the activated [ligand-occupied, monoclonal antibody (mAb) 12G10-reactive] pool of β1 integrin receptors (Ng *et al.*, 1999a). Overexpression of PKCα in MCF-10A human breast cells enhances cell motility, which is subject to control by the small GTPase Rac1 (Sun and Rotenberg, 1999). By using dominant inhibitor constructs, the activity states of RhoA, Rac1 and Rab5 have been shown to influence 12-*O*-tetradecanoylphorbol-13-acetate (TPA)-induced disassembly/reassembly of actin stress fibres and focal adhesions in MDCK cells (Imamura *et al.*, 1998). In NIH 3T3 cells, growth factor-induced Rac1 activation is sensitive to PKC inhibition, also placing PKC upstream of Rac in this cell system (Buchanan *et al.*, 2000).

ERM proteins (ezrin, radixin and moesin) are F-actin-binding proteins that affect actin cytoskeletal turnover and hence the maintenance of cell shape and lamellipodial extension (Crepaldi *et al.*, 1997; Lamb *et al.*, 1997; reviewed by Mangeat *et al.*, 1999; Bretscher *et al.*, 2000). Depending on individual cell types, ERM proteins have been reported to be localized to different structures including microvilli, ruffles, filopodia, uropods, retraction fibres and cell adhesion sites (reviewed by Tsukita and Yonemura, 1999).

The crystal structure of a dormant moesin N-terminal FERM (band four-point-one, ezrin, radixin, moesin homology domains)–C-terminal tail complex reveals the C-terminal segment to be bound as an extended peptide masking a large surface of the FERM domain (Pearson *et al.*, 2000). The activation of ERM proteins is mediated by both C-terminal threonine phosphorylation (T567 in ezrin, T564 in radixin and T558 in moesin) (Matsui *et al.*, 1999; Nakamura *et al.*, 1999; Gautreau *et al.*, 2000; Pearson *et al.*, 2000) and exposure to polyphosphoinositides (reviewed by Mangeat *et al.*, 1999). *In vitro*, the T558-phosphorylated form of moesin interacts with F-actin only in the presence of polyphosphoinositides such as phosphatidylinositol 4,5-bisphosphate [PI(4,5)P_2] (Nakamura *et al.*, 1999).

Two protein kinases, namely PKCθ (Pietromonaco *et al.*, 1998) and Rho-kinase/ROCK (Matsui *et al.*, 1998; Tran Quang *et al.*, 2000), were found to phosphorylate the

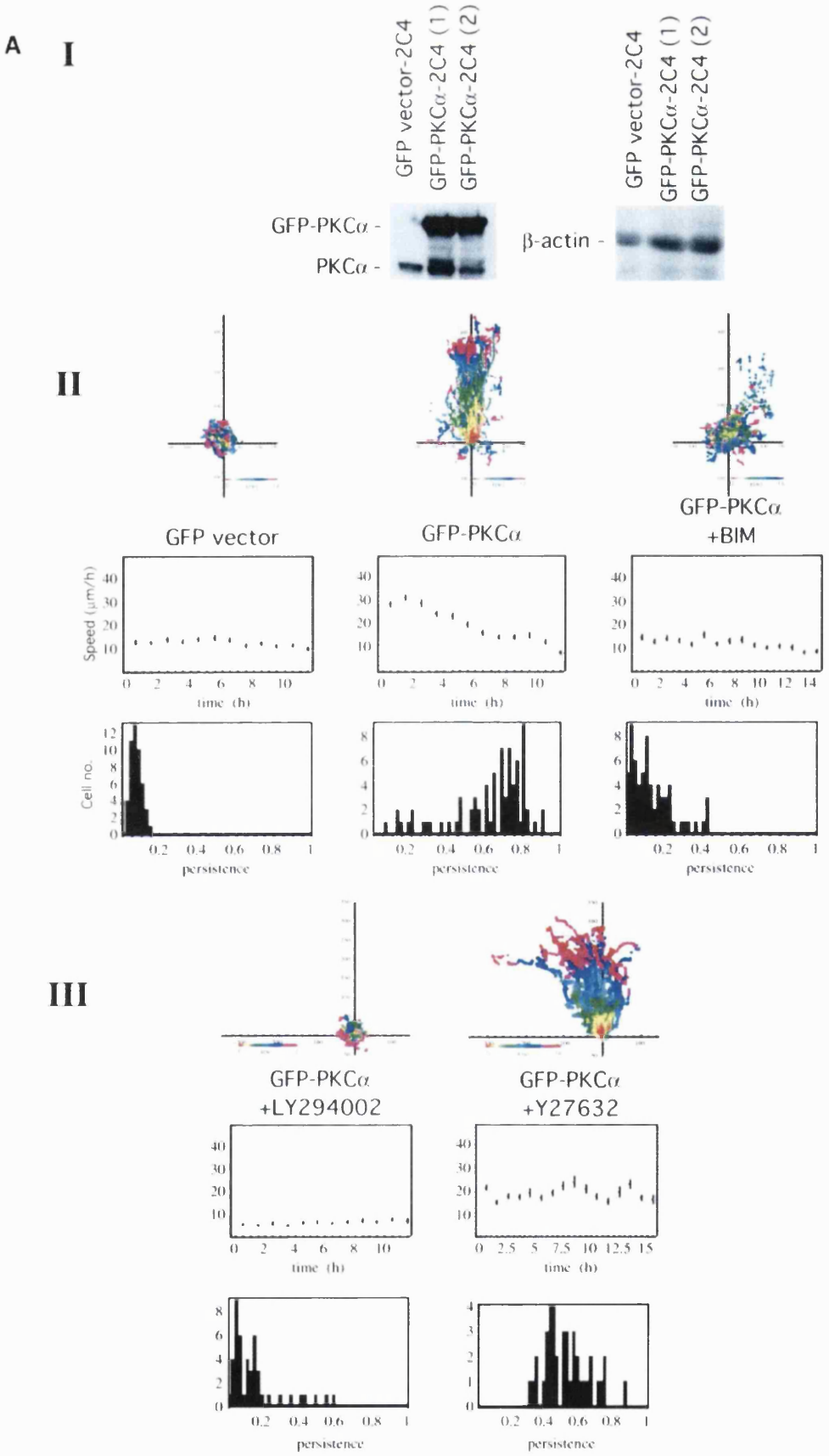
A
I
GFP vector-2C4
GFP-PKCα-2C4 (1)
GFP-PKCα-2C4 (2)
GFP-PKCα -
PKCα -
β-actin -
II
GFP vector
GFP-PKCα
GFP-PKCα +BIM
Speed (μm/h)
time (h)
Cell no.
persistence
III
GFP-PKCα +LY294002
GFP-PKCα +Y27632

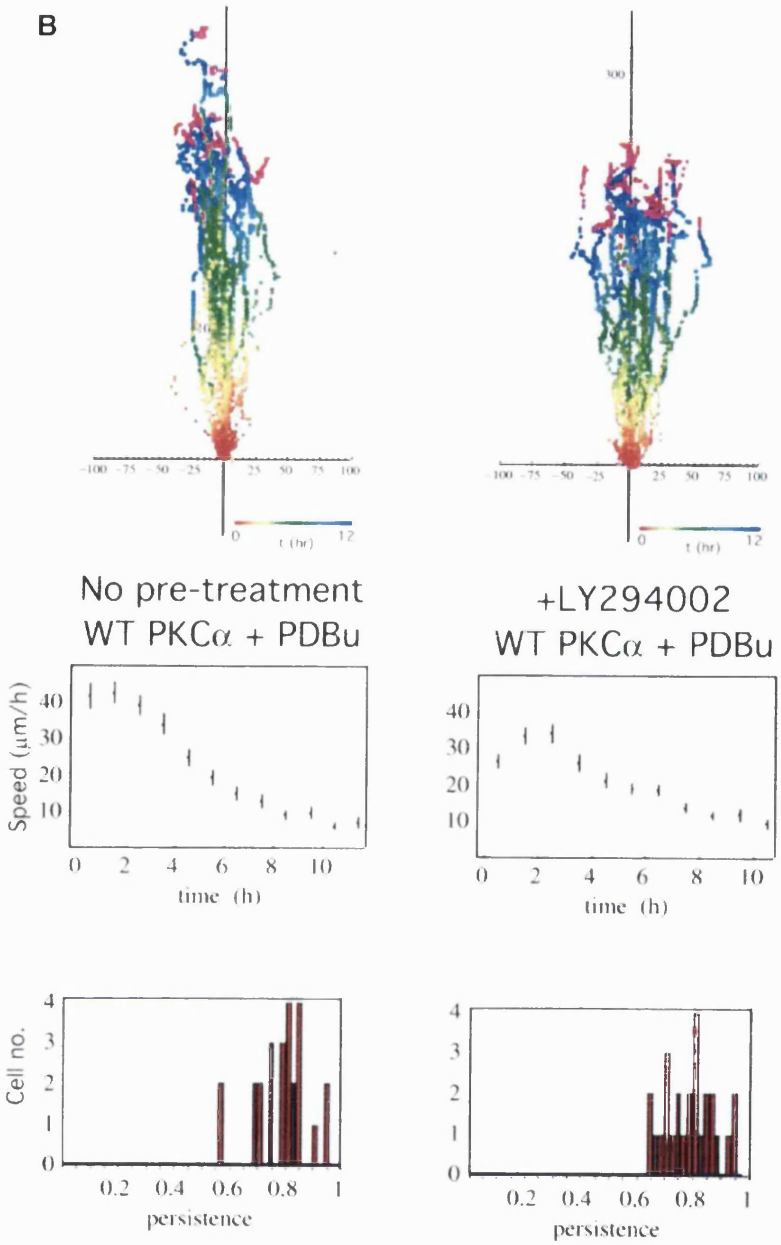

Fig. 1. PKC-driven wound closure response in 2C4 fibrosarcoma cells stably transfected with GFP–PKCα. (**A**) Confluent 2C4 fibrosarcoma cells stably transfected with GFP–PKCα (GFP–PKCα-2C4) or the GFP control vector were wounded and the wound closure response was recorded by time-lapse microscopy. Part I: the total level of PKCα, as detected by a PKCα C-terminal polyclonal antibody, in two different batches of the GFP–PKCα-2C4 cell line (1) and (2), in comparison with that in the vector control cell line. Loading control was provided by stripping the blot and reprobing with an anti-β-actin mAb. In both GFP–PKCα-2C4 lanes, both the exogenous GFP-tagged and untagged forms of PKCα are apparent, with the latter possibly representing a cleavage product of the expressed protein. Overall, the ratio of the levels of PKCα expressed in GFP–PKCα-2C4 versus the GFP control vector line was 3:1. In both parts II and III, the upper panels show all the cell trajectories during the entire time course of each experiment. Each dot represents a cell position at a particular time point that is indicated by the pseudocolour scale (t in h) beneath each set of cell tracks. The scale of the cell track axes is in μm. Middle panels show the changes in mean speed (of all tracked cells ± SD) with time, and the lower panels show the distribution of persistence within the cell populations in each treatment group. Speed and persistence were derived from the analysis of tracked cells from at least four independent experiments (except for the +Y-27632 data where $n = 2$) as described in Materials and methods. Persistence of motility measured for each cell was calculated as the ratio of the resultant displacement in 16 h over the sum of individual 5 min displacements. GFP–PKCα-2C4 cells (GFP–PKCα) ($n = 75$, mean persistence = 0.63 ± 0.2) showed a significant increase in persistence of migration into a wound space overnight ($P < 0.01$) when compared with 2C4 cells stably expressing GFP control vector (GFP vector) ($n = 48$, mean persistence = 0.08 ± 0.03). In cultures wounded in the presence of 10 μM BIM (GFP–PKCα + BIM) ($n = 66$, mean persistence = 0.14 ± 0.1) or LY294002 (10 μM) (GFP–PKCα + LY294002) ($n = 46$, mean persistence = 0.15 ± 0.14), there was a loss of cell persistence. The Rho kinase (ROCK) inhibitor Y-27632 (GFP–PKCα + Y27632) ($n = 40$, mean persistence = 0.53 ± 0.1) had no effect on the persistence of migration compared with untreated cultures. (**B**) GFP–PKCα-2C4 cells were wounded after a 30 min incubation in media containing LY294002 (10 μM) (+LY294002) ($n = 26$, mean persistence = 0.79 ± 0.09). PDBu (1 μM) was added to the media after wounding and the wound closure response was monitored. Results from two independent experiments were analysed. The P-value for the difference between the LY294002-treated group and the no pre-treatment control (WT PKCα + PDBu) ($n = 25$, mean persistence = 0.79 ± 0.09) was derived using ANOVA.

C-terminal threonine residue of the ERM proteins *in vitro*. However, the authors who first showed that ROCK phosphorylates the site *in vitro* (Matsui *et al.*, 1998) subsequently reported that the C-terminal threonine phosphorylation of ERM is in fact insensitive to ROCK inhibition *in vivo* (Matsui *et al.*, 1999). To date, the protein serine/threonine kinase(s) that is responsible *in vivo* for the phosphorylation of the ERM C-terminal threonine residue has yet to be identified.

In the present study, we have found both green fluorescent protein (GFP)–PKCα and β1 integrins to co-localize with endogenous ezrin *in vivo*. Using fluorescence lifetime imaging microscopy (FLIM) and co-immunoprecipitation, GFP–PKCα was confirmed to form a molecular complex with vesicular stomatitis virus (VSV) G-tagged ezrin in MCF-7 cells. The C-terminal threonine phosphorylation of ERM is dependent on the catalytic domain function of PKC (not ROCK) in an *in vivo* model of cell migration. Finally, a phosphorylation site mutant of ezrin that is incapable of interacting with the cytoskeleton but retains the ability to bind PKC is shown here to exert a dominant inhibitory effect on PKC-driven cell migration.

Results

PKC-enhanced cell migration in response to wounding

Previously we observed that transient expression of GFP–PKCα increased the haptotactic response of MCF-7 cells towards β1 (but not αvβ5) integrin substrates (Ng *et al.*, 1999a). In this study, we confirmed that stable expression of a GFP–PKCα full-length construct also significantly enhanced the 'persistence' of 2C4 fibrosarcoma cell migration in response to wounding in comparison with cells stably expressing the corresponding GFP control vector [$P < 0.01$ by analysis of variance (ANOVA), Figure 1A].

The cumulative speed profile of GFP–PKCα-2C4 cells in Figure 1A showed faster cell movement than that of the vector control cell line during the initial 4 h post-wounding but, when the whole time course was analysed statistically, the speed of the GFP–PKCα-expressing cells based on 5 min displacements was not different from the speed of the control cells by ANOVA. The total level of PKCα expressed in GFP–PKCα-2C4 cells (which is a mixed clone), after correction with the β-actin control, was ~3 times that of the endogenous protein present in the vector control cells (Figure 1A). In GFP–PKCα-2C4 cell cultures wounded in the presence of the PKC inhibitor bisindolylmaleimide I (BIM, 10 μM) or the phosphatidylinositol 3-kinase (PI3K) inhibitor LY294002 (10 μM), there was a loss of the wound closure response ($P < 0.01$ by ANOVA for all three inhibitors, showing a significant loss of persistence of the wound closure response compared with no treatment control). Persistence of motility measured for each cell was calculated as the ratio of the resultant displacement in 16 h over the sum of individual 5 min displacements. The ROCK inhibitor Y-27632 had no effect on the wound-induced migratory response (persistence or speed) compared with untreated cultures ($P = 0.49$ by ANOVA showing no significant difference in persistence of the wound response compared with no treatment control). An analysis of the speed data by ANOVA, however, indicated a significant reduction in speed with LY294002 compared with no treatment control.

Activation of PKC with phorbol 12,13-dibutyrate (PDBu) treatment (post-wounding) was shown to reverse the inhibition of cell migration by LY294002 [$P = 0.096$ by ANOVA, comparing the wound migratory response following pre-treatment with LY294002 (+PDBu) with control treatment, i.e. +PDBu post-wounding alone; Figure 1B].

PKC control of ERM C-terminal phosphorylation in response to wounding

A monoclonal antibody (297S) that recognizes the C-terminal threonine-phosphorylated (T567 in ezrin, T564 in radixin and T558 in moesin; Nakamura *et al.*, 1999) form of ERM proteins (CPERM) was used to monitor their phosphorylation in relation to PKC activation. In MCF-10A monolayer culture, endogenous PKCα redistributed to a vesicular compartment at the wound edge (Figure 2A). This redistribution was coincident with an increase in PKCα phosphorylation at the Thr250 site (Ng *et al.*, 1999b), indicative of PKC activation at the wound edge (T.Ng, unpublished observations). Endogenous ERM protein phosphorylation at the C-terminal threonine residue is low in confluent monolayer cultures (observed for MCF-7, MCF-10A epithelial cells and GFP–PKCα-2C4 fibrosarcoma cell cultures) (Figures 2 and 3). An increase in ERM C-terminal threonine phosphorylation in response to wounding was observed at the wound edge. Pre-treatment of MCF-7 cells at the wound edge with alkaline phosphatase, following paraformaldehyde fixation, significantly reduced the recognition of endogenous ERM proteins by mAb 297S, confirming the phosphospecificity of the antibody (data not shown). The anti-CPERM staining partially co-localized with both the GFP-tagged and endogenous PKCα at the wound edge. The site of PKC/CPERM co-localization at the wound edge varied according to cell type. Co-localization was seen predominantly in intracellular vesicular structures in mammary epithelial cells such as MCF-10A and at cell ruffles in the case of 2C4 fibrosarcoma cells (Figure 2).

ERM C-terminal threonine phosphorylation at the wound edge was sensitive to PKC inhibition by BIM and PI3K inhibition by LY294002, but was not affected by the ROCK inhibitor Y-27632 (Ishizaki *et al.*, 2000) (Figure 2). In 2C4 fibrosarcoma cells stably transfected with GFP–PKCα, the abrogation of the ERM C-terminal threonine phosphorylation by these inhibitors was mirrored by a reduction of the wound closure response (Figure 1A).

GFP–PKCα complexes with VSVG–ezrin in vivo

Of the ERM proteins, ezrin has been shown to be an effector of growth factor-mediated cell migration (Crepaldi *et al.*, 1997). To determine whether ezrin forms part of the PKC–integrin complex, we assessed whether PKCα and ezrin associate upon PKC activation. FLIM was undertaken to determine the extent of fluorescence resonance energy transfer (FRET) between GFP–PKCα (donor) and VSVG-tagged ezrin stained with a Cy3 (acceptor)-conjugated antibody to the VSVG epitope. The spatial separation (R_0) between GFP and Cy3 at which the resonance energy transfer efficiency is 50% is 6 nm; however, detectable energy transfer can occur up to 9 nm

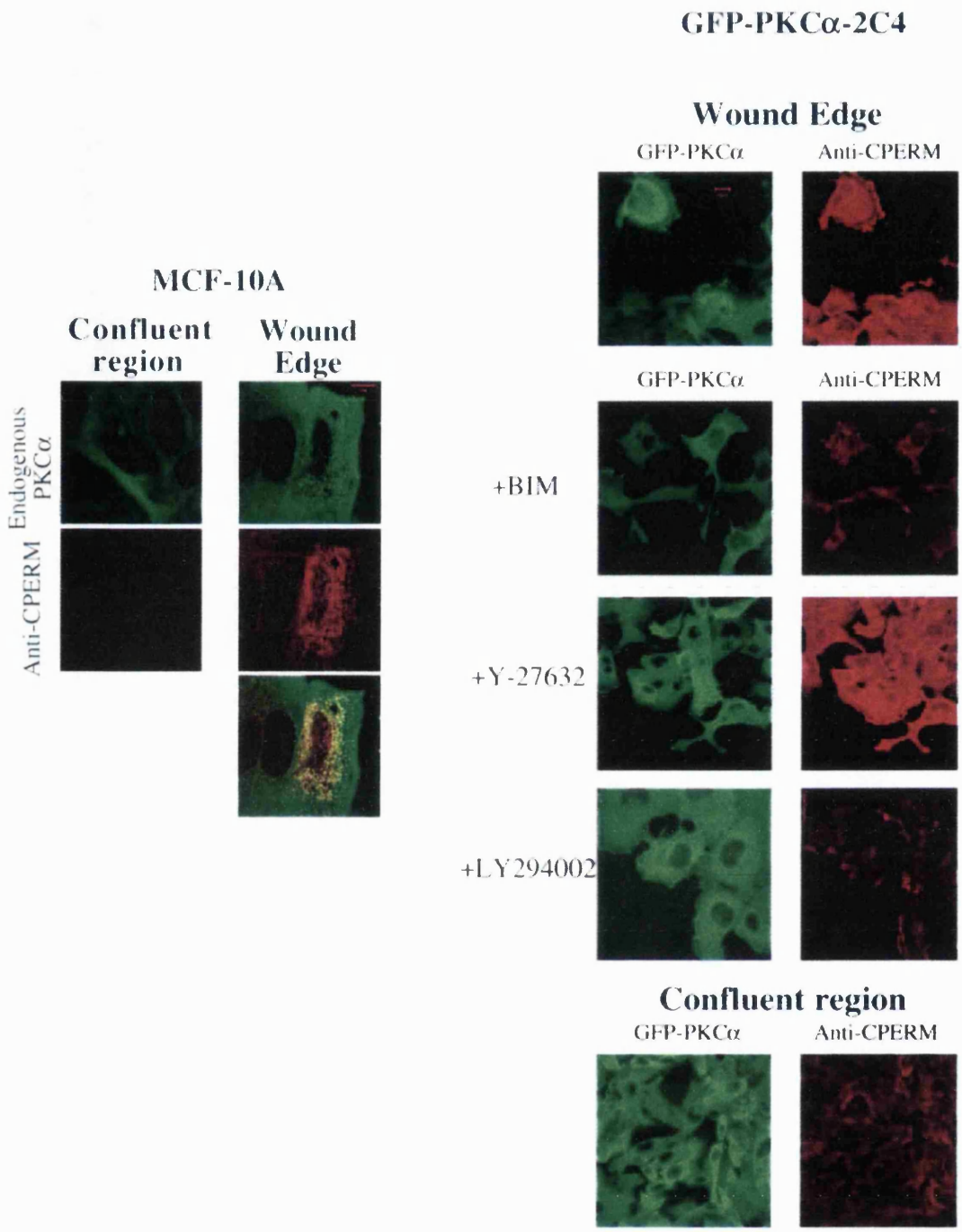

Fig. 2. PKC control of ERM C-terminal threonine phosphorylation in response to wounding. Confluent MCF-10A cells or 2C4 fibrosarcoma cells stably expressing GFP–PKCα (GFP–PKCα-2C4) were wounded and ERM C-terminal threonine phosphorylation (CPERM) was detected by confocal microscopy using an anti-CPERM mAb 297S as described in Materials and methods. Each image represents a two-dimensional projection of 2–3 slices in the Z-series, taken across the mid-depth of the cell at 0.2 μm intervals. Left: in wounded MCF-10A cells, endogenous PKCα was stained with mAb MC5 and its partial co-localization with anti-CPERM staining was shown. Representative scale bar = 10 μm. Right: GFP–PKCα-2C4 cells were pre-treated for 1 h and incubated with the following compounds for 4 h after wounding, before fixation: BIM (10 μM), LY294002 (10 μM) and ROCK inhibitor Y-27632 (10 μM). Representative scale bar = 20 μm. In both cell types, there was an increase in ERM C-terminal threonine phosphorylation (anti-CPERM) at the wound edge compared with the confluent region of the monolayer. The effects of the various inhibitors are shown.

(Ng *et al.*, 1999b). FRET results in a shortening of the GFP (donor) fluorescence lifetime that is measured by two independent parameters, the phase shift (τ_p) and relative modulation depth (τ_m). Therefore, FRET should only be detected between two proteins that are closely associated or complexed *in vivo*.

When GFP–PKCα- and VSVG–ezrin-expressing cells were stained with VSVG-Cy3 following PDBu stimulation and fixation, it was evident that fluorescence lifetime, <τ>, measured as the average phase shift and relative modulation depth [(τ_p + τ_m)/2] for GFP was decreased at the plasma membrane and cell cortex beneath the membrane (Figure 3A). The presence of FRET (from GFP to Cy3) in these structures was confirmed by photobleaching the Cy3 acceptor, resulting in a lengthening of the donor <τ> after acceptor photobleaching (Figure 3C and data not shown). The FRET efficiency (Eff) pseudocolour plots, which only apply to the +anti-VSVG-Cy3 lifetime maps, give a qualitative indication of the pixel-to-pixel variation in the amount of PKC molecules that are complexed to ezrin. [Eff = $1 - \tau_{da}/\tau_d$ where τ_{da} is the lifetime map of the donor in the presence of acceptor and τ_d is the average lifetime of the donor in the absence of acceptor (average of the mean<τ> of at least five GFP–PKC alone control cells).] The efficiencies are approximately proportional to the fraction of the total steady-state fluorescence that originates from donor molecules in their bound state. Since the donor-tagged molecules transfer energy to the acceptor when they are in a complex, their lifetimes are reduced and hence the number of photons emitted would be reduced fractionally.

Statistical analysis of cumulative results from all the cells at each time point confirmed that there was a time-dependent, PDBu-enhanced association between GFP–PKCα and VSVG–ezrin [see two-dimensional lifetime histograms and pixel counts versus Eff (%) profile in the lower panels of Figure 3A]. The maximal levels of acceptor fluorescence intensity (anti-VSVG ezrin-Cy3) were similar in both untreated and PDBu-stimulated cells, and there was no significant correlation between <τ> and the intensity of acceptor fluorescence at each pixel of the cell (data not shown). The increase in association by PKC activation observed in Figure 3A is therefore not an artefact due to protein overexpression. Phorbol esters bind to the C1 domains of conventional and novel PKCs, and thereafter induce a conformational change that results in a disruption of the intramolecular interaction between the pseudosubstrate site in the regulatory domain (RD) and the kinase domain. Figure 3B shows that the expression of the PKCα RD + V3 (hinge region) alone, without the catalytic domain, renders the PKC–ezrin association constitutive. This implies that the PDBu effect is mediated at least in part through a conformational change in the PKC regulatory domain, and that the association is not merely a kinase domain–substrate binding.

The ezrin-bound and uncomplexed subpopulations of GFP–PKCα are associated with distinct fluorescence lifetimes (τ_1 and τ_2, respectively). Quantitative maps of the populations of each form were derived using a global FLIM analysis as previously described (Verveer *et al.*, 2000a,b), and two pseudocolour cell plots are presented in Figure 3B as 'percentage population of PKC complexed to ezrin'. A cumulative analysis of all the cell data showed that the average populations of the ezrin-complexed form of PKCα RD + V3 were 0.48 ± 0.08 (mean ± SD, $n = 7$; $\tau_1 = 0.56$ ns and $\tau_2 = 2.12$ ns) and 0.51 ± 0.12 ($n = 7$; $\tau_1 = 0.46$ ns and $\tau_2 = 2.06$ ns), before and after 20 min of PDBu treatment, respectively. This is in perfect agreement with the equivalent cumulative pixel counts versus Eff (%) profiles in the lowest panel, which show that PKC–ezrin association was rendered constitutive by expressing the RD + V3 alone. There is no linear relationship between the two quantities (i.e. populations versus Eff); hence, the contrast in the Eff cell plots in Figure 3B appears to be slightly different from the population images. Importantly though, the biological conclusions drawn from the cumulative/statistical analysis of these two parameters are identical.

Figure 3C shows that the non-phosphorylatable T567A mutant of VSVG–ezrin, which associates poorly with the actin cytoskeleton (Gautreau *et al.*, 2000; Tran Quang *et al.*, 2000), still interacts with PKCα. Cell morphology and the degree of PKC/ezrin co-localization were similar between wild-type and T567A ezrin-co-transfected cells, in agreement with previous observations made in LLC-PK1 cells (Gautreau *et al.*, 2000). Thus, phosphorylation at the C-terminal threonine residue is not a prerequisite for complex formation.

Co-sedimentation of GFP–PKCα and ezrin

Previously we found by cryoelectron microscopy that the 12G10-reactive β1 integrin localized to the filopodia and multivesicular bodies in breast carcinoma cells (Ng *et al.*, 1999a). In pulse–chase experiments coupled with immunofluorescence staining, the vesicular structures containing activated β1 integrins were shown to recycle and co-localize with transferrin receptors. By sucrose gradient fractionation, GFP–PKCα and β1 integrin were found to co-sediment through both velocity (VG) and equilibrium (EG) sucrose gradients prior to and following PDBu stimulation (Figure 5A and B and data not shown). Consistent with the FLIM results, in unstimulated MCF-7 cells there was no significant co-sedimentation between GFP–PKCα and endogenous ezrin (Figure 4A). In PDBu-stimulated cells, however, ezrin became highly enriched in PKCα- and β1 integrin-containing EG fractions (Figure 4B). Among the post-PDBu EG fractions, endogenous transferrin receptors were only detected in fractions 1–4, which were enriched in GFP–PKCα, β1 integrin and endogenous ezrin (data not shown), indicating that these fractions contained recycling endosomes.

T567 hyperphosphorylation of the PKCα-associated ezrin subpopulation

To corroborate the FLIM and sucrose gradient co-sedimentation data, we determined whether a PKCα–ezrin complex could be demonstrated by co-immunoprecipitation. Immunoprecipitation of endogenous PKCα from PDBu-stimulated MDA-MB-231 (which, unlike MCF-7, contains a sufficient amount of endogenous PKCα detectable by immunoblotting) with the antibody MC5 and western analysis with an anti-ezrin rabbit serum reveals that endogenous ezrin can be co-immunoprecipitated with PKCα (Figure 5A). The pool of ezrin in the PKCα-bound fraction was composed predominantly of a slower electrophoretic mobility form (labelled ezrin*) when compared with the unbound ezrin. The type of large resolving acrylamide gels used in these precipitation assays was shown previously to distinguish the mature phosphorylated form of PKCα (80 kDa) from its dephosphorylated variant (with an apparent mol. wt of 76 kDa) (Cazaubon *et al.*, 1994). Figure 5B shows a similar co-precipitation of

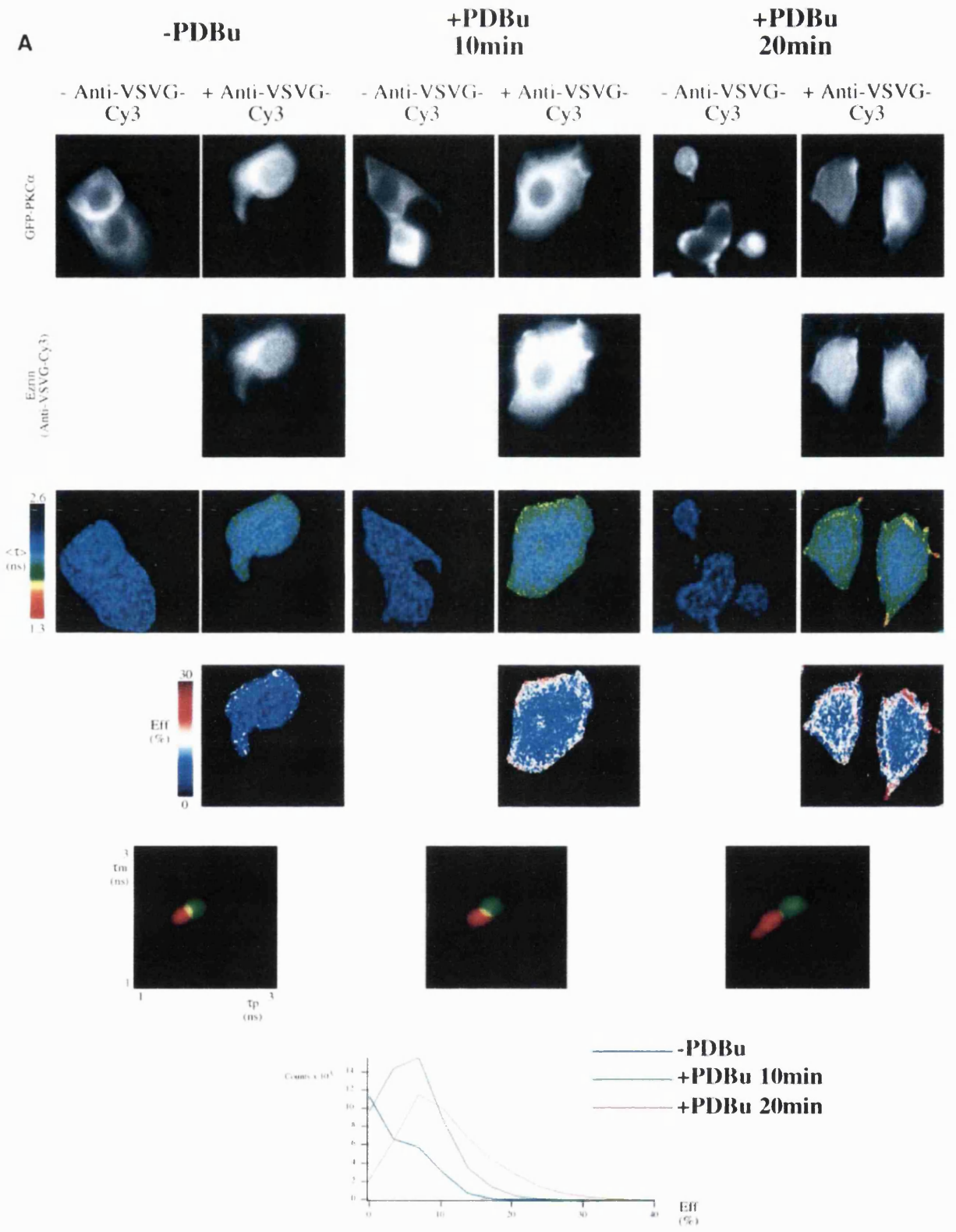

Fig. 3. (Continued over page)

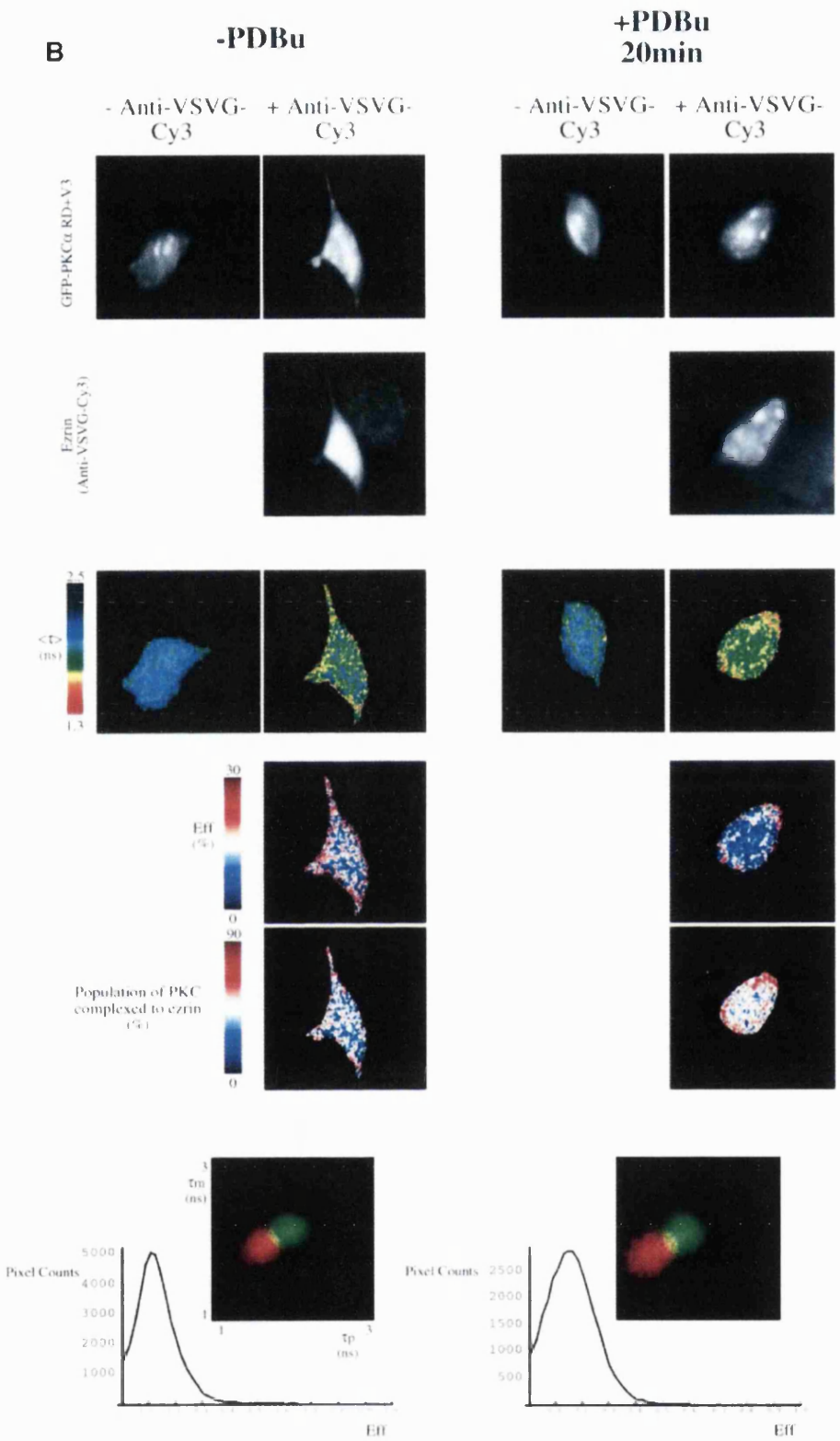

Fig. 3. PKC–ezrin association in MCF-7 cells detected by FLIM. (**A**) MCF-7 cells were dually transfected with both a GFP–PKCα- and a VSVG-tagged ezrin construct. After 36 h, cells were stimulated with PDBu (1 μM) for the times indicated, then fixed in ice-cold methanol for 4 min (–20°C). Cells were stained with a Cy3-labelled anti-VSVG mAb. FRET results in a shortening of the GFP (donor) fluorescence lifetime that is measured by two independent parameters, the phase shift (τ_p) and relative modulation depth (τ_m). The fluorescence images from the donor (GFP–PKCα) and acceptor (anti-VSVG-Cy3), the donor fluorescence lifetime <τ> (the average of τ_p and τ_m) and its corresponding pseudocolour scales are shown.

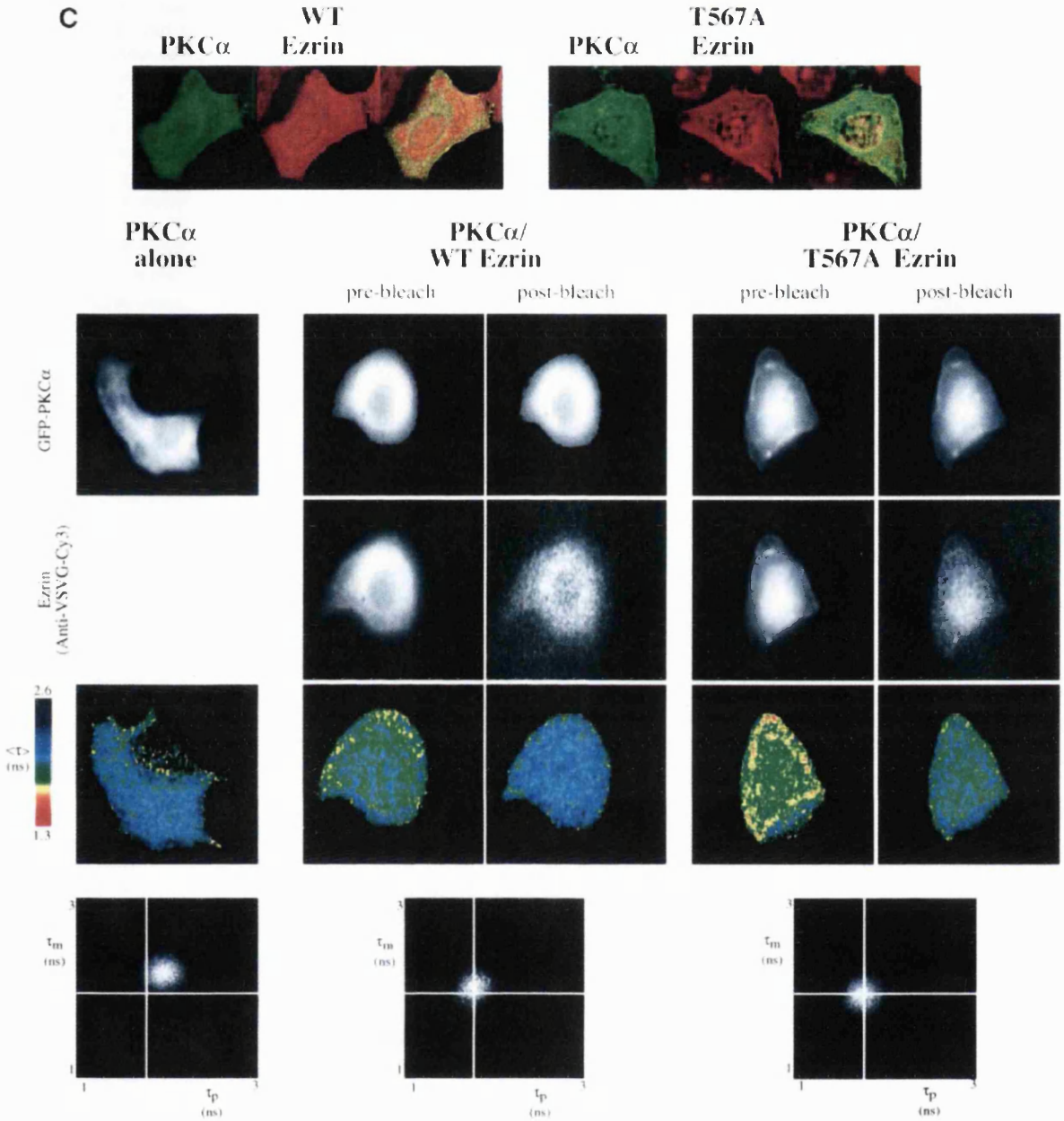

Eff is the pixel-by-pixel FRET efficiency represented on a pseudocolour scale [Eff = 1 – τ_{da}/τ_d, where τ_{da} is the lifetime map of the donor in the presence of acceptor and τ_d is the average lifetime <τ> of the donor in the absence of acceptor (numerically taken as the average of mean <τ> of five GFP–PKC alone control cells at each time point)]. The cumulative lifetimes of GFP–PKCα alone (green) and that measured in the presence of the acceptor fluorophore (red) are plotted on the two-dimensional histograms in the lower panels (n = 5 for each time point). The pixel counts versus Eff (%) profile in the bottom panel summarizes all the FRET efficiency data at each time point. (**B**) Repeat experiment in which MCF-7 cells were co-transfected with GFP–PKCα RD + V3 and wild-type VSVG–ezrin and stimulated with PDBu for 20 min before fixation. n = 7 for PDBu treatment and no treatment control. For cumulative analysis, in addition to the pixel counts versus Eff (%) profiles in the lowest panel, quantitative maps of the populations of both the ezrin-bound and unbound forms of GFP–PKCα RD + V3 were derived using a global FLIM analysis, and two representative pseudocolour cell plots are presented as 'percentage population of PKC complexed to ezrin'. (**C**) Repeat experiment in which MCF-7 cells were co-transfected with GFP–PKCα and either wild-type (WT) or T567A ezrin and stimulated with PDBu for 20 min before fixation. The confocal images in the upper panels are two-dimensional projections of 2–3 slices in the Z-series, taken across the mid-depth of the cell at 0.2 μm intervals, illustrating the similarity in terms of cell morphology and the degree of PKC/ezrin co-localization between WT and T567A ezrin-co-transfected cells. n = 4 for transfection with GFP–PKCα alone as well as for each PKC/ezrin co-transfection. Co-transfection with either WT or T567A ezrin and subsequent staining with the Cy3-labelled anti-VSVG antibody resulted in lifetime shortening (compared with GFP–PKCα alone controls), which was partially reversed after 4 min bleaching of the Cy3 acceptor as shown by the <τ> pseudocolor maps of the cells. The fluorescence images from the donor (GFP–PKCα) and acceptor (anti-VSVG-Cy3), before and after partial bleaching, are shown. Pre-bleach, before Cy3 acceptor photobleaching; post-bleach, after 4 min of photobleaching. The two-dimensional histograms represent the cumulative lifetimes.

GFP–PKCα with endogenous ezrin from PDBu-stimulated GFP–PKCα-2C4 cells, in two independent experiments (cultures 1 and 2); again the slow mobility form ezrin* was detected predominantly in the PKCα-bound fraction. The ratio of ezrin*:ezrin in the 'bound' fraction on the total ezrin blot in Figure 5B was 0.7 and 1.4 for cultures 1 and 2, respectively. An increase in the amount of the C-terminal threonine-phosphorylated form of ERM proteins (detected by an affinity-purified polyclonal rabbit anti-CPERM IgG) was found in the PKCα-bound pool, when compared with the unbound fraction. From densitometric analysis, the mean ratio of CPERM in PKC-bound versus unbound fraction ± SEM = 2.3 ± 0.3 (n = 7 independent cultures) and, when corrected for the total amount of ezrin present in each lysate, the mean ratio of CPERM in bound versus unbound ± SEM = 10.7 ± 3.1. The PKCα-associated ERM pool is therefore hyperphosphorylated at the C-terminal threonine residue. The phosphospecificity of this affinity-purified polyclonal IgG is demonstrated in Figure 5D.

The relative proportion of total ezrin/radixin/moesin bound to GFP–PKCα in unstimulated GFP–PKCα-2C4 cells was investigated by co-precipitation and is presented in Figure 5C. A comparison with Figure 5B and other similar experiments (n = 7 independent cultures) shows that in unstimulated cells, there is no C-terminal hyperphosphorylation of ERM in the PKC-associated fraction. The ezrin* band is not apparent under these conditions. A negligible amount of radixin was bound to PKCα. The stoichiometry of pull-down for moesin (PKCα-bound: unbound ~0.2) was less than that for ezrin (PKCα-bound:unbound ~0.7). Ezrin is therefore the predominant ERM protein that is associated with PKCα under these conditions.

Enrichment of GFP–PKCα and ezrin at plasma membrane protrusions

The precise localization of GFP–PKCα and ezrin was examined by immunoelectron microscopy (EM). Our initial efforts to localize PKCα by GFP immunogold labelling were unsuccessful using transiently transfected MCF-7 cells; the amount of endogenous ERM proteins in these cells was also below the detection limit using an affinity-purified rabbit anti-ezrin IgG (S.Gschmeissner and T.Ng, unpublished observations). A fibrosarcoma cell line stably expressing GFP–PKCα (GFP–PKCα-2C4) and transiently transfected with a VSVG-tagged ezrin was therefore chosen for EM studies. Electron micrographs in Figure 6A and B show the distribution of both VSVG-tagged ezrin [detected by an affinity-purified rabbit anti-ezrin IgG + 10 nm protein A–gold (PAG)] and GFP–PKCα (detected by a rabbit anti-GFP antiserum + 5 nm PAG) in the cytoplasm and plasma membrane of PDBu-stimulated GFP–PKCα-2C4 cells. Both proteins were found to be particularly enriched at plasma membrane protrusions. In contrast, there was no detectable labelling of other membranous structures including the mitochondria, Golgi and the nucleus. Control experiments where the second antibody (anti-GFP or anti-ezrin IgG) was omitted revealed no cross-reactivity of the 5 nm PAG with the first antibody (anti-ezrin or anti-GFP IgG, respectively) (data not presented). Figure 6C and D shows the immunolocalization of wild-type and T567A, VSVG-tagged ezrin in

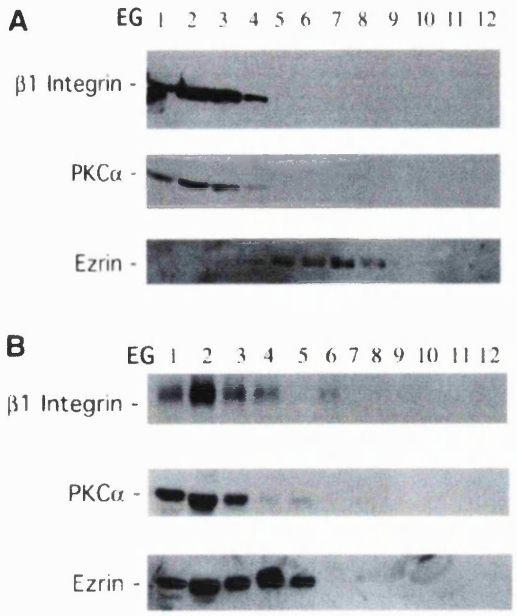

Fig. 4. Co-sedimentation of GFP–PKCα, β1 integrin and ezrin in sucrose gradient fractions derived from PDBu-activated MCF-7 cells. (**A**) PKCα and β1 integrin (recognized by mAbs MC5 and 8E3, respectively) were found in a light vesicle pool (fractions 2–3) from unstimulated, GFP–PKCα-transfected MCF-7 cell post-nuclear supernatant fractionated by velocity sucrose gradient (VG) centrifugation as described in Materials and methods (data not shown). Equilibrium gradient (EG) fractions were derived from this light vesicle pool (VG fractions 2–3) of unstimulated MCF-7 cell post-nuclear supernatant. EG fractions 1–4 were enriched in both GFP–PKCα and β1 integrin. There was a partial overlap with the EG fractions (4–8) containing endogenous ezrin. (**B**) The same as (A), with the exception that GFP–PKCα-transfected MCF-7 cells were stimulated with 1 μM PDBu for 10 min prior to fractionation. PKCα and β1 integrin were found to co-sediment in a light vesicle pool (fractions 2–3) from PDBu-stimulated, GFP–PKCα-transfected MCF-7 cell post-nuclear supernatant fractionated by VG centrifugation (data not shown). EG fractions were derived from these VGs. EG fractions 1–4 were enriched in GFP–PKCα and β1 integrin, as well as endogenous ezrin. Among the post-PDBu EG fractions, endogenous transferrin receptors were only detected in fractions 1–4 (data not shown).

GFP–PKCα-2C4 cells, respectively (stained with an anti-VSVG mAb P5D4 + 10 nm PAG). The distribution is remarkably similar. Also the distinction between the membrane- and cytoskeleton-associated subpopulations of wild-type versus T567 ezrin would be difficult, even at the EM level of resolution.

PKCα phosphorylates ezrin in vitro

The activation-enhanced association/proximity between PKCα and ezrin (Figure 3) as well as the significant diminution of ERM C-terminal threonine phosphorylation by PKC inhibition (Figure 2) suggest that ERM proteins may be *in vivo* substrates of PKCα. The only PKC isoform that has been documented to phosphorylate the ERM proteins *in vitro* to date is PKCθ (Pietromonaco *et al.*, 1998). Figure 7A shows that recombinant human PKCα can also phosphorylate full-length glutathione *S*-transferase (GST)-tagged ezrin *in vitro* in a Ca^{2+}/TPA/phospholipid-dependent manner. After 30 min of *in vitro* phosphorylation at 37°C, the stoichiometry was 1.5 mol ATP incorporated per mol ezrin. The ratio of ^{32}P

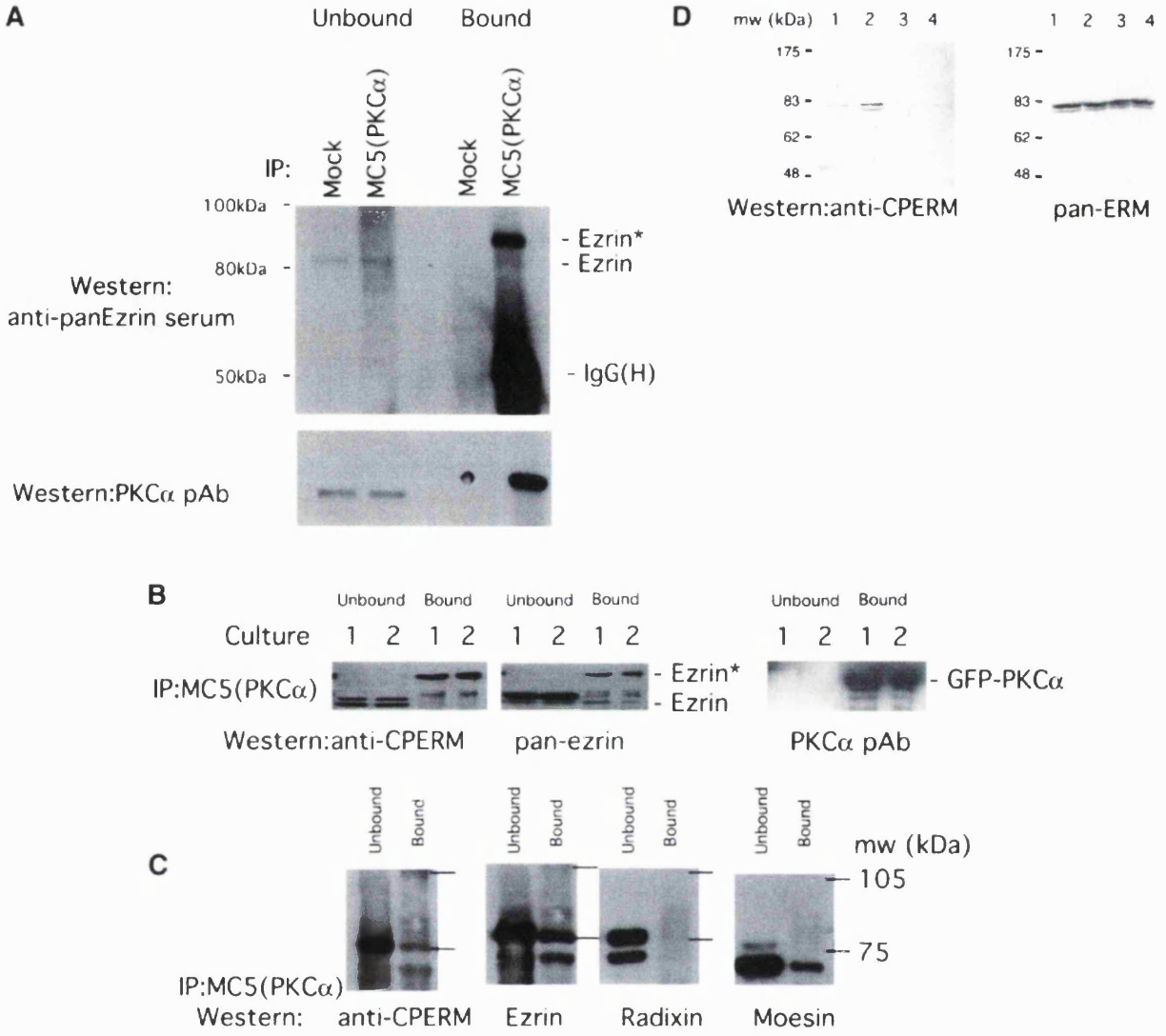

Fig. 5. Association of endogenous ERM proteins with PKCα *in vivo* correlated with an increase in C-terminal threonine phosphorylation. (**A**) MDA-MB-231 cells stimulated with PDBu. Co-precipitation of endogenous PKCα (immunoprecipitated with an anti-PKCα mAb MC5) with endogenous ezrin detected by an anti-ezrin rabbit serum. All the bound proteins on the protein G beads (bound) and 1/30 of the unbound proteins left in the cell extract supernatant after the first centrifugation post-precipitation (unbound) were loaded. Ezrin* is a subset of ezrin that exhibits a slower electrophoretic mobility and is only detected in the PKCα-bound ezrin pool. The blot was stripped and reprobed with an anti-PKCα pAb. Mock, control immunoprecipitation in which the precipitating antibody was omitted; IgG(H), immunoglobulin heavy chain. Approximate positions of the molecular weight markers are shown. (**B**) GFP–PKCα-2C4 cells stimulated with PDBu. Co-precipitation of GFP–PKCα with endogenous ezrin. All the bound proteins on the protein G beads (bound) and 1/100 of the unbound proteins left in the cell extract supernatant after the first centrifugation post-precipitation (unbound) were loaded. The blot containing MC5 immunoprecipitates, derived from two independent experiments (cultures 1 and 2), was detected first with a polyclonal rabbit anti-CPERM IgG, stripped and reprobed with an anti-ezrin rabbit serum, then stripped and reprobed again with an anti-PKCα pAb. (**C**) Relative proportion of total ERM bound to GFP–PKCα in unstimulated GFP–PKCα-2C4 cells. MC5 immunoprecipitates from three untreated cultures were pooled and one-third of the pooled bound proteins on the protein G beads (bound) were loaded. Similarly, 1/300 of the pooled unbound proteins left in the cell extract supernatant after the first centrifugation post-precipitation (unbound) were loaded. The blot was cut into three strips and stained with (i) an affinity-purified polyclonal rabbit anti-CPERM IgG and crude sera raised against radixin (ii) and moesin (iii), respectively. The anti-CPERM blot (i) was then stripped and reprobed with an affinity-purified anti-ezrin IgG that has been cross-adsorbed for moesin and radixin. (**D**) In total LLC-PK1 cell lysates, immunoreactivity of ERM proteins with the affinity-purified polyclonal rabbit anti-CPERM IgG was abolished by pre-treatment of cells with staurosporine (a broad spectrum protein kinase inhibitor) before cell lysis, and enhanced by calyculin A, a protein serine/threonine phosphatase 1 (PP1)/PP2A inhibitor. ERM, immunoblot developed with a mixture of antibodies specific for ERM (Gautreau *et al.*, 2000). Lane 1, untreated; lane 2, treated with calyculin A (100 nM, 10 min); lanes 3 and 4, treated with 1 and 5 μM staurosporine, respectively, for 10 min. Approximate positions of the molecular weight markers are shown.

incorporation in ezrin ± PKC activators was ~3:1. Full-length ezrin was a better PKC substrate than the GST–C-terminal ezrin (amino acids 280–585) (<0.3 mol ATP incorporated per mol ezrin; data not shown), implying that components in the N-terminal part of ezrin might be required for kinase–substrate contact.

We next investigated the ability of immunoprecipitated PKCα to phosphorylate its associated endogenous ezrin at

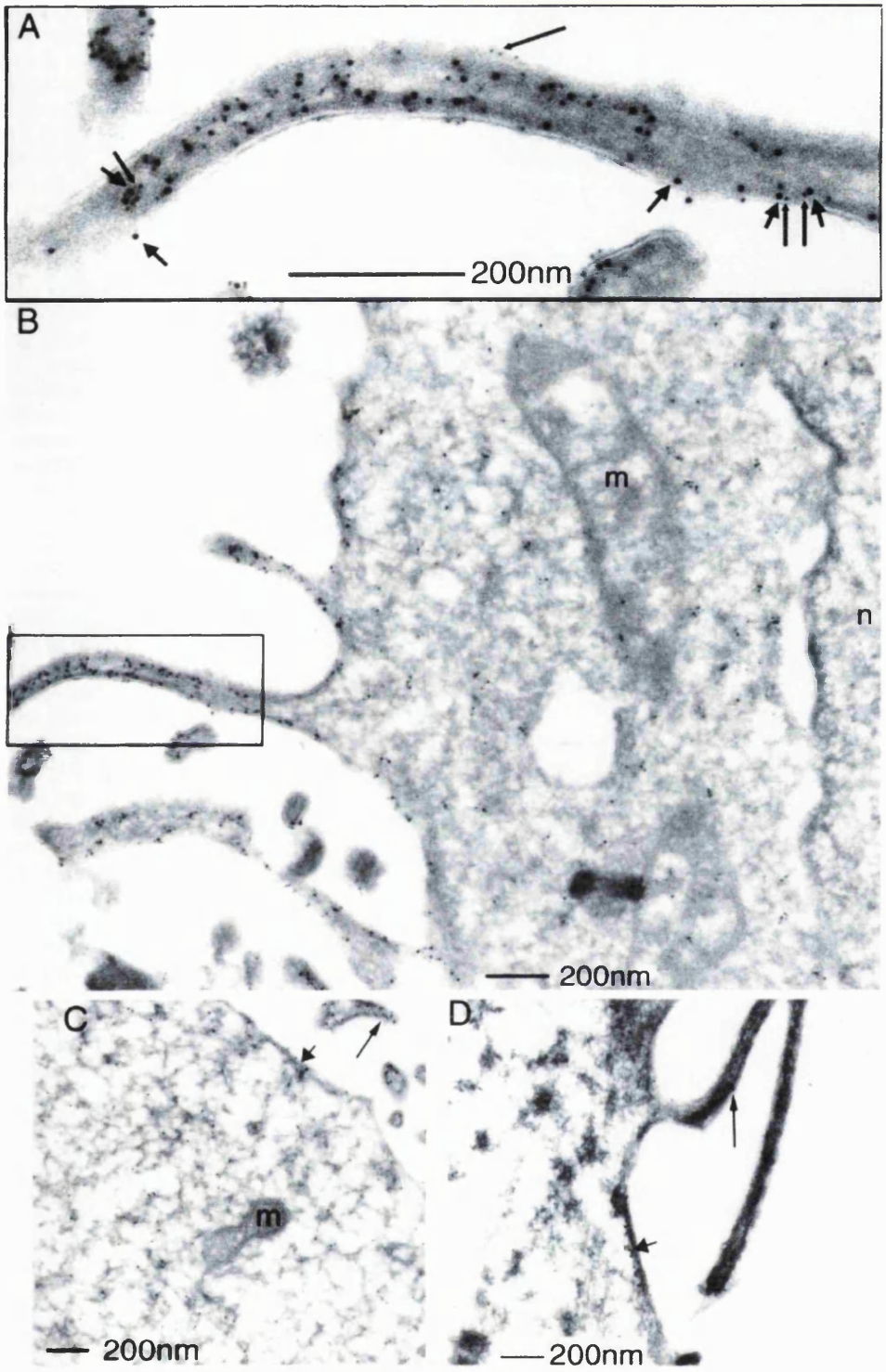

Fig. 6. Enrichment of GFP–PKCα and ezrin at plasma membrane protrusions. (A and B) The main immunoelectron micrograph (**B**) shows the localization of both VSVG-tagged ezrin (detected by an affinity-purified rabbit anti-ezrin IgG + 10 nm protein A–gold; short arrows) and GFP–PKCα (detected by a rabbit anti-GFP antiserum + 5 nm protein A–gold; long arrows). The inset (**A**) represents an enlarged view of a plasma membrane protrusion showing isolated and clusters of the 5 and 10 nm protein A–gold labels. m = mitochondrium, n = nucleus. (**C** and **D**) The immunolocalization of wild-type and T567A, VSVG-tagged ezrin in GFP–PKCα-2C4 cells, respectively (stained with an anti-VSVG mAb P5D4 + 10 nm protein A–gold). The long and short arrows show the localization of ezrin in the plasma membrane protrusion and a peripheral (cortical) area of the cell, respectively.

the C-terminal threonine residue *ex vivo* (procedure described in the legend of Figure 7B). In view of the findings in Figure 2, pre-treatment with LY294002 (10 μM for 6 h) was used to reduce the basal ERM C-terminal threonine phosphorylation in GFP–PKCα-2C4 cells, or more specifically in the PKCα-bound ERM proteins (–Mg/ATP, anti-CPERM 'bound' lane in Figure 7B). Notably, the PKC-associated ezrin* band was barely detectable in the total ezrin blot from cells pre-treated with LY294002 when compared with the untreated cultures shown in Figure 5B. After the *ex vivo* phosphorylation reaction (+Mg/ATP, anti-CPERM 'bound' lane in Figure 7B), there was an ~3-fold increase in the amount of CPERM on beads, indicating that PKCα, or a PKCα-associated serine/threonine kinase, is capable of phosphorylating the ERM C-terminal threonine residue within a kinase–ezrin molecular complex.

In order to address further the identity of the CPERM that is bound to PKCα, the PKCα immunoprecipitation experiment was repeated with GFP–PKCα-2C4 cells that had been pre-treated with LY294002 (10 μM for 6 h) to reduce the basal ERM C-terminal threonine phosphorylation before lysis. Under conditions where ERM C-terminal threonine phosphorylation is reduced, the CPERM in the PKC-bound fraction had the same apparent molecular weight as that in the unbound fraction. Using a large resolving acrylamide gel, the major band in the anti-CPERM blot (indicated by a filled arrowhead in Figure 7C) co-migrated with the major band in the anti-ezrin blot (developed with an affinity-purified anti-ezrin IgG that has been cross-adsorbed for moesin and radixin; Algrain *et al.*, 1993). Very little radixin that corresponds to the major radixin band in the unbound fraction was found in the PKCα immunoprecipitate. The major moesin band had a similar apparent molecualr weight but the stoichiometry (PKCα-bound:unbound ~0.1) of pull-down was less than that for ezrin (PKCα-bound:unbound ~0.2). Ezrin is therefore also the predominant ERM protein that remains associated with PKCα under conditions where ERM C-terminal threonine phosphorylation is reduced.

Ezrin T567A mutant inhibits PKCα-driven migration in wound closure

To investigate the role of ERM proteins in PKCα-dependent migration, GFP–PKCα-2C4 cells transiently co-expressing ezrin (wild-type/T567A variant) were tracked during overnight wound migration assays. The T567A mutant of VSVG–ezrin associates poorly with the actin cytoskeleton (Gautreau *et al.*, 2000; Tran Quang *et al.*, 2000) but retains the capacity to interact with PKCα *in vivo* (Figure 3C). Figure 8 demonstrates that the injection of a wild-type ezrin plasmid into GFP–PKCα-2C4 cells did not affect the PKCα-stimulated wound closure response. However, introduction of the T567A phosphorylation site mutant had a dominant inhibitory effect on PKCα-induced cell migration (P = 0.02 by ANOVA for the difference between wild-type- and T567A ezrin-injected cells, showing a significant loss of persistence of the wound closure response due to T567A ezrin expression). There was no significant cell toxicity associated with T567A ezrin expression, as assessed by the propidium iodide exclusion assay (data not shown).

Discussion

The results here demonstrate that on activation, PKCα co-localizes and interacts with ezrin at the plasma membrane and cell cortex beneath the membrane, particularly at the membranous protrusions of the cell. Associated with this interaction, ERM proteins become phosphorylated on the C-terminal threonine residue, and agents that block this phosphorylation also abrogate PKCα-dependent migration. In addition, PKC-associated endogenous ERM proteins are shown to be hyperphosphorylated preferentially at the C-terminal threonine residue, i.e. activated. Among the endogenous ERM proteins, ezrin is the predominant ERM protein that is associated with PKCα. Recombinant human PKCα is capable of phosphorylating full-length GST-tagged ezrin *in vitro* in a Ca^{2+}/TPA/phospholipid-dependent manner. Full-length ezrin is a better PKC substrate than the GST–C-terminal ezrin, implying that components in the N-terminal part of ezrin might be required for stabilizing kinase–substrate contact. The expression of the regulatory domain of PKCα alone is sufficient to support this interaction. We have also provided the first evidence that PKCα, or a PKCα-associated serine/threonine kinase, is capable of phosphorylating the ERM C-terminal threonine residue within a kinase–ezrin molecular complex in cells.

The pool of ERM proteins bound to PKCα contains a higher proportion of the C-terminal threonine-phosphorylated form than the 'unbound' pool. The increase in C-terminal threonine phosphorylation in the bound fraction correlates with the finding of a subset of ezrin that is associated with a slower electrophoretic mobility (ezrin*). The increase in the apparent molecular weight of ezrin* is likely to be related to its phosphorylation by PKC (or a PKCα-associated serine/threonine kinase) within an intermolecular complex, as well as any additional biochemical modification that occurs as a consequence of the phosphorylation. This is because in unstimulated cells where there is no C-terminal hyperphosphorylation of ERM in the PKC-associated fraction (Figure 5C), or under conditions where ERM C-terminal threonine phosphorylation is reduced (Figure 7C), the CPERM in the PKC-bound fraction has the same apparent molecular weight as that in the unbound fraction. The ezrin* band is also not apparent under these conditions.

Recent work (Gautreau *et al.*, 2000) clearly demonstrates that the C-terminal threonine-phosphorylated form is enriched in the membrane and exists as a monomer. One possible consequence of the C-terminal threonine phosphorylation within the PKC–ezrin molecular complex is therefore to promote a transition of ERM from the oligomeric to monomeric state (active form). The activated form of ERM then acts as a downstream effector of PKCα involved in the control of polarized cell movement. The observed dominant inhibitory effect of expressing the T567A mutant of ezrin on PKC-enhanced wound closure can be explained in a number of ways. First, the T567A variant has an almost identical cytosol/membrane distribution as the wild-type protein but associates poorly with the cytoskeleton (Gautreau *et al.*, 2000). This is not surprising since the T567A variant can oligomerize with endogenous ERM proteins and localize to the same compartments in cells. The localization of the T567A

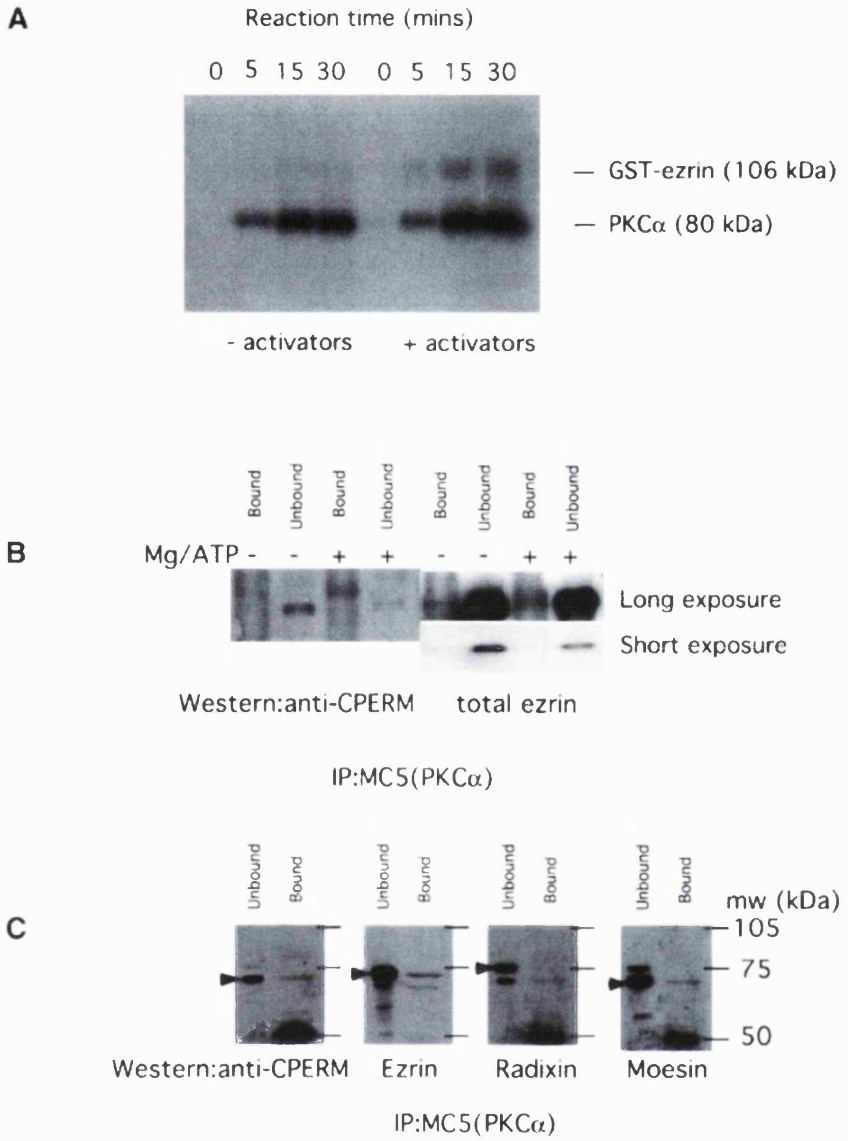

Fig. 7. *In vitro* phosphorylation of ezrin by PKCα. (**A**) *In vitro* phosphorylation of a GST–wild-type ezrin (106 kDa) with human recombinant PKCα was carried out as described in Materials and methods. The time courses of the autophosphorylation of PKCα and TPA/lipids/Ca^{2+} (activators)-induced, PKC-mediated ezrin phosphorylation (representative of >3 experiments) are shown. (**B**) GFP–PKCα was immunoprecipitated with an anti-PKCα mAb MC5 from whole-cell lysates of 80% confluent GFP–PKCα-2C4 cell monolayer cultures that were pre-treated for 6 h with LY294002 (10 μM). One-hundredth of the unbound proteins left in the cell extract supernatant after the first centrifugation post-precipitation were loaded in the lanes marked 'unbound'. The protein G beads were washed at 4°C, post-precipitation, twice with the modified RIPA buffer, then twice with 70 μl of a 0.05 M HEPES/0.5 mM EGTA buffer containing a cocktail of protease inhibitors, calyculin A (10 nM) and sodium orthovanadate (1 mM). In the +Mg/ATP lane, this was exchanged for an equivalent buffer containing in addition 12.5 mM $MgCl_2$ and 0.1 mM ATP. The beads were then incubated at 30°C for 30 min in a shaking heating block. The phosphorylation reaction was stopped by centrifugation in a cooling microcentrifuge (4°C) and by adding 70 μl of modified Laemmli's sample buffer (containing final concentrations of 2% SDS, 4 M urea and 10 mM EDTA) to the beads post-centrifugation. All the bound proteins on the protein G beads were loaded in the lanes marked 'bound'. Western blotting with the polyclonal rabbit anti-CPERM IgG showed an ~300% increase in the amount of CPERM in the PKC-co-precipitated material on beads after the *ex vivo* phosphorylation reaction. The amount of ezrin on beads (total ezrin) in the – Mg/ATP or +Mg/ATP lane was similar. The ratio of the 'bound:unbound total ezrin' was, however, notably lower in the LY294002-treated cultures (<0.2 in both the – Mg/ATP and +Mg/ATP lanes) compared with untreated cultures (mean ± SEM = 0.6 ± 0.08; Figure 5 and data not shown). A shorter exposure of the pan-ezrin blot shows that the amount of total ezrin in the 'unbound' fraction of the +Mg/ATP lane was slightly lower than that of the –Mg/ATP lane but these were derived from different cultures. (**C**) Repeat of the PKCα immunoprecipitation experiment with GFP–PKCα-2C4 cells that had been pre-treated with LY294002 (10 μM for 6 h) to reduce the basal ERM C-terminal threonine phosphorylation before lysis. One-hundredth of the unbound proteins left in the cell extract supernatant after the first centrifugation post-precipitation were loaded in the lanes marked 'unbound'. The protein G beads were washed at 4°C, post-precipitation, twice with the modified RIPA buffer, then once with a 10 mM Tris pH 7.4 buffer containing a cocktail of protease and phosphatase inhibitors before elution with 70 μl of Laemmli's sample buffer. All the bound proteins on the protein G beads were loaded in the lanes marked 'bound'. The blot was probed with an anti-CPERM IgG, then stripped and reprobed with an affinity-purified anti-ezrin IgG that had been cross-adsorbed for moesin and radixin, followed by anti-radixin and anti-moesin detection, respectively, with the appropriate rabbit sera. The major band of reactivity in each blot is indicated by a filled arrowhead. The approximate positions of molecular weight markers are shown and, after sufficient exposure times, a 50 kDa band appeared and corresponds to the immunoglobulin heavy chain.

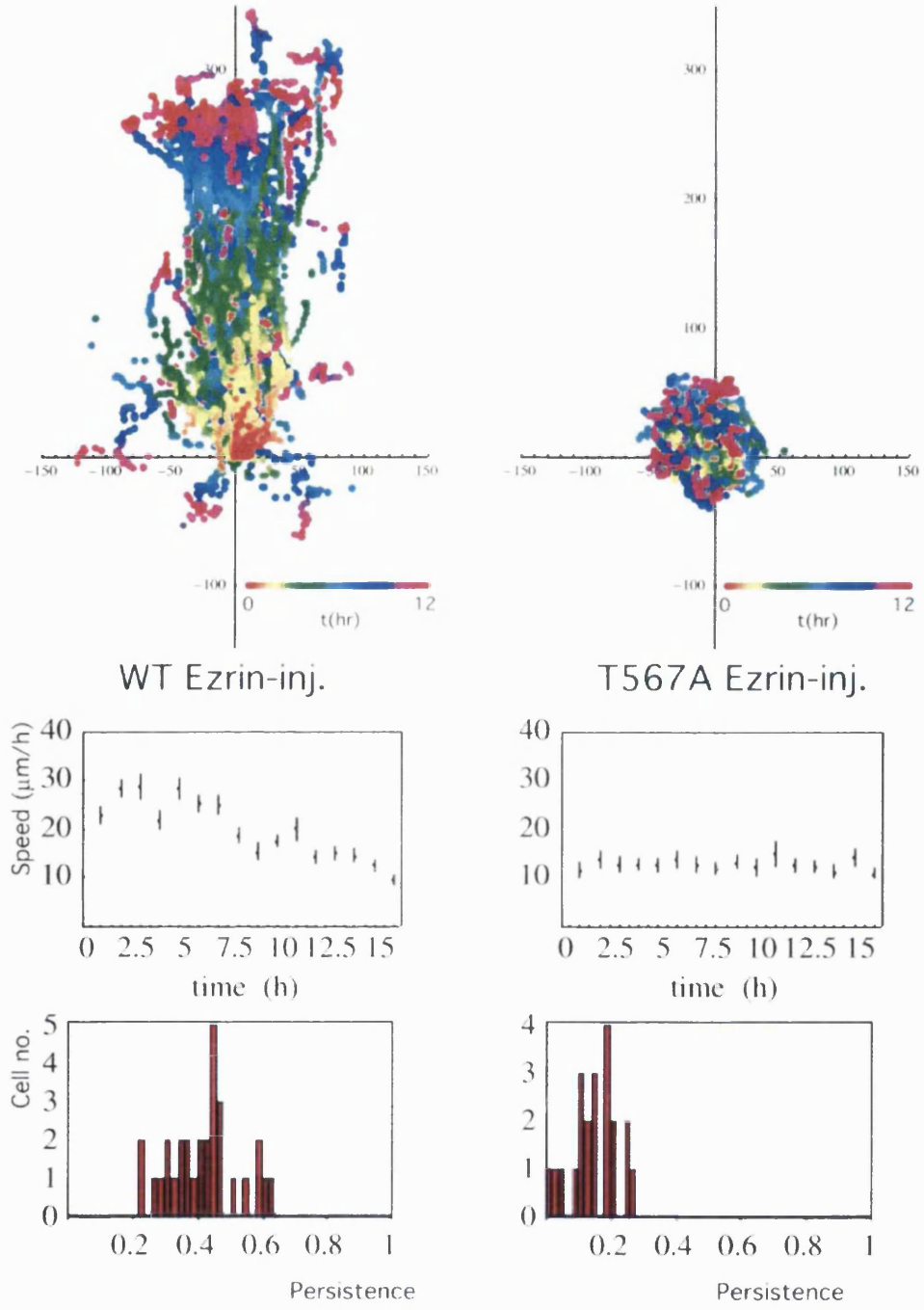

Fig. 8. Dominant inhibitory effect of the T567A ezrin variant on the PKCα-induced wound migratory response. A wild-type or T567A VSVG-tagged ezrin plasmid (100 μg/ml) was microinjected into the nuclei of confluent GFP–PKCα-2C4 cells along with a Cy3-conjugated anti-transferrin receptor antibody as a marker to identify the injected cells subsequently. The monolayer was wounded and the migration response was recorded by time-lapse microscopy. Upper panels: all the cell trajectories during the entire time course of each experiment. Each dot represents a cell position at a particular time point that is indicated by the pseudocolour scale (t in h) beneath each set of cell tracks. The scale of the cell track axes is in μm. Left, wild-type ezrin-injected cell (WT Ezrin-inj.); right, a representative T567A ezrin-injected cell (T567A Ezrin-inj.). Middle panel: the changes in mean speed with time. Lower panel: the distribution of persistence within the cell populations in each treatment group. Speed and persistence were derived from the analysis of tracked cells from three independent experiments (total number of cells tracked = 30 for WT Ezrin-inj. and 21 for T567A Ezrin-inj.). The mean persistences = 0.42 ± 0.1 (SD) and 0.15 ± 0.07 (SD) for the WT Ezrin-inj. and T567A Ezrin-inj. cultures, respectively. The P-value for the difference between the two treatment groups was derived using ANOVA.

variant is indistinguishable from that of the wild-type protein, even at the EM level (Figure 6). Through oligomerization with endogenous ERM proteins, this mutant may exert a dominant inhibitory effect by sequestering the active (C-terminally phosphorylated) form of ERM. Alternatively, since T567A ezrin will still interact with PKCα in intact cells, it may sequester the kinase away from foci of actin polymerization.

In MDCK cells, PKCα (not PKCδ or ζ) is the only PKC isotype that changes its cellular localization concomitantly with the development of Ca^{2+}-dependent desmosomes in response to wounding (Wallis *et al.*, 2000). Treatment with an antisense oligonucleotide to PKCα abolishes the reversal of desmosomes to Ca^{2+} dependence at the wound edge, illustrating the important role that this specific PKC isozyme plays in the wounding response. The molecular mechanisms underlying the wound closure migratory response are, hitherto, poorly understood. After an overnight incubation, an intermediate zone of subconfluent cells is usually observed between the wound edge and the unperturbed part of the confluent monolayer culture. Cells in this subconfluent zone are motile and have less extensive intercellular contact than cells from the confluent region. PKC-induced wound closure (such as that shown in Figure 1A) is characterized by an increase in 'persistence' in the direction of cell movement, particularly in this intermediate zone where there is less contact inhibition of cell migration. Based on our previous work using the Transwell chamber migration sytem where the filter was coated with either bovine serum albumin (BSA; random motility) or specific integrin substrates (Ng *et al.*, 1999a), the expression of PKCα in MCF-7 cells was observed significantly to enhance random motility as well as haptotaxis towards β1 integrin substrates on filters. Here we conclude that stable expression of a GFP–PKCα full-length construct significantly enhances the 'persistence' of 2C4 fibrosarcoma cell migration in response to wounding. GFP–PKCα-2C4 cells tend to undergo a more accelerated cell movement (speed) during the initial 4 h post-wounding in comparison with the vector control. Speed is a measure of random motility (Surtees, 1964) and is mathematically an entirely independent entity from persistence/directionality. These conclusions do not just apply to confluent cells induced to move in response to wounding, since the expression of PKCα in subconfluent MCF-7 cells also significantly enhances the directional cell movement in a chemotaxis assay (M.Parsons *et al.*, in preparation).

ERM C-terminal phosphorylation at the wound edge is sensitive to PI3K inhibition with LY294002, but not the ROCK inhibitor Y-27632. The PKC-driven wound closure response is significantly impaired by these same inhibitors that abolish the ERM C-terminal threonine phosphorylation; this response is also insensitive to Y-27632. PI3K has long been implicated in the control of cell migration/haptotaxis (Wang *et al.*, 1996; Derman *et al.*, 1997; Shaw *et al.*, 1997; Meng and Lowell, 1998; Ng *et al.*, 1999a; Vanhaesebroeck *et al.*, 1999). At least in NIH 3T3 fibroblasts, the di-C_{16}-phosphatidylinositol-3,4,5-trisphosphate (PtdIns-P_3)-induced cell motility involves PKC and can be inhibited by calphostin C (Derman *et al.*, 1997). Also, in lymphocytes, PI3K blockade has an inhibitory effect on moesin redistribution to the uropod during migration (Vicente-Manzanares *et al.*, 1999). Here we demonstrate that in a GFP–PKCα stably transfected fibrosarcoma cell line (GFP–PKCα-2C4), ERM C-terminal threonine phosphorylation, which is sensitive to inhibition of the catalytic activity of PKC *in vivo*, is also subject to PI3K control. PI3K may, by enhancing phospholipase C-γ activity *in vivo* (Bae *et al.*, 1998), increase the availability of diacylglycerol (DAG), which in turn activates PKC and ERM phosphorylation. This would be consistent with the inhibitory effect that calphostin has (via competition for the DAG-binding site on PKC; Bruns *et al.*, 1991) on PtdIns-P_3-induced cell motility (Derman *et al.*, 1997). Furthermore, we show that activation of PKC with PDBu treatment can reverse the inhibition of the wound migratory response by LY294002, placing allosteric activation of conventional or novel PKC isozymes downstream of PI3K (Figure 1B). These data further define the functional relationship between PI3K and PKC as downstream effectors of the integrin signalling axes (Berrier *et al.*, 2000). Finally, the p85 regulatory subunit of PI3K has been shown to bind to the N-terminal part of ezrin; a point mutant of ezrin that does not interact with PI3K has an inhibitory effect on the activation of Akt, a downstream effector of the PI3K pathway (Gautreau *et al.*, 1999). This complex array of feedback mechanisms between PKC, PI3K and ezrin may constitute an important mechanism for signal amplification and cell migratory function.

The PKC isozymes constitute a major family of protein kinases that influence cell motility through a variety of mechanisms that are involved in the regulation of cytoskeletal turnover (Arber *et al.*, 1998) and possibly microtubule function (Steiner *et al.*, 1990). Some of the downstream components may, like ezrin, form stable complexes with PKC in response to appropriate physiological stimuli, while others, such as cofilin, may be regulated indirectly through other signalling proteins (Arber *et al.*, 1998). Further studies are needed to integrate our current knowledge of these individual signal components in a physiological context with the aim of intervening in these PKC-dependent processes in a pathological milieu such as tumour cell metastasis.

Materials and methods

Cell culture and plasmid constructs

Human breast carcinoma cells (MCF-7 cells) were cultured in Dulbecco's modified Eagle's medium (DMEM) containing 10% fetal calf serum at 37°C, in a 10% CO_2 atmosphere. In addition, the MCF-7 cultures were grown in media supplemented with insulin (10 μg/ml). MCF-10A cells were established originally from mammary tissue of a patient with fibrocystic breast disease and display characteristics of luminal epithelial cells. Transient transfection was performed using Fugene (Boehringer Mannheim). 2C4 fibrosarcoma cells (derivative of HT1080 cells) were transfected with either GFP–PKCα plasmid (Ng *et al.*, 1999a,b) or the control vector. At 48 h after transfection was initiated, cells were replated in complete medium at a 1:5 ratio. Selection for neomycin resistance was started the following day by the addition of the antibiotic G418 (Sigma) to 400 μg/ml. GFP-expressing cells were enriched by fluorescence activated cell sorting. After 10–14 days, G418-resistant cells were isolated as a mixed clone (see Figure 1A for the level of exogenous PKCα) and subsequently maintained in complete growth medium containing 40 μg/ml G418. Stable transfectants were cultured for up to 20 passages. The GFP–PKCα RD + V3 (Ng *et al.*, 1999a) was made by subcloning the corresponding PKCα sequence encoding amino acids 1–337 into the pEGFP-N1 vector (Clontech), permitting fusion of the coding sequence of eGFP. The VSVG-tagged ezrin (wild-type and T567A variant) constructs were published previously (Gautreau *et al.*, 2000).

Antibodies and direct conjugation to fluorophores, and Fab fragment generation

Anti-VSVG mAb was purchased from Boehringer Mannheim. MC5 is a murine mAb that recognizes the V3 region of PKCα (Young *et al.*, 1988). 8E3 is a pan-β1 integrin murine mAb (a kind gift of M.Humphries). The rat mAb (297S) that recognizes the C-terminal threonine-phosphorylated (T567 in ezrin, T564 in radixin and T558 in moesin; Nakamura *et al.*, 1999) form of ERM was a kind gift of S.Tsukita (Kyoto, Japan). A similar polyclonal rabbit anti-CPERM antibody was obtained by immunizing with a keyhole limpet haemocyanin (KLH)-coupled CRDKYKT*LRQIR peptide (the asterisk indicates the phosphorylated residue) and purifying the serum obtained through a GST–ezrin C(280–585) column to eliminate the non-phosphospecific antibodies. Phosphospecific antibodies were then affinity purified on a column coupled to the immunizing peptide. Goat polyclonal IgG against the C-terminus of ezrin was purchased from Santa Cruz and used in immunocytochemical staining. For western blotting, both a crude rabbit serum against ezrin and its affinity-purified IgG that has been cross-adsorbed for moesin and radixin (Algrain *et al.*, 1993) were used. Also, crude sera raised against radixin and moesin (kind gifts of Professor Paul Mangeat, Universite Montpellier II) were used for blotting. Fab fragments were generated and isolated from mouse IgG using the ImmunoPure Fab preparation kit (Pierce) according to the manufacturer's protocol. Direct conjugation of IgG/IgG Fab fragments to the fluorophores Cy3 and Cy5 (Amersham Life Science) was performed at pH 8.5 (IgG) or pH 9.0 (IgG Fab) as described previously (Bastiaens and Jovin, 1998).

Wound migration assays

Cells were plated at confluence onto 22 mm coverslips and allowed to adhere. In the inhibitor studies, compounds were added to the media and cells were pre-incubated for 1 h prior to wounding. A single wound was made using a plastic pipette tip through the confluent monolayer and media were changed. For the ezrin studies, a wild-type or T567A VSVG-tagged ezrin construct was microinjected into the nuclei of confluent cells using an Eppendorf system, along with a Cy3-labelled anti-transferrin IgG for the subsequent identification of injected cells. Monolayers were then wounded in such a way that most of the injected cells would remain at the wound edge. Cell migration at the wound edge was recorded overnight at a 5 min lapse interval using a 10× objective, and the images were acquired using Kinetic Imaging (Merseyside, UK) AQM software.

Cell tracking and statistical analysis of migration

Cell trajectories were acquired by manually tracking all the cells over the sequence of time-lapse digital images (Motion Analysis, Kinetic Imaging, Merseyside, UK). The data were used to calculate speed as distance in μm per 5 min and converted to μm per h. Another important aspect of the migration response is the persistence of motility that we measured for each cell as the ratio of the resultant displacement in 16 h over the sum of individual 5 min displacements (Figures 1A and B, and 8). Comparisons between different groups of experiments were made by applying ANOVA to the persistence data. We used ANOVA with a hierarchical and unbalanced model that allows more general testing between treatment groups, and takes into account possible variations between experiments and among different cells in our recordings.

Immunocytochemical staining and confocal microscopy

Immunocytochemical staining was performed as described elsewhere (Kiley and Parker, 1997) except for the following modifications. Cells were permeabilized with 0.2% (v/v) Triton X-100/phosphate-buffered saline (PBS) following fixation in 4% (w/v) paraformaldehyde, with the exception of the slides processed for the GFP–PKCα/VSVG–ezrin association study by FLIM, which were fixed in methanol for 4 min at −20°C, due to the Triton X-100 extractability of some of the ezrin constructs. Cells processed for the determination of ERM C-terminal threonine phosphorylation were first fixed in 10% ice-cold trichloroacetic acid (TCA) as described (Matsui *et al.*, 1998). Primary antibodies were diluted 1:200 in PBS containing 1% BSA, except for the fluorophore-conjugated antibodies that were used at 1:20–1:50. The Cy5-labelled anti-rat conjugate was obtained from Jackson ImmunoResearch Laboratories. Confocal images were acquired on a confocal laser scanning microscope (model LSM 510, Carl Zeiss Inc.) equipped with both 40×/1.3Plan-Neofluar and 63×/1.4Plan-Apochromat oil immersion objectives. Each image represents a two-dimensional projection of 2–3 slices in the Z-series, taken across the mid-depth of the cell at 0.2 μm intervals.

FRET determination by FLIM measurements

A detailed description of the FLIM apparatus used for FRET determination in this work can be found elsewhere (Squire and Bastiaens, 1999). The lifetime instrument performs phase- and modulation-based imaging fluorimetry by microscopy. All images were taken using a Zeiss Plan-Apochromat 100×/1.4NA phase 3 oil objective and the homodyne phase-sensitive images recorded at a modulation frequency of 80.224 MHz. The donor (GFP–PKCα) was excited using the 488 nm line of an argon–krypton laser and the resultant fluorescence separated using a combination of dichroic beamsplitter (Q 505 LP; Chroma Technology Corp.) and narrow band emitter filter (BP514/10; Lys and Optik). Acceptor images (Cy3-conjugated IgG or Fabs) were recorded using a 100 W mercury arc lamp (Zeiss Attoarc) as a source of sample illumination combined with a high Q Cy3 filter set (exciter: HQ 535/50, dichroic: Q 565 LP, emitter: HQ 610/75 LP; Chroma Technology Corp.). Global analysis was performed to calculate the precise fraction of donor molecules that have a reduced lifetime due to FRET (i.e. the fraction of GFP–PKCα RD + V3 bound to ezrin) as described (Verveer *et al.*, 2000a,b).

Cellular fractionation by sucrose gradient centrifugation

GFP–PKCα-transfected MCF-7 cells were scraped from plates, washed and homogenized using a cell cracker in 0.25 M sucrose, 10 mM HEPES–KOH pH 7.2 containing 1 mM EDTA and 1 mM magnesium acetate. The post-nuclear supernatant was loaded onto a velocity gradient as described (Dittie *et al.*, 1997). PKCα and β1 integrin were enriched in VG fractions 2 and 3 (T.Ng and P.J.Parker, unpublished data). EG fractions were subsequently prepared from these VG fractions as described (Dittie *et al.*, 1997). Proteins were precipitated from these fractions in 10% TCA overnight, washed with ethanol/acetone (50/50), then denatured in Laemmli's sample buffer, separated on an 8% polyacrylamide gel under reducing conditions and transferred electrophoretically to a polyvinylidene difluoride (PVDF) membrane. Incubation with primary antibodies was performed overnight at 4°C. Detection was with enhanced chemiluminescence (ECL; Amersham) according to recommended procedures.

Immunoprecipitation and western blotting

GFP-tagged or endogenous PKCα was immunoprecipitated from whole-cell lysates (each derived from an 80% confluent cell monolayer in a 15 cm round tissue culture dish, pre-treated with 1 μM PDBu for 20 min) using 10–20 μg of protein G-coupled MC5 as described previously (Kanner *et al.*, 1989), except that 1% (w/v) *n*-octyl β-D-glucopyranoside was used instead of NP-40. The samples were separated on large 8% resolving polyacrylamide gels. Blots were then probed with a rabbit IgG that recognizes anti-CPERM (in 0.1% TBS-Tween containing 3% BSA) followed by an anti-rabbit-horseradish peroxidase (HRP) conjugate (Amersham). The same membrane was stripped and reprobed (according to procedures recommended by Amersham) with an affinity-purified rabbit anti-ezrin IgG, then subsequently with an anti-PKCα C-terminal polyclonal serum. Incubation with primary antibodies was performed overnight at 4°C. Detection was with ECL according to recommended procedures.

Immunogold electron microscopy

Cells were scraped carefully and fixed in 4% paraformaldehyde for 1 h, before being processed for routine sectioning on a Leica ultra-cryotome for immunolabelling. Single and double labelling was carried out as described previously (Slot and Geuze, 1985). In the double labelling, the first antibody used was an affinity-purified rabbit polyclonal anti-ezrin IgG (cross-adsorbed against moesin and radixin) recognized by 10 nm PAG; this was followed, after an additional glutaraldehyde fixation step (1% monomeric glutaraldehyde for 5 min to cross-link the primary antibody), by a rabbit anti-GFP antiserum (a kind gift of D.Shima, ICRF) detected with 5 nm PAG. In some studies, the second antibody was omitted to control for cross-reactivity of the 5 nm PAG with the first antibody. After antibody labelling, sections were examined using a Jeol 1010 microscope.

In vitro kinase assays with recombinant or PKCα-co-precipitated endogenous ezrin

The potential phosphorylation of GST-tagged full-length ezrin by PKCα was examined in an *in vitro* ^{32}P incorporation assay where 5 μl (0.27 μg) of human recombinant PKCα (PanVera Corporation) were put in a 35 μl reaction buffer containing 5 μl (1.7 μg) of GST–ezrin, 5 μl (0.8 mM) of ATP containing 1 μCi of [^{32}P]ATP (255 c.p.m./pmol), 5 μl each of $MgCl_2$ (0.1 M) and $CaCl_2$ (6 mM), 10 μl of a pure lipid sonicated suspension of 50 μg of phosphatidylserine, 5 μg of phosphatidylinositol 4,5-bis-

phosphate and 0.05 μg of TPA in 0.2 M HEPES pH 7.5/2 mM EGTA. The control reaction was carried out in the absence of lipids/TPA. The *in vitro* phosphorylation reactions were incubated at 30°C and stopped after various time points by adding 40 μl of modified Laemmli's sample buffer (containing final concentrations of 2% SDS, 4 M urea and 10 mM EDTA). The samples were then separated on an 8% polyacrylamide gel and the phosphorylated proteins were detected by autoradiography. The *in vitro* phosphorylation assay was also performed with protein G–agarose bead-bound, PKCα-co-precipitated endogenous ERM (see the legend of Figure 7B for experimental details).

Acknowledgements

We wish to thank Dr Gipi Schiavo and Professor Ian Hart (ICRF) for their valuable comments. 2C4 fibrosarcoma cells stably expressing GFP–PKCα (GFP–PKCα-2C4) or GFP control vector were kindly provided by B.Lillemeier. We also thank Professor Clare Isacke (Imperial College, London) and Professor Paul Mangeat (Universite Montpellier II, Montpellier) for kindly providing the GST-tagged ezrin plasmid and crude sera against radixin and moesin, respectively. We thank Christine T.Quang for many helpful discussions. This study was supported by the Imperial Cancer Research Fund (UK) and the UK Medical Research Council (in the form of a Clinician Scientist Grant awarded to T.N.).

References

Algrain,M., Turunen,O., Vaheri,A., Louvard,D. and Arpin,M. (1993) Ezrin contains cytoskeleton and membrane binding domains accounting for its proposed role as a membrane–cytoskeletal linker. *J. Cell Biol.*, **120**, 129–139.

Arber,S., Barbayannis,F.A., Hanser,H., Schneider,C., Stanyon,C.A., Bernard,O. and Caroni,P. (1998) Regulation of actin dynamics through phosphorylation of cofilin by LIM-kinase. *Nature*, **393**, 805–809.

Bae,Y.S., Cantley,L.G., Chen,C.S., Kim,S.R., Kwon,K.S. and Rhee,S.G. (1998) Activation of phospholipase C-γ by phosphatidylinositol 3,4,5-trisphosphate. *J. Biol. Chem.*, **273**, 4465–4469.

Bastiaens,P.I.H. and Jovin,T.M. (1998) Fluorescence resonance energy transfer microscopy. In Celis,J. (ed.), *Cell Biology: A Laboratory Handbook*. Academic Press, New York, NY, pp. 136–146.

Berrier,A.L., Mastrangelo,A.M., Downward,J., Ginsberg,M. and LaFlamme,S.E. (2000) Activated R-Ras, Rac1, PI 3-kinase and PKCε can each restore cell spreading inhibited by isolated integrin β1 cytoplasmic domains. *J. Cell Biol.*, **151**, 1549–1560.

Bretscher,A., Chambers,D., Nguyen,R. and Reczek,D. (2000) ERM-Merlin and EBP50 protein families in plasma membrane organization and function. *Annu. Rev. Cell Dev. Biol.*, **16**, 113–143.

Bruns,R.F., Miller,F.D., Merriman,R.L., Howbert,J.J., Heath,W.F., Kobayashi,E., Takahashi,I., Tamaoki,T. and Nakano,H. (1991) Inhibition of protein kinase C by calphostin C is light-dependent. *Biochem. Biophys. Res. Commun.*, **176**, 288–293.

Buchanan,F.G., Elliot,C.M., Gibbs,M. and Exton,J.H. (2000) Translocation of the Rac1 guanine nucleotide exchange factor Tiam1 induced by platelet-derived growth factor and lysophosphatidic acid. *J. Biol. Chem.*, **275**, 9742–9748.

Cazaubon,S., Bornancin,F. and Parker,P.J. (1994) Threonine-497 is a critical site for permissive activation of protein kinase Cα. *Biochem. J.*, **301**, 443–448.

Crepaldi,T., Gautreau,A., Comoglio,P.M., Louvard,D. and Arpin,M. (1997) Ezrin is an effector of hepatocyte growth factor-mediated migration and morphogenesis in epithelial cells. *J. Cell Biol.*, **138**, 423–434.

Derman,M.P., Toker,A., Hartwig,J.H., Spokes,K., Falck,J.R., Chen,C.S., Cantley,L.C. and Cantley,L.G. (1997) The lipid products of phosphoinositide 3-kinase increase cell motility through protein kinase C. *J. Biol. Chem.*, **272**, 6465–6470.

Dittie,A.S., Thomas,L., Thomas,G. and Tooze,S.A. (1997) Interaction of furin in immature secretory granules from neuroendocrine cells with the AP-1 adaptor complex is modulated by casein kinase II phosphorylation. *EMBO J.*, **16**, 4859–4870.

Gautreau,A., Poullet,P., Louvard,D. and Arpin,M. (1999) Ezrin, a plasma membrane–microfilament linker, signals cell survival through the phosphatdiylinositol 3-kinase/Akt pathway. *Proc. Natl Acad. Sci. USA*, **96**, 7300–7305.

Gautreau,A., Louvard,D. and Arpin,M. (2000) Morphogenic effects of ezrin require a phosphorylation-induced transition from oligomers to monomers at the plasma membrane. *J. Cell Biol.*, **150**, 193–203.

Imamura,H., Takaishi,K., Nakano,K., Kodama,A., Oishi,H., Shiozaki,H., Monden,M., Sasaki,T. and Takai,Y. (1998) Rho and Rab small G proteins coordinately reorganize stress fibers and focal adhesions in MDCK cells. *Mol. Biol. Cell*, **9**, 2561–2575.

Ishizaki,T., Uehata,M., Tamechika,I., Keel,J., Nonomura,K., Maekawa,M. and Narumiya,S. (2000) Pharmacological properties of Y-27632, a specific inhibitor of rho-associated kinases. *Mol. Pharmacol.*, **57**, 976–983.

Kanner,S.B., Reynolds,A.B. and Parsons,J.T. (1989) Immunoaffinity purification of tyrosine-phosphorylated cellular proteins. *J. Immunol. Methods*, **120**, 115–124.

Kiley,S.C. and Parker,P.J. (1997) Defective microtubule reorganization in phorbol ester-resistant U937 variants: reconstitution of the normal cell phenotype with nocodazole treatment. *Cell Growth Differ.*, **8**, 231–242.

Kiley,S.C., Clark,K.J., Goodnough,M., Welch,D.R. and Jaken,S. (1999) Protein kinase Cδ involvement in mammary tumor cell metastasis. *Cancer Res.*, **59**, 3230–3238.

Lamb,R.F., Ozanne,B.W., Roy,C., McGarry,L., Stipp,C., Mangeat,P. and Jay,D.G. (1997) Essential functions of ezrin in maintenance of cell shape lamellipodial extension in normal and transformed fibroblasts. *Curr. Biol.*, **7**, 682–688.

Mangeat,P., Roy,C. and Martin,M. (1999) ERM proteins in cell adhesion and membrane dynamics. *Trends Cell Biol.*, **9**, 187–192.

Matsui,T., Maeda,M., Doi,Y., Yonemura,S., Amano,M., Kaibuchi,K. and Tsukita,S. (1998) Rho-kinase phosphorylates COOH-terminal threonines of ezrin/radixin/moesin (ERM) proteins and regulates their head-to-tail association. *J. Cell Biol.*, **140**, 647–657.

Matsui,T., Yonemura,S. and Tsukita,S. (1999) Activation of ERM proteins *in vivo* by Rho involves phosphatidylinositol 4-phosphate 5-kinase and not ROCK kinases. *Curr. Biol.*, **9**, 1259–1262.

Meng,F. and Lowell,C.A. (1998) A β1 integrin signaling pathway involving Src-family kinases, Cbl and PI-3 kinase is required for macrophage spreading and migration. *EMBO J.*, **17**, 4391–4403.

Nakamura,F., Huang,L., Pestonjamasp,K., Luna,E.J. and Furthmayr,H. (1999) Regulation of F-actin binding to platelet moesin *in vitro* by both phosphorylation of threonine 558 and polyphosphatidylinositides. *Mol. Biol. Cell*, **10**, 2669–2685.

Ng,T., Shima,D., Squire,A., Bastiaens,P.I.H., Gschmeissner,S., Humphries, M.J. and Parker,P.J. (1999a) PKCα regulates β1 integrin-dependent motility, through association and control of integrin traffic. *EMBO J.*, **18**, 3909–3923.

Ng,T. *et al.* (1999b) Imaging PKCα activation in cells. *Science*, **283**, 2085–2089.

Pearson,M.A., Reczek,D., Bretscher,A. and Karplus,P.A. (2000) Structure of the ERM protein moesin reveals the FERM domain fold masked by an extended actin binding tail domain. *Cell*, **101**, 259–270.

Pietromonaco,S.F., Simons,P.C., Altman,A. and Elias,L. (1998) Protein kinase C-θ phosphorylation of moesin in the actin-binding sequence. *J. Biol. Chem.*, **273**, 7594–7603.

Platet,N., Prevostel,C., Derocq,D., Joubert,D., Rochefort,H. and Garcia,M. (1998) Breast cancer cell invasiveness: correlation with protein kinase C activity and differential regulation by phorbol ester in estrogen receptor-positive and -negative cells. *Int. J. Cancer*, **75**, 750–756.

Shaw,L.M., Rabinovitz,I., Wang,H.H.F., Toker,A. and Mercurio,A.M. (1997) Activation of phosphoinositide 3-OH kinase by the α6β4 integrin promotes carcinoma invasion. *Cell*, **91**, 949–960.

Slot,J.W. and Geuze,H.J. (1985) A new method of preparing gold probes for multiple-labeling cytochemistry. *Eur. J. Cell Biol.*, **38**, 87–93.

Squire,A. and Bastiaens,P.I. (1999) Three dimensional image restoration in fluorescence lifetime imaging microscopy. *J. Microsc.*, **193**, 36–49.

Steiner,B. *et al.* (1990) Phosphorylation of microtubule-associated protein tau: identification of the site for Ca^{2+}-calmodulin dependent kinase and relationship with tau phosphorylation in Alzheimer tangles. *EMBO J.*, **9**, 3539–3544.

Sun,X.G. and Rotenberg,S.A. (1999) Overexpression of protein kinase C α in MCF-10A human breast cells engenders dramatic alterations in morphology, proliferation and motility. *Cell Growth Differ.*, **10**, 342–352.

Surtees,G. (1964) Laboratory studies on dispersion behaviour of adult beetles in grain. VIII Spontaneous activity in three species and a new approach to analysis of kinetic mechanism. *Anim. Behav.*, **12**, 374.

Tang,S., Morgan,K.G., Parker,C. and Ware,J.A. (1997) Requirement for

protein kinase C θ for cell cycle progression and formation of actin stress fibers and filopodia in vascular endothelial cells. *J. Biol. Chem.*, **272**, 28704–28711.

Tran Quang,C., Gautreau,A., Arpin,M. and Treisman,R. (2000) Ezrin function is required for ROCK-mediated fibroblast transformation by the Net and Dbl oncogenes. *EMBO J.*, **19**, 4565–4576.

Tsukita,S. and Yonemura,S. (1999) Cortical actin organization: lessons from ERM (ezrin/radixin/moesin) proteins. *J. Biol. Chem.*, **274**, 34507–34510.

Vanhaesebroeck,B., Jones,G.E., Allen,W.E., Zicha,D., Hooshmand-Rad,R., Sawyer,C., Wells,C., Waterfield,M.D. and Ridley,A.J. (1999) Distinct PI(3)Ks mediate mitogenic signalling and cell migration in macrophages. *Nature Cell Biol.*, **1**, 69–71.

Verveer,P.J., Squire,A. and Bastiaens,P.I. (2000a) Global analysis of fluorescence lifetime imaging microscopy data. *Biophys. J.*, **78**, 2127–2137.

Verveer,P.J., Wouters,F.S., Reynolds,A.R. and Bastiaens,P.I. (2000b) Quantitative imaging of lateral ErbB1 receptor signal propagation in the plasma membrane. *Science*, **290**, 1567–1570.

Vicente-Manzanares,M. *et al.* (1999) Involvement of phosphatidyl-inositol 3-kinase in stromal cell-derived factor-1-α-induced lymphocyte polarization and chemotaxis. *J. Immunol.*, **163**, 4001–4012.

Wallis,S., Lloyd,S., Wise,I., Ireland,G., Fleming,T.P. and Garrod,D. (2000) The α isoform of protein kinase C is involved in signaling the response of desmosomes to wounding in cultured epithelial cells. *Mol. Biol. Cell*, **11**, 1077–1092.

Wang,M.H., Montero-Julian,F.A., Dauny,I. and Leonard,E.J. (1996) Requirement of phosphatidylinositol-3 kinase for epithelial cell migration activated by human macrophage stimulating protein. *Oncogene*, **13**, 2167–2175.

Young,S., Rothbard,J. and Parker,P.J. (1988) A monoclonal antibody recognising the site of limited proteolysis of protein kinase C. Inhibition of down-regulation *in vivo*. *Eur. J. Biochem.*, **173**, 247–252.

Zigmond,S.H. (1996) Signal transduction and actin filament organization. *Curr. Opin. Cell Biol.*, **8**, 66–73.

Received November 30, 2000; revised and accepted April 5, 2001